



**HAL**  
open science

# Yttrium-90 quantification using SiPM PET and Monte Carlo simulations for radioembolisation monitoring

Joey Labour

► **To cite this version:**

Joey Labour. Yttrium-90 quantification using SiPM PET and Monte Carlo simulations for radioembolisation monitoring. Medical Imaging. Université de Lyon, 2021. English. NNT : 2021LYSEI054 . tel-03552477

**HAL Id: tel-03552477**

**<https://theses.hal.science/tel-03552477v1>**

Submitted on 2 Feb 2022

**HAL** is a multi-disciplinary open access archive for the deposit and dissemination of scientific research documents, whether they are published or not. The documents may come from teaching and research institutions in France or abroad, or from public or private research centers.

L'archive ouverte pluridisciplinaire **HAL**, est destinée au dépôt et à la diffusion de documents scientifiques de niveau recherche, publiés ou non, émanant des établissements d'enseignement et de recherche français ou étrangers, des laboratoires publics ou privés.



N°d'ordre NNT : 2021LYSEI054

**THESE de DOCTORAT DE L'UNIVERSITE DE LYON**  
opérée au sein de  
**Institut National des Sciences Appliquées, INSA - Lyon**

**Ecole Doctorale N° 160**  
**(ÉLECTRONIQUE, ÉLECTROTECHNIQUE, AUTOMATIQUE)**

**Spécialité/ discipline de doctorat :**  
Traitement du Signal et de l'Image

Soutenue publiquement le 21/09/2021, par :  
**Joey Labour**

---

**Yttrium-90 quantification using SiPM PET and Monte Carlo simulations for radioembolisation monitoring**

---

Devant le jury composé de :

Christian, Morel	Professeur des Universités/Directeur de recherche, Aix-Marseille Université, CPPM, Marseille	Président
Yuni, Dewaraja	Professeure des Universités, University of Michigan, Ann Arbor	Rapporteure
Etienne, Garin	Professeur des Universités/Médecin Nucléaire, Université de Rennes, Centre Eugène Marquis, Rennes	Rapporteur
Emilie, Roncali	Directrice de recherche, University of California Davis, Davis	Examinatrice
Arnaud, Dieudonné	Physicien Médical, Centre Henri Becquerel, Rouen	Examineur
David, Sarrut	Directeur de recherche, CNRS, Lyon	Directeur de thèse
Jean-Noël, Badel	Physicien Médical, Centre Léon Bérard, Lyon	Co-directeur de thèse
Sandrine, Parisse-Di Martino	Médecin Nucléaire, Centre Léon Bérard, Lyon	Invitée



## Département FEDORA – INSA Lyon - Ecoles Doctorales

SIGLE	ECOLE DOCTORALE	NOM ET COORDONNEES DU RESPONSABLE
<b>CHIMIE</b>	<b><u>CHIMIE DE LYON</u></b> <a href="https://www.edchimie-lyon.fr">https://www.edchimie-lyon.fr</a> Sec. : Renée EL MELHEM Bât. Blaise PASCAL, 3e étage secretariat@edchimie-lyon.fr	<b>M. Stéphane DANIELE</b> C2P2-CPE LYON-UMR 5265 Bâtiment F308, BP 2077 43 Boulevard du 11 novembre 1918 69616 Villeurbanne <a href="mailto:directeur@edchimie-lyon.fr">directeur@edchimie-lyon.fr</a>
<b>E.E.A.</b>	<b><u>ÉLECTRONIQUE, ÉLECTROTECHNIQUE, AUTOMATIQUE</u></b> <a href="https://edeea.universite-lyon.fr">https://edeea.universite-lyon.fr</a> Sec. : Stéphanie CAUVIN Bâtiment Direction INSA Lyon Tél : 04.72.43.71.70 secretariat.edeea@insa-lyon.fr	<b>M. Philippe DELACHARTRE</b> INSA LYON Laboratoire CREATIS Bâtiment Blaise Pascal, 7 avenue Jean Capelle 69621 Villeurbanne CEDEX Tél : 04.72.43.88.63 <a href="mailto:philippe.delachartre@insa-lyon.fr">philippe.delachartre@insa-lyon.fr</a>
<b>E2M2</b>	<b><u>ÉVOLUTION, ÉCOSYSTÈME, MICROBIOLOGIE, MODÉLISATION</u></b> <a href="http://e2m2.universite-lyon.fr">http://e2m2.universite-lyon.fr</a> Sec. : Sylvie ROBERJOT Bât. Atrium, UCB Lyon 1 Tél : 04.72.44.83.62 secretariat.e2m2@univ-lyon1.fr	<b>M. Philippe NORMAND</b> Université Claude Bernard Lyon 1 UMR 5557 Lab. d'Ecologie Microbienne Bâtiment Mendel 43, boulevard du 11 Novembre 1918 69 622 Villeurbanne CEDEX <a href="mailto:philippe.normand@univ-lyon1.fr">philippe.normand@univ-lyon1.fr</a>
<b>EDISS</b>	<b><u>INTERDISCIPLINAIRE SCIENCES-SANTÉ</u></b> <a href="http://ediss.universite-lyon.fr">http://ediss.universite-lyon.fr</a> Sec. : Sylvie ROBERJOT Bât. Atrium, UCB Lyon 1 Tél : 04.72.44.83.62 secretariat.ediss@univ-lyon1.fr	<b>Mme Sylvie RICARD-BLUM</b> Institut de Chimie et Biochimie Moléculaires et Supramoléculaires (ICBMS) - UMR 5246 CNRS - Université Lyon 1 Bâtiment Raulin - 2ème étage Nord 43 Boulevard du 11 novembre 1918 69622 Villeurbanne Cedex Tél : +33(0)4 72 44 82 32 <a href="mailto:sylvie.ricard-blum@univ-lyon1.fr">sylvie.ricard-blum@univ-lyon1.fr</a>
<b>INFOMATHS</b>	<b><u>INFORMATIQUE ET MATHÉMATIQUES</u></b> <a href="http://edinfomaths.universite-lyon.fr">http://edinfomaths.universite-lyon.fr</a> Sec. : Renée EL MELHEM Bât. Blaise PASCAL, 3e étage Tél : 04.72.43.80.46 infomaths@univ-lyon1.fr	<b>M. Hamamache KHEDDOUCI</b> Université Claude Bernard Lyon 1 Bât. Nautibus 43, Boulevard du 11 novembre 1918 69 622 Villeurbanne Cedex France Tél : 04.72.44.83.69 <a href="mailto:hamamache.kheddouci@univ-lyon1.fr">hamamache.kheddouci@univ-lyon1.fr</a>
<b>Matériaux</b>	<b><u>MATÉRIAUX DE LYON</u></b> <a href="http://ed34.universite-lyon.fr">http://ed34.universite-lyon.fr</a> Sec. : Yann DE ORDENANA Tél : 04.72.18.62.44 yann.de-ordenana@ec-lyon.fr	<b>M. Stéphane BENAYOUN</b> Ecole Centrale de Lyon Laboratoire LTDS 36 avenue Guy de Collongue 69134 Ecully CEDEX Tél : 04.72.18.64.37 <a href="mailto:stephane.benayoun@ec-lyon.fr">stephane.benayoun@ec-lyon.fr</a>
<b>MEGA</b>	<b><u>MÉCANIQUE, ÉNERGÉTIQUE, GÉNIE CIVIL, ACOUSTIQUE</u></b> <a href="http://edmega.universite-lyon.fr">http://edmega.universite-lyon.fr</a> Sec. : Stéphanie CAUVIN Tél : 04.72.43.71.70 Bâtiment Direction INSA Lyon mega@insa-lyon.fr	<b>M. Jocelyn BONJOUR</b> INSA Lyon Laboratoire CETHIL Bâtiment Sadi-Carnot 9, rue de la Physique 69621 Villeurbanne CEDEX <a href="mailto:jocelyn.bonjour@insa-lyon.fr">jocelyn.bonjour@insa-lyon.fr</a>
<b>ScSo</b>	<b><u>ScSo*</u></b> <a href="https://edsciencessociales.universite-lyon.fr">https://edsciencessociales.universite-lyon.fr</a> Sec. : Mélina FAVETON INSA : J.Y. TOUSSAINT Tél : 04.78.69.77.79 melina.faveton@univ-lyon2.fr	<b>M. Christian MONTES</b> Université Lumière Lyon 2 86 Rue Pasteur 69365 Lyon CEDEX 07 <a href="mailto:christian.montes@univ-lyon2.fr">christian.montes@univ-lyon2.fr</a>

\*ScSo : Histoire, Géographie, Aménagement, Urbanisme, Archéologie, Science politique, Sociologie, Anthropologie



# Abstract

Selective internal radiation therapy (SIRT) or radioembolisation using Yttrium-90 ( $^{90}\text{Y}$ ) microspheres is a treatment for unresectable hepatic malignancies and metastases that can be monitored with positron emission tomography (PET) imaging. PET is today the most sensitive functional imaging modality for studying molecular interactions in the human body. This monitoring is of prime importance for patient safety and to move towards personalised dosimetry. However, during  $^{90}\text{Y}$  decay, only few  $\beta^+$  particles are emitted (around 32 positrons per million decays), which makes quantitative PET imaging challenging. State-of-the-art PET systems are equipped with silicon photomultipliers (SiPMs) replacing conventional photomultiplier tubes (PMTs), thus allowing an overall improvement in performance and in particular in the time-of-flight (TOF) resolution.

The objective of this thesis was twofold. First to develop and validate a Monte Carlo model of the Vereos PET SiPM system. Second, to investigate  $^{90}\text{Y}$  PET quantitative imaging for  $^{90}\text{Y}$  microspheres treatment monitoring. The proposed model of the Vereos PET was developed with the GATE platform and validated against experimental data following NEMA standardised protocols. The model can support a number of future projects, in particular to optimise imaging performance, evaluate new reconstruction and correction methods, among others. The second contribution focused on the evaluation of reconstruction parameters on the quantitative accuracy in  $^{90}\text{Y}$  dosimetry and investigate on the gain over the acquisition time provided by the Vereos PET/CT. To that aim, experiments using phantoms were carried out and parameters were varied to estimate their influence on absorbed dose distributions. Here, contrary to previous works, the whole evaluation was performed with absorbed dose (in Gy) via dose-volume histograms (DVHs) instead of activity (in MBq). The results have finally been applied to the clinical settings in our institution. A third contribution provides a preliminary assessment of the predictive value of the  $^{99m}\text{Tc}$ -macro-aggregated albumin (MAA) surrogate particles to  $^{90}\text{Y}$ -microspheres used in treatment planning. Consistent approaches were suggested for image registration between pre-treatment single photon emission computed tomography (SPECT)/CT and per-treatment PET/CT, using patient datasets from the Léon Bérard cancer research center (CLB) where  $^{90}\text{Y}$ -radioembolisation therapy is regularly performed.



# Résumé

La radiothérapie interne sélective (SIRT), connue également sous le terme de radioembolisation, par microsphères d'Yttrium-90 ( $^{90}\text{Y}$ ) est un traitement des tumeurs malignes et métastases hépatiques non résecables qui peut être suivi par la tomographie par émission de positons (TEP). La TEP est aujourd'hui la modalité d'imagerie fonctionnelle la plus sensible pour étudier les interactions moléculaires dans le corps humain. Ce suivi est de première importance pour la sécurité des patients et pour évoluer vers une dosimétrie personnalisée. Cependant, lors de la désintégration de  $^{90}\text{Y}$ , seules quelques particules  $\beta^+$  sont émises (environ 32 positons par million de désintégrations), ce qui rend la quantification à partir d'une image TEP délicate. Les systèmes TEP les plus modernes sont cependant équipés de photomultiplicateurs au silicium (SiPMs) qui remplacent les tubes photomultiplicateurs (PMTs) conventionnels, ce qui permet une amélioration globale des performances et en particulier de la résolution du temps-de-vol (TOF).

L'objectif de cette thèse était double : d'une part, développer et valider un modèle Monte Carlo du système TEP Vereos, qui est équipé de SiPM, et d'autre part, étudier l'apport de l'imagerie TEP à  $^{90}\text{Y}$  pour le suivi du traitement par microsphères d' $^{90}\text{Y}$ , en contexte clinique. La première contribution de cette thèse a donc été le développement d'un modèle de simulation GATE du système TEP Vereos qui a été évalué par rapport aux données expérimentales suivant les protocoles standardisés du NEMA. Le modèle peut être utilisé pour un certain nombre de projets futurs, notamment pour optimiser les performances d'imagerie, ou encore évaluer de nouvelles méthodes de reconstruction et de correction. La deuxième contribution s'est concentrée sur l'évaluation des paramètres de reconstruction sur la précision quantitative de la dosimétrie à  $^{90}\text{Y}$  et sur l'étude du gain sur le temps d'acquisition apporté par le Vereos TEP/TDM. Des expérimentations utilisant des fantômes ont été réalisées et les paramètres de reconstructions ont été variés pour évaluer leur influence sur les distributions de dose absorbée. Une troisième contribution propose une évaluation préliminaire de la valeur prédictive des particules de macroagrégats d'albumine ( $^{99m}\text{Tc-MAA}$ ), utilisées dans la planification du traitement par radioembolisation en substitution aux microsphères d' $^{90}\text{Y}$ . Des approches cohérentes ont été proposées pour le recalage d'images avec la tomographie par émission monophotoniques (TEMP)/TDM, en utilisant des ensembles de données de patients du Centre de lutte contre le cancer Léon Bérard (CLB), où la thérapie par radioembolisation à  $^{90}\text{Y}$  est régulièrement effectuée.





### ***Ti poem melodi***

*Si pa ti enan twa, parol ti pou rezonn fos. Patriotis to pios. Disan ek la swer ki koulé, ekrire tou paz nou lavenir. **Sa mem inn vinn nou rev, ti obliz nou avanse.***

*Si pa ti enan twa, kouma karay ti pou kriyé. La koz to tras trasé. To pa inn res lebra krwazé, enn ti roupi to inn gagné, pou enn bousé manzé, pou to fami prosperé.*

*Lakoz énan twa, zot dir nou leker dan la main. Plis solidarité. Travay volonter, drwa imain, pénan traka, pénan voler, dormi laport ouvert, met tou dan la main Bondié.*

*Pou zot saki zoli, fer nou leker flote dan lekstaz. Ti poem melodi. Enn tablo top kouler pei, Zistwar depi nou leritaz. Kadans balans lérein, nou sant ansam nou refrain.*

*Parol bers nou lespri, zarden dedenn dan paradi. **Enn tipa nunn grandi.** Bondié akonpagn nou simen, pa tombé, nek trap mo lamén. Pa kil lespri sen, persevere, pans demen*

*Se pou sa, kan nou guetté partout vert, la mer li blé, disab blan doré, le ciel pénan niaz, la briz dan feyaz.*

*Se pou sa, kan nou guetté, mem aswar, mille zétwal apé brillé, pou fer maréntwar rekilé, pénan mirak, pénan mazik. **Fodré énan tou, pou fer enn sel.***

***Persevere, pans demen.***



# Remerciements

Mo rémercié David Sarrut pou so lencadrement san fay, san ki mo pa ti pou ressi. Mo rémercié Jean-Noël Badel pou so lencadrement ek banne diskisyon. Merci pou tou moyen ki zot inn met en plas pou mo ressi fini sa travay la. Merci pu zot conseil. Mo rémercié oussi Nicolas Rossetto pou tou laide ki linn fourni mwan. Mo exprim mo gratitud pou tou dimoune ki monn cotoyé dan travay, Aurélien, Antoine, Ferial, Mélanie, Pierre-Antoine, Madalina, Laure, Francesca, Olga, Ahmad, Jean Michel, Simon, Nils, Sandrine, Fouzi, Pascale ek tou lezot kinn contribié dan enn sans ou enn lot. Pou Ane avek ki nou inn partaz mem biro ek bann bon momen, ek Thomas kinn aide mwan boukou dan réalizasyon sa travay la. Saken dant zot inn ran sa laventir la bien pli incroyab. Mo rémercié tou membre mo jury kinn accepté lir mo manuscrit, kinn pose mwan boukou kestion interessan ek inn permet mwan vive enn soutenance rempli ek émotion.

Sa trwa lannin la inn passe bien vite, ek monn ressi réaliz enn dé mo bann rev. Enn gran létap pou mwan ki mo ti touzour envi réaliser. Ek zordi mo p ressi fer momem sa cado la. Zordi mo pense Mam ek Pap ek mo senti zot la zoie, mo trouv zot boner ek zot émerveymen. Ek dan mo leker, enn kantité papiyon envoler ek toussala renforce mo pilyer pou mo ale pli lwin. Sa trwa lannin la pa ti facile, inn deman mwan boukou sacrifice lwin ek mo fami, mo sœur, mo bann bon camarad. Lwin ek mo pays. Mais mo inn ressi arriv kot mo ti p envi arrivé.

Mo bisin dir tou dimoune kinn encouraz mwan dan mo lavi en dehor travay merci. Merci parski letour mwan, enan enn kantité dimoune ki crwar dan mwan. Mo rémercié Catheline ek Milaine, mo penan mot pou exprime zot mo sentiment. Mo pa pou enan assé reconnaissance pou tou sa bann maman kinn la pou mwan tout long mo lavi ziska aster. Zot mem mo la force.

Mo pa pou bliyer tou mo bann camarad dan Rodrigues ek la France kinn aide mwan sirmonte bann éprev. Mo pa pou bliyer Henri, Adama ek Véronique dan sa réalisation la. Finalement, mo dir merci Alexis, kinn guet dan mo direksyon ansam avek moi, ek kinn apport mwan so lamitié ek sipor ki mo ti bizin tout long sa parcour la. San twa oussi, mo pa ti pou ressi. Merci Mam, Pap ek Cloey pou zot l'amour ek sippport incondisyonel.



# Contents

<b>Abstract</b>	<b>v</b>
<b>Résumé</b>	<b>vii</b>
<b>Remerciements</b>	<b>xi</b>
<b>Acronyms</b>	<b>xxvii</b>
<b>Introduction</b>	<b>1</b>
<b>I State of the art</b>	<b>3</b>
<b>1 Clinical context</b>	<b>5</b>
1.1 Liver cancer . . . . .	5
1.1.1 Statistics . . . . .	5
1.1.2 Treatment overview . . . . .	7
1.2 Radioembolisation rationale . . . . .	8
1.2.1 Microspheres properties . . . . .	8
1.2.2 Vascular considerations in radioembolisation . . . . .	8
1.3 $^{90}\text{Y}$ -radioembolisation . . . . .	11
1.3.1 Part I: $^{99m}\text{Tc}$ -MAA pre-treatment simulation step . . . . .	12
1.3.2 Part II: $^{90}\text{Y}$ -radioembolisation treatment step . . . . .	15
1.4 $^{90}\text{Y}$ activity planning . . . . .	16
1.4.1 Image-based metrics . . . . .	16
1.4.2 Glass microspheres . . . . .	18
1.4.3 Resin microspheres . . . . .	19
1.5 Radionuclide alternatives to $^{90}\text{Y}$ for radioembolisation . . . . .	20
1.6 Dosimetry calculations in internal radiotherapy . . . . .	21
1.6.1 Definitions . . . . .	21
1.6.2 Monte Carlo approach . . . . .	22
1.6.3 The MIRD schema for absorbed dose calculation . . . . .	23
1.6.4 Voxel <i>S-values</i> convolution approach . . . . .	26
1.6.5 Local deposition method approach . . . . .	27
1.6.6 Dose point kernel approach . . . . .	27
1.6.7 Clinical softwares for absorbed dose calculation . . . . .	30
1.7 Limitations and perspectives . . . . .	30
1.8 Conclusion . . . . .	33
<b>2 Positron emission tomography</b>	<b>35</b>
2.1 Radionuclides used in PET . . . . .	36
2.2 Beta-plus ( $\beta^+$ ) decay . . . . .	36
2.2.1 Positron emission . . . . .	36
2.2.2 Positron mean free path . . . . .	38

2.2.3	Annihilation effect . . . . .	39
2.2.4	$2-\gamma$ s non-collinearity . . . . .	40
2.3	0.511 MeV $\gamma$ interactions with matter . . . . .	41
2.4	Photon attenuation . . . . .	42
2.5	PET imaging principles . . . . .	42
2.5.1	Types of events for coincidence detection . . . . .	44
2.6	Sources of error contributing to PET spatial resolution . . . . .	45
2.6.1	Positron physics and $2-\gamma$ non-collinearity . . . . .	45
2.6.2	Detectors . . . . .	45
2.6.3	Depth of interaction . . . . .	45
2.6.4	Intercrystal Compton scattering and multiplexing . . . . .	45
2.6.5	Sampling and reconstruction algorithms . . . . .	46
2.6.6	Total spatial resolution . . . . .	46
2.6.7	Additional factors . . . . .	47
2.7	Time-of-flight PET . . . . .	47
2.7.1	Cerenkov light and TOF PET . . . . .	49
2.8	Scintillator crystals . . . . .	49
2.9	Operating principles of photodetectors . . . . .	51
2.9.1	Photomultiplier tubes (PMTs) . . . . .	51
2.9.2	Avalanche photodiodes (APDs) . . . . .	52
2.9.3	Silicon photomultipliers (SiPMs) . . . . .	53
2.10	Digital photon counting dSiPMs . . . . .	56
2.10.1	Architecture . . . . .	56
2.10.2	Data acquisition state machine . . . . .	57
2.10.3	Characteristics of the DPC SiPM . . . . .	58
2.11	Developments in PET detection . . . . .	59
2.11.1	Depth of interaction . . . . .	59
2.11.2	Ortho-positronium detection using JPET . . . . .	59
2.12	Performance of actual PET systems . . . . .	60
2.13	PET data acquisition and reconstruction . . . . .	62
2.13.1	Data acquisition . . . . .	62
2.13.2	Data format . . . . .	63
2.14	PET tomographic reconstruction . . . . .	65
2.14.1	Analytical reconstruction . . . . .	65
2.14.2	Iterative reconstruction . . . . .	68
<b>3</b>	<b>The physics of <math>^{90}\text{Y}</math> for PET imaging</b> . . . . .	<b>71</b>
3.1	$^{90}\text{Y}$ radiation physics . . . . .	71
3.1.1	Properties and decay scheme of $^{90}\text{Y}$ . . . . .	71
3.1.2	Internal pair production and its branching ratio . . . . .	71
3.2	Confounding factors in $^{90}\text{Y}$ PET imaging . . . . .	75
3.2.1	Low $\beta^+$ production . . . . .	75
3.2.2	Natural background radioactivity . . . . .	75
3.2.3	Bremsstrahlung radiation from $\beta^-$ radiation . . . . .	75
3.3	Other factors limiting quantification in PET . . . . .	77
3.4	Post-treatment radioembolisation monitoring . . . . .	77
3.4.1	$^{90}\text{Y}$ emission tomography imaging . . . . .	77
3.4.2	Imaging alternatives for $^{90}\text{Y}$ radioembolisation monitoring . . . . .	78
3.5	Conclusion . . . . .	78

<b>II</b>	<b>Contributions</b>	<b>79</b>
<b>4</b>	<b>Monte Carlo simulation of the DPC-PET</b>	<b>81</b>
4.1	Introduction . . . . .	81
4.2	Materials and methods . . . . .	82
4.2.1	The Vereos DPC-PET/CT . . . . .	82
4.2.2	PET scanner model in GATE . . . . .	83
4.2.3	Simulation physics parameters . . . . .	84
4.2.4	Photon detection and coincidence events . . . . .	84
4.2.5	Image reconstruction . . . . .	90
4.2.6	PET model validation . . . . .	91
4.3	Results . . . . .	96
4.3.1	Count rates, NECR and scatter fraction . . . . .	96
4.3.2	TOF and energy resolutions . . . . .	98
4.3.3	Sensitivity . . . . .	98
4.3.4	Intrinsic spatial resolution . . . . .	98
4.3.5	Image quality . . . . .	98
4.3.6	Monte Carlo statistical uncertainty . . . . .	101
4.4	Discussion . . . . .	103
4.5	Conclusion . . . . .	106
<b>5</b>	<b>Yttrium-90 quantitative study using DPC-PET</b>	<b>107</b>
5.1	Introduction . . . . .	107
5.2	Materials and methods . . . . .	109
5.2.1	Experimental setup . . . . .	109
5.2.2	Image acquisition . . . . .	111
5.2.3	Image reconstruction . . . . .	111
5.2.4	Absorbed dose computation . . . . .	112
5.2.5	Dosimetry-based figures of merit . . . . .	113
5.2.6	Clinical application . . . . .	114
5.3	Results . . . . .	115
5.3.1	Cylindrical phantoms Ph1 and Ph2 . . . . .	115
5.3.2	NEMA IEC body phantom Ph3 . . . . .	116
5.3.3	Clinical application . . . . .	122
5.4	Discussion . . . . .	124
5.5	Conclusion . . . . .	130
<b>6</b>	<b>Predictive and per-treatment image-based dosimetry</b>	<b>131</b>
6.1	Introduction . . . . .	131
6.2	Materials and methods . . . . .	133
6.2.1	Patient characteristics . . . . .	134
6.2.2	Imaging and reconstruction protocols . . . . .	134
6.2.3	Delineation of volumes of interest . . . . .	136
6.2.4	Absorbed dose calculation . . . . .	138
6.2.5	Exported input data . . . . .	138
6.2.6	Propagation of contours . . . . .	138
6.2.7	Analysis . . . . .	140
6.3	Results . . . . .	141
6.3.1	Comparison of registration methods. . . . .	142
6.3.2	Comparison of predictive and per-treatment dosimetries . . . . .	148
6.4	Discussion . . . . .	154



6.4.1	Comparisons . . . . .	154
6.4.2	Limitations . . . . .	157
6.4.3	Future directions . . . . .	158
6.5	Conclusion . . . . .	158
<b>Conclusions and perspectives</b>		<b>161</b>
<b>Résumé étendu</b>		<b>165</b>
<b>Appendices</b>		<b>203</b>
<b>A</b>	<b>Evaluation of reconstruction parameters using DVH</b>	<b>205</b>
A1	37 mm sphere . . . . .	205
A2	28 mm sphere . . . . .	207
A3	22 mm sphere . . . . .	208
A4	17 mm sphere . . . . .	209
A5	13 mm sphere . . . . .	210
A6	10 mm sphere . . . . .	211
<b>B</b>	<b>Evaluation of reconstruction parameters using RMSD</b>	<b>213</b>
<b>C</b>	<b>Influence of acquisition duration</b>	<b>215</b>
<b>D</b>	<b>Comparing pre- and per-treatment DVHs</b>	<b>217</b>
D1	Delineated volumes. . . . .	217
D2	Whole liver . . . . .	219
D3	Perfused liver . . . . .	221
D4	Activity distribution . . . . .	223
D5	Non-perfused liver . . . . .	226
D6	Total tumour . . . . .	228
D7	Target normal liver . . . . .	230
D8	Whole normal liver . . . . .	232
<b>Bibliography</b>		<b>235</b>

# List of Figures

1.1	Age-standardised rate (ASR) statistics on liver cancer in Europe from IARC/WHO <sup>2</sup> , all ages confounded showing male predominance. . . .	5
1.2	Primary liver cancer origin: HCC develop from the main liver cells (by malignant transformation of hepatocytes) and ICC develop from the small intrahepatic bile duct epithelium ( <i>Source: Cancer Research UK/Wikimedia Commons</i> ). . . . .	6
1.3	SIRT transarterial procedure. A branch of the hepatic artery feeding the tumour is selected where activity is administered by catheterisation ( <i>Source: Macmillan Cancer Support (UK)</i> ). . . . .	10
1.4	Comparison between particle sizes in TAE or TACE ( <i>right</i> ) and SIRT ( <i>left</i> ). <sup>90</sup> Y and <sup>166</sup> Ho microspheres of ~35 μm (gray colour) provide short range radiation to the tumour for SIRT, whilst larger beads provide an ischemia effect during TAE and eventually expose tumour cells to high concentrations of cytotoxic agents during TACE. Extracted from Sangro, Iñarrairaegui, and Bilbao (2012). . . . .	11
1.5	Hepatic angiography after arterial embolisation using a C-arm CBCT ( <i>Source: CBCT</i> ). . . . .	13
1.6	Anterior and posterior planar scintigraphy images of both lungs and the total liver following injection of <sup>99m</sup> Tc-MAA (pre-treatment) for a patient at the CLB. . . . .	14
1.7	Pre-treatment <sup>99m</sup> Tc-MAA imaging. <i>Top</i> : Anterior and posterior planar scintigraphy images of the total liver. <i>Bottom</i> : SPECT/CT images for the same patient. Extracted from Bilbao, Reiser, et al. (2008). . . . .	14
1.8	<sup>90</sup> Y-SIRT procedure at the CLB. <i>Top left</i> : Administration system for microspheres (TheraSphere™) and physicians placing the catheter to the selected hepatic artery in interventional radiology before microspheres injection. <i>Top right</i> : Performing angiography for catheterisation monitoring to the selected region to be perfused by the interventional radiologist. <i>Bottom left</i> : Injection procedure of microspheres to the patient by the nuclear physicist. <i>Bottom right</i> : Dosimeter for radioprotection control. . . . .	16
1.9	<i>Left</i> : Pre-treatment distribution of <sup>99m</sup> Tc-MAA using SPECT/CT. <i>Middle</i> : Post-SIRT distribution of <sup>90</sup> Y using SPECT/CT. <i>Right</i> : Post-SIRT distribution of <sup>90</sup> Y using PET/CT. Extracted from Bilbao, Reiser, et al. (2008). . . . .	17
1.10	Simple representations of a DPK. . . . .	28
1.11	Total DPKs for <sup>90</sup> Y using GATE (Papadimitroulas et al., 2012). . . . .	28
1.12	Sequence diagram of absorbed dose computation by means of DPK. Adapted from Peer-Firozjahi et al. (2021). . . . .	29

2.1	Errors related to the positron physics are depicted. 1. Range error ( <i>green</i> ) - the effective range considered is not the actual positron range (mean free path). 2. Non-collinearity error ( <i>orange</i> ) - back-to-back $\gamma$ s angular uncertainty. Extracted and adapted from Cherry, Sorenson, and Phelps (2012) . . . . .	38
2.2	The number of annihilations at a given radial distance (3D) from a point source for different $\beta^+$ emitters, normalised to the same value at the maximum. <i>Left</i> : Point sources in water for different isotopes used in PET. <i>Right</i> : Point sources for $^{18}\text{F}$ in different media. Extracted from Cal-González et al. (2013). . . . .	39
2.3	Comparison of positron range for different isotopes from different studies. <i>Top-left</i> : $^{11}\text{C}$ , <i>Top-right</i> : $^{13}\text{N}$ , <i>Bottom-left</i> : $^{68}\text{Ga}$ and <i>Bottom-right</i> : $^{82}\text{Rb}$ . Extracted from Cal-González et al. (2013). . . . .	40
2.4	<i>Left</i> : Most probable interactions of 0.511 MeV photons with varying $Z$ . <i>Right</i> : Example of mass attenuation coefficient for NaI(Tl) crystals. Human soft tissues and bones have an effective $Z$ around 7 and 14, respectively. Extracted from Cherry, Sorenson, and Phelps (2012) who themselves generated the graph using the <b>NIST Standard Reference Database</b> . . . . .	41
2.5	Simplified coincidence logic in PET imaging. LOR detection is limited by the reduced geometrical efficiency of the axial FOV. . . . .	43
2.6	From <i>left</i> to <i>right</i> : Illustration of <i>true</i> , <i>scatter</i> , <i>random</i> and <i>multiple</i> coincidences. . . . .	44
2.7	The sampling depends on the position in the FOV, especially near the center. Extracted from Moses (2011). . . . .	46
2.8	Contributions to the degradation of spatial resolution. Adapted from Moses (2011). . . . .	47
2.9	<i>Left</i> : Illustration of the Gaussian coincidence peak using TOF information, showing higher probability of interaction position. <i>Right</i> : Illustration of image quality based on TOF ( <i>bottom</i> ) and non-TOF ( <i>top</i> ) PET with decreasing (better) CTR. Figure adapted from the <b>10 ps challenge website</b> . . . . .	48
2.10	Principles of the PMT, the primary components being the photocathode followed by a series of electrodes which are the dynodes and an anode recuperating the amplified electron swarm. The overall structure is enclosed in a vacuum tube. The dynodes are progressively biased at higher voltages. Extracted from Cherry, Sorenson, and Phelps (2012) . . . . .	51
2.11	Principle of APD and SPAD operation. <i>Left</i> : Avalanche breakdown process in a reverse biased p-n junction. <i>Right</i> : I-V characteristics (Jiang, Chalich, and Deen, 2019). . . . .	53
2.12	Schematic representation of the sensing electronics based on aSiPMs (top) and dSiPMs (bottom). Extracted from (Jiang, Chalich, and Deen, 2019). . . . .	55
2.13	DPC-type sensor architecture. <i>Top, left to right</i> : Representation of a tile. 1 tile = 16 dice. 1 die = 4 pixels (Liu et al., 2016). <i>Bottom, left to right</i> : Representation of a die (Frach et al., 2010) and 1 pixel = 4 subpixels (coupled to one crystal). See <i>Haemisch Y. (Philips)</i> and Schaart et al. (2016). . . . .	56
2.14	State machine for DPC acquisition. Extracted from Schaart et al. (2016). 57	57

2.15	Differences between 2D and 3D PET acquisition modes. Direct ( <i>red</i> ) and oblique ( <i>blue</i> ) planes forming LORs. Oblique LORs ( <i>green</i> ) cannot be formed when using <i>septa</i> in 2D PET. All LORs are accepted in 3D PET. Adapted from Alessio, Kinahan, et al. (2006). . . . .	62
2.16	<i>Left</i> : The projection $p(x_r, \varphi)$ according to the line integral model obtained by the integration along parallel LORs, at an angle $\varphi$ ( <i>orange</i> ). The fixed tomograph reference frame $(x, y)$ ( <i>blue</i> ) and the rotating frame $(x_r, y_r)$ ( <i>green</i> ) which define the LORs are depicted. <i>Right</i> : <b>A</b> . Storage of coincidences data in a sinogram. Adapted from Wernick and Aarsvold (2004) and see lecture on medical physics. <b>B</b> . and <b>C</b> . are realistic representations of a 2D object consisting of several circular regions of different activities and the sinogram of the object, respectively (Etxebeste Barrena, 2017). . . . .	64
3.1	Radioactive decay scheme of the parent isotope $^{90}\text{Y}$ to the stable daughter isotope $^{90}\text{Zr}$ . $^{90}\text{Y}$ is considered a pure $\beta^-$ emitter ( $\beta_{00}^-$ , $\beta_{01}^-$ , $\beta_{02}^-$ transitions). A minor (rare) branch, $\beta_{01}^-$ of $^{90}\text{Y}$ in its disintegration goes to the first excited $0^+$ state of $^{90}\text{Zr}$ where the origin of the $\beta^+$ production can be explained following a rare monopole transition (E0) between the $0^+$ / $0^+$ states of $^{90}\text{Zr}$ resulting in internal pair creations. The $2^+$ excited state of $^{90}\text{Zr}$ is also depicted but the branching ratio for this transition to happen is negligible. Other excited states of $^{90}\text{Zr}$ exist, which are above the 2.28 MeV beta spectrum of $^{90}\text{Y}$ . Extracted from LNHB (France), Bé et al. (2006). . . . .	72
3.2	$\beta^-$ spectrum of $^{90}\text{Y}$ for all decay branches. Data downloaded from ICRP publications (Eckerman, 2008) for $^{90}\text{Y}$ . . . . .	73
3.3	$\beta^+$ spectrum from the monopole transition of $^{90}\text{Zr}$ . Extracted from Dryák and Šolc (2020). . . . .	74
3.4	Bremsstrahlung photon spectrum following emission of $\beta^-$ particles during $^{90}\text{Y}$ disintegration. <i>Top</i> : Total bremsstrahlung spectra extracted from Stabin et al. (1994). <i>Bottom</i> : The 511 keV annihilation photon peak embedded in the background bremsstrahlung photons around the 511 keV energy extracted from Dryák and Šolc (2020). . . . .	76
4.1	The Vereos DPC dSiPM-based TOF-PET/CT from Philips installed at the CLB. . . . .	83
4.2	GATE geometry model of the Philips DPC-PET. The four depth levels components are illustrated on the right of the image. 18 <i>modules</i> are repeated in one ring. Each module contains 4 tangentially $\times$ 5 axially arranged <i>stacks</i> . Each stack is subdivided into $4 \times 4$ <i>dice</i> and each die contains $2 \times 2$ LYSO <i>crystals</i> . The system is composed of a total of 23,040 crystals. . . . .	85
4.3	Digitizer chain used in GATE simulations. . . . .	87
4.4	Background noise obtained by linear regression, fitted on low counts ( $< 3 \text{ kBq.mL}^{-1}$ ) and the influence of deadtime at higher counts for one module. . . . .	89
4.5	<b>A</b> : Position of line source in the cylindrical scatter phantom from NEMA (2018). <b>B</b> : Scatter phantom positioned in the real system. <b>C</b> : Modelled phantom and PET geometry in GATE for illustration (the table geometry has not been depicted). The line source (red) is placed 45 mm below the central axis z. . . . .	92

4.6	Sensitivity phantom used for experiments and modelled for simulations. . . . .	93
4.7	Determination of $\overline{SA}$ for the calculation of intrinsic spatial resolution for a LOR inside the tomograph's FOV. . . . .	94
4.8	Simulated and experimental count rates according to activity concentrations. <b>A:</b> Single count rates. <b>B:</b> Prompt, delay, true and scatter count rates. <b>C:</b> NECRs. The vertical dashed lines correspond approximately to the upper level of activity concentrations usually used in clinical routine for $^{18}\text{F}$ (black line) and $^{82}\text{Rb}$ (red line) PET exams. . . . .	96
4.9	<b>A:</b> TOF and energy resolutions according to activity concentrations for both simulated (o) and experimental ( $\times$ ) data, over a wide range of activities. <b>B:</b> Example, for $5.2 \text{ kBq.mL}^{-1}$ activity concentration, of the normalized TOF and energy histograms used to compute the FWHM values. . . . .	99
4.10	<b>A:</b> Total count sensitivities measured according to NEMA standards for simulated and experimental data, for increasing thicknesses of aluminium sleeves and with the exponential regressions providing attenuation-free count sensitivities. <b>B:</b> Sensitivities of contiguous axial slices according to the distances from camera centres. . . . .	100
4.11	Example of histograms and corresponding FWHM of the shortest distances between source and LORs projected along the X,Y and Z axis, obtained from experimental and simulated data. . . . .	100
4.12	<b>A:</b> Comparison between simulated and experimental images of the relationships between contrast recovery coefficient and background relative noise, according to the number of OSEM iteration and for the 10 and 22 mm diameter hot spheres and the 37 mm cold sphere. <b>B:</b> Cross-sectional slices passing through the spheres of the IEC phantom and reconstructed with 2 OSEM iterations and 10 subsets from simulated and experimental data. A parallelepiped profile of 6 mm cross-section and passing through the hot spheres of 10 mm and 22 mm diameter is compared between simulated and experimental images. . . . .	102
5.1	Axial slices of PET/CT images of <b>A:</b> Ph1, <b>B:</b> Ph2 and <b>C:</b> Ph3. <b>D:</b> Geometry of Ph3 modelled in GATE for reference. <b>E</b> and <b>F:</b> Examples of segmentation of liver VOIs following radioembolisation for patients #2 and #3, respectively. . . . .	110
5.2	Quantitative accuracy of $^{90}\text{Y}$ acquisitions for image reconstructions with <i>Recon1</i> . <b>A:</b> $AC_{pet}$ against $AC_{ref}$ for both Ph1 and Ph2. <b>B</b> and <b>C:</b> Comparisons of $DVH_{pet}^{VSV}$ (blue lines) and $DVH_{pet}^{LDM}$ (green lines) to $DVH_{ref}^{MC}$ (red lines) for Ph1 at $AC_{ref} = 0.29 \text{ MBq.mL}^{-1}$ and Ph2 at $AC_{ref} = 1.71 \text{ MBq.mL}^{-1}$ , respectively. . . . .	116
5.3	The $DVH_{pet}^{VSV}$ for 8 different reconstructions are compared to $DVH_{ref}^{MC}$ (black curves) for each sphere of Ph3. Sphere sizes are represented in <b>A:</b> 37 mm, <b>B:</b> 28 mm, <b>C:</b> 22 mm, <b>D:</b> 17 mm, <b>E:</b> 13 mm and <b>F:</b> 10 mm. . . . .	118
5.4	RMSD between $DVH_{pet}^{VSV}$ and $DVH_{ref}^{MC}$ . <b>A:</b> RMSD for all reconstructions for the 28 mm sphere against filter size. <b>B:</b> RMSD against sphere sizes for reconstructions using a 2 mm FWHM post-reconstruction Gaussian filter only. . . . .	119

5.5	Effect of acquisition duration on $DVH_{pet}^{VSV}$ for all spheres. <b>A:</b> 37 mm, <b>B:</b> 28 mm, <b>C:</b> 22 mm, <b>D:</b> 17 mm, <b>E:</b> 13 mm and <b>F:</b> 10 mm. Reconstructions were performed using i3s10-2mm. . . . .	120
5.6	Recovery coefficients against sphere diameter for varying $AC_{ref}$ over 6 days. <b>A:</b> $RC_{AC}$ . <b>B:</b> $RC_{Dose}$ . Reconstructions were performed using i3s10-2mm. . . . .	121
5.7	Effect of acquisition duration on $DVH_{pet}^{VSV}$ for 5 patients. Reconstructions were performed using i3s10-2mm. . . . .	123
5.8	Reference Monte Carlo $DVH_{ref}^{MC}$ (black) dosimetry in ideal conditions, image-based $DVH_{pet}^{VSV}$ (blue) and image-based $DVH_{pet}^{MC}$ (red) for the <b>A:</b> 28 mm and <b>B:</b> 13 mm spheres. . . . .	129
6.1	Defined VOIs for the WLV, PLV and $TV_{Total}$ using the $^{99m}Tc$ -macro-aggregated albumin (MAA) SPECT/CT pre-treatment acquisition. The $NPLV$ , $NLV_{Target}$ and $NLV_{WholeLiver}$ are derived from the first three.	137
6.2	Scheme showing the <i>steps</i> (1) to (7) for the comparison between predictive and actual $^{90}Y$ microspheres absorbed dose distributions. <i>Step</i> (1): Predictive SPECT/CT. <i>Step</i> (2): VOI contouring on SPECT/CT images. <i>Step</i> (3): Calculation of absorbed dose. <i>Step</i> (4): Treatment monitoring PET/CT. <i>Step</i> (5): Calculation of absorbed dose. <i>Step</i> (6): Propagation of $RT-struct_{SPECT}$ to obtain $RT-struct_{PET}$ , see Figure 6.3. <i>Step</i> (7): Comparison of absorbed doses using DVHs. . . . .	139
6.3	Scheme showing the different image transformations performed at the <i>Step</i> (6) in Figure 6.2. Methods 2, 3 and 4 implement first the method 1 with a $rigid_{global}$ transformation. . . . .	140
6.4	Two patient cases are represented for the WLV. The $DVH_{j,treatment}$ for the corresponding $j$ methods are represented as: $rigid_{global}$ (red), $deformable_{global}$ (cyan), $rigid_{local}$ (blue) and $rigid_{local,functional}$ (green). The $^{99m}Tc$ -MAA SPECT/CT-based $DVH_{predicted}$ (black) are also depicted for comparison to the $DVH_{j,treatment}$ . . . . .	142
6.5	Two patient cases are represented for the PLV. The $DVH_{j,treatment}$ for the corresponding $j$ methods are represented as: $rigid_{global}$ (red), $deformable_{global}$ (cyan), $rigid_{local}$ (blue) and $rigid_{local,functional}$ (green). The $^{99m}Tc$ -MAA SPECT/CT-based $DVH_{predicted}$ (black) are also depicted for comparison to the $DVH_{j,treatment}$ . . . . .	143
6.6	Two patient cases are represented for the NPLV. The $DVH_{j,treatment}$ for the corresponding $j$ methods are represented as: $rigid_{global}$ (red), $deformable_{global}$ (cyan), $rigid_{local}$ (blue) and $rigid_{local,functional}$ (green). The $^{99m}Tc$ -MAA SPECT/CT-based $DVH_{predicted}$ (black) are also depicted for comparison to the $DVH_{j,treatment}$ . . . . .	144
6.7	Two patient cases are represented for the $TV_{Total}$ . The $DVH_{j,treatment}$ for the corresponding $j$ methods are represented as: $rigid_{global}$ (red), $deformable_{global}$ (cyan), $rigid_{local}$ (blue) and $rigid_{local,functional}$ (green). The $^{99m}Tc$ -MAA SPECT/CT-based $DVH_{predicted}$ (black) are also depicted for comparison to the $DVH_{j,treatment}$ . . . . .	146

- 6.8 The  $RT\text{-}struct_{PET}$  obtained from the propagated  $RT\text{-}struct_{SPECT}$  for the  $TV_{Total}$ , following the  $rigid_{global}$  (cyan) and  $rigid_{local,functional}$  (green) transformations. *Top-left*: The SPECT/CT following the  $rigid_{global}$  method. *Bottom-left*: The SPECT/CT following the  $rigid_{local,functional}$  method. *Right*: The PET/CT and position of the propagated  $TV_{Total}$  if the  $rigid_{global}$  (cyan) and  $rigid_{local,functional}$  (green) transformations are used. The position of the  $TV_{Total}$  falls outside the perfused region using the  $rigid_{global}$  method. . . . . 147
- 6.9 Two patient cases are represented for the  $NLV_{Target}$ .  $DVH_{j,treatment}$  for the corresponding  $j$  methods are represented as:  $rigid_{global}$  (red),  $deformable_{global}$  (cyan),  $rigid_{local}$  (blue) and  $rigid_{local,functional}$  (green). The  $^{99m}Tc\text{-}MAA$  SPECT/CT-based  $DVH_{predicted}$  (black) are also depicted for comparison to the  $DVH_{j,treatment}$ . . . . . 148
- 6.10 Two patient cases are represented for the  $NLV_{WholeLiver}$ .  $DVH_{j,treatment}$  for the corresponding  $j$  methods are represented as:  $rigid_{global}$  (red),  $deformable_{global}$  (cyan),  $rigid_{local}$  (blue) and  $rigid_{local,functional}$  (green). The  $^{99m}Tc\text{-}MAA$  SPECT/CT-based  $DVH_{predicted}$  (black) are also depicted for comparison to the  $DVH_{j,treatment}$ . . . . . 149

# List of Tables

1.1	Properties of microspheres used for liver SIRT. Nuclear data were obtained from LNHB (France) (Bé et al., 2006) . . . . .	9
1.2	Comparison of algorithms. Adapted from Huizing, Verheij, Stokkel, et al. (2018) and others (Dieudonné et al., 2010; Lanconelli et al., 2012; Götz et al., 2019) . . . . .	31
2.1	Positron emitters used in PET imaging. . . . .	37
2.2	Linear attenuation coefficient of different absorbers at 0.511 MeV related to PET imaging. Adapted from Cherry and Dahlbom (2006) and Cherry, Sorenson, and Phelps (2012). . . . .	43
2.3	Physical properties of common scintillators in PET. LYSO is highlighted since the PET used for studies in this thesis is LYSO-equipped. Data obtained from Lecomte (2009) and Cherry, Sorenson, and Phelps (2012). Data for plastic scintillators obtained from Kapłon et al. (2014) and Wieczorek (2017). Data for TlBr obtained from Ariño-Estrada et al. (2018). . . . .	50
2.4	Comparison of the commercially available SiPM PET systems (at the time of writing this thesis). The characteristics of the actual 3 commercialised clinical SiPM-based PET/CTs are outlined, the: 1) GE Discovery MI, 2) Siemens Biograph Vision and 3) Philips DPC Vereos. Characteristics for the SiPM-based PET/MR GE Signa and SiPM-based extended FOV (106 cm) PET/CT Siemens Biograph Vision Quadra, are also reported. Respective values are from [a]: Pan et al. (2019), [b]: Grant et al. (2016) and Caribé et al. (2019), [c]: Reddin et al. (2018) and Van Sluis et al. (2019), [d]: Prenosil et al. (2021), and [e]: Zhang, Maniawski, and Knopp (2018) and Rausch et al. (2019) . . . . .	60
3.1	Properties of $^{90}\text{Y}$ decay for $\beta^-$ and $\gamma$ transitions. Values are from LNHB (France), Bé et al. (2006). . . . .	73
3.2	Experimentally determined positron branching ratio ( $w_p/w_\beta$ ) from published studies. . . . .	74
4.1	Key specifications of the Vereos from Philips (which can be found in literature, e.g. Schaart et al. (2016), Moreau (2019)). . . . .	83
4.2	Parameter values of the digitizer chain. . . . .	86
4.3	Sensitivity phantom characteristics. . . . .	93



4.4	Comparison of the characteristics of the DPC-PET for NECR and scatter fraction between the experimental and Monte Carlo simulated data in this study. Additional comparison is added from experimental data published from Rausch et al. (2019) and Zhang, Maniawski, and Knopp (2018). Values marked with an asterisk (*) represent 'maximum' instead of peak values since the system did not show a peak value beyond which the NECR began to decrease with increasing activity. . . . .	97
4.5	Maximum relative differences between simulated and experimental data are reported for activity concentration ranges for clinical $^{18}\text{F}$ scans and $^{89}\text{Rb}$ cardiac perfusion scans. . . . .	98
4.6	FWHM defined before reconstruction for intrinsic spatial resolution along all dimensions for ten positions recommended by NEMA standards, for both simulated (Sim.) and experimental (Exp.) data. The columns to the right give their absolute difference. . . . .	99
4.7	Comparison of the intrinsic FWHM obtained before reconstruction for the (0,1,0) cm central position, with FWHM obtained after reconstruction. . . . .	100
4.8	Monte Carlo relative statistical uncertainty for the true, scatter and delay event rates. . . . .	101
4.9	Published clinical whole body PET models validated in GATE and compared to experimental data. Some brain and breast systems are also included. A more exhaustive list referencing prototype and small animal systems can be found in Sarrut et al. (2021b). . . . .	103
5.1	Parameter sets used for listmode data reconstructions. . . . .	112
5.2	Patient characteristics. . . . .	115
5.3	Comparison of absorbed dose calculation methods through the $D_{mean}$ and $D_{50\%}$ for Ph1 at $0.29 \text{ MBq}\cdot\text{mL}^{-1}$ and Ph2 at $1.71 \text{ MBq}\cdot\text{mL}^{-1}$ , for both $VOI_{outer}$ and $VOI_{inner}$ . Reconstructions were performed using <i>Recon1</i> . . . . .	116
5.4	Comparison between absorbed dose estimations for all spheres ( $\varnothing_{imm}$ ). Reconstructions were performed using i3s10-2mm. All values in the table are in Gy. . . . .	122
5.5	Comparison of LDM to VSV convolution absorbed dose calculation methods through $D_{mean}$ , $D_{50\%}$ and $D_{2\%}$ for patients #1 and #2 and different volume of interest (VOI)s. Reconstructions were performed using i3s10-2mm. . . . .	124
5.6	Summary of phantom studies with hot spheres for $^{90}\text{Y}$ , for several PET/CT and PET/MR systems, SBR and $AC_{ref}$ . The four last columns to the right summarise the type of evaluation done in the different studies. <b>Contrast:</b> Qualitative evaluation using definitions such as in the NEMA NU-2 standards for image quality. <b>Activity:</b> Quantitative evaluation either based on activity or $RC_{AC}$ estimates. <b>Dose:</b> Quantitative evaluation based on $RC_{Dose}$ or dose-volume histogram (DVH) estimates. <b>Optim:</b> Studies which aimed at varying reconstruction parameters to find optimised reconstruction parameters. Only variable parameters for OSEM reconstructions with time-of-flight (TOF) are reported. . . . .	129

6.1	Patient characteristics who had $^{90}\text{Y}$ -radioembolisation treatment at the CLB. . . . .	134
6.2	Recorded information for the treatment planning $^{99m}\text{Tc}$ -MAA injection and treatment $^{90}\text{Y}$ microspheres injection for patients who received radioembolisation at the CLB. The last column provides the time interval between the $^{99m}\text{Tc}$ -MAA SPECT/CT scan and the post-treatment $^{90}\text{Y}$ PET/CT scan. . . . .	135
6.3	Parameters used for image acquisition and reconstruction for both pre-treatment $^{99m}\text{Tc}$ -MAA SPECT/CT and post-treatment $^{90}\text{Y}$ PET/CT. . . . .	136
6.4	Defined VOIs using the $^{99m}\text{Tc}$ -MAA SPECT/CT pre-treatment acquisition. All VOIs were registered to the SPECT images and exported as $RT\text{-struct}_{\text{SPECT}}$ . . . . .	137
6.5	The methods used for image registration. . . . .	138
6.6	$\bar{D}_{\text{treatment}}$ for the WLW using different registration methods between SPECT/CT and PET/CT images. Values for $\bar{D}_{\text{predicted}}$ are also provided. Patients with the largest differences are highlighted in pink. . . . .	143
6.7	$\bar{D}_{\text{treatment}}$ for the PLV using different registration methods between SPECT/CT and PET/CT images. Values for $\bar{D}_{\text{predicted}}$ are also provided. Patients with the largest differences are highlighted in pink. . . . .	144
6.8	$\bar{D}_{\text{treatment}}$ for the NPLV using different registration methods between SPECT/CT and PET/CT images. Values for $\bar{D}_{\text{predicted}}$ are also provided. Patients with the largest differences are highlighted in pink. . . . .	145
6.9	$\bar{D}_{\text{treatment}}$ for the $\text{TV}_{\text{Total}}$ using different registration methods between SPECT/CT and PET/CT images. Values for $\bar{D}_{\text{predicted}}$ are also provided. Patients with the largest differences are highlighted in pink. . . . .	146
6.10	$\bar{D}_{\text{treatment}}$ for the $\text{NLV}_{\text{Target}}$ using different registration methods between SPECT/CT and PET/CT images. Values for $\bar{D}_{\text{predicted}}$ are also provided. Patients with the largest differences are highlighted in pink. . . . .	147
6.11	$\bar{D}_{\text{treatment}}$ for the $\text{NLV}_{\text{WholeLiver}}$ using different registration methods between SPECT/CT and PET/CT images. Values for $\bar{D}_{\text{predicted}}$ are also provided. Patients with the largest differences are highlighted in pink. . . . .	149
6.12	Predicted absorbed doses compared to obtained absorbed doses following treatment for the WLW, using the $\text{rigid}_{\text{local,functional}}$ . . . . .	150
6.13	Predicted absorbed doses compared to obtained absorbed doses following treatment for the PLV, using the $\text{rigid}_{\text{local,functional}}$ . . . . .	151
6.14	Predicted absorbed doses compared to obtained absorbed doses following treatment for the NPLV, using the $\text{rigid}_{\text{local,functional}}$ . . . . .	151
6.15	Predicted absorbed doses compared to obtained absorbed doses following treatment for the $\text{TV}_{\text{Total}}$ , using the $\text{rigid}_{\text{local,functional}}$ . . . . .	152
6.16	Predicted absorbed doses compared to obtained absorbed doses following treatment for the $\text{NLV}_{\text{Target}}$ , using the $\text{rigid}_{\text{local,functional}}$ . . . . .	153
6.17	Predicted absorbed doses compared to obtained absorbed doses following treatment for the $\text{NLV}_{\text{WholeLiver}}$ , using the $\text{rigid}_{\text{local,functional}}$ . . . . .	154
6.18	Summary of: 1) $\Delta_{\text{method}}^{\%}$ and $\Delta_{\text{method}}^{\text{abs}}$ obtained between the methods, and 2) $\Delta_{\text{predict-treatment}}^{\%}$ and $\Delta_{\text{predict-treatment}}^{\text{abs}}$ between the predictive and mean absorbed dose obtained using the $\text{rigid}_{\text{local,functional}}$ method. The ratio between parentheses, e.g. (8/10) gives the number of patient VOIs which have differences lower than or equal to the recorded difference. . . . .	155



# Acronyms

**1D** 1 dimensional

**2D** 2-dimensional

**3D** 3-dimensional

**ADC** analogue-to-digital converters

**ADV<sub>5%</sub>** activity distribution volume using a 5% threshold

**AI** Artificial Intelligence

**APD** avalanche photodiode

**AQR** active quenching and reset

**ASIC** application-specific integrated circuit

**aSiPM** analog silicon photo-multiplier

**BCLC** Barcelona Clinic Liver Cancer

**BED** biologically effective dose

**BGO** bismuth germanium oxide

**BPF** Back-projection filtered

**BPL** Bayesian Penalised Likelihood

**BremSPECT** bremsstrahlung single photon emission computed tomography

**BRN** Background relative noise

**BSA** body surface area

**BSC** best supportive care

**BV** background variation

**CASToR** Customizable and Advanced Software for Tomographic Reconstruction

**CBCT** cone beam computed tomography

**CFD** Computational fluid dynamics

**CLB** Centre de lutte contre le cancer Léon Bérard

**CLI** Cerenkov luminescence imaging

**CRC** contrast recovery coefficient

**CREATIS** Centre de Recherche en Acquisition et Traitement de l'Image pour la Santé

**CSDA** continuous slowing down approximation

**CST** Central Slice theorem

**CT** X-ray computed tomography

**CTAC** X-ray computed tomography-derived attenuation correction

**CTR** coincidence timing resolution

**DCR** dark count rate

**DICOM** Digital Imaging and Communications in Medicine

**DOI** depth of interaction

**DPC** Digital Photon Counting

**DPC-PET** Digital Photon Counting positron emission tomography

**DPK** dose point kernel

**dSiPM** digital silicon photo-multiplier

**DVH** dose-volume histogram

**EANM** European Association of Nuclear Medicine

**EBRT** External beam radiation therapy

**ECOG-PS** Eastern Cooperative Oncology Group Performance Status scale

**eFOV** extended field-of-view

**EGS** Electron Gamma Shower

**EM** Expectation Maximisation

**ETRAN** Electron TRANsport

**EU** European Union

**EUBED** equivalent uniform biologically effective dose

**EUD** equivalent uniform dose

**FBP** Filtered back-projection

**FF** fill-factor

**FLUKA** FLUktuierende KAskade

**FORE** Fourier rebinning

**FOV** field-of-view

**FPGA** field-programmable gate array

**FWHM** full-width at half-maximum

**GANs** generative adversarial networks

**GATE** Geant4 Application for Tomographic Emission

**Geant4** GEometry ANd Tracking 4

**GI** gastrointestinal

**HCC** hepatocellular carcinoma

**HIFU** high-intensity focused ultrasound

**IARC** International Agency for Research on Cancer

**ICC** intrahepatic cholangiocarcinoma

**IMT** immunotherapy

**J-PET** Jagiellonian Positron Emission Tomograph

**LDM** local deposition method  
**LEHR** low-energy high-resolution  
**LET** linear energy transfer  
**LMOSEM** relaxed List Mode Ordered Subset Expectation Maximisation  
**LOR** line-of-response  
**LSF** lung shunt fraction  
**LSO** lutetium oxyorthosilicate  
**LUT** look-up table  
**LYSO** lutetium–yttrium oxyorthosilicate  
  
**MAA** macro-aggregated albumin  
**MCP** microchannel plate  
**mCRC** secondary hepatic metastases from colorectal cancer  
**MIRD** Medical Internal Radiation Dose  
**ML** Maximum Likelihood  
**MLEM** Maximum-Likelihood Expectation-Maximization  
**MNCP** Monte Carlo N-Particle  
**MNCPX** Monte Carlo N-Particle extended  
**mNETs** secondary hepatic metastases from neuroendocrine tumours  
**MRD** maximum ring difference  
**MRI** magnetic resonance imaging  
**MSRB** multi-slice rebinning  
**MWA** microwave ablation  
  
**NEC** Noise equivalent count  
**NECR** noise equivalent count rate  
**NEMA** National Electrical Manufacturers Association  
**NLV<sub>Target</sub>** target normal liver volume  
**NLV<sub>WholeLiver</sub>** whole normal liver volume  
**NN** neural network  
**NPLV** non-perfused liver volume  
  
**OARs** organs at risk  
**OSEM** Ordered Subset Expectation-Maximization  
  
**PDE** photon detection efficiency  
**PEI** percutaneous ethanol injection  
**PENELOPE** PENetration and Energy LOss of Positrons and Electrons  
**PET** positron emission tomography  
**PET/CT** positron emission tomography combined with X-ray computed tomography  
**PK** point kernel

**PL** Penalised Likelihood  
**PLV** perfused liver volume  
**PMMA** polymethyl methacrylate  
**PMT** photo-multiplier tubes  
**PMT** photo-multiplier tube  
**PNLV** perfused normal liver volume  
**PQR** passive quenching and reset  
**PS** position-sensitive  
**PSF** point-spread function  
**PTV** planning target volume  
**PVE** partial-volume effect

**QE** quantum efficiency  
**QF** quality factors  
**QVH** quality-volume histogram

**RFA** radiofrequency ablation  
**RLI** radioluminescence imaging  
**RMSD** root-mean-square deviation  
**ROI** region of interest

**SBR** sphere-to-background ratio  
**SBRT** stereotactic body radiation therapy  
**SF** scatter fraction  
**SHM** secondary hepatic metastases  
**SI** International System of units  
**SiPM** silicon photo-multipliers  
**SiPM** silicon photo-multiplier  
**SIRT** selective internal radiation therapy  
**SNR** signal-to-noise ratio  
**SPAD** single-photon avalanche diode  
**SPECT** single photon emission computed tomography  
**SPECT/CT** single photon emission computed tomography combined with X-ray computed tomography  
**SPTR** single photon timing resolution  
**SSRB** single-slice rebinning  
**STR** single timing resolution

**T/N** tumour-to-non-tumour ratio  
**TACE** transarterial chemoembolisation  
**TAE** transarterial embolization  
**TDC** time-to-digital converters

**TlBr** thallium bromide  
**TLV** total liver volume  
**TOF** time-of-flight  
**TRT** targeted radiotherapy  
**TTLV** tumour-to-total liver ratio  
**TV** tumour volume  
**TV<sub>Total</sub>** total tumour volume  
**US** ultrasound  
**VK** voxel-kernel  
**VOI** volume of interest  
**VOR** volume-of-response  
**VRT** variance reduction technique  
**VSV** voxel S-value  
**WLV** whole liver volume





# Introduction

Liver is one of the rising cause of cancer-related mortality in both sexes at a time when the mortality from most cancers is decreasing<sup>1</sup>. Depending on the diagnosis, stage of the disease, relative health and physical condition of each liver cancer patient, several treatment alternatives are however available, including treatment by radioembolisation, also known as selective internal radiation therapy (SIRT). Radioembolisation therapy using <sup>90</sup>Y encapsulated in glass, or labelled-to resin, microspheres is an intra-arterial method used in clinical practice to treat unresectable and chemoresistant hepatic malignancies. During <sup>90</sup>Y-radioembolisation, millions of microspheres are administered through selected branches of the hepatic artery which feed the tumours. High energy  $\beta^-$  particles are emitted from the decay of <sup>90</sup>Y, which deliver high absorbed doses to the surrounding tissues in the liver where the tumours are located, while preserving the non-perfused healthy regions and other organs at risk (OARs) from irradiation. Following <sup>90</sup>Y-radioembolisation treatment delivery, positron emission tomography (PET) imaging can be performed to monitor the <sup>90</sup>Y microspheres biodistribution and evaluate the technical success of the procedure. This monitoring is of prime importance for patient safety and to move towards personalised dosimetry, enabling to perform an assessment of the spatial absorbed dose distribution and make further predictions about the outcome of the treatment.

PET is today the most sensitive functional imaging modality for studying molecular interactions in the human body. In constant evolution, it has recently been equipped with silicon photo-multipliers (SiPM), replacing more conventional photo-multiplier tubes (PMT), thus enabling an overall improvement in performance and in particular in the resolution in TOF. PET was also found interesting through its performance for imaging <sup>90</sup>Y. Indeed, <sup>90</sup>Y is a pure  $\beta^-$  emitter, but possesses a branching ratio related to an internal pair production of  $32.6 \times 10^{-6}$  pairs/decay (Dryák and Šolc, 2020). Even if there are conditions of low positron production statistics, PET imaging since the last decade has become the gold standard for the monitoring of <sup>90</sup>Y-radioembolisation.

The context of this thesis falls under the scope of the monitoring of radioembolisation treatment with <sup>90</sup>Y microspheres using silicon photo-multiplier (SiPM)-based PET imaging and Monte Carlo calculations. <sup>90</sup>Y-radioembolisation is usually delivered in the local institution hospital where my thesis was conducted, the Centre de lutte contre le cancer Léon Bérard (CLB), but, however, no absorbed dose calculation is systematically performed following treatment although a PET imaging is always carried out. The technical success of the treatment is only evaluated by the visual distribution of radioactivity of the PET images.

The aim during this thesis was twofold. First, emphasis was made on the simulation of the Vereos in the Geant4 Application for Tomographic Emission (GATE) platform to make it available to the scientific community for research purposes. Then, the thesis focused on the evaluation of image reconstruction parameters and imaging conditions using <sup>90</sup>Y towards an improvement in absorbed dose quantification

---

1. See [The Surveillance, Epidemiology and End Results \(SEER\) Program \(USA\)](#)

for  $^{90}\text{Y}$ -radioembolisation. Analyses were carried out using phantom data but also applied to patient data. Finally, preliminary comparisons between the predictive  $^{99m}\text{Tc}$ -MAA and  $^{90}\text{Y}$  microspheres dosimetries were performed.

The manuscript is divided into two parts, each of which consists of three chapters. *Part I* (Chapters 1 to 3) provides a thorough description of the state-of-the-art on the radioembolisation treatment using  $^{90}\text{Y}$  microspheres and PET imaging. It outlines the patient workup and dosimetry techniques for treatment monitoring using PET imaging and the related issues. *Part II* (Chapters 4 to 6) provides the different contributions made during this thesis including the Monte Carlo simulations of the Philips Vereos PET in GATE, the experimental phantom studies for the evaluation of Ordered Subset Expectation-Maximization (OSEM) reconstruction parameters for  $^{90}\text{Y}$  PET imaging and applied on patient data for absorbed dose calculations.

*Chapter 1* first describes the rationale and clinical context of radioembolisation treatment. It also provides a state-of-the-art on present methods for absorbed dose calculations in targeted radiotherapy (TRT) using single photon emission computed tomography (SPECT) and PET voxelised images. *Chapter 2* is a generic state-of-the-art on PET from positron emission to annihilation photon detection and image reconstruction. Furthermore, it provides the concepts of the Digital Photon Counting (DPC) SiPM, which is used in the Vereos system, and summarises the performance of several actual clinical novel PET systems. *Chapter 3* finally describes the physics of  $^{90}\text{Y}$  decay and the related confounding factors to PET imaging for quantification.

*Chapter 4* details the work carried out for the first contribution made during this thesis on the Monte Carlo simulation of the DPC SiPM PET, describing the simulated performance of the system, with comparison to experimental data in accordance with NEMA guidelines, and has been published in EJNMMI Physics (Labour et al., 2020). *Chapter 5* provides the results of the second contribution made during this thesis on the quantitative study using the Vereos for  $^{90}\text{Y}$  imaging, aiming at evaluating the OSEM reconstruction parameters and at the same time aiming at reducing the acquisition duration with acceptable degradation in accuracy of the information obtained in reconstructed images. This contribution, at the time of writing this thesis, has been accepted for publication and should be published shortly in EJNMMI Physics (Labour et al., 2021). *Chapter 6* uses the results of selected reconstruction and acquisition parameters in the contribution in *Chapter 5* on a set of patient data who had  $^{90}\text{Y}$ -radioembolisation in our hospital. A preliminary assessment of the predictive value of the  $^{99m}\text{Tc}$ -MAA surrogate to  $^{90}\text{Y}$ -microspheres by suggesting consistent approaches for image registration was performed.

# **Part I**

## **State of the art**



## Chapter 1

# Clinical context

## 1.1 Liver cancer

### 1.1.1 Statistics

The worldwide incidence and mortality of liver cancers are outlined by the International Agency for Research on Cancer (IARC)<sup>1</sup>. In 2018, the number of recorded new cases for liver cancer in both sexes was 841,100 for 781,600 deaths (Bray et al., 2018), making it the sixth most commonly diagnosed cancer and the fourth leading cause of cancer mortality (Bray et al., 2018; Dasgupta et al., 2020). Figure 1.1 provides some statistics about the incidence and mortality rates for countries of the European Union (EU), where France is ranked third and fourth in incidence and mortality rates, respectively. In addition, liver cancer is a male-dominated disease, associated with increasing age and many types of chronic liver diseases consequent to hepatitis B or C virus infections, alcoholic-related liver disease or non-alcoholic fatty liver tissue, which is tightly linked to the metabolic syndrome and obesity.

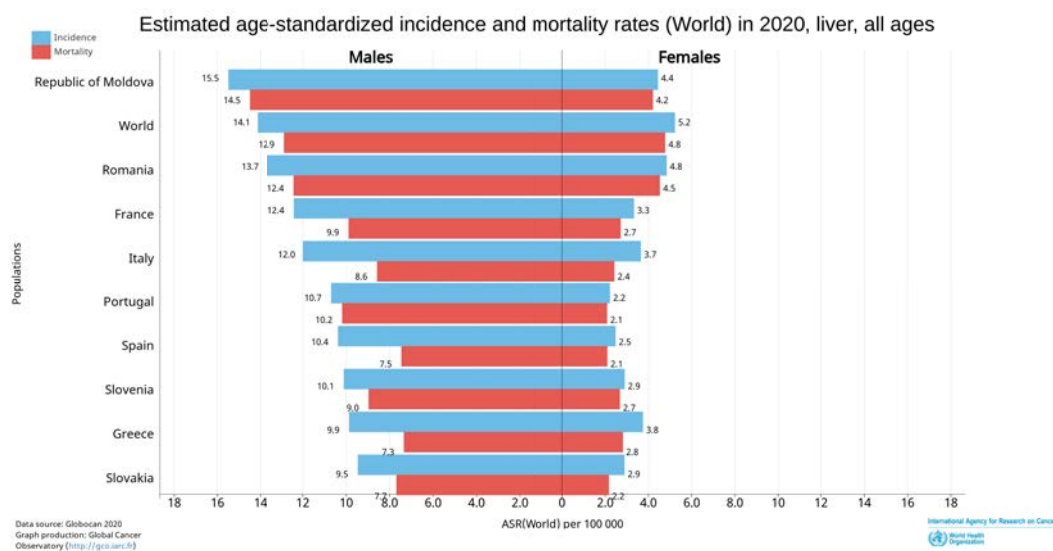


FIGURE 1.1 – Age-standardised rate (ASR) statistics on liver cancer in Europe from IARC/WHO<sup>2</sup>, all ages confounded showing male predominance.

The two most feared primary cancers of the liver are hepatocellular carcinoma (HCC), which accounts for 75%-85% of the total burden of primary malignant liver

1. See [Global Cancer Observatory \(GCO\) - IARC/WHO \(France,UN\)](#)

cancers, followed by intrahepatic cholangiocarcinoma (ICC) which accounts for 10%-15% of cases, as well as some other rare types (Tischoff and Tannapfel, 2007; Bray et al., 2018). Figure 1.2 outlines the difference of origin for HCC and ICC. HCC was ranked the fifth most common cancer in men, the ninth most common cancer in women and the second most common cause of cancer death worldwide (Knudsen, Gopal, and Singal, 2014).

The liver is also a common metastatic site for a wide variety of primary tumours from other sites in the body (Namasivayam, Martin, and Saini, 2007), such as adenocarcinomas of the gastrointestinal (GI) tract (e.g. colorectal cancers). This could be due to the double blood supply to the liver through the portal vein and the hepatic artery which facilitates the trapping of circulating cancer cells, leading to secondary hepatic metastases (SHM) (Ananthakrishnan, Gogineni, and Saeian, 2006; Ridder et al., 2016). Metastatic liver tumours are more prevalent than primary tumours. In clinical practice, the majority of secondary liver cancers are secondary hepatic metastases from colorectal cancer (mCRC).

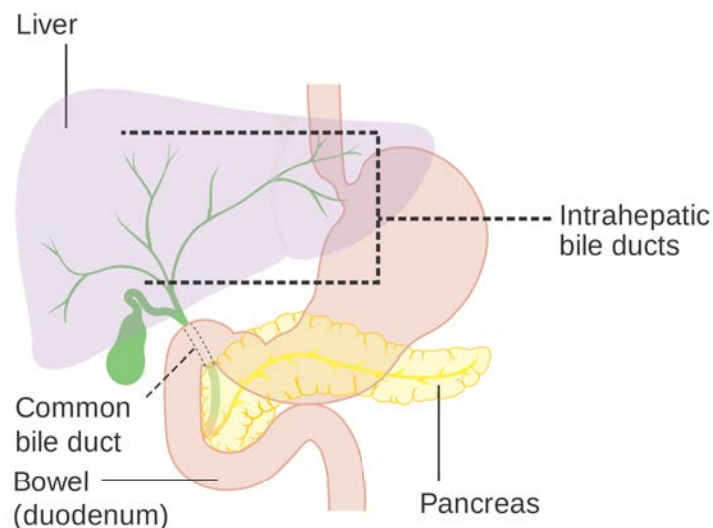


FIGURE 1.2 – Primary liver cancer origin: HCC develop from the main liver cells (by malignant transformation of hepatocytes) and ICC develop from the small intrahepatic bile duct epithelium (*Source: Cancer Research UK/Wikimedia Commons*).

Noninvasive medical imaging modalities are of key importance in the diagnosis, staging and follow-up of liver tumours. Different techniques such as ultrasound (US), contrast enhanced dynamic X-ray computed tomography (CT) and magnetic resonance imaging (MRI) are used to detect abnormal liver damage (Jiang et al., 2018). Treatment decisions are based on these different imaging modalities to determine the site of the tumour in the liver, the type of malignancy (HCC, ICC, SHM), the size of the tumour and whether it has spread (the stage), the remaining healthy and functional liver parenchyma, and so on. However, the diagnosis of liver cancer is often followed by a poor prognosis, and treatment alternatives generally preclude surgical resection that could lead to a cure, due to the hypervascular nature of the organ or a late staging diagnosis.

## 1.1.2 Treatment overview

Depending on the diagnosis, staging, relative health and physical fitness of each liver cancer patient, a multidisciplinary team will discuss the appropriate treatment to be administered. Although the prognosis is often poor, there are many alternatives for the treatment of liver cancer, ranging from cure to palliative care or best supportive care (BSC). Patients whose cancer is detected at an early stage have a wider range of treatment possibilities and are more likely to live longer, compared to those who present at a later stage.

### 1.1.2.1 Liver cancer staging algorithms.

The stage is one of the most important prognostic factors for liver cancer. The most commonly used algorithm for the staging and treatment of patients with HCC is that of the Barcelona Clinic Liver Cancer (BCLC) (Llovet, Fuster, and Bruix, 2004), based on the Eastern Cooperative Oncology Group Performance Status scale (ECOG-PS) and the Child-Pugh system<sup>2</sup>. People with liver cancer that is BCLC stage 0 (very early stage) or stage A (early stage) have a more favorable prognosis leading to cure than people with liver cancer that is BCLC stage B (intermediate stage), C (advanced stage) or D (terminal end-stage disease).

**Early diagnosis.** The main treatments for primary liver cancers are first surgery, including liver resection or transplantation which can be curative, but most people with liver cancer are inoperable due to already damaged parenchyma (e.g. liver cirrhosis), a too large tumour volume, the tumour being near to a blood vessel making it hard to remove, difficulties to find a donor for transplant, and so forth. Local ablative therapies including radiofrequency ablation (RFA), microwave ablation (MWA), high-intensity focused ultrasound (HIFU) (Ji et al., 2020) and percutaneous ethanol injection (PEI) (for small tumours) are also alternatives which can be curative. With the increasing incidence of HCC, surgery in the form of liver resection which provides optimal outcomes in patients of good performance status with limited liver disease, or transplantation, remains the mainstay of curative treatment with ablation for small tumours.

External radiotherapy using the stereotactic body radiation therapy (SBRT) approach with high energy X-ray beams is also a non-invasive treatment option that can precisely deliver ablative absorbed doses to the targeted lesions, while limiting radiation to adjacent healthy tissues and OARs. However, due to the proximity to the stomach, bowel and other organs to the liver, see Figure 1.2, SBRT is not a common choice for liver cancer treatment to limit irradiation to these adjacent organs. Furthermore, the delivery of fractional high radiation during SBRT is not a simple task owing to intra- and inter- fractional variations in patient setup, organ movement and deformation. There are frequently large mismatches in absorbed dose compared with the plan in liver, with higher absorbed doses than expected during SBRT (Schmid et al., 2019). This can lead to toxicity when an absorbed dose of more than 35 Gy of radiation is given to the liver parenchyma (Lawrence et al., 1995; Miften et al., 2018).

**Late diagnosis.** Due to late stage presentation and diagnosis of liver cancers, therapeutic options become limited and most patients are offered palliative treatments

2. See [Cancer Research UK for summary on BCLC, ECOG-PS and Child-Pugh system](#)



or supportive care. An alternative local treatment which can be administered is chemoembolisation or transarterial chemoembolisation (TACE), which is a form of chemotherapy directed into the liver and restricting the blood supply of the tumour, performed in interventional radiology. Radioembolisation or SIRT (See Section 1.2) is another alternative treatment for liver cancer. It is a type of internal radiotherapy aiming at delivering dose from radioactive emitters into the hepatic arterial circulation to chosen tumoral liver regions. SIRT, which is the treatment of interest for this thesis, is a palliative treatment which however, is becoming efficacious in liver cancer patients and now trending to be considered as curative. For liver cancer that has spread (advanced stage), the patient might have a targeted cancer drug, such as sorafenib. In addition, new therapeutic options are being developed such as immunotherapy (IMT) with tangible hope for long term survival and there is still progress to be made in this field.

In France, SIRT is reimbursed by the health insurance scheme for the treatment of HCC, ICC and mCRC. There are stages of the disease to be considered, the patient must be in satisfactory general condition, preserved liver function and must fulfil certain other factors and biological criteria. It depends also on the medical device considered, see Haute Autorité de Santé, France (2018, 2020).

## 1.2 Radioembolisation rationale

Radioembolisation or SIRT is an intra-arterial method used in clinical practice to treat unresectable and chemoresistant hepatic malignancies (Lau et al., 1994; Salem et al., 2010; Sangro et al., 2011; Tafti and Padia, 2019). During SIRT, millions of microspheres are administered into an artery, delivering high absorbed doses to the selected perfused regions of the liver where the hepatic lesions are located, while preserving the non-perfused healthy regions of the liver and other OARs from irradiation (Kennedy et al., 2012), see Figure 1.3. SIRT can be administered to patients with liver malignancies which are well-vascularised since the microspheres are carried by the blood to the tumour, ranging from HCC and ICC primary tumours to mCRC, secondary hepatic metastases from neuroendocrine tumours (mNETs) and SHM from breast cancer, and so on.

### 1.2.1 Microspheres properties

Currently, SIRT can be performed with two isotopes, either with  $^{90}\text{Y}$  or  $^{166}\text{Ho}$  microspheres. Three types of medical devices exist, SIR-Spheres® (Sirtex Medical Limited, North Sydney NSW, Australia, 2020) and TheraSphere™ (Boston Scientifics, Massachusetts, United States, 2020) for  $^{90}\text{Y}$  microspheres, and QuiremSpheres® for  $^{166}\text{Ho}$  microspheres (Quirem Medical BV, Deventer, the Netherlands, 2020). The properties of the three types of microspheres are resumed in Table 1.1.

### 1.2.2 Vascular considerations in radioembolisation

The liver has the advantage of having a double blood supply which is of benefit to SIRT. While the liver parenchyma is mainly supplied with blood by the portal vein, tumours that appear in the liver are in turn predominantly supplied by the circulation of the hepatic artery (Bierman et al., 1951; Dezso et al., 2009). The specific configuration of the vascularisation of the liver organ therefore offers something that can be exploited for the treatment of cancer.

TABLE 1.1 – Properties of microspheres used for liver SIRT. Nuclear data were obtained from LNHB (France) (Bé et al., 2006)

Specifications	Therasphere™	SIR-Sphere®	QuiremSpheres®
Isotope	$^{90}\text{Y}$	$^{90}\text{Y}$	$^{166}\text{Ho}$
Microsphere material	Glass	Resin	Poly-L-lactic acid
Isotope is	Incorporated into glass matrix	Attached to the surface	Attached to the surface
$T_{1/2}$ (h)	64.04	64.04	26.80
$E_{\beta_{max}}$ (keV)	2278.7 (99.98%)	2278.7 (99.98%)	1854.5 (48.2%) and 1773.9(50.5%)
$E_{\beta_{mean}}$ (keV)	926.7 (99.98%)	926.7 (99.98%)	693.8 (48.2%) and 651.1 (50.5%)
$E_{\gamma}$ (keV)	no $\gamma$ emission	no $\gamma$ emission	81.57 (6.6%)
$r_{max}$ (mm)	11	11	8.7
$r_{mean}$ (mm)	2.5	2.5	2.2
Range (average) of particle diameter ( $\mu\text{m}$ )	20-30 (25)	20-60 (32.5)	15-60 (30)
Density ( $\text{g.cm}^3$ )	3.6	1.6	1.4
Activity per microsphere (Bq) at calibration	2500	50	< 450
Activity per commercially available vial (GBq) at calibration	3, 5, 7, 10, 15, 20	3 (can be divided)	Patient specific dose
Relative embolic effect	Mild	Moderate	-
Number of particles instilled	4 million	50 million	30 million
Scout dose	$^{99m}\text{Tc}$ -MAA	$^{99m}\text{Tc}$ -MAA	$^{166}\text{Ho}$ -MS or $^{99m}\text{Tc}$ -MAA
Activity calculation	Compartmental MIRD, voxel-based personalised dosimetries	Compartmental MIRD, voxel-based personalised dosimetries, BSA methods	Compartmental MIRD, dosimetry
Imaging modality	BremSPECT or PET	BremSPECT or PET	SPECT or MRI
Reimbursement (in France)	HCC, ICC, mCRC	HCC,ICC	Not reimbursed

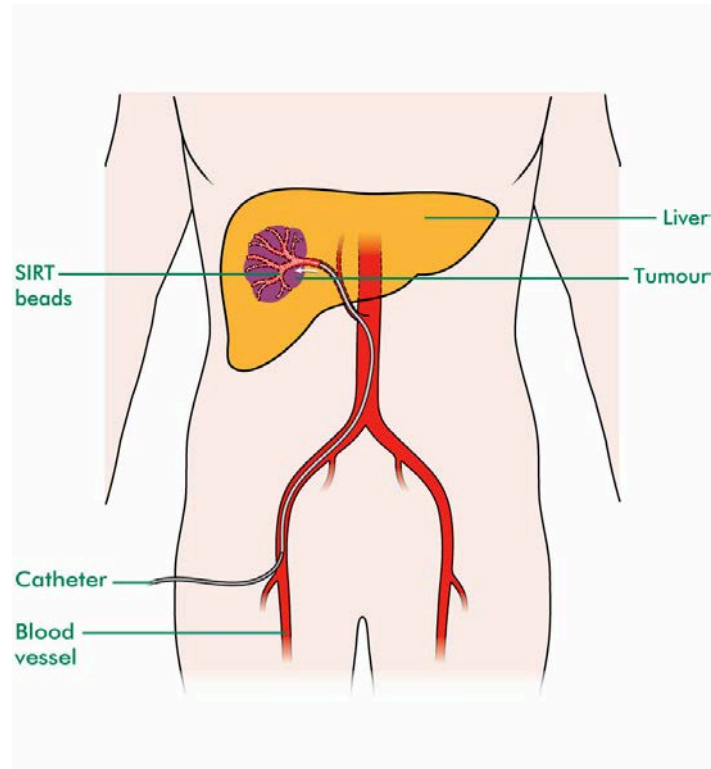


FIGURE 1.3 – SIRT transarterial procedure. A branch of the hepatic artery feeding the tumour is selected where activity is administered by catheterisation (*Source: Macmillan Cancer Support (UK)*).

For the record, this feature of the liver benefit to transarterial embolization (TAE) treatment<sup>3</sup>, where the tumour has its supply cut off by the injection of tiny gelatin sponges or beads, and so the nutrients sustaining the cancer by the blood are removed, and the tumour dies from ischaemia and subsequently tissue necrosis. TACE, which is a treatment given to tumours intermediate stage BCLC B, applies the same approach as TAE, whilst at the same time providing a second hit from directly injecting chemotherapeutic agents or drug-eluting beads laced with toxic drugs. The latter enhance cancer cell death. TAE/TACE particles have a diameter which are 3-10 times larger than microspheres used in SIRT, see Table 1.1 for SIRT microsphere sizes, which results in the occlusion of medium to large arteries and there is blood flow stagnation or interruption (Sangro, Iñarrairaegui, and Bilbao, 2012).

Figure 1.4 depicts the difference in the effects brought by TAE/TACE and SIRT mechanisms according to the sphere size. SIRT differs substantially from TAE/TACE where the source of radiation has to access the network of tumoral neovessels after being injected into the hepatic arteries. It should be pointed out that the beneficial and deleterious effects of SIRT come both from the radiation delivered by the isotope and from the poorly understood effects of micro-embolisation, but not from the ischaemia due to occlusion of the vessels (Sangro, Iñarrairaegui, and Bilbao, 2012). Moreover, contrary to TAE/TACE, there is not significant reduction in the arterial blood flow during SIRT. This in turn adds an aspect to the treatment, where together with the lack of ischaemic effect, lobar or even whole liver SIRT can be performed safely without inducing acute liver decompensation (Sangro et al., 2011). Therefore,

3. See [National Cancer Institute \(USA\)](#)

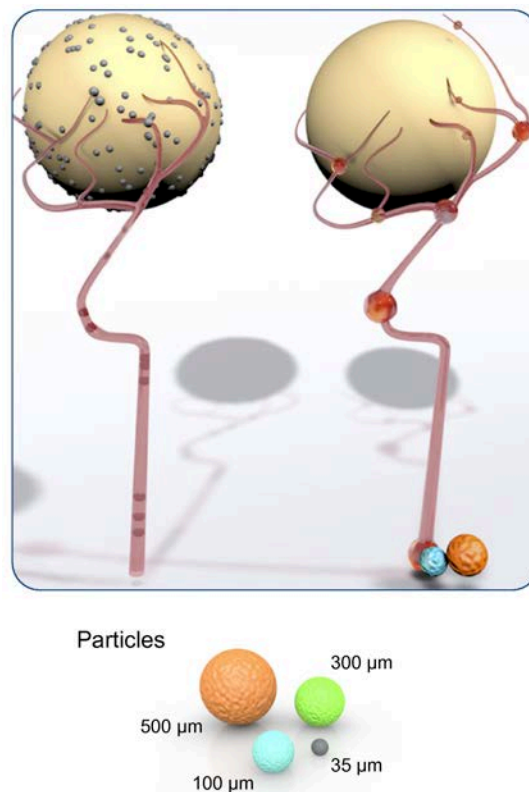


FIGURE 1.4 – Comparison between particle sizes in TAE or TACE (*right*) and SIRT (*left*).  $^{90}\text{Y}$  and  $^{166}\text{Ho}$  microspheres of  $\sim 35\ \mu\text{m}$  (gray colour) provide short range radiation to the tumour for SIRT, whilst larger beads provide an ischemia effect during TAE and eventually expose tumour cells to high concentrations of cytotoxic agents during TACE. Extracted from Sangro, Iñarrairaegui, and Bilbao (2012).

the therapeutic effect of SIRT largely depends on factors such as hepatic arterial flow distribution and the arterial vascularisation of the target tumour.

An overview of the SIRT procedure using  $^{90}\text{Y}$  is given in the following sections, which is the main interest for this thesis. In France<sup>4</sup> (or elsewhere), the decision to implement the treatment and post-treatment follow-up must be taken, in agreement with the patient, in a multidisciplinary consultation meeting specialised in hepatic tumours, including at least: an oncologist, a hepatologist, a radiotherapist, a digestive surgeon, an interventional radiologist, a nuclear physician and a palliative care physician. Treatment planning, see Section 1.4, must be reserved for multidisciplinary teams comprising: a nuclear physician, an interventional radiologist with expertise in hepatic embolisation in cancerology, a medical physicist and a radiopharmacist.

### 1.3 $^{90}\text{Y}$ -radioembolisation

During  $^{90}\text{Y}$ -SIRT, the high energy  $\beta^-$  emitter  $^{90}\text{Y}$  particles which are encapsulated in glass or labelled-to resin microspheres, see Table 1.1, are administered through selected branches of the hepatic artery which feed the tumours. This method ensures

4. See Haute Autorité de Santé reports (France): SIR-Spheres® (2018) and TheraSphere™ (2020)

a regional biodistribution of the  $^{90}\text{Y}$ -microspheres delivering a highly localised absorbed dose to the perfused regions, sparing nearby OARs and healthy tissues with the advantage of a negligible radiation burden to both non-embolized portions and extra-hepatic tissues (considering the maximum range of  $\beta^-$  particles around the deposition site), see Figure 1.3. The  $^{90}\text{Y}$ -SIRT method is widely used owing to its clinical efficacy and relative safety (Lau et al., 1994; Sato et al., 2008; Kennedy et al., 2009; Salem et al., 2010; Sangro et al., 2011; Garin et al., 2021).

Prior to SIRT treatment, patients undergo a thorough angiography to map the arterial vessels supplying the tumour and surrogate particles which mimic the distribution of microspheres are administered to assess the presence of pulmonary and GI shunts. These different steps are necessary for an individualised treatment planning to maximise and ensure the safety and efficacy of the therapy.

### 1.3.1 Part I: $^{99m}\text{Tc}$ -MAA pre-treatment simulation step

Unlike other forms of brachytherapy (*curiethérapie* in French) where the position of the implanted radioactive material can be more precisely known, an accurate dosimetry cannot be predicted in SIRT since the radioactive microspheres are liberated in the bloodstream rather than being directly implanted. Complications in patients after  $^{90}\text{Y}$ -SIRT might therefore arise due to non-target intrahepatic and extrahepatic deposition of radioactive particles during the treatment procedure. To avoid or limit the impact of possible side-effects and toxicity, a pre-treatment mock examination procedure is performed before and not more than 2 weeks prior to  $^{90}\text{Y}$ -SIRT (because of possible disease progression) using the surrogate  $^{99m}\text{Tc}$ -MAA particles, which roughly commensurate to microspheres sizes.  $^{99m}\text{Tc}$  is a pure gamma ( $\gamma$ ) emitter with a photon energy peak of 140 keV and its physical half life is relatively short ( $\sim 6$  hours), allowing for a wide range of scanning procedures, keeping the total patient radiation exposure low. The properties of  $^{99m}\text{Tc}$ -MAA are given in Table 1.1.

During this step, the suitability of the patient for  $^{90}\text{Y}$ -SIRT is assessed by anticipating the microspheres distribution and the absorbed dose distribution of radiation that could be delivered to tumour and healthy liver regions. The amount of  $^{90}\text{Y}$  activity to administer during the treatment phase (See Section 1.3.2) is therefore determined at this step. The approach also allows to predict the toxicity, since it is more likely that there will be no deposition of microspheres during the treatment phase where there is no  $^{99m}\text{Tc}$ -MAA deposition.

#### 1.3.1.1 Angiography workup and $^{99m}\text{Tc}$ -MAA injection.

The distribution of activity depends on several factors, first regarding the hepatic vasculature distribution itself. Thus, examinations of the latter is performed upstream and monitored during  $^{99m}\text{Tc}$ -MAA injection. To evaluate the hepatic vasculature feeding the tumour and select the right artery or artery parts for activity injection, a C-arm cone beam computed tomography (CBCT) or other hybrid angiography/CT angiographic imaging (Orth et al., 2008) is performed by injecting at first contrasted agents by catheterisation through the selected artery feeding the tumoral region. CBCT may identify branches of the hepatic artery which feed the tumours that CT or MRI fail to detect (Louie et al., 2009). Hybrid CT/angiography is preferred to CBCT when possible (Levillain et al., 2021).

Figure 1.5 depicts the workup angiography for a patient. This allows to detect, and in due course coil-embolise any artery branches (or move the injection position

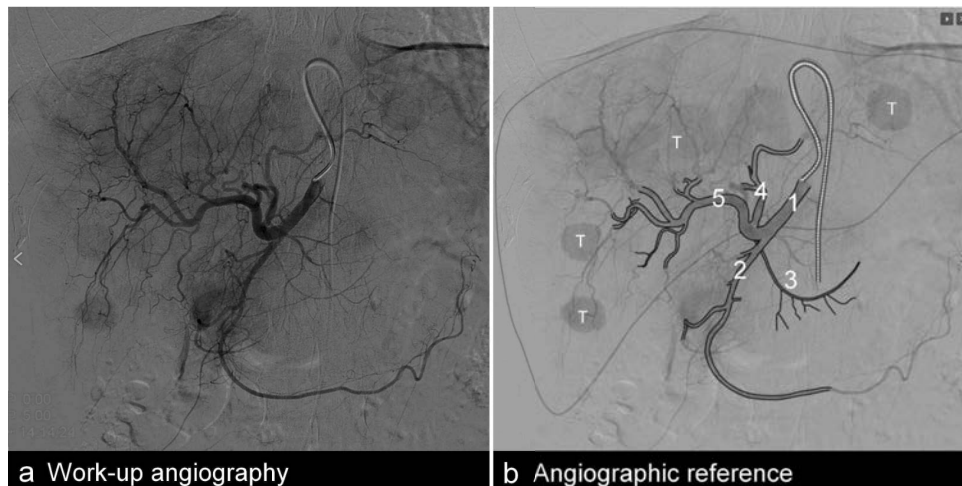


FIGURE 1.5 – Hepatic angiography after arterial embolisation using a C-arm CBCT (Source: CBCT).

beyond the ostium of the arteries that we do not want to catheterise, which does not require a coil) which might transport radioactive particles to other non-desired parts of the liver or nearby and extrahepatic OARs. It allows also to determine if different injection positions are required before injecting  $^{99m}\text{Tc}$ -MAA in a second step, under the same catheter placements. Once the right artery is selected, the surrogate  $^{99m}\text{Tc}$ -MAA particles can be administered by the interventional radiologist in the same procedure and monitoring of activity administration is accompanied by the same angiographic techniques.

### 1.3.1.2 Gamma-camera imaging after $^{99m}\text{Tc}$ -MAA injection.

Following injection of  $^{99m}\text{Tc}$ -MAA, a planar scintigraphy and/or if available a 3-dimensional (3D)-SPECT gamma-camera imaging are performed, as depicted in Figures 1.6 and 1.7. The use of the last two platforms is many-fold. They allow to: (1) also detect any extrahepatic deposition of activity transported by the hepatic vasculature to non-targeted liver parenchyma or OARs, (2) calculate the lung shunt fraction (LSF) which is the proportion of radioactive material which reached the lungs presumably due to leakage via hepatopulmonary shunts, see Section 1.4.1.1, (3) simulate the outcome of the spatial distribution of  $^{90}\text{Y}$  during the treatment phase, (4) adapt the  $^{90}\text{Y}$  activity to be injected during treatment which is dependant of the microsphere type and (5) estimate if possible the absorbed dose distribution by in the perfused tumoral regions of interest and liver tissue. Imaging should be performed within one hour from injection due to degradation of  $^{99m}\text{Tc}$ -MAA (Grosser et al., 2016).

The pre-treatment phase is essential to maximize the  $^{90}\text{Y}$  activity to be administered to tumoral regions while concurrently preserving healthy liver parenchyma and other OARs, minimising side-effects for the patient. The LSF is also a decisive criteria in the recommendations for  $^{90}\text{Y}$ -SIRT follow-up. Section 1.4 outlines in further details about the  $^{90}\text{Y}$  microspheres prescriptions using the  $^{99m}\text{Tc}$ -MAA pre-treatment phase.

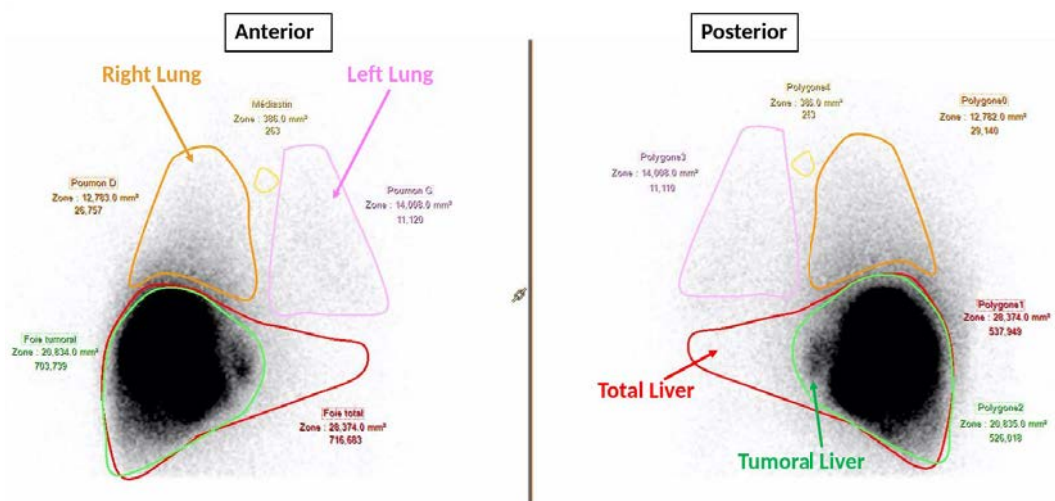


FIGURE 1.6 – Anterior and posterior planar scintigraphy images of both lungs and the total liver following injection of  $^{99m}\text{Tc}$ -MAA (pre-treatment) for a patient at the CLB.

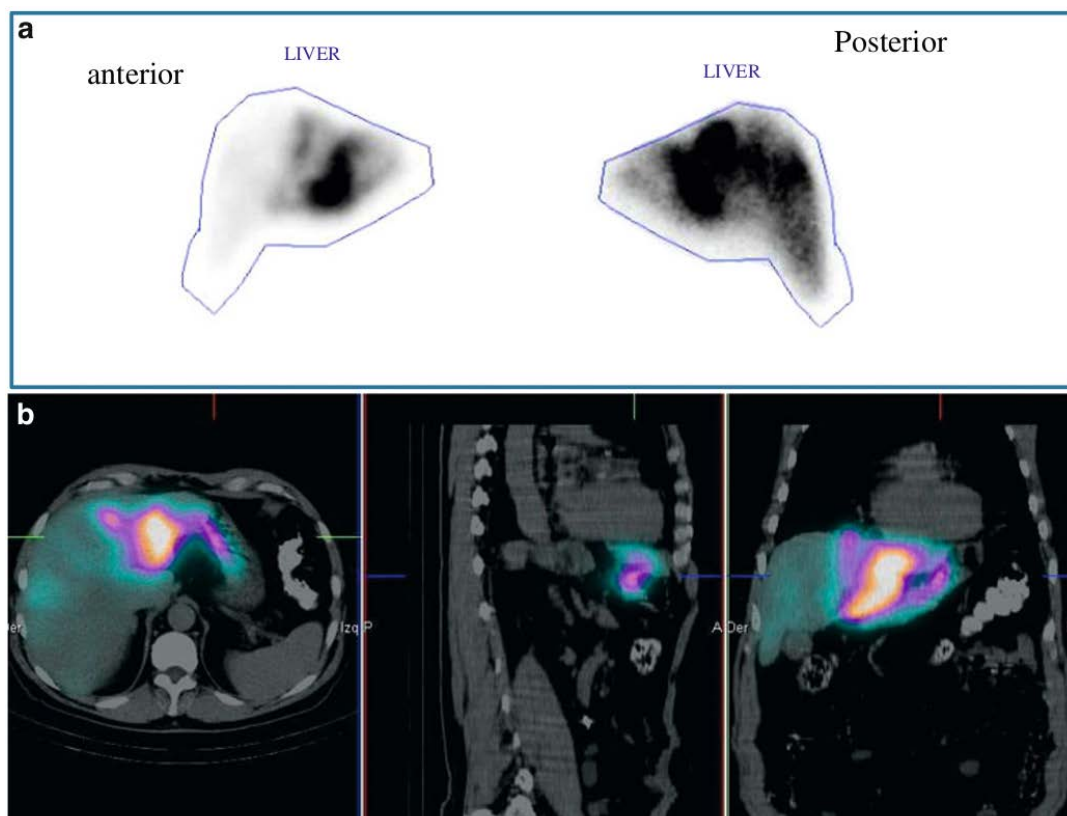


FIGURE 1.7 – Pre-treatment  $^{99m}\text{Tc}$ -MAA imaging. *Top*: Anterior and posterior planar scintigraphy images of the total liver. *Bottom*: SPECT/CT images for the same patient. Extracted from Bilbao, Reiser, et al. (2008).

### 1.3.2 Part II: $^{90}\text{Y}$ -radioembolisation treatment step

Within two weeks after the  $^{90}\text{Y}$  has been prescribed (Dezarn et al., 2011; Salem et al., 2019) with the mock procedure using the surrogate  $^{99m}\text{Tc}$ -MAA as explained in the previous Section 1.3.1, the administration of  $^{90}\text{Y}$ -microspheres is performed using the same catheterisation position in the selected hepatic vasculature which is the treatment site. Levillain et al. (2021) recommend (recommendation R17) to conduct SIRT as soon as possible after the simulation and no more than four weeks after simulation for  $^{90}\text{Y}$ -resin microspheres.

#### 1.3.2.1 Administration procedure and monitoring

The administration equipment sets are different for the glass and resin microspheres. The integrity of the equipment is assured by the nuclear physician and the interventional radiologist. Without going into much details, resin microspheres are injected by alternating small bursts of spheres, until all the spheres have been injected. The catheter placement and stasis/reflux can be regularly verified using contrasted agents and performing planar angiography. CBCT can be cumbersome during injection since it revolves around the patient. Glass microspheres injection is much faster by injecting in bolus. No per procedure control is required for glass microspheres. Figure 1.8 depicts the SIRT procedure at the CLB using glass microspheres.

In case the totality of the activity cannot be administered, the undelivered activity should be measured. The approximate administered activity is calculated using Equation 1.1.

$$\text{Administered activity} = \text{Prepared activity} \times \left(1 - \frac{\text{Dose rate after}}{\text{Dose rate before}}\right) \quad (1.1)$$

where the dose rates can be obtained by measuring around the delivery box before and after the treatment. The final activity delivered to the patient must be recorded and used for dosimetric purposes.

#### 1.3.2.2 Post-treatment monitoring

Although if the lung shunt calculated by the scout images using  $^{99m}\text{Tc}$ -MAA predicts the lung shunt for  $^{90}\text{Y}$ -microspheres (Jha et al., 2012), differences might arise between the biodistribution of MAA and microspheres, providing inaccurate predictions (See Section 1.7 and Chapter 6 for  $^{99m}\text{Tc}$ -MAA limitations). Therefore, there should be a monitoring of the microspheres biodistribution following the SIRT administration procedure to evaluate the technical success of the procedure and detect possible non-target deposition to take necessary actions as early as possible after treatment if there are any extrahepatic depositions (e.g. in the GI tract). The gold standards for this monitoring can be actually performed using either single photon emission computed tomography combined with X-ray computed tomography (SPECT/CT) or positron emission tomography combined with X-ray computed tomography (PET/CT), which moreover enable to perform an assessment of the spatial absorbed dose distribution and make further predictions about the outcome of the treatment (Lhommel et al., 2010; D'Arienzo et al., 2012). Figure 1.9 gives a visual comparison of the images obtained following the predictive  $^{99m}\text{Tc}$ -MAA injection and the post-SIRT following  $^{90}\text{Y}$ -microspheres injection.



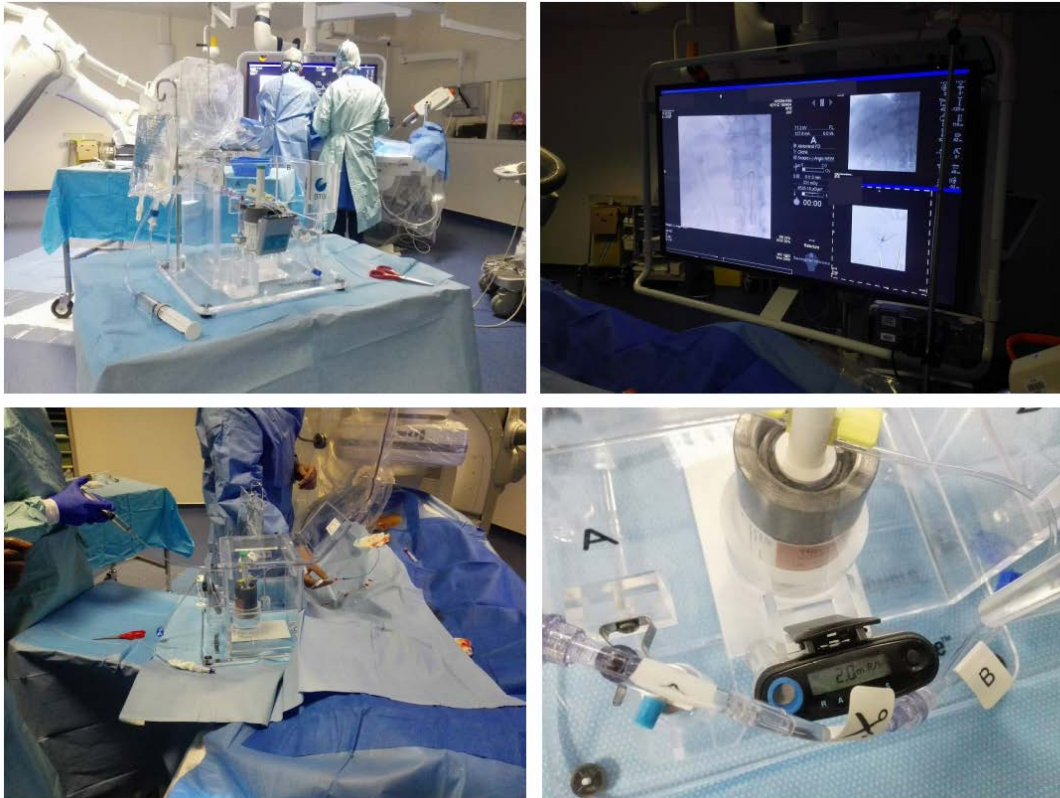


FIGURE 1.8 –  $^{90}\text{Y}$ -SIRT procedure at the CLB. *Top left*: Administration system for microspheres (TheraSphere™) and physicians placing the catheter to the selected hepatic artery in interventional radiology before microspheres injection. *Top right*: Performing angiography for catheterisation monitoring to the selected region to be perfused by the interventional radiologist. *Bottom left*: Injection procedure of microspheres to the patient by the nuclear physicist. *Bottom right*: Dosimeter for radioprotection control.

## 1.4 $^{90}\text{Y}$ activity planning

This section describes the methods used to adapt  $^{90}\text{Y}$  activity to each patient. As seen in the previous sections (See Section 1.3.1), within 1 hour from the scout  $^{99m}\text{Tc}$ -MAA injection, planar scintigraphic images from the upper thoracic to the lower abdominal cavities are acquired, see Figure 1.6. Lately, SPECT/CT is being used, see Figure 1.7, overcoming the limitations of planar images such as lack of 3D information, tissue densities and heterogeneities and attenuation correction. The endpoint of this assessment is the adaptation of the  $^{90}\text{Y}$  activity to be administered during SIRT for a personalised dosimetry for each patient.

### 1.4.1 Image-based metrics

The definitions of the LSF, tumour-to-non-tumour ratio (T/N) and tumour-to-total liver ratio (TTLV) are provided hereafter. They are considered when determining the  $^{90}\text{Y}$  activity to administer for an individual patient depending on the the prescription method and microsphere type.

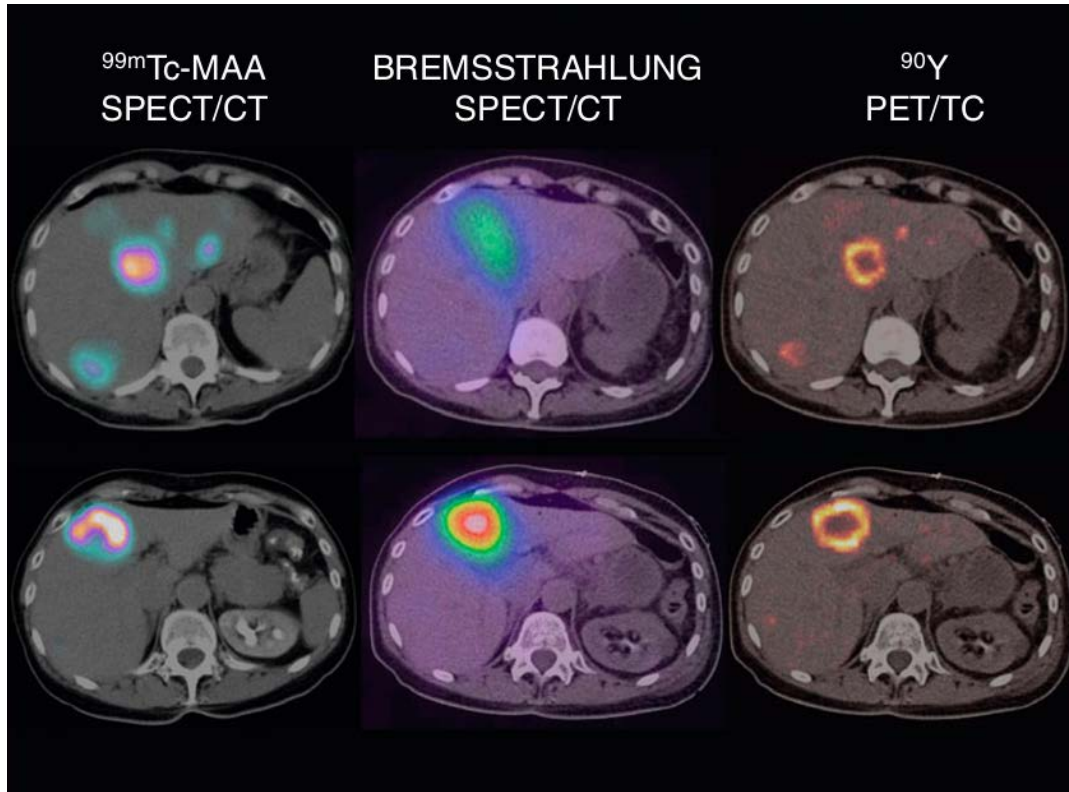


FIGURE 1.9 – *Left*: Pre-treatment distribution of  $^{99m}\text{Tc}$ -MAA using SPECT/CT. *Middle*: Post-SIRT distribution of  $^{90}\text{Y}$  using SPECT/CT. *Right*: Post-SIRT distribution of  $^{90}\text{Y}$  using PET/CT. Extracted from Bilbao, Reiser, et al. (2008).

#### 1.4.1.1 The lung shunt fraction (LSF)

LSF from  $^{99m}\text{Tc}$ -MAA is more commonly calculated from planar scintigraphy imaging. The anterior and posterior images are used to define region of interest (ROI)s for each lung and the total liver, see Figure 1.6. The total number of counts in each ROI is obtained enabling to calculate the LSF, as expressed in Equation 1.2.

$$LSF(\%) = \frac{C_{ROI,lungs}}{C_{ROI,lungs} + C_{ROI,liver}} \times 100 \quad (1.2)$$

where  $C_{ROI,lungs}$  and  $C_{ROI,liver}$  are the total counts in the lungs and liver ROIs, respectively.

Concomitantly, a 3D distribution of  $^{99m}\text{Tc}$ -MAA is obtained from the reconstructed and corrected SPECT image. Up to date, SPECT images benefit from corrections from photon attenuation (using X-ray computed tomography-derived attenuation correction (CTAC)), scattered radiation (using multiple energy windows) and accompanied by resolution compensation (e.g. using distance dependent resolution compensation). Compared to planar scintigraphy, SPECT/CT enables more personalised  $^{90}\text{Y}$ -SIRT treatment planning with the evaluation of counts in each 3D VOI instead of overlapped accumulated counts in a 2-dimensional (2D) ROI. Furthermore, it is nowadays possible to co-register SPECT images to other tomographic imaging modalities used pre- or post-treatment such as SPECT itself, PET, CT and MRI. SPECT/CT therefore helps to design better the treatment compared to planar

scintigraphy with a better localisation and centering of the perfused VOI and extrahepatic activity deposition. SPECT alone (without CTAC) has been shown to be accurate to delimit visually large perfused VOI, but not for small volumes (Garin et al., 2012).

#### 1.4.1.2 The tumour-to-non-tumour ratio (T/N)

The T/N is defined by Equation 1.3, assuming that the distribution of  $^{99m}\text{Tc}$ -MAA in the tumoral and non-tumoral regions are similar to that of  $^{90}\text{Y}$  microspheres.

$$T/N = \frac{(A_{\text{tumour}} / M_{\text{tumour}})}{(A_{\text{liver}} / M_{\text{liver}})} \quad (1.3)$$

where  $A_{\text{tumour}}$  and  $A_{\text{liver}}$  are the total activities measured in the tumour and the normal (non-tumoral) liver determined from  $^{99m}\text{Tc}$ -MAA images, respectively.  $M_{\text{tumour}}$  and  $M_{\text{liver}}$  are the masses of the tumour and normal liver, respectively.

#### 1.4.1.3 Tumour-to-total liver ratio (TTLV)

The percentage involvement by the tumour in the liver (or TTLV), is defined by

$$\text{TTLV}(\%) = \frac{V_{\text{tumour}}}{V_{\text{tumour}} + V_{\text{normal liver}}} \times 100\% \quad (1.4)$$

where  $V_{\text{tumour}}$  and  $V_{\text{normal liver}}$  are the tumour and normal liver volumes, respectively.

There are no standardised methods used for the calculation of LSF, T/N and TTLV and they are more accurately determined using SPECT/CT (Giammarile et al., 2011). The prescription of  $^{90}\text{Y}$  activity is microsphere dependant and based on manufacturer's specifications as detailed in the following sections.

### 1.4.2 Glass microspheres

The properties of glass microspheres can be found in Table 1.1. Two methods are recommended for the determination of personalised  $^{90}\text{Y}$  activity ( $A_{90\text{Y},\text{prescribed}}$ ) using glass microspheres: the *single-compartment model* and the *multi-compartment model*. Equation 1.5, derived from the Medical Internal Radiation Dose (MIRD) convention is used for the calculation of  $A_{90\text{Y},\text{prescribed}}$  (Salem et al., 2019; Garin et al., 2021).

$$A_{90\text{Y},\text{prescribed}} = \frac{\overline{D}_{\text{absorbed}}(r_T) \times M_{r_T}}{50 [\text{Gy.kg.GBq}^{-1}]} \quad (1.5)$$

where  $M_{r_T}$  and  $\overline{D}_{\text{absorbed}}(r_T)$  are the target liver mass to be perfused and the desired mean absorbed dose in the target liver, respectively. An absorbed dose of approximately  $50 \text{ Gy.kg}^{-1}$  in tissue per GBq of  $^{90}\text{Y}$  as the denominator is used, see Section 1.6.3 on the MIRD principle for more details.

The desired  $\overline{D}_{\text{absorbed}}(r_T)$  is set with assumptions of an homogeneous distribution and a total absorption of  $A_{90\text{Y},\text{prescribed}}$  and energy over the target volume in the liver. The equation is independent of the LSF. A limiting factor to calculate the  $A_{90\text{Y},\text{prescribed}}$  is the mean absorbed dose to the lungs which should not exceed 30 Gy, which is approximately equal to an  $^{90}\text{Y}$  activity lung shunt of 610 MBq if we assume

a total mass of 1 kg of lung tissue (Boston Scientifics, Massachusetts, United States, 2020).

The *multi-compartmental model* dosimetry approach is also based on the MIRD scheme, where the mean absorbed dose is calculated in more than one VOI (Gulec, Mesoloras, and Stabin, 2006; Salem et al., 2019) and obtain separate analysis for multiple tumours and the normal liver (Morán et al., 2020). Voxel-based dosimetry can also be performed, for example using the Simplicit $^{90}\text{Y}^{\text{TM}}$  software (Mirada Medical, Oxford, UK).

### 1.4.3 Resin microspheres

Three methods are suggested for the calculation of individual  $^{90}\text{Y}$  activity using resin microspheres suggested by the manufacturer (Sirtex Medical Limited, North Sydney NSW, Australia, 2020), these being: 1) the empirical model, 2) the body surface area (BSA) model and 3) the partition model. For all methods, the final prescribed activity for  $^{90}\text{Y}$  SIR-Spheres $^{\text{®}}$  is re-adapted empirically depending on the LSF, see Equation 1.6.

$$A_{90\text{Y},\text{prescribed}}(\text{LSF}) = \begin{cases} A_{90\text{Y},\text{prescribed}} \times 1 & \text{if LSF} < 10\% \\ A_{90\text{Y},\text{prescribed}} \times 0.8 & \text{if } 10\% < \text{LSF} < 15\% \\ A_{90\text{Y},\text{prescribed}} \times 0.6 & \text{if } 15\% < \text{LSF} < 20\% \\ \text{no treatment otherwise.} & \end{cases} \quad (1.6)$$

The empirical method is outdated and the most commonly used method is the BSA (Bastiaannet et al., 2018) even if it presents some inherent pitfalls. For better personalised activity prescription, MIRD equations and the multi-compartmental method (or even voxel-based dosimetry if possible) are preferred (Levillain et al., 2021).

#### 1.4.3.1 Empirical method.

The empirical method is based on safety margins based on published clinical data (Gray et al., 2001).  $^{90}\text{Y}$  activity to be prescribed is determined based on the TTLV. The recommended  $^{90}\text{Y}$  activities are determined using Equation 1.7.

$$A_{90\text{Y},\text{prescribed}}(\text{TTLV}) = \begin{cases} 2.0 & \text{if TTLV} < 25\% \\ 2.5 & \text{if } 25\% < \text{TTLV} < 50\% . \\ 3.0 & \text{if } 50\% < \text{TTLV} \end{cases} \quad (1.7)$$

This method is the most-basic that can be used, has no theoretical background and treatment personalisation, and due to clinically observed side-effects using this model, the BSA-based method was elaborated.

#### 1.4.3.2 BSA method.

The BSA-based method is a semi-empirical model based on the assumption that the BSA predicts the total liver volume in the healthy population (Vauthey et al., 2002), removing the need for cross-sectional imaging. The calculation of the prescribed  $^{90}\text{Y}$  activity by the BSA method is based on the patient's body measurements (weight and height) and the TTLV, according to Equation 1.8.

$$A_{90\text{Y},prescribed} = (BSA - 0.2) + \frac{TTLV(\%)}{100} \quad (1.8)$$

where the BSA is modelled by Equation 1.9.

$$BSA[m^2] = 0.20247 \times (\text{height}[m])^{0.725} \times (\text{weight}[kg])^{0.425} \quad (1.9)$$

However, the pitfalls of the BSA method are the assumption that the BSA is correlated with the total liver volume (TLV) is not always the case with patients with liver tumours, and small patients with large livers will receive relatively low doses on the liver and the other way round (Lam et al., 2014; Bastiaannet et al., 2018), leading to under/over treatment (Levillain et al., 2021).

### 1.4.3.3 Partition multi-compartment method.

The partition model (Ho et al., 1996) selects the maximum  $^{90}\text{Y}$  activity that can be prescribed, based on absorbed dose thresholds that can receive the healthy liver (max. 80 Gy) and lungs (max. 20 Gy), therefore maximising the absorbed dose to the tumour tissue and limiting toxicity. Dosimetry for the three considered compartments, which are the tumour, healthy liver and lungs, are based on the  $^{99m}\text{Tc}$ -MAA scans. Segmentation of the compartments is performed using reconstructed images.

The  $A_{90\text{Y},prescribed}$  is based on the T/N. Subsequently,  $A_{90\text{Y},prescribed}$  can be calculated according to Equation 1.10, given the calculated LSF, T/N and compartment masses (Gulec, Mesoloras, and Stabin, 2006).

$$A_{90\text{Y},prescribed} = D_{tumour} \times \frac{T/N \times M_{tumour} + M_{normal\ liver}}{49.67 \times T/N \times (1 - LSF)} \quad (1.10)$$

The partition model can only be used when the tumour mass is a discrete region in the liver. This is more likely the case with primary HCC or ICC tumours. SHM are usually spread in regions of the liver, making it difficult to define the tumour and the healthy liver parenchyma. However, the partition model is still not routinely used today (Lau et al., 2012; Smits et al., 2015).

## 1.5 Radionuclide alternatives to $^{90}\text{Y}$ for radioembolisation

Microspheres containing  $^{166}\text{Ho}$  (Quirem Medical BV, Deventer, the Netherlands, 2020) provide an alternative to  $^{90}\text{Y}$  microspheres. The specifications of  $^{166}\text{Ho}$  in comparison to  $^{90}\text{Y}$  microspheres are also provided in Table 1.1.  $^{166}\text{Ho}$  microspheres emits low-energy  $\gamma$ -rays, therefore the visualisation of microspheres perfused in patients is possible using SPECT/CT; but the additional specificity being that  $^{166}\text{Ho}$  and its decay product  $^{166}\text{Er}$  are both lanthanides<sup>5</sup> and thus present paramagnetic properties. The visualisation of microspheres is therefore possible by MRI of the metal. However, even if MRI has a higher resolution and can easily be combined with anatomical scans, it is not suitable for tissues containing air or tissues containing metals (such as coils placed for treatment) (Reinders et al., 2019). Owing to the shorter half life than  $^{90}\text{Y}$  and differences in the energy spectra, more activity is needed when using  $^{166}\text{Ho}$  to attain comparable absorbed doses. As a consequence, 90% of the radiation is released within the first 4 days of radiation, compared to 11 days for  $^{90}\text{Y}$ .

5. See [Wikipedia/Lanthanides](https://en.wikipedia.org/wiki/Lanthanides)

**Treatment procedure overview for  $^{166}\text{Ho}$ -SIRT.** A sham procedure, same as with  $^{90}\text{Y}$ -SIRT is performed, see Section 1.3.1, to assess the safety of the treatment. Here, a small but clinically safe amount of  $^{166}\text{Ho}$  particles can be used for the scout dose. The  $^{166}\text{Ho}$  particles (around 250 MBq for the scout dose) have identical shape and size to the  $^{166}\text{Ho}$  microspheres and therefore can better predict the intrahepatic and extrahepatic distributions of the microspheres (Elschot et al., 2014). Activity calculation for  $^{166}\text{Ho}$  microspheres is currently based on the MIRD model assuming a homogeneous distribution of the microspheres and the target volume or liver weight.  $A_{^{166}\text{Ho},prescribed}$ , which is the activity to administer, is calculated using Equation 1.11, based on the recommended total liver absorbed dose around 60 Gy (Reinders et al., 2019).

$$A_{^{166}\text{Ho},prescribed} = 3.781[\text{GBq.kg}^{-1}] \times M_{r_T} \quad (1.11)$$

The  $M_{r_T}$  of the patient's liver can be determined using CT (CBCT) or MRI.

## 1.6 Dosimetry calculations in internal radiotherapy

This section outlines the different possible algorithms for calculating the absorbed dose for TRT and for SIRT. Computational methods for TRT dosimetry start from reference most common model-based macrodosimetry using *S-values* for whole target organs. The latter method however neglects heterogeneities in the biological radioactive source distributions and the target tissue densities and are not representative of all variations in real patient body morphology.

Other methods based on non-uniform activity distributions have been proposed to provide means for more accurate voxel-based dosimetry. Current ones employ numerical Monte Carlo simulations, analytical convolution methods using point kernel (PK) or voxel-kernel (VK) modellings using *S-values* and the MIRD formalism (Bolch et al., 2009) and also an analytical more simplified MIRD voxel dosimetry using the local deposition method (LDM). The last methods account for more realistic source distributions and when possible also account for tissue heterogeneities, but with different levels of accuracy.

Internal dosimetry calculations can be performed over a broad range of target dimensions from whole organs, small-scale tissue to cellular levels. However, they depend on available imaging modalities and the resolution of the output image datasets, which nowadays are preferably presented by means of 3D voxel maps. Functional SPECT and PET images are generally employed in clinical patient dosimetry to assess radiopharmaceutical biological uptake while the anatomical CT modality can provide information about tissue compositions. Nowadays, bi-modal systems such as SPECT/CT and PET/CT imaging have been benchmarked for absorbed dose calculation in nuclear medicine applications.

### 1.6.1 Definitions

#### 1.6.1.1 Absorbed dose

The mean absorbed dose,  $\bar{D}_{absorbed}$ , is defined as the energy deposited in a target region or tissue,  $r_T$ , per unit target tissue mass, expressed as

$$\bar{D}_{absorbed}(r_T) = \frac{E_{absorbed}(r_T)}{M_{r_T}} \quad (1.12)$$

where  $\bar{D}_{absorbed}(r_T)$  is the mean absorbed dose in  $r_T$  in [Gy],  $E_{absorbed}(r_T)$  is the absorbed energy in  $r_T$  in [J] and  $M_{r_T}$  is the mass of  $r_T$  in [kg] (Loevinger, Budinger, and Watson, 1991; Bolch et al., 2009; Thomas, 2012).

It is measured in *gray* (Gy), with one *gray* defined as the absorption of one *joule* of radiation energy *per kilogram* of matter ( $J.kg^{-1}$ ). The special name *gray* (*sievert* for equivalent dose (Thomas, 2012)) instead of *joule per kilogram* was given to avoid dangers to human health arising from mistakes involving the International System of units (SI), in case they were incorrectly taken to identify the different quantities involved (Göbel, Mills, and Wallard, 2006). The estimation of the absorbed dose depends on different parameters: (1) the types (electrons, photons, charged particles) and energy of particles emitted from a particular isotope, (2) the size and spatial distribution of the source volume containing the activity, and target tissue where energy is deposited and (3) the distance separating the source and target as well as the density variations of materials between them.

### 1.6.1.2 Time-integrated activity

The time-integrated activity (or cumulated activity),  $\tilde{A}(r_S, T_D)$ , is the number of disintegrations occurring in a radioactive source region,  $r_S$ , over a period of time,  $T_D$ , expressed by Equation 1.13. If the activity-time curve is known,  $\tilde{A}(r_S, T_D)$  can also be calculated by the area under the curve.

$$\tilde{A}(r_S, T_D) = \int_0^{T_D} A(r_S, t) dt = A_0 \int_0^{T_D} f_{r_S}(t) e^{-(\lambda_p + \lambda_b)t} dt \quad (1.13)$$

where  $A(r_S, t) = A_0 \cdot e^{-(\lambda_p + \lambda_b)t}$ ,  $f_{r_S}(t)$  is the fractional uptake in  $r_S$ ,  $\lambda_p$  and  $\lambda_b$  being the physical and biological decay constants of the radiopharmaceutical or medical device. If we assume no biological clearance and a total uptake of activity in  $r_S$ ,  $f_{r_S}(t) = 1$  and  $\lambda_b = 0$ .

### 1.6.1.3 Time-integrated activity coefficient

$\tilde{A}(r_S, T_D)$  is sometimes expressed in terms of the time residence,  $\tau(r_S, T_D)$  (Loevinger, Budinger, and Watson, 1991), or the time-integrated activity coefficient,  $\tilde{a}(r_S, T_D)$ , (Bolch et al., 2009), representing the cumulative number of nuclear transformations occurring in  $r_S$  per unit administered activity, defined as

$$\tau(r_S, T_D) = \tilde{a}(r_S, T_D) = \frac{1}{A_0} \int_0^{T_D} A(r_S, t) dt = \int_0^{T_D} f_{r_S}(t) e^{-(\lambda_p + \lambda_b)t} dt \quad (1.14)$$

## 1.6.2 Monte Carlo approach

Monte Carlo simulations compared to analytical approaches have the capability for modelling full radiation transport in voxelised geometries, thus achieving better reliability and accuracy. They are based on iterative statistical processes which stochastically estimate interactions positions, energy and relative pathways of particles traversing media, taking into account variations in tissue densities when a particle is being tracked in heterogeneous matter. Monte Carlo methods allow therefore to perform 3D voxel-based dosimetry with the major uncertainty arising from the input 3D image voxel cartography from imaging modalities which depends on the intrinsic performance of modern quantitative tomographs in specific imaging conditions. The input images can also be biased by image reconstruction parameters.

Input images for the calculation of absorbed dose using Monte Carlo simulations are: (1) the normalised SPECT or PET image considered as the heterogeneous radioactive emission source distribution and (2) the CT image co-registered to the emission tomography image to take into account tissue heterogeneity at the voxel level. Numerous inputs other than the source and the transport medium are required to tune the simulation. These are necessarily: 1) the physics behaviour list of interactions for Compton scattering, photon absorption, generation of secondaries or any physical interaction with matter in specific media, 2) each voxel density attribution based on the CT and look-up table (LUT) models, 3) the source type and the number of primaries in the source and 4) energy and absorbed dose scorers during the simulation to obtain the voxelised absorbed dose maps. If necessary, particle range threshold cuts and variance reduction technique (VRT) can be applied aiming at reducing simulation duration. The choice of the different parameters will determine the accuracy and duration of the simulations and might depend on the computation infrastructure made available to the user.

Although Monte Carlo simulations are quite extensive and provide the main advantages of 3D voxelised source and tissue heterogeneities considerations, accurate models for particle tracking traversing matter, induction of secondary particles and patient-specific organ lesions and geometries (Huizing, Verheij, Stokkel, et al., 2018), they still demand huge computation time and infrastructure for clinical routine calculations. They are mostly used in the validation of developing new algorithms such as described in the following Sections 1.6.3-1.7. Monte Carlo simulations are also requisites to pre-calculate input data in other algorithms, such as *S-values* and kernels for voxel dosimetry and general research purposes (Götz et al., 2019). Nevertheless, for absorbed dose calculations, Monte Carlo simulations can be relatively fast, with 2-3 hours simulation (Dieudonné et al., 2013), or much less in minutes if multiple cluster nodes are available.

### 1.6.3 The MIRD schema for absorbed dose calculation

The MIRD is a recognised method applied for estimating absorbed dose from radiopharmaceuticals used in nuclear medicine (Loevinger, Budinger, and Watson, 1991; Bolch et al., 2009). The first schema for internal radiation therapy using radioactive isotopes was presented in 1968 as the MIRD Pamphlet No.1 (Loevinger and Berman, 1968a,b) and has been superseded by the MIRD Primer for absorbed dose calculations (Loevinger, Budinger, and Watson, 1988, 1991). Since then, the MIRD committee<sup>6</sup> has published 20 dose estimate reports for several radionuclides and 26 Pamphlets. The MIRD formalism has been extended to an image voxel-based level and cellular level dosimetry (Bolch et al., 1999; Howell et al., 1999) and has been generalised to both nuclear medicine and radiation protection (Bolch et al., 2009) with standardised nomenclature.

#### 1.6.3.1 MIRD principle for an organ-based source and target

In this section, the derivation of the MIRD formalism is detailed starting with the simplest case: which is radioactive emission from one homogeneous source organ to a target organ considering one type of radiation only. The MIRD Primer by Loevinger, Budinger, and Watson (1991) and the generalised formalism from Bolch et al. (2009) stipulate that following the multiple nuclear transitions that can occur during radioactive decay of a specific isotope in a source region,  $r_S$ , the mean energy

---

6. See [MIRD Committee](#)



emitted for radiation type  $i$  is calculated for each discrete nuclear transition using Equation 1.15.

$$\Delta_i = Y_i \times E_i \quad (1.15)$$

where  $Y_i$  is the number of  $i^{\text{th}}$  nuclear transitions per nuclear transformation,  $E_i$  is the mean energy emitted of the  $i^{\text{th}}$  nuclear transition and  $\Delta_i$  is their product, i.e. the mean energy emitted of the  $i^{\text{th}}$  nuclear transition per nuclear transformation.

Only part of  $\Delta_i$  will be absorbed in the target region,  $r_T$ , depending on the aforementioned variable parameters in Section 1.6.1.1. This fraction is called the absorbed fraction,  $\phi_i(r_T \leftarrow r_S)$ , which is the fraction of radiation energy  $E_i$  emitted within  $r_S$  that is absorbed in  $r_T$ . Therefore, the mean absorbed energy absorbed in  $r_T$  from energy emitted within  $r_S$  from radiation type  $i$ ,  $\bar{E}_{\text{absorbed},i}(r_T \leftarrow r_S)$ , can be calculated using Equation 1.16.

$$\bar{E}_{\text{absorbed},i}(r_T \leftarrow r_S) = \tilde{A}(r_S) \times \Delta_i \times \phi_i(r_T \leftarrow r_S) \quad (1.16)$$

where  $\tilde{A}(r_S)$  is the cumulated activity obtained using the activity-time curve (see Section 1.6.1.2).

Dividing Equation 1.16 by the mass of the  $r_T$ ,  $M_{r_T}$ , simply gives the mean absorbed dose in the  $r_T$  from emitted radiation type  $i$  from  $r_S$ ,  $\bar{D}_{\text{absorbed},i}(r_T \leftarrow r_S)$ , as expressed in Equation 1.17, where the specific absorbed fraction,  $\Phi_i(r_T \leftarrow r_S)$ , is introduced, defined as the ratio of the absorbed fraction and the target mass.

$$\begin{aligned} \bar{D}_{\text{absorbed},i}(r_T \leftarrow r_S) &= \tilde{A}(r_S) \times \Delta_i \times \frac{\phi_i(r_T \leftarrow r_S)}{M_{r_T}} \\ &= \tilde{A}(r_S) \times \Delta_i \times \Phi_i(r_T \leftarrow r_S) \end{aligned} \quad (1.17)$$

Equation 1.17 can be further reduced to Equation 1.18 since the product of  $\Phi_i$  and  $\Delta_i$  can be taken under a common term, giving the specific quantity called the *S-values*,  $S_i(r_T \leftarrow r_S)$ , which is the mean absorbed dose to  $r_T$  per unit activity in  $r_S$  for radiation type  $i$ .

$$\bar{D}_{\text{absorbed},i}(r_T \leftarrow r_S) = \tilde{A}(r_S) \times S_i(r_T \leftarrow r_S) \quad (1.18)$$

Further expressing the absorbed dose in terms of mean absorbed dose per administered activity,  $\bar{d}_{\text{absorbed},i}(r_T \leftarrow r_S)$ , Equation 1.19 is obtained.

$$\begin{aligned} \frac{\bar{D}_{\text{absorbed},i}(r_T \leftarrow r_S)}{A_0} &= \frac{\tilde{A}(r_S)}{A_0} \times S_i(r_T \leftarrow r_S) \\ \bar{d}_{\text{absorbed},i}(r_T \leftarrow r_S) &= \tilde{a}(r_S) \times S_i(r_T \leftarrow r_S) \end{aligned} \quad (1.19)$$

where  $A_0$  is the administered activity and  $\tilde{a}(r_S)$  is the time-integrated activity coefficient or residence time (See Section 1.6.1.2).

The MIRD principle is not precluded to other scenarios and can be extended to a wide range of possibilities, to multiple source contributing to a target regions, from whole organs, tissue subregions, voxelised tissue, cellular levels and so on, depending on the appropriate available data (e.g. images) for dosimetry calculation. The following Section 1.6.3.2 provides the formulation used for voxel-based dosimetry, in which we are more interested for this thesis.

### 1.6.3.2 MIRD principle extended to multiple sources

Equations 1.15-1.19 can be extended to account for multiple  $r_S$  with multiple cumulative types of radioactive emissions  $i$  contributing to the absorbed dose in a  $r_T$  (e.g. one image target voxel surrounded by several image source voxels). If we consider one source, the standard, time-independent MIRD equation when the mass of the source and target regions remain constant over the period of irradiation,  $T_D$ , can be given by Equation 1.20 (Bolch et al., 2009).

$$\begin{aligned}\bar{D}_{absorbed}(r_T \leftarrow r_S, T_D) &= \tilde{A}(r_S, T_D) \times \sum_i \Delta_i \times \frac{\Phi_i(r_T \leftarrow r_S)}{M_{r_T}} \\ &= \tilde{A}(r_S, T_D) \times \sum_i \Delta_i \times \Phi_i(r_T \leftarrow r_S) \\ &= \tilde{A}(r_S, T_D) \times S(r_T \leftarrow r_S)\end{aligned}\quad (1.20)$$

where  $S(r_T \leftarrow r_S)$  is the  $S$ -value for all types of irradiation combined. Therefore, an  $S$ -value summarises the complex radiation-matter interactions in  $r_T$ , and describes the resulting absorbed dose in  $r_T$  per nuclear decay in  $r_S$ .

To account for more than one  $r_S$  contributing to absorbed dose in one  $r_T$ , individual source contributions to the target absorbed doses can be cumulated, as expressed in Equation 1.21.

$$\begin{aligned}\bar{D}_{absorbed}(r_T, T_D) &= \sum_{r_S} \bar{D}_{absorbed}(r_T \leftarrow r_S, T_D) \\ &= \sum_{r_S} \tilde{A}(r_S, T_D) \times S(r_T \leftarrow r_S)\end{aligned}\quad (1.21)$$

Furthermore, the previous equation can also be expressed as the mean absorbed dose to  $r_T$  per unit administered activity like in Equation 1.19, termed  $\bar{d}_{absorbed}(r_T, T_D)$  becoming Equation 1.22.

$$\bar{d}_{absorbed}(r_T, T_D) = \sum_{r_S} \tilde{a}(r_S, T_D) \times S(r_T \leftarrow r_S)\quad (1.22)$$

### 1.6.3.3 Data availability for MIRD organ-based calculations

Data including absorbed fractions, specific absorbed fractions and  $S$ -values for absorbed dose calculations using the MIRD formulae can be found in several publications from the MIRD committee (Snyder et al., 1975a,b). Published data tables were obtained by Monte Carlo simulations using several computational phantoms. These phantoms represent reference individuals of a given age, sex, total-body mass, and height to model different target and source organs (also sub-organs, voxels from SPECT/PET images or at the cellular level). Data values are for several radionuclides, types and energy of particles emitted (Petoussi-Henss et al., 2007; Divoli et al., 2009; Eckerman, 2008). The most widely used Monte Carlo codes for the generation of the data tables are Electron Gamma Shower (EGS), FLUK-tuierende KAskade (FLUKA), GATE, GEometry ANd Tracking 4 (Geant4), Monte Carlo N-Particle (MNCP) and PENetration and Energy LOss of Positrons and Electrons (PENELOPE) (Chauvin et al., 2020).

Using the MIRD compilation data tables, absorbed dose calculation is simplified and the user has only to provide the  $\tilde{A}(r_S)$  (Equation 1.21) or  $\tilde{a}(r_S)$  (Equation 1.22).

A dataset for 7 different radionuclides and 13 different voxel sizes was provided by Lanconelli et al. (2012). The OpenDose collaboration<sup>7</sup> by Chauvin et al. (2020) facilitates the practice of dosimetry in nuclear medicine by providing the  $\Phi_i(r_T \leftarrow r_S)$  and  $S(r_T \leftarrow r_S)$  since 2019 and are implementing a module named Slicer3D<sup>8</sup>, which performs full 3D dosimetry for molecular radiotherapy procedures using multiple time point 3D datasets, using either SPECT/CT or PET/CT.

We described in the previous sections the compartmental source contribution to target organs or sub-organ tissues for the estimation of absorbed dose in TRT. The voxelised concept is detailed in Sections 1.6.4 and 1.6.6, where dose kernels extend the MIRD formalism.

#### 1.6.4 Voxel $S$ -values convolution approach

Absorbed dose calculation by the voxel  $S$ -value (VSV) convolution approach is performed following the MIRD formalism at the voxel level from PET and SPECT images (Bolch et al., 1999; Pacilio et al., 2009; Reiner, Blaickner, and Rattay, 2009; Dieudonné et al., 2010; Fernández et al., 2013; Pacilio et al., 2015). Model-based  $S$ -values and voxel-based absorbed dose kernels follow the same principle, since in both cases the absorbed dose to a specified  $r_T$  is calculated as the superposition of the radiation contributions from each  $r_S$ .

Dieudonné et al. (2010) presented a revised VSV approach for dosimetry in TRT. VSVs at a fine resolution were generated using the Monte Carlo N-Particle extended (MNCPIX) and the radionuclide decay schemes for 9 radionuclides including  $^{18}\text{F}$ ,  $^{90}\text{Y}$ ,  $^{99m}\text{Tc}$ ,  $^{111}\text{In}$ ,  $^{123}\text{I}$ ,  $^{131}\text{I}$ ,  $^{177}\text{Lu}$ ,  $^{186}\text{Re}$  and  $^{201}\text{Tl}$  published by Eckerman and Endo (2007). Several assumptions and approximations were made to make a compromise between the calculation time and absorbed dose accuracy. For electrons, the fine-resolution VSV matrix was set to 0.5 mm, whereas for photons, it was set to 1.0 mm. Other assumptions made are the bremsstrahlung photons contribute negligibly to the dose matrix and the VSV kernels were generated for an array distance up to the continuous slowing down approximation (CSDA) range of the most energetic electron particle in the decay scheme for each radionuclide. For photons, VSVs were calculated with the direct Monte Carlo approach, out to a distance for which the angular dependence of the VSV becomes negligible. Beyond this distance, VSVs were calculated using the PK approach (Dieudonné et al., 2010). The VSVs calculated in their study had sufficient histories to provide an uncertainty below 1% within the fine resolution VSV matrices.

A resampling algorithm is then used to obtain the desired VSV matrix defined by the SPECT or PET image resolution from the isotropic fine resolution VSV matrix using necessary interpolations. After the resampling step, the VSVs are generated at the appropriate voxel size and can be used using the MIRD principle, for which the average absorbed dose to a target voxel  $r_T$  resulting from the contributions of itself and each surrounding source voxel  $r_S$  can be calculated using Equation 1.21. The equation can then be implemented by a discrete convolution using fast Hartley transform<sup>9</sup>, where the VSV matrix, computed for a given radionuclide and voxel dimensions, is used as kernel to convolve the cumulated activity map from SPECT or PET images, and obtain the average absorbed dose for each voxel of the cumulated activity map.

7. See [The OpenDose collaboration website](#)

8. See [Github: OpenDose Slicer3D](#)

9. See [Wikipedia/Hartley Transform](#)

The VSV convolution approach could be regarded as approximating a continuous spatial distribution of point sources (Lanconelli et al., 2012; Götz et al., 2019), described in the next Section 1.6.6, the advantage being that the size of the voxel can be chosen arbitrarily, since the kernel can be scaled (Reiner, Blaickner, and Rattay, 2009; Dieudonné et al., 2010; Fernández et al., 2013; Pacilio et al., 2015).

### 1.6.5 Local deposition method approach

The LDM is a simplified alternative for absorbed dose calculation in internal radiotherapy to Monte Carlo simulations and VSV convolution. It is an analytic method where all the emitted energy is assumed to be absorbed within the voxel where decay occurred. This method is relevant when the size of the target tissue (or voxel) is significantly larger than the particle range in tissue, e.g. for  $\alpha$ -particles having short ranges (50-100  $\mu\text{m}$ ) and high linear energy transfer (LET) (30-300  $\text{keV}\cdot\mu\text{m}^{-1}$ ) (Eckerman and Endo, 2007; Marcatili, 2015). The paths associated with the electronic emissions of most of the isotopes used in TRT are often less than the spatial samplings in SPECT (4-10 mm) and PET (3-4 mm) imaging. Therefore, the absorbed fraction  $\phi_i(r_T \leftarrow r_S)$  tends to one and Equation 1.20 can be simply expressed as

$$\begin{aligned}\bar{D}_{absorbed}(r_T) &= \tilde{A}(r_S) \times \sum_i \Delta_i \times \frac{1}{M_{r_T}} \\ &= \frac{A_0}{M_{r_T}} \times \frac{T_{1/2}}{\ln(2)} \times \sum_i \Delta_i \\ &= \frac{A_0}{M_{r_T}} \times C\end{aligned}\quad (1.23)$$

where the constant  $C$  equals to  $49.7 \text{ Gy}\cdot\text{kg}\cdot\text{GBq}^{-1}$  for  $^{90}\text{Y}$  decay (Dieudonné et al., 2011) and equals to  $15.87 \text{ Gy}\cdot\text{kg}\cdot\text{GBq}^{-1}$  for  $^{166}\text{Ho}$ . The  $C$  coefficient is dependant of the isotope and no clearance of the radiopharmaceutical is assumed.

The LDM is therefore a fast analytical method which does not require much computing power by multiplying each image voxel by a constant coefficient from the MIRD database, knowing the initial activity and the mass of the voxel for a specific radionuclide (Eckerman and Endo, 2007).

### 1.6.6 Dose point kernel approach

The dose point kernel (DPK) is an alternative absorbed dose calculation method. A DPK represents the radial distribution of the mean absorbed dose around an isotropic point source of radiation or interaction point embedded in an infinite homogeneous transport medium (Bochkarev et al., 1972; Bolch et al., 1999; Bardiès, Kwok, and Sgouros, 2002; Pérez et al., 2011). Figure 1.10 outlines the elementary definition of a DPK representing the mean absorbed dose per unit distance around a point source. The energy emitted from the center and absorbed between each consecutive spherical concentric shell to the source is scored and divided by the mass between them to give the absorbed dose.

A DPK can be calculated either for a monoenergetic electron or photon source of radiation (e.g. for calculation of absorbed dose in external radiotherapy or a beta ( $\beta^-/\beta^+$ ) or gamma ( $\gamma$ ) decay emission spectra for a specific radionuclide (e.g. in TRT). A DPK in TRT is therefore dependant on the medium and the emission types

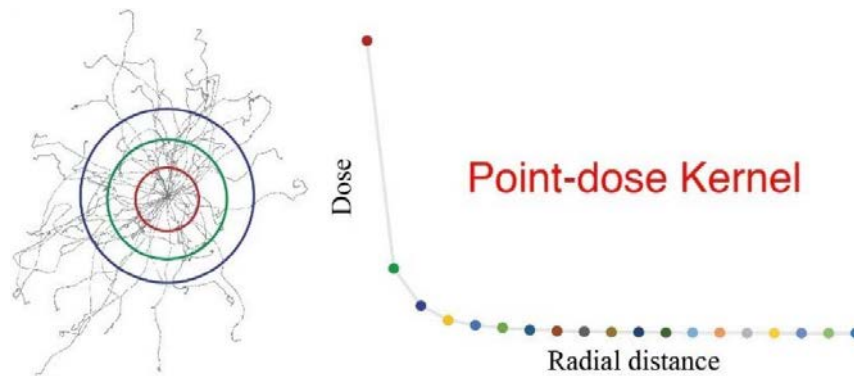


FIGURE 1.10 – Simple representations of a DPK.

from the radioactive source and suitable kernel databases over a wide range of configurations are required for computing absorbed dose distributions, for each type and energy of  $\beta^-$ ,  $\beta^+$  and  $\gamma$  particle emissions in a specific transport medium density.

Electrons emitted from isotopes dominates self-organ absorbed dose but the photon contribution to adjacent organs should not be neglected. Several models are used for the calculation of DPKs, based on the CSDA for electrons in terms of Monte Carlo-based stopping power information (*NIST: Description of the ESTAR database; NIST stopping-power and range tables: Electrons, protons, and helium ions*), e.g. as described following Equation 1.24.

$$DPK(x, E_0) = 4\pi r^2 \times R_{CSDA} \times \Phi(r, E_0) \quad (1.24)$$

where  $E_0$  is the energy of the corresponding monoenergetic point source,  $R_{CSDA}$  is CSDA electron range,  $r$  is the radial distance travelled by the electron,  $x$  represents the scaled distance given by  $r/R_{CSDA}$  and  $\Phi(r, E_0)$  is the specific absorbed fraction given this time by  $S(E(r))/4\pi r^2 E_0$  with  $S(E(r))$  being the stopping power function (Scarinci, Valente, and Pérez, 2013).

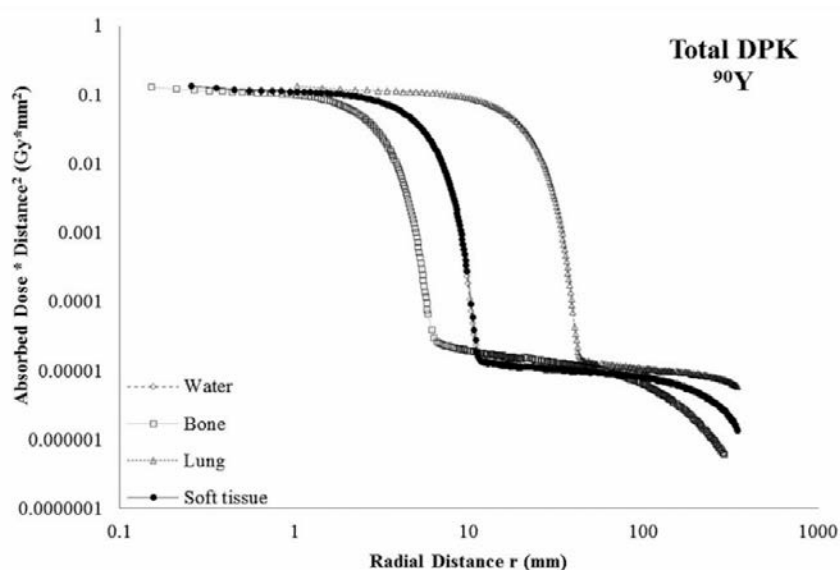


FIGURE 1.11 – Total DPKs for  $^{90}\text{Y}$  using GATE (Papadimitroulas et al., 2012).

Once suitable DPKs are calculated, as shown in Figure 1.11 for  $^{90}\text{Y}$ , if one considers the activity within the source region as a discrete 3D grid of point sources, the absorbed dose at a target point is a superposition of contributions from all DPKs surrounding this target point. The  $\bar{D}_{absorbed}(r)$  at any location  $\vec{r}$  can be calculated by the convolution of the cumulated activity input geometrical term  $\tilde{A}(\vec{r})$  by the input physical  $DPK(\vec{r})$  term as described in Equation 1.25

$$\bar{D}_{absorbed}(r) = DPK(\vec{r}) * \tilde{A}(\vec{r}) \quad (1.25)$$

This convolution is a time-consuming mathematical process and therefore, considering discrete voxels, Equation 1.25 to calculate  $\bar{D}_{absorbed}(r)$  can be written as Equation 1.26 using Fourier transforms.

$$\bar{D}_{absorbed}(i, j, k) = \mathcal{F}^{-1}\{\mathcal{F}\{DPK(i, j, k)\} \cdot \mathcal{F}\{\tilde{A}(i, j, k)\}\} \quad (1.26)$$

where  $\mathcal{F}$  and  $\mathcal{F}^{-1}$  are the discrete operators for Fourier transforms representing the forward and inverse Fourier transforms, respectively. Indices  $i, j$  and  $k$  are the 3D indices of the PET or SPECT input images. Fast Fourier or fast Hartley transforms can be used to solve the operation in Equation 1.26 and increase the computational speed, as in the VSV convolution approach.

Figure 1.12 summarises the steps in calculating absorbed doses from DPK functions and voxelised cumulated activity maps, adapted from Peer-Firozjahi et al. (2021), describing the different steps mentioned above.

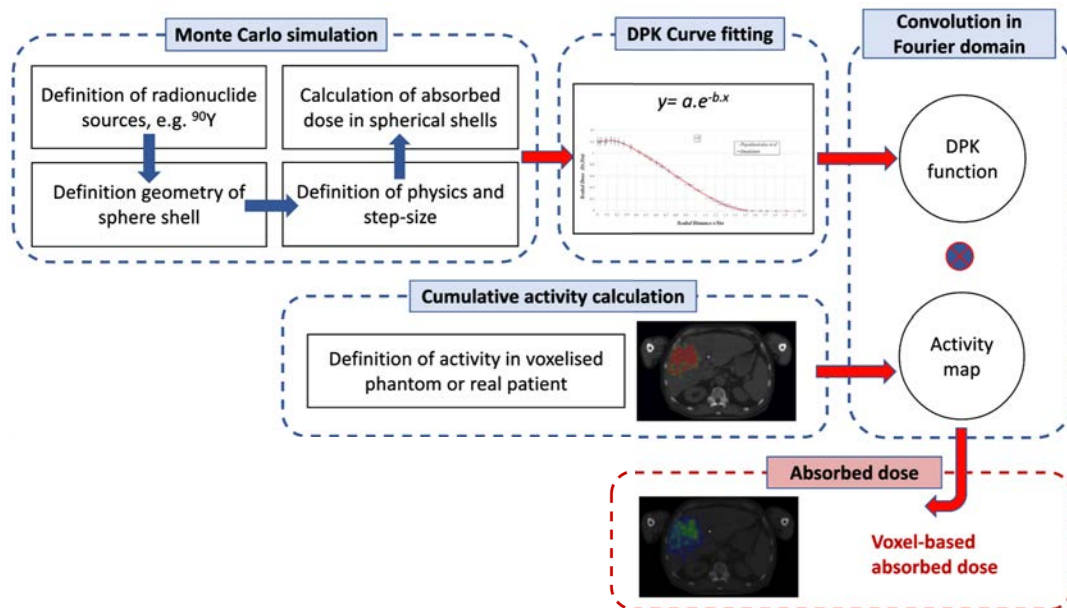


FIGURE 1.12 – Sequence diagram of absorbed dose computation by means of DPK. Adapted from Peer-Firozjahi et al. (2021).

Several evaluations and datasets of DPKs have been calculated and published by several authors for electrons, photons,  $\beta$  and  $\gamma$  emitting isotopes, using many Monte Carlo codes including MNCP, EGS, FLUKA, Electron TRANsport (ETRAN), Geant4, PENELOPE and GATE (Uusijärvi et al., 2009; Botta et al., 2011; Papadimitroulas et al., 2012; Peer-Firozjahi et al., 2021). Figure 1.11 depicts total DPKs where the whole isotope spectrum is simulated considering all possible interaction mechanisms for  $^{90}\text{Y}$  in GATE in different media from a study by Papadimitroulas et al. (2012). The study also includes total DPKs for  $^{67}\text{Ga}$ ,  $^{68}\text{Ga}$ ,  $^{99m}\text{Tc}$ ,  $^{111}\text{In}$ ,  $^{124}\text{I}$ ,  $^{125}\text{I}$ ,  $^{153}\text{Sm}$ ,  $^{177}\text{Lu}$ ,

$^{186}\text{Re}$  and  $^{188}\text{Re}$ . For further reading, a recent study from Götz et al. (2021) used neural network (NN) to generate DPKs and provided satisfactory results compared to Monte Carlo simulations.

### 1.6.7 Clinical softwares for absorbed dose calculation

A number of 3D software tools can take the distribution of  $^{99m}\text{Tc}$ -MAA or  $^{90}\text{Y}$  microspheres for a given patient (from SPECT or PET) and combine it with anatomical information (from CT or MRI) to produce absorbed dose estimates. Of those (among others) are PLANET®Dose/DOSIsoft, Simplicit $^{90}\text{Y}$ ™/Mirada and SurePlan™ LiverY90/MIM software. The first one has been mostly used for absorbed dose calculations during this thesis.

## 1.7 Limitations and perspectives

*Differences in medical devices.* Glass and resin microspheres for  $^{90}\text{Y}$ -SIRT are useful devices in the treatment of patients with unresectable liver cancer. Glass microspheres have been found to have a lower incidence of gastrointestinal and pulmonary adverse events in the treatment of HCC than resin microspheres (Kallini et al., 2017). This might be due to the specific activity difference between the devices, requiring more microspheres for an equivalent activity using resin microspheres, besides being made of different materials, see Table 1.1. Their radiobiological properties may also differ (Garin et al., 2016). Furthermore, conditions and practices vary widely from institution to institution, and results differ depending on the “learning curve” and experience of the operator.

*Prediction using  $^{99m}\text{Tc}$ -MAA and dosimetric approach.* MAA particles are biodegradable compared to microspheres which are not. Their sizes are not well controlled, estimated to range from 10 to 100  $\mu\text{m}$ . Furthermore, difficulties might arise with uncertainties in the labelling of MAA particles and it is recommended to perform imaging shortly after injection (De Gersem et al., 2013), to limit the presence of free  $^{99m}\text{Tc}$  particles in other organs and high LSF which might contraindicate SIRT treatment. The risk of embolic effects associated with the use of resin microspheres, as mentioned in the previous paragraph, may therefore mean that the dosimetric assessment based on the MAA may be inaccurate. Other confounding factors are discussed by Garin et al. (2016), including tumor type, size and vascularisation, prior therapy, reproducibility of injection of MAA during workup and microspheres in the treatment phase, among others. Despite the limitations, predictive dosimetry using  $^{99m}\text{Tc}$ -MAA is the only readily available tool for use that can have a direct impact on the treatment plan. Several studies found a strong correlation between the predictive  $^{99m}\text{Tc}$ -MAA dosimetry to the post-treatment monitoring dosimetry (Kao et al., 2013a). This is further discussed in Chapter 6 in the contributions made during this thesis.

*Emission tomography imaging.* SPECT/CT, PET/CT or planar scintigraphy imaging modalities are of key importance to internal radiation therapy. They allow in the case of SIRT the planning and monitoring of treatment although they present inherent and intrinsic performance weaknesses, such as spatial resolution (among

TABLE 1.2 – Comparison of algorithms. Adapted from Huizing, Verheij, Stokkel, et al. (2018) and others (Dieudonné et al., 2010; Lanconelli et al., 2012; Götz et al., 2019)

Method	Assumptions	Advances	Drawbacks	Clinical application
<b>Monte Carlo simulations</b>	Simulation of a certain number of particles. Manual particle energy cut-off values.	Very accurate, handles tissue density heterogeneities, non-uniform source distributions and cross-fire dose.	Many simulation parameters. Long-calculation times.	Not applicable for clinical routine. Calculation of <i>S-values</i> and dose kernels.
<b>Organ-based <i>S-values</i></b>	Homogeneous radioactivity distribution in tissue.	Fast, easy, commonly used and generally accepted. Tabulated pre-calculated <i>S-values</i> available, calculated from Monte Carlo simulations.	Based on reference phantoms. Spatial variations in the distribution of radioactivity, tissue composition and hence absorbed dose within the macroscopic volumes $r_S$ and $r_T$ are not considered.	Organs and lesions without superimposition. Toxicity studies.
<b>Voxel <i>S-values</i></b>	Homogeneous radioactivity distribution within one voxel. Discrete and finite-sized voxel kernel.	Rapid computation and still-good dosimetric accuracy. Not requiring volume integrations of the DPK over sources and target. Kernels can be scaled to arbitrary voxel sizes. DVH and isodose lines. Patient specific.	Calculated for each radionuclide and given configuration of voxel geometry and dimensions. Not always feasible for clinicians to perform dedicated Monte Carlo simulations to derive <i>S-values</i> . Difficulties to account for absorbed dose stemming from $\gamma$ -radiation.	Most applied concept in clinic. Comply to the familiar MIRD formalism. Patient specific voxel-based tumour and normal tissue dosimetry.
<b>Dose point kernels</b>	Homogeneous radioactivity distribution within one voxel.	Rapid computation and still-good dosimetric accuracy. DVH and isodose lines. Patient specific.	Radionuclide-specific, determined for specific tissues. Mean absorbed dose per voxel.	Patient specific voxel-based tumour and normal tissue dosimetry.
<b>Local energy deposition</b>	All energy is absorbed in the source voxel.	Rapid computation. DVH and isodose lines. Patient specific.	Not suitable for photons.	Primarily for $\beta$ - and $\alpha$ emitters.



others) limited to several millimetres which might limit image interpretation. However, confounding factors can be quantified in emission tomography and where possible corrected for. Issues related to PET imaging are detailed in Chapter 2. PET and SPECT imaging can provide quantitative activity data in voxels of several millimeters in size. For smaller voxel sizes (sub-millimetric), it is currently impossible to obtain accurate data with the existing imaging technology. For sub-millimetric scales, autoradiographic methods can be used when tissue is obtained by biopsy or autopsy (Bolch et al., 1999).

**Physical absorbed dose calculation methods.** Table 1.2 provides a comparison for absorbed dose calculation methods. Voxel-based absorbed dose estimations are only appropriate for radionuclides which predominantly emit massive particles of short range in tissue.  $^{90}\text{Y}$  is considered, being a  $\beta^-$ -emitter whose electrons have an  $r_{\text{mean}}$  of 2.5 mm in tissue. One limitation of voxel-based absorbed dose estimations is the compromise between high spatial resolution and estimation of absorbed dose contributions stemming from  $\gamma$ -radiation, see Götz et al. (2019). Also, very few studies adapt their research for heterogeneity in tissue composition. Dieudonné et al. (2013) suggested a simple density-correction method when using voxel *S-values*, compared to reference Monte Carlo simulations, but presented only 3 patient cases. Khazae Moghadam et al. (2016) suggested another technique considering tissue-specific absorbed dose kernels using GATE, but was not tested on real patient data. A recent patient ( $n = 26$ ) study from Götz et al. (2019) for  $^{177}\text{Lu}$  radionuclide therapies using four different voxel-based methods (and compared to Monte Carlo simulations) demonstrated that no adaptation for voxel kernels was required when considering soft-tissues, which might be the case of absorbed dose calculation in the liver following SIRT. However, for high (bone) and low (lung) density tissues, adaptation of the absorbed dose kernel provided better agreement to the Monte Carlo simulations. Götz et al. (2021) further conducted their studies to predict voxel kernels using a NN, which yielded superior results compared to standard method.

**Radiobiology perspectives towards EBRT approaches.** Cell irradiation between TRT and *conventional* External beam radiation therapy (EBRT) differ due to (1) a much lower absorbed dose rate in TRT (cells have more time to repair), (2) high heterogeneity of irradiation at cellular level in TRT (homogeneous in EBRT) and (3) unlabelled cytotoxicity associated with the radiopharmaceutical which needs to be considered (Marcatili, 2015). Therefore, the assumption of proportionality between radiation-induced biological effects and delivered absorbed dose is not straightforward for TRT as in EBRT. SIRT and EBRT are therefore different from a radiobiological point of view, and 1 Gy using both techniques will not produce the same radiobiological disorder (Garin et al., 2016). In addition, the radiobiological properties of resin and glass microspheres are also believed to differ, due to differences in specific activity and the quantity of injected spheres. Walrand et al. (2014) suggest that implementation of the physiological model of the arterial tree including a microsphere transport model will further enhance the understanding of microsphere efficiency.

**Vascular and other considerations towards  $^{90}\text{Y}$ -SIRT.** Taebi et al. (2020) used Computational fluid dynamics (CFD) and CBCT input images (for hepatic arterial tree segmentation) to simulate the blood flow in the hepatic artery for the prediction and optimisation of the distribution of  $^{90}\text{Y}$  microspheres by maximising tumour targeting, as an alternative of using surrogate  $^{99m}\text{Tc}$ -MAA. They developed a new

dosimetry approach for personalised treatment planning called CFDose (Roncali et al., 2020) making use of CFD to predict the heterogeneous distribution of  $^{90}\text{Y}$  microspheres, based on careful choice of patient-specific parameters and conditions for the simulations. The suggested method might provide a more realistic and personalised dosimetry for effective radioembolization treatment (Taebi, Vu, and Roncali, 2021).

## 1.8 Conclusion

$^{90}\text{Y}$ -radioembolisation requires the use of several imaging techniques in order to plan, deliver and monitor the treatment. Several methods exist for prescribing microsphere activity and recommendations have recently been published by Salem et al. (2019) and Levillain et al. (2021) in order to best tailor the treatment to each patient for each type of microsphere. The use of SPECT/CT for the pre-treatment as well as PET/CT for the follow-up of the treatment procedures are crucial to personalise the treatment (Garin et al., 2021). Emphasis on PET/CT imaging is made in the next chapter, being studied in this thesis for  $^{90}\text{Y}$ -radioembolisation.



## Chapter 2

# Positron emission tomography

Major progress has been made in recent years in PET imaging. In addition to the improved accuracy in interaction position and signal-to-noise ratio (SNR) gain by the incorporation of TOF information in tomographic reconstruction, significant developments with the emergence of SiPM technology and faster electronics allow more efficient coincidence detection capabilities. SiPMs provide supplementary benefits, enhancing the role of PET in the diagnosis and staging of human diseases.

Indeed, SiPM for photon detection has recently superseded the conventional photo-multiplier tube (PMT) owing to the practical limits of the latter, which provide an improved TOF resolution and thus better precision on the location of the  $\beta^+$  annihilation. Most latest commercialised and still-prototype systems being developed today are being equipped with SiPM technologies. Furthermore, a major step forward has been taken with the installation of the first clinical and commercial extended field-of-view (eFOV) whole-body PET in 2020<sup>1</sup> (Alberts et al., 2021), featuring a 1 metre compared to traditional 15-30 centimetres long axial field-of-view (FOV)s, besides being SiPM-equipped. Benefiting from larger solid angles for detection, PET therefore provides an even more fortifying technology and impact in clinical use. Future directions promise substantial progress with reduced radiation dose to patients for diagnostic, reduced acquisition durations improving patient comfort and at the same time permitting dynamic image acquisitions with eFOV systems.

A quest for a 10 picoseconds timing resolution<sup>2</sup> has also been launched, which may allow PET technology to bypass the use of reconstruction algorithms (Lecoq, 2017; Lecoq et al., 2020) which add further bias on quantitative data independent of PET performance. Indeed, the TOF information alone will be enough to obtain an activity concentration distribution with an improved timing resolution and subsequently spatial resolution.

PET seems therefore to remain the most sensitive functional imaging modality in nuclear medicine allowing to visualise the metabolism of cells and organs, as apposed to the morphological CT or MRI which allow the anatomy to be imaged with good spatial resolution. Today, all PET systems are readily equipped with a CT (or MRI) that provides additional information to help locate functional abnormalities more accurately, with photon attenuation (CTAC) and partial-volume effect (PVE) corrections.

This chapter provides a state-of-the-art on the intrinsic positron emission and PET physics, the related novel technologies, from the PMT to newer SiPM implementations. The bias added on the accuracy of coincidence detection and the confounding factors that affect spatial resolution are detailed, as well as a short description of the reconstruction algorithms used in the clinic.

1. The Biograph Vision Quadra™ installed in Bern (Switzerland)
2. See [the 10 ps challenge website](#)

## 2.1 Radionuclides used in PET

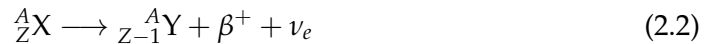
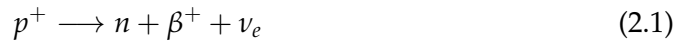
PET imaging benefits before anything else from the physics of positron ( $\beta^+$  or  $e^+$ ) emitting isotopes. The properties of a list of radionuclides used in PET are presented in Table 2.1. Many of the most used emitters have short half lives ( $T_{1/2}$ ), e.g.  $^{15}\text{O}$  and  $^{13}\text{N}$ , hence restraining their use in research or hospitals to the availability of an on-site or nearby-site cyclotron<sup>3</sup>. It is also possible to produce isotopes using generators, e.g.  $^{68}\text{Ge}/^{68}\text{Ga}$  and  $^{82}\text{Sr}/^{82}\text{Rb}$  generators (Knapp and Mirzadeh, 1994; Dash and Chakravarty, 2019).

$^{90}\text{Y}$  which is the isotope of interest for this thesis, is however a pure  $\beta^-$  emitter, meaning that it decays by emitting 100% electrons and no positrons. Nevertheless,  $^{90}\text{Y}$  decays to an excited state of  $^{90}\text{Zr}$  which in turn emits positrons by a monopole transition to the stable state, with possible detection of annihilation photons by PET. The  $^{90}\text{Y}$  physics will be detailed in Chapter 3. For the record, the primary intent of using  $^{90}\text{Y}$  is for treatment purposes, exploiting medical imaging for treatment monitoring. Once positrons are emitted, the physics of annihilation and detection remain the same as outlined in the following parts of this current chapter.

## 2.2 Beta-plus ( $\beta^+$ ) decay

### 2.2.1 Positron emission

The positron ( $e^+$ ) is the antiparticle of the electron ( $e^-$ ). They have similar masses but differ in that a positron has positive electric charge, whilst an electron has a negative charge. Positrons are emitted by the  $\beta^+$  nuclear decay process from unstable nuclei which have an excess of protons ( $p$ ), thus  $\beta^+$  emission is mediated by the weak interaction<sup>4</sup>. Fundamentally, a proton in the nucleus of the atom is transformed into a neutron ( $n$ ) and a positron as shown in Equations 2.1 and 2.2, the second being generic for any decaying parent isotope  $^A_Z\text{X}$  to its daughter product  $^A_{Z-1}\text{Y}$ , and the atom regains its nuclear stability.



The positron is ejected from the nucleus accompanied by a neutrino ( $\nu_e$ ). Examples of radionuclides which emit  $\beta^+$  radiation are  $^{18}\text{F}$  and  $^{15}\text{O}$ , which decay to  $^{18}\text{O}$  and  $^{15}\text{N}$ , see Equations 2.3 and 2.4, respectively.



According to the Einstein's theory of relativity, the energy balance following the  $\beta^+$  decay of any  $^A_Z\text{X}$  can be given by Equation 2.5.

$$Q_{\beta^+} = (m_{^A_Z\text{X}} - m_{^A_{Z-1}\text{Y}} - m_{\beta^+}) \cdot c^2 \quad (2.5)$$

3. See [Wikipedia/Cyclotron](#)

4. See [Wikipedia/Weak interaction](#)

TABLE 2.1 – Positron emitters used in PET imaging.

Atom	$T_{half}$ (min)	$\beta^+$ branching ratio (%)	$E_{max,\beta^+}$ (MeV) ( $R_{max,\beta^+}$ (mm))	$E_{mean,\beta^+}$ (MeV) ( $R_{mean,\beta^+}$ (mm))	$\gamma$ branching ratio (%)	$E_{mean,\gamma}$ (MeV)	Production mode	Purposes
<b>Pure beta+ emitters</b>								
$^{11}\text{C}$	20.4	99.8	0.960 (4.2)	0.386 (1.2)	-	-	Cyclotron	Parkinson diseases. Cerebral neoplasia. Cardiology.
$^{13}\text{N}$	10	99.8	1.119 (5.5)	0.492 (1.8)	-	-	Cyclotron	Myocardial blood flow.
$^{15}\text{O}$	2.0	99.9	1.732 (8.4)	0.735 (3.0)	-	-	Cyclotron	Blood flow.
$^{18}\text{F}$	110	96.9	0.634 (2.4)	0.250 (0.6)	-	-	Cyclotron	Glucose metabolism in tumours and tissue. Most sensitive diagnosis method. Many applications.
$^{22}\text{Na}$	2.6 (years)	90.3	1820.2 (2.28)	220.3(0.53)	-	-	-	Point sources for daily PET calibration.
$^{62}\text{Cu}$	9.74	97.0	2.93 (-)	-	-	-	Generator (from $^{62}\text{Zn}$ )	Myocardial and cerebral perfusion
$^{64}\text{Cu}$	762	17.5	0.653 (2.5)	0.216 (0.7)	-	-	Cyclotron	Theranostic agent for malignancies.
$^{89}\text{Zr}$	4704	22.7	0.902 (3.8)	0.396 (1.3)	-	-	Cyclotron	Slow pharmacokinetics visualisation.
<b>Non-pure beta+ emitters</b>								
$^{68}\text{Ga}$	67.8	87.7 1.2	1.899 (-) 0.821 (-)	-	3.2	1.077	Generator (from $^{68}\text{Ge}$ )	Cardiac diseases.
$^{76}\text{Br}$	972	25.8 6.3	3.382 (-) 0.871 (-)	-	74.0 15.9	0.559 0.657	Cyclotron	Measurement of cell proliferation
$^{82}\text{Rb}$	1.3	81.8 13.1	3.378 (-) 2.601 (-)	-	15.1	0.777	Generator (from $^{82}\text{Sr}$ )	Cardiac diseases
$^{86}\text{Y}$	882	11.9 5.6	1.221 (-) 1.545 (-)	-	82.5 32.6	1.077 0.627	Cyclotron	Radionuclide pair $^{90}\text{Y}/^{86}\text{Y}$
$^{124}\text{I}$	6012	11.7 10.7	1.535 (-) 2.138 (-)	-	62.9 11.2	0.602 1.691	Cyclotron	Potential use for thyroid disease, cardiovascular imaging and dosimetry of malignant diseases.
<b>Isotope of interest for this thesis (<math>\beta^-</math>) emitter</b>								
$^{90}\text{Y}^+$	3841	$3.86 \times 10^{-6}$	739 (-)	-	-	-	Seperation from its parent isotope $^{90}\text{Sr}$	Theranostics. SPECT/PET treatment monitoring

$^{90}\text{Y}$  properties are also reported for comparison purposes, although being a pure  $\beta^-$  emitter.

The emitted energy  $Q_{\beta^+}$  is shared between the daughter product  ${}_{Z-1}^AY$  of  ${}_{Z}^AX$ , the  $\beta^+$  and  $\nu_e$  particles. Thus, the positron has a spectrum of energy with varying intensities between minimum 0 and maximum  $Q_{\beta^+}$  MeV, and accordingly, varying mean free paths or range of the positrons in different media, further explained in the following Section 2.2.2.

The positron range distribution differs according to the emitter used, summarised in Table 2.1 as  $E_{mean,\beta^+}$  and  $E_{max,\beta^+}$  for the mean and maximum energies with their corresponding  $R_{mean,\beta^+}$  and  $R_{max,\beta^+}$  ranges in water, respectively.

## 2.2.2 Positron mean free path

Owing to the succession of collisions, the trajectory of the positron is tortuous. The actual total distance travelled by the positron before it thermalises and captures an electron, is therefore much greater than its mean free path, as depicted in Figure 2.1. The positron mean free path or range is defined as the average distance between the emission of the positron and the phenomenon of annihilation. It contributes to one of the inherent physical limitations to the spatial resolution of PET scanners, together with others as further underlined in Section 2.6. An error on the position of annihilation interaction is introduced since the range of the positron on the line-of-response (LOR) is then given by determining the smallest distance separating the LOR and the positron first emission site from nuclear disintegration (the effective positron range), as shown in Figure 2.1.

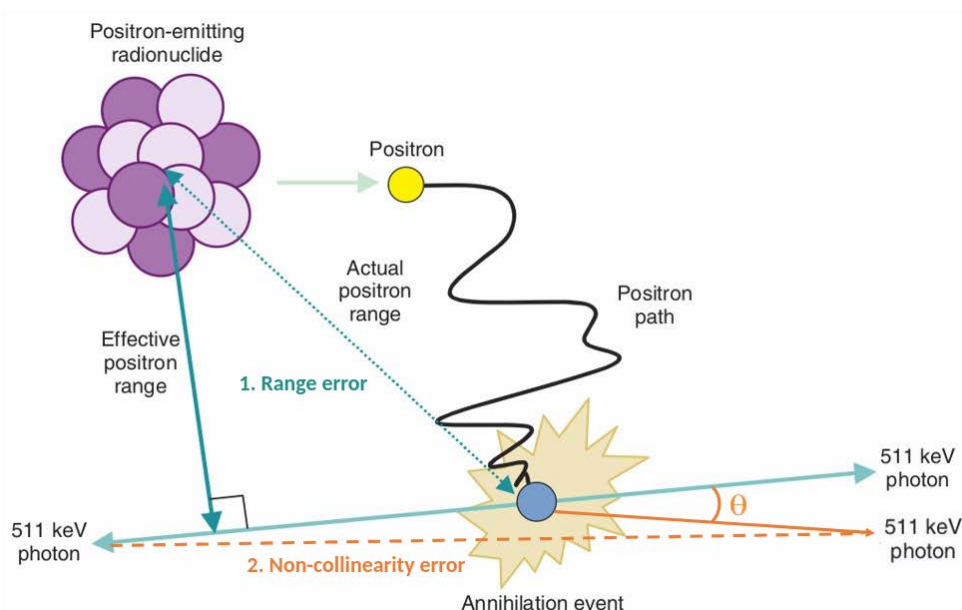


FIGURE 2.1 – Errors related to the positron physics are depicted. 1. Range error (*green*) - the effective range considered is not the actual positron range (mean free path). 2. Non-collinearity error (*orange*) - back-to-back  $\gamma$ s angular uncertainty. Extracted and adapted from Cherry, Sorenson, and Phelps (2012)

The range of positrons in different materials are the main detector-independent contributions to the blurring of PET imaging, and can partly (subsequently) be corrected in image reconstruction, see Section 2.14.2.3, if appropriate estimates are provided. The error becomes more important as the kinetic energy of the positron particle increases, and therefore depends on the isotope considered. Two interesting

figures regarding positron energy and range estimations which can be found in the literature are from Cal-González et al. (2013). The first one, Figure 2.2, depicts the positron range of different  $\beta^+$  emitting isotopes and in different tissue compositions, from the less dense (lungs) to the more dense (cortical bone).

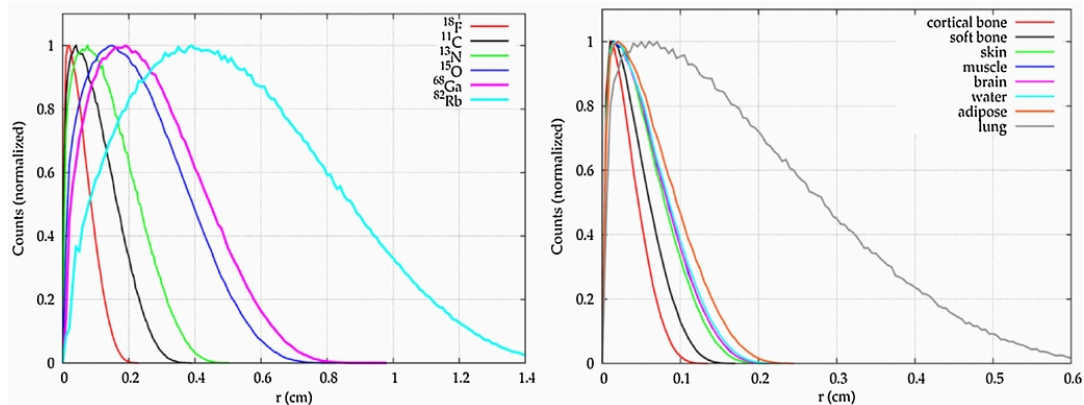


FIGURE 2.2 – The number of annihilations at a given radial distance (3D) from a point source for different  $\beta^+$  emitters, normalised to the same value at the maximum. *Left*: Point sources in water for different isotopes used in PET. *Right*: Point sources for  $^{18}\text{F}$  in different media. Extracted from Cal-González et al. (2013).

The second one, Figure 2.3, depicts the differences in positron ranges for different isotopes and the significant variability amongst previous studies. The differences are probably due to different theoretical energy spectra (e.g. using the Fermi function or others), different simulation models/codes implemented and different platforms used in these different studies. The positron ranges in the study of Cal-González et al. (2013) were estimated using 3D radial distributions by counting the number annihilations per unit distance bin, using the PeneloPET Monte Carlo simulation toolkit (España et al., 2009). For further reading, several other publications can be of reference (Derenzo, 1979; Levin and Hoffman, 1999; Champion and Le Loirec, 2007; Alessio and MacDonald, 2008).

### 2.2.3 Annihilation effect

The positron quickly thermalises after being ejected from the nucleus. As soon as it has thermalised, either it combines directly with an electron of opposite spin being at rest, resulting in a 2 gamma photons (2- $\gamma$ ) annihilation or it may form short lived ( $10^{-7}\text{s}$ ) neutral particles called positronium (the bound state of an electron and a positron). Positronium exist in the form of either para-positronium which results also in a 2- $\gamma$  annihilation, or an ortho-positronium which decays into 3- $\gamma$  (Harpen, 2003). Refer to Section 2.11.2 for a short presentation of ortho-positronium detection, which is out of scope here. Even so, most annihilations in tissue result in a useful 2- $\gamma$  ray emission (Harpen, 2003), which is the basis of PET detection.

The two charged particles ( $e^-$  and  $e^+$ ) being almost at rest during annihilation, the conservation of the mass requires a liberated energy of approximately 1.022 MeV in the form of electromagnetic energy (the 2- $\gamma$ s), following Equation 2.6.

$$E_{2-\gamma} = (m_{e^-} + m_{e^+})c^2 = 1.022 \text{ MeV} \quad (2.6)$$

With the previous assumption ( $e^-$  and  $e^+$  being at rest), the  $E_{2-\gamma}$  is then distributed between the two photons, with 0.511 MeV each. The conservation of the



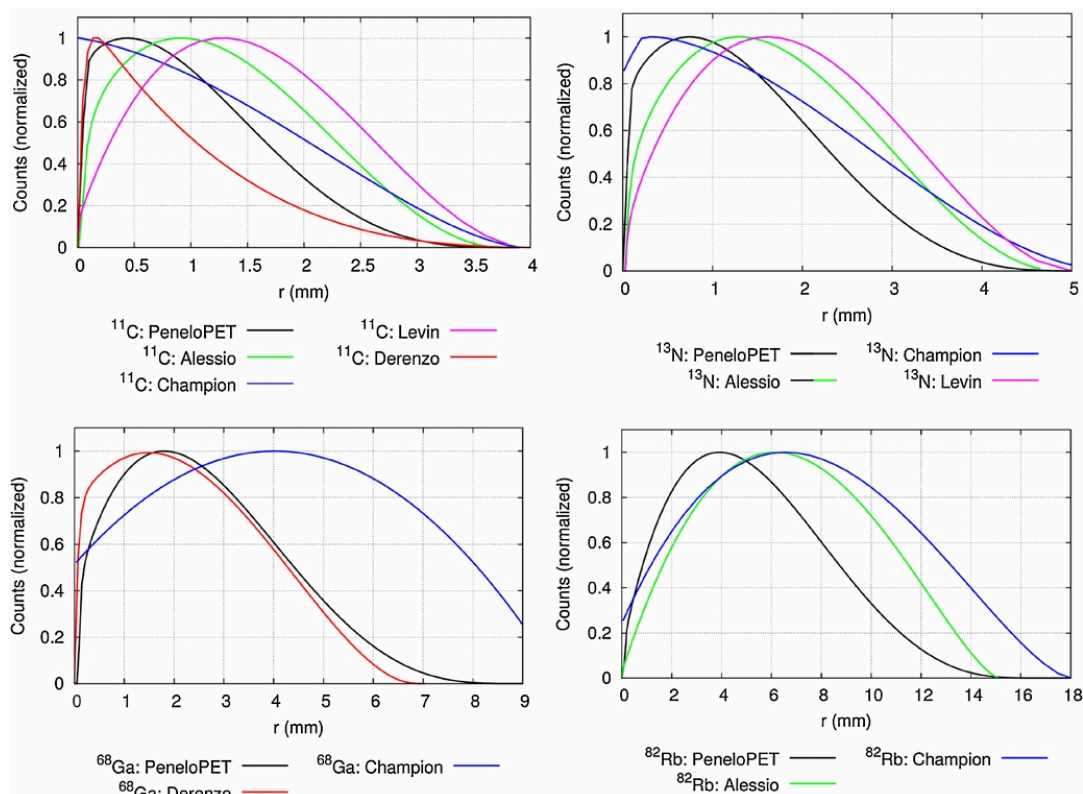


FIGURE 2.3 – Comparison of positron range for different isotopes from different studies. *Top-left*:  $^{11}\text{C}$ , *Top-right*:  $^{13}\text{N}$ , *Bottom-left*:  $^{68}\text{Ga}$  and *Bottom-right*:  $^{82}\text{Rb}$ . Extracted from Cal-González et al. (2013).

momentum requires also that the emission of two collinear photons should be made in opposition to each other, i.e. emitted at  $180^\circ$ , see Figure 2.1. However, this is not perfectly the case, as described in the following section.

## 2.2.4 2- $\gamma$ s non-collinearity

In fact, before annihilation, the positron possesses a kinetic energy, as well as a residual quantity of motion. The energy of each  $\gamma$  photon ( $E_\gamma$ ) is therefore accompanied by an uncertainty,  $0.511 \text{ MeV} \pm \Delta E_\gamma$ , and similarly for the angle ( $\theta$ ) separating them,  $180^\circ \pm \Delta\theta$ . The energy  $\Delta E_\gamma$  and angular  $\Delta\theta$  dispersions when the positron annihilates in water, follow both Gaussian laws with full-width at half-maximum (FWHM)s equal to  $<0.003 \text{ MeV}$  and  $\sim 0.54^\circ$ , respectively (Iwata, Greaves, and Surko, 1997; Shibuya et al., 2007; Tang et al., 2020). Thus,  $\Delta\theta$  constitutes a second intrinsic limit of spatial resolution in PET, together with the positron range as depicted in Figure 2.1. The angular uncertainty leads to a Gaussian blur which is directly proportional to the radial FOV of the PET detector ring (Moses, 2011). On the other hand,  $\Delta E_\gamma$  represents only 0.5% of the 0.511 MeV and can be considered as negligible, given the energy resolutions of current pre-clinical and clinical PET systems, which are around 10% at best. See Table 2.4 for energy resolution information of some actual clinical PET systems.

## 2.3 0.511 MeV $\gamma$ interactions with matter

As a reminder, the definitions of the different interactions of photons in matter are given hereafter. The photoelectric effect and Compton scattering are the two main photonic interactions of interest in PET. Photons do not cause ionisations directly as it happens with the transport of charged particles (which will not be detailed here), but can be classified as secondary ionisation radiation. The most probable interactions of 0.511 MeV photons are depicted in Figure 2.4 (left).

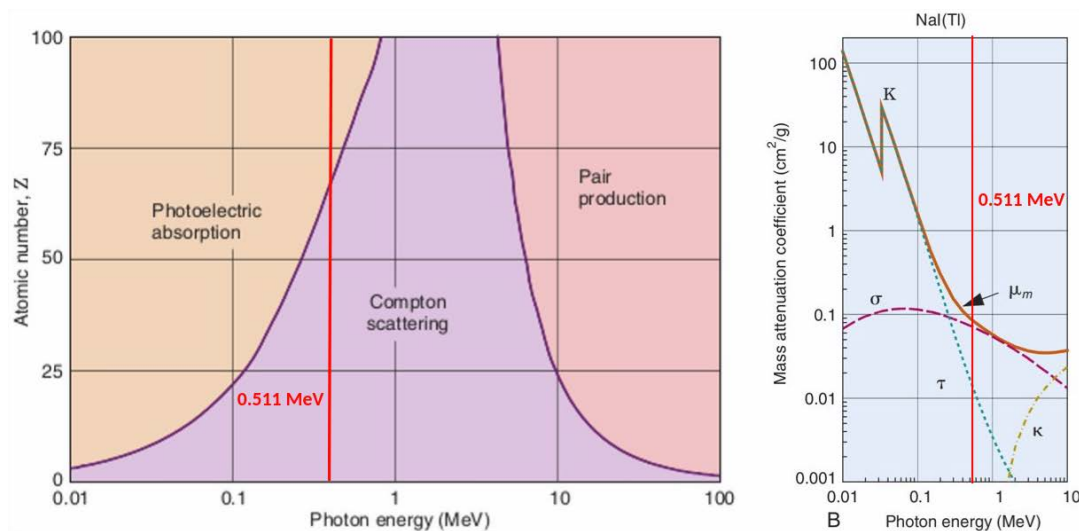


FIGURE 2.4 – *Left*: Most probable interactions of 0.511 MeV photons with varying  $Z$ . *Right*: Example of mass attenuation coefficient for NaI(Tl) crystals. Human soft tissues and bones have an effective  $Z$  around 7 and 14, respectively. Extracted from Cherry, Sorenson, and Phelps (2012) who themselves generated the graph using the [NIST Standard Reference Database](#).

**The photoelectric effect.** The photon undergoes a photoelectric effect when it is completely absorbed by an atom and the totality of its energy transferred to an orbital electron in the inner layers. If the  $E_\gamma$  is greater than the binding energy of the electron, the latter electron gains enough energy and escapes from its orbital (the photoelectron), leaving a vacancy in the inner electron shell. In turn, there is the release of energy (due to an outer layer electron shifting to the vacant inner shell) which can cause the emission of an X-ray fluorescence photon, or transmitted to an atomic electron which will be ejected from the atom, called the Auger electron. The higher the atomic number ( $Z$ ) or effective  $Z$  ( $Z_{eff}$ ) of the medium, the more likely the photoelectric interaction will occur. At 0.511 MeV, this probability is roughly proportional to  $Z^{3 \text{ or } 4}$ ,  $E_\gamma^{-3 \text{ to } -5}$  and varies linearly with the density ( $\rho$ , i.e. the mass per unit volume) of materials.

**Incoherent or Compton scattering.** The photon undergoes an interaction rather with an outer shell orbiting electron, transferring part of its energy (greater than the binding energy) to the electron. This electron is ejected (the recoil electron) and the photon is deflected through a scattering angle with its remaining energy. A clear relationship exists between the  $E_\gamma$  of the scattered photon and the scattering angle  $\theta$  considering laws of conservation of energy and momentum (which will not be detailed here, see Agarwal (1991), Cherry and Dahlbom (2006), and Cherry, Sorenson,

and Phelps (2012)). Since the Compton scattering interaction depends mainly on electrons considered as 'free' with loose bonds to the nucleus, it depends therefore less on  $Z$  and  $E_\gamma$  of the incident electron, but predominantly on the electronic density  $\rho_e$ . The Compton scattering is the main type of interaction of photons in soft tissue.

At 0.511 MeV, the photon has too much or too little energy and it is less probable for it to undergo a coherent scattering or a pair production (respectively) than a photoelectric effect or Compton scattering.

## 2.4 Photon attenuation

Photons do not directly cause ionisations, when traversing matter but are attenuated by the diverse interactions, depending on their own kinetic energy  $E_\gamma$  and properties of  $Z$  or  $Z_{eff}$ , density  $\rho$  and thickness  $D$  of the transport medium. Photon attenuation can be calculated using Equation 2.7.

$$I(x = D) = I_0 \cdot e^{-\int_0^D \mu_l(E_\gamma, x) dx} \quad (2.7)$$

where  $I_0$  and  $I(x = D)$  are the photon intensities: 1) without attenuating materials (absorbers, e.g. patient's body with different tissue densities) and 2) transmitted after traversing the absorbers (e.g. the patient's body with varying thickness  $0 \leq x \leq D$ ), respectively. The parameter  $\mu_l(E_\gamma, x)$  is the linear attenuation coefficient. It corresponds to the probability of interaction per unit distance depending on  $E_\gamma$ , and  $x$ .  $\mu_l$  can be given by Equation 2.8 considering the linear attenuation for photoelectric ( $\mu_{photoelectric}$ ) and Compton scattering ( $\mu_{Compton}$ ).

$$\mu_l \approx \mu_{photoelectric} + \mu_{Compton} \quad (2.8)$$

The mass attenuation coefficient,  $\mu_m(E_\gamma, Z)$ , i.e. the probability that a photon will experience a particular interaction. At and around 0.511 MeV,  $\mu_m$  is therefore composed of mostly the photoelectric effect ( $\tau$ ) and the Compton scattering ( $\sigma$ ), such as

$$\mu_m \approx \tau + \sigma \quad (2.9)$$

$\mu_m$  and  $\mu_l$  are measured in [ $cm^2 \cdot g^{-1}$ ] and [ $cm^{-1}$ ], respectively. They are related according to Equation 2.10.

$$\mu_m [cm^2 \cdot g^{-1}] = \frac{\mu_l [cm^{-1}]}{\rho [g \cdot cm^{-3}]} \quad (2.10)$$

In the case of PET imaging, three types of media are likely to attenuate annihilation photons: 1) body soft tissues and bones, 2) scintillator materials such as lutetium oxyorthosilicate (LSO)/lutetium–yttrium oxyorthosilicate (LYSO) and 3) materials used for shielding. Table 2.2 gives  $\mu_l$  at 0.511 MeV in different materials susceptible to act as absorbers in PET imaging.

## 2.5 PET imaging principles

PET uses the knowledge about the previously described particle physics. Annihilation photons with  $0.511 \pm \Delta E_\gamma$  MeV are emitted at  $180^\circ \pm \Delta\theta$  in coincidence and are detected by detectors placed in opposite directions, on one or several rings for

TABLE 2.2 – Linear attenuation coefficient of different absorbers at 0.511 MeV related to PET imaging. Adapted from Cherry and Dahlbom (2006) and Cherry, Sorenson, and Phelps (2012).

Material	$\mu_{photoelectric}[cm^{-1}]$	$\mu_{Compton}[cm^{-1}]$	$\mu_l[cm^{-1}]$
Soft tissue	$\sim 0.00002$	$\sim 0.096$	$\sim 0.096$
Bone	$\sim 0.001$	$\sim 0.169$	$\sim 0.17$
BGO	0.40	0.51	0.96
LSO/LYSO	0.30	0.58	0.88
Lead	0.89	0.76	1.78
Tungsten	1.09	1.31	2.59

3D detection. A simplified coincidence detection logic is illustrated in Figure 2.5. A bunch of novel 3D detection methods and state-of-the-art improved electronics are used to discriminate the arriving photons, since different types of primary and secondary photon radiations can be emitted confounding annihilation photon detection.

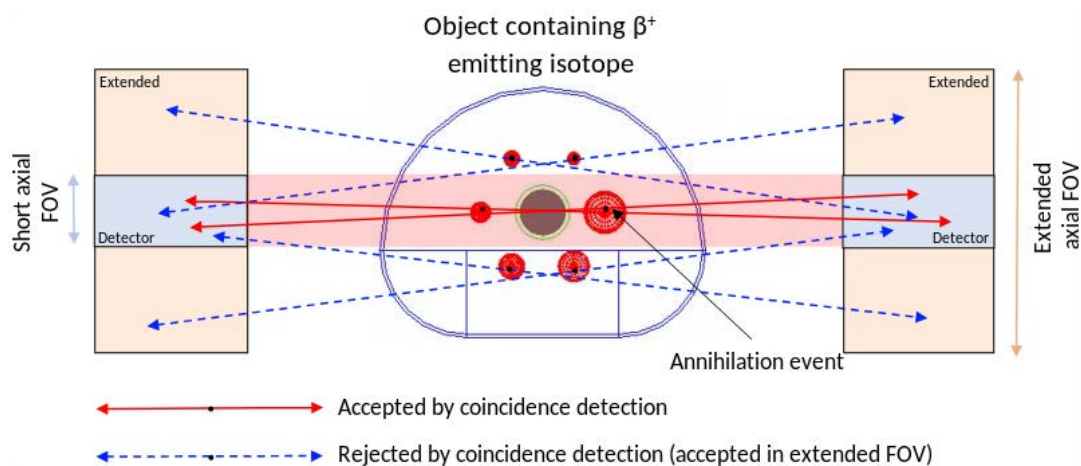


FIGURE 2.5 – Simplified coincidence logic in PET imaging. LOR detection is limited by the reduced geometrical efficiency of the axial FOV.

Straightforwardly, the detection process starts once a photon reaches a detector where first a photon energy discrimination is made using an energy window centred on the 0.511 MeV energy (more or less to take into account photons which underwent Compton scattering and lost part of their energy). Indeed, as soon as a first photon hits a detector and falls into the energy window, a timing window opens (of a few ns) to detect whether the opposite photon emitted by the same annihilation hits the opposite detector, recording a coincidence between the two accepted single events if this is the case. A LOR is created on which the position of annihilation interaction has taken place can be determined. This is the fundamental hypothesis on which PET imaging is based.

The coincidence detection is limited geometrically by the FOV covered by the detectors, see Figure 2.5, which is between 15-30 cm in actual clinical systems and in consequence provides a reduced detection efficiency by the modest solid angle coverage around the patient. The performance of some clinical short-FOV systems are provided later in Section 2.12 (see Tables 2.4). Efforts are being made with the

development of larger FOV systems covering the whole body and have provided more than satisfactory results in terms of performance, opening the way to greater perspectives using PET. At the time of writing this thesis, the first clinical whole-body PET has been installed at the Bern University Hospital, Switzerland, with a 1 m long FOV (See Biograph Vision Quadra™ in Table 2.4 also).

### 2.5.1 Types of events for coincidence detection

Once a coincidence event is recorded through a LOR, the position of photon interaction (in the detector), energy and arrival time in the coincidence windows of each pair of photon are recorded. The TOF difference between the two photons is also recorded, see Section 2.7. However, due to the performance and limits of detection systems and interactions of photons in the emission volume (e.g. human body), the information of all LORs do not provide the correct information and the detection is confounded by undesirable events. Coincidences are classified in four different groups: the *true*s (the only desired ones), the *scatters* and *randoms* (undesired ones), and the *multiples* (an ambiguous choice must be made for the right LOR in this case). Each one of them is called a *prompt coincidence*, depicted in Figure 2.6.

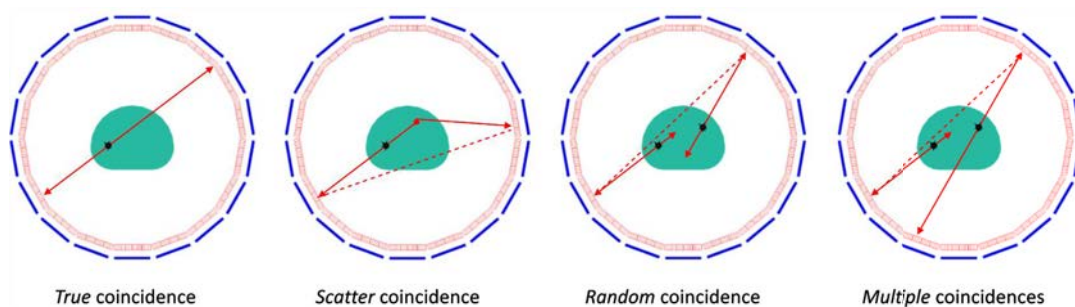


FIGURE 2.6 – From left to right: Illustration of *true*, *scatter*, *random* and *multiple* coincidences.

*True coincidences* are the ones obtained under ideal conditions, with partner photons originating from the same annihilation interaction on the LOR, neither deviated, nor lost energy when crossing matter until detection. *Scatter coincidences* occur when one or both photons undergo a Compton interaction and changed direction causing an incorrect localisation of the LOR even if the partner photons originate from the same annihilation. *Random coincidences* occur due to the reduced solid angle coverage, with two different photons from two different annihilations falling in the energy and timing discrimination windows and being detected in coincidence. Finally, *multiple coincidences* might also occur at rather high count rates, where more than two photons are detected in the same coincidence window generating more than one LOR and an ambiguous choice should be made to discard or select the right LOR.

*True coincidences* are the only ones that provide useful information for PET imaging. Therefore, the *prompt coincidences* must be corrected for confounding data which degrade image quality. Since the *random coincidences* arise from photons emitted by different annihilations, they contain no spatial information on the distribution of activity and are relatively easy to estimate and correct using the simple coincidence rate or a second delayed coincidence window. On the other way, *scattered coincidences* account for a high fraction of the total number of prompts, around 30%, and more difficult to correct. *Multiple coincidences* are easily identifiable and depending on the case, they are either rejected or kept.

## 2.6 Sources of error contributing to PET spatial resolution

Different sources of error impinge on the spatial resolution of PET systems. Intrinsic bias (before PET image reconstruction) in PET detection has been discussed in the previous sections, see Figure 2.1 for the positron range and annihilation photon non-collinearity errors. Contributions from other sources of error are discussed and quantitatively described in this section.

### 2.6.1 Positron physics and 2- $\gamma$ non-collinearity

The contribution of the range of positrons and the non-collinearity of annihilation photons have been described for many years, for example as in Derenzo et al. (1982), Levin and Hoffman (1999), and Moses (2011). As examples, the effective blurring (in water medium) is 0.54, 2.46 and 6.14 mm FWHM for  $^{18}\text{F}$ ,  $^{15}\text{O}$  and  $^{82}\text{Rb}$ , respectively (Moses, 2011). The FWHMs quoted here are for non-Gaussian fits but 'cusp-like' functions. The contribution due to the non-collinearity of annihilation photons is however modelled by Gaussian function where the  $FWHM = 0.0022D$  for any isotope,  $D$  being the diameter of the system (Levin and Hoffman, 1999).

### 2.6.2 Detectors

Due to the solid angle coverage and the fact that the position of interaction of the annihilation photon is not determined in the crystal, the detector size plays a role in the measured spatial resolution. Assuming a point source placed at the centre of the system, the sensitivity is maximum at the centre of the crystal and nearly 0 at the edges, therefore the response function is modelled by a triangular function, whose  $FWHM = d/2$ ,  $d$  being the detector width and  $d \ll D$  (Hoffman et al., 1982).

### 2.6.3 Depth of interaction

If a photon is not normally incident to the detector ring and hits a scintillator crystal in an oblique direction, it might travel a certain distance and reach another neighbouring crystal to the one that it hit primarily. Therefore, the wrong position is assigned by the crystal indexes. This is caused mainly by annihilation photons originating away from the PET scanner axis and the magnitude of this effect is proportional as a point source moves radially outward, and is known as *radial elongation*. For bismuth germanium oxide (BGO) or LSO/LYSO crystals, the penetration is modelled by a Gaussian whose FWHM is given by Equation 2.11.

$$FWHM = \frac{12.5r}{\sqrt{r^2 + (D/2)^2}} \quad (2.11)$$

where  $r$  is the radius for a point source from the centre of the radial FOV.

### 2.6.4 Intercrystal Compton scattering and multiplexing

Intercrystal Compton scatter can be a source of positioning error. Furthermore, most PET scanners have more scintillators than photodetector elements to reduce the number of electronics channels and this contributes to a degradation in the spatial resolution. This effect is however minimised today with the use of SiPM compared to PMT technology output multiplexing. These can be compensated in the detector designs.

### 2.6.5 Sampling and reconstruction algorithms

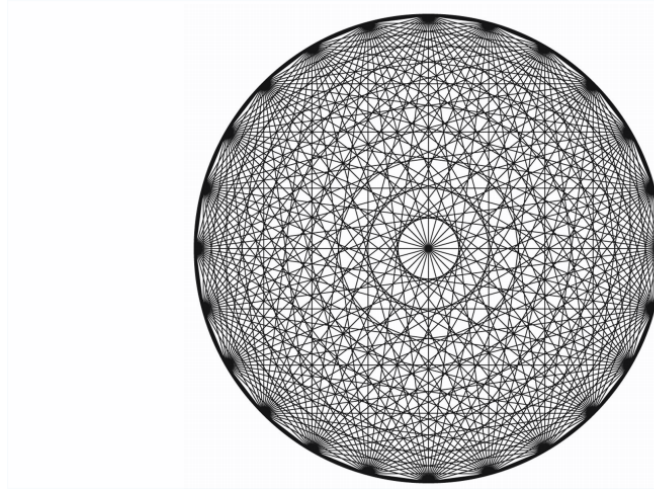


FIGURE 2.7 – The sampling depends on the position in the FOV, especially near the center. Extracted from Moses (2011).

The LORs are separated by the crystal width and create a degradation factor in the spatial resolution. Figure 2.7 depicts the non-uniform sampling of the LOR inside the FOV of the PET. The sampling error has been quantified to amplify all the other factors by a factor of 1.25 on a specific tomograph with BGO crystals (Derenzo et al., 1981; Moses, 2011), see Equation 2.12.

### 2.6.6 Total spatial resolution

A summary of the different contributions to spatial resolution are schematised in Figure 2.8. They are assumed to add in quadrature (although not all are described by Gaussian functions). Therefore, the reconstructed spatial resolution  $\Gamma$  for a point source located at a radius  $r$  from the centre of the radial FOV is described by Equation 2.12.

$$\Gamma \text{ [mm at FWHM]} = 1.25 \sqrt{(d/2)^2 + s^2 + (0.0022D)^2 + b^2 + \frac{(12.5r)^2}{r^2 + (D/2)^2}} \quad (2.12)$$

where  $s$  is the range of the positron and  $b$  is the crystal decoding factor error ( $b = d/3$  for detectors which use optical decoding or 0 otherwise).

#### 2.6.6.1 Ideal spatial resolution

The quest for the ultimate spatial resolution in PET would eliminate some terms in Equation 2.12 to give Equation 2.13.

$$\Gamma \text{ [mm at FWHM]} = \sqrt{(d/2)^2 + s^2 + (0.0022D)^2} \quad (2.13)$$

The remaining terms being fundamental where solutions exist to lower their contribution but they are not practical, e.g. lowering to  $-4^\circ\text{C}$  or  $-44^\circ\text{C}$  to reduce non-collinearity of annihilation photons contribution by factors of 1.5 and 5, respectively

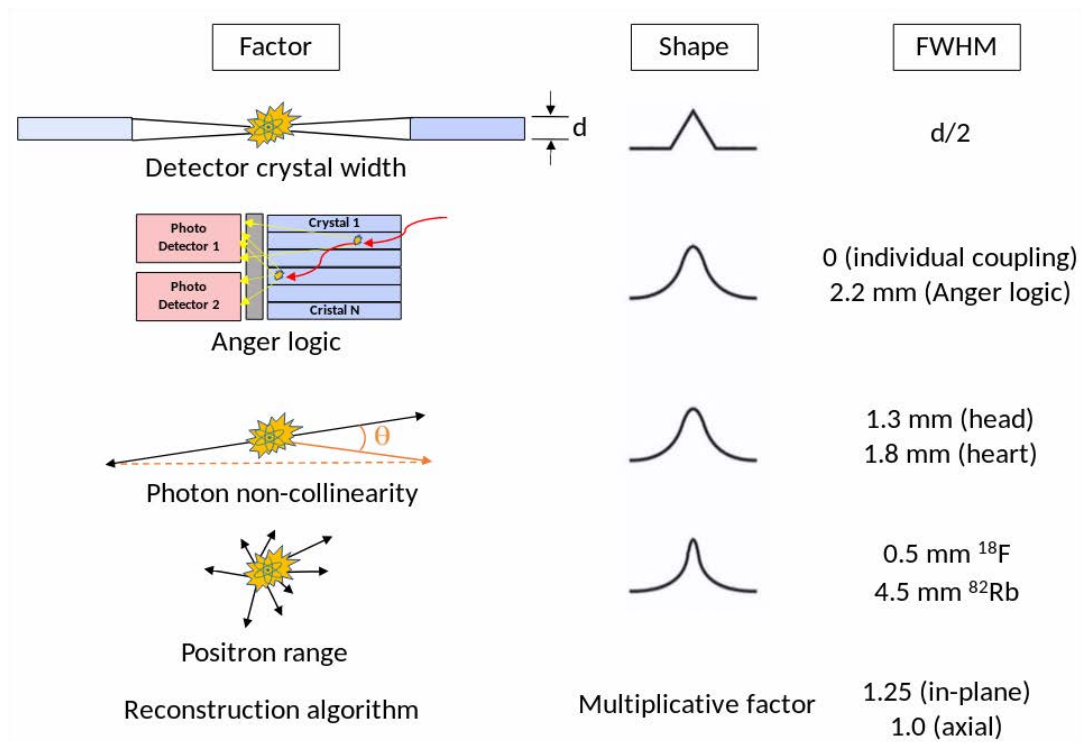


FIGURE 2.8 – Contributions to the degradation of spatial resolution.  
Adapted from Moses (2011).

(See Colombino, Fiscella, and Trossi (1965) and Moses (2011)). Improvement in spatial resolution can also be made using depth of interaction (DOI) information, see Section 2.11.1.

### 2.6.7 Additional factors

Statistical noise due to the finite number of detected events contributes to the degradation of SNR and it is not easy to quantify since it depends on several factors (number of counts, distribution of activity in the object and activity concentration in each voxel). Other bias are also added using reconstruction algorithms, whether using analytical or statistical algorithms will not yield the same result. Readers can refer to Section 2.14 for PET tomographic reconstruction algorithms.

## 2.7 Time-of-flight PET

The incorporation of TOF in PET systems have improved the capabilities of PET imaging (Surti, 2015), enhancing the Noise equivalent count (NEC) and SNR, hence image quality. The localisation of the point of emission of annihilation photons depends on the TOF information, i.e. the detection of the time difference between the two annihilation photons as depicted in Figure 2.9, where the back-projection of the information on the LOR is constrained to a limited number of voxels using TOF compared to non-TOF PET in the reconstructed image matrix, see reconstruction algorithms in Section 2.13. Equation 2.14 provides the simple relationship to determine the position of interaction  $\Delta X$  from the centre of the LOR (i.e. distance between two opposite detectors).



$$\Delta X = \frac{|t_2 - t_1| \times c}{2} = \frac{\Delta T \times c}{2} \quad (2.14)$$

where  $c$  is the speed of light and  $\Delta T$  the time information difference, refer to Figure 2.9.

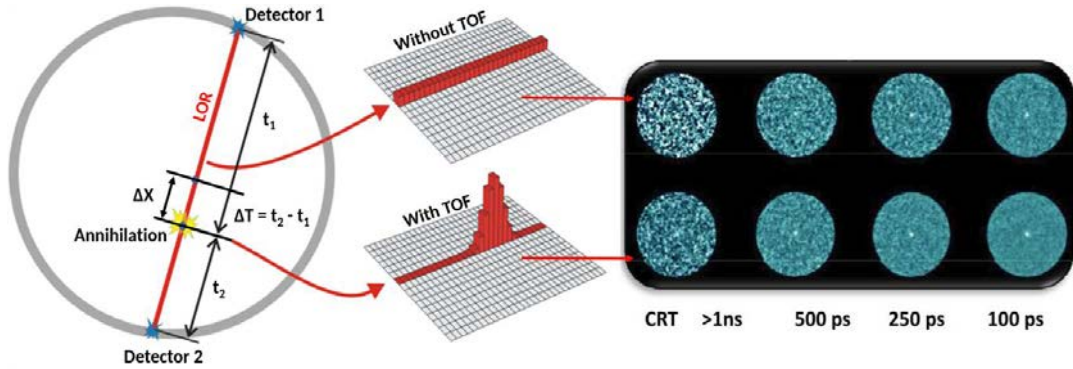


FIGURE 2.9 – *Left*: Illustration of the Gaussian coincidence peak using TOF information, showing higher probability of interaction position. *Right*: Illustration of image quality based on TOF (*bottom*) and non-TOF (*top*) PET with decreasing (better) CTR. Figure adapted from the [10 ps challenge website](#).

According to Equation 2.14, the smaller is  $\Delta T$ , the smaller is  $\Delta X$ . As quoted from Conti (2011), "In order to achieve a 2-mm single pixel spatial resolution, a 10-ps time resolution would be required". With such time resolutions, the TOF information can in theory allow for the formation of tomographic images without reconstruction algorithms if the intrinsic or fundamental limits to spatial resolution as explained previously are minimised.

Such timing resolutions are however not achievable on actual PET scanners and the position of interaction is blurred by a time measurement uncertainty, the coincidence timing resolution (CTR) which is the measure for the accuracy of TOF. The better the CTR, the better the TOF performance of the scanner, see Figure 2.9 (*right*). The TOF information is therefore implemented in the reconstruction algorithms, making the tomographic reconstruction being less ill-conditioned and less sensitive to small errors which might cause large errors in tomographic reconstruction. The overall benefit using TOF is the reduced noise, higher contrast recovery, and hence, higher SNR. As reviewed by Conti (2011), the TOF SNR gain, i.e. the ratio between  $SNR_{TOF}$  and  $SNR_{non-TOF}$  is given by Equation 2.15, where TOF reconstruction acts as a sensitivity amplifier for a PET scanner, i.e. a gain in SNR can be taken as a gain in counts ( $SNR \propto \sqrt{NEC}$  (Strother, Casey, and Hoffman, 1990)). This is due to the simple fact that each individual event may be forced to take place in a smaller volume in the process of reconstruction.

$$SNR_{TOF} = \sqrt{\frac{D}{\Delta X}} SNR_{non-TOF} \quad (2.15)$$

where  $D$  here is the effective diameter (e.g. for a patient) (Budinger, 1983; Lecomte, 2009).

### 2.7.1 Cerenkov light and TOF PET

Promptly emitted Cerenkov light is produced by the interaction of annihilation photons, for example in thallium bromide (TlBr) (Ariño-Estrada et al., 2018) or even BGO (Brunner and Schaart, 2017) and can be collected using dedicated photodetectors. Cerenkov radiation has been shown to provide alternatives for the detection of annihilation photons interacting in the crystals, based on the crystal index of refraction, which is higher in TlBr (2.63) than LYSO (1.82) and BGO (2.15), values in brackets given at 570 nm, see Table 2.3 in the following Section 2.8. TlBr seems to be a good candidate for Cerenkov luminescence production since it has a lower energy threshold favouring this effect compared to LYSO or BGO. Furthermore, it is mostly transparent in the visible part of the spectrum (it should not be highly absorbed within the crystal). To put it concisely, the timing of annihilation photons can be derived using Cerenkov luminescence signal using photodetectors to obtain fast sub-ns timing resolutions.

## 2.8 Scintillator crystals

The photon detection system is based on two detectors assembled together, the scintillator (organic or inorganic) and the photodetector (e.g. PMTs, photodiodes, SiPMs). The principles of the scintillators used in PET are described in this section. Scintillators convert the energy deposited by 0.511 MeV  $\gamma$ s by luminescence into visible photons (also extending to ultraviolet spectrum) and are detected by photodetectors, described later in Section 2.9. For PET imaging, inorganic scintillators in the form of solid crystals are used. Table 2.3 provides the properties of different intrinsic and extrinsic activated (e.g. Ce-doped impurity) scintillator crystals commonly used in PET.

One important parameter of scintillators as described by Lecomte (2009) is the initial photon rate  $I_0$  following the scintillation event which determines the timing performance of the detector.  $I_0$  is itself related to 1) the decay time  $\tau_s$  which is a limit to the count rate capability at higher counts due to pile-up effects and 2) the light output  $R$  which mainly determines the energy resolution of the detector. Equation 2.16 describes the relationship between  $R$ ,  $I_0$  and  $\tau_s$ .

$$R = \int_0^{\infty} I(t)dt = \int_0^{\infty} I_0 e^{-t/\tau_s} dt = I_0 \tau_s \quad (2.16)$$

Detectors for use in PET require also high stopping power or attenuation length materials ( $1/\mu$  at 0.511 MeV) to optimise the sensitivity of the system.  $1/\mu$  itself depends on the density  $\rho$  and the effective atomic number  $Z_{eff}$  of the scintillator material. One related parameter is the photoelectric absorption probability (PE) which has a direct consequence on the 0.511 MeV photon detection efficiency (PDE).

Other factors are detailed in Table 2.3, and today, LSO/LYSO crystals offer the best combination of luminosity and coincidence detection efficiency, benefiting from the possibility to be doped with cerium ions ( $Ce^{3+}$ ) for faster and more efficient scintillation mechanisms, see Lecomte (2009) and Cherry, Sorenson, and Phelps (2012) for further reading.

TABLE 2.3 – Physical properties of common scintillators in PET. LYSO is highlighted since the PET used for studies in this thesis is LYSO-equipped. Data obtained from Lecomte (2009) and Cherry, Sorenson, and Phelps (2012). Data for plastic scintillators obtained from Kapłon et al. (2014) and Wiczorek (2017). Data for TlBr obtained from Ariño-Estrada et al. (2018).

Properties	NaI	BGO	GSO	LSO	LYSO	LGSO	LuAP	YAP	LaBr3	TlBr*	Plastic**
Peak emission wavelength (nm)	410	480	440	420	<b>420</b>	415	365	350	360	-	391-404
Index of refraction	1.85	2.15	1.85	1.82	<b>1.81</b>	1.8	1.94	1.95	1.9	2.63	1.58-1.59
Light output R ( $10^3$ ph.MeV <sup>-1</sup> )	41	9	8	30	<b>30</b>	16	12	17	60	-	10-10.88
Decay time $\tau_s$ (ns)	230	300	60	40	<b>40</b>	65	18	30	16	-	1.5-2.4
$I_0$ @ 0.511 MeV (ph/ns)	90	21	60	380	<b>380</b>	125	340	290	1900	-	-
$\Delta E/E$ (%) @ 0.662 MeV	6	10	8	10	<b>10</b>	9	15	4.5	3	1.66	-
Density $\rho$ (g.cm <sup>-3</sup> )	3.67	7.13	6.71	7.35	<b>7.19</b>	6.5	8.34	5.5	5.3	7.56	1.023-1.032
Effective Z ( $Z_{eff}$ )	50	73	58	65	<b>64</b>	59	65	33	46	74	-
$1/\mu$ @ 0.511 MeV (mm)	25.9	11.2	15.0	12.3	<b>12.6</b>	14.3	11.0	21.3	22.3	9.7	-
PE (%)	18	44	26	34	<b>33</b>	28	32	4.4	14	-	-
Magnetic susceptibility	No	No	Yes	No	<b>No</b>	Yes	No	No	No	-	No
Hygroscopic	Yes	No	No	No	<b>No</b>	No	No	No	Yes	-	No

\*TlBr for the detection of Cerenkov light.

\*\*various plastic scintillators studied for the Jagiellonian-PET (see website).

## 2.9 Operating principles of photodetectors

This section describes the the most commonly employed photodetectors coupled to scintillator crystals in PET imaging, such as PMTs and SiPMs.

### 2.9.1 Photomultiplier tubes (PMTs)

In this section, the basic operating principles of PMT technology are described. Further details can be found in various books and reviews which can be of reference for further reading, see Cherry and Dahlbom (2006), Knoll (2010), Grupen and Buvat (2011), Cherry, Sorenson, and Phelps (2012), and Jiang, Chalich, and Deen (2019), and others. PMT converts scintillation light into a detectable electric pulse by electron multiplication. PMTs were the first to be employed for PET imaging but are now being superseded by recent progress in SiPM technology for optical photon detection, described later in Section 2.9.3.

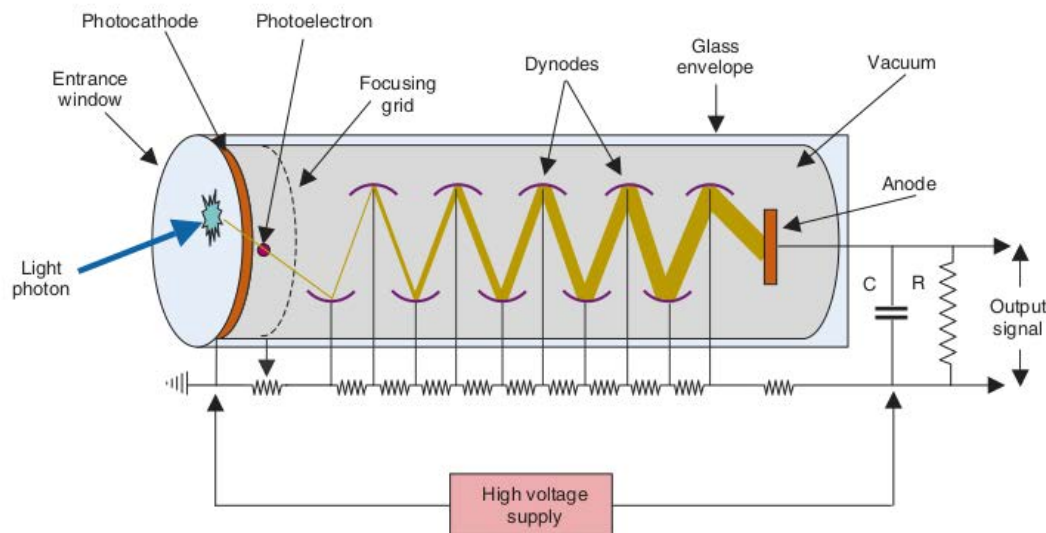


FIGURE 2.10 – Principles of the PMT, the primary components being the photocathode followed by a series of electrodes which are the dynodes and an anode recuperating the amplified electron swarm. The overall structure is enclosed in a vacuum tube. The dynodes are progressively biased at higher voltages. Extracted from Cherry, Sorenson, and Phelps (2012)

A sketch of the structure of a conventional PMT is depicted in Figure 2.10, composed of a photocathode and several electrodes enclosed in a vacuum tube (made of glass, ceramics, metals) within an electric field. Some of the photons impinging the photosensitive material on the photocathode and liberate electrons by the photoelectric effect. The primary generated photoelectrons are focused and accelerated to the first dynode (positively charged electrode) by the high internal electric field. Each electron which strike the first dynode generates more secondary electrons (3 to 5 multiplicative factor) and are accelerated by the progressively increasing potential differences between the dynodes, to the next dynode. This process is amplified on successively arranged dynodes, until reaching the anode where finally a high photocurrent pulse ( $\sim$ mA) is generated by the collection of a large number of electrons (Grupen and Buvat, 2011). A final multiplication factor (gain,  $G$ ) of  $10^5 - 10^6$

can be achieved, which is the number of electrons collected for each generated photoelectron.  $G$  depends on the applied potential difference  $U$  and is given by Equation 2.17.

$$G = AU^{kn} \quad (2.17)$$

where  $k \approx 0.7 - 0.8$  depending on the dynode material,  $n$  the number of successive dynodes and  $A$  is a constant depending on  $n$  (Gruppen and Buvat, 2011).

Some alternative types of PMTs are the microchannel plate (MCP) and position-sensitive (PS) PMTs, which are based on the same acceleration and gain effect, see Jiang, Chalich, and Deen (2019). However, even if they could provide advantages (good timing and spatial resolutions, tolerance to magnetic fields, ...), MCP PMTs have very short life time and have rather long recovery time per channel Gruppen and Buvat (2011). PS PMT provides the estimation of the position sensitivity of the incident photons on the photocathode by multiple anodes, which are processed individually, therefore requiring multiple readout channels and increases complexity, power consumption and cost.

PMTs are capable of detecting and amplifying signals provided by single photons with high  $G$ . They provide high timing resolution adding to their ruggedness and stability. However, they present the drawbacks of being bulky, sensitive to magnetic fields and mechanical variations, operate at high voltages and can be costly. They require Anger logic decoding for the position of interactions. Owing to these drawbacks, photosensors such as avalanche photodiode (APD)s and SiPMs have been developed and they have overcome the widespread use of PMT in clinical applications.

The following sections outline the functioning of silicon semiconductors.

## 2.9.2 Avalanche photodiodes (APDs)

**Standard photodiodes.** A photodiode consists of a P-N junction in a reverse bias mode. When a photon of sufficient energy impinges on the diode in its depletion region, it generates an electron-hole ( $e^- - h^+$ ) pair by means of a photoelectric effect, as depicted in Figure 2.11, and a photocurrent is produced which is measured. Standard P-N photodiodes were found not suitable for use in PET imaging owing to no internal gain where only one electron-hole pair is detected per scintillation photon. They provide a signal which is  $\sim$ six orders or magnitude lower than a PMT, which deteriorates the SNR of the impulse and limits the energy resolution and cause long integration times incompatible with TOF implementations for PET imaging.

**Avalanche photodiodes.** APDs are based on the same structure as the standard silicon P-N photodiodes but with an improved mechanism for the internal electric gain from avalanche multiplication. Compared to standard photodiodes, a larger reverse potential difference bias is applied at the electrodes of the APD. The electrical field in the depletion or space-charge region is sufficiently large such that when a primary photoelectron is generated there by an interacting optical photon, it is accelerated and gains enough energy to generate by itself an electron-hole pair by ionisation. This process is repeated by the primary photo-electron and subsequent ones, resulting in an avalanche of reactions similar to that in a PMT. This yields in a significant increase in the detectable current with an gain in amplification between  $10^2$  and  $10^3$  which is a significant improvement over the standard photodiodes but still does not

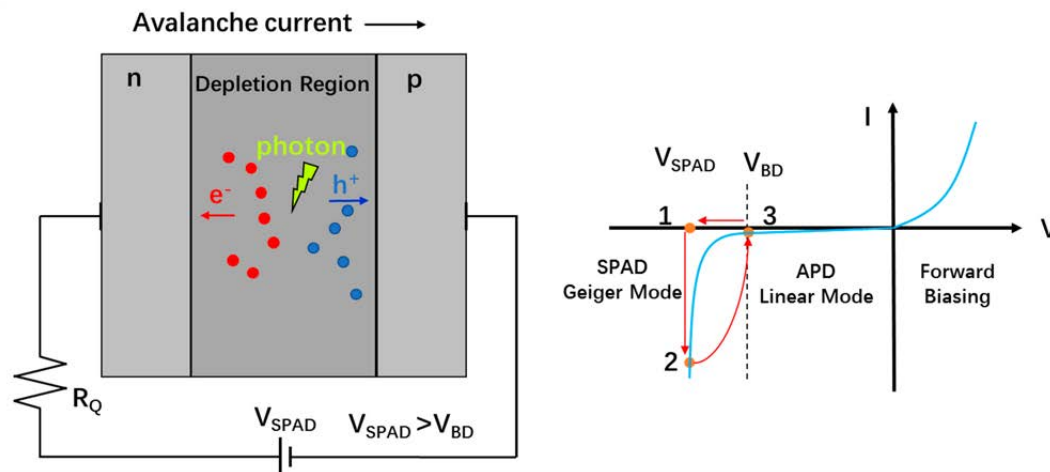


FIGURE 2.11 – Principle of APD and SPAD operation. *Left*: Avalanche breakdown process in a reverse biased p-n junction. *Right*: I-V characteristics (Jiang, Chalich, and Deen, 2019).

match the performance achieved by PMT and does not allow for single photon detection.

Although being three to four orders of magnitude below the performance regarding gain with respect to PMTs, APDs offer some benefits such as their relatively smaller sizes, reduced cost and insensitivity to magnetic fields. This led to the development of the first commercial APD-based PET for small animals imaging, the LabPET (Bergeron et al., 2009) followed by the LabPET II (Berard et al., 2008), with achieved 1.3 mm and sub-millimeter resolutions, respectively. The non-sensitivity to magnetic fields allowed for an easier integration of bi-modal systems and the development of the first commercial whole body PET-MRI system, the Siemens Biograph mMR which is based on APD technology (Delso et al., 2011). Compared to CT, MRI reduces the risk of ionising radiation and provides necessary information for photon attenuation and scattering corrections.

### 2.9.3 Silicon photomultipliers (SiPMs)

The major development in photon detection for PET imaging during this last decade is the SiPM technology. They use arrays of single-photon avalanche diode (SPAD)s, which are APDs working in a reverse bias mode a few volts above the breakdown voltage, functioning in the Geiger mode, see Figure 2.11. SiPMs offer much more benefits than APDs. They can be much smaller in size ( $\mu\text{m}$  sides) and can be compacted by thousands. They allow single photon detection with an excellent timing resolution (the single photon timing resolution (SPTR)) due to the lower timing jitter in the Geiger mode (exponential increase of current) and the narrow amplification region where the signal is produced. SPADs provide better control for linearity, improved timing and spatial resolutions and TOF applications for PET imaging, compared to APDs, see Section 2.10. They have a gain comparable to PMT, around  $10^6$  and can operate digitally by counting incident photons instead of producing an amplified current as with APD. An overview of the principles of the basic component SiPM cell, i.e., the SPAD, and existing types of SiPMs: analog silicon photo-multiplier (aSiPM) and digital silicon photo-multiplier (dSiPM), are discussed

in the following Sections 2.9.3.1 to 2.9.3.3. The DPC dSiPM is then described in further details in Section 2.10 since it is the PET system of interest studied throughout all of this thesis.

### 2.9.3.1 Single-photon avalanche diodes (SPADs)

A SPAD is a solid state (silicon semi-conductor) P-N junction which is reverse biased with an overvoltage of  $V_{excess}$  above the breakdown voltage  $V_{breakdown}$ , thus operating in Geiger mode. Compared to APDs, SPADs have a large enough potential difference which enables not only to the generated primary photoelectrons (from the interaction of visible photon) in the depletion zone to initiate an avalanche reaction, but also to the holes to create avalanches. As a result, avalanches occur in the P- and N-doped areas and the diode becomes conductive. This is illustrated in Figure 2.11. A large avalanche of current carriers develops exponentially and can be triggered from a single photon, see Figure 2.11 (left). The SPAD therefore requires a structure that allows operation without damage or too much noise due to the exponential increase of the conducted current. This structure can be passive using a resistor or active using a transistor, see Section 2.9.3.2.

Figure 2.11 (right) outlines the basic operating mode of a SPAD and its regulation using a quenching resistor. At phase 1, before a charge carrier is created in the depletion zone by a scintillator photon, the reverse potential difference is set to  $V_{SPAD} = V_{breakdown} + V_{excess}$ . As soon as a self-sustaining avalanche is generated, the SPAD conducts a high current which grows exponentially. Therefore, at phase 2, a quenching resistor ( $R_Q$  in Figure 2.11 (left)) allows for the voltage in the depletion region to be reduced below  $V_{breakdown}$  and thus force the polarisation of the diode at a level at which avalanches can no longer be continued. At phase 3, the SPAD is quenched and is recharged back to its initial polarised state to  $V_{SPAD}$  by a recharging circuit which may also be active or passive as the quenching circuit, see Section 2.9.3.2.

Active regulatory circuits for SPAD are better controlled, more stable with feedback and generally have lower dead time than passive ones.

### 2.9.3.2 Quench and reset circuits

Two categories exist to regulate the avalanche and recharge of SPAD to  $V_{SPAD}$  for the next photon detection: either a passive quenching and reset (PQR) or an active quenching and reset (AQR) circuit. PQR can easily occupy a smaller area than AQR, therefore a higher fill-factor (FF) for SiPMs, but solutions exist for AQR circuits to be implemented together with each compacted SPAD to overcome this drawback, but can be costly for fabrication.

### 2.9.3.3 Analog and digital SiPMs

*Analog.* For PET systems, the configuration of SPAD in an aSiPM can be depicted as in Figure 2.12 (top). The SPAD are connected in parallel and the output signal is the analog sum of the currents from all the cells, and use a PQR circuit. A very large number of aSiPM must be used for PET applications and the coupling of each detector to its own complex analog reading chain can pose design and cost problems. Similar to PMTs, the detected signal of the aSiPM is amplified and further needs a reading application-specific integrated circuit (ASIC) to obtain information about the time, with the time-to-digital converters (TDC), and energy, with the analogue-to-digital converters (ADC), of the detected photons. Therefore, the flaw of using this

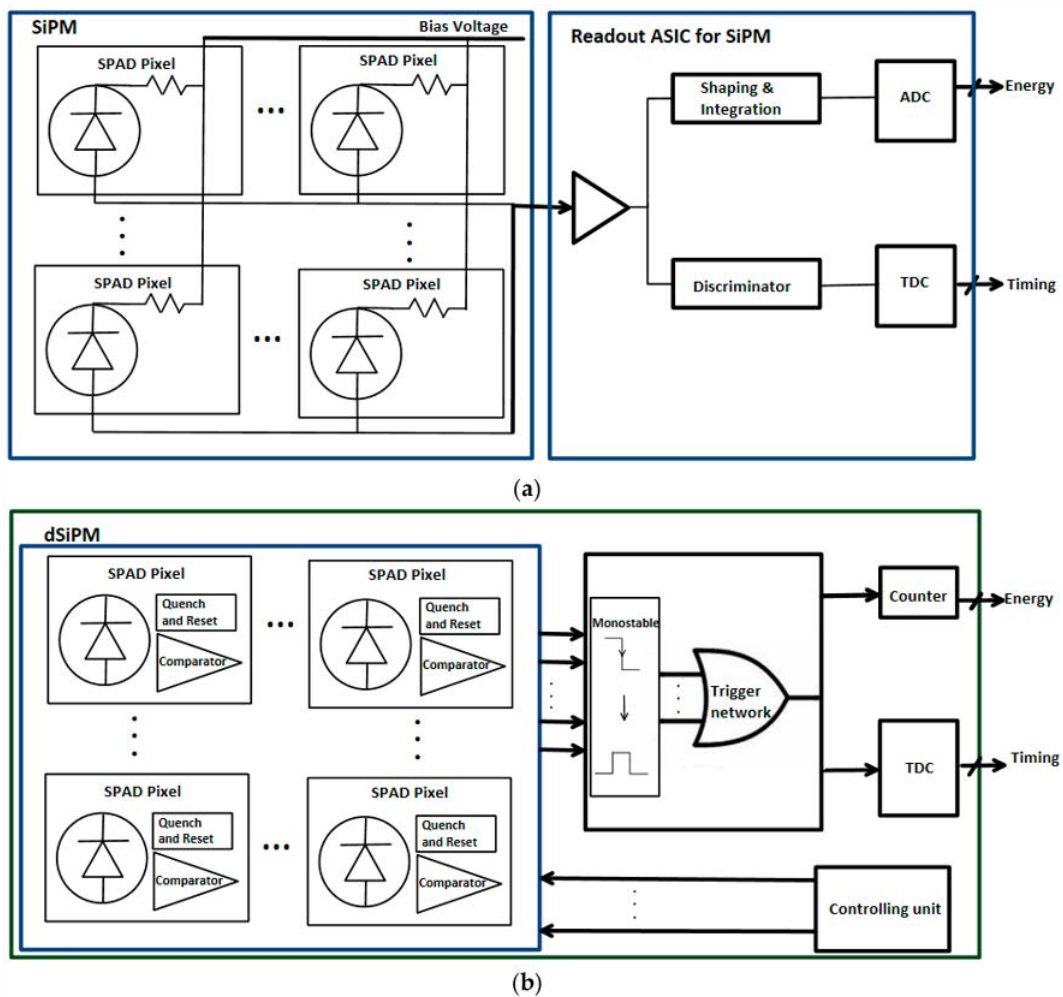


FIGURE 2.12 – Schematic representation of the sensing electronics based on aSiPMs (top) and dSiPMs (bottom). Extracted from (Jiang, Chalich, and Deen, 2019).

system is that the excellent intrinsic performance of the SPAD is not fully utilised because the output signal is degraded by the additional analog detection chain which can cause interference, electronic noise and other parasitics between connections, bond wires and external loads. They are also susceptible to temperature variations. Nevertheless, aSiPM have been developed and are used in commercial whole body PET systems from Siemens (Biograph Vision and Vision Quadra) and GE (Discovery MI).

**Digital.** The alternative exists to directly digitise the scintillation signal by connecting each cell to its own reading electronics. These are called dSiPMs, depicted in Figure 2.12 (bottom). The SPAD array can be integrated simultaneously with the necessary circuits on one only chip including AQR rather than PQR circuits using transistors (allowing better management of dead time and therefore improved counting capabilities compared to aSiPMs), TDC, ADC, and so on as depicted in Figure 2.12 (bottom). The TDC is the most important element influencing the temporal resolution of the whole chip. There is therefore a fully digital readout and processing circuits on the same chip which allow them to reach better timing resolution compared to



PMTs, APD and aSiPMs, which is attractive for PET. However, there is a large number of electrical connections on a limited space on a unique sensor tile using ASICs or field-programmable gate array (FPGA)s. Further description is given in the next Section 2.10 for the DPC dSiPM technology used in the Vereos from Philips which is the PET system of interest for this thesis.

## 2.10 Digital photon counting dSiPMs

The basics of DPC dSiPM developed by Philips is briefly described in this section, referring to several publications (among others) describing its principle of operation (Frach et al., 2009; Degenhardt et al., 2009; Frach et al., 2010; Degenhardt et al., 2010; Haemisch et al., 2012; Heller et al., 2013; Schaart et al., 2016; Liu et al., 2016; Jiang, Chalich, and Deen, 2019).

### 2.10.1 Architecture

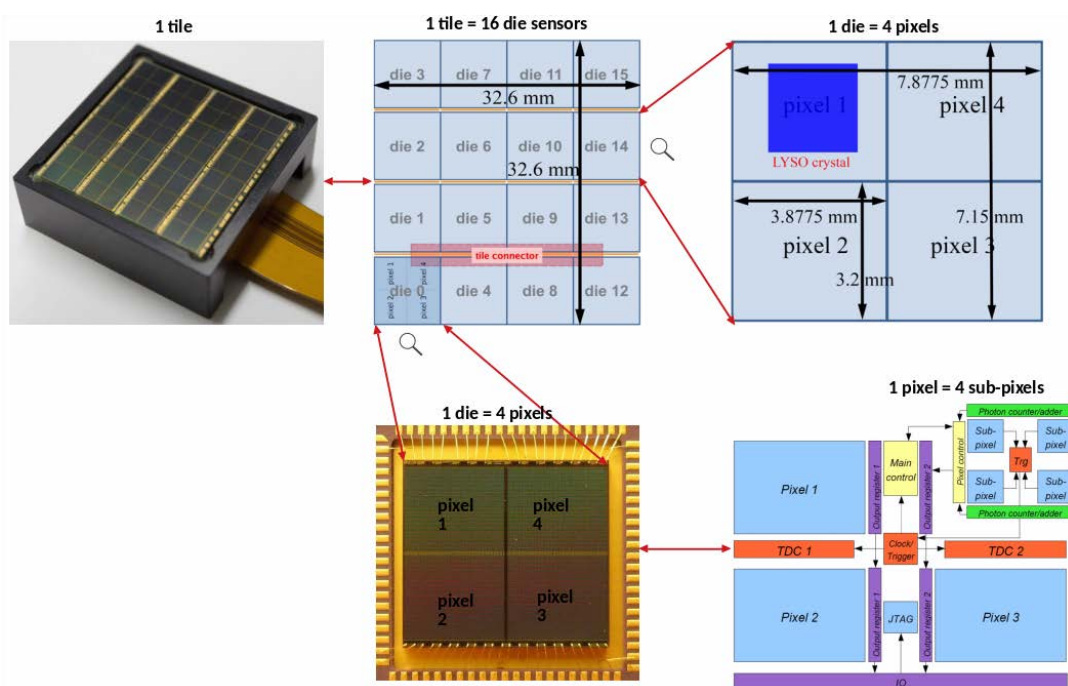


FIGURE 2.13 – DPC-type sensor architecture. *Top, left to right*: Representation of a tile. 1 tile = 16 dice. 1 die = 4 pixels (Liu et al., 2016). *Bottom, left to right*: Representation of a die (Frach et al., 2010) and 1 pixel = 4 subpixels (coupled to one crystal). See Haemisch Y. (Philips) and Schaart et al. (2016).

The type of photodetector used in the Philips Vereos PET system is the DPC3200-22 depicted in Figure 2.13. It consists of a *tile* (32.6 mm × 32.6 mm) which in turn consists of 16 *die sensors* (7.15 mm × 7.8775 mm each) arranged in a 4 × 4 grid. Each *die sensor* is composed of 4 digital photodetectors called *pixels* (the dSiPMs) (3.8775 mm × 3.2 mm each) arranged in a 2 × 2 grid. Each *pixel* is again subdivided in *subpixels* arranged in a 2 × 2 grid. Each *subpixel* contains 800 SPADs being the basic cells of the SiPM operating in the Geiger mode. Each SPAD in turn measures 59.4 μm × 64 μm and there is a total of 3200 SPAD per *pixel*. Furthermore, each dSiPM/*pixel* has

its own photon counter. The FF is 82.9% for the SPAD array and 77.7% for the whole system.

Further separating the *pixels* into *subpixels* make the discrimination process of events less complex compared to a full custom design. Therefore, the data readout duration is halved and the implementation of various trigger thresholds is simplified, being implemented in a fully digital way using logic operations. There are four logic combinations schemes possible, depending on the number of photons first hitting the SPAD and triggering individual subpixels to produce one *master trigger* to the main controller and starting the signal of the TDC, (See Frach et al. (2009) for more details). A pair of TDCs (around 20 ps time resolution) and one acquisition controller are coupled to each *die* of 4 *pixels* for measuring photon arrival time and generates a single timestamp. Therefore, the *die* is the readout level of the sensor, and the Philips Vereos PET system has 5720 trigger channels.

The generation of the timestamp is dependent on the configured trigger threshold based on the number of detected photons, going from one to four. As soon as the photon trigger threshold is reached and the timestamp activated, the data acquisition chain of the DPC-dSiPM starts, controlled by a state machine, see Figure 2.14, implemented in the *die* and FPGA on the backside of the *tile*. A bit of memory is allocated to each SPAD to allow selective inhibition to control dark noise events in case some of them become faulty.

### 2.10.2 Data acquisition state machine

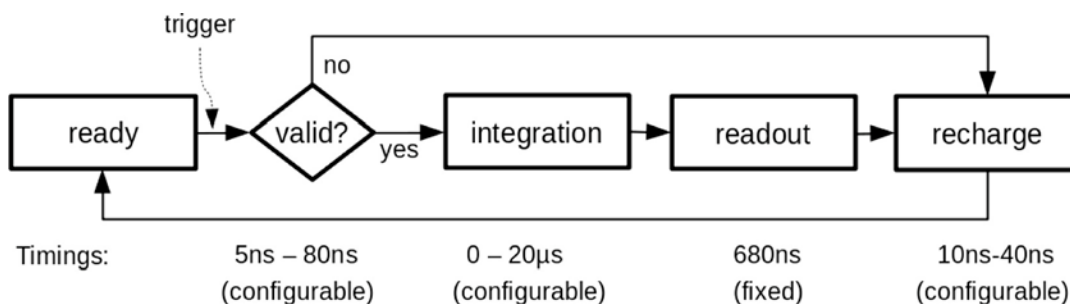


FIGURE 2.14 – State machine for DPC acquisition. Extracted from Schaart et al. (2016).

In this section, the data acquisition of a scintillator crystal coupled to a dSiPM is described. Each SPAD of the subpixels can detect and store only one photon at a time from the moment the photon hits a SPAD in the *ready* state to the moment the information is read or rejected and the global pixel is reset in the *recharged* state.

**Ready state.** The pixel starts in the *ready* state where all the SPAD are in the Geiger mode at  $V_{SPAD}$ , see Figure 2.11, and the recharge transistors of the AQR are open. As soon as the *master trigger* threshold is passed for at least one *pixel* of a *die*, a single time-stamp is produced per *die* and the entire die stops to accept further triggers, and the pixel controller changes the state to *validate*.

**Validate state.** This is a second higher-level threshold implemented to determine if an event is valid or is a dark count, based on the fact that a large number of photons is detected at different mutually exclusive regions of the pixels at the very beginning of the light pulse, which is very improbable for dark counts in this short time span.

A validation period is configured by the user, and launched as soon as the main trigger threshold is reached. Once a light pulse is validated, the state machine goes to the *integration* state. Else, if it is a dark count event, a fast pixel reset is performed with the SPAD recharged to  $V_{SPAD}$  and ready to detect again new events. This minimises the dead time of the sensor, but at the cost of a slight reduction in temporal resolution.

**Integration state.** In the *integration* or *collect* state, the number of photons hitting the SPAD accumulates and the pixel waits for the scintillator pulse to decay during again a user-defined duration. Each time a SPAD is hit by a photon, the avalanche occurs, the SPAD is actively quenched and the information stored for later readout. At the termination of the timer, the whole pixel is ready to be read. The timing chosen relies on the decay time of the employed scintillator crystal.

**Readout state.** Each row is read individually in a successive manner and the number of photons detected in each row is added to the photon counter. While reading out row number  $n$ , the preceding row ( $n - 1$ ) is recharged by the AQR circuitry (the quenching transistor is also disconnected) to avoid large power surges if the whole *pixel* is reset at once.

**Recharge state.** Finally, the pixel controller goes to the *reset* state for a global recharge and TDC reset, and loop back to the *ready* state.

### 2.10.3 Characteristics of the DPC SiPM

Some characteristics of the DPC dSiPM are presented in this section, which are the saturation of SPADs, dark count rate, photon detection efficiency, optical crosstalk and temperature sensitivity.

**Saturation of SPADs.** Each SPAD in dSiPMs cannot detect more than one photon during a cycle. Therefore, when there is more active cells ( $N_{cells}$  at the *ready state*) than the light photon shower from the scintillator crystal, i.e. at low photon count, the detector pixel is not saturated. As soon as the number of photons impinging on the SPAD is greater than the number of  $N_{cells}$ , i.e. a high photon count, a saturation correction is employed using Equation 2.18 to estimate the number of detected photons  $N_{detected}$ .

$$N_{detected} = N_{cells} \left( 1 - e^{-\frac{PDE \cdot N_{photons}}{N_{cells}}} \right) \quad (2.18)$$

A correction LUT per pixel can be provided as the number of  $N_{cells}$  differ from one pixel to the other to solve for  $N_{photons}$  (Frach et al., 2009).

**Dark count rate.** When implemented SPADs on a dSiPM present failures and produce dark counts, a dark count rate (DCR) map can be obtained, which is the triggers per unit time without light. This helps in the reduction of the deadtime by switching off the SPADs (they cannot be replaced) with the highest DCRs (around 5 to 10% of SPADs). Switching off 5% of cells halves the cumulative DCR for the whole pixel. A bit of memory is dedicated to each SPAD to be able to selectively activate individual cells.

**Photon detection efficiency.** PDE describes the probability to detect a photon of a certain wavelength ( $\lambda$ ). It is proportional to the product of the FF, quantum efficiency (QE) of silicon due to different interaction and absorption behaviours of light with different wavelengths in silicon, and the avalanche generation probability in the Geiger mode.

**Optical crosstalk.** Optical crosstalk is the consequence of photons generated during the avalanche discharge of the diode, creating a secondary avalanche in neighbouring diodes. Reducing the current in the SPAD reduces the photoemissions and optical crosstalk. Optical crosstalk can be also reduced by optical isolation between SPAD and can be measured using a 'light generator' diode and validated events recorded minus the dark counts.

**Temperature sensitivity.** Temperature affects the ionisation coefficients of electrons and holes, leading to a drift in the  $V_{breakdown}$  of the SPAD. dSiPMs are insensitive to any change in  $V_{breakdown}$  as compared to aSiPMs since the potential difference is sensed by a digital circuit and logic gate. The temperature sensitivity of dSiPMs is mainly due to the change in PDE caused by the temperature-dependent avalanche probability. This can be compensated for only by adapting the bias voltage of the device. The TDC and trigger might present drifts, being implemented next to the dSiPM, but can be measured and compensated for.

## 2.11 Developments in PET detection

Two developments in PET are described hereafter, including DOI and ortho-positronium detection.

### 2.11.1 Depth of interaction

PET resolution can be enhanced using DOI information, based on the transport of scintillation light among multiple detectors, considering their attenuation over the multiple detector crystals. Indeed, DOI encoding techniques have been studied in different scintillator geometries to avoid parallax errors in longer crystals. In fact, increasing the length of the crystals increases the sensitivity of detection of photons but have a degraded timing resolution and more uncertainty in the interaction position of the annihilation photon in the crystal. Bibliography concerning DOI determination suggested methods such as using phoswich detectors, stacked discrete layers of scintillators, monolithic crystals, double-sided readout schemes, are described in a recent study from Zatcepin et al. (2020) (see also Pizzichemi et al. (2016) and Sanaat and Zaidi (2020)).

### 2.11.2 Ortho-positronium detection using JPET

As described earlier in Section 2.2.3, PET records 511 keV photons emitted photons from annihilation of  $e^+e^-$  pairs. It turns out that it is also possible to image the three-photon annihilation of ortho-positronium, which can provide additional and complementary information for diagnosis (Moskal et al., 2019). A prototype scanner has been built with a large axial FOV, called the Jagiellonian Positron Emission Tomograph (J-PET), built from long-strips of plastic scintillators (Niedźwiecki et al., 2017), see Table 2.3 for plastic scintillators characteristics. The J-PET can detect and

reconstruct using information from 511 keV  $2 - \gamma$  photons, as well as detect ortho-positronium  $3 - \gamma$  decays in a single plane in the J-PET detector Gajos et al. (2016). The system provides several benefits, being cost-effective with a large eFOV which can be modular, a good timing resolution (220 ps), is MRI compatible, and so on. Its main drawback is the low detection efficiency. The National Electrical Manufacturers Association (NEMA) performances of the J-PET system (using GATE) can be found in Kowalski et al. (2018). A list of articles is available on the [JPET website](#).

## 2.12 Performance of actual PET systems

The characteristics of the state-of-the-art SiPM-based PET/CT clinical systems are summarised and compared in Table 2.4. Systems with axial eFOVs (e.g. the Siemens Biograph Vision Quadra), provide better sensitivities than standard axial FOVs.

TABLE 2.4 – Comparison of the commercially available SiPM PET systems (at the time of writing this thesis). The characteristics of the actual 3 commercialised clinical SiPM-based PET/CTs are outlined, the: 1) GE Discovery MI, 2) Siemens Biograph Vision and 3) Philips DPC Vereos. Characteristics for the SiPM-based PET/MR GE Signa and SiPM-based extended FOV (106 cm) PET/CT Siemens Biograph Vision Quadra, are also reported. Respective values are from [a]: Pan et al. (2019), [b]: Grant et al. (2016) and Caribé et al. (2019), [c]: Reddin et al. (2018) and Van Sluis et al. (2019), [d]: Prenosil et al. (2021), and [e]: Zhang, Maniawski, and Knopp (2018) and Rausch et al. (2019)

	Manufacturer				
	GE		Siemens		Philips
References	[a]	[b]	[c]	[d]	[e]
Model name	Discovery MI	SIGNA* (5 rings)	Biograph Vision 600	Biograph Vision Quadra	DPC Vereos
Characteristics					
Scintillator material	LYSO	LYSO	LSO	LSO	LYSO
Scintillator size ( $Tr. \times Ax. \times Dep. mm^3$ )	$3.9 \times 5.3 \times 25$	$3.9 \times 5.3 \times 25$	$3.2 \times 3.2 \times 20$	$3.2 \times 3.2 \times 20$	$4 \times 4 \times 19$
Sensor	SiPM	SiPM	SiPM	SiPM	dSiPM
N° of scintillators	24480	20160	60800	-	23040
N° of sensors	12240	1680	48640	-	23040
Coupling	2:1	$4 \times 9 : 1 \times 3$	$4 \times 9 : 1 \times 3$	$5 \times 5 : 4 \times 4$	1:1
Radial FOV (mm)	700	600	820	820	764
Axial FOV (mm)	250	250	263	1060	164
Energy Window (keV)	425-650	425-650	435-585	435-585	450-613
Performances					
Sensitivity ( $cps.kBq^{-1}$ )	20.84	23.3	16.4	83.4† 176.0‡	5.2
NECR peak ( $kcps @ kBq.mL^{-1}$ )	266 @ 20.8	218 @ 17.8	306 @ 32.6	1.641 @ 28.3† 3.018 @ 28.3‡	153.4@ 54.9
Scatter fraction (%) @ peak NECR (ps)	40.2	43.6	38.7	36.5† 37.0‡	33.9
Spatial resolution** FWHM (mm)	$4.3 \times 4.3 \times 5.0$	$4.4 \times 4.1 \times 5.3$	$3.5 \times 3.7 \times 3.6$	$3.3 \times 3.4 \times 3.8$	$4.2 \times 4.2 \times 4.2$
TOF resolution (ps)	381.7	< 400	210	225† 227‡	310
Energy resolution (%)	9.55	10.3	9.0	9.0	11.2

\*PET/MR system, \*\* At the centre of FOV, † for a maximum ring difference (MRD) of 85, ‡ for a MRD of 322.

## 2.13 PET data acquisition and reconstruction

The aim of image reconstruction in PET is to transform information from acquired individual LORs into 3D quantitative data, which is the activity concentration in  $Bq.mL^{-1}$  in each reconstructed voxel present in the FOV. This section outlines PET image reconstruction and algorithms, starting from the raw data acquisition modes.

### 2.13.1 Data acquisition

The 2D and 3D acquisition modes for PET imaging are outlined here, with emphasis on the 3D mode. Both modes result in 3D images, the classification (2D or 3D modes) only refers to the type of data acquired. Their fundamental differences are depicted in Figure 2.15.

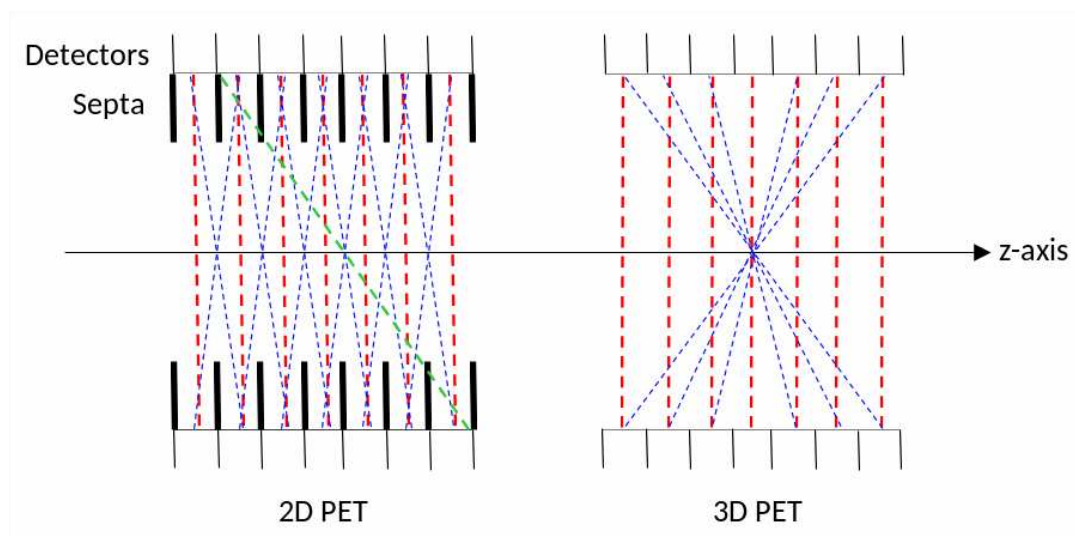


FIGURE 2.15 – Differences between 2D and 3D PET acquisition modes. Direct (*red*) and oblique (*blue*) planes forming LORs. Oblique LORs (*green*) cannot be formed when using *septa* in 2D PET. All LORs are accepted in 3D PET. Adapted from Alessio, Kinahan, et al. (2006).

**2D acquisition mode.** PET data collection before reconstruction were at a time performed in a 2D mode using tungsten or lead interplane *septa* for collimation. Each single 2D slice was reconstructed independently and the cross planes in the FOV were combined together with the help of oblique LORs delimited by adjusting the length of the *septa* to form a 3D image. The use of *septa* reduced the data storage needs at the cost of loss in sensitivity and SNR.

**3D acquisition mode.** State-of-the-art commercial PET systems today achieve 3D acquisitions accepting all LORs (direct and oblique) in any detector ring, despite the large data storage and computing power required. Higher proportion of scattered and random coincidences need therefore to be properly corrected in 3D, owing to higher sensitivity improved by a factor between 4 and 6 compared to 2D (Fahey, 2002), on which the SNR benefits. 3D reconstruction methods are also more complex and time consuming than 2D methods. Today, sensitivity using eFOV PET systems improved by several factors and efforts seem to be actually made to circumvent the

associated computation issues linked to the 3D acquisition mode (compare sensitivity values in Table 2.4).

### 2.13.2 Data format

Data can be stored in different formats: *histograms* which store the number of events detected in each LOR index, *sinograms* which are based on the line integral approximation and *listmodes*, the last two being the most common ones as presented below.

#### 2.13.2.1 Sinogram format

**Line integral approximation.** A sinogram in PET is fundamentally a 2D matrix where the number of events detected in each LOR connecting two detectors,  $d_1$  and  $d_2$ , is stored as a function of the shortest radial distance,  $x_r$ , between the LOR and the centre of the FOV and its orientation angle,  $\varphi$ . Figure 2.16 depicts how sinograms are organised, considering a 2D activity distribution in an object  $f(x, y)$  present in a cross-section,  $(x, y)$  being the fixed coordinates of the PET. The coincidence data in each LOR are essentially linear projections of the tracer distribution. Indeed, a LOR instead of a *volume-of-response* (VOR) joining the two detectors is considered. The average number of coincidence events detected in each LOR,  $p(x_r, \varphi)$ , is the **line integral** through  $f(x, y)$  at given  $x_r$  and given  $\varphi$ , described by Equation 2.19.

$$\begin{aligned} p(x_r, \varphi) &= \int_{-\infty}^{+\infty} f(x, y) dy_r \\ &= \int_{-\infty}^{+\infty} f(\cos\varphi.x_r - \sin\varphi.y_r, \sin\varphi.x_r + \cos\varphi.y_r) dy_r \end{aligned} \quad (2.19)$$

$(x_r, y_r)$ , which is the rotating reference frame is related to the angle  $\varphi$  of the LOR and to the fixed frame  $(x, y)$  by Equation 2.20.

$$\begin{bmatrix} x \\ y \end{bmatrix} = \begin{bmatrix} \cos\varphi & -\sin\varphi \\ \sin\varphi & \cos\varphi \end{bmatrix} \begin{bmatrix} x_r \\ y_r \end{bmatrix} \quad (2.20)$$

**Radon transform.** The **Radon transform** (Radon, 1986) of  $f(x, y)$ ,  $R[f(x, y)]$ , is the complete collection of line integrals  $p(x_r, \varphi)$  for  $x_r \in \mathbb{R}$  and  $\varphi \in [0, \pi]$ . A line of the sinogram therefore corresponds to the set of parallel LORs associated with the same angle  $\varphi$  and the image of a point is a sinusoid, as depicted in Figure 2.16 A. The sinogram of the activity distribution  $f(x, y)$  is a superposition of sinusoids, as depicted in Figures 2.16 B and C provided as example.

#### 2.13.2.2 Listmode format

Nowadays, the *listmode* format is preferred to the more conventional *sinogram* data format due to better handling and practicality, e.g. when the coordinates of the coincidence or even singles need to be recorded, and due to the flexibility of post-processing it brings. This is already the case for the manufacturer Philips, whose current generation of PET scanners record data only in *listmode*. Single *listmodes* can be processed to obtain coincidence *listmodes* and *sinograms* to adapt to reconstruction algorithms if needed.



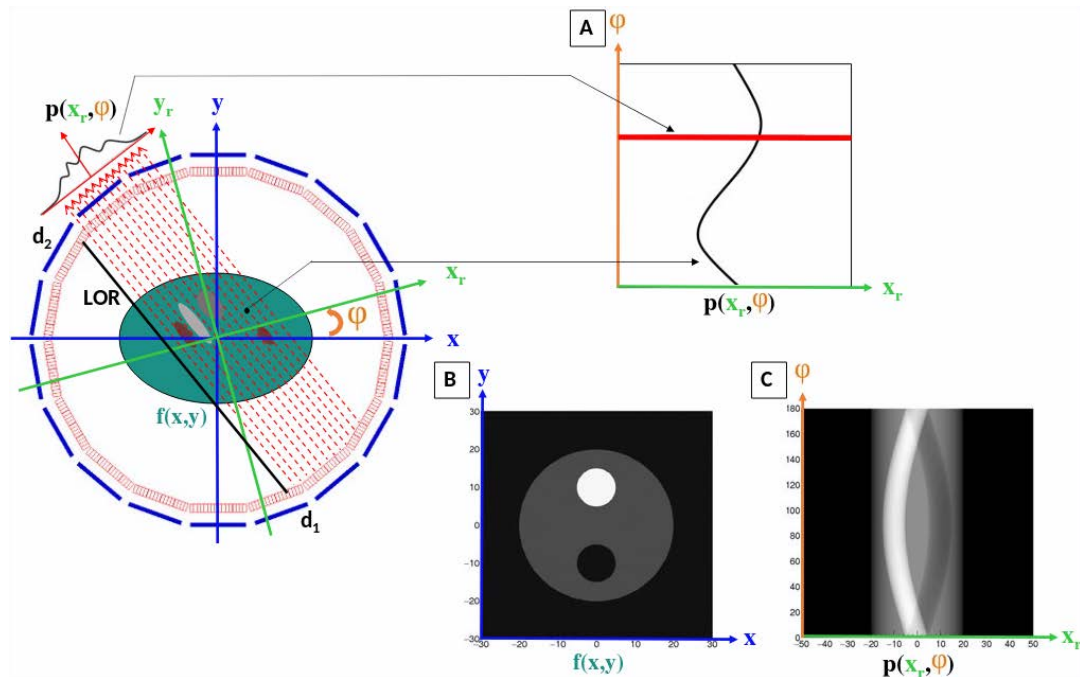


FIGURE 2.16 – *Left*: The projection  $p(x_r, \varphi)$  according to the line integral model obtained by the integration along parallel LORs, at an angle  $\varphi$  (orange). The fixed tomograph reference frame  $(x, y)$  (blue) and the rotating frame  $(x_r, y_r)$  (green) which define the LORs are depicted. *Right*: **A**. Storage of coincidences data in a sinogram. Adapted from Wernick and Aarsvold (2004) and see [lecture on medical physics](#). **B**. and **C**. are realistic representations of a 2D object consisting of several circular regions of different activities and the sinogram of the object, respectively (Etxebeste Barrena, 2017).

The *listmode* thus consists of a binary file where for each coincidence, a line is recorded containing the indexes of the coincident detectors ( $d_1, d_2$ ) (see Figure 2.16), the measured energy of the two photons ( $E_{\gamma_1}, E_{\gamma_2}$ ), and their TOF differences,  $\Delta T$ . There is no data resampling as required in the other formats and the exact information of the event is stored. The *listmode* format allows to record all necessary information for every event and the inherent large file size limitation (which depends on the counts statistics) is circumvented with the considerable improvement in storage capacity in recent years.

## 2.14 PET tomographic reconstruction

The imaging system can be represented as a discrete linear model as per Equation 2.21.

$$\mathbf{g} = \mathbf{H}\mathbf{f} + \mathbf{n} \quad (2.21)$$

where  $\mathbf{g}$  is the set of observations which are the measured projections of the activity along different directions (the recorded data of all LORs),  $\mathbf{H}$  is the known system model,  $\mathbf{f}$  is the unknown image of the activity distribution in the object, and  $\mathbf{n}$  is the error in the observations.

Data values are modelled in two main groups as deterministic or stochastic, although they are inherently stochastic due to the physical effects of PET imaging, such as the radioactive decay process, the attenuation of photons in the object and the statistical nature of gamma ray detection.

**Deterministic approach.** A unique and exact solution exists using inversion formulas (Townsend and Defrise, 1993), assuming measurements  $\mathbf{g}$  free of statistical noise ( $\mathbf{n} = 0$ ) and an idealised system model  $\mathbf{H}$ . Physical aspects (attenuation, scatter, detector size) are not considered. This approach is used in analytical reconstruction algorithms, making the problem solving simple, and fast with a linear and predictable behaviour. However, as the noise in the measurements is ignored, the reconstructed images using deterministic approaches can suffer from a lower image quality (Alessio, Kinahan, et al., 2006).

**Stochastic approach.** A more accurate description of the imaging and detection process can be implemented considering random noise structure. In this case, an exact solution is not possible and the computed solution,  $\hat{\mathbf{f}}$ , is an iterative approximation of the real activity distribution  $\mathbf{f}$ . Stochastic approaches are therefore iterative reconstruction methods.

The two approaches (deterministic and stochastic) are described in the following sections.

### 2.14.1 Analytical reconstruction

#### 2.14.1.1 Foundation principles

**Radon inverse transform.** The Radon transform has been defined by Equation ???. The tomographic reconstruction problem then consists of inverting the Radon transform, in order to estimate the radioactive distribution and recover  $f(x, y)$  from the measured projections  $p(x_r, \varphi)$ , as in the following equation.

$$f(x, y) = R^{-1}[p(x_r, \varphi)](x, y) \quad (2.22)$$

The Radon transform is a continuous operator, it can only be inverted for an infinite number of projections. However, since a PET acquisition is intrinsically sampled, the coordinates  $(x_r, \varphi)$  of the LOR are discrete in nature. This results in a non-uniqueness of the solution. Several methods for problem solving are detailed in the following sections.

**The Central Slice theorem.** The Central Slice theorem (CST)<sup>5</sup> is a fundamental theorem in analytical methods for image reconstruction (Alessio, Kinahan, et al., 2006). It states that for a given angle  $\varphi$ , the 1 dimensional (1D) Fourier transform ( $\mathcal{F}_{1D}$ ) of a projection  $p(x_r, \varphi)$  (i.e.  $P(v_{x_r}, \varphi)$  in the Fourier space, see Equation 2.23) of an object  $f(x, y)$  is equal to the values of the 2D Fourier transform ( $\mathcal{F}_{2D}$ ) of  $f(x, y)$  along a line drawn through the centre of the  $\mathcal{F}_{2D}$  plane. To prove this, let us start from the Fourier transform of  $p(x_r, \varphi)$ .

$$P(v_{x_r}, \varphi) = \mathcal{F}_{1D}\{p(x_r, \varphi)\} = \int_{-\infty}^{+\infty} p(x_r, \varphi) e^{-i2\pi x_r v_{x_r}} dx_r \quad (2.23)$$

where  $v_{x_r}$  is the Fourier space conjugate (frequency coordinates) of  $x_r$ . Replacing Equation 2.19 in Equation 2.23, yields the following equation

$$P(v_{x_r}, \varphi) = \int_{-\infty}^{+\infty} \int_{-\infty}^{+\infty} f(\cos\varphi \cdot x_r - \sin\varphi \cdot y_r, \sin\varphi \cdot x_r + \cos\varphi \cdot y_r) e^{-i2\pi x_r v_{x_r}} dx_r dy_r \quad (2.24)$$

Since  $x_r = x \cos\varphi + y \sin\varphi$  and  $d_{x_r} d_{y_r} = dx dy$  (see Figure 2.16) we obtain the following equation

$$\begin{aligned} P(v_{x_r}, \varphi) &= \int_{-\infty}^{+\infty} \int_{-\infty}^{+\infty} f(x, y) e^{-i2\pi(x \cos\varphi + y \sin\varphi)v_{x_r}} dx dy \\ &= F(v_{x_r} \cos\varphi, v_{x_r} \sin\varphi) \\ &= F(v_x, v_y) \Big|_{\substack{v_x = v_{x_r} \cos\varphi \\ v_y = v_{x_r} \sin\varphi}} \end{aligned} \quad (2.25)$$

where  $v_x$  and  $v_y$  represent the frequency coordinates of  $x$  and  $y$  in the Fourier space, respectively. The theorem states that if one knows the projections of the 2D slice of  $f(x, y)$  at angles  $0 \leq \varphi \leq \pi$ , in a continuous frame, one can recover the object by reconstructing the 2D Fourier transform of the object from the 1D Fourier transforms of the projections and taking the inverse of the 2D Fourier transform. In practice, angularly and spatially sampled projections are recorded and therefore, the sampling density will be lower for high frequencies which can lead to degradation of the reconstructed images. Alternatives exist to recover  $f(x, y)$  as described in the following parts.

### 2.14.1.2 Back-projection

An alternative but straightforward manner to provide a first estimation of  $f(x, y)$ , denoted  $f^*(x, y)$ , is by back-projecting  $p(x_r, \varphi)$  for all  $\varphi$ , using Equation 2.26.

$$f^*(x, y) = \int_0^\pi p(x_r, \varphi) d\varphi = \int_0^\pi p(x \cos\varphi - y \sin\varphi, \varphi) d\varphi \quad (2.26)$$

Back-projection does not reverse the Radon transform. A constant value is distributed uniformly along the LORs. The knowledge of the origin of the value in the LOR is thus lost, resulting in a blurred reconstructed image with frequency streak artefacts, due to the oversampling at the centre and less sampling at the edges of the object, originating from the Fourier transforms (Defrise and Kinahan, 1998).

5. See also Irène Buvat/Tomographic reconstruction.

### 2.14.1.3 Back-projection and filters

In order to compensate for the oversampling issues, filtered projections  $p_F(x_r, \varphi)$  can be used to estimate an artefact-free  $f^*(x, y)$ .  $p_F(x_r, \varphi)$  is obtained by the convolution of  $p(x_r, \varphi)$  at a given  $\varphi$  with a filter,  $h(x_r)$ , as described in the following Fourier space equation

$$p_F(x_r, \varphi) = p(x_r, \varphi) * h(x_r) = \mathcal{F}_{1D}^{-1}\{P(v_{x_r}, \varphi) \cdot H(v_{x_r})\} \quad (2.27)$$

with  $\mathcal{F}_{1D}^{-1}$  the inverse 1D Fourier transform.

**Back-projection filtered (BPF)** In this method,  $f(x, y)$  is obtained by 1) back-projecting the projected data but this operation needs a larger matrix size than the size needed for the final result as the backprojection has infinite support, 2) filtering in the frequency space, and 3) performing the inverse Fourier transform.

**Filtered back-projection (FBP).** It is the most common technique used in PET analytical reconstruction. To put it concisely, the projections must be filtered in order to recover  $f(x, y)$ . A 1D ramp filter can deduced from the CST. The object  $f(x, y)$  is obtained by 1) filtering each projection for each angle in the Fourier space, 2) performing the inverse Fourier of the filtered projections and 3) back-projecting the latter in the image space. To find the FBP formula, we start from the inverse 2D Fourier transform of the object

$$f(x, y) = \int_{-\infty}^{+\infty} \int_{-\infty}^{+\infty} F(v_x, v_y) e^{i2\pi(v_x x + v_y y)} dv_x dv_y \quad (2.28)$$

$v_x = v_{x_r} \cos \varphi$ ,  $v_y = v_{x_r} \sin \varphi$ ,  $dv_x dv_y = v_{x_r} dv_{x_r} d\varphi$  and  $x_r = x \cos \varphi + y \sin \varphi$ , see Figure 2.16, if we do a change of variables, the following equation is obtained,

$$\begin{aligned} f(x, y) &= \int_0^\pi \int_{-\infty}^{+\infty} P(v_{x_r}, \varphi) |v_{x_r}| e^{i2\pi v_{x_r} x_r} dv_{x_r} d\varphi \\ &= \int_0^\pi p_F(x_r, \varphi) d\varphi \end{aligned} \quad (2.29)$$

where  $|v_{x_r}|$  and  $p_F(x_r, \varphi)$  are the 1D ramp filter allowing the exact inversion of the Radon transform and the filtered projections, respectively.

Some limitations of FBP are as follows. FBP assumes continuous projections for angles  $0 \leq \varphi \leq \pi$  and noiseless data, when intrinsic data collection is sampled and there is statistical noise in the measurements, thus the exact solution cannot be found. Also, due to the discrete sampling ( $\Delta x_r$ ), the maximum recoverable frequency is the Nyquist frequency ( $\nu_N = 1/2\Delta x_r$ ), limiting the maximum frequency that can be recovered without aliasing artefacts. Conversely, due to the presence of statistical noise in the measured projections, the Fourier transform of these projections is dominated by noise above a certain frequency and the ramp filter amplifies these high frequency components, causing a degradation in the SNR.

Regularisation<sup>6</sup> is therefore required, typically for the FBP using an apodising function using the Hamming window ( $W_H$ ) in the Fourier space, a smoothing function applied to suppress the contribution of noise above a cut-off frequency,  $\nu_c$ , which determines the trade-off between spatial resolution and noise in the images. It is described as follows

$$W_H(\nu_{x_r}) = \begin{cases} \alpha + (1 - \alpha)\cos\left(\frac{\pi\nu_{x_r}}{\nu_c}\right) & |\nu_{x_r}| < \nu_c \\ 0 & |\nu_{x_r}| \geq \nu_c \end{cases} \quad (2.30)$$

where  $0.5 \leq \alpha \leq 1$  controls the shape of the window. The regularised and filtered projections back-projection can thus be expressed as Equation 2.31.

$$f(x, y) \approx \int_0^\pi \mathcal{F}_{1D}^{-1}\{W_H(\nu_{x_r})|\nu_{x_r}|P(\nu_{x_r}, \varphi)\} d\varphi \quad (2.31)$$

The recovery of  $f(x, y)$  is therefore largely bounded by the statistical noise in the projections recorded, data sampling, together with the uncertainty on the corrections made in the estimation of line integrals.

#### 2.14.1.4 3D analytical reconstruction

2D FBP can be adapted for 3D FBP reconstructions using different methods. One alternative is the 3D reprojection algorithm from Kinahan and Rogers (1988), an extension of the 2D FBP. However, the method is computer intensive and requires rebinning methods such as the single-slice rebinning (SSRB) (Daube-Witherspoon and Muehllehner, 1987), multi-slice rebinning (MSRB) (Lewitt, Muehllehner, and Karp, 1994) and Fourier rebinning (FORE) (Defrise et al., 1997).

#### 2.14.2 Iterative reconstruction

Unlike analytical methods, iterative reconstructions proceed by incrementally estimating the distribution of activity in  $f(x, y)$  rather than doing a direct inversion of the line integral model. They are more flexible due to their discrete models using matrices and thus enable the implementation of stochastic noise, the statistical nature of the data, the physical processes involved (positron range, non-collinearity, attenuation, scatter, ...) or any a priori known information about the object to be reconstructed. Iterative methods can be classified in two categories: algebraic and statistical methods. Algebraic methods are no longer used because it is not possible to model stochastic noise events with these methods. Iterative-statistical algorithms consist of different elements which are 1) the image model, 2), the data (noise) model, 3) system model, 4) objective cost function and 5) optimisation algorithm (Fessler, 2002; Hoeschen, Rafecas, and Aspelmeier, 2011). A comprehensive description of iterative and correction methods can be found in Moreau (2019) and Salvadori (2020).

##### 2.14.2.1 Maximum-Likelihood Expectation Maximisation

Maximum-Likelihood Expectation-Maximization (MLEM) has been introduced by Shepp and Vardi (1982) and is based on the maximisation of the logarithm of the Poisson likelihood cost function (Maximum Likelihood (ML)) using Expectation Maximisation (EM) optimising algorithm. MLEM can be readily adapted to perform

6. See [Wikipedia/Regularisation \(mathematics\)](https://en.wikipedia.org/wiki/Regularisation_(mathematics))

reconstructions using the *listmode* data format (Parra and Barrett, 1998; Reader et al., 1998).

MLEM is attractive as it provides the possibility to modify and incorporate prior information and data can be described using realistic models. The algorithm is valid for 3D data, without estimating missing projections. Convergence to the ML solution is guaranteed but might be slow since during each iteration, where a forward and a backward projections are required. Image noise increases with number of iterations due to statistical noise. However, even if the computation is bigger than FBP, MLEM provides more accurate reconstructions with an ameliorated SNR and less streak artefacts.

### 2.14.2.2 Ordered-Subset Expectation Maximisation

OSEM accelerates the reconstruction process of MLEM using ordered subsets of projection data (Hudson and Larkin, 1994). Succinctly, the entire data is sub-divided into  $N$  subsets and at each  $k$  iteration an MLEM algorithm is applied to each subset, taking the estimated image from the previous subset,  $N - 1$ . The image is updated  $N$  times. OSEM thus reaches the ML solution  $N$  times faster than MLEM.

OSEM is equivalent to MLEM algorithm if  $N = 1$ . The main drawback of OSEM is that convergence is not guaranteed compared to MLEM which improves monotonically the ML solution. The way the subsets are chosen and ordered has an effect on the resulting reconstructions, and hence, an evaluation and optimisation of the number of iterations and subsets is necessary when the algorithm is applied to real noisy data (Takahashi and Ogawa, 1997).

### 2.14.2.3 Corrections during reconstruction

Different biases have an influence on the quantification of reconstructed data due to technical and physical influences which should be corrected for to obtain accurate true coincidences on which accurate reconstruction relies. The effects can be multiplicative,  $m_i$ , or additive,  $a_i$ , for each LOR  $i$ , and can be corrected as

$$g_{i,corr} = m_i g_i + a_i \quad (2.32)$$

where  $g_{i,corr}$  is the corrected measured data. For iterative reconstructions,  $m_i$  and  $a_i$  can be incorporated in the matrix system model, which however might substantially increase computation time, rendering the algorithms not suitable for clinical practice. For these practical reasons, generally only  $m_i$  are implemented in the system matrix and  $a_i$  are considered after the projection step. It is also important to keep in mind that when corrections are implemented, the Poisson statistics of the recorded data should be preserved.



## Chapter 3

# The physics of $^{90}\text{Y}$ for PET imaging

As outlined in Chapter 1,  $^{90}\text{Y}$  is used as a radioisotope for the treatment of liver cancers by radioembolisation. While it is a pure beta emitter, making it suitable for therapy, there is also the phenomenon of internal production of pairs ( $e^-e^+$ ) in the disintegration scheme of  $^{90}\text{Y}$ , arising from a rare electric monopole transition (E0) between the  $0^+ / 0^+$  states of  $^{90}\text{Zr}$ . This property can be therefore be exploited for the detection of 0.511 MeV annihilation photons using PET imaging systems, for which a state-of-the-art is provided in Chapter 2.

Indeed,  $^{90}\text{Y}$  has multiple characteristics that make it an interesting radionuclide for targeted internal therapy and imaging. This chapter provides an overview on the physics of  $^{90}\text{Y}$  and the internal pair production following its decay which can be exploited for personalised dosimetry using PET imaging for post-radioembolisation monitoring.

### 3.1 $^{90}\text{Y}$ radiation physics

#### 3.1.1 Properties and decay scheme of $^{90}\text{Y}$

$^{90}\text{Y}$  is a pure  $\beta^-$  emitter, producing only electrons during its disintegration to its daughter products, mainly to the  $^{90}\text{Zr}$  fundamental level, and to a much lesser extent to an excited state of  $^{90}\text{Zr}$ . It is one of a minority of radionuclides that do not emit gamma rays at a significant rate after decay. Its decay scheme is provided in Figure 3.1. The properties of  $^{90}\text{Y}$  have been provided in Table 1.1 in Chapter 1.  $^{90}\text{Y}$  has a half life of 64.04 h. The mean energy of the  $\beta^-$  spectrum is equal to 0.927 MeV (with a maximum of 2.28 MeV). The whole  $\beta^-$  spectrum is depicted in Figure 3.2. We will see in the next Section 3.1.2 that there is also a very small positron production during the disintegration process of  $^{90}\text{Y}$ , which is of interest for this thesis.

When radiation transport is calculated in water (close to soft tissue medium), emitted particles following  $^{90}\text{Y}$  disintegration have mean and maximum ranges of 2.5 and 11 mm (respectively) and 90% of the energy emitted is deposited within 5.3 mm.  $^{90}\text{Y}$  is therefore of interest for nuclear medicine applications owing to its long life producing  $\beta^-$  particles with short ranges in water, considering the fact that proper targeting can be achieved and allowing for high absorbed doses into the targeted tissue between embolised capillaries during radioembolisation.

#### 3.1.2 Internal pair production and its branching ratio

##### 3.1.2.1 $0^+ \rightarrow 0^+$ transition of $^{90}\text{Zr}$

The decay scheme of  $^{90}\text{Y}$  is shown in Figure 3.1 with ( $\beta_{00}^-$ ) representing almost 100% ( $\approx 99.98\%$ ) of the radioactive decay.  $^{90}\text{Y}$  has a rare part of its branching ratio



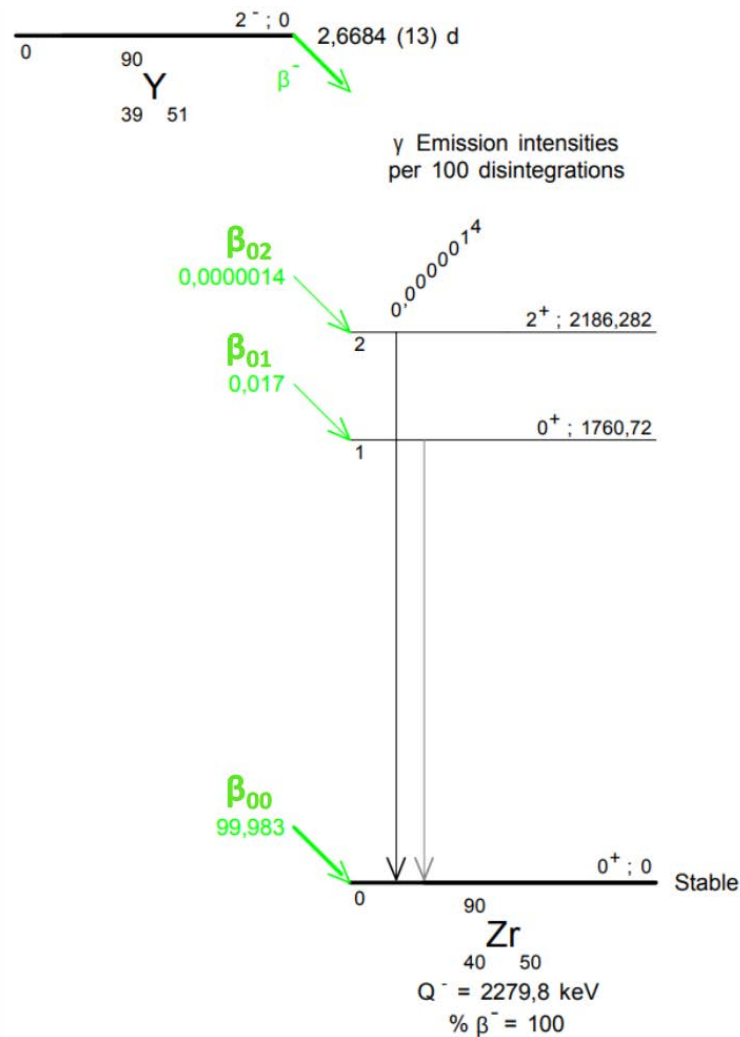


FIGURE 3.1 – Radioactive decay scheme of the parent isotope  $^{90}\text{Y}$  to the stable daughter isotope  $^{90}\text{Zr}$ .  $^{90}\text{Y}$  is considered a pure  $\beta^-$  emitter ( $\beta_{00}^-$ ,  $\beta_{01}^-$ ,  $\beta_{02}^-$  transitions). A minor (rare) branch,  $\beta_{01}^-$ , of  $^{90}\text{Y}$  in its disintegration goes to the first excited  $0^+$  state of  $^{90}\text{Zr}$  where the origin of the  $\beta^+$  production can be explained following a rare monopole transition (E0) between the  $0^+/0^+$  states of  $^{90}\text{Zr}$  resulting in internal pair creations. The  $2^+$  excited state of  $^{90}\text{Zr}$  is also depicted but the branching ratio for this transition to happen is negligible. Other excited states of  $^{90}\text{Zr}$  exist, which are above the 2.28 MeV beta spectrum of  $^{90}\text{Y}$ . Extracted from LNHB (France), Bé et al. (2006).

( $\beta_{01}^-$ ) which disintegrates to the  $0^+$  first excited state of  $^{90}\text{Zr}$  at an energy level equal to 1.76 MeV. A third branching ratio ( $\beta_{02}^-$ ) represents the transition of  $^{90}\text{Y}$  to the  $2^+$  excited state of  $^{90}\text{Zr}$ , but the branching ratio for the latter is even more scarce. Table 3.1 provides the branching ratio for the three respective  $\beta^-$  transitions, as well as for  $\gamma$  transitions.

The de-excitation which follows from the  $0^+$  first excited to the ground stable state of  $^{90}\text{Zr}$  can result in two possible transitions, either 1) an internal conversion process where the excited nucleus interacts electromagnetically with an orbital electron of the atom which is ejected from the atom (causing subsequent characteristic X-ray and Auger emissions), or 2) an electron-positron ( $\beta^-/\beta^+$ ) internal pair creation if the excited energy is higher than 1.022 MeV. A third transition with a two-photon

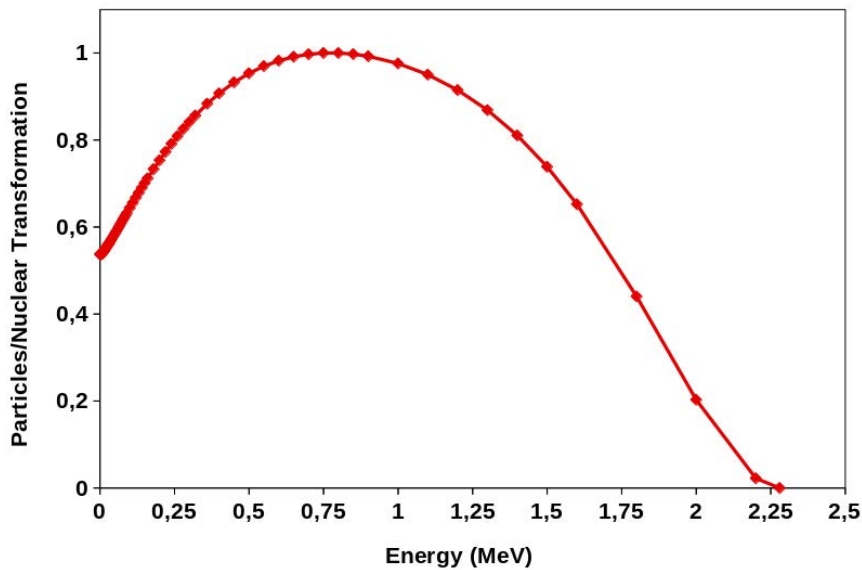


FIGURE 3.2 –  $\beta^-$  spectrum of  $^{90}\text{Y}$  for all decay branches. Data downloaded from ICRP publications (Eckerman, 2008) for  $^{90}\text{Y}$ .

TABLE 3.1 – Properties of  $^{90}\text{Y}$  decay for  $\beta^-$  and  $\gamma$  transitions. Values are from LNHB (France), Bé et al. (2006).

Transition	Energy (keV)	Probability ( $\times 100$ )
$\beta_{00}^-$	2279,8	99,983
$\beta_{01}^-$	519,1	0,017
$\beta_{02}^-$	93,5	0,0000014
$\gamma_{10}$	1760,7	0,017
$\gamma_{20}$	2186,282	0,0000014

emission can occur but is negligibly small compared to the two first ones.

The transition which occurs is an electric monopole transition  $0^+ \rightarrow 0^+$  of  $^{90}\text{Zr}$  and there is no modification in the nucleus composition of the parent (excited) and daughter (stable) nuclei and single gamma transitions are absolutely forbidden (unlike in typical excited states). As stated by D’Arienzo (2013), this may be visualised as a “breathing” mode without change of shape. For a detailed review on the decay modes of  $^{90}\text{Y}$  and explanation the monopole transition  $0^+ \rightarrow 0^+$  states of  $^{90}\text{Zr}$ , readers can refer to D’Arienzo (2013) and Deutsch (1957) (among others).

### 3.1.2.2 Positron branching ratio and historical background

Ford (1955) theoretically expected that the first excited state of  $^{90}\text{Zr}$  might be a  $0^+$ . This prediction has been put in evidence during the same year by Johnson, Johnson, and Langer (1955) working in the same laboratory. At the time, they observed a 1.75 MeV transition line (with a FWHM of 0.5%) on their spectrometer in their experimental setup using an  $^{90}\text{Y}$  source corresponding to internal conversion events with an intensity of 0.005% relative to the 2.26 MeV  $\beta^-$  spectrum. They also noticed a weak positron distribution with an intensity of  $0.020 \pm 0.010\%$  relative to the 2.26 MeV  $\beta^-$  spectrum and an energy distribution with about a maximum of 0.8 MeV. They presumed it arose from internal pair creations. They did not detect any

gamma-ray in their experimental setup line in the 1.75 MeV region. This transition was therefore assumed to be that of a monopole between two  $0^+$  states of  $^{90}\text{Zr}$ .

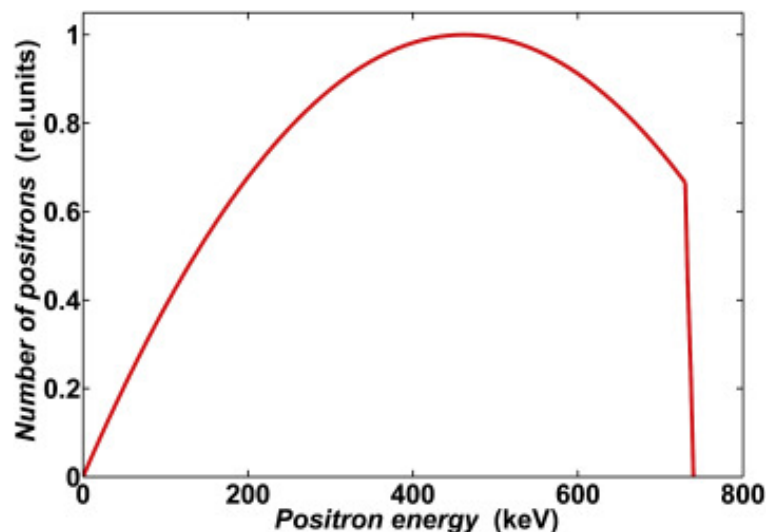


FIGURE 3.3 –  $\beta^+$  spectrum from the monopole transition of  $^{90}\text{Zr}$ . Extracted from Dryák and Šolc (2020).

Several experimental studies followed to measure more precisely the internal pair production per  $\beta^-$  decay,  $w_p/w_\beta$ . The values found in literature are provided in Table 3.2. The  $\beta^+$  spectrum following the monopole transition states of  $^{90}\text{Zr}$  is depicted in Figure 3.3. The last study was from Dryák and Šolc (2020), where they determined the  $w_p/w_\beta$  ratio from the number of 511 keV photons originating from positron annihilation using two calibrated high purity germanium detectors. A theoretical continuous  $\beta^+$  spectrum with a maximum energy of 738 keV was used to calculate the detection efficiency of the 511 keV photons using Monte Carlo calculations (MNCPIX) to support the measurements, as depicted in Figure 3.3. The authors found the  $w_p/w_\beta$  ratio to be  $3.26 \pm 0.04 \times 10^{-5}$ .

TABLE 3.2 – Experimentally determined positron branching ratio ( $w_p/w_\beta$ ) from published studies.

Reference	$w_p/w_\beta$
Johnson, Johnson, and Langer (1955)	$0.020 \pm 0.010 \times 10^{-2}$
Greenberg and Deutsch (1956)	$3.6 \pm 0.9 \times 10^{-5}$
Langhoff and Hennies (1961)	$3.4 \pm 0.4 \times 10^{-5}$
Selwyn et al. (2007)	$3.186 \pm 0.047 \times 10^{-5}$
Dryák and Šolc (2020)	$3.26 \pm 0.04 \times 10^{-5}$

An accurate knowledge of the branching ratio is necessary for an accurate quantification of the yttrium accumulated in the target region. Else, the last recorded positron branching ratio by Dryák and Šolc (2020) differ by around 2.3% from the one in the previous study by Selwyn et al. (2007), the latter being implemented in all clinical PET systems for quantification.

## 3.2 Confounding factors in $^{90}\text{Y}$ PET imaging

For the record, the primary purpose of using  $^{90}\text{Y}$  in nuclear medicine is therapy. Its radioactive emission characteristics allow for post-treatment monitoring using emission tomography imaging. The use of SPECT and its inherent drawbacks has been highlighted in the previous chapters (see also Section 3.4.1 below).

$^{90}\text{Y}$  is also an unfavourable PET tracer compared to those commonly used for diagnostic purposes. This section outlines and discusses the confounding factors in quantification using PET for  $^{90}\text{Y}$  imaging. These are the low statistics from the small  $\beta^+$  branching ratio described previously and the challenge to detect useful counts among the natural background radioactivity of  $^{176}\text{Lu}$  emitting gamma prompts which fall into the energy window for coincidence detection present in the LYSO/LSO crystals and the X-ray radiation from  $^{90}\text{Y}$  disintegration spectrum around the 511 keV peak.

### 3.2.1 Low $\beta^+$ production

The relatively low  $^{90}\text{Y}$  positron branching ratio,  $w_p/w_\beta$ , (from the  $0^+ \rightarrow 0^+$  states monopole transition of  $^{90}\text{Zr}$  described above) is therefore the main limiting and confounding factor in  $^{90}\text{Y}$  PET imaging. The low statistics cause long scan times and noisy images due to a low true coincidence rate. Post  $^{90}\text{Y}$ -radioembolisation patients undergo a 15-20 min/bed PET acquisition on actual systems, longing 30 to 40 minutes per patient if two bed positions are acquired.

### 3.2.2 Natural background radioactivity

A well known confounding factor associated to  $^{90}\text{Y}$  imaging is the presence of  $^{176}\text{Lu}$  in LYSO/LSO crystals, with an isotropic abundance of 2.59% (Luo and Kong, 2006).  $^{176}\text{Lu}$  has a long half life,  $3.56 \times 10^{10}$  years as measured by Luo and Kong (2006), and emits gamma prompts which might fall into the coincidence energy selection window. For other conventional PET tracers such as  $^{18}\text{F}$ , the background radioactivity can be considered negligible due to the difference in orders of magnitude between  $^{176}\text{Lu}$  background counts and counts from annihilation processes. Due to the low positron statistics considering  $^{90}\text{Y}$ , background radiation can cause degradation in the quantification accuracy.

The choice of LYSO/LSO relative to another crystal composition is due to their faster light decay time,  $\tau_s$  (40 ns for LYSO/LSO vs. 300 ns for BGO), and to better energy resolution relative to other scintillators, refer to Table 2.3.

### 3.2.3 Bremsstrahlung radiation from $\beta^-$ radiation

Figure 3.4 illustrates the bremsstrahlung X-ray photons fluence spectrum created by the  $\beta^-$  emission during the disintegration of  $^{90}\text{Y}$  (Top) and its contribution around the 511 keV region (Bottom). Dryák and Šolc (2020) quantified this contribution to the 511 keV peak to be around 0.14% to the total number of 511 keV photons, with a branching ratio of  $4.4 \times 10^{-8}$ , compared to the the  $3.186 \times 10^{-5}$  positron branching ratio from Selwyn et al. (2007). As stated by Pasciak et al. (2014), low energy bremsstrahlung photons are attenuated by the patient's body, at few keVs below 20 keV, see Figure 3.4 Top. The spectrum is quite constant up to around 500 keV and drops significantly afterwards until the 2.28 MeV maximum.

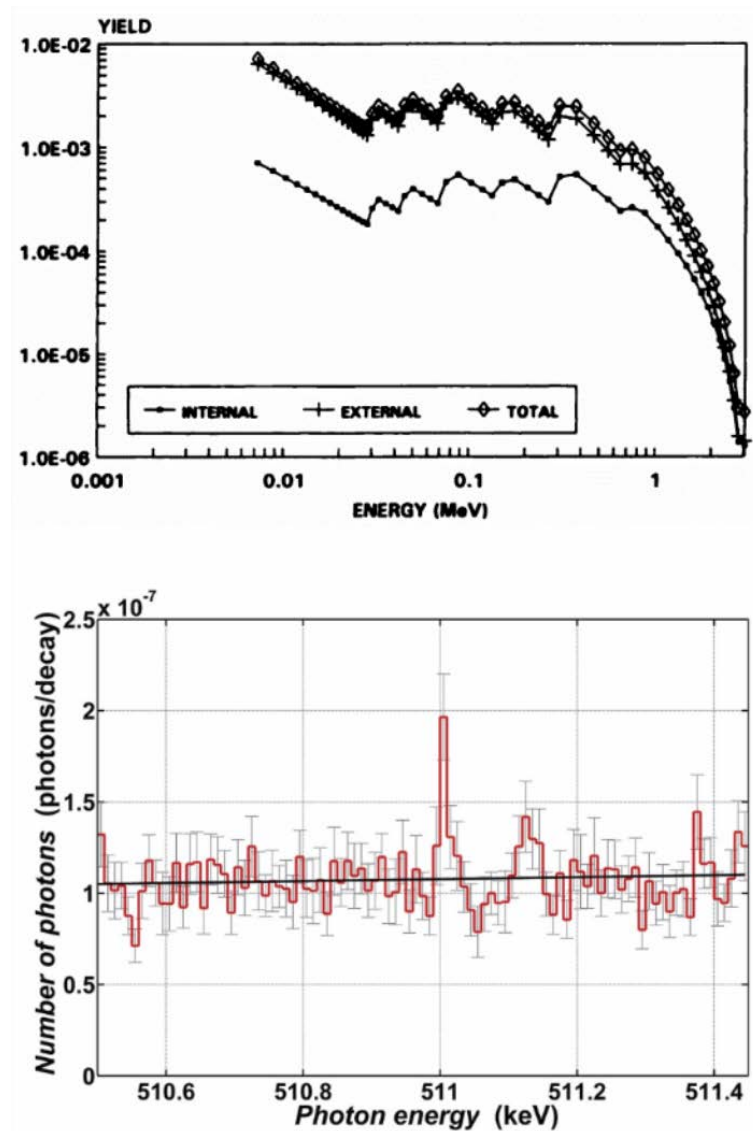


FIGURE 3.4 – Bremsstrahlung photon spectrum following emission of  $\beta^-$  particles during  $^{90}\text{Y}$  disintegration. *Top*: Total bremsstrahlung spectra extracted from Stabin et al. (1994). *Bottom*: The 511 keV annihilation photon peak embedded in the background bremsstrahlung photons around the 511 keV energy extracted from Dryák and Šolc (2020).

The fear previously associated with the bremsstrahlung photons is the PET detector saturation with the *singles* rates which exceeds the true counts rate, degrading image quality and therefore the accuracy in quantification. However, this does not seem to be a major issue, despite the high activity of  $^{90}\text{Y}$  that may be present inside the FOV (a few GBq). State-of-the-art PET systems and technologies presented in Chapter 2 showed improved performance. Several studies proved the feasibility of  $^{90}\text{Y}$  imaging using PET, especially using TOF (Lhommel et al., 2009).

The study from Lhommel et al. (2009) used a 2.5 mm thickness of copper ring into the gantry to limit the arrival of bremsstrahlung photons to the detectors and limit saturation. Later on, Strydhorst et al. (2016) demonstrated and confirmed that quantitative  $^{90}\text{Y}$  can be achieved with the same methods as for  $^{18}\text{F}$  and that there was little potential for improvement in taking into account the peculiarities of  $^{90}\text{Y}$

PET imaging with the presence of bremsstrahlung X-rays in the single data.

Indeed, Strydhorst et al. (2016) investigated the impact of the confounding factors compromising  $^{90}\text{Y}$  quantification using PET, comparing their phantom experiments (comparing  $^{90}\text{Y}$  and  $^{18}\text{F}$  measurements) to Monte Carlo simulations using GATE. To summarise their findings, no significant influence was detected on the quantification of  $^{90}\text{Y}$  that could be attributed to the presence of random counts using simulations and meet findings from Carlier et al. (2015), allowing data to be decay corrected to obtain correct quantification.

### 3.3 Other factors limiting quantification in PET

Several other factors confound the quantification in emission tomography, less specific to one specific PET radiotracer. The limitations of the physical processes involved (positron range, non-collinearity, attenuation, scatter) and PET detection system have been presented in Chapter 2 and add further bias on activity quantification, see Section 2.6 and Figure 2.8. In PET, several correction methods are available in to limit these degrading factors, including arc effects, normalisation, attenuation, random and scattered coincidences, deadtime and pile-up and partial volume effects corrections. The correction methods will not be detailed in this thesis, but a complete state-of-the-art on can be found in Salvadori (2020), *Partie I-Chapitre VI-Corrections et quantification*.

## 3.4 Post-treatment radioembolisation monitoring

### 3.4.1 $^{90}\text{Y}$ emission tomography imaging

$^{90}\text{Y}$  SPECT imaging exploits bremsstrahlung X-rays, with various published energy windows and has been used for post-SIRT evaluation. However, despite the common use of SPECT/CT, it represents number of drawbacks. SPECT suffers from noise and challenging quantitative analysis, from lower image quality compared to conventional radiotracers used in SPECT. Quantification using  $^{90}\text{Y}$  bremsstrahlung single photon emission computed tomography (BremSPECT) images also requires specialised techniques which might confound accuracy of output images (Clarke et al., 1992; Kappadath, 2010). However, some recent studies using Monte Carlo and deep learning methods have shown substantial improvement over  $^{90}\text{Y}$  SPECT of the past without significant degradation in image noise or intensive computational requirements (Dewaraja et al., 2017; Xiang et al., 2020).

Nickles et al. (2004) first exploited the minor positron branching ratio for  $^{90}\text{Y}$  PET imaging to show the distribution of the regional absorbed dose delivered by  $^{90}\text{Y}$  therapies. Activity distribution assessment after  $^{90}\text{Y}$ -SIRT was proved feasible in 2010 by Lhommel et al., 2009, 2010, with the help of TOF information added on PET/CT systems. Other studies followed and showed that TOF PET compared to non-TOF PET provided improved recovery in reconstructed quantitative data. Although it was shown that routine PET scanners can produce good-quality  $^{90}\text{Y}$  images, further studies are needed to determine which reconstruction methods and acquisition parameters should be used (Van Elmbt et al., 2011; Pasciak et al., 2014).

### 3.4.2 Imaging alternatives for $^{90}\text{Y}$ radioembolisation monitoring

Although beyond the scope of this thesis, optical detection and imaging of  $^{90}\text{Y}$  radioactivity by Cerenkov luminescence is feasible. Cerenkov radiation is emitted by high-energy beta particles when these particles travel faster than the relative speed of light in an aqueous medium (Ciarrocchi and Belcari, 2017). These charged particles change the local electromagnetic field and cause orbital electrons to be displaced and polarised. These polarised electrons then return to their initial equilibrium state by emitting visible and ultraviolet photons.

There are non-invasive imaging systems with high sensitivity to detect Cerenkov radiation, known as Cerenkov luminescence imaging (CLI) and has been used for example for  $^{18}\text{F}$  and  $^{68}\text{Ga}$  as positron emitters, and  $^{90}\text{Y}$  as  $\beta^-$  emitter which is the most efficient medical isotope for Cerenkov light production (Wright et al., 2015). The advantages of CLI are that it is non-invasive, provides high spatial resolution images, and imaging is performed in seconds compared to more than 10-20 minutes for SPECT and PET. In addition, they are much cheaper than small animal SPECT or PET systems and several small animals can be imaged simultaneously. However, CLI has all the disadvantages of optical imaging, i.e. reduced penetration depth and complex tissue transport.

For more information on CLI and the interest in it, the reader can refer to Wright et al. (2015) and Ciarrocchi and Belcari (2017). Indeed, more research is needed in this area to move from a qualitative molecular imaging technique to a proper quantitative technique. Another technique, called radioluminescence imaging (RLI), has also been explored (Spinelli and Boschi, 2015).

## 3.5 Conclusion

PET/CT with implemented TOF information in image reconstruction provides the potential to accurately measure  $^{90}\text{Y}$  activity concentration despite the low  $^{90}\text{Y}$  positron branching ratio, with a reasonable degree of accuracy.  $^{90}\text{Y}$  TOF-PET is therefore useful, providing better image quality than  $^{90}\text{Y}$  BremSPECT. It has been confirmed that the contribution of bremsstrahlung X-ray and the background radioactivity have negligible contribution on the quantification of  $^{90}\text{Y}$  PET and there is few margin to take into account these specific  $^{90}\text{Y}$  properties. The main limitations being the  $^{90}\text{Y}$  scarce positron production, the PET performance itself (e.g. spatial resolution) and the accuracy of reconstruction algorithms. It is therefore necessary to select carefully the reconstruction parameters which can improve quantitative accuracy and the best choice will depend on the scanner and reconstruction software.

# **Part II**

# **Contributions**





## Chapter 4

# Monte Carlo simulation of the DPC-PET

*In this chapter, a GATE Monte Carlo model of the Philips Vereos Digital Photon Counting positron emission tomography (DPC-PET) imaging system using SiPM detectors is proposed. This chapter is adapted from Labour et al. (2020) and the publication is the result of a successful and still-ongoing collaboration with Julien Salvadori from the IADI Laboratory in Nancy. Julien Salvadori and I are equal contributors to the publication as joint first authors.*

### 4.1 Introduction

Positron emission tomography (PET) imaging has an essential role in modern medicine for both diagnostic and follow-up of oncology treatments (Cherry, Sorenson, and Phelps, 2012), as described in Part I in this thesis. It has been shown that PET technology has experienced tremendous improvements in performance over recent decades and new trends make use of SiPM detectors, such as the Philips Vereos DPC PET/CT introduced in 2013, the GE Discovery<sup>TM</sup> MI PET/CT launched in 2016 and the Siemens Biograph Vision<sup>TM</sup> and eFOV Vision Quadra<sup>TM</sup> PET/CTs launched in 2018 and 2020, respectively.

For the record, as it has been described in Chapter 2, the precision in the location of the annihilation has been improved with the use of TOF information, which spatially constrains the location of the event on the LOR, increasing the SNR in the reconstructed image (Lewellen, 1998). The TOF resolution improved with the use of SiPMs, due to their lower intrinsic timing resolution than conventional PMTs or APDs, with a more compact electronic configuration (Otte et al., 2006). Detecting and processing signals using dSiPMs bypasses the need to treat analogous signals by a direct binary count of optical photons, reducing noise in the processed output, providing better conditions for imaging than PMTs at low counts as described in Chapters 1 and 3.

The Vereos DPC system has the characteristics of a 1:1 coupling between the crystal array and the dSiPM array, which decreases uncertainty in the interaction position and ultimately improves the volumetric resolution on reconstructed images. The Vereos DPC system has been previously evaluated according to the experimental NEMA guidelines (Zhang, Maniawski, and Knopp, 2018; Rausch et al., 2019). The spatial resolution, defined as the FWHM was found to be 4.2 mm at the centre of the FOV, the average sensitivity was estimated to be 5200 counts per second (cps)/MBq, and the peak noise equivalent count rate (NECR) was 153.4 kcps at an activity concentration of  $^{18}\text{F}$  of 54.9 kBq.mL<sup>-1</sup>, according to Rausch et al. (2019). Several studies have shown that the Vereos DPC can improve the image quality of PET images compared to analogous systems, such as in Wright et al. (2018), Salvadori

et al. (2019a,b), and López-Mora et al. (2019). Moreover, diagnostic confidence and accuracy for oncology diseases is also improved (Nguyen et al., 2015; Wright et al., 2017a; Fuentes-Ocampo et al., 2019).

Simulations using Monte Carlo models are important and useful tools for PET imaging. They help to design, optimise and assess imaging systems, predict the performance, optimise acquisition parameters and reconstruction algorithms and evaluate the effects of confounding factors in image quality. Sarrut et al. (2021b) reviewed the latest advances in simulating current detectors and presented a detailed report on the imaging systems that have been simulated and evaluated in GATE<sup>1</sup>/Geant4<sup>2</sup> platform (Jan et al., 2004; Jan et al., 2011; Sarrut et al., 2014). The review benefited from the work provided during this thesis (Labour et al., 2020), and has been a collaborative work from the OpenGATE collaboration<sup>1</sup>.

Several works have been proposed to simulate PET systems using GATE. Various clinical PET imaging systems have been modeled and compared to experimental measurements, such as the ECAT PET systems HRRT (Bataille et al., 2004) and EXACT HR+ (Jan et al., 2005; Karakatsanis et al., 2006), Philips PET systems Allegro and GEMINI (Lamare et al., 2004; Lamare et al., 2006), GE PET systems Advance and Discovery LS (Schmidtlein et al., 2006) and Siemens PET systems Biograph 2 (Karakatsanis et al., 2006), Biograph 6 (Gonias et al., 2007), Biograph mcT (Poon et al., 2015) and Inveon (Lu et al., 2016). Others include studies from Buvat and Castiglioni (2002), Assie et al. (2004), Lamare et al. (2004), Michel et al. (2006), Lamare et al. (2006), Stute et al. (2011), Poon et al. (2012), and Lee, Gregor, and Osborne (2013). Refer to Table 1 in Sarrut et al. (2021b) for a complete bibliography including commercialised and prototype clinical and preclinical small animal systems. Several platforms are also available for Monte Carlo simulations such as SimSET (Badawi et al., 1999; MacDonald et al., 2008; Guérin and El Fakhri, 2008; Poon et al., 2015), PeneloPET (Abushab et al., 2016) (Penelope), SORTEO (Boisson et al., 2013), Eidolon (Zaidi and Morel, 1999) (MCNP), PETSIM (Thompson, Moreno-Cantu, and Picard, 1992), Geant4 (Moehrs et al., 2006) or GAMOS (Mikhaylova et al., 2011, 2013).

To our knowledge, no whole body clinical SiPM-PET Monte Carlo model has been proposed and made OpenSource for research purposes. In this work, the Philips Vereos DPC-PET system was modelled using the GATE platform and compared to measurements performed according to the NEMA protocols NU 2-2018 (NEMA NU 2-2018 - Performance measurements of positron emission tomographs 2018). All comparisons were performed using listmode data in order to remain independent of the image reconstruction algorithm.

## 4.2 Materials and methods

### 4.2.1 The Vereos DPC-PET/CT

The Vereos PET/CT installed at the CLB is depicted in Figure 4.1. It acquires data in a 3D mode using *listmode* data format. It consists of a total of 23,040 LYSO:Ce crystals of dimensions  $4 \times 4 \times 19$  mm<sup>3</sup> each, distributed on 18 *modules* forming the detector ring. The ring comprises a total of 360 *DPC-tiles* (or *stacks*), arranged 4 tangentially  $\times$  5 axially per *modules*. Each *DPC-tile* consists of a  $4 \times 4$  array of *DPC-sensors* (or *dice*), which are again sub-divided into  $2 \times 2$  *DPC-pixels*. It is at this level where there is a 1:1 coupling between each LYSO:Ce crystal and each *DPC-pixel*, thus

- 
1. See [OpenGATE collaboration](#)
  2. See [Geant4 overview](#)

avoiding the need for Anger logic decoding for crystal identification (Schaart et al., 2016). Other specifications of the Vereos are provided in Table 4.1 and the principle of operation of the DPC dSiPM is described in Section 2.10.1.



FIGURE 4.1 – The Vereos DPC dSiPM-based TOF-PET/CT from Philips installed at the CLB.

TABLE 4.1 – Key specifications of the Vereos from Philips (which can be found in literature, e.g. Schaart et al. (2016), Moreau (2019)).

Vereos specifications	
Acquisition mode	3D
Data format	Listmode
Crystal composition	LYSO:Ce
Detector design	dSiPM (DPC)
Number of modules	18
Number of stacks	360 (20/module)
Number of dice	5760 (320/module)
Number of crystals	23,040 (1280/module)
Number of photodetectors	23,040
Crystal to photodetector coupling	1:1
Crystal dimensions	$4 \times 4 \times 19 \text{ mm}^3$
Ring diameter	764 mm
Axial FOV	164 mm
Coincidence window ( $2\tau$ )	4.0 ns
Energy discrimination window	449.68-613.20 keV

#### 4.2.2 PET scanner model in GATE

The DPC-PET scanner was modelled with GATE 8.2 (Jan et al., 2004; Jan et al., 2011; Sarrut et al., 2014, 2021b) using Geant4 10.5. The geometry, dimensions and

material composition of the scanner were provided by Philips. The cylindrical PET was defined by a set of hierarchically arranged elements with four different depth levels as described in the previous Section 4.2.1. The first level component was the *module* (1<sup>st</sup> level). The 18 modules were arranged in one ring and each module was composed of an array of  $4 \times 5$  blocks, the *stacks* (2<sup>nd</sup> level). The stacks were individually subdivided into  $4 \times 4$  *dice* (3<sup>rd</sup> level). Each die consisted of a grid of  $2 \times 2$  LYSO scintillator *crystal* elements (4<sup>th</sup> level). Spacing and packing materials between the different detector blocks were taken into account. The final configuration leads to one detector ring with the total of 23,040 LYSO scintillator crystals required, with individual dimensions of  $4 \times 4 \times 19 \text{ mm}^3$ , resulting in an axial FOV of 164 mm and a detector cylinder of 764 mm inner diameter, see Table 4.1. Figure 4.2 shows the geometry of the PET model. In addition to the detector rings, the model included the lead shielding rings (which reduces the interference from activity outside the FOV), the inner diameter plastic cover and all the back compartments to take into account scatter in surrounding materials. The bed and different NEMA phantoms used were also modelled to take into account photon attenuation.

### 4.2.3 Simulation physics parameters

Simulations using the modelled PET corresponding to the different NEMA tests discussed in this study, were carried out (see NEMA description in Section 4.2.6). In all simulations, the physics list named `emstandard_opt4` was used<sup>3</sup>. It contains the Geant4 most accurate standard and low-energy models for electromagnetic processes recommended for medical applications (Beaudoux et al., 2019; Arce et al., 2021). Range production cuts were set to 0.1 mm for electrons and photons in the whole geometry. In Geant4, it means that secondary particles are only created and tracked when their expected range in the current material is larger than this distance. No variance reduction technique was used. The radioactive sources of  $^{18}\text{F}$  were simulated by  $\beta^+$  sources with energy spectra parameterized according to the Landolt-Börnstein tables (Jan et al., 2004). The number of primary particles was adapted for all simulations according to the NEMA protocol.

### 4.2.4 Photon detection and coincidence events

In a PET imaging system, coincidence events are detected by scintillation detectors coupled with photo-detector systems. Incident annihilation photons of 511 keV interact in the inorganic crystal (here: LYSO:Ce) and generate, by scintillation, thousands of flash optical photons that are detected by the photo-detector (here: dSiPM). Even if Monte Carlo tracking of optical photons can be performed (Stockhoff et al., 2017), it would require a tremendous amount of computation time to perform a complete simulation, estimated to be three orders of magnitude longer than without optical photons. Instead, because the number of generated scintillation photons is proportional to the energy deposited in the crystal, an analytical model is used through a specific *digitizer module* that converts photon interactions in the crystal into digital counts and manages the timestamp of all events (Jan et al., 2004). The *digitizer* is composed of successive signal processing operations that mimics the photo-detection process<sup>4</sup>.

Figure 4.3 gives the schematic representation of the proposed signal processing chain. Individual particle interactions within the crystal are called *hits*. They are

3. See `Geant4/PhysicsList`

4. See `OpenGATE/readthedocs`

## Scanner geometry: Philips Vereos DPC-PET

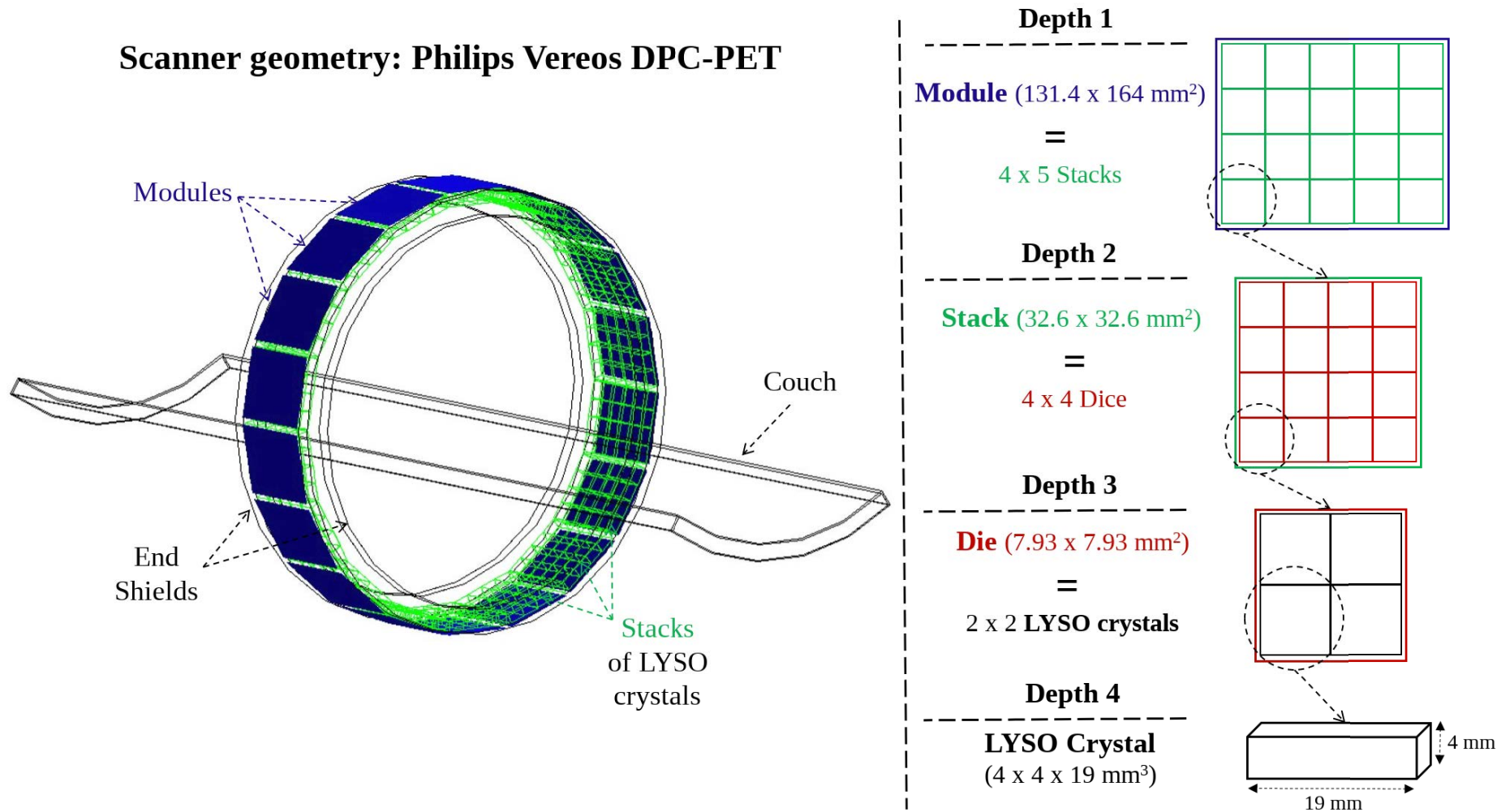


FIGURE 4.2 – GATE geometry model of the Philips DPC-PET. The four depth levels components are illustrated on the right of the image. 18 *modules* are repeated in one ring. Each module contains 4 tangentially  $\times$  5 axially arranged *stacks*. Each stack is subdivided into  $4 \times 4$  *dice* and each die contains  $2 \times 2$  LYSO *crystals*. The system is composed of a total of 23,040 crystals.

gathered into *pulses*, converted into *singles* and sorted into final *coincidences*. Along the chain, several models and parameters values have been chosen: the 1) adder, 2) readout, 3) background noise, 4) energy resolution, 5) detection efficiency, 6) temporal resolution, 7) pile-up, 8) deadtime, 9) energy thresholds and 10) coincidence window. Some parameters have been set according to constructor data, others according to a method adapted from Guez et al. (2008). They are described below, with Figure 4.3 providing a schematic illustration of the *digitizer chain* and Table 4.2 reporting all parameter values. The choice of each parameter is explained in the following sections.

TABLE 4.2 – Parameter values of the digitizer chain.

Single event processing parameters	
Background noise level	461 kHz
Crystal blurring	11.2% @ 511 keV
Detection efficiency	86.5%
Temporal resolution (STR)	220 ps
Pile-up	5.9 ns
Deadtime	5.9 ns
Energy window	449.68-613.20 keV
Coincidence builder	
Coincidence window ( $\tau$ )	2.0115 ns
Delayed window offset	100 ns
Multiple coincidences	<i>takeAllGoods</i>
Acceptance angle	80° max.

#### 4.2.4.1 Adder and readout

**Adder.** It consists of the first module of the *digitizer chain*, gathering multiple *hits* generated by a particle in a crystal (depth 4, the sensitive detector) into a *pulse*. The energy deposited in each crystal is therefore recorded, as well as the interaction position calculated as an energy-weighted centroid of the different *hit* positions, describing the *pulse*. The timestamp of the *pulse* corresponds to the timestamp of the first interaction in the sensitive detector.

**Readout.** Two different approaches are available in GATE to choose for the readout process, i.e., the segmentation level and logic at which data is read. These are the *winner-takes-all* and *energy-centroid* policies. The first one models an APD- or SiPM-like readout and the *depth* variable should be set to determine at which level of the hierarchy the grouping of pulses should be performed. The interaction position in the crystals is the one that provides the highest energy pulse. The second one models a PMT-like readout, forcing the depth of the grouping to the sensitive detector (the crystal level), and all the pulses belonging to a level higher than the crystal level (and having the same ID) are summed together. For both policies, the readout output is the sum of different pulses having the same level ID regrouped in a single pulse. The next step is to emulate the response of the detectors and convert this readout

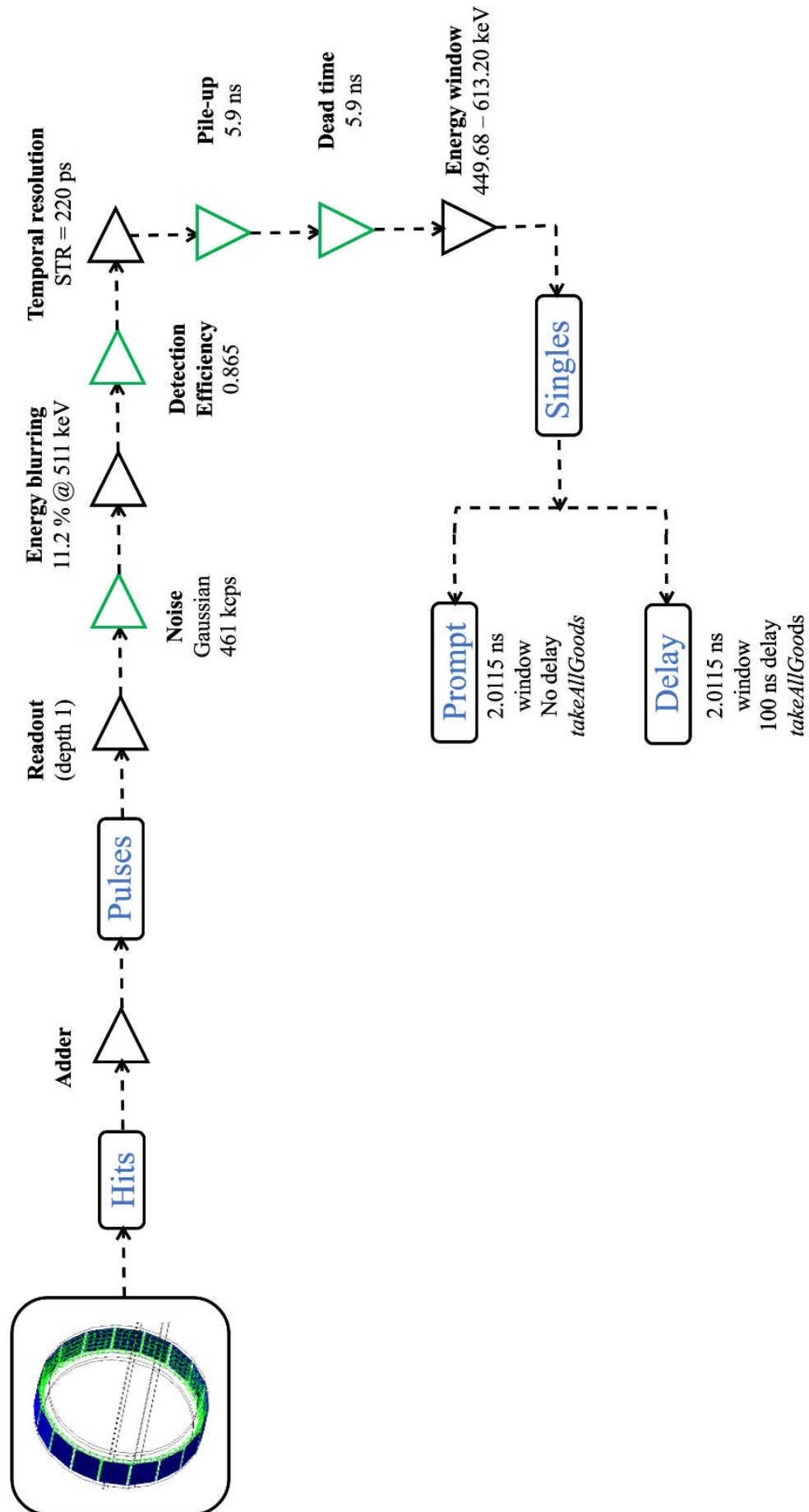


FIGURE 4.3 – Digitizer chain used in GATE simulations.



pulse into a single, which simulate the physical observables of a detector's response to a particle interacting with it.

The readout process takes place at the level of the *die* (depth 3) for the DPC-sensor. Therefore, theoretically, the *winner-takes-all* policy set at depth 3 would more accurately model the readout process using the digitizer. However, during the optimisation process, this combination provided an underestimation of about 40% of the simulated data compared to the experimental number of counts. On the other hand, on tuning, when the readout was set on the module (depth 1), the count rates were much more consistent with the experimental data. Therefore, the final combination using *winner-takes-all* set at depth 1 was used.

#### 4.2.4.2 Background noise, deadtime, pile-up and detection efficiency

The *background noise* can be due to the electronics and the natural radioactivity of the crystals ( $^{176}\text{Lu}$  in the LYSO crystals). Background noise cannot be neglected at low activities below a few MBq (or at low count statistics). Background noise in the simulations in this study was modelled using stochastic energy according to a Gaussian distribution centred on 511 keV, and inter-event time intervals according to a Poisson process. The *deadtime* is the time after each event during which the system is not able to record another event. *Pile-up* events can occur when the, possibly partial, sum of the deposited energies from the two events is recorded as one single event instead of two separate events. The *detection efficiency* takes into account the quantum efficiency of the crystals and light transfer between the crystals and the SiPMs, and corresponds to the probability to detect a photon by the photodetectors.

The above described parameters were not communicated by the manufacturer to be implemented in the model for better accuracy in event counts at low (concerning background noise and detection efficiency) and high (concerning deadtime and pile-up) activity concentrations. Following Guez et al. (2008), all parameters have been determined and proposed from experimental measurements and simulations for this work.

**Deadtime and background noise.** First, we used the *singles* data from the phantom acquisition, as stated in the NEMA NU 2-2018 guidelines for measurement of the scatter fraction, count losses and randoms, further described in Section 4.2.6.1 below. In GATE, the deadtime can be applied on any level of the system hierarchy, but not on the system as a whole. The *readout* has been defined at *depth 1* on the *modules* and it is consistent to apply the deadtime on the *modules* as well. However, during an experimental acquisition, the number of *singles* obtained is for the system as a whole and information about the number of *singles* per module is obtained assuming that each module detect the same number of events. Therefore,

$$S_{\text{module}} = \frac{S_{\text{total}}}{18} \quad (4.1)$$

where  $S_{\text{total}}$  is the total number of singles from the *listmode* data, and  $S_{\text{module}}$  is the number of singles estimated for each module.

For the low activity range, below  $3 \text{ kBq.mL}^{-1}$ , linear regression was performed to estimate the theoretical *singles* rate in ideal conditions, in the absence of deadtime and pile-up influence for each module. The fitted line was extrapolated to the origin to estimate the background noise level, as depicted in Figure 4.4.

The deadtime  $\tau_d$  was then estimated using a paralyzable model, using the following equation.

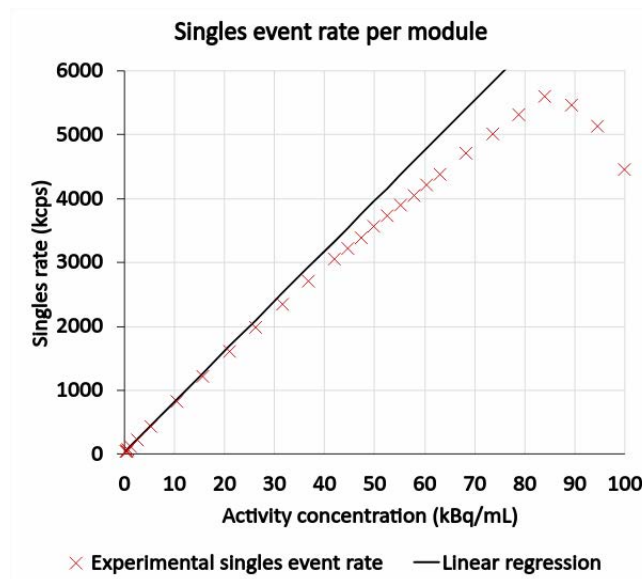


FIGURE 4.4 – Background noise obtained by linear regression, fitted on low counts ( $< 3 \text{ kBq}\cdot\text{mL}^{-1}$ ) and the influence of deadtime at higher counts for one module.

$$\tau_d = \frac{-1}{S_{ideal}} \ln\left(\frac{S_{module}}{S_{ideal}}\right) \quad (4.2)$$

where  $S_{ideal}$  is the estimation of the *singles* rate without the effect of deadtime obtained by the linear regression in Figure 4.4 (Usman and Patil, 2018).

**Detection efficiency.** Once background noise has been modelled, the simulated and experimental single rates were compared by computing their ratio. This ratio should be constant at low activity concentrations and provides the system detection efficiency where deadtime effects can be neglected.

**Pile-up effects.** The pile-up influence is more difficult to model accurately compared to the deadtime, background noise and detection efficiency. An optimisation process was therefore performed using several simulations with the aim of reducing the percentage error between simulated singles and experimental ones. The dead-time and pile-up modules in the digitizer chain was placed before the coincidence energy window (449.68-613.20 keV), since the integration time (which characterises pile-up effects) must be modelled before the energy discrimination.

Final retained values were a frequency of 461 kcps for the noise, 5.9 ns for both the deadtime and pile-up values, and 86.5% for the detection efficiency. It should be noted that deadtime and pile-up were modeled before the energy windows and therefore their values differ from estimated experimental values which are determined at the end of the chain of acquisition, see Table 4.2.

#### 4.2.4.3 Energy and temporal resolutions

Both the energy and temporal (CTR) resolutions were set according to data from the manufacturer. The energy resolution was set to 11.2% at 511 keV for each crystal

and the temporal resolution applied to *singles* (single timing resolution (STR)) was set to 220 ps on each detector, leading to a coincidence temporal resolution of 311 ps ( $CTR = \sqrt{2} \cdot STR$ ).

#### 4.2.4.4 Energy thresholds and coincidence window

**Energy and coincidence timing windows.** As in the experimental setup, an energy window discriminator of 449.68-613.20 keV was used. The exiting *singles* were sorted by a  $\tau = 2.0115$  ns coincidence timing window using the coincidence sorter module (Strydhorst and Buvat, 2016)

**Coincidence sorter.** Two different approaches are available in GATE to sort for coincidences from the singles. These are the *single-window* and the *multiple-window* policies. In the first one, a coincidence window ( $\tau$ ) is opened once a single is detected and no other single event can open its own coincidence window until the current window closes. In the second one, each single opens its own window and coincidences are selected by performing a logical OR between all the individual signals. The *multiple-window* approach has been selected, providing a better model for modern PET systems.

**Randoms coincidences.** A second coincidence module was added with an offset of 100 ns in order to estimate the number of *random* counts in the simulation within a same window width.

**Acceptance angle.** In line with the experimental setup and the real system, an acceptance angle of  $80^\circ$  minimum is set for all LORs. This corresponds to the angle covered by 4 modules, since a module covers an angle of  $20^\circ$ . This is modelled in GATE by the parameter *minSectorDifference* set to 5, corresponding to the minimum difference between the indexes of the two modules for valid coincidences.

**Multiple coincidences.** When more than two *singles* are detected in the coincidence window (due to its finite size), several types of models could be used to select the coincidence(s). In GATE, 9 different policies are available (see OpenGATE/readthedocs<sup>4</sup>). The *takeAllGoods* multiples policy was selected. It considers all pairs of *singles* in the list of possible *coincidences* within geometric constraints. As described by Moraes *et al.* (Moraes *et al.*, 2015), the design choices currently implemented in modern PET systems are best modeled in GATE by choosing the *takeAllGoods* coincidence policy. Also, this combination (*multiple-window* and *takeAllGoods*) provides a better estimation of the number of *randoms* using the delayed window (Strydhorst and Buvat, 2016).

#### 4.2.5 Image reconstruction

As explained earlier, the evaluation of the simulation was performed before image reconstruction to be independent of the algorithm, but examples of reconstructions were performed to illustrate image quality. For both reconstructed and simulated data, reconstructions were made with the open-source software Customizable and Advanced Software for Tomographic Reconstruction (CASToR) (Merlin *et al.*, 2018), using OSEM (Shepp and Vardi, 1982) with Joseph line projector (Joseph, 1982). All CASToR reconstruction developments have been mostly part of the thesis

of Julien Salvadori (Salvadori, 2020) and will not be detailed here. For more details about CASToR using both the experimental and GATE simulated DPC-PET data, see *Partie III-Chapitre II* in Salvadori (2020).

#### 4.2.6 PET model validation

The proposed DPC-PET simulation model was evaluated following the *NEMA NU 2-2018 - Performance measurements of positron emission tomographs* (2018). The NEMA guidelines for PET provide a uniform and consistent method for experimental measurement and reporting performance parameters. The evaluation tests chosen for the validation were (1) count rates, NECR and scatter fraction, (2) TOF resolution and energy resolution, (3) sensitivity and (4) pre-reconstruction spatial resolution. The first three tests are independent of image reconstruction. For the spatial resolution, a LOR-based method was proposed in order to estimate spatial resolution from *listmode* data, before image reconstruction.

Monte Carlo simulations were performed following the configurations described in the NEMA guidelines and compared to experimental measurements. The different tests and phantoms used are described in the following sections. Moreover, both experimental and simulated data were used to reconstruct images with the same reconstruction parameters to illustrate the image quality. Additional NEMA tests related to the accuracy of corrections and PET/CT registration accuracy were not performed.

##### 4.2.6.1 Count rates, NECR and scatter fraction

**Cylindrical scatter phantom.** Evaluations based on count rates were performed with a cylindrical scatter phantom of 102 mm radius and 700 mm length, composed of polyethylene and centred in the FOV of the DPC-PET, as depicted in Figure 4.5. The phantom was filled with a 1.6 mm radius line source of 1.78 GBq of  $^{18}\text{F}$ , off-centred at a radial distance of 45 mm from the central axis of the cylinder. Twenty-six different measurement time points were performed over 16 hours and with increasing acquisition times (while the activity in the phantom decreases). The activity during the last time point was less than 10 MBq. In order to reduce the computation time, the simulations were performed with the exact activity but with a reduced acquisition time such that each acquisition contained a minimum of  $2 \times 10^6$  prompts. The experimental *listmode* data sets were truncated at  $2 \times 10^6$  prompts for comparison with simulated data. For this test, the NEMA protocol defines the effective activity concentration as the ratio of the activity present in the source to the volume of the cylindrical polyethylene phantom.

The number of counts over the integration period of time can be extracted as well as the derived NEC and scatter fraction (SF) from the *listmode* data according to NEMA standards. Scatter counts,  $C_{sc}$ , is the number of falsely located coincidence events resulting from gamma rays scattering inside the phantom,  $C_t$  is the number of true coincidences,  $C_r$  is the number of random (accidental) coincidences. Therefore, the total number of detected coincidences or prompts is given by the following equation.

$$C_{tot} = C_{sc} + C_t + C_r \quad (4.3)$$

Finally, NEC which is a global measure of the scanner's ability to detect useful counts (Chang et al., 2012) and SF are defined as in Equations 4.4 and 4.5, respectively.

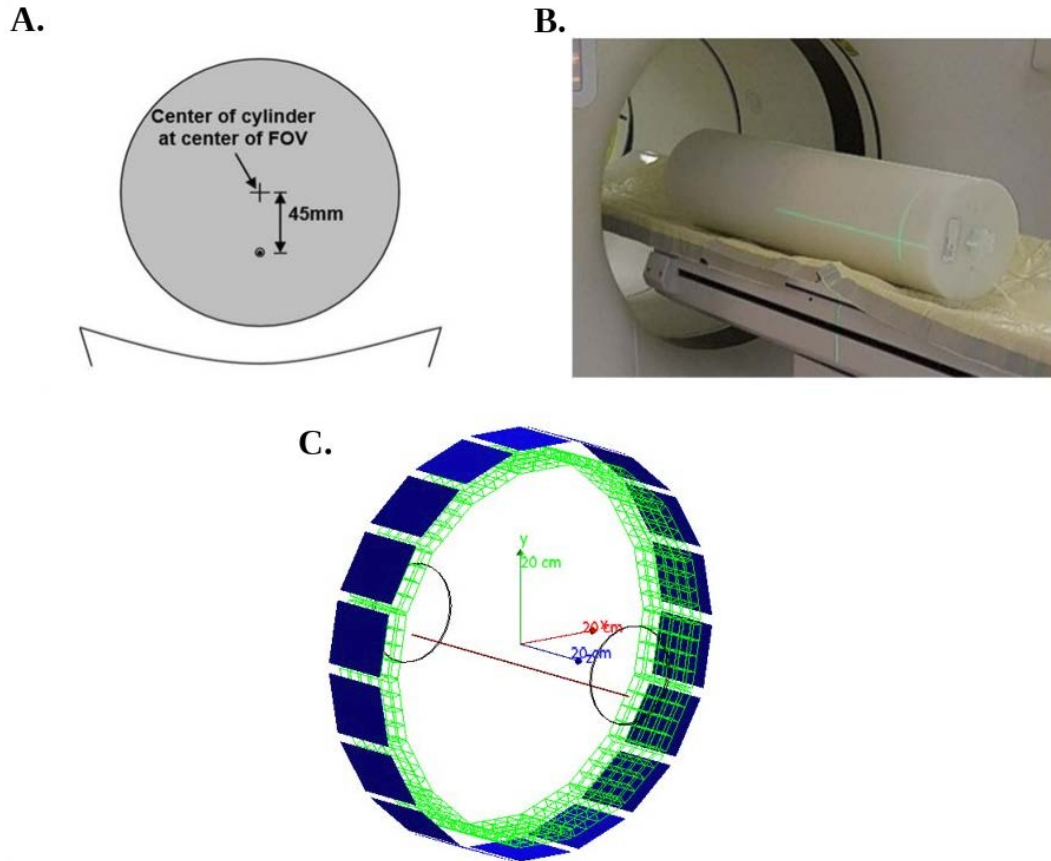


FIGURE 4.5 – **A:** Position of line source in the cylindrical scatter phantom from NEMA (2018). **B:** Scatter phantom positioned in the real system. **C:** Modelled phantom and PET geometry in GATE for illustration (the table geometry has not been depicted). The line source (red) is placed 45 mm below the central axis  $z$ .

$$NEC = \frac{C_t^2}{C_{tot}} \quad (4.4)$$

$$SF = \frac{C_{sc}}{C_t + C_{sc}} \quad (4.5)$$

Count rates are the counts divided by the acquisition time.

#### 4.2.6.2 TOF and energy resolutions

The experimental and simulation setups were the same as for the previous test (Section 4.2.6.1, see Figure 4.5). TOF resolution was determined for increasing count rates with the FWHM of the timing error histogram computed from the listmode data. This method is based on the work of Wang *et al.* (Wang *et al.*, 2016) and was recently added to the NEMA NU 2 (2018). There are two main differences compared to the daily quality control procedure, which uses a point source of  $^{22}\text{Na}$ . First, because of the 45 mm offset of the linear source used for the NECR measurement, the difference in detection time of coincident photons is no longer 0 and, therefore, it is necessary to compute a timing offset correction for each LOR, to account for the off-center source location. Second, scatter from the phantom must be corrected.

The energy resolution was assessed with the FWHM value of the energy histogram computed from all true *coincidences* extracted from the same listmode data.

#### 4.2.6.3 Sensitivity

**Sensitivity phantom.** Sensitivity was measured and simulated using a 700 mm long and 1 mm inner diameter line source filled with 8 MBq of  $^{18}\text{F}$  and centered in the FOV, as depicted in Figure 4.6. Five acquisitions of 120 s were performed by placing the source successively inside one to five concentric aluminium sleeves of 1.25 mm thickness each.



FIGURE 4.6 – Sensitivity phantom used for experiments and modelled for simulations.

TABLE 4.3 – Sensitivity phantom characteristics.

Tube number	Inside diameter (mm)	Outside diameter (mm)	Thickness (mm)	Length L (mm)
1	3.9	6.4	1.5	700
2	7.0	9.5	1.5	700
3	10.2	12.7	1.5	700
4	13.4	15.9	1.5	700
5	16.6	19.1	1.5	700
Plastic tube	1	3	1	700

Sensitivity for each thickness was computed in  $\text{cps.MBq}^{-1}$  and the sensitivity without attenuation was extrapolated to zero thickness, to obtain effective sensitivity,  $S_{eff}$ , in the absence of scattering medium, defined by Equation 4.6.

$$S_{eff} = \frac{R_0}{A_{cal}} \quad (4.6)$$

where  $R_0$  and  $A_{cal}$  are the count rates in the absence of attenuation and the activity at calibration, respectively. The sensitivity of each slice  $i$ ,  $S_i$ , is given by Equation 4.7

$$S_i = \frac{R_{1,i}}{R_1} \cdot S_{eff} \quad (4.7)$$

where  $R_1$  is the count rates obtained using tube number 1.

#### 4.2.6.4 Spatial resolution

Spatial resolution was assessed for 10 positions using a  $2.2 \text{ GBq} \cdot \text{mL}^{-1} \text{ } ^{18}\text{F}$  point source: 5 in the centre of the axial FOV ( $z = 0 \text{ cm}$ ) positioned at  $(0,1,0)$ ,  $(0,10,0)$ ,  $(0,20,0)$ ,  $(10,0,0)$  and  $(20,0,0) \text{ cm}$ , and 5 with an offset of  $1/8$  of the edge of the FOV ( $z = 6.15 \text{ cm}$ ) positioned at  $(0,1,6.15)$ ,  $(0,10,6.15)$ ,  $(0,20,6.15)$ ,  $(10,0,6.15)$  and  $(20,0,6.15) \text{ cm}$ . *Listmode* data was acquired and simulated until a minimum of 3 million prompt events was reached for each position. In contrast to the experimental measurements, the simulations can be performed with a perfectly isotropic point source. Resolutions in all three directions (radial, tangential and axial) can therefore be obtained from a single simulation at each desired position.

**Intrinsic spatial resolution.** Spatial resolution is usually determined after reconstruction, using the FWHM of the point-spread function (PSF) of a point source. However, in order to remain independent of the reconstruction software for both experimental and simulation data, an original method was developed to estimate and compare spatial resolution from *listmode* data. Figure 4.7 provides a description of the method used. The positions  $\vec{L}_1$  and  $\vec{L}_2$  as well as the unit vector  $\vec{u}$ , defined by Equation 4.8, were determined for each LOR in the Cartesian coordinates  $(x, y, z)$  of the tomograph, based on the indexes  $(t_1, z_1)$  and  $(t_2, z_2)$  of the opposed detectors in coincidence, where  $t$  and  $z$  are the transverse and axial indexes of each crystal, respectively.

$$\vec{u} = (\vec{L}_2 - \vec{L}_1) / \|\vec{L}_2 - \vec{L}_1\| \quad (4.8)$$

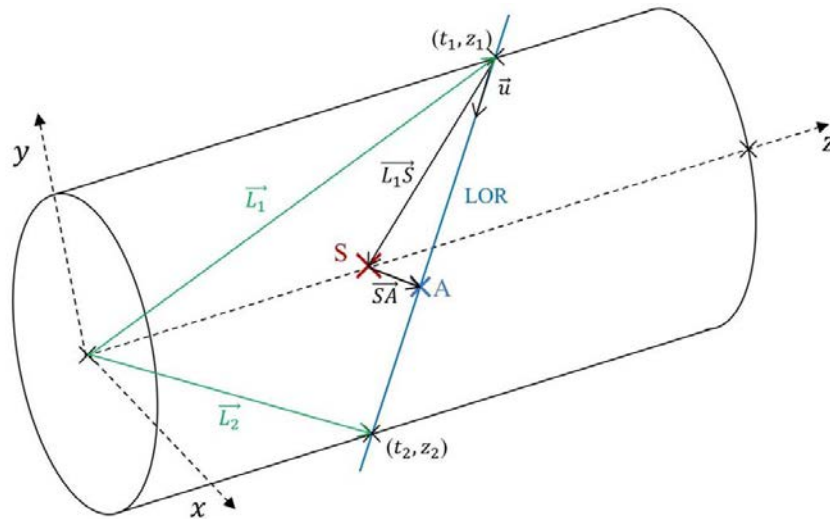


FIGURE 4.7 – Determination of  $\vec{SA}$  for the calculation of intrinsic spatial resolution for a LOR inside the tomograph's FOV.

For each event in the *listmode*, the orthogonal projection ( $A$ ) of the point source ( $S$ ) onto the LOR defined by the event was computed. The vector  $\vec{SA}$ , which represents the smallest vector between the LOR and the source, was projected along each axis  $x$ ,  $y$  and  $z$ . Only coincidences with a distance to the source of less than  $10 \text{ mm}$  ( $\|\vec{SA}\| < 10 \text{ mm}$ ) were kept for analysis. Each projected distance distribution along  $x$ ,  $y$  and  $z$  was then binned into histograms and the intrinsic spatial resolution for a given direction was determined by the FWHM. FWHM values were determined

as preconised in the NEMA standard for the spatial resolution test (NEMA (2018)). This method requires a precise knowledge of the source position, which is the case for simulation but not for experimental data. The exact location of the point source for experimental data was therefore determined by an optimisation process aimed at minimising the mean distance  $\|\vec{S\hat{A}}\|$  over all LORs with a distance of less than 10 mm ( $\|\vec{S\hat{A}}\| < 10$  mm).

Due to the cylindrical shape of PET scanner, radial frequency increases with the distance from the center of the FOV. This non-uniform sampling in the transverse direction could lead to distortion of high spatial frequency and non-uniform spatial resolution across the FOV. Hence, listmode data was first resampled at a uniform sample rate of 2 LOR.mm<sup>-1</sup> in the radial direction by the *arc correction* method (Fahy, 2002; Farsaii, 2005) before doing the previously described analysis.

**Reconstructed spatial resolution.** In order to illustrate the difference between pre-reconstruction (intrinsic) and post-reconstruction spatial resolution, experimental and simulated data of the central point source at (0,1,0) cm were reconstructed with 576 × 576 mm FOV, 1 mm voxels, using OSEM with 5 iterations and 10 subsets. No correction was applied before or during the reconstruction. Two types of reconstructions were performed using CASToR. The first one with 4 mm isotropic Gaussian filter applied during the forward and backward model (the standard image-based PSF modelling), in order to match the FWHM of the DPC-PET at the centre of the FOV (Rausch et al., 2019) according to the NEMA NU 2 (2018) standard (i.e. in air and with a FBP algorithm). The second was performed with an additional 4 mm isotropic Gaussian filter applied to the final reconstructed image (the standard method of *Sieve* (Snyder and Miller, 1985)). Spatial resolution was then determined using the FWHM of the reconstructed PSF along the three main directions (axial, tangential, radial) as described in the NEMA.

#### 4.2.6.5 Image quality

Illustrative reconstructed images were compared with the following protocol. A three minutes PET acquisition of the International Electrotechnical Commission (IEC) torso phantom was performed. The phantom was filled with <sup>18</sup>F of 5.3 kBq.mL<sup>-1</sup> for the background activity and four times higher in four spheres of 10, 13, 17 and 22 mm diameters. The 28 and 37 mm diameter spheres were left cold as in the *NEMA NU 2-2012 - Performance measurements of positron emission tomographs* (2012). Images were reconstructed using CASToR using OSEM with 10 subsets and varying iterations from 1 to 10. Reconstructions were performed using the *Sieve* method (PSF modelling and post-reconstruction convolution) using a 4 mm FWHM kernel. For experimental data, all corrections required for quantitative reconstruction (attenuation, scatter (Ye, Song, and Hu, 2014), random (Brasse et al., 2005), normalisation (Wang, Hu, and Gagnon, 2007)) were precomputed outside CASToR using a software provided by Philips. For simulated data, only random and attenuation corrections were computed. Other corrections were not available. Consequently, all scatter events were discarded during reconstruction. The delayed window method was used to estimate random correction factors. An attenuation coefficient map was computed for the IEC phantom. Background relative noise (BRN) and contrast recovery coefficient (CRC) for all six spheres were computed as described in Salvadori et al. (2020a).



### 4.2.6.6 Implementation

In total, 41 PET listmode acquisitions were performed: 26 with the scatter phantom, 5 with the sensitivity analysis and 10 with point sources for the spatial resolution estimation. All corresponding simulations were performed with the same set of digitizer parameters. Experiments have been done on a Philips Vereos system installed at Nancy University Hospital (Nancy, France). Simulations were conducted on a cluster with Intel Xeon CPU E5-2640 v4 @ 2.40GHz, with 12 GB memory<sup>5</sup>. The GATE macros used for the simulations are available on the website of the OpenGATE collaboration.

## 4.3 Results

### 4.3.1 Count rates, NECR and scatter fraction

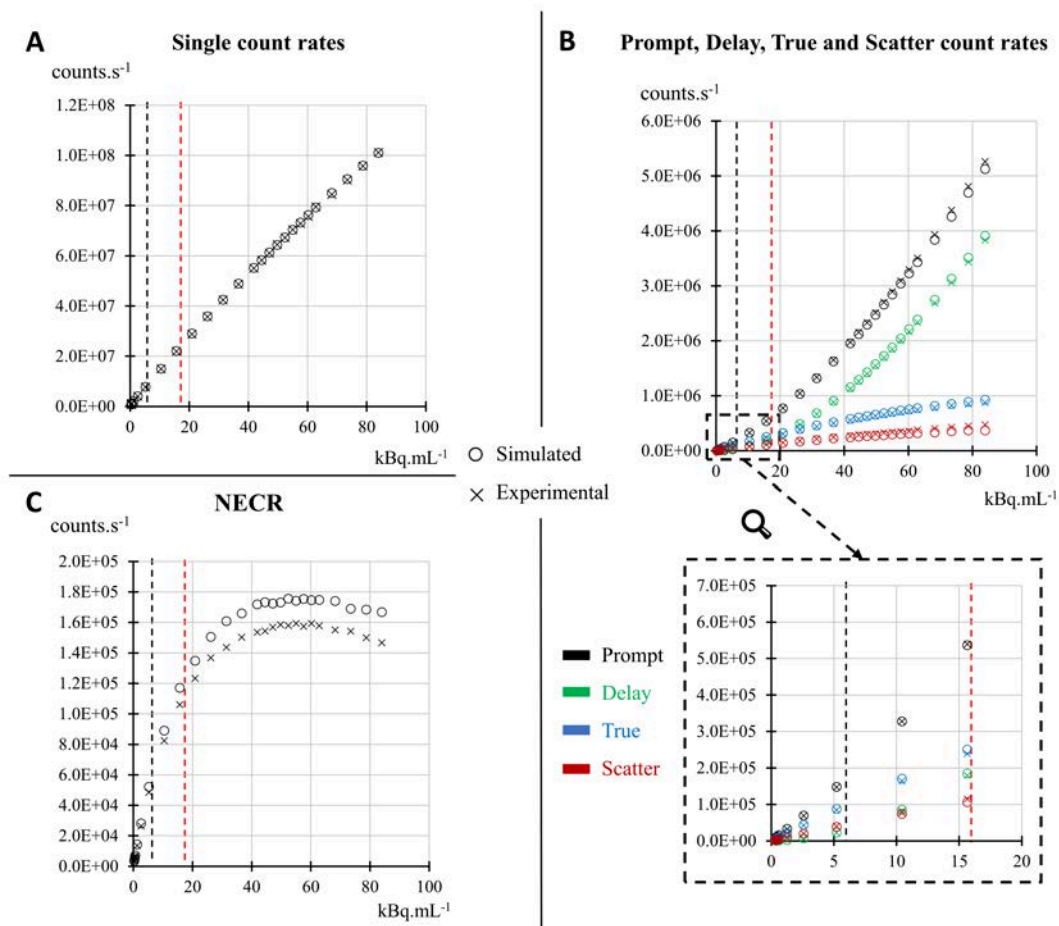


FIGURE 4.8 – Simulated and experimental count rates according to activity concentrations. **A:** Single count rates. **B:** Prompt, delay, true and scatter count rates. **C:** NECRs. The vertical dashed lines correspond approximately to the upper level of activity concentrations usually used in clinical routine for <sup>18</sup>F (black line) and <sup>82</sup>Rb (red line) PET exams.

5. See [IN2P3 Computing Centre](#)

**Singles.** As depicted in Figure 4.8A, a good agreement was obtained between simulations and experiments for *single* event rates, with a maximum of 0.7% relative difference up to an activity concentration of 80 kBq.mL<sup>-1</sup>. Note that usual activities used clinically with <sup>18</sup>F-FDG tracer do not exceed around 6 kBq.mL<sup>-1</sup> (Sluis et al., 2019).

**Prompts, trues, randoms and scatters.** Maximum relative differences between simulated and experimental data, up to 80 kBq.mL<sup>-1</sup>, were 3%, 3%, 5% and 18% for *total*, *random*, *true* and *scatter* coincidence count rates, respectively (Figure 4.8B). The difference for scatter count rate stayed below 5% up to a concentration of 10 kBq.mL<sup>-1</sup>.

TABLE 4.4 – Comparison of the characteristics of the DPC-PET for NECR and scatter fraction between the experimental and Monte Carlo simulated data in this study. Additional comparison is added from experimental data published from Rausch et al. (2019) and Zhang, Maniawski, and Knopp (2018). Values marked with an asterisk (\*) represent ‘maximum’ instead of peak values since the system did not show a peak value beyond which the NECR began to decrease with increasing activity.

Parameter	Experimental	MC simulation	Rausch et al. (2019)	Zhang et al. (2018)
NECR @ peak value	159.4 kcps @ 54.9 kBq.mL <sup>-1</sup>	175.6 kcps @ 52.4 kBq.mL <sup>-1</sup>	153.4 kcps @ 54.9 kBq.mL <sup>-1</sup>	171 kcps* @ 50.5 kBq.mL <sup>-1</sup>
NECR @ 5.3 kBq.mL <sup>-1</sup>	48.5 kcps	52.2 kcps	47.2 kcps	n/a
Scatter fraction @ peak NECR	33.2% @ 54.9 kBq.mL <sup>-1</sup>	29.2% @ 52.4 kBq.mL <sup>-1</sup>	33.9% @ 54.9 kBq.mL <sup>-1</sup>	30.8%* @ 50.5 kBq.mL <sup>-1</sup>
Scatter fraction @ low count rates	31.8% @ 0.4 kBq.mL <sup>-1</sup>	30.3% @ 0.4 kBq.mL <sup>-1</sup>	31.7% @ 0.4 kBq.mL <sup>-1</sup>	n/a

**NECR and scatter fraction.** As a result, less than 13% relative difference was obtained between simulated and experimental NECR (Figure 4.8C). The peak NECR was close between simulated and experimental data with 175.6 kcps at 52.4 kBq.mL<sup>-1</sup> and 159.4 kcps at 54.9 kBq.mL<sup>-1</sup>, respectively. At these peak values, the corresponding scatter fractions were found to be 29.2% and 33.2% for simulated and experimental data, respectively.

Due to the systematic difference between simulated and experimental *scatter* events at high count rates, the simulated scatter fraction was also slightly underestimated, with a relative difference increasing from 5% at 4 kBq.mL<sup>-1</sup> to 15% at 80 kBq.mL<sup>-1</sup>. However, this difference in *scatter* event rate only becomes important for activities that are much higher than those commonly used in routine clinical practice. Values for peak NECR and scatter fraction are reported in Table 4.4. The maximum relative differences between simulated and experimental values, depicted in Table 4.5, were below 11% for all event rates as well as for NECR and scatter fraction, for activity concentrations of 2-6 kBq.mL<sup>-1</sup> and 11-16 kBq.mL<sup>-1</sup>, which correspond to the clinical ranges found in <sup>18</sup>F-FDG whole-body exams and in <sup>82</sup>Rb cardiac exams (Sluis et al., 2019), respectively.

TABLE 4.5 – Maximum relative differences between simulated and experimental data are reported for activity concentration ranges for clinical  $^{18}\text{F}$  scans and  $^{89}\text{Rb}$  cardiac perfusion scans.

	$^{18}\text{F}$ [2-6 kBq.mL $^{-1}$ ]	$^{89}\text{Rb}$ [11-16 kBq.mL $^{-1}$ ]
Single	-0.6 %	-0.6 %
Prompt	1.2 %	-0.5 %
Delay	-3.1 %	-3.4 %
True	4.1 %	4.8 %
Scatter	-4.7 %	-7.6 %
Scatter fraction	-5.8 %	-8.3 %
NECR	7.5 %	10.3 %

### 4.3.2 TOF and energy resolutions

As depicted in Figure 4.9A, a good agreement was obtained with less than 4% relative difference observed between simulated and experimental data for both TOF and energy resolutions over the entire range of activity concentrations explored in this study. Examples of TOF and energy histograms from which the FWHM values were extracted, obtained for an activity concentration of 5.2 kBq.mL $^{-1}$  are presented in Figure 4.9B.

### 4.3.3 Sensitivity

The measured and simulated sensitivities for each aluminium thickness together with the extrapolation for determining the attenuation-free sensitivity are provided in Figure 4.10A. A 7.9% agreement was found between the attenuation-free sensitivity for simulated and experimental data, showing 5591 and 5184 cps.MBq $^{-1}$ , respectively. As shown in Figure 4.10B, the axial sensitivity profiles between simulated and experimental data were in good agreement. Largest relative differences were within 14% for the low sensitivity slices on both sides of the FOV. Sensitivity decreases according to the distance from the camera center due to 3D acquisition geometry.

### 4.3.4 Intrinsic spatial resolution

Table 4.6 depicts the FWHM for intrinsic spatial resolution the 10 positions recommended by the NEMA standards. An overall agreement of less than 0.25 mm absolute difference was obtained between simulated and experimental data, except for Z-axis (axial) where values up to 0.92 mm were obtained. Figure 4.11 provides an example of the histograms from which the PSF were extracted for the (0,20,0) cm transverse position. Table 4.7 depicts the FWHM at the central position (0,1,0) cm obtained 1) before, 2) after reconstruction with image-based PSF modelling and 3) after reconstruction with the standard method of *Sieve*.

### 4.3.5 Image quality

The tradeoff between CRC and BRN was analysed for two hot spheres (10 and 22 mm) and one cold sphere (37 mm) of the IEC phantom. Curves representing the evolution of CRC according to BRN as a function of the number of iterations

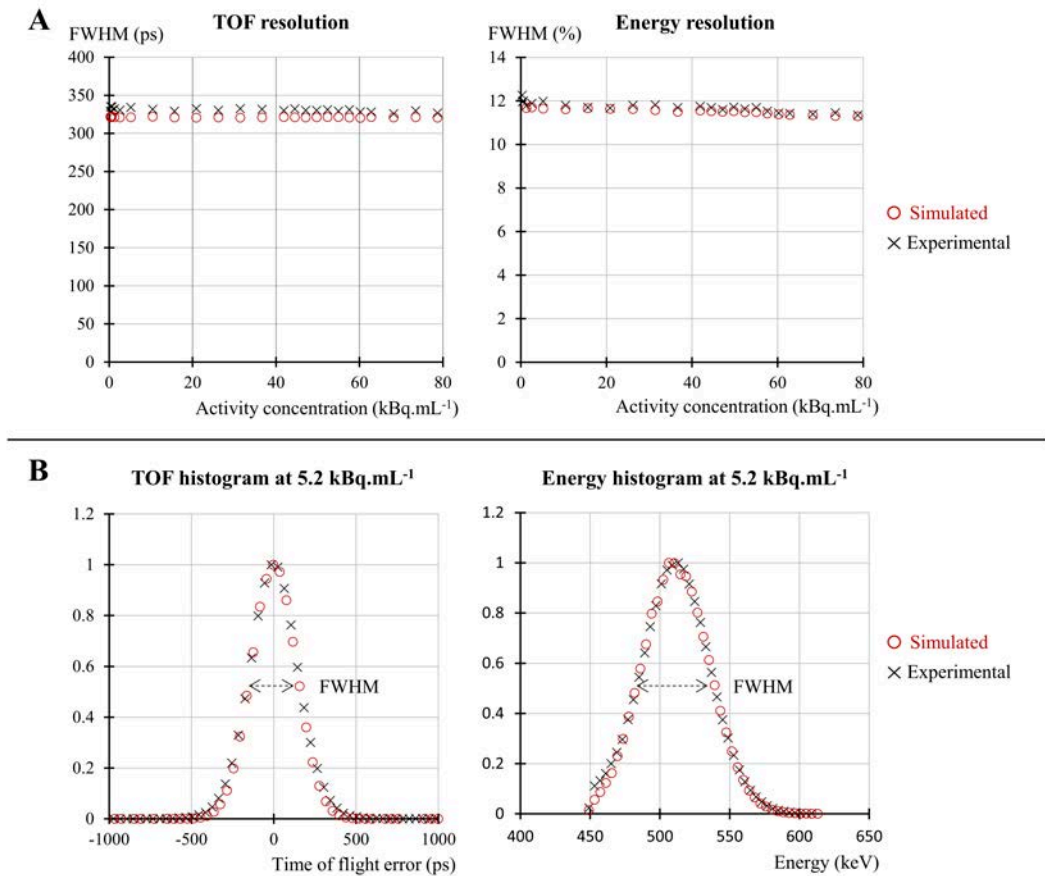


FIGURE 4.9 – **A**: TOF and energy resolutions according to activity concentrations for both simulated (o) and experimental (×) data, over a wide range of activities. **B**: Example, for 5.2 kBq.mL<sup>-1</sup> activity concentration, of the normalized TOF and energy histograms used to compute the FWHM values.

TABLE 4.6 – FWHM defined before reconstruction for intrinsic spatial resolution along all dimensions for ten positions recommended by NEMA standards, for both simulated (Sim.) and experimental (Exp.) data. The columns to the right give their absolute difference.

Position (cm)	Sim. FWHM (mm)			Exp. FWHM (mm)			Abs. diff. (mm)		
	X	Y	Z	X	Y	Z	X	Y	Z
(0,1,0)	1.73	1.48	1.91	1.93	1.71	2.37	-0.20	-0.23	-0.46
(0,10,0)	1.87	1.97	2.81	1.97	2.09	3.51	-0.10	-0.12	-0.70
(0,20,0)	1.77	2.19	2.99	1.90	2.18	3.37	-0.13	0.01	-0.38
(10,0,0)	1.82	1.69	2.76	1.95	1.87	3.50	-0.13	-0.18	-0.74
(20,0,0)	1.77	1.73	3.01	1.89	1.90	3.40	-0.13	-0.17	-0.40
(0,1,6.15)	1.62	1.41	n/a	1.70	1.47	n/a	-0.08	-0.06	n/a
(0,10,6.15)	1.92	1.77	2.39	1.94	1.80	3.31	-0.02	-0.03	-0.92
(0,20,6.15)	2.08	1.76	n/a	2.09	1.67	n/a	-0.01	0.09	n/a
(10,0,6.15)	1.56	1.72	2.50	1.61	1.84	3.34	-0.05	-0.12	-0.84
(20,0,6.15)	1.43	1.99	n/a	1.46	2.08	n/a	-0.03	-0.09	n/a

are shown in Figure 4.12A. In overall, the trade-off was slightly better for simulated compared to experimental images. At early iterations, simulated images show better CRC with a maximum relative difference of 13% (at 1 iteration), while for further iterations, BRN is better with a maximum relative difference of 14% reached for 5 iterations. Figure 4.12B shows that simulated and experimental images were visually

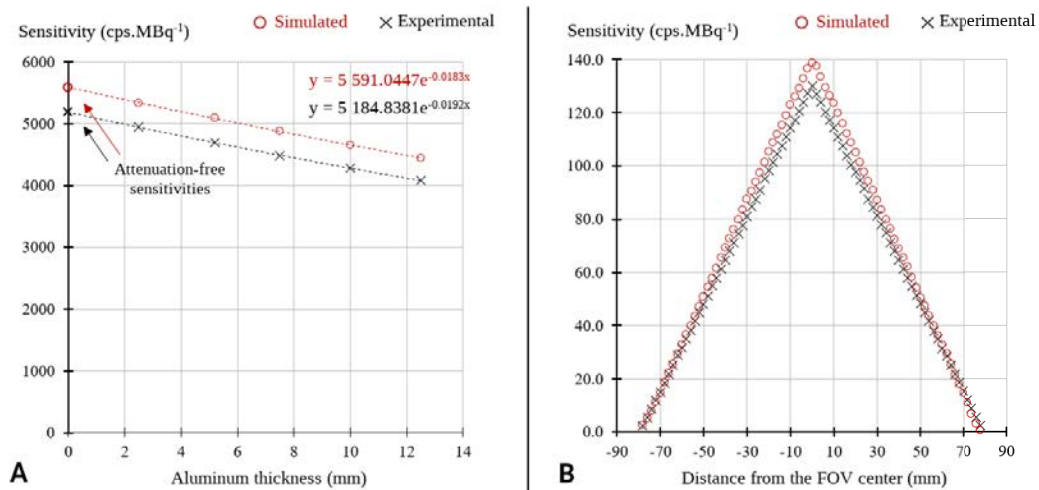


FIGURE 4.10 – **A**: Total count sensitivities measured according to NEMA standards for simulated and experimental data, for increasing thicknesses of aluminium sleeves and with the exponential regressions providing attenuation-free count sensitivities. **B**: Sensitivities of contiguous axial slices according to the distances from camera centres.

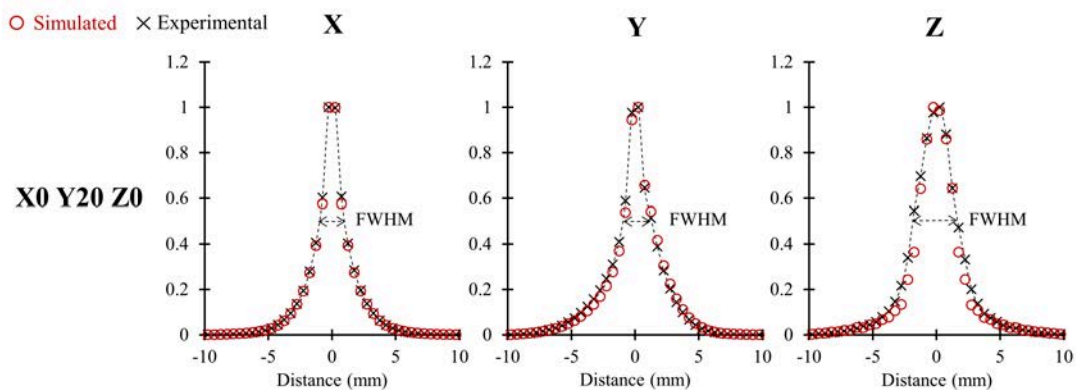


FIGURE 4.11 – Example of histograms and corresponding FWHM of the shortest distances between source and LORs projected along the X,Y and Z axis, obtained from experimental and simulated data.

TABLE 4.7 – Comparison of the intrinsic FWHM obtained before reconstruction for the (0,1,0) cm central position, with FWHM obtained after reconstruction.

Position (0,1,0) cm	Sim. FWHM (mm)			Exp. FWHM (mm)			Abs. diff. (mm)		
	X	Y	Z	X	Y	Z	X	Y	Z
Intrinsic	1.73	1.48	1.91	1.93	1.71	2.37	-0.20	-0.23	-0.46
4 mm PSF	1.95	1.92	1.88	1.84	1.57	1.67	0.10	0.35	0.22
4 mm Sieve	4.37	4.37	4.31	4.45	4.46	4.33	-0.08	-0.09	-0.02

very close. The depicted profiles passing through both the 10 and 22 mm spheres were almost identical.

#### 4.3.6 Monte Carlo statistical uncertainty

In order to estimate the statistical uncertainty from the Monte Carlo simulations, 10 different simulations of the NEMA count rate test were performed at both  $5.2 \text{ kBq.mL}^{-1}$  and  $42 \text{ kBq.mL}^{-1}$ , using  $2 \times 10^6$  *prompts*. The coefficient of variation (ratio of the standard deviation to the mean) over the 10 values for the *true*, *scatter* and *delay* event rates were calculated and reported in Table 4.8.

TABLE 4.8 – Monte Carlo relative statistical uncertainty for the true, scatter and delay event rates.

	$5.2 \text{ kBq.mL}^{-1}$	$42 \text{ kBq.mL}^{-1}$
True	0.2 %	0.3 %
Scatter	0.4 %	0.9 %
Delay	0.2 %	0.1 %

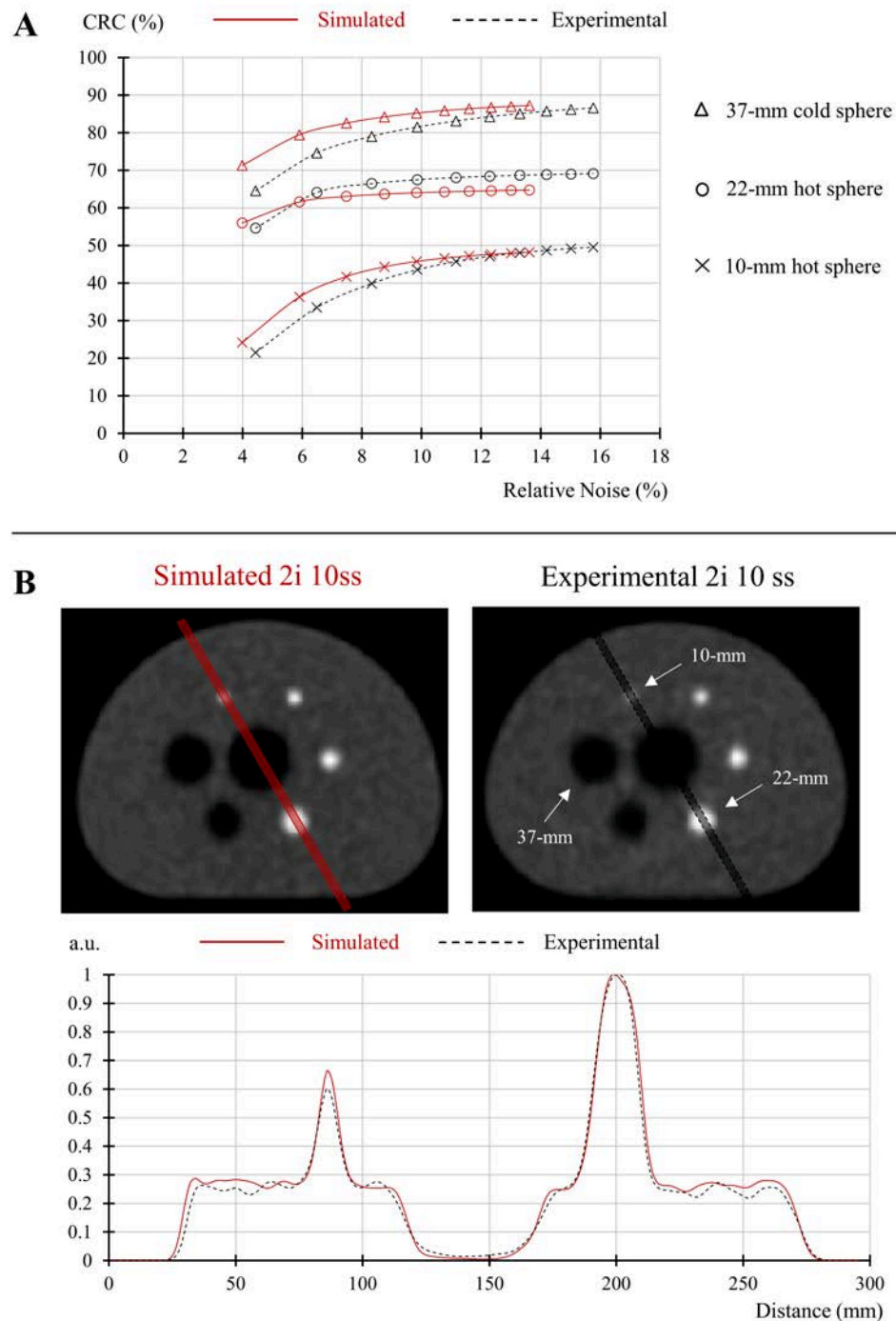


FIGURE 4.12 – **A**: Comparison between simulated and experimental images of the relationships between contrast recovery coefficient and background relative noise, according to the number of OSEM iteration and for the 10 and 22 mm diameter hot spheres and the 37 mm cold sphere. **B**: Cross-sectional slices passing through the spheres of the IEC phantom and reconstructed with 2 OSEM iterations and 10 subsets from simulated and experimental data. A parallelepiped profile of 6 mm cross-section and passing through the hot spheres of 10 mm and 22 mm diameter is compared between simulated and experimental images.

## 4.4 Discussion

**Context.** In this study, a GATE model of the Vereos DPC-PET was developed and validated by comparing simulated data with experimentally obtained data using NEMA tests. This work has been published Labour et al. (2020), and to our best knowledge, provides for the first time the Monte Carlo model of a clinical whole body SiPM- or dSiPM-based PET system. Table 4.9 summarises the published Monte Carlo models of clinical PET systems using GATE. A more exhaustive list for published preclinical and small animal validated PET systems can be found in Sarrut et al. (2021b), Table 1, where the present study has been enhanced.

TABLE 4.9 – Published clinical whole body PET models validated in GATE and compared to experimental data. Some brain and breast systems are also included. A more exhaustive list referencing prototype and small animal systems can be found in Sarrut et al. (2021b).

Study	Clinical PET system	Technology
Bataille et al. (2004)	ECAT HRRT (brain)	LSO/PMT
Jan et al. (2005)	ECAT EXACT HR+	BGO/PMT
Karakatsanis et al. (2006)	ECAT EXACT HR+	BGO/PMT
	Siemens Biograph 2	LSO/PMT
Lamare et al. (2006)	Philips Allegro	GSO/PMT
	Philips Gemini	
Michel et al. (2006)	Siemens Biograph HiRez	LSO/PMT
Schmidtlein et al. (2006)	GE Advance	BGO/PMT
	GE Discovery LS	
Gonias et al. (2007)	Siemens Biograph 6	LSO/PMT
Geramifar et al. (2009)	4 different GE scanners	BGO-LYSO/PMT
Poon et al. (2012)	Siemens Biograph mCT	LSO/PMT
Trindade et al. (2012)	Philips Gemini TF	LYSO/PMT
	Philips TruFlight Select	
Moraes et al. (2015)	Siemens Biograph mCT	LSO/PMT
Poon et al. (2015)		
Aklan et al. (2015)	Siemens Biograph mMR	LSO/APD
Monnier et al. (2015)		
Sheikhzadeh et al. (2017)	PDS NeuroPET (brain)	LYSO/SiPM
Li et al. (2017)	ARRAYS SMIC Ray-San 64	BGO/PMT
Emami et al. (2020)	Oncovision MAMMI (breast)	LYSO/PMT
<b>Labour et al. (2020)</b> <b>(This present study)</b>	<b>Philips Vereos DPC</b>	<b>LYSO/dSiPM</b>

**Count rates.** In general, the proposed simulation model has been favourably compared to measurements. Excellent agreement was found between simulated and experimental *singles* count rates with relative differences below 1% over the whole activity concentration range ( $< 80 \text{ kBq.mL}^{-1}$ ). For *total*, *random* and *true* coincidence rates, agreements were found with maximum differences equal to or less than 5% on overall. However, for *scatter* count rates, the percentage difference increased with increasing activity concentration from 3% to 5% at 1 and 30  $\text{kBq.mL}^{-1}$  (respectively)



and reached a maximum of 18% difference at  $80 \text{ kBq.mL}^{-1}$ . The cause of this discrepancy at high activity is not yet explained; it might be due to elements which produce scattered radiation being included in the simulation by simplified geometrical models, such as the cooling plates, the Lexan cover or the patient table. It could also be due to the simulated composition of the materials of the cylindrical phantom which might not be exactly the same as in the real phantom. However, for scatter fraction below  $10 \text{ kBq.mL}^{-1}$ , the percentage differences were within 6% between simulated and experimental values and stayed within 15% for higher activity concentrations.

**Peak NECR.** Experimental peak NECR was in agreement to the study of Rausch et al. (2019) showing 3.8% and  $< 1\%$  differences for the NECR value and the corresponding activity concentration, respectively. The simulated peak NECR value was 175.6 kcps at  $52.4 \text{ kBq.mL}^{-1}$ , which represents a relative difference from the experimental values of 10.2% for the peak NECR and 4.6% for the corresponding activity concentration.

As a consequence, the proposed model reproduces all experimental counting rates with less than 8% relative errors on the range of clinical activity concentrations found in  $^{18}\text{F}$ -FDG whole-body exams ( $2\text{-}6 \text{ kBq.mL}^{-1}$ ) and up to  $10.3 \text{ kBq.mL}^{-1}$ , and less than 11% until the upper limit of  $16 \text{ kBq.mL}^{-1}$  found in the first pass (first 30 s) of dynamic  $^{82}\text{Rb}$  cardiac exams.

**Adder and readout modules.** Setting the policy as *winner-takes-all* and the reader module at *depth 3* on the *dice* (see Figure 4.2) theoretically describes a model which meets the architecture of integration of the DPC-PET. However, this configuration led to an underestimation of the count rates and sensitivity of the order of 40% compared to the experimental measurements. On the other hand, by setting the reading domain at *depth 1* (the highest level corresponding to the *module*), the results obtained in terms of count rate and sensitivity were much more consistent with experimental data. This could be due to scattered events (into the crystals) which are rejected at lower depths since all their energy will not be integrated and deposited in other parts of the *module*. As the modelling in GATE recovering scattered events is not yet available, it was decided to define the *readout* at the highest level on the modules at *depth 1*. Other modules recently developed by Mehadji (2021) and Lenz (2021) can be tested in our model but were not available yet when performing this study.

**Deadtime.** One of the main features of the Vereos DPC-PET, in comparison with conventional analogue PET, is its good count rate performances characterised by low deadtime and pile-up effects. This property is mainly due to the use of SiPM allowing a 1:1 coupling with the scintillation crystals due to their small dimensions and allowing for more trigger channels. As a result, the relative difference between the theoretical and the experimental *singles* rate obtained by the low activity linear regression in the absence of deadtime, was less than 5% up to an activity concentration of  $15 \text{ kBq.mL}^{-1}$ . However, even if the loss due to deadtime was relatively low with the Vereos DPC-PET, it was necessary to model this effect to obtain accurate counting rates, especially for high activity concentrations.

**Background noise.** At activity concentrations observed in clinical routine, background noise from electronics and natural radioactivity from crystals are often considered negligible and is thus not modelled in Monte Carlo PET simulations. However, it was necessary in order to reproduce the experimental low-activity counting curves. For example, at the lowest measured concentration of  $0.3 \text{ kBq.mL}^{-1}$ , the background noise represented 60% of the total number of detected *singles*. This percentage decreased with activity concentration, but was still 6% at  $5 \text{ kBq.mL}^{-1}$  which is representative of clinical  $^{18}\text{F}$ -FDG activity. It dropped below 1% as from an activity concentration of  $35 \text{ kBq.mL}^{-1}$ .

**TOF and energy resolutions.** Figure 4.9A shows the stability of TOF and energy resolutions up to  $80 \text{ kBq.mL}^{-1}$ . An agreement within 4% between both the simulated and experimental timing and energy resolutions was found over the whole activity range. Simulation values were slightly lower than experimental ones.

**Sensitivity.** The sensitivity value obtained by simulation ( $5591 \text{ cps.MBq}^{-1}$ ) was found to be 7.9% higher than the experimental one ( $5184 \text{ cps.MBq}^{-1}$ ). A good agreement was obtained between the axial sensitivity profiles (Figure 4.10B), with a maximum difference of 13% at the edges of the FOV. However, in comparison with published values from Zhang *et al.* ( $5721 \text{ cps.MBq}^{-1}$ ) (Zhang, Maniawski, and Knopp, 2018) and from the Philips white paper ( $5390 \text{ cps.MBq}^{-1}$ ) (Miller, 2016), the agreement was closer with 2.3% and 3.7% relative differences, respectively. This disparity between the experimental sensitivity values could be explained by the uncertainty on the activity calibration as well as on the phantom positioning which is critical for this test.

**Intrinsic spatial resolution.** The estimation of intrinsic spatial resolution before reconstruction was close between simulation and experimental data, with less than 0.25 mm difference between FWHM for transverse directions ( $x, y$ ). Intrinsic spatial resolutions were better in the transverse direction than in the axial direction ( $z$ ) which reached 0.92 mm difference simulated and experimental data, see Figure 4.11 and Table 4.6.

This PSF asymmetry in the three directions is inherent to the proposed method. Indeed, due to the cylindrical shape of the scanner, only a few azimuthal angles are available in the axial direction. The projected distance along  $z$  can only take values between a scalar  $b = \|\vec{S}\vec{A}\| \cos(\theta_{max})$  and  $\|\vec{S}\vec{A}\|$ , with  $\theta_{max}$  being the maximum azimuthal angle for a given distance  $\|\vec{S}\vec{A}\|$ . Furthermore, the value of  $b$  depends on the axial position due to the truncation of the axial data in 3D PET. Therefore, the lowest projected distance values (between 0 and  $b$ ) were not present in the distribution of the axial  $z$  projected distance, resulting in a degraded FWHM in comparison with those measured in the transverse  $x$  and  $y$  directions. In addition, the truncation of the projections also results in non-uniform axial sampling, making the resolution measurement inaccurate with the presented method for positions too far from the centre of the axial FOV. One solution to improve this method would be to use an exact rebinning algorithm, such as the one proposed by Defrise *et al.* (1997), followed by resampling to achieve an axial sample rate comparable of that obtained transversely.

**Reconstructed spatial resolution.** Regardless of the type of convolution chosen, good agreement was observed between simulated and experimental reconstructed

resolutions with a maximum absolute difference of 0.35 mm, see Table 4.7. It is interesting to note that only when the convolution was applied in the reconstruction model and when the OSEM algorithm converged sufficiently (5 iterations and 10 subsets), that FWHM values were close to those obtained with the intrinsic resolution method developed. When post-reconstruction convolution filters were added, FWHM values were close to the manufacturer's evaluation (around 4 mm).

**Illustrative image reconstructions.** Reconstructed images were in good agreement between the simulated and reconstructed data with a maximum relative deviation of 13% for the CRC and 14% for the BRN. The tradeoff between CRC and BRN was consistently slightly better for simulated than with experimental data. This difference can be explained by the scattered coincidences that have not been equally corrected: the experimental data were corrected by the standard single-scatter simulation (SSS) method (Ye, Song, and Hu, 2014), which only corrects for single-photon scattering, whereas the simulated data were reconstructed ignoring all scattered coincidences (ideal case).

**Statistical uncertainty.** Monte Carlo relative statistical uncertainty were lower than 1% on the estimated count rates. Simulation computation times were relatively large, with an average of about 3000 simulated primary  $\beta^+$  particles per second, leading to, for example, about 80 hours of computation time for one of the 26 acquisitions with the scatter cylindrical phantom. No particular attention has been paid to gain speed. In particular, the slowest physic list (emstandard\_opt4) has been used and the production and tracking cuts have not been optimized. The optimal trade-off between computation speed and accuracy remains to be studied, but this work can serve as reference for optimal accuracy results. Fast methods, such as the SMART software (Pfaehler et al., 2018), may be used to speed up the simulation.

## 4.5 Conclusion

As a conclusion, the proposed GATE PET model was validated with respect to NEMA NU 2-2018 compliant experimental data. To our knowledge, this is the first time a full Monte Carlo model of a DPC-based PET system is proposed and validated. This model can be useful for numerous studies such as to optimise imaging performance, evaluate reconstruction algorithms and estimate the effects of confounding factors in image quality.

## Chapter 5

# Yttrium-90 quantitative study using DPC-PET

*PET imaging of  $^{90}\text{Y}$ -microsphere distribution following radioembolisation is challenging due to the count-starved statistics from the low branching ratio of  $e^+/e^-$  pair production during  $^{90}\text{Y}$  decay. PET systems using SiPMs have shown better  $^{90}\text{Y}$  image quality compared to conventional PMTs.*

*This chapter is adapted from Labour et al. (2021), which has been published in the European Journal of Nuclear Medicine and Molecular Imaging (Physics) journal. The main goal was to evaluate reconstruction parameters for different phantom configurations and varying listmode acquisition lengths to improve quantitative accuracy in  $^{90}\text{Y}$  dosimetry, using DPC-PET.*

### 5.1 Introduction

**Short review.** Liver radioembolisation or SIRT, has been reviewed in Chapter 1 and is an intra-arterial method used in clinical practice to treat unresectable hepatic malignancies (Salem et al., 2010; Sangro et al., 2011). Currently, SIRT can be performed either with  $^{90}\text{Y}$  or  $^{166}\text{Ho}$  microspheres. During  $^{90}\text{Y}$ -SIRT, the high energy  $\beta^-$  emitter  $^{90}\text{Y}$  particles which are encapsulated-in glass or labelled to resin microspheres are administered through selected branches of the hepatic artery which feed the tumours. This method ensures a regional biodistribution of the  $^{90}\text{Y}$ -microspheres delivering a highly localised absorbed dose to the perfused regions, sparing nearby organs at risk and healthy tissues with the advantage of a negligible radiation burden to both non-embolized portions and extra-hepatic tissues. The  $^{90}\text{Y}$ -SIRT method is widely used owing to its clinical efficacy and relative safety (Lau et al., 1994; Sato et al., 2008; Kennedy et al., 2009; Salem et al., 2010; Sangro et al., 2011).

At present, the prediction of the biodistribution of  $^{90}\text{Y}$ -microspheres is generally performed using  $^{99m}\text{Tc}$ -labelled MAA prior to treatment, see Section 1.3.1. However,  $^{99m}\text{Tc}$ -MAA biodistribution does not always match with post-therapy  $^{90}\text{Y}$  microspheres distribution (Cremonesi et al., 2014; Garin et al., 2016; Gnesin et al., 2016; Haste et al., 2017; Richetta et al., 2019) and an assessment of the radionuclide biodistribution must be performed following treatment either by SPECT or PET. This assessment is mainly done to detect any possible extrahepatic deposition of microspheres and determine the intrahepatic microsphere distribution over the perfused tumorous and non-tumorous liver tissue.

$^{90}\text{Y}$  SPECT imaging exploits bremsstrahlung photons, with various published energy windows, collimator size, with or without correction (Dezarn et al., 2011; Wright et al., 2015) and has been used for post-SIRT treatment evaluation (Walrand et al., 2011). However, SPECT suffers from scatter, low spatial resolution and

challenging quantitative analysis. Alternatively,  $^{90}\text{Y}$  PET imaging exploits a minor positron decay (Johnson, Johnson, and Langer, 1955; Ford, 1955), see Chapter 3. In 2004, Nickles et al. (2004) first exploited this property to show the distribution of the regional absorbed dose delivered by  $^{90}\text{Y}$  therapies using PET, although difficult and time-consuming due to the count-starved statistics for annihilation photons. Activity distribution assessment after  $^{90}\text{Y}$ -SIRT was proved feasible in 2010 by Lhommel et al. (2009, 2010) with the help of TOF information added on PET/CT systems. Other studies followed and showed that TOF PET compared to non-TOF PET provided improved recovery in reconstructed quantitative data (Lhommel et al., 2009, 2010; Elschot et al., 2011; Carlier et al., 2013; Gates et al., 2011; Kao et al., 2012; Kao et al., 2013a), outperforming at the same time  $^{90}\text{Y}$  bremsstrahlung SPECT (Walrand et al., 2011; Elschot et al., 2011). In 2007, Selwyn et al. (2007) verified the branching ratio related to  $e^+ / e^-$  pair production during  $^{90}\text{Y}$  decay to be  $(31.86 \pm 0.47) \times 10^{-6}$ , following de-excitation from the  $0^+$  excited state of  $^{90}\text{Zr}$ . The latest published value was from Dryák and Šolc (2020) in 2020, who measured the branching ratio to be  $(32.6 \pm 0.4) \times 10^{-6}$ .

The recent digital PET systems are equipped with SiPM technology that replaces conventional PMTs, see Chapter 2. They allow enhanced TOF capability and CTR owing to faster and more compact electronics (Lecoq, 2017; Gundacker et al., 2020). They demonstrate better performances for sensitivity, spatial resolution, count rates and overall image quality (Zhang, Maniawski, and Knopp, 2018; Rausch et al., 2019; Van Sluis et al., 2019; Labour et al., 2020; Gnesin et al., 2020; Chicheportiche, Marciano, and Orevi, 2020).

*Context of this present study.* Reviewing previous studies, assessments for  $^{90}\text{Y}$  imaging were performed largely using criteria based on NEMA guidelines, *NEMA NU 2-2012 - Performance measurements of positron emission tomographs* (2012) (or earlier), and by evaluating detectability for diagnostic purposes rather than dosimetry calculations. Willowson et al. (2012) and Carlier et al. (2013) showed that with the help of TOF information, higher detectability was reached with a small number of OSEM iterations on Siemens Biograph mCT systems. Few studies evaluated OSEM reconstruction parameters using absorbed dose calculation tools. In 2014, Pasciak, Bourgeois, and Bradley (2014) based on previous findings of Willowson et al. (2012) and Carlier et al. (2013) found that an additional 4.5 mm FWHM PSF modelling improved accuracy in absorbed dose distributions using DVHs. Siman et al. (2019) studied a GE D690 PET/CT and found that 3 iterations with 12 subsets with additional PSF modelling and a 5.2 mm FWHM post-reconstruction Gaussian filter size provided the least root-mean-square deviation (RMSD) between their experimental and reference DVH.

This study focuses on the use of a DPC-PET for  $^{90}\text{Y}$  quantification for dosimetry purposes following SIRT. We considered the fully digital SiPM-equipped Philips Vereos PET/CT system described in Section 4.2.1, with a 1:1 coupling between the LYSO scintillator crystals and the SiPMs (Zhang, Maniawski, and Knopp, 2018), showing improved timing resolution and SNR compared to conventional PMT-PET (Salvadori et al., 2020b). Wright et al. (2016, 2017b) and Wright et al. (2018) showed that DPC-PET detection of annihilation photons following  $^{90}\text{Y}$ -SIRT is feasible, showing concordant visualisation with improved  $^{90}\text{Y}$ -to-background contrast of microsphere distribution with the DPC-PET compared to SPECT and PMT-PET systems.

Previous studies (Willowson et al., 2012; Carlier et al., 2013; Pasciak, Bourgeois, and Bradley, 2014; Siman et al., 2019) evaluated OSEM reconstruction parameters for

PMT-PET systems with TOF resolutions around 550 ps. Therefore, suggested parameters in the literature might not be suitable for the DPC-PET with a TOF resolution around 320 ps (Rausch et al., 2019; Zhang, Maniawski, and Knopp, 2018; Labour et al., 2020), due to the dependence of the convergence of OSEM-based algorithms on the TOF information (Salvadori et al., 2020b). Moreover, implementations of OSEM-based algorithms differ within systems and the OSEM algorithm implemented in the DPC-PET is based on listmode data, instead of sinograms, and use spherically symmetric volume elements to model the image, instead of voxels (Wang et al., 2006; Narayanan and Perkins, 2013).

In this study, we investigated the accuracy of  $^{90}\text{Y}$  DPC-PET by evaluating the effect of OSEM reconstruction parameters and acquisition duration on estimating the absorbed dose distribution based on DVHs (Drzymala et al., 1991), as proposed by Siman et al. (2019).

## 5.2 Materials and methods

In order to evaluate the accuracy of image-based absorbed dose estimations from  $^{90}\text{Y}$  DPC-PET/CT, 3 phantoms were selected and imaged using a range of parameters. Acquired PET images were used as input activity maps to compute the absorbed dose distributions and DVHs. Obtained image-based distributions were compared to reference absorbed dose distributions computed with Monte Carlo simulations and the impact of several parameters, including VOIs, activity levels, reconstruction parameters and acquisition lengths, were evaluated. The following subsections describe 1) the phantoms, 2) the acquisition and reconstruction parameters, 3) the algorithms used to compute the absorbed dose, 4) the figures of merit and 5) the clinical application using several patient image datasets acquired on the same DPC-PET/CT following  $^{90}\text{Y}$ -SIRT treatment.

### 5.2.1 Experimental setup

#### 5.2.1.1 Phantoms

**Cylindrical phantoms, Ph1 and Ph2.** A 6800 mL uniform cylindrical phantom (Ph1) (diameter  $\varnothing$  21.6 cm; height  $h$  18.6 cm) and a 5950 mL cylindrical phantom ( $\varnothing$  19.6 cm;  $h$  19.7 cm) with a 300 mL cylindrical fillable insert ( $\varnothing$  4.5 cm;  $h$  18.7 cm) (Ph2), were used for validation of quantitative recovered data following PET calibration for  $^{90}\text{Y}$ . All materials of Ph1 and Ph2 are made of polymethyl methacrylate (PMMA). PET/CT fusion images of Ph1 and Ph2 are depicted in Figures 5.1A and 5.1B, respectively.

**NEMA IEC body phantom, Ph3.** A NEMA IEC body phantom (Ph3) in Figure 5.1C, was then used for quantitative measurements for dosimetry evaluations, consisting of a background compartment of approximately 9700 mL, a lung insert and an insert with six fillable spheres of diameters, 10, 13, 17, 22, 28 and 37 mm. The corresponding nominal volumes of the spheres ranged between 0.52 and 26.52 mL. The phantoms used in this study allow for quantitative activity recovery (or activity concentration recovery) and dosimetry evaluations in objects of different sizes.

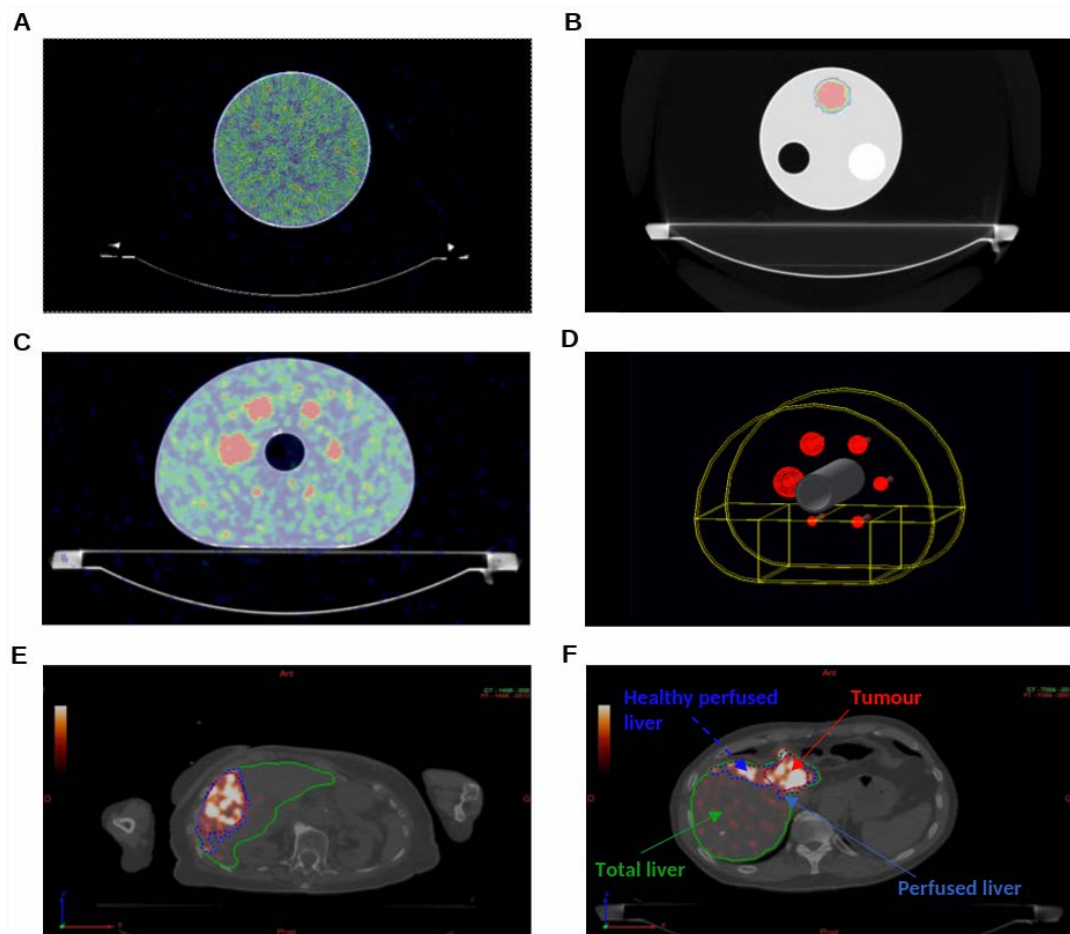


FIGURE 5.1 – Axial slices of PET/CT images of **A:** Ph1, **B:** Ph2 and **C:** Ph3. **D:** Geometry of Ph3 modelled in GATE for reference. **E** and **F:** Examples of segmentation of liver VOIs following radioembolisation for patients #2 and #3, respectively.

### 5.2.1.2 Activities

Prior to phantom preparations, 100  $\mu\text{L}$  of diethylenetriaminepentaacetic acid (DTPA) with a concentration of 5  $\text{mg}\cdot\text{mL}^{-1}$  was added to two vials, each containing 2850 MBq of  $^{90}\text{YCl}_3$  in 1.03 mL. This was done to prevent the known effect of adsorption of  $^{90}\text{YCl}_3$  on the inner PMMA walls of plastic phantoms which may negatively affect PET quantitative imaging studies (Willowson, Tapner, Bailey, et al., 2015). Activities were measured using an Easypharma HE Lemer Pax activimeter calibrated for  $^{90}\text{Y}$  under national standards. Prepared syringes used for filling Ph1, Ph2 and Ph3 were flushed several times to transfer the maximum amount of activity into the phantom volumes. All syringes were also measured for residual activity to allow for the calculation of the net transferred activity.

**Cylindrical phantoms, Ph1 and Ph2.** Ph1 was filled with 2130 MBq of  $^{90}\text{YCl}_3$  in water. The 300 mL water insert in Ph2 was filled with 540 MBq of  $^{90}\text{YCl}_3$  and placed in a cold water background. The reference initial activity concentrations at injection ( $AC_{ref,init}$ ) were 0.31  $\text{MBq}\cdot\text{mL}^{-1}$  and 1.83  $\text{MBq}\cdot\text{mL}^{-1}$ , which are the total net injected activity ( $A_{ref,init}$ ) in each region divided by the volume of the considered region, for Ph1 and the insert in Ph2, respectively.

**NEMA IEC body phantom, Ph3.** A stock solution was prepared for filling the spheres by combining 225 MBq of  $^{90}\text{YCl}_3$  with 100 mL of water. An activity of 2355 MBq of  $^{90}\text{YCl}_3$  was added to the 9700 mL water background. The  $AC_{ref,init}$  in the spheres and background compartment were 2.25  $\text{MBq}\cdot\text{mL}^{-1}$  and 0.24  $\text{MBq}\cdot\text{mL}^{-1}$  at injection, respectively. A sphere-to-background ratio (SBR) of 9:1 was obtained, similar to that in the QUEST study (Willowson, Tapner, Bailey, et al., 2015).

## 5.2.2 Image acquisition

Image acquisitions for all phantoms were performed over six consecutive days (two half lives of  $^{90}\text{Y}$ ) to analyse the response of the PET with decreasing activity concentrations. Markers were placed to allow for reproducible placement of the phantoms between daily scans. Data acquisitions were performed in *listmode* format. The acquisition lengths were 30 minutes per bed (min/bed) for both Ph1 and Ph2 and 15 min/bed for Ph3.

## 5.2.3 Image reconstruction

**Reconstruction algorithms.** All image reconstructions were performed with TOF information and using relaxed relaxed List Mode Ordered Subset Expectation Maximisation (LMOSEM) algorithm (Wang et al., 2006) implemented on Philips PET systems, with isotropic voxels of  $2 \times 2 \times 2 \text{ mm}^3$ . They were post-treated with a regularised version of the Richardson-Lucy algorithm for resolution recovery (Richardson, 1972; Lucy, 1974) with the default recommended parameters of the PSF modelling (1 iteration with a 6 mm FWHM regularisation kernel) which provide reasonable contrast recovery without noticeable Gibbs artefacts (Narayanan and Perkins, 2013; Golla, Lammertsma, and Boellaard, 2015).

**Reconstruction parameters.** The listmode data for Ph1 and Ph2 were reconstructed with *Recon1*, the default clinical setup recommended by Philips, see Table 5.1.



Several parameters were compared for Ph3, also listed in Table 5.1. The number of iterations were fixed to 1, 2 or 3 to limit image noise amplification. The number of subsets were varied with 10, 20 or 30 subsets to cover the range of suggested number of subsets used in previous studies (which are listed in the Discussion Section 5.4 in Table 5.6). Post-reconstruction Gaussian filters of varying sizes were applied, between 0 (no filter) and 8 mm FWHM with increments of 2 mm.

TABLE 5.1 – Parameter sets used for listmode data reconstructions.

Reconstruction parameter set	Iterations	Subsets	Gaussian filter (mm @ FWHM)	PSF	TOF
<i>Various*</i>	1, 2 or 3	10, 20 or 30	0, 2, 4, 6 or 8	Yes	Yes
<i>Recon1</i>	3	5	2	Yes	Yes
<i>Recon2</i>	3	12	5.2	Yes	Yes
<i>Recon3</i>	1	21	5	Yes	Yes

\*45 possible combinations of parameters for evaluation.

In total, 45 combinations for reconstructions were compared for Ph3. Reconstruction parameter sets suggested in the literature were also tested, *Recon2* (Siman et al., 2019) and *Recon3* (Willowson et al., 2012; Carrier et al., 2013; Pasciak, Bourgeois, and Bradley, 2014). Reconstruction parameters are denoted i3s5-2mm for example for 3 iterations with 5 subsets and a 2 mm FWHM post-reconstruction Gaussian filter, with implemented PSF and TOF modellings.

Finally, thanks to listmode data, datasets for Ph3 were rebinned into various acquisition lengths, from 5 to 15 min/bed, in order to evaluate the impact of the counts statistics on dosimetry and investigate if shorter acquisitions might be used.

## 5.2.4 Absorbed dose computation

Monte Carlo simulations were used to estimate the reference absorbed dose distributions in the 3 phantoms and inserts therein, according to the known  $AC_{ref,init}$  in each region at injection. These reference absorbed dose distributions were compared to the ones that can be estimated from the  $^{90}\text{Y}$  PET reconstructed images. The image-based absorbed dose computations were performed first with the VSV kernel-based convolution method, see Section 1.6.4, for the various reconstruction parameters applied (see Table 5.1). The LDM, see Section 1.6.5, was also used for comparison purposes.

**Reference absorbed dose.** Monte Carlo simulations were performed with the GATE platform 9.0 (Jan et al., 2011; Sarrut et al., 2014) using Geant4 10.5 (Collaboration, Agostinelli, et al., 2003). The geometry, dimensions and material composition of each phantom were modelled. The modelled geometry for Ph3 is shown in Figure 5.1D. The physics list named `emstandard_opt4` was used<sup>1</sup>. It contains the Geant4 most accurate standard and low-energy models for electromagnetic processes recommended for medical applications (Beaudoux et al., 2019) and deemed to offer the best performance in terms of accuracy at the cost of CPU efficiency (Arce et al., 2021), considering Geant4 10.5.

Range production cuts were set to 1 mm for electrons and photons in the whole geometry. In Geant4, it means that secondary particles are only created and tracked when their expected range in the current material is larger than this distance. No

1. See <https://geant4.web.cern.ch/node/1731>

variance reduction technique was used. The  $\beta^-$  radioactive sources of  $^{90}\text{Y}$  were simulated by homogeneous *generic ion sources* in each sphere and the background compartment. The absorbed doses were scored with  $2 \times 2 \times 2 \text{ mm}^3$  voxels sizes. The number of primary particles was adapted for each phantom region in a single simulation for an entire phantom according to the relative experimental  $AC_{ref,init}$  in each region, such as to reach a statistical Type-A uncertainty of lower than 1% on the estimated mean absorbed dose values. This corresponds for example to about  $6 \times 10^5$  primary generated particles for the smallest 10 mm sphere in Ph3. Final absorbed dose values were scaled according to the known accumulated activities in all injected regions.

**Image-based absorbed dose.** Absorbed dose distributions were first computed from the PET images with DOSIsoft® (Cachan, France) with the VSV dose kernel convolution algorithm following the MIRD formalism (Bolch et al., 2009; Dieudonné et al., 2010, 2011), see Sections 1.6.3 and 1.6.4. It is considered as a compromise between more simplified calculation models (such as the LDM multiplicative approach) and Monte Carlo calculations, allowing to achieve accurate absorbed dose distribution information in clinic (Dieudonné et al., 2010; Gardin et al., 2003; Sarfaraz et al., 2004; Dieudonné et al., 2011; Ferrari et al., 2012). Calculations were also performed using LDM for comparison purposes.

**Partition model.** Mean absorbed dose estimations were also carried out with the simplified MIRD formalism ( $D_{MIRD}$ ) for  $^{90}\text{Y}$ , using the partition model (Ho et al., 1996) (see Section 1.4.3.3), according to:

$$D_{MIRD} = \frac{A_{ref,init}(GBq)}{M(kg)} \times 49.67 \quad (5.1)$$

where  $M$  is the mass of each phantom region injected with  $A_{ref,init}$ , respectively.

## 5.2.5 Dosimetry-based figures of merit

For Ph1 and the filled insert in Ph2, VOIs were defined using the co-registered CT to PET images, using at first the exact complete internal dimensions of intended VOIs, denoted  $VOI_{outer}$ , and secondly using reduced dimensions to avoid edge PVE, denoted  $VOI_{inner}$ . For Ph3, spherical VOIs were defined for the 6 spheres using the exact internal diameter of each sphere on the CT images. The DVH of each VOI was computed as suggested in Siman et al. (2019).

### 5.2.5.1 DVH and RMSD

The reference Monte Carlo, image-based VSV convolution and image-based LDM DVHs are denoted  $DVH_{ref}^{MC}$ ,  $DVH_{pet}^{VSV}$  and  $DVH_{pet}^{LDM}$ , respectively. For each parameter set,  $r$ , used for image reconstruction and sphere size,  $\varnothing$ , in Ph3, differences between the absorbed dose distributions using VSV convolution were evaluated by the RMSD between their respective  $DVH_{ref,\varnothing}^{MC}$  and  $DVH_{pet,\varnothing}^{VSV}$ , see Equation 5.2.

$$RMSD_{\varnothing,r} = \sqrt{\frac{\sum_{i=0}^{N-1} (DVH_{ref,\varnothing,i}^{MC} - DVH_{pet,\varnothing,r,i}^{VSV})^2}{N}} \quad (5.2)$$

where  $N$  is the total number of points in which the absorbed dose-axes of the DVHs are sampled.

Comparisons using RMSD as in Equation 5.2 were also performed between different DVHs obtained by varying acquisition lengths, e.g. between a 15 and a 10 min/bed acquisitions for Ph3.

### 5.2.5.2 $D_{mean}$ and $D_{50\%}$

For all phantoms, comparisons between  $DVH_{ref}^{MC}$ ,  $DVH_{pet}^{LDM}$  and  $DVH_{pet}^{VSV}$  were performed using differences in the mean absorbed doses,  $D_{mean}$ .  $D_{mean}$  is denoted as  $\overline{D}_{ref}^{MC}$ ,  $\overline{D}_{pet}^{VSV}$  and  $\overline{D}_{pet}^{LDM}$  for the reference Monte Carlo simulations, VSV convolution and LDM, respectively. Similar comparisons were made using the absorbed doses at 50% volume,  $D_{50\%}$ , denoted  $D_{ref,50\%}^{MC}$ ,  $D_{pet,50\%}^{VSV}$  and  $D_{pet,50\%}^{LDM}$  for each corresponding calculation method.

### 5.2.5.3 $RC_{AC}$ and $RC_{Dose}$

In addition, instead of the NEMA CRC definition NEMA (2018) that aims at lesion detection rather than absorbed dose estimation, we used the mean activity concentration recovery coefficient ( $RC_{AC}$ ) and the mean absorbed dose recovery coefficient ( $RC_{Dose}$ ) using VSV convolution for quantitative analysis with decreasing activity concentrations, see Equations 5.3 and 5.4.

$$RC_{AC,\varnothing} = \frac{AC_{pet,\varnothing}}{AC_{ref,\varnothing}} \quad (5.3)$$

$$RC_{Dose,\varnothing} = \frac{\overline{D}_{pet,\varnothing}^{VSV}}{\overline{D}_{ref,\varnothing}^{MC}} \quad (5.4)$$

where for each  $\varnothing$ ,  $AC_{pet,\varnothing}$  is the mean activity concentration measured from reconstructed PET images,  $AC_{ref,\varnothing}$  is the reference activity concentration at the start of each acquisition.

## 5.2.6 Clinical application

The dosimetric impact of reducing PET acquisition duration was investigated on five patients treated by  $^{90}\text{Y}$ -SIRT in the local hospital, see Table 5.2. The initial acquisition length was 15 min/bed position. Listmode datasets were used to artificially decrease the acquisition length down to 10 and 5 min/bed position during the reconstruction step. Each patient's listmode data was reconstructed using the reconstruction parameters chosen following the evaluation using DVH and RMSD on Ph3 (see results in Section 5.3.2.2, paragraph *Choice of reconstruction parameter set*).

For all considered patients, different VOIs were delineated by an experienced clinician following the local hospital protocol, including: 1) whole liver volume (WLV), 2) perfused liver volume (PLV), 3) tumour volume (TV) and 4) perfused normal liver volume (PNLV). 3D segmentations were performed using the DOSIsoft® software and the registered CT and PET images. The WLV and TV were manually segmented using the CT images. Only the largest visible lesion on the CT was selected per patient as the TV for illustration in this study. The PLV was delineated

TABLE 5.2 – Patient characteristics.

Patient	Sex, Age	Tumour type	Microsphere material	Injected $^{90}\text{Y}$ activity (GBq)	Treatment approach	WLTV-PLV-TV ( $\text{cm}^3\text{-cm}^3\text{-cm}^3$ )
#1	M,65	HCC	Glass	2.463	Lobar	2470-635-365
#2	F,92	mCRC	Resin	0.716	Segmental	870-330-380
#3	M,67	mCRC	Resin	0.800	Lobar	1010-127-50
#4	F,16	FLC	Resin	1.752	Whole liver	2900-1020-70
#5	F,67	mCRC	Resin	1.479	Whole liver	4240-2610-230

*HCC* hepatocellular carcinoma, *FLC* fibrolamellar carcinoma, *mCRC* hepatic metastases from colorectal cancer

using a threshold of 5% of the maximum activity in the liver on the PET images. The PNLV was considered as the subtraction of the TV from the PLV.

Figures 5.1E and 5.1F depict axial slices of liver VOI segmentations for patients #2 and #3, respectively. DVH analysis was performed on the different VOIs, using the VSV convolution and LDM algorithms implemented in DOSIsoft®. The metrics used for comparison are the  $D_{mean}$  and  $D_{50\%}$  as in phantoms, as well as the absorbed doses at 2% volume,  $D_{2\%}$ , denoted  $D_{pet,2\%}^{VSV}$  and  $D_{pet,2\%}^{LDM}$  for VSV convolution and LDM, respectively.

## 5.3 Results

### 5.3.1 Cylindrical phantoms Ph1 and Ph2

The first test was a sanity check to evaluate the PET response. Figure 5.2A depicts the measured mean activity concentrations from reconstructed PET images,  $AC_{pet}$ , versus  $AC_{ref}$ , for both Ph1 and Ph2 using  $VOI_{outer}$  (the exact internal dimensions of the VOI).  $AC_{ref}$  ranged from 0.08 to 0.29  $\text{MBq.mL}^{-1}$  for Ph1, and from 0.49 to 1.71  $\text{MBq.mL}^{-1}$  for Ph2.

**Activity comparisons.** On the first imaging day (highest  $AC_{ref}$ ), relative percentage differences between  $AC_{pet}$  and  $AC_{ref}$  were  $-1.1\%$  and  $+0.1\%$  for Ph1 at 0.29  $\text{MBq.mL}^{-1}$  and Ph2 at 1.71  $\text{MBq.mL}^{-1}$ , respectively. The maximum relative percentage differences obtained over the range of activity concentrations studied were  $-19.6\%$  and  $-4.5\%$  for Ph1 at 0.08  $\text{MBq.mL}^{-1}$  and Ph2 at 0.49  $\text{MBq.mL}^{-1}$ , corresponding to an absolute difference of  $-0.02 \text{ MBq.mL}^{-1}$  for both Ph1 and Ph2 at the reported  $AC_{ref}$ , respectively.

**Absorbed dose comparisons.** Figures 5.2B and 5.2C depict the calculated DVHs for Ph1 and Ph2, respectively, according to the computation methods used:  $DVH_{ref}^{MC}$  (reference absorbed dose),  $DVH_{pet}^{VSV}$  and  $DVH_{pet}^{LDM}$  (PET image-based absorbed doses). The obtained DVHs illustrate the loss of accuracy brought by the use of images in the calculation of absorbed dose distributions. DVHs calculated with  $VOI_{outer}$  regions suffer from edge PVE effects compared to the ones based on  $VOI_{inner}$  regions for the known geometries. LDM compared to VSV convolution seems to favour the amplification of the maximum absorbed dose ( $D_{max}$ ) to the detriment of intermediate ones. Table 5.3 provides the  $D_{mean}$  and  $D_{50\%}$  for both phantoms computed with each absorbed dose calculation method. Their percentage differences to the reference Monte Carlo simulations are also provided.

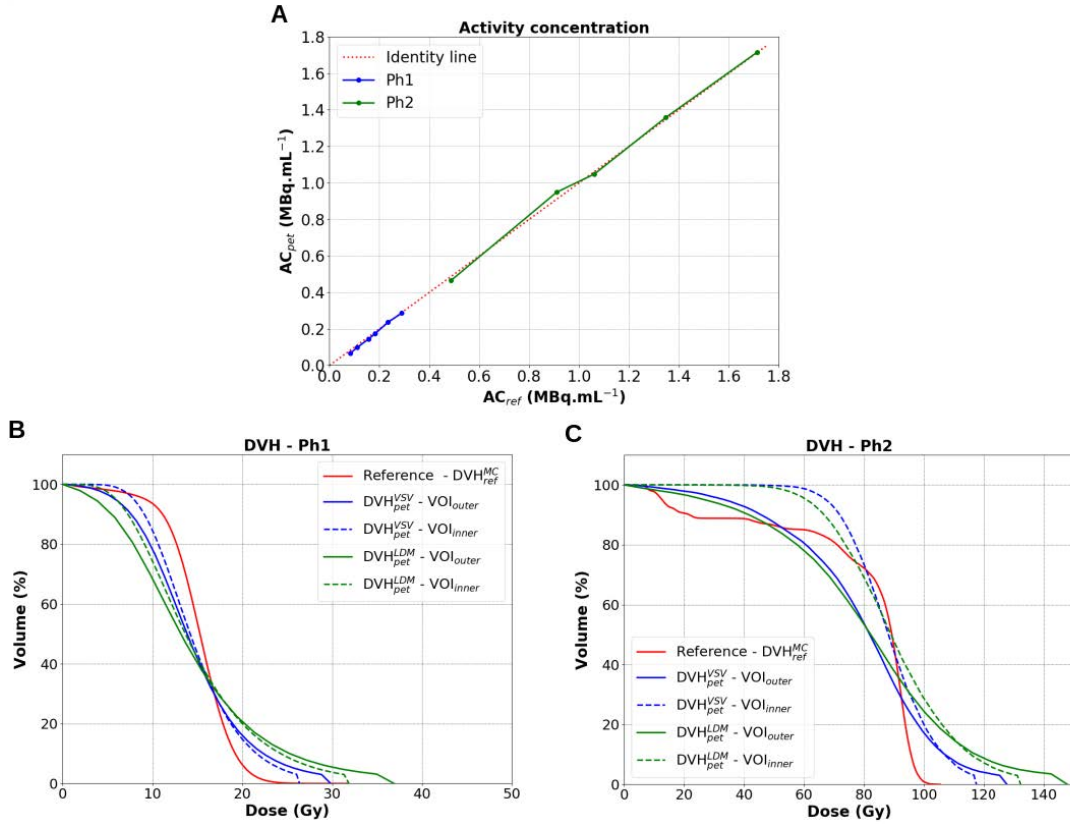


FIGURE 5.2 – Quantitative accuracy of <sup>90</sup>Y acquisitions for image reconstructions with *Recon1*. **A**:  $AC_{pet}$  against  $AC_{ref}$  for both Ph1 and Ph2. **B** and **C**: Comparisons of  $DVH_{pet}^{VSV}$  (blue lines) and  $DVH_{pet}^{LDM}$  (green lines) to  $DVH_{ref}^{MC}$  (red lines) for Ph1 at  $AC_{ref} = 0.29$  MBq.mL<sup>-1</sup> and Ph2 at  $AC_{ref} = 1.71$  MBq.mL<sup>-1</sup>, respectively.

TABLE 5.3 – Comparison of absorbed dose calculation methods through the  $D_{mean}$  and  $D_{50\%}$  for Ph1 at  $0.29$  MBq.mL<sup>-1</sup> and Ph2 at  $1.71$  MBq.mL<sup>-1</sup>, for both  $VOI_{outer}$  and  $VOI_{inner}$ . Reconstructions were performed using *Recon1*.

Calculation method	Ph1 <sub>VOI,inner</sub>		Ph1 <sub>VOI,outer</sub>		Ph2 <sub>VOI,inner</sub>		Ph2 <sub>VOI,outer</sub>	
	$D_{mean}$	$D_{50\%}$	$D_{mean}$	$D_{50\%}$	$D_{mean}$	$D_{50\%}$	$D_{mean}$	$D_{50\%}$
Ref. MC (Gy)	15.1	15.2	15.1	15.2	83.7	89.2	83.7	89.2
VSV conv. (Gy)	14.9	14.2	14.7	13.9	88.8	88.1	79.9	81.9
LDM (Gy)	15.0	13.7	14.8	13.1	90.5	89.0	82.7	82.2
Percent diff. (%)								
MC vs VSV	-1.3	-6.6	-2.6	-8.6	+6.1	-1.3	-4.5	-8.2
Percent diff. (%)								
MC vs LDM	-0.7	-9.9	-2.6	-13.8	+8.1	-0.2	-1.1	-7.8

### 5.3.2 NEMA IEC body phantom Ph3

In this section, we proceed in the comparison of different reconstruction parameters for Ph3 using  $DVH_{pet}^{VSV}$  and  $DVH_{ref}^{MC}$  and their RMSD at the imaging point where  $AC_{ref}$  was equal to  $2.18$  MBq.mL<sup>-1</sup> ( $AC_{ref,init}$  was  $2.25$  MBq.mL<sup>-1</sup>). We also evaluate the effect of acquisition length on absorbed dose distributions. The response of the PET is then evaluated using the  $RC_{AC}$  and  $RC_{Dose}$  for different  $AC_{ref}$

over two  $^{90}\text{Y}$  radioactive periods following phantom preparation. Comparisons using  $DVH_{pet}^{LDM}$  are also reported.

### 5.3.2.1 Evaluation using $DVH_{pet}^{VSV}$

In total, 270 image-based  $DVH_{pet}^{VSV}$  (45 reconstruction parameter sets described in Section 5.2.3 for the 6 spheres) have been computed, and 6 reference  $DVH_{ref}^{MC}$ , corresponding to each sphere, have been simulated. For each sphere and each reconstruction, the  $DVH_{pet}^{VSV}$  has been compared to the  $DVH_{ref}^{MC}$ . Figure 5.3 depicts the simulated  $DVH_{ref}^{MC}$  (black curves) for each sphere and the  $DVH_{pet}^{VSV}$  for 8 reconstructions per sphere (only extremes are depicted: 1 and 3 iterations, 10 and 30 subsets, 0 and 8 mm FWHM filter sizes).

**Varying post-reconstruction Gaussian filter.** As expected for all spheres, increasing the filter size reduced the  $D_{max}$  of the  $DVH_{pet}^{VSV}$ , e.g. between i1s30-0mm and i1s30-8mm, as seen in Figure 5.3. It could be observed that too large a filter could not be suitable for dosimetry, specially with decreasing sphere sizes where the area under the curve can be significantly reduced (comparing cyan and green  $DVH_{pet}^{VSV}$  in Figures 5.3D, 5.3E and 5.3F).

**Varying subsets.** As expected, increasing the number of subsets led to an increase in the  $D_{max}$  of the  $DVH_{pet}^{VSV}$  for all spheres, e.g. between i3s10-0mm and i3s30-0mm, as seen in Figure 5.3. For the largest 28 and 37 mm spheres, 30 iterations compared to 10 iterations favoured noise amplification to the detriment of intermediate absorbed doses (comparing red and blue  $DVH_{pet}^{VSV}$ ).

**Varying iterations.** The relationship in varying the number of iterations was less clear and intuitive than with the size of post-reconstruction filter or number of subsets. For spheres  $> 20$  mm (22, 28 and 37 mm), increasing the number of iterations did not incur significant change in the shape of the  $DVH_{pet}^{VSV}$  or resulted in a slight increase in the  $D_{max}$ , e.g. between i1s10-0mm and i3s10-0mm, as shown on Figure 5.3. Increasing iterations from 1 to 3 did not seem to favour noise amplification for the largest spheres. On the other hand, more variations were observed for spheres  $< 20$  mm (10, 13, 17 mm) using the same comparison, e.g. between i1s10-0mm and i3s10-0mm.

**Equivalent updates.** Equivalent number of updates (product of the number of iterations and subsets) did not provide the same accuracy in  $DVH_{pet}^{VSV}$  as would be expected, e.g. between i1s30-0mm and i3s10-0mm or between i1s30-8mm and i3s10-8mm.

Results for all reconstructions are provided in Appendix A for the 6 spheres, with 45 reconstructions per sphere, totalling the 270  $DVH_{pet}^{VSV}$ .

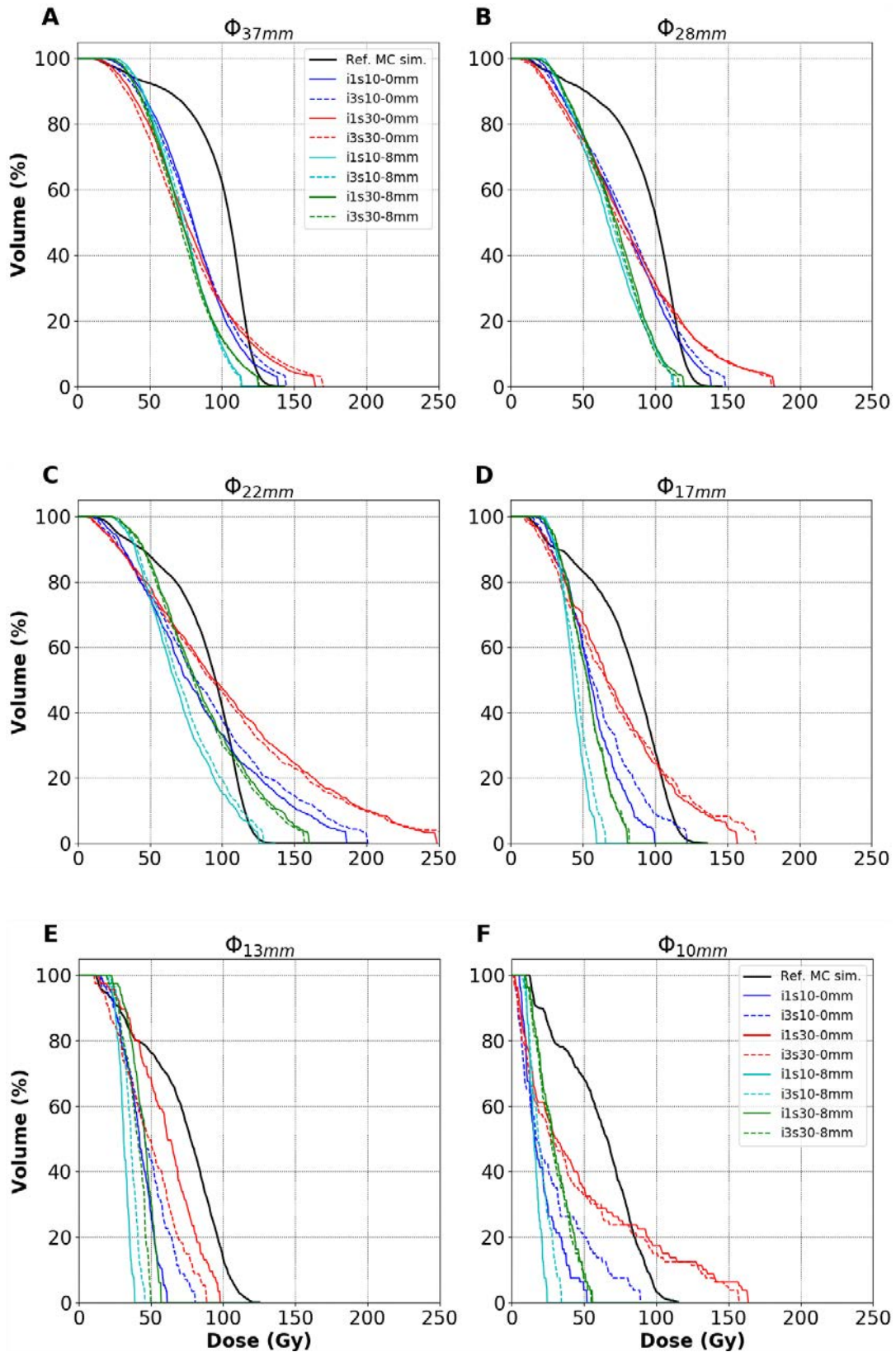


FIGURE 5.3 – The  $DVH_{pet}^{VSV}$  for 8 different reconstructions are compared to  $DVH_{ref}^{MC}$  (black curves) for each sphere of Ph3. Sphere sizes are represented in **A**: 37 mm, **B**: 28 mm, **C**: 22 mm, **D**: 17 mm, **E**: 13 mm and **F**: 10 mm.

### 5.3.2.2 Comparison using RMSD

Figure 5.4A outlines the RMSD between  $DVH_{pet}^{VSV}$  and  $DVH_{ref}^{MC}$  for the 28 mm sphere as an example, corresponding to 45 reconstructions (9 combinations of iterations and subsets each with 5 filter sizes). The figure also shows three additional RMSD values for *Recon1-3* in Table 5.1. Independent of the combination of iterations and subsets, the RMSD between  $DVH_{pet}^{VSV}$  and  $DVH_{ref}^{MC}$  were smallest when no (0 mm), or a 2 mm FWHM post-reconstruction Gaussian filter was applied. Similar observations were made for all spheres, except for the 22 mm sphere where the  $D_{max}$  could be amplified when no filter was applied, and agreed with the observations made in Figure 5.3 when increasing the filter size.

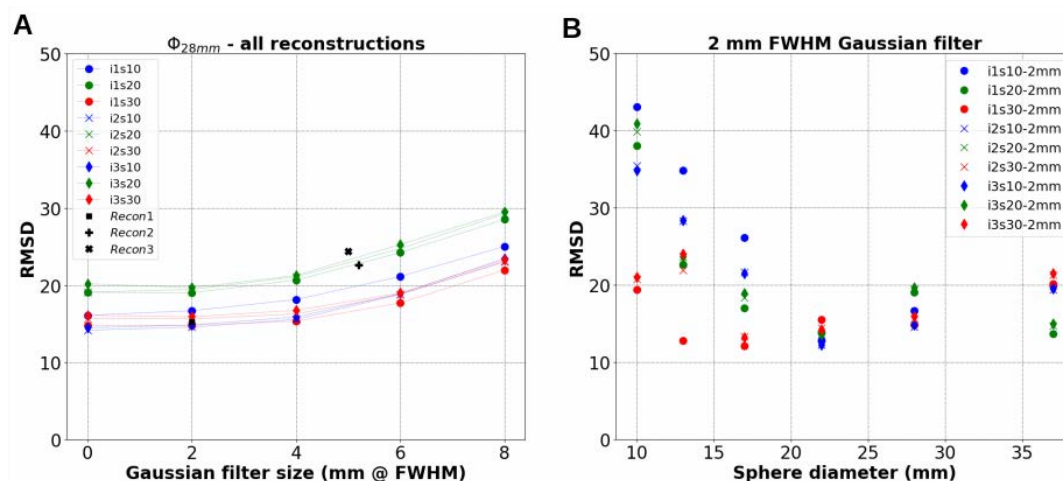


FIGURE 5.4 – RMSD between  $DVH_{pet}^{VSV}$  and  $DVH_{ref}^{MC}$ . **A:** RMSD for all reconstructions for the 28 mm sphere against filter size. **B:** RMSD against sphere sizes for reconstructions using a 2 mm FWHM post-reconstruction Gaussian filter only.

**Choice of post-reconstruction filter size.** From the previous findings, we now consider the use of a post-reconstruction Gaussian filter size of 2 mm FWHM for dosimetry, which can reduce noise in the reconstructed image while keeping the same accuracy as when no filter is applied. Figure 5.4B depicts the RMSD for all spheres obtained for reconstructions with a 2 mm FWHM filter only. Larger variations in RMSD were found for spheres < 20 mm than spheres > 20 mm. For the 10 to 17 mm spheres, i1s30-2mm provided the smallest RMSD. For the 22 to 37 mm spheres, the smallest RMSD were obtained using two combinations: i3s10-2mm for both the 22 and 28 mm spheres, and i1s20-2mm for the 37 mm sphere.

**Choice of reconstruction parameter set.** The reconstruction parameter set i3s10-2mm, as depicted by Figure 5.3, provides a good compromise in reducing  $D_{max}$  and provides more accurate intermediate absorbed doses ( $D_{20\%}$ - $D_{80\%}$ ) for the larger spheres (22-37 mm). It also shows relatively low RMSDs in Figure 5.4 for these spheres. This parameter set is therefore selected for image reconstructions in the following sections.

Figures depicting RMSD values against the post-reconstruction Gaussian filter size for all spheres (45 reconstruction per sphere) are provided in Appendix B.



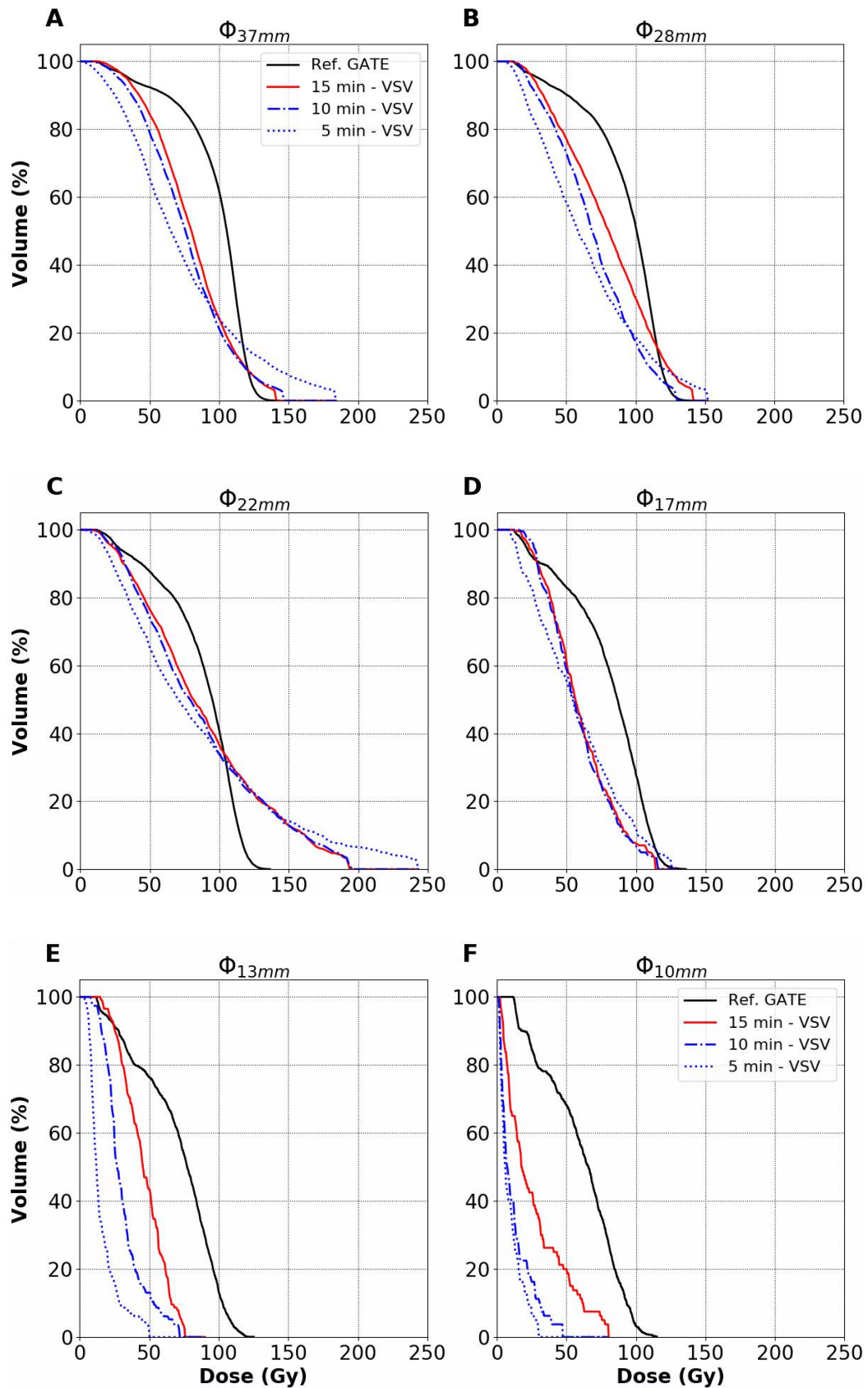


FIGURE 5.5 – Effect of acquisition duration on  $DVH_{pet}^{VSV}$  for all spheres. **A:** 37 mm, **B:** 28 mm, **C:** 22 mm, **D:** 17 mm, **E:** 13 mm and **F:** 10 mm. Reconstructions were performed using i3s10-2mm.

### 5.3.2.3 Effect of acquisition duration

Figure 5.5 depicts the effect of the acquisition duration on the  $DVH_{pet}^{VSV}$ , for the 6 spheres of Ph3. The RMSDs when comparing a 15 to a 10 min/bed acquisitions  $DVH_{pet}^{VSV}$  were 3.2, 8.0, 1.6, 1.8, 23.2 and 19.4 for the 37 to 10 mm spheres, respectively. These corresponding RMSDs increased to 10.1, 12.7, 5.6, 6.8, 43.6 and 24.2, when comparing a 15 to a 5 min/bed  $DVH_{pet}^{VSV}$ , respectively.

Figures depicting the  $DVH_{pet}^{VSV}$  variation (5, 10, 11, 12, 13, 14 and 15 mins.) for all spheres are provided in Appendix C.

### 5.3.2.4 $RC_{AC}$ and $RC_{Dose}$

Figures 5.6A and 5.6B depict the  $RC_{AC}$  and  $RC_{Dose}$  using VSV convolution (see Equations 5.3 and 5.4) for all the spheres with decreasing  $AC_{ref}$ , respectively.  $AC_{ref}$  ranged between 0.61 and 2.18 MBq.mL<sup>-1</sup>. The activity concentration recovery performance is influenced by the count statistics related to the total activity present in the PET's FOV.  $RC_{AC}$  and  $RC_{Dose}$  both decrease with decreasing  $AC_{ref}$  in the spheres. Overall,  $RC_{AC}$  and  $RC_{Dose}$  were comparable for all spheres and  $AC_{ref}$ .  $RC_{Dose}$  was slightly greater than  $RC_{AC}$  for most of the considered object sizes as visible by comparison of Figure 5.6A to Figure 5.6B.

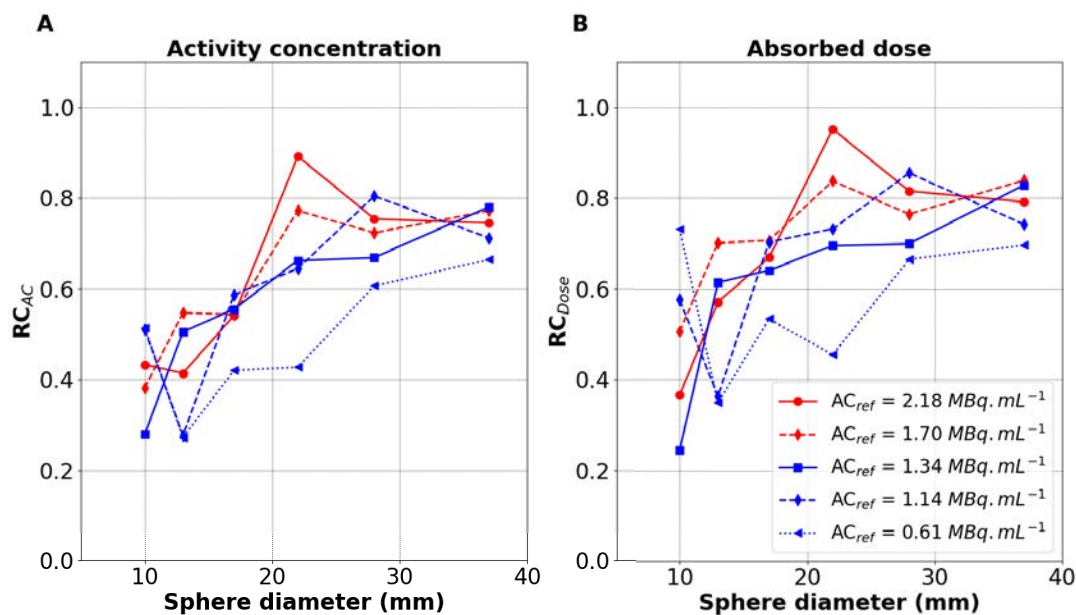


FIGURE 5.6 – Recovery coefficients against sphere diameter for varying  $AC_{ref}$  over 6 days. A:  $RC_{AC}$ . B:  $RC_{Dose}$ . Reconstructions were performed using i3s10-2mm.

### 5.3.2.5 Comparison of absorbed dose calculation methods.

Table 5.4 provides a comparison for Ph3 between the  $D_{mean}$  obtained with different calculation methods ( $D_{MIRD}$ ,  $\bar{D}_{ref}^{MC}$ ,  $\bar{D}_{pet}^{VSV}$  and  $\bar{D}_{pet}^{LDM}$ , see Sections 5.2.4 and 5.2.5) and their corresponding  $D_{50\%}$ , for the image acquisition where  $AC_{ref}$  was largest (2.18 MBq.mL<sup>-1</sup>). As expected,  $\bar{D}_{ref}^{MC}$  decreased with decreasing sphere sizes since

the sphere surface-to-volume ratio increases, leading to more absorbed dose delocalisation due to electrons exiting the spherical VVOI. Moreover,  $\overline{D}_{pet}^{VSV}$  dropped when estimated from the PET image compared to  $\overline{D}_{ref}^{MC}$ , e.g. from 89.5 Gy to 59.8 Gy for the 17 mm sphere.  $D_{mean}$  and  $D_{50\%}$  were comparable for each calculation method. Overall,  $D_{mean}$  values estimated by LDM were closer than VSV convolution to Monte Carlo simulated values.

TABLE 5.4 – Comparison between absorbed dose estimations for all spheres ( $\varnothing_{imm}$ ). Reconstructions were performed using i3s10-2mm. All values in the table are in Gy.

VOI	$D_{MIRD}$	Ref. Monte Carlo		VSV convolution		LDM	
		$\overline{D}_{ref}^{MC}$	$D_{ref,50\%}^{MC}$	$\overline{D}_{pet}^{VSV}$	$D_{pet,50\%}^{VSV}$	$\overline{D}_{pet}^{LDM}$	$D_{pet,50\%}^{LDM}$
$\varnothing_{10mm}$	112	73.3	66.1	26.8	17.3	31.3	12.6
$\varnothing_{13mm}$	112	81.1	77.4	46.3	45.3	51.2	48.7
$\varnothing_{17mm}$	112	89.5	86.8	59.8	55.9	66.3	58.0
$\varnothing_{22mm}$	112	93.8	95.2	89.2	81.0	96.4	84.8
$\varnothing_{28mm}$	112	97.8	101.1	79.7	80.5	84.7	81.1
$\varnothing_{37mm}$	112	101.8	105.8	80.5	80.0	83.7	78.5

### 5.3.3 Clinical application

#### 5.3.3.1 Reducing acquisition duration.

Figure 5.7 shows the influence of acquisition duration on the absorbed dose distributions for post  $^{90}\text{Y}$ -SIRT patient acquisitions, using i3s10-2mm reconstruction parameters, as previously recommended. Only minor differences were observed between  $DVH_{pet}^{VSV}$  calculated for 10 and 15 min/bed acquisitions, for each of the liver VOIs delineated for all patients. The RMSDs between 10 and 15 min/bed acquisitions for patient #1 were 0.3, 1.2, 1.5 and 0.9 for the WL, PL, TV and PNLV, respectively. The RMSDs for each VOI between 5 and 15 min/bed acquisitions for patient #1 increased to 2.8, 18.3, 12.4 and 24.1 for the WL, PL, TV and PNLV, respectively.

Due to the size of the liver, the local protocol for the post  $^{90}\text{Y}$ -SIRT patients generally includes a two bed, 15 min/bed acquisition. The reduction of acquisition duration on the specific patients studied here appeared to have no significant impact on dosimetry via  $DVH_{pet}^{VSV}$ . Also, the visual interpretation made by physicians were similar when comparing 10 to a 15 min/bed patient acquisitions. Therefore, we suggest a reduction of the acquisition duration from 15 to 10 min/bed, resulting in a total of 20 minutes instead of 30 minutes for 2 bed positions, helping to improve patient comfort.

#### 5.3.3.2 Comparison of absorbed dose calculation methods.

Table 5.5 provides results for patients #1 and #2 for comparisons between VSV convolution and LDM.  $D_{mean}$ ,  $D_{50\%}$  and  $D_{2\%}$  values are reported. LDM resulted in a systematically higher  $D_{2\%}$  than VSV convolution for all VOIs, e.g. 247.9 Gy for LDM to 214.1 Gy for VSV convolution.  $D_{mean}$  and  $D_{50\%}$  between the two calculation methods were comparable for all VOIs for all patients.

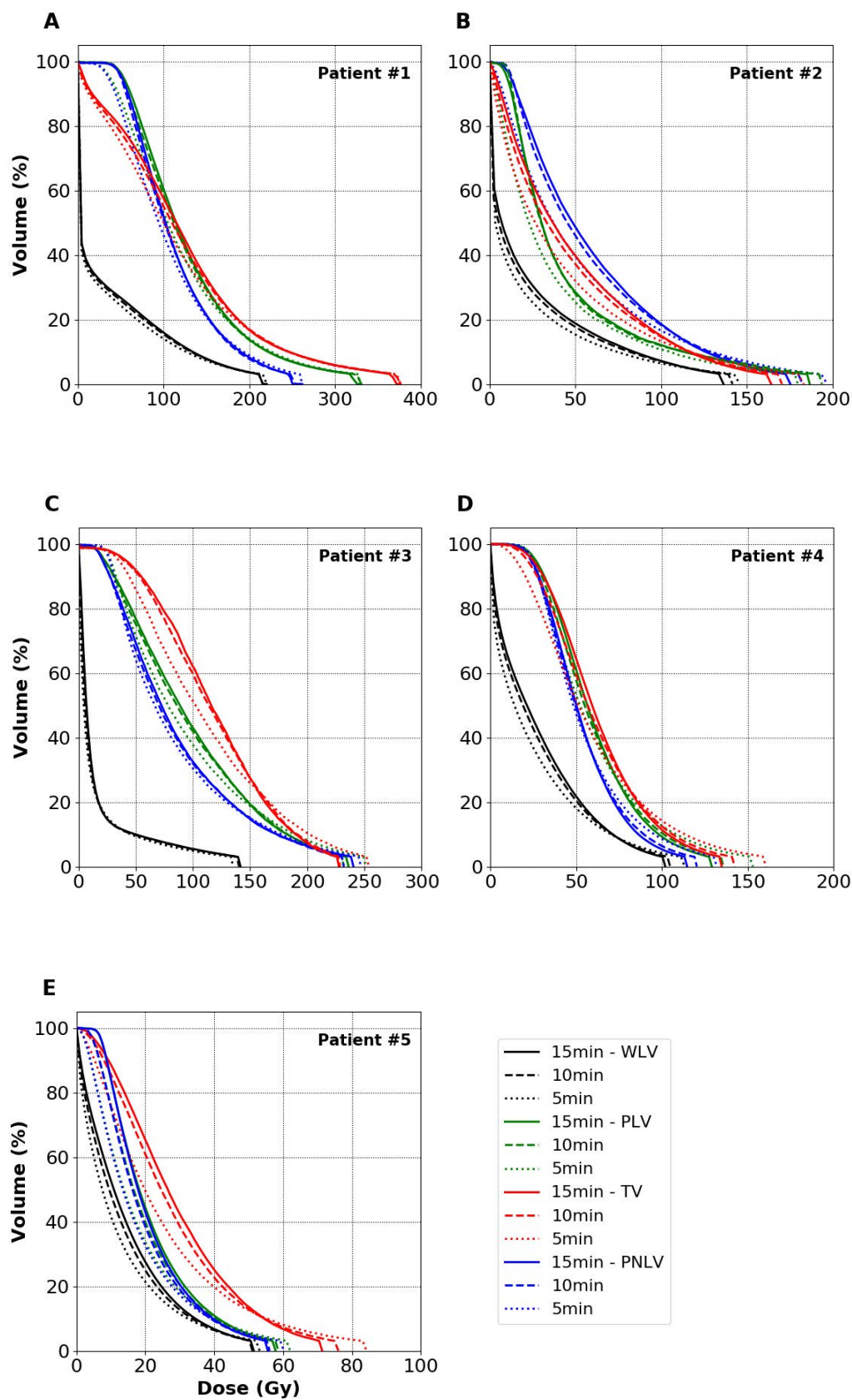


FIGURE 5.7 – Effect of acquisition duration on  $DVH_{pet}^{VSV}$  for 5 patients. Reconstructions were performed using i3s10-2mm.

TABLE 5.5 – Comparison of LDM to VSV convolution absorbed dose calculation methods through  $D_{mean}$ ,  $D_{50\%}$  and  $D_{2\%}$  for patients #1 and #2 and different VOIs. Reconstructions were performed using i3s10-2mm.

Patient, VOI	VSV convolution			LDM		
	$\overline{D}_{pet}^{VSV}$	$D_{pet,50\%}^{VSV}$	$D_{pet,2\%}^{VSV}$	$\overline{D}_{pet}^{LDM}$	$D_{pet,50\%}^{LDM}$	$D_{pet,2\%}^{LDM}$
#1, WLW	38.1	1.3	242.7	38.5	0.9	263.4
#1, PLV	131.0	112.2	365.7	133.8	111.2	401.4
#1, TV	126.4	109.8	417.1	127.8	104.5	459.5
#1, PNLV	113.9	101.2	270.7	116.9	101.3	305.7
#2, WLW	25.1	5.4	157.8	25.5	3.6	178.1
#2, PLV	61.0	45.4	197.7	62.6	43.7	231.9
#2, TV	49.5	33.4	183.8	50.4	30.0	215.8
#2, PNLV	48.5	30.0	214.1	51.8	30.6	247.9

## 5.4 Discussion

**Context.** The main goal of this work was to evaluate the influence of the acquired count statistics (acquisition length), phantom configuration and reconstruction parameters using a DPC-PET to improve quantitative accuracy in  $^{90}\text{Y}$  dosimetry for PET imaging. An initial check was performed using two cylindrical uniform phantoms. A third NEMA IEC body phantom was used to evaluate the relaxed LMOSEM algorithm parameters implemented in Philips reconstruction platforms for PET imaging. OSEM parameters were varied to find combinations of iterations, subsets and post-reconstruction Gaussian filter sizes which would provide the least difference between the  $DVH_{ref}^{MC}$  using GATE and  $DVH_{pet}^{VSV}$  using DOSIsoft® (Cachan, France). TOF and PSF modellings were considered in all reconstructions. The acquisition duration was varied by rebinning listmode phantom and patient datasets to determine the shortest acquisition duration that maintains an acceptable accuracy. Using the method suggested by Siman *et al.*, the RMSD between  $DVH_{ref}^{MC}$  and  $DVH_{pet}^{VSV}$  was used to compare absorbed doses obtained with different datasets and dosimetry methodologies. Analysis using  $DVH_{pet}^{LDM}$  was also performed, using specific reconstruction parameters following evaluation. No special intent was made toward improving image quality using NEMA standards on performance measurements, NEMA (2018), since the goal was to improve dosimetry accuracy.

**Ph1 and Ph2.** Considering mean activity concentrations and mean absorbed doses for Ph1 (at  $AC_{ref}$  equal to  $0.29 \text{ MBq.mL}^{-1}$ ) and Ph2 (at  $AC_{ref}$  equal to  $1.71 \text{ MBq.mL}^{-1}$ ), the DPC-PET was shown to produce accurate results ( $< 5\%$  using  $VOI_{outer}$ ) with large phantoms. Relative percentage differences between  $AC_{pet}$  and  $AC_{ref}$  using  $VOI_{outer}$  were  $-1.1\%$  for Ph1 and  $+0.1\%$  for Ph2, see Figure 5.2A. Absolute differences remained around  $\pm 0.02 \text{ MBq.mL}^{-1}$  for all  $AC_{ref}$  measured for both phantoms, suggesting an adequate calibration of the DPC-PET used in this study for  $^{90}\text{Y}$  imaging at these activities. Relative percentage differences between  $D_{mean}$  values ( $\overline{D}_{pet}^{VSV}$  or  $\overline{D}_{pet}^{LDM}$  to  $\overline{D}_{ref}^{MC}$ ) using  $VOI_{outer}$  for Ph1 were  $-2.6\%$  for both VSV convolution and LDM, and for Ph2 were  $-4.5\%$  for VSV convolution and  $-1.1\%$  for LDM, see Table 5.3. However, differences were obtained in calculations of absorbed dose distributions comparing  $DVH_{pet}^{VSV}$  and  $DVH_{pet}^{LDM}$  to  $DVH_{ref}^{MC}$ , as shown in Figures 5.2B and 5.2C for the two phantoms, illustrating the loss of accuracy brought by

the use of the PET images compared to the ideal reference Monte Carlo simulations. The two figures also illustrate the PVEs on distributions of intermediate absorbed doses when using  $VOI_{outer}$  (the exact CT dimensions of the considered phantom VOIs) and  $VOI_{inner}$  (the reduced dimensions). Adding to PVE, there are also the low statistics and noise conditions in which imaging was performed, which could cause heterogeneity in the activity distribution and therefore in the absorbed dose distribution.

**Ph3 and evaluation through DVH.** The differences in  $DVH_{ref}^{MC}$  and  $DVH_{pet}^{VSV}$  are also depicted in Figures 5.3, 5.4 and 5.5. The limitation due to the intrinsic poor statistics and the PVE compromise the accurate quantification of small objects, showing  $DVH_{pet}^{VSV}$  and RMSDs which have large variations depending on the reconstruction parameters used. Siman *et al.* also showed relative large RMSDs between their reference and PET image-based DVHs, illustrating the loss of accuracy brought by the use of the images. Figures 5.5E and 5.5F depict the limit of reducing acquisition duration for small lesions. RMSDs between a 10 to a 15 min/bed acquisitions were significant for the 10 and 13 mm spheres compared to the other 4 larger spheres. On the other hand, acquisition duration can be reduced to 10 min/bed using a DPC-PET if the size of the lesion is at least 17 mm in diameter based on the obtained absorbed dose distributions in this study. The results found that in both the phantom and patient data, the difference in  $DVH_{pet}^{VSV}$  between 10 and 15 minutes acquisitions was small, as depicted in Figure 5.7.

**Variation of OSEM parameters.** The evaluation of the reconstruction parameters for dosimetry is necessary for each system, first owing to different PET performances in terms of sensitivity, spatial resolution, counts rates, energy and timing resolutions (Labour *et al.*, 2020; Rausch *et al.*, 2019; Vandendriessche *et al.*, 2019; Carlier *et al.*, 2020). Second, for different reconstruction algorithms, e.g. the OSEM or Bayesian Penalised Likelihood (BPL), where the implementations of OSEM-based algorithms vary from one manufacturer to another, and third, due to the very specific configurations of imaging protocols from one hospital to another.

The combination of parameters for OSEM reconstructions is not a simple choice and is specific for one configuration of SBR,  $AC_{ref}$ , image voxel size and lesion size. In this study, the variation of iterations, limited from 1 to 3, did not have a significant impact on the calculated absorbed dose distributions, see Figure 5.3. On the other hand, varying subsets and the FWHM of the post-reconstruction Gaussian filter had an impact. The use of 30 subsets could help in improving accuracy in dosimetry for the small spheres, but could favour noise amplification in the image compared to 10 subsets. The number of updates, which is the product of the number of iterations and subsets was not used as objective criteria for evaluation since different combinations for the same number of updates could provide different results, e.g. 30 updates for both i1s30-0mm and i3s10-0mm in Figure 5.3.

**DVH comparisons using RMSD.** We evaluated the reconstruction parameters using RMSD comparisons between DVHs as suggested by Siman *et al.* (2019), but this could not be a relevant criteria for assessing absorbed dose distributions. Variations in RMSD will be observed depending on the range chosen for calculation, e.g.  $D_{0\%}-D_{100\%}$ ,  $D_{10\%}-D_{90\%}$  and  $D_{20\%}-D_{80\%}$ , as explained by Siman *et al.* (2019) themselves. In this study, whole range ( $D_{0\%}-D_{100\%}$ ) was chosen for evaluation, even if larger RMSD would be obtained to include all factors which could affect the dosimetry.

It was found that the use of DVH is necessary and sufficient to make a choice on the reconstruction parameters. However, it depends on the information required ( $D_{mean}$ ,  $D_{max}$ ,  $D_{20\%}$ ,  $D_{50\%}$ ,  $D_{80\%}$ , etc.), and the size of the VOI. For example, for the 22-37 mm spheres in Figure 5.3, a compromise can be made between intermediate absorbed doses, e.g. between  $D_{20\%}$  and  $D_{80\%}$ , and the  $D_{max}$ , where 13s10-0mm (or 13s10-2mm) can be suitable for reconstruction.

**$RC_{AC}$  and  $RC_{Dose}$ .** Owing to the few statistical production of positrons during  $^{90}\text{Y}$  decay, PVE and other confounding factors, the  $RC_{AC}$  does not reach 100% for any of the spheres in Ph3, as it can be the case for  $^{18}\text{F}$  imaging. This is true for all 69 PET systems evaluated in the QUEST multicentric study (Willowson, Tapner, Bailey, et al., 2015) in 2014, for any kind of reconstruction. No SiPM systems were included in the QUEST evaluation, due to SiPM PET systems only being commercialised from 2013 for Philips, 2016 for GE (Discovery<sup>TM</sup> MI) and 2018 (Biograph Vision<sup>TM</sup>) and 2020 (Biograph Vision Quadra<sup>TM</sup>) for Siemens. Since activity recovery has not reached at 100% for spheres up to 37 mm, absorbed doses for such lesion sizes are expected to suffer from poor quantitative accuracy and corrections in the absorbed dose estimations still need to be investigated and accounted for post  $^{90}\text{Y}$ -SIRT dosimetry. For the largest 28 and 37 mm spheres, the  $RC_{Dose}$  were around 0.8, and the  $\overline{D}_{pet}^{VSV}$  seems to be underestimated by about roughly 20% if we compare to  $\overline{D}_{ref}^{MC}$ . The two smallest 10 and 13 mm spheres have underestimations on the mean absorbed dose which can be greater than 50%. The latter still suffer from greater PVE due to the spatial resolution, which is around 4 mm FWHM (Zhang, Maniawski, and Knopp, 2018; Rausch et al., 2019; Labour et al., 2020). In an attempt to compare to  $^{18}\text{F}$  imaging but for qualitative studies and diagnostic purposes, Salvadori et al. (2020b) obtained CRCs which were less than 50% using 1 to 3 OSEM iterations for the 10 mm sphere on the DPC-PET, showing the limits of small spheres even for high  $\beta^+$  production statistics.

**Absorbed dose calculations.** VSV convolution for absorbed dose calculation is based on pre-calculated kernels by Monte Carlo methods and has been validated and proved to be clinically suitable for  $^{90}\text{Y}$  post-SIRT dosimetry (Dieudonné et al., 2011). LDM is a fast voxel-based method and easy to apply in clinic, which requires no post-processing and where a multiplicative factor similar to Equation 5.1 is applied in a voxel-wise manner, as opposed to a pre-calculated convolution kernel for VSV. LDM is an alternative providing good accuracy as suggested by Pasciak, Bourgeois, and Bradley (2014). Monte Carlo simulations were used in this study but did not aim at replacing clinical dosimetry using VSV convolution or LDM. It was used as a tool to obtain a reference in absorbed dose distributions and was easier to use than industrial software for batch processing. It has not been detailed here, but absorbed dose distributions using VSV convolution were compared to PET image-based Monte Carlo simulations where excellent agreements were obtained between them, again illustrating the major image degradation coming from the non-ideal PET performance impacting on the absorbed dose distributions.

**Comparison of VSV convolution to LDM.** LDM would probably be a good method for absorbed dose computation, as shown by Pasciak, Bourgeois, and Bradley (2014), since the PET derived  $^{90}\text{Y}$  absorbed dose distribution is already blurred by PVE and organ movement due to respiration, and indeed, there might be no need to blur even more the PET signal with a kernel. Results in this study show comparable

$\bar{D}_{pet}^{VSV}$  and  $\bar{D}_{pet}^{LDM}$  for phantoms and patients, see Tables 5.3, 5.4 and 5.5. However, LDM has the tendency to favour amplification of the  $D_{max}$  as seen on Figures 5.2B and 5.2C (green DVHs), which adds a bias on the  $D_{mean}$  by increasing its value. In fact, considering Table 5.4, the  $\bar{D}_{pet}^{LDM}$  is closer than  $\bar{D}_{pet}^{VSV}$  to  $\bar{D}_{ref}^{MC}$  for all spheres. If we consider Table 5.5,  $D_{2\%}$  for LDM is 20 to 40 Gy higher than VSV convolution for different VOIs in patients. The same observations can be made using reference phantom data.

LDM seems to favour amplification of high absorbed doses compared to VSV convolution if compared to Monte Carlo simulations, to the detriment of intermediate absorbed doses. Therefore, this study suggests that considering the  $D_{mean}$  would not be the the best criteria to assess absorbed doses using LDM. Finally, LDM and VSV convolution methods are both available for clinical practice. Even though more difficult to implement than LDM, VSV convolution is also fast (approx. 30 seconds for calculation per reconstructed image) and clinically feasible for each patient and both can be used if DVH comparisons are performed.

**Comparison to previous studies.** Following the improvements in photon detection in PET systems, PET/CT is an established and recommended method for  $^{90}\text{Y}$  treatment verification after SIRT as it provides improved accuracy for dosimetry (Levilain et al., 2021). A number of phantom studies have been performed with  $^{90}\text{Y}$  on different PET systems (Werner et al., 2010; Van Elmbt et al., 2011; Bagni et al., 2012; D'Arienzo et al., 2012; Willowson et al., 2012; Elschot et al., 2013; Carlier et al., 2013; Attarwala et al., 2014; Martí-Climent et al., 2014; Pasciak, Bourgeois, and Bradley, 2014; Willowson, Tapner, Bailey, et al., 2015; Strydhorst et al., 2016; D'Arienzo et al., 2017; Rowley et al., 2017; Siman et al., 2019; Maughan et al., 2018; Scott and McGowan, 2019; Seo et al., 2020; Hou et al., 2020). They are summarised in Table 5.6.

Some studies focused on qualitative and detection performances through image quality reports (Willowson et al., 2012; Elschot et al., 2013; Martí-Climent et al., 2014; Strydhorst et al., 2016; Scott and McGowan, 2019; Rowley et al., 2017; Seo et al., 2020; Hou et al., 2020), such as the CRC and the background variation (BV) following the NEMA NU-2 standards and guidelines. Some other studies focused on a more quantitative evaluation on activity concentrations using  $RC_{AC}$  (Werner et al., 2010; Van Elmbt et al., 2011; Bagni et al., 2012; Scott and McGowan, 2019; D'Arienzo et al., 2012; Willowson et al., 2012; Carlier et al., 2013; Attarwala et al., 2014; Willowson, Tapner, Bailey, et al., 2015; D'Arienzo et al., 2017; Siman et al., 2019; Maughan et al., 2018; Hou et al., 2020).

Fewer phantom studies focused on improving dosimetric quantification using  $RC_{Dose}$  or other dosimetric clinical routine metrics (Elschot et al., 2013; Pasciak, Bourgeois, and Bradley, 2014; D'Arienzo et al., 2017; Siman et al., 2019; Hou et al., 2020). Elschot et al. (2013) showed through DVH that  $^{90}\text{Y}$  dosimetry is more accurate for PET than SPECT imaging. Strydhorst et al. (2016) showed in their study that the bremsstrahlung radiation from  $^{90}\text{Y}$  decay had negligible effects on PET-image image quality using Monte Carlo simulations. D'Arienzo et al. (2017) concluded that the post-SIRT dosimetry is possible even in conditions of low statistics and high random fraction, provided that accurate PET calibration is performed and acquisition durations are sufficiently long.

Pasciak, Bourgeois, and Bradley (2014), Siman et al. (2019) and the latest study from Hou et al. (2020) were the only studies which suggested optimised reconstruction algorithm parameters using either, or both,  $RC_{Dose}$  and DVH estimations on phantoms. However, the suggested OSEM parameters from Pasciak, Bourgeois, and



Ref.	Scanner	Spheres phantom set					Optim. (Variable parameters)
		SBR	$AC_{ref}$ (MBq.mL <sup>-1</sup> )	Contrast	Activity	Dose	
Werner et al. (2010)	Biograph Hi-Rez 16	N/A	3.6	-	x	-	-
Van Elmbt et al. (2011)	Gemini TF Ecat Exact HR+	3:1	1.3	-	x	-	-
Bagni et al. (2012) D'Arienzo et al. (2012)	Discovery ST	10:1	1.92	-	x	-	-
Willowson et al. (2012)	Biograph mCT-S(64)	8:1	3.9	x	x	-	OSEM (i1, i2, i3, s14, s21, s24)
Elschot et al. (2013)	Biograph mCT	1:0 9:1	2.4	x	-	x	-
Carlier et al. (2013)	Biograph mCT 40	40:1	8.1	-	x	-	OSEM (i1, i3)
Attarwala et al. (2014)	Biograph mCT 40	8:1	2.38	-	x	-	OSEM (i1 to i12)
Martí-Climent et al. (2014)	Biograph mCT-TrueV	5:1	1	x	-	-	OSEM (i1, i2, i3, 2mm, 4mm, 6mm)
Pasciak, Bourgeois, and Bradley (2014)	Biograph mCT Flow	3:1	2.2	-	-	x	PSF at FWHM (mm) (2 to 12)
Willowson, Tapner, Bailey, et al. (2015) (The QUEST study)	Various*	8:1	N/A	-	x	-	-
Strydhorst et al. (2016)	Biograph mCT	8:1	N/A	x	-	-	-
D'Arienzo et al. (2017)	Discovery ST	8:1	2.28	-	x	x	-
Siman et al. (2019)	Discovery 690	4:1 13:1	1.6 4.8	-	x	x	OSEM (i1 to i12, 0mm, 2.6mm, 5.2mm, 7.8mm, 10.4mm)
Maughan et al. (2018) (The MR-QUEST study)	Biograph mMR**	8:1	N/A	-	x	-	-
Scott and McGowan (2019)	Discovery 710	8:1	N/A	x	x	-	PL
Rowley et al. (2017)	Discovery 710	8:1	3.3	x	-	-	PL
Seo et al. (2020)	SIGNA (PET/MR)	4:1	N/A	x	-	-	-
Hou et al. (2020)	Discovery 690	7.5:1	2.45	x	x	x	PL
Labour et al. (2021) (The present study)	Vereos DPC	9:1	2.25	-	x	x	OSEM (i1, i2, i3, s10, s20, s30, 0mm, 2mm, 4mm, 6mm, 8mm 5, 10, 15 min/bed)

\*The QUEST phantom study including 69 PET/CT systems (GE, Siemens, Philips)

\*\* The MR-QUEST phantom study including 8 PET/MR systems (Siemens)

TABLE 5.6 – Summary of phantom studies with hot spheres for  $^{90}\text{Y}$ , for several PET/CT and PET/MR systems, SBR and  $AC_{ref}$ . The four last columns to the right summarise the type of evaluation done in the different studies. **Contrast:** Qualitative evaluation using definitions such as in the NEMA NU-2 standards for image quality. **Activity:** Quantitative evaluation either based on activity or  $RC_{AC}$  estimates. **Dose:** Quantitative evaluation based on  $RC_{Dose}$  or DVH estimates. **Optim:** Studies which aimed at varying reconstruction parameters to find optimised reconstruction parameters. Only variable parameters for OSEM reconstructions with TOF are reported.

Bradley (2014) (i1s21-0mm + 4.5 mm FWHM PSF + TOF) were different from Siman et al. (2019) (i3s12-5.2mm + PSF + TOF) and were for different PET systems. Hou et al. (2020) evaluated reconstructions on GE systems using a Penalised Likelihood (PL) algorithm.

**Reference absorbed dose calculations.** The reference absorbed doses were not taken as a PET image-based Monte calculated DVHs, denoted  $DVH_{pet}^{MC}$ , since they depend on the PET performance and reconstruction parameters. Figure 5.8 depicts a quick cursory comparison between the reference and image-based Monte Carlo calculated DVHs,  $DVH_{ref}^{MC}$  and  $DVH_{pet}^{MC}$  (respectively), and the image-based  $DVH_{pet}^{VSV}$ . It can be seen that the major impact on quantification is the performance of the PET system.

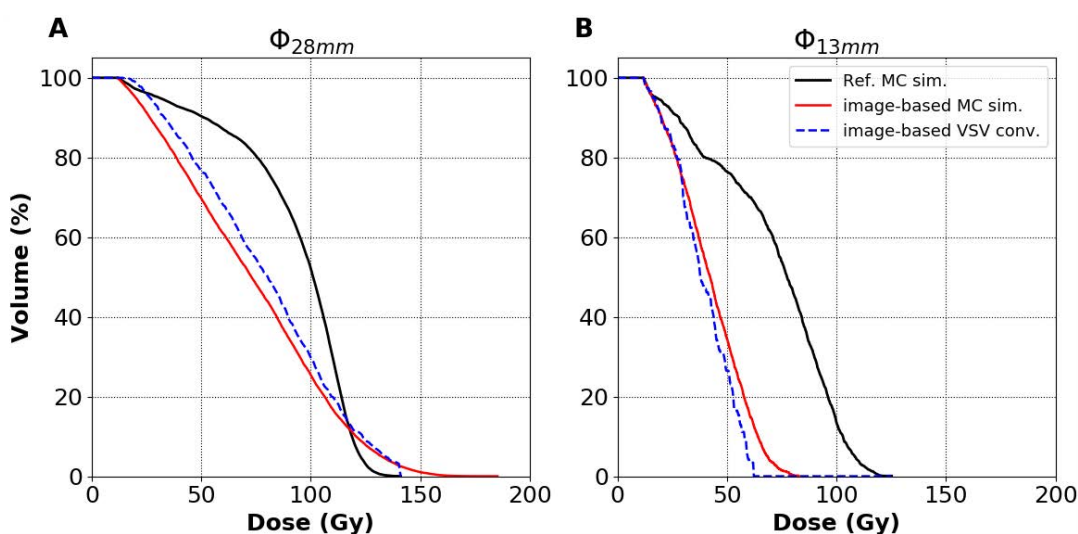


FIGURE 5.8 – Reference Monte Carlo  $DVH_{ref}^{MC}$  (black) dosimetry in ideal conditions, image-based  $DVH_{pet}^{VSV}$  (blue) and image-based  $DVH_{pet}^{MC}$  (red) for the **A:** 28 mm and **B:** 13 mm spheres.

**Limitations.** In the present study, we evaluated several  $DVH_{pet}^{VSV}$  for the acquisition in specific conditions (SBR of 9:1, isotropic image voxel size of 2 mm,  $AC_{ref}$  of  $2.18 \text{ MBq.mL}^{-1}$ ). For further investigation, evaluations of  $DVH_{pet}^{VSV}$  should be made for the different  $AC_{ref}$  present in the spheres at different imaging times and also by varying the image resolution, for example for voxels of 4 mm instead of 2 mm.

Evaluations varying SBR would require more experimental data, with a different experimental setup for each SBR. Evaluations by varying and tuning the parameters chosen for the regularised version of the Richardson-Lucy algorithm for resolution recovery (fixed to 1 iteration with a 6 mm regularisation kernel in this study according to recommendations) and their influence on the accuracy of quantitative recovered information in the reconstructed images can be the topic for future studies. Selected reconstruction parameters were based on evaluations using VSV convolution, but similar evaluations can be performed using LDM. The results presented here can be useful in the choice of OSEM reconstruction parameters for example in studies such as published by Wei et al. (2020), Levillain et al. (2020), Morán et al. (2020) and Hesse et al. (2020) for better accuracy in absorbed dose calculation following  $^{90}\text{Y}$ -SIRT using the DPC-PET.

## 5.5 Conclusion

This study aimed to evaluate various parameters for  $^{90}\text{Y}$ -PET imaging with a DPC-PET Philips system for post-SIRT image-based dosimetry. To our knowledge, no previous study concerning the evaluation of acquisition and reconstruction parameters through DVHs have been published previously for SiPM PET systems. Overall, for dosimetry purposes, we recommend to apply a 2 mm FWHM post-reconstruction Gaussian filter size, which could reduce noise in the reconstructed image while keeping the same accuracy as when no filter is applied. The selected reconstruction parameter set could be i3s10-2mm for large spheres, but this choice depends on the absorbed dose information required. This study can be useful in the choice of reconstruction parameters using the DPC-PET, depending on imaging conditions for  $^{90}\text{Y}$ . The acquisition length can also be reduced from 15 to 10 min/bed for  $^{90}\text{Y}$ -SIRT with acceptable accuracy degradation in the absorbed dose distribution, improving patient comfort.

## Chapter 6

# Predictive and per-treatment image-based dosimetry

*This chapter provides preliminary results for dosimetric comparisons between predictive SPECT/CT images using  $^{99m}\text{Tc}$ -MAA as surrogate for  $^{90}\text{Y}$  microspheres and per  $^{90}\text{Y}$ -radioembolisation monitoring PET/CT images. Because images may depict spatial differences, different image registration techniques are proposed and compared. Image datasets for several patients which had radioembolisation treatment at the Centre Léon Bérard have been retrospectively assessed. Therefore, this study contributes as a preliminary assessment of the predictive value of the MAA surrogate to microspheres through the spatial distribution of absorbed dose in different volumes of interest in the liver, together with an evaluation of, and comparison to, the absorbed dose distribution following radioembolisation treatment. The primary aim here is the choice of the most suitable registration method which would allow for better match of volumes without the need to proceed to manual registrations and perform comparisons. This present work and the prospective results will be presented at the future 2021 European Association of Nuclear Medicine (EANM) congress as an oral presentation.*

### 6.1 Introduction

Unlike other forms of radiotherapy or brachytherapy, performing accurate pre-treatment dosimetry is challenging to predict the technical feasibility and outcome of radioembolisation treatment.  $^{99m}\text{Tc}$ -MAA surrogate particles have been suggested and is the common practice today for the simulation prior to radioembolisation treatment administration using  $^{90}\text{Y}$  microspheres, as described in Chapter 1, Section 1.3.1.  $^{99m}\text{Tc}$ -MAA is injected through selective parts of the liver and after injection, a planar scintigraphy and/or, if available, 3D-SPECT/CT images are acquired. The prediction is mainly performed for the reasons 1 to 5 given in Section 1.3.1.2.

Following  $^{90}\text{Y}$ -radioembolisation treatment delivery, either BremSPECT/CT or preferably nowadays TOF-PET/CT is performed to evaluate the technical success of the treatment, see Section 1.3.2.2. Several flaws and challenges have been discussed in literature, for example associated with the limited image quality and spatial resolution of  $^{90}\text{Y}$  BremSPECT, and lack of positron statistics following  $^{90}\text{Y}$  disintegration using PET. Nevertheless, it is still an asset to be able to verify systematically the delivery of the treatment and assess intra- and extra-hepatic absorbed dose distributions.

It is also an asset to be able to use images to predict the treatment outcome, which allows for a more personalised treatment planning, gives more confidence in treatment delivery and removes the need for follow-up imaging. However, the correlations found between  $^{99m}\text{Tc}$ -MAA and  $^{90}\text{Y}$  microspheres distributions still remain

controversial. A non-exhaustive list of publications reviewing retrospective studies which evaluated the significance of  $^{99m}\text{Tc}$ -MAA predictions are reviewed hereafter.

Ahmadzadehfar et al. (2010) showed that  $^{99m}\text{Tc}$ -MAA SPECT/CT is appropriate to minimise side effects by minimising extra-hepatic depositions on 76 patients with several types of diseases, with a comparison between planar, non-attenuation-corrected SPECT and SPECT/CT, but did not assess the intrahepatic  $^{99m}\text{Tc}$ -MAA distributions. Knešaurek et al. (2010) also compared  $^{90}\text{Y}$  microspheres and MAA distributions for 20 patients and highlighted that the accuracy strongly depends on the matching of images in all 3 dimensions. The automatic rigid transforms they used could not provide accurate enough matching between CT images due to different positioning of patients between MAA and  $^{90}\text{Y}$  scans, and therefore proceeded to manual registrations in such cases. They obtained a range of correlations from highly to very poor correlated results between the predictive and actual activity distributions. Their findings therefore suggested that the prediction of the response of the therapy may not be accurate if it is based on MAA distributions. Wondergem et al. (2013) conducted another study on 31 patients, and made the same conclusion that there is not an accurate prediction of activity distribution with the clinical practices at the time, and that specific recommendations may lead to more personalised dosimetry.

Garin et al. (2012) conducted a study on 36 patients with HCC treated with glass microspheres to assess if the response and patient survival can be predicted using the dosimetry from  $^{99m}\text{Tc}$ -MAA SPECT/CT exams. They concluded that MAA SPECT/CT dosimetry provides accurate predictions, but that studies should be conducted for SHM setups (Garin et al., 2016). Studies conducted by Song et al. (2015) on 23 patients with liver malignancies and Gnesin et al. (2016) on 25 patients with HCC led to similar conclusions with close relations between MAA activity planning and  $^{90}\text{Y}$  microspheres distributions. Kao et al. (2013b) also obtained good correlations on 23 patients and encouraged further research on the predictive dosimetry for a more personalised dosimetry. Haste et al. (2017) performed similar studies using  $^{90}\text{Y}$  glass microspheres distribution in 62 patients with HCC. They found however that there was a large variability in absorbed dose distributions for the defined tumour regions, even though a good correlation was found for the whole normal liver tissue. They concluded that  $^{99m}\text{Tc}$ -MAA was a poor surrogate to quantitatively predict subsequent  $^{90}\text{Y}$  microspheres distributions for HCC. Kafrouni et al. (2019) did the same comparisons for 23 patients with HCC using glass microspheres, investigating factors related clinical hazards and equipment issues, such as activity preparation and delivery, the imaging modality used and interventional radiology. They found a good correlation between the prediction using  $^{99m}\text{Tc}$ -MAA and  $^{90}\text{Y}$  absorbed dose distributions in the normal liver and tumour volumes. They however highlighted the importance of the reproducibility of the position of the catheter tip in the agreement between predictive and actual dose distributions where discrepancies were found. A study from Jadoul et al. (2019) also concluded that  $^{90}\text{Y}$  absorbed dose distributions in the normal liver can be reasonably predicted using MAA, but fairly reasonable in the tumour, for both HCC and metastases, regardless of the type of microspheres.

More recent studies revolving around the controversial subject are from Morán et al. (2020) which studied the impact of four different dosimetry approaches for the calculation of  $^{90}\text{Y}$  absorbed doses on 14 patients and found large discrepancies

among the methods. They suggested that 3D voxel-based approaches (dose kernel convolution and LDM) can be indistinctly used. They, however, did not compare predictive MAA and  $^{90}\text{Y}$  microsphere distributions for these patients. Levillain et al. (2020) combined DVH and the quality-volume histogram (QVH) concept (Vanderstraeten et al., 2006) to enhance radioembolisation dosimetry and obtained promising results although they did not conclude on the clinical outcome on the matching between predictive and post-treatment dosimetry on patients. Their method should be validated in prospective studies.

The aforementioned publications list is not exhaustive and further references can be found in literature. It can be observed that the correlation between MAA and microspheres distributions still remains unclear and prospective studies need to be performed. There are uncertainties at several stages of the treatment, as described above, and the reason for the mismatch between these activity distributions can be due to a number of factors, such as variations in catheter position, injection procedures, difference in particle dimensions and flux between microspheres and MAA, disease progression between pre- and per-treatment steps, and the difference in radiation energy between the  $^{90}\text{Y}$  and  $^{99\text{m}}\text{Tc}$ . Furthermore, during steps of image processing, several types of uncertainties add to the quantification of the distribution of activity in the liver parts: such as the intrinsic non-ideal performance of the different imaging modalities used (SPECT for prediction and PET for monitoring) and the choice of reconstruction parameters which adds bias on the recovery of information in reconstructed images, as evaluated in Chapter 5. Finally, differences in the absorbed doses should be taken into account using different dosimetry methods (Morán et al., 2020).

**Context of this study.** The Vereos DPC PET/CT system (dSiPM-based) has been installed at the CLB since 2018, and  $^{90}\text{Y}$ -radioembolisation treatment monitoring has since then been performed using this system. Microspheres can thereby be compared to the predictive MAA distributions as described in the above referenced studies. To that aim, image registration is required for relating pre and post-treatment images. Several studies have reported mismatching and proceeded to manual registrations between the predictive and post-treatment monitoring images.

The aim of this work was therefore to provide a consistent approach for image comparisons without proceeding to manual registrations in case of mismatch with existing tools. Different schemes to match pre-treatment  $^{99\text{m}}\text{Tc}$ -MAA SPECT/CT delineated VOIs to post-treatment  $^{90}\text{Y}$  PET/CT are compared. Indeed, the choice of the image registration method is a potential parameter which can be responsible for quantitative discrepancies in the absorbed dose distributions when performing this comparison due to ill-positioned delineated structures (e.g. small tumours), owing to known, but difficultly corrected effects of internal organ displacements and respiratory motion. This retrospective study presents however only preliminary results and will serve as a perspective following this thesis for future studies.

## 6.2 Materials and methods

In this study, the predictive  $^{99\text{m}}\text{Tc}$ -MAA SPECT/CT was used to calculate the intrahepatic distribution of absorbed doses in patients, simulating  $^{90}\text{Y}$  microsphere distribution. When possible, the workup and treatment phases were performed during the same day, with no more than three weeks between the two procedures.  $^{90}\text{Y}$ -SIRT treatment monitoring was performed using PET/CT and the intrahepatic

distribution of absorbed doses calculated. The predictive MAA and microspheres distributions following treatment were compared using four different image registration schemes. Absorbed doses were compared through DVHs and extracted absorbed dose values.

### 6.2.1 Patient characteristics

Out of all patients who had SIRT with  $^{90}\text{Y}$  microspheres, since October 2018 up to May 2021, a database of 45 patient *listmodes* files for both  $^{99m}\text{Tc}$ -MAA SPECT/CT acquisitions and their corresponding  $^{90}\text{Y}$  PET/CT acquisitions have been stored which can be used for further retrospective analysis. Patients were treated either with glass or resin microspheres. For this retrospective work, the last 10 patients were selected and enrolled indistinctively for analysis, regardless of the liver tumour type and type of microspheres used. The characteristics of the patients studied are provided in Table 6.1. No inclusion or exclusion criteria was selected, but will be the case in future studies, the aim being first to compare and select the most appropriate registration method(s) for propagation of contours between the predictive SPECT/CT and and post-treatment PET/CT.

TABLE 6.1 – Patient characteristics who had  $^{90}\text{Y}$ -radioembolisation treatment at the CLB.

Patient Number	Sex	Age	Tumour type	Treatment approach
#1	M	84	ICC	Left liver
#2	M	68	ICC	Right liver
#3	M	88	ICC	Different injection points
#4	F	79	SHM	Different injection points
#5	F	62	SHM	Right liver
#6	M	82	ICC	Right liver
#7	F	78	SHM	Right liver
#8	F	61	SHM	Different injection points
#9	M	65	ICC	Total liver
#10	F	52	SHM	Different injection points

**Treatment procedure.** Patients received around 185 MBq (range 150-545 MBq) of  $^{99m}\text{Tc}$ -MAA prior to SIRT in the treatment planning step in the selected part (or parts) of the liver to be treated. The different targeting procedures for each patient are detailed in Table 6.1. After administration, the LSF calculation was performed using both planar scintigraphy and SPECT/CT. SPECT/CT was also used for  $^{90}\text{Y}$  microspheres activity prescription. In all patients studied, the LSF was less than 10%.  $^{90}\text{Y}$  microspheres activity prescriptions were performed using voxel-based calculations for either types of  $^{90}\text{Y}$  microspheres.  $^{90}\text{Y}$  activities were measured using an Easypharma HE Lemer Pax activimeter calibrated for  $^{90}\text{Y}$  under national standards. The total activities injected during the treatment phases ranged between 1024 and 5691 MBq of  $^{90}\text{Y}$  microspheres. The activities used for each patient are provided in Table 6.2.

### 6.2.2 Imaging and reconstruction protocols

This section describes the imaging protocols used for both  $^{99m}\text{Tc}$ -MAA SPECT/CT and  $^{90}\text{Y}$  microspheres PET/CT, which are summarised in Table 6.3.

TABLE 6.2 – Recorded information for the treatment planning  $^{99m}\text{Tc}$ -MAA injection and treatment  $^{90}\text{Y}$  microspheres injection for patients who received radioembolisation at the CLB. The last column provides the time interval between the  $^{99m}\text{Tc}$ -MAA SPECT/CT scan and the post-treatment  $^{90}\text{Y}$  PET/CT scan.

Patient Number	$^{99m}\text{Tc}$ -MAA activity (MBq)	LSF (%)	Microsphere type	Injected $^{90}\text{Y}$ microsphere activity (GBq)	Time interval between procedures (days)
#1	200	2.70	glass	2945	17
#2	185	2.10	resin	2972	same day
#3	172	2.50	glass	1146+294	20
#4	2 × 185	1.70	glass	760 + 758	7
#5	2 × 185	3.11	resin	1292	12
#6	2 × 185	9.88	glass	1898 + 1905 + 1888	13
#7	150	2.4	resin	1132	same day
#8	180+175+170	2.77	resin	965+228+531	16
#9	182+176	3.89	glass	1063+2046	9
#10	178	2.1	resin	1200	13

### 6.2.2.1 $^{99m}\text{Tc}$ -MAA SPECT/CT

For each patient, workup  $^{99m}\text{Tc}$ -MAA SPECT/CT images were acquired using a GE Discovery 670 SPECT/CT with an axial FOV of 400 mm centered over the liver area. Imaging was performed within 1 hour after injection. A low-energy high-resolution (LEHR) collimator was used with an energy window centred at 140 keV and 10% wide (126.45-154.55 keV). 120 frames (60 projections, 25 s per projection) were acquired in a 3D-mode. Images were reconstructed with CT-based attenuation and window-based scatter corrections, and calibrated in  $\text{MBq}\cdot\text{mL}^{-1}$ , using an OSEM algorithm with 8 iterations and 4 subsets, with an additional post-reconstruction Gaussian filter size of 8.4 mm at FWHM. Reconstructions were performed for isotropic voxel sizes of 4.4 mm and an image matrix of  $128 \times 128$  voxels. The CT scan was performed with a  $0.98 \text{ mm} \times 0.98 \text{ mm} \times 1.25 \text{ mm}$  spacing, 120 kVp, 4 mAs and a  $512 \times 512$  matrix size.

### 6.2.2.2 $^{90}\text{Y}$ microspheres DPC PET/CT

The time interval between the  $^{99m}\text{Tc}$ -MAA and  $^{90}\text{Y}$  microspheres injections are provided in Table 6.2. Radioembolisation treatment monitoring images were acquired on average 16 hours after injection using the DPC TOF PET/CT, the latter described in the previous chapters, with an axial FOV of 164 mm. The acquisition duration for each patient was 10 min/bed, centred on the liver region. For some patients, two bed positions were required. Images were reconstructed using the evaluated and chosen OSEM reconstruction parameters with 3 iterations and 10 subsets with an additional post-reconstruction Gaussian filter size of 2 mm at FWHM, based on the previous findings (see Chapter 5). The default recommended parameters of the PSF modelling (1 iteration with a 6 mm FWHM regularisation kernel) for resolution recovery was used. Reconstructions were performed for isotropic voxel sizes of 2 mm sides and an image matrix of  $288 \times 288$  voxels. The CT scan was performed with a  $1.17 \text{ mm} \times 1.17 \text{ mm} \times 2.0 \text{ mm}$  spacing, 120 kVp, 49 mAs and a  $512 \times 512$  matrix size.



TABLE 6.3 – Parameters used for image acquisition and reconstruction for both pre-treatment  $^{99m}\text{Tc}$ -MAA SPECT/CT and post-treatment  $^{90}\text{Y}$  PET/CT.

	$^{99m}\text{Tc}$ -MAA SPECT/CT acquisitions	$^{90}\text{Y}$ DPC PET/CT acquisitions
Average time interval between injection and acquisition (h)	1	16
Emission acquisition duration	25 s per projection for 60 projections	10 min/bed
Collimator	LEHR	n/a
Energy window (keV)	126.45-154.55	449.68-613.20
Corrections	CT-attenuation and Scatter	Multiple corrections
Reconstruction algorithm	OSEM	OSEM
Iterations	8	3
Subsets	4	10
Gaussian filter size (FWHM)	8.4	2.0
PSF modelling	Yes	Yes
Voxel size (mm <sup>3</sup> )	4.4 x 4.4 x 4.4	2 x 2 x 2
Matrix size	128 x 128	288 x 288
CT parameters	120 kVp, 4 mAs 1.25 mm axial sampling	120 kVp, 49 mAs 2.0 mm axial sampling

### 6.2.3 Delineation of volumes of interest

For each patient, contours for liver structures were used. They were defined by clinicians using local clinical protocols at the CLB using the Planet Onco clinical workstation from DOSIsoft® (Cachan, France). Primary defined VOIs were: 1) WLW, 2) total tumour volume ( $TV_{Total}$ ) and 3) PLV, depicted in Figure 6.1. Other VOIs for comparison could be defined using the first three structures, which were: 4) target normal liver volume ( $NLV_{Target}$ ), 5) non-perfused liver volume (NPLV), and 6) whole normal liver volume ( $NLV_{WholeLiver}$ ).

The WLW and  $TV_{Total}$  (as only one tumoral volume) were contoured on the CT acquired during the workup SPECT/CT acquisition. When the CT image lacked contrast for clear tumour delimitation, it was contoured with the help of SPECT images and diagnostic scans prior to radioembolisation by clinicians. The PLV, which was considered as the treated volume was defined as the intersection of the WLW and an automatic segmentation using a 5% threshold from the maximum activity distribution (activity distribution volume using a 5% threshold ( $ADV_{5\%}$ )) using the co-registered SPECT workup image. The PLV is indeed taken as such since activity might fall outside the WLW structure due to motion and respiratory artefacts which are not corrected.

The  $NLV_{Target}$  is the normal (non-tumoral), target liver volume which has received irradiation, defined as the PLV excluding the  $TV_{Total}$ . The NPLV is the WLW excluding the PLV, considered as the part of the liver which should not receive any irradiation. The  $NLV_{WholeLiver}$  is defined as the WLW excluding the  $TV_{Total}$ , which might further help in the interpretation of results.

All VOIs are summarised in Table 6.4. They were all propagated and registered

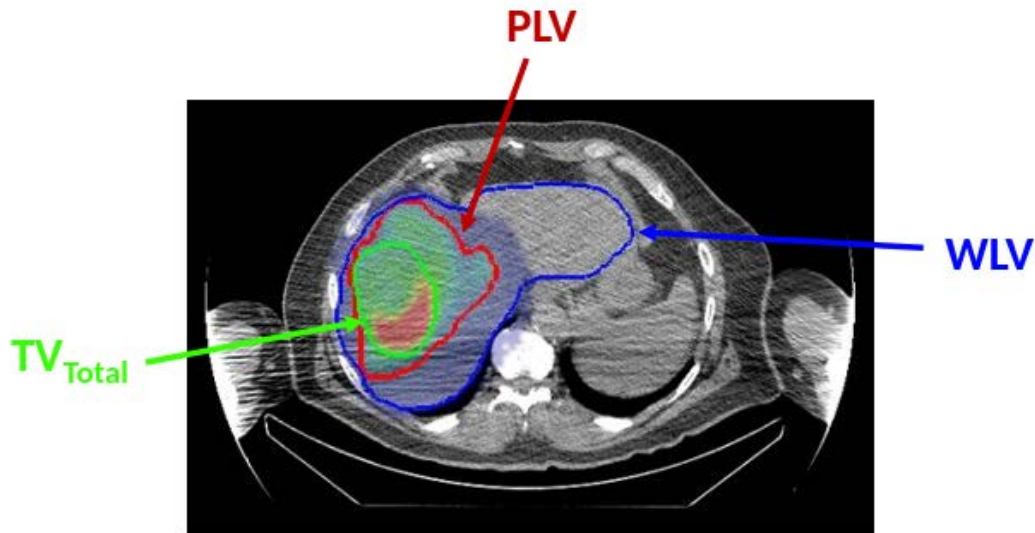


FIGURE 6.1 – Defined VOIs for the WLW, PLV and  $TV_{Total}$  using the  $^{99m}\text{Tc}$ -MAA SPECT/CT pre-treatment acquisition. The NPLV,  $NLV_{Target}$  and  $NLV_{WholeLiver}$  are derived from the first three.

to the SPECT images. Each delineated VOI was then exported as a *RT-struct* (Radiotherapy structure) in the Digital Imaging and Communications in Medicine (DICOM) format to be used by an in-house Python script for analysis. The *RT-struct* based on the predictive SPECT images are denoted  $RT\text{-}struct_{SPECT}$ , which serve as the reference structures for comparisons and were further propagated to PET images. The workflow for the propagation of contours is detailed later in Section 6.2.6.

TABLE 6.4 – Defined VOIs using the  $^{99m}\text{Tc}$ -MAA SPECT/CT pre-treatment acquisition. All VOIs were registered to the SPECT images and exported as  $RT\text{-}struct_{SPECT}$ .

$RT\text{-}struct_{SPECT}$	Name	Definition
WLW	Whole liver volume	CT-defined
$TV_{Total}$	Total tumour volume	CT-defined
$ADV_{5\%}$	Activity distribution volume	SPECT-defined, 5% threshold from maximum
PLV	Perfused liver volume	$WLW \cap ADV_{5\%}$
NPLV	Non-perfused liver volume	$WLW - PLV$
$NLV_{Target}$	Target normal liver volume	$PLV - TV_{Total}$
$NLV_{WholeLiver}$	Whole normal liver volume	$WLW - TV_{Total}$

### 6.2.4 Absorbed dose calculation

Absorbed dose maps for each patient were computed independently from the: 1)  $^{99m}\text{Tc}$ -MAA SPECT to predict  $^{90}\text{Y}$  distribution and 2) post-treatment monitoring PET images for the actual  $^{90}\text{Y}$  microspheres distribution using the Planet Onco workstation. The VSV dose kernel convolution algorithm following the MIRD formalism (Bolch et al., 2009; Dieudonné et al., 2010, 2011) was used for absorbed dose computations, see Sections 1.6.3 and 1.6.4. Calculations using the LDM algorithm also available in the software was not performed. Indeed, as stated by Morán et al. (2020), 3D voxel-based absorbed dose calculations are pretty similar in both the healthy liver and individual tumours for  $^{90}\text{Y}$  microspheres.

All absorbed dose distributions were exported as *RT-dose* (Radiotherapy dose distributions) objects in the DICOM format to be used by an in-house Python script for analysis. The *RT-dose* based on the predictive SPECT/CT and post-treatment monitoring PET/CT images are denoted  $RT\text{-dose}_{SPECT}$  and  $RT\text{-dose}_{PET}$ , respectively.

### 6.2.5 Exported input data

At this step, the different  $RT\text{-struct}_{SPECT}$  defined in Section 6.2.3, and the independently calculated  $RT\text{-dose}_{SPECT}$  and  $RT\text{-dose}_{PET}$  for each patient described in Section 6.2.4 have been exported out of the clinical workstation to be used as input and analysis. The predictive SPECT/CT and post-treatment PET/CT image datasets were also exported for each patient to be used as input for image registration and propagation of contours, respectively. Figure 6.2 summarises the workflow for obtaining input data for analysis.

### 6.2.6 Propagation of contours

The alignment of image datasets was performed using the `elastix` software<sup>1</sup>, which consists of a collection of algorithms that are commonly used to solve medical image registration problems (Klein et al., 2009). Different image registration workflows were developed and compared. The  $RT\text{-struct}_{SPECT}$  contours were propagated to PET images using four registration methods, denoted: 1)  $rigid_{global}$ , 2)  $deformable_{global}$ , 3)  $rigid_{local}$  and 4)  $rigid_{local,functional}$ . By "global", we mean that all the voxels of the images are used for the registration, while with "local", only voxels belonging to a given VOI were used during the registration process. Table 6.5 provides a summary of the methods used and they are described in the following sections. Figure 6.3 provides a scheme to summarise the workflow used for the propagation of contours at the *step* (6) in Figure 6.2. Volumes of the WLV, PLV and  $TV_{Total}$  are provided in the tables in *Appendix D1*.

TABLE 6.5 – The methods used for image registration.

Method	Image transformation	Transformation type	Region
$rigid_{global}$	$\mathbf{T}_{CT_{SPECT} \rightarrow CT_{PET}}$	rigid	global
$deformable_{global}$	$\mathbf{T}_{CT_{SPECT} \rightarrow CT_{PET}}$	deformable	global
$rigid_{local}$	$\mathbf{T}_{CT_{SPECT} \rightarrow CT_{PET}}$	rigid	local
$rigid_{local,functional}$	$\mathbf{T}_{SPECT \rightarrow PET}$	rigid	local

1. See [elastix software webpage](#)

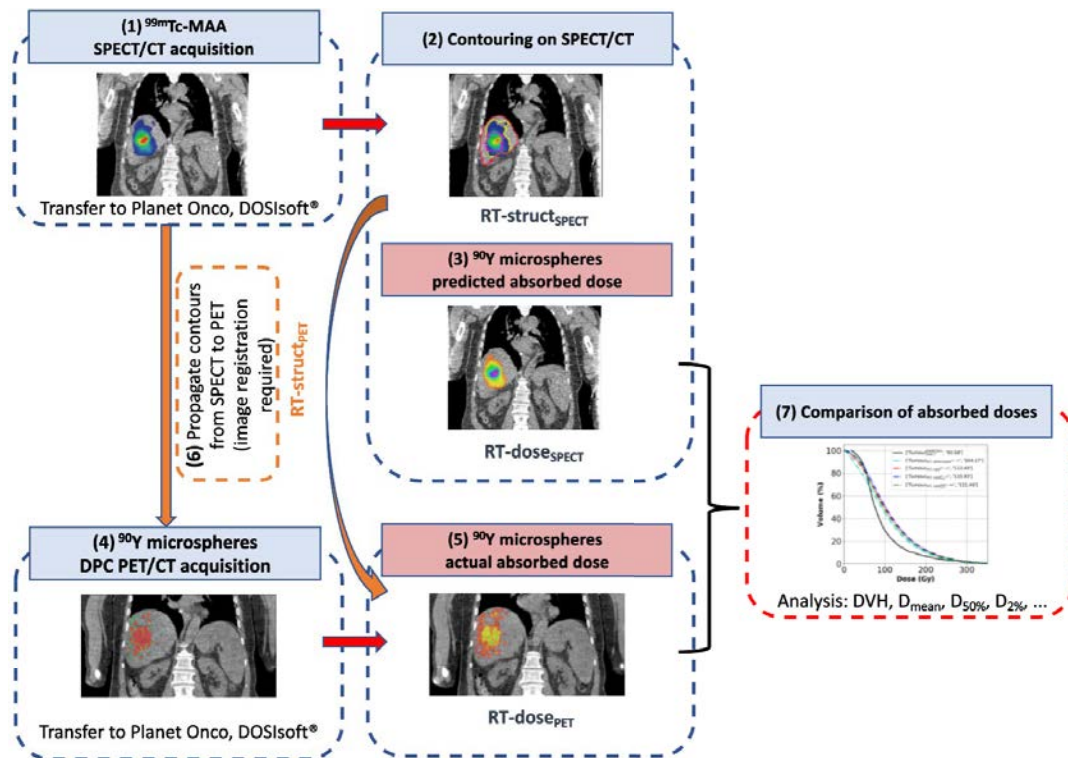


FIGURE 6.2 – Scheme showing the *steps* (1) to (7) for the comparison between predictive and actual  $^{90}\text{Y}$  microspheres absorbed dose distributions. *Step* (1): Predictive SPECT/CT. *Step* (2): VOI contouring on SPECT/CT images. *Step* (3): Calculation of absorbed dose. *Step* (4): Treatment monitoring PET/CT. *Step* (5): Calculation of absorbed dose. *Step* (6): Propagation of  $\text{RT-struct}_{\text{SPECT}}$  to obtain  $\text{RT-struct}_{\text{PET}}$ , see Figure 6.3. *Step* (7): Comparison of absorbed doses using DVHs.

### 6.2.6.1 The $\text{rigid}_{\text{global}}$ method

This method considers a  $\text{CT}_{\text{SPECT}}$  to  $\text{CT}_{\text{PET}}$  rigid transformation (CTs from the SPECT/CT and PET/CT acquisitions, respectively), denoted  $\mathbf{T}_{\text{CT}_{\text{SPECT}} \rightarrow \text{CT}_{\text{PET}}}$ . The rigid transformation is performed on the global image. The EulerTransform transform was used. It is defined by a rotation matrix parametrised by three angles in the 3D Euler space and a 3D translation vector. The  $\text{rigid}_{\text{global}}$  method therefore consists of 6 parameters, for 3 translations,  $(t_x, t_y, t_z)$ , in the 3D  $(x, y, z)$  space accompanied by 3 rotations,  $(\theta_x, \theta_y, \theta_z)$ , around each axis. Therefore, the treated image is neither re-scaled nor stretched. The  $\text{rigid}_{\text{global}}$  method was systematically employed before testing the three other methods described hereafter.

### 6.2.6.2 The $\text{deformable}_{\text{global}}$ method

This method considers also a  $\mathbf{T}_{\text{CT}_{\text{SPECT}} \rightarrow \text{CT}_{\text{PET}}}$  but using a deformable, non-rigid transformation on the global image. The BSplineTransform transform was used, where instead of only 6 translation and rotation parameters used as in the  $\text{rigid}_{\text{global}}$ , much more parameters are required ( $\sim 10^5$  parameters) for the rescaling and stretching of the moving image for a better match. BSpline control points grid spacing were 12 mm (about 40000 control points per image), allowing smooth and limited deformation.

### 6.2.6.3 The $rigid_{local}$ method

This method also considers a  $\mathbf{T}_{CT_{SPECT} \rightarrow CT_{PET}}$  rigid transformation between the two CTs, but centred on the liver region only compared to the global image for the  $rigid_{global}$  method. To consider the liver region only, the WLV was dilated with a spherical kernel with a radius of 10 pixels.

### 6.2.6.4 The $rigid_{local,functional}$ method

This method considers a rigid local transformation but between the functional images instead of the anatomical CTs. A transformation is applied to the SPECT image to match the PET image, denoted  $\mathbf{T}_{SPECT \rightarrow PET}$ , centred on the liver region. The same region than in  $rigid_{local}$  method was used here to perform the registration.

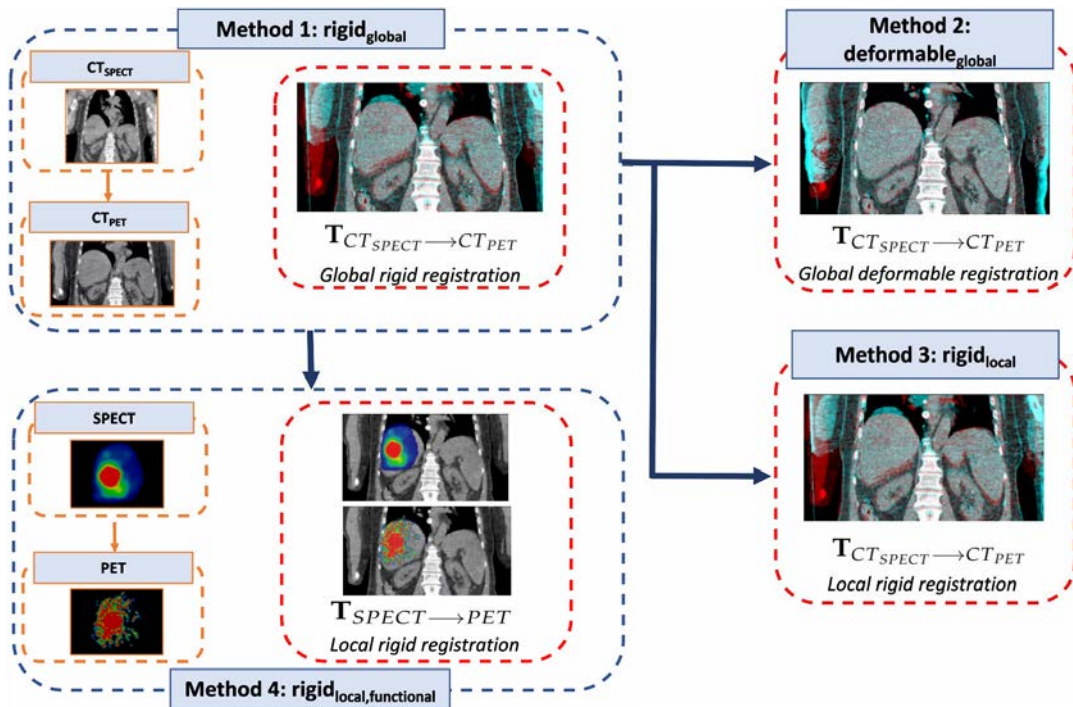


FIGURE 6.3 – Scheme showing the different image transformations performed at the *Step (6)* in Figure 6.2. Methods 2, 3 and 4 implement first the method 1 with a  $rigid_{global}$  transformation.

Once the transformation matrix is defined from the fixed (PET) to the moving (SPECT) images, from either method, it is applied to the  $RT-struct_{SPECT}$  to obtain the  $RT-struct_{PET}$ , i.e. the different structures registered to the PET images.

## 6.2.7 Analysis

As depicted in Figure 6.2 (*Step (7)*),  $RT-struct_{SPECT}$  and  $RT-struct_{PET}$  were used to extract DVH information from the predictive  $RT-dose_{SPECT}$  and post-treatment  $RT-dose_{PET}$ , respectively. DVHs based on the predictive SPECT/CT are denoted  $DVH_{predicted}$ . DVHs based on the monitoring post-treatment PET/CT for each registration technique,  $j$ , are denoted  $DVH_{j,treatment}$ .

### 6.2.7.1 Comparing registration methods

Mean absorbed doses ( $\bar{D}$ ) obtained following treatment,  $\bar{D}_{treatment}$ , were considered for comparing the four methods. The maximum absolute differences (in Gy) in  $\bar{D}_{treatment}$ ,  $\Delta_{method}^{abs}$ , between the four registration techniques are reported, calculated as in Equation 6.1.

$\Delta_{method}^{\%}$ , the maximum relative percentage differences in  $\bar{D}_{treatment}$  obtained between the different methods for the post-treatment monitoring PET/CT images, were also reported, calculated as in Equation 6.2.

$$\Delta_{method}^{abs} \text{ (Gy)} = |\bar{D}_{treatment,max} - \bar{D}_{treatment,min}| \quad (6.1)$$

$$\Delta_{method}^{\%} \text{ (\%)} = \frac{\Delta_{method}^{abs}}{\bar{D}_{treatment,max}} \times 100\% \quad (6.2)$$

where  $\bar{D}_{treatment,min}$  and  $\bar{D}_{treatment,max}$  are the minimum and maximum mean absorbed doses obtained following treatment, obtained within the four registration techniques.  $\Delta_{method}^{abs}$  and  $\Delta_{method}^{\%}$  were calculated for each patient and each VOI in each patient.

### 6.2.7.2 Comparison to predictive dosimetry

The  $DVH_{predicted}$  and  $DVH_{j,treatment}$  were then compared using  $\bar{D}$  and the absorbed doses at 2% and 50% volumes,  $D_{2\%}$  and  $D_{50\%}$ , respectively. They are denoted by  $\bar{D}_{predicted}$ ,  $D_{predicted,50\%}$  and  $D_{predicted,2\%}$  for the predicted absorbed doses, respectively. Similarly, the two lasts are denoted by  $D_{treatment,50\%}$  and  $D_{treatment,2\%}$  for the absorbed doses obtained following treatment.

$\Delta_{predict-treatment}^{abs}$ , the absolute differences between  $\bar{D}_{predicted}$  and  $\bar{D}_{treatment}$ , were reported, using the following Equation 6.3.

$\Delta_{predict-treatment}^{\%}$ , the percentage differences between the  $\bar{D}_{predicted}$  and  $\bar{D}_{treatment}$ , were also reported using the following Equation 6.4.

$$\Delta_{predict-treatment}^{abs} \text{ (Gy)} = |\bar{D}_{treatment} - \bar{D}_{predicted}| \quad (6.3)$$

$$\Delta_{predict-treatment}^{\%} \text{ (\%)} = \frac{\Delta_{predict-treatment}^{abs}}{\bar{D}_{predicted}} \times 100\% \quad (6.4)$$

$\Delta_{predict-treatment}^{abs}$  and  $\Delta_{predict-treatment}^{\%}$  are calculated for each patient and each VOI in each patient, for specific registration methods.

## 6.3 Results

The Section 6.3.1 hereafter provides a comparison between the four registration techniques. Then, the Section 6.3.2 provides the preliminary results comparing the predictive and post-treatment monitoring absorbed dose distributions for each patient. The results are further discussed in the Section 6.4 and summarised in Table 6.18 in the *Discussion* section.

### 6.3.1 Comparison of registration methods.

Each of the Sections 6.3.1.1 to 6.3.1.6 hereafter are written in a similar format, reporting data as described in the previous Section 6.2.7.1 for each of the 6 delineated VOIs. Specific cases of patients are provided in each section. The reader is helped with the number of the VOI ranging from 1 to 6 and can refer to specific VOIs only, e.g. (1/6) for the WLW in Section 6.3.1.1.

Examples of DVHs are depicted for two patients #1 and #2 for each VOI in each section. Even if  $DVH_{predicted}$  are also depicted in all figures, they provide only a cursory comparison and are not discussed. The DVHs for the complete set of patients are provided in Appendix D. Tables 6.6 to 6.11 provide the mean absorbed dose values found using the different registration methods for comparison.

#### 6.3.1.1 Whole liver volume (1/6)

Figure 6.4 depicts the  $DVH_{j,treatment}$  obtained for the WLW for patients #1 and #2. Table 6.6 provides the  $\bar{D}_{treatment}$  using each registration method for the 10 patients studied. Supplementary figures are provided in Appendix D2 for the WLW for the complete set of patients.

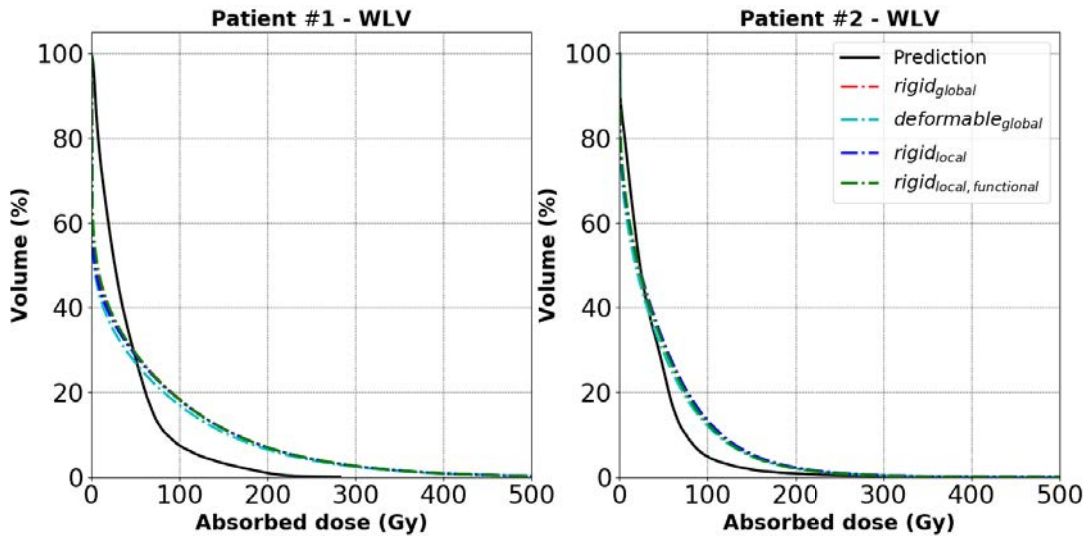


FIGURE 6.4 – Two patient cases are represented for the WLW. The  $DVH_{j,treatment}$  for the corresponding  $j$  methods are represented as:  $rigid_{global}$  (red),  $deformable_{global}$  (cyan),  $rigid_{local}$  (blue) and  $rigid_{local,functional}$  (green). The  $^{99m}Tc$ -MAA SPECT/CT-based  $DVH_{predicted}$  (black) are also depicted for comparison to the  $DVH_{j,treatment}$ .

$\Delta_{method}^{\%}$  ranged between 1.8 and 8.8%, which represent  $\Delta_{method}^{abs}$  ranging between 0.6 and 4.6 Gy within the four different methods, except for highlighted patients in pink in Table 6.6. For these two specific patients #4 and #8,  $\Delta_{method}^{\%}$  of 34.7% and 20.2% were obtained, corresponding to  $\Delta_{method}^{abs}$  of 25.1 and 10.2 Gy, respectively.

Less than 6.2% differences were found between the  $rigid_{local,functional}$  and  $rigid_{global}$  methods, except for the same patients #4 (34.7%) and #8 (13.2%).

TABLE 6.6 –  $\bar{D}_{treatment}$  for the WLV using different registration methods between SPECT/CT and PET/CT images. Values for  $\bar{D}_{predicted}$  are also provided. Patients with the largest differences are highlighted in pink.

Patient number	Mean absorbed doses in Gy - WLV				Predictive SPECT/CT
	Post-treatment PET/CT				
	$rigid_{global}$	$deformable_{global}$	$rigid_{local}$	$rigid_{local,functional}$	
#1	49.4	45.7	48.7	49.7	39.1
#2	41.7	39.6	42.8	41.8	34.2
#3	14.5	15.9	14.5	14.6	19.1
#4	72.5	66.6	72.5	47.3	70.6
#5	33.2	33.6	33.1	33.0	40.8
#6	40.0	40.9	40.8	42.0	44.3
#7	26.3	24.9	27.0	25.8	23.4
#8	46.7	50.4	40.2	40.5	39.7
#9	29.3	27.9	27.4	27.9	37.9
#10	74.5	76.5	73.4	69.9	66.3

### 6.3.1.2 Perfused liver volume (2/6)

The PLV corresponds to the liver parts which received irradiation, containing the tumour to be treated but also healthy normal tissue. Figure 6.5 depicts the  $DVH_{j,treatment}$  obtained for the PLV for patients #1 and #2. Table 6.7 provides the  $\bar{D}_{treatment}$  using each method for the 10 patients studied. Supplementary figures are provided in Appendix D3 for the PLV for the complete set of patients.

Figures depicting the DVHs for the  $ADV_{5\%}$  which were used to define the PLV, and tables reporting absorbed doses for the  $ADV_{5\%}$  are also provided in Appendix D4.

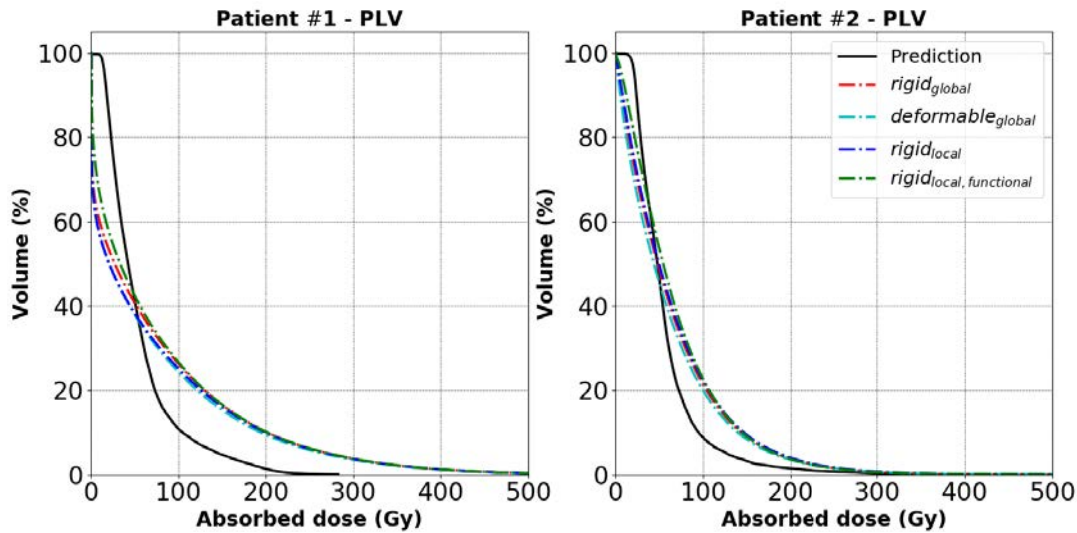


FIGURE 6.5 – Two patient cases are represented for the PLV. The  $DVH_{j,treatment}$  for the corresponding  $j$  methods are represented as:  $rigid_{global}$  (red),  $deformable_{global}$  (cyan),  $rigid_{local}$  (blue) and  $rigid_{local,functional}$  (green). The  $^{99m}Tc$ -MAA SPECT/CT-based  $DVH_{predicted}$  (black) are also depicted for comparison to the  $DVH_{j,treatment}$ .



TABLE 6.7 –  $\bar{D}_{treatment}$  for the PLV using different registration methods between SPECT/CT and PET/CT images. Values for  $\bar{D}_{predicted}$  are also provided. Patients with the largest differences are highlighted in pink.

Patient number	Mean absorbed doses in Gy - PLV				Predictive SPECT/CT
	Post-treatment PET/CT				
	$rigid_{global}$	$deformable_{global}$	$rigid_{local}$	$rigid_{local,functional}$	
#1	69.1	64.6	66.2	71.9	53.9
#2	63.9	60.6	65.9	68.7	55.9
#3	23.5	24.9	23.2	24.3	32.9
#4	86.0	88.3	88.0	85.9	136.8
#5	65.7	64.6	64.5	66.7	89.9
#6	66.1	70.7	67.4	70.2	72.5
#7	34.2	31.5	35.1	34.3	38.0
#8	55.7	62.0	58.4	58.2	61.7
#9	93.6	116.0	109.2	111.8	158.4
#10	105.2	105.5	103.5	101.3	95.3

$\Delta_{method}^{\%}$  ranged between 2.7% and 11.7%, which correspond to  $\Delta_{method}^{abs}$  ranging between 2.2 and 8.0 Gy within the methods, except for patient #9. For the specific patient #9, a  $\Delta_{method}^{\%}$  of 19.3% was found, corresponding to a  $\Delta_{method}^{abs}$  of 22.3 Gy.

Less than 7.0% differences were found between the  $rigid_{local,functional}$  and  $rigid_{global}$  methods, except for patient #9 (16.3%).

### 6.3.1.3 Non-perfused liver volume (3/6)

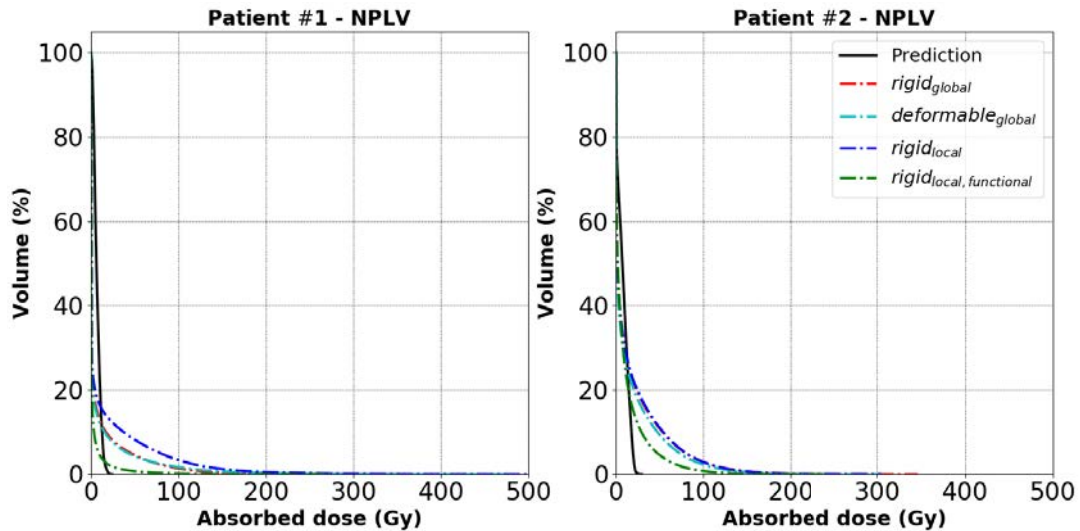


FIGURE 6.6 – Two patient cases are represented for the NPLV. The  $DVH_{j,treatment}$  for the corresponding  $j$  methods are represented as:  $rigid_{global}$  (red),  $deformable_{global}$  (cyan),  $rigid_{local}$  (blue) and  $rigid_{local,functional}$  (green). The  $^{99m}Tc$ -MAA SPECT/CT-based  $DVH_{predicted}$  (black) are also depicted for comparison to the  $DVH_{j,treatment}$ .

The NPLV by definition refers to the liver parts which should not receive irradiation. Figure 6.6 depicts the  $DVH_{j,treatment}$  obtained for the NPLV for patients #1 and

#2. Table 6.8 provides the  $\bar{D}_{treatment}$  using each method for the 10 patients studied. Supplementary figures are provided in Appendix D5 for the NPLV for the complete set of patients.

TABLE 6.8 –  $\bar{D}_{treatment}$  for the NPLV using different registration methods between SPECT/CT and PET/CT images. Values for  $\bar{D}_{predicted}$  are also provided. Patients with the largest differences are highlighted in pink.

Patient number	Mean absorbed doses in Gy - NPLV				Predictive SPECT/CT
	Post-treatment PET/CT				
	$rigid_{global}$	$deformable_{global}$	$rigid_{local}$	$rigid_{local,functional}$	
#1	6.6	6.7	11.0	1.9	6.9
#2	15.0	13.4	15.3	9.6	7.9
#3	4.9	6.9	5.2	4.2	4.6
#4	59.2	46.8	58.3	9.6	4.9
#5	11.7	13.2	12.4	10.8	8.4
#6	5.5	5.9	5.6	4.7	6.5
#7	16.0	15.8	16.5	14.7	4.3
#8	32.2	33.4	11.6	12.6	4.1
#9	10.7	5.2	3.9	3.8	2.3
#10	24.2	25.7	23.9	18.4	18.1

Owing to the relatively low absorbed doses reported for the NPLV compared to the other VOIs, large  $\Delta_{method}^{\%}$  were obtained, ranging between 10.9% and 83.8% for all patients. These correspond however to  $\Delta_{method}^{abs}$  ranging between 1.2 and 9.1 Gy, excluding the highlighted patients in Table 6.8. For these two specific patients #4 and #8,  $\Delta_{method}^{abs}$  of 49.6 and 20.9 Gy were found, respectively.

Less than 6.9 Gy differences were found between the  $rigid_{local,functional}$  and  $rigid_{global}$  methods, except for the same patients #4 (49.6 Gy) and #8 (19.6 Gy).

#### 6.3.1.4 Total tumour volume (4/6)

$TV_{Total}$  was delineated for 7 out of the 10 patients and Figure 6.7 depicts the  $DVH_{j,treatment}$  obtained for patients #1 and #2. Table 6.9 provides the  $\bar{D}_{treatment}$  using each method for the patients where the  $TV_{Total}$  was delineated. Supplementary figures are provided in Appendix D6 for the 7 patients.

$\Delta_{method}^{\%}$  were within 10.1% for four patients (#2, #3, #5 and #10).  $\Delta_{method}^{\%}$  were 21.6%, 23.0% and 82.2% for the three other patients #6, #7 and #1, respectively. For patient #1, the mean absorbed dose found using the  $rigid_{local,functional}$  method (using a  $T_{SPECT \rightarrow PET}$  transformation) was 169.2 Gy, compared to less than 43.6 Gy for the three other methods using  $T_{CT_{SPECT} \rightarrow CT_{PET}}$  transformations. Therefore, large  $\Delta_{method}^{abs}$  were found for the  $TV_{Total}$  as shown in Table 6.9.

The specific case of patient #1 shows the necessity to apply different registration techniques depending on the patient case. The  $RT-struct_{SPECT}$  for the  $TV_{Total}$  propagated to the PET images using the  $rigid_{global}$  seemed to mismatch to the actual liver structures, as depicted in Figure 6.8. The PET/CT-based absorbed dose map is depicted at the right of the figure, where the cyan and green  $RT-struct_{PET}$  positions were obtained following the  $rigid_{global}$  and  $rigid_{local,functional}$  methods, respectively.

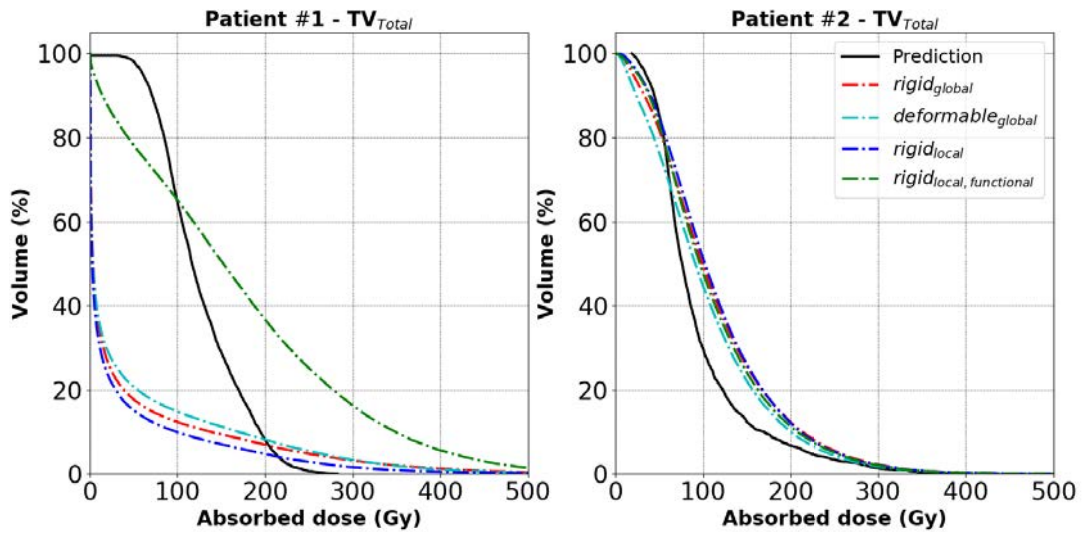


FIGURE 6.7 – Two patient cases are represented for the  $TV_{Total}$ . The  $DVH_{j,treatment}$  for the corresponding  $j$  methods are represented as:  $rigid_{global}$  (red),  $deformable_{global}$  (cyan),  $rigid_{local}$  (blue) and  $rigid_{local,functional}$  (green). The  $^{99m}Tc$ -MAA SPECT/CT-based  $DVH_{predicted}$  (black) are also depicted for comparison to the  $DVH_{j,treatment}$ .

TABLE 6.9 –  $\bar{D}_{treatment}$  for the  $TV_{Total}$  using different registration methods between SPECT/CT and PET/CT images. Values for  $\bar{D}_{predicted}$  are also provided. Patients with the largest differences are highlighted in pink.

Patient number	Mean absorbed doses in Gy - $TV_{Total}$				Predictive SPECT/CT
	Post-treatment PET/CT				
	$rigid_{global}$	$deformable_{global}$	$rigid_{local}$	$rigid_{local,functional}$	
#1	39.1	43.6	30.2	169.2	125.4
#2	113.4	104.2	115.9	111.6	93.6
#3	121.5	128.5	122.5	125.9	71.6
#4	-	-	-	-	-
#5	85.0	79.7	80.9	87.8	170.5
#6	57.7	57.8	54.4	69.4	120.0
#7	43.5	42.7	45.2	55.4	90.3
#8	-	-	-	-	-
#9	-	-	-	-	-
#10	254.0	251.6	255.4	232.6	214.4

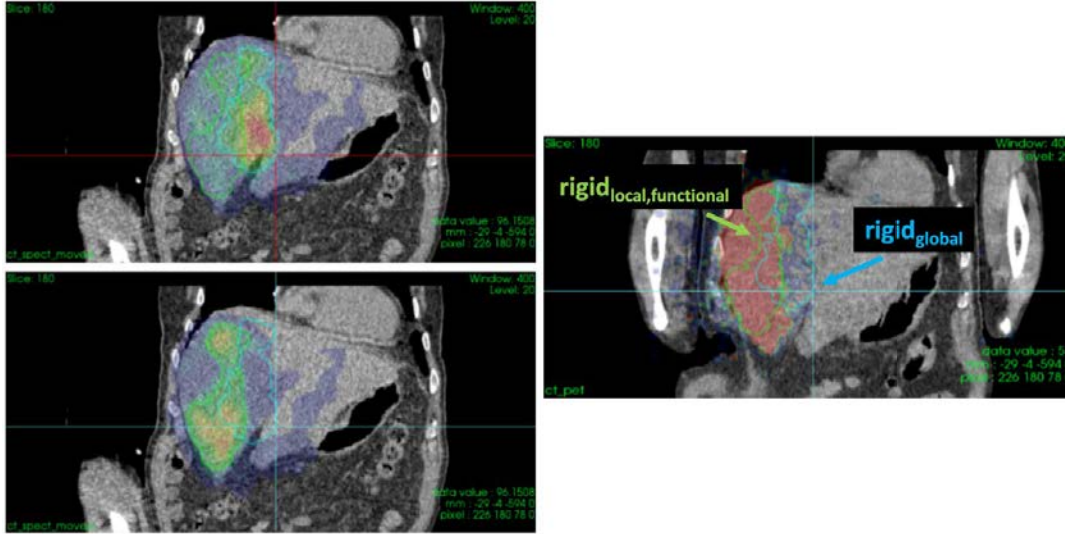


FIGURE 6.8 – The  $RT\text{-}struct_{PET}$  obtained from the propagated  $RT\text{-}struct_{SPECT}$  for the  $TV_{Total}$ , following the  $rigid_{global}$  (cyan) and  $rigid_{local,functional}$  (green) transformations. *Top-left*: The SPECT/CT following the  $rigid_{global}$  method. *Bottom-left*: The SPECT/CT following the  $rigid_{local,functional}$  method. *Right*: The PET/CT and position of the propagated  $TV_{Total}$  if the  $rigid_{global}$  (cyan) and  $rigid_{local,functional}$  (green) transformations are used. The position of the  $TV_{Total}$  falls outside the perfused region using the  $rigid_{global}$  method.

### 6.3.1.5 Target normal liver volume (5/6)

The  $NLV_{Target}$  corresponds to the normal, non-tumoral, liver volume which received irradiation and was delineated for 7 out of the 10 patients. Figure 6.9 depicts the  $DVH_{j,treatment}$  obtained for the  $NLV_{Target}$  for patients #1 and #2. Table 6.10 provides the  $\bar{D}_{treatment}$  using each method for the patients where the  $NLV_{Target}$  was delineated. Supplementary figures are provided in Appendix D7 for the 7 patients.

TABLE 6.10 –  $\bar{D}_{treatment}$  for the  $NLV_{Target}$  using different registration methods between SPECT/CT and PET/CT images. Values for  $\bar{D}_{predicted}$  are also provided. Patients with the largest differences are highlighted in pink.

Patient number	Mean absorbed doses in Gy - $NLV_{Target}$				Predictive SPECT/CT
	Post-treatment PET/CT				
	$rigid_{global}$	$deformable_{global}$	$rigid_{local}$	$rigid_{local,functional}$	
#1	74.7	69.0	72.9	53.5	40.0
#2	51.2	46.7	53.3	57.9	46.9
#3	15.9	17.3	15.4	16.3	29.8
#4	-	-	-	-	-
#5	58.0	58.7	57.9	58.2	57.2
#6	67.2	73.3	69.5	69.7	61.3
#7	32.9	29.9	33.6	31.3	30.7
#8	-	-	-	-	-
#9	-	-	-	-	-
#10	64.3	61.2	61.2	64.7	62.2

$\Delta_{method}^{\%}$  ranged between 1.5% and 11.2%, which correspond to  $\Delta_{method}^{abs}$  ranging between 0.9 and 6.1 Gy, except for the patients highlighted in Table 6.10. For these two

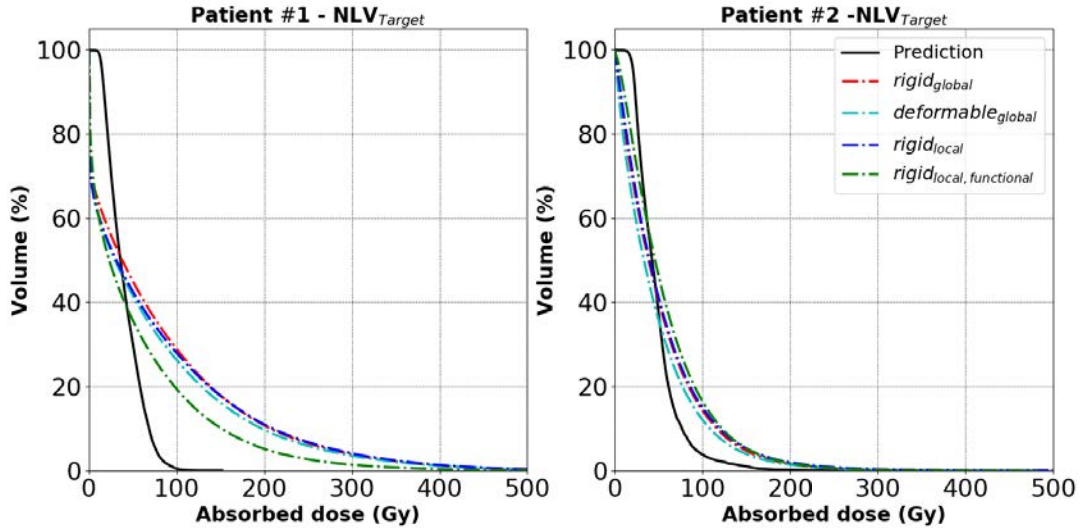


FIGURE 6.9 – Two patient cases are represented for the  $NLV_{Target}$ .  $DVH_{j,treatment}$  for the corresponding  $j$  methods are represented as:  $rigid_{global}$  (red),  $deformable_{global}$  (cyan),  $rigid_{local}$  (blue) and  $rigid_{local,functional}$  (green). The  $^{99m}Tc$ -MAA SPECT/CT-based  $DVH_{predicted}$  (black) are also depicted for comparison to the  $DVH_{j,treatment}$ .

specific patients #1 and #2,  $\Delta_{method}^{\%}$  of 28.4% and 19.3% were found, corresponding to  $\Delta_{method}^{abs}$  of 21.2 and 11.2 Gy, respectively.

Less than 4.9% differences were found between the  $rigid_{local,functional}$  and  $rigid_{global}$  methods, except for the same patients #1 (28.4%) and #2 (11.4%).

### 6.3.1.6 Whole normal liver volume (6/6)

The  $NLV_{WholeLiver}$  corresponds to the normal, non-tumoral, liver volume which received irradiation, or not. Figure 6.10 depicts the  $DVH_{j,treatment}$  obtained for the  $NLV_{WholeLiver}$  for patients #1 and #2. Table 6.11 provides the  $\bar{D}_{treatment}$  using each method for 7 out of the 10 patients where the  $NLV_{WholeLiver}$  was delineated. Supplementary figures are provided in Appendix D8 for the 7 patients.

$\Delta_{method}^{\%}$  ranged between 3.2% and 14.2%, which correspond to  $\Delta_{method}^{abs}$  ranging between 1.2 and 3.7 Gy, except for patient #1. For patient #1, a  $\Delta_{method}^{\%}$  of 31.0% was found, corresponding to  $\Delta_{method}^{abs}$  of 15.8 Gy.

Less than 5.9% differences were found between the  $rigid_{local,functional}$  and  $rigid_{global}$  methods, except for patient #1, where a 30.4% difference was found.

## 6.3.2 Comparison of predictive and per-treatment dosimetries

Each of the Sections 6.3.2.1 to 6.3.2.6 hereafter are also written in a similar format, reporting data as described in the previous Section 6.2.7.2 for each of the 6 delineated VOIs, using the  $rigid_{local,functional}$  method. Specific cases of patients are provided in each section. The reader is helped with the number of the VOI ranging from 1 to 6 and can refer to specific VOIs only.

Tables 6.12 to 6.17 provide the absorbed dose values for comparisons between the predicted and post-treatment images using the  $rigid_{local,functional}$  method only for each delineated VOI for all patients. Ranges for  $D_{50\%}$  as well as  $D_{2\%}$  are reported,

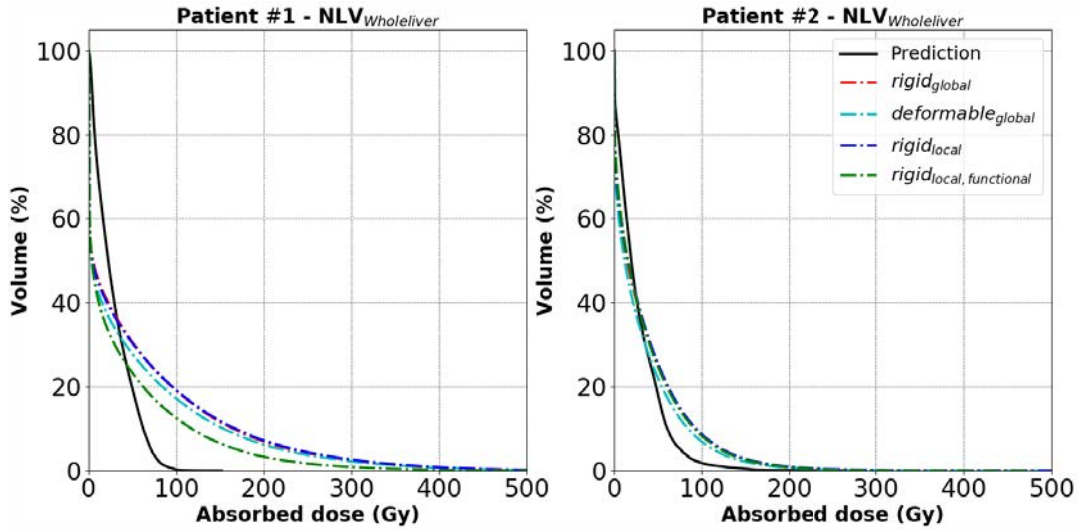


FIGURE 6.10 – Two patient cases are represented for the  $NLV_{WholeLiver}$ .  $DVH_{j,treatment}$  for the corresponding  $j$  methods are represented as:  $rigid_{global}$  (red),  $deformable_{global}$  (cyan),  $rigid_{local}$  (blue) and  $rigid_{local,functional}$  (green). The  $^{99m}Tc$ -MAA SPECT/CT-based  $DVH_{predicted}$  (black) are also depicted for comparison to the  $DVH_{j,treatment}$ .

TABLE 6.11 –  $\bar{D}_{treatment}$  for the  $NLV_{WholeLiver}$  using different registration methods between SPECT/CT and PET/CT images. Values for  $\bar{D}_{predicted}$  are also provided. Patients with the largest differences are highlighted in pink.

Patient number	Mean absorbed doses in Gy - $NLV_{WholeLiver}$				Predictive SPECT/CT
	Post-treatment PET/CT				
	$rigid_{global}$	$deformable_{global}$	$rigid_{local}$	$rigid_{local,functional}$	
#1	50.5	46.0	50.9	35.2	28.3
#2	32.7	29.5	33.8	33.2	27.2
#3	10.4	11.9	10.3	10.2	17.0
#4	-	-	-	-	-
#5	26.6	27.9	26.9	26.0	24.0
#6	37.8	38.8	39.0	38.7	12.7
#7	25.0	23.5	25.6	23.5	18.5
#8	-	-	-	-	-
#9	-	-	-	-	-
#10	46.7	46.0	44.9	44.4	43.1

and provide only a cursory comparison until other objective metrics are used in future analyses.

### 6.3.2.1 Whole liver volume (1/6)

Table 6.12 compares the predicted and obtained absorbed doses following treatment for the 10 patients studied for the WLV.

$\bar{D}$ .  $\bar{D}_{predicted}$  was within 44.3 Gy for all patients, except for patients #4 and #10.  $\bar{D}_{treatment}$  were within 49.7 Gy, except for patient #10.

TABLE 6.12 – Predicted absorbed doses compared to obtained absorbed doses following treatment for the WLW, using the  $rigid_{local,functional}$ .

Patient number	Absorbed doses in Gy - WLW					
	Prediction SPECT/CT			Treatment monitoring PET/CT		
	$\bar{D}$	$D_{50\%}$	$D_{2\%}$	$\bar{D}$	$D_{50\%}$	$D_{2\%}$
#1	39.1	26.7	174.4	49.7	7.0	322.4
#2	34.2	23.1	173.7	41.8	21.5	199.6
#3	19.1	12.6	88.3	14.6	1.0	17.2
#4	70.6	22.9	306.7	47.3	4.2	276.0
#5	40.8	18.2	253.1	33.0	14.5	161.9
#6	44.3	25.0	183.4	42.0	18.1	194.9
#7	23.4	12.5	147.1	25.8	15.5	126.0
#8	39.7	30.4	151.9	40.5	32.3	145.4
#9	37.9	1.5	345.9	27.9	1.9	234.7
#10	66.3	33.6	363.7	69.9	27.7	426.1

$\Delta_{predict-treatment}^{\%}$  for all patients ranged between 2.1% and 27.2%, corresponding to  $\Delta_{predict-treatment}^{abs}$  ranging between 0.8 and 10.6 Gy, except for patient #4 where an absolute difference of 23.2 Gy was found.

$D_{50\%}$ .  $D_{predicted,50\%}$  ranged between 1.5 and 33.6 Gy and  $\bar{D}_{post-treatment,50\%}$  ranged between 1.0 and 32.3 Gy for all patients.

$D_{2\%}$ .  $D_{predicted,2\%}$  ranged between 88.3 and 363.7 Gy and  $\bar{D}_{post-treatment,2\%}$  ranged between 17.2 and 426.1 Gy for all patients.

### 6.3.2.2 Perfused liver volume (2/6)

Table 6.13 compares the predicted and obtained absorbed doses following treatment for the 10 patients studied for the PLV.

$\bar{D}$ .  $\bar{D}_{predicted}$  ranged between 32.9 to 158.4 Gy for all patients.  $\bar{D}_{treatment}$  ranged between 24.3 and 111.8 Gy.

$\Delta_{predict-treatment}^{\%}$  up to 37.2% were found. The associated  $\Delta_{predict-treatment}^{abs}$  were within 8.6 Gy for 5 patients (#3, #6, #7, #8 and #10), were within 23.3 Gy for 3 patients (#1, #2 and #5), were 46.6 and 50.9 Gy for patients #9 and #4, respectively.

$D_{50\%}$ .  $D_{predicted,50\%}$  ranged between 22.3 and 136.8 Gy and  $\bar{D}_{post-treatment,50\%}$  ranged between 22.8 and 91.6 Gy.

$D_{2\%}$ .  $D_{predicted,2\%}$  ranged between 112.1 and 408.0 Gy and  $\bar{D}_{post-treatment,2\%}$  ranged between 144.8 and 483.4 Gy.

TABLE 6.13 – Predicted absorbed doses compared to obtained absorbed doses following treatment for the PLV, using the  $rigid_{local,functional}$ .

Patient number	Absorbed doses in Gy - PLV					
	Prediction SPECT/CT			Treatment monitoring PET/CT		
	$\bar{D}$	$D_{50\%}$	$D_{2\%}$	$\bar{D}$	$D_{50\%}$	$D_{2\%}$
#1	53.9	42.4	188.3	71.9	33.4	356.6
#2	55.9	47.8	176.8	68.7	54.3	233.0
#3	32.9	25.7	112.1	24.3	3.1	230.6
#4	136.8	121.3	340.1	85.9	66.5	325.7
#5	89.9	69.6	357.8	66.7	56.1	204.0
#6	72.5	63.0	204.8	70.2	58.5	221.3
#7	38.0	22.3	178.5	34.3	22.8	144.8
#8	61.7	52.8	178.6	58.2	55.4	159.8
#9	158.4	136.8	408.0	111.8	91.6	432.6
#10	96.0	46.9	393.1	101.3	48.6	483.4

### 6.3.2.3 Non-perfused liver volume (3/6)

Table 6.14 compares the predicted and obtained absorbed doses following treatment for the 10 patients studied for the NPLV.

TABLE 6.14 – Predicted absorbed doses compared to obtained absorbed doses following treatment for the NPLV, using the  $rigid_{local,functional}$ .

Patient number	Absorbed doses in Gy - NPLV					
	Prediction SPECT/CT			Treatment monitoring PET/CT		
	$\bar{D}$	$D_{50\%}$	$D_{2\%}$	$\bar{D}$	$D_{50\%}$	$D_{2\%}$
#1	6.9	6.2	16.2	1.9	1.3	21.9
#2	7.9	7.3	21.0	9.6	2.1	72.0
#3	4.6	3.6	13.6	4.2	0.3	41.5
#4	4.9	1.8	23.0	9.6	2.3	126.8
#5	8.4	4.7	31.3	10.8	1.2	81.2
#6	6.5	5.9	17.1	4.7	0.6	41.9
#7	4.3	3.8	10.6	14.7	8.5	72.9
#8	4.1	1.1	18.3	12.6	2.8	87.3
#9	2.3	0.9	16.5	3.8	0.7	32.2
#10	18.1	18.5	28.7	18.4	12.4	77.7

$\bar{D}$ .  $\bar{D}_{predicted}$  ranged between 2.3 and 18.1 Gy for all patients.  $\bar{D}_{treatment}$  ranged between 1.9 and 18.4 Gy.



Owing to the low  $\bar{D}_{predicted}$ , large  $\Delta_{predict-treatment}^{\%}$  were obtained. However, the  $\Delta_{predict-treatment}^{abs}$  were within 5.0 Gy for 8 patients (#1 to #6, #9 and #10), and within 10.4 Gy for the remaining 2 patients (#7 and #8).

$D_{50\%}$ .  $D_{predicted,50\%}$  ranged between 0.9 and 18.5 Gy and  $\bar{D}_{post-treatment,50\%}$  ranged between 0.3 and 12.4 Gy.

$D_{2\%}$ .  $D_{predicted,2\%}$  ranged between 10.6 and 28.7 Gy and  $\bar{D}_{post-treatment,2\%}$  ranged between 21.9 and 126.8 Gy.

### 6.3.2.4 Total tumour volume (4/6)

Table 6.15 compares the predicted and obtained absorbed doses following treatment for 7 out of the 10 patients studied for the  $TV_{Total}$ .

TABLE 6.15 – Predicted absorbed doses compared to obtained absorbed doses following treatment for the  $TV_{Total}$ , using the  $rigid_{local,functional}$ .

Patient number	Absorbed doses in Gy - $TV_{Total}$					
	Prediction SPECT/CT			Treatment monitoring PET/CT		
	$\bar{D}$	$D_{50\%}$	$D_{2\%}$	$\bar{D}$	$D_{50\%}$	$D_{2\%}$
#1	125.4	116.7	228.7	169.5	152.6	478.9
#2	93.6	76.1	286.6	111.6	96.3	300.9
#3	71.6	60.1	193.3	125.9	77.6	580.7
#4	-	-	-	-	-	-
#5	170.5	125.0	479.4	87.8	75.8	228.7
#6	120.0	116.5	274.8	69.7	55.3	218.3
#7	91.3	72.6	262.8	55.4	40.5	192.7
#8	-	-	-	-	-	-
#9	-	-	-	-	-	-
#10	214.4	199.7	446.4	232.6	203.9	650.2

$\bar{D}$ .  $\bar{D}_{predicted}$  ranged between 71.6 to 214.4 Gy for the 7 patients.  $\bar{D}_{treatment}$  ranged between 55.4 and 232.6 Gy.

$\Delta_{predict-treatment}^{\%}$  up to 75.7% were obtained. The found absorbed doses following treatment were therefore far from predictions.  $\Delta_{predict-treatment}^{abs}$  ranged between 18.1 and 82.7 Gy.

$D_{50\%}$ .  $D_{predicted,50\%}$  ranged between 60.1 and 199.7 Gy and  $\bar{D}_{post-treatment,50\%}$  ranged between 40.5 and 203.9 Gy.

$D_{2\%}$ .  $D_{predicted,2\%}$  ranged between 193.3 and 479.4 Gy and  $\bar{D}_{post-treatment,2\%}$  ranged between 192.7 and 650.2 Gy.

### 6.3.2.5 Target normal liver volume (5/6)

Table 6.15 compares the predicted and obtained absorbed doses following treatment for 7 out of the 10 patients studied for the  $NLV_{Target}$ .

TABLE 6.16 – Predicted absorbed doses compared to obtained absorbed doses following treatment for the  $NLV_{Target}$ , using the  $rigid_{local,functional}$ .

Patient number	Absorbed doses in Gy - $NLV_{Target}$					
	Prediction SPECT/CT			Treatment monitoring PET/CT		
	$\bar{D}$	$D_{50\%}$	$D_{2\%}$	$\bar{D}$	$D_{50\%}$	$D_{2\%}$
#1	40.0	36.1	86.1	53.5	23.2	271.2
#2	57.9	45.7	193.1	53.3	39.3	197.9
#3	29.8	24.5	90.3	16.3	2.1	143.0
#4	-	-	-	-	-	-
#5	57.2	54.2	97.8	58.2	47.7	186.9
#6	61.3	55.1	150.5	69.7	58.3	221.2
#7	30.7	20.0	145.4	31.3	21.1	132.2
#8	-	-	-	-	-	-
#9	-	-	-	-	-	-
#10	62.2	41.3	292.4	64.7	34.5	373.2

$\bar{D}$ .  $\bar{D}_{predicted}$  ranged between 29.8 to 62.2 Gy for the 7 patients.  $\bar{D}_{treatment}$  ranged between 16.3 and 69.7 Gy.

$\Delta_{predict-treatment}^{\%}$  up to 45.4% were obtained.  $\bar{D}_{treatment}$  differed to the predictions with  $\Delta_{predict-treatment}^{abs}$  ranging between 0.6 to 13.5 Gy.

$D_{50\%}$ .  $D_{predicted,50\%}$  ranged between 20.0 and 55.1 Gy and  $\bar{D}_{post-treatment,50\%}$  ranged between 2.1 and 58.3 Gy.

$D_{2\%}$ .  $D_{predicted,2\%}$  ranged between 90.3 and 292.4 Gy and  $\bar{D}_{post-treatment,2\%}$  ranged between 132.2 and 373.2 Gy.

### 6.3.2.6 Whole normal liver volume (6/6)

Table 6.17 compares the predicted and obtained absorbed doses following treatment for 7 out of the 10 patients studied for the  $NLV_{WholeLiver}$ .

$\bar{D}$ .  $\bar{D}_{predicted}$  ranged between 17.0 to 43.1 Gy for the 7 patients.  $\bar{D}_{treatment}$  ranged between 10.2 and 44.4 Gy.

$\Delta_{predict-treatment}^{\%}$  up to 40.0% were obtained.  $\bar{D}_{treatment}$  differed to the predictions with  $\Delta_{predict-treatment}^{abs}$  ranging between 1.4 and 6.9 Gy.

$D_{50\%}$ .  $D_{predicted,50\%}$  ranged between 11.3 and 29.9 Gy and  $\bar{D}_{post-treatment,50\%}$  ranged between 0.8 and 22.2 Gy.

TABLE 6.17 – Predicted absorbed doses compared to obtained absorbed doses following treatment for the  $NLV_{WholeLiver}$ , using the  $rigid_{local,functional}$ .

Patient number	Absorbed doses in Gy - $NLV_{WholeLiver}$					
	Prediction SPECT/CT			Treatment monitoring PET/CT		
	$\bar{D}$	$D_{50\%}$	$D_{2\%}$	$\bar{D}$	$D_{50\%}$	$D_{2\%}$
#1	28.3	22.5	81.3	35.2	3.9	238.4
#2	27.2	19.7	97.9	33.2	15.9	161.7
#3	17.0	11.8	70.4	10.2	0.8	93.7
#4	-	-	-	-	-	-
#5	24.0	13.1	90.6	26.0	8.8	137.3
#6	35.4	18.5	133.3	38.7	12.7	190.8
#7	18.5	11.3	108.5	23.5	14.4	113.3
#8	-	-	-	-	-	-
#9	-	-	-	-	-	-
#10	43.1	29.9	231.2	44.4	22.2	298.3

$D_{2\%}$ .  $D_{predicted,2\%}$  ranged between 70.4 and 231.2 Gy and  $\bar{D}_{post-treatment,2\%}$  ranged between 93.7 and 298.3 Gy.

## 6.4 Discussion

*Context.* The main goal of this study was to investigate several workflows for the propagation of delineated contours from SPECT/CT to PET/CT acquisitions for  $^{90}\text{Y}$ -radioembolisation. These allow to perform comparisons between the predictive and post-treatment dosimetries by selecting appropriate image transformations to adjust as best as possible reference the structures from one image to another. Indeed, retrospective studies still need to be performed to assess the predictive value of  $^{99m}\text{Tc}$ -MAA SPECT/CT imaging for  $^{90}\text{Y}$ -radioembolisation for different scenarios, as described in the *Introduction* Section 6.1.

Contour propagation methods and VOI segmentation itself still remain limiting factors for an accurate assessment of dosimetry (Morán et al., 2020). The current study focused on this source of uncertainty to obtain necessary tools and reinforce future dosimetric analysis on patient datasets at the CLB. It clearly demonstrates that, depending on the patient case, different registration techniques should be applied. This study quantifies the influence of a good match or mismatch between predictive and post-treatment dosimetry on patients.

### 6.4.1 Comparisons

Table 6.18 provides a summary of the differences obtained, 1) between the four methods, and 2) between the prediction and the mean absorbed doses following treatment. A first difficulty lies in the fact that it is not clear how to set threshold values to assess whether the results obtained are correct, but the extent of the differences can be observed between the different VOIs.

TABLE 6.18 – Summary of: 1)  $\Delta_{method}^{\%}$  and  $\Delta_{method}^{abs}$  obtained between the methods, and 2)  $\Delta_{predict-treatment}^{\%}$  and  $\Delta_{predict-treatment}^{abs}$  between the predictive and mean absorbed dose obtained using the *rigid<sub>local,functional</sub>* method. The ratio between parentheses, e.g. (8/10) gives the number of patient VOIs which have differences lower than or equal to the recorded difference.

Region	Comparisons			
	Methods		Prediction vs. Treatment	
	$\Delta_{method}^{\%}$ (%)	$\Delta_{method}^{abs}$ (Gy)	$\Delta_{predict-treatment}^{\%}$ (%)	$\Delta_{predict-treatment}^{abs}$ (Gy)
WLV	8.8 (8/10)	4.6 (8/10)	27.2 (9/10)	10.6 (9/10)
PLV	11.7 (9/10)	8.0 (9/10)	26.2 (7/10)	12.7 (6/10)
NPLV	83.1 (8/10)	9.1 (8/10)	>100 (10/10)	10.4 (10/10)
TV <sub>Total</sub>	23.0 (6/7)	22.8 (6/7)	48.5 (6/7)	54.3 (6/7)
NLV <sub>Target</sub>	11.2 (5/7)	6.1 (5/7)	45.4 (7/7)	13.5 (7/7)
NLV <sub>WholeLiver</sub>	14.2 (6/7)	3.7 (6/7)	40.0 (7/7)	6.9 (7/7)

**WLV (1/6)** On overall for the WLV, as reported in Table 6.18, all four methods were within agreements of 8.8% ( $\Delta_{method}^{\%}$ ). The found mean absorbed doses differed by a maximum of 4.6 Gy ( $\Delta_{method}^{abs}$ ). As expected, the *rigid<sub>global</sub>* method in most cases was found suitable for the liver as a whole organ. Absolute differences of less than 3.7, 1.9, and 4.6 Gy were found between the *rigid<sub>global</sub>* and each of the *deformable<sub>global</sub>*, *rigid<sub>local</sub>* and *rigid<sub>local,functional</sub>* methods among the patients, respectively.

Largest variations (> 10 Gy) were found in patients #4 and #8. For patient #4, a  $\bar{D}_{treatment}$  of 47.3 Gy was found using the *rigid<sub>local,functional</sub>* method, compared to more or less 70 Gy for the three other methods. This was due to a misplacement the WLV after registration using of the *rigid<sub>local,functional</sub>* method, therefore should not be used for this specific patient. For patient #8, around 40 Gy were obtained with methods using *local* registration methods, whereas higher mean absorbed doses (46.7 and 50.4 Gy) were obtained using registration methods using the voxels of the *global* images. A misplacement of the WLV after registration using of the *rigid<sub>local,functional</sub>* method was also observed for this patient. The *deformable<sub>global</sub>* method seemed to provide a better match in the case of patient #8, where it was clear that the liver size was different in the workup and treatment procedures.

$\bar{D}_{treatment}$  were within 50 Gy for all the patients where the prediction was within 50 Gy. For the two patients (#4 and #8) where  $\bar{D}_{treatment}$  were around 70 Gy, their predictions were also around 70 Gy (discarding the *rigid<sub>local,functional</sub>* method). A visual interpretation comparing the DVHs using the 10 figures for the 10 patients for the WLV in Appendix D2 would let us suggest that the predictions matched obtained results following radioembolisation, requiring however further analysis for interpretation.

**PLV (2/6)** As reported in Table 6.18, all four methods were within agreements of 11.7% ( $\Delta_{method}^{\%}$ ) for the PLV. The found mean absorbed doses differed by a maximum of 8.0 Gy ( $\Delta_{method}^{abs}$ ). As for the WLV, the *rigid<sub>global</sub>* method in most cases was found suitable for the PLV compared to the other methods, with a maximum percentage difference in  $\bar{D}_{treatment}$  of 7.0% compared to *rigid<sub>local,functional</sub>*, corresponding to a maximum absolute difference of 4.8 Gy.

Largest variations between the methods were found for patient #9.

A  $\bar{D}_{treatment}$  of 93.6 Gy was found using the  $rigid_{global}$  method, whereas higher doses were obtained for the three other methods. The  $deformable_{global}$  method provided satisfactory visual match for patient #9.

$\bar{D}_{treatment}$  had large variations to predictions among patient. If we broadly try to classify, using the  $rigid_{global}$ , an absolute difference of less than 12.7 Gy was found for 6 out of 10 patients. Larger differences of 15.2, 50.8, 24.2 and 46.6 Gy were found for the other 4 patients #1, #4, #5 and #9, respectively. A visual interpretation comparing the DVHs for the PLV in *Appendix D3* would let us suggest that the predictions can be close to obtained results following radioembolisation (for 7 patients #2, #3, #5, #6, #7, #8 and #10), and that the mean absorbed dose criteria is not enough for comparisons.

**NPLV (3/6)** As reported in Table 6.18, large percentage differences ( $\Delta_{method}^{\%}$ ) were obtained for the NPLV but all four methods were within good agreements, with maximum absolute differences ( $\Delta_{method}^{abs}$ ) within 9.1 Gy.

Largest variations between the methods were found for patients #4 and #8. For patient #4, even if a  $\bar{D}_{treatment}$  of 9.6 Gy was obtained using the  $rigid_{local,functional}$  compared to around 50 Gy for the three other methods, it should not be considered owing to the misplacement of the WLW following the  $rigid_{local,functional}$  method. For patient #8,  $\bar{D}_{treatment}$  of 11.6 and 12.6 Gy were found using the  $rigid_{local}$  and  $rigid_{local,functional}$  methods, whereas 32.2 and 33.4 Gy were found using the  $rigid_{global}$  and  $deformable_{global}$  methods, respectively.

Considering the  $rigid_{local,functional}$  method,  $\bar{D}_{treatment}$  were within 14.7 Gy for all the patients and the predictions were within 8.4 Gy, but may not be the most suitable method for some patients even if low absorbed doses are obtained. For patient #10 where the found  $\bar{D}_{treatment}$  was 18.4 Gy, its prediction was 18.1 Gy. A visual interpretation comparing the DVHs for the NPLV in *Appendix D5* would let us suggest that the predictions matched obtained results following radioembolisation, except for patients #4 and #8.

**TV<sub>Total</sub> (4/6)** As reported in Table 6.18, all four methods for the TV<sub>Total</sub> were within agreements of 10.1% ( $\Delta_{method}^{\%}$ ) for 4 out of 7 patients (#2 #3, #5 and #10). The found mean absorbed doses differed by a maximum of 11.8 Gy ( $\Delta_{method}^{abs}$ ) for these patients.

For the 3 other patients, (#1, #6 and #7), the  $rigid_{global}$ ,  $deformable_{global}$  and  $rigid_{local}$  methods had better agreements between themselves, than with the  $rigid_{local,functional}$  method, see Table 6.9. For example for patient #1, the mean absorbed dose using the  $rigid_{local,functional}$  method differed largely, showing 169.2 Gy compared to less than 43.6 Gy to the other three methods.

The  $\bar{D}_{treatment}$  for the TV<sub>Total</sub> using  $rigid_{local,functional}$  were on overall higher than for the PLV, which would mean that the NLV<sub>Target</sub> received less irradiation than the defined tumour. Among all defined VOIs, the TV<sub>Total</sub> showed the largest differences between the found mean absorbed doses following treatment and their predictions. As it can be shown in the figures in *Appendix D6*, only patients #2 and #10 showed good visual match between the DVHs.

**NLV<sub>Target</sub> (5/6)** As reported in Table 6.18, all four methods for the NLV<sub>Target</sub> were within agreements of 11.2% ( $\Delta_{method}^{\%}$ ) for 5 over 7 patients. The found mean absorbed doses differed by a maximum of 3.8 Gy ( $\Delta_{method}^{abs}$ ) for these patients.

The  $\bar{D}_{treatment}$  found in the NLV<sub>Target</sub> are smaller than the PLV, and therefore than in the TV<sub>Total</sub>. For example for patient #10, using the  $rigid_{local,functional}$  method, the

$\bar{D}_{treatment}$  was 101.26, 232.6 and 64.7 Gy for the PLV,  $TV_{Total}$  and  $NLV_{Target}$ , respectively.

A visual interpretation comparing the DVHs using the figures for the 7 patients with defined  $NLV_{Target}$  in Appendix D7 would let us suggest that the predictions matched obtained results following radioembolisation, excluding patient #1.

**$NLV_{WholeLiver}$  (6/6)** As reported in Table 6.18, all four methods for the  $NLV_{WholeLiver}$  were within agreements of 14.2% ( $\Delta_{method}^{\%}$ ) for 6 out of 7 patients. The found mean absorbed doses differed by a maximum of 3.7 Gy ( $\Delta_{method}^{abs}$ ) for these patients.

For patient #1 where a  $\Delta_{method}^{\%}$  of 31.0% was found, the  $rigid_{global}$ ,  $deformable_{global}$  and  $rigid_{local}$  methods had better agreements between themselves, ranging between 46.0 and 50.9 Gy, than with the  $rigid_{local,functional}$  method with 35.2 Gy, see Table 6.11.

Considering the  $rigid_{local,functional}$  method,  $\bar{D}_{treatment}$  were within 43.1 Gy for all the patients and the predictions were within 44.4 Gy. Not more than 6.9 Gy difference were obtained between the prediction and obtained absorbed doses following treatment. A visual interpretation comparing the DVHs in the figures in Appendix D8 for the  $NLV_{WholeLiver}$  would let us suggest that the predictions matched obtained results following radioembolisation, except for patient #1.

**Predictive dosimetry.** If an accurate prediction of the different VOIs can be performed, patient selection can be optimised and it can provide an individualised effective treatment planning. The predicted mean absorbed doses for the large volumes which are the WLV,  $NLV_{WholeLiver}$  and NPLV in this study were within 10 Gy from obtained values following treatment. However, this is not the case for the PLV and  $TV_{Total}$  where much larger differences were found as described earlier.

The difference in the predictions and mean absorbed doses following treatment using the  $rigid_{local,functional}$  method for the  $NLV_{Target}$  ranged between 0.6 and 13.6 Gy. The PLV is the sum of the  $TV_{Total}$  and  $NLV_{Target}$ . This would mean therefore that the prediction using the mean absorbed dose to the  $TV_{Total}$  is not accurate. Indeed, differences between the prediction and  $\bar{D}_{treatment}$  ranged between 18.1 to 82.7 Gy using the  $rigid_{local,functional}$  method.

Comparisons using  $D_{50\%}$  and  $D_{2\%}$  between predictions and absorbed doses obtained as presented in Section 6.3.2 remain only cursory until further analysis are used for comparison.

## 6.4.2 Limitations

**Defined volumes of interest.** For the purpose of this study, the defined VOIs were used as reference volumes for comparison of the image registration methods studied, detailed in Section 6.2.6. However, only one tumoral zone was selected per patient instead of individual tumours, the target volume was selected as a 5% threshold (the PLV) instead of delimiting the planned volume as the treated liver parts, as in Table 6.1 (treatment approach). A different workflow defining VOIs such as in Morán et al. (2020) and Levillain et al. (2020) should be used, defining a planning target volume (PTV) based on the treatment approach instead of a PLV which might be useful in future studies following this preliminary one. Individual tumours also should be delineated. To that aim, diagnostic contrasted images (contrast-enhanced-CT or MRI) should be available which might not be the case. They are also usually performed several weeks before treatment, which might not be appropriate for VOI delimitation due to disease progression and internal organ movement.

**Inclusion and exclusion criteria.** No selection on the 10 patients were performed for this retrospective study. Patients with different types of primary and secondary hepatic malignancies were included. The 10 patients had different treatment approaches and treated with both resin and glass microspheres. For future studies, patients should be classified in different groups, for example the tumour and microsphere types. Also, only 10 patients were included. Tumours were delineated for 7 of them. The complete datasets of patients (around 45) can be classified in different groups to be included in future studies. Patients with visible motion artefacts should also be excluded from the study as explained below.

**Respiratory motion.** For some patients, clearly visible respiration motion artefacts in the hepatic region could be found which lead to misplaced activity activity distributions outside the liver parts. This is a limitation to an actual accurate quantification. The use of 4D PET for motion correction could be an alternative to circumvent this effect, but is not performed in our centre for  $^{90}\text{Y}$ -SIRT PET monitoring. Concerning SPECT/CT, research in our group is being performed to reconstruct 4D respiration-gated SPECT images using a data driven approach (Robert et al., 2019). Their respiration-gated SPECT reconstruction improves the estimation of the activity on the tumour, applied to  $^{90}\text{Y}$ -radioembolisation, without the need for extra hardware and forms part as a perspective for comparisons to absorbed doses obtained following treatment.

**Other confounding factors.** Residual  $^{90}\text{Y}$  activity calculation by measuring the dose rates around the injection box does not provide an accurate measurement of the activity and is still a limitation to compute the net administered activity. Uncertainties related to acquisition and reconstruction parameters and PVE, as seen in the previous Chapter 5 also add bias on voxel-based dosimetry. Finally, the way contours are delineated and propagated remain a source of error.

### 6.4.3 Future directions

This preliminary study evaluated the impact of registration methods for contour propagation on the quantification of absorbed dose in the liver following  $^{90}\text{Y}$ -radioembolisation. The absorbed dose distributions to the treated regions as well as the normal, non-tumoral, parenchymal volumes were performed. Prospective studies can implement metrics suggested by Morán et al. (2020), with QVHs which are based on a voxel-to-voxel absorbed dose comparison and deal with absorbed dose differences directly. However, their method should be validated in prospective studies that could reinforce this validation to bring additional information in the assessment of the compliance between the predictive and absorbed dose distributions following treatment.

The results in this study can also be useful to adapt registration methods depending on the patient case, avoiding manual registrations when mismatching during contour propagation occurs.

## 6.5 Conclusion

This work was performed to validate a workflow for image registration techniques before performing further retrospective studies using the same image

datasets. It allowed to evaluate the extent to which differences can be obtained depending on the registration method and raises awareness of the large differences which can lead to the misinterpretation of data. Therefore, different methods should be adapted for each patient case. On overall, the  $rigid_{global}$  was sufficient for large volumes such as the WL<sub>V</sub>, but not for smaller ones such as the TV<sub>Total</sub>.





# Conclusions and perspectives

The objective of this thesis was twofold, being first to provide a validated Monte Carlo model of the Vereos SiPM-based PET system, and second to investigate on the sources of error which could have an impact on the quantification of  $^{90}\text{Y}$  using Monte Carlo simulations for monitoring  $^{90}\text{Y}$ -radioembolisation treatment. During the course of this thesis, we have 1) proposed a Monte Carlo model of the DPC PET/CT, validated using GATE simulations against experimental measurements; 2) studied the influence of OSEM reconstruction parameters and *listmode* acquisition lengths on the quantitative accuracy in  $^{90}\text{Y}$  dosimetry and 3) provided a preliminary assessment of the predictive value of the  $^{99m}\text{Tc}$ -MAA surrogate to  $^{90}\text{Y}$ -microspheres by suggesting consistent approaches for image registration.

## Monte Carlo PET model

The Monte Carlo model of the Vereos presented in *Chapter 4* can be useful for numerous studies. Instead of performing experiments, whole evaluations can be performed using the model to tune parameters, such as the experimental evaluation of reconstruction parameters performed during this thesis using  $^{90}\text{Y}$ . One short term perspective to follow the work during this thesis could be to validate a workflow using the CASToR software for the reconstruction of GATE output data for  $^{90}\text{Y}$  imaging. This validation can be carried out comparing simulated against  $^{90}\text{Y}$  experimental data acquired during this thesis. An OSEM reconstruction workflow has been validated against  $^{18}\text{F}$  data by Salvadori (2020) which could help in designing the same workflow for  $^{90}\text{Y}$ . This done, studies for example evaluating the extent of PVEs (Soret, Bacharach, and Buvat, 2007) on objects of different complex shapes and sizes, and containing variable activity concentrations can be performed. Absorbed dose recovery coefficients can be derived using simulated data, and corrected for using known geometries and derived metrics.

Furthermore, evaluations of reconstruction parameters as carried out in *Chapter 5* can be continued for different scenarios using the Monte Carlo PET model, by varying the activity concentrations for different SBRs, which is experimentally quite time-consuming and raises radiation protection issues. This could provide a complete set of evaluated reconstruction parameters which can be adapted to specific cases of patients or specific regions of activity distributions, and this for different isotopes used in PET imaging, which could form part of individualised patient dosimetries. Indeed, evaluated parameters during this thesis were for a SBR of 9:1 throughout the experiments using the NEMA body phantom, and might vary in patient setups. More complex phantom geometries than spherical volumes can be studied. Also, confounding factors to image quality and quantification can be studied as in Strydhorst et al. (2016) for several isotopes.

In a longer term perspective, the model can be useful also for: 1) generation of datasets for machine learning purposes and 2) testing and validation of generated

data using image reconstruction with the workflow as described above. For example in a future research project, named as the MoCaMed ANR project (2021-2025)<sup>2</sup> in collaboration with different research teams (CREATIS, LATIM, LIRIS and CLB) starting in September 2021, the model can be of potential use to validate the generated *phase space* files, storing particles leaving the imaged patient, such as in a study recently published in our research team in Lyon applied to external radiotherapy by Sarrut, Krahe, and Létang (2019) using generative adversarial networks (GANs), and the proof of concept to SPECT imaging by Sarrut et al. (2021a). These *phase space* files can be used as input in Monte Carlo simulations of nuclear imaging systems and our PET model. The model could also be useful for other coming PhD positions in our Centre de Recherche en Acquisition et Traitement de l'Image pour la Santé (CREATIS) team in collaboration to other institutions, on the use of artificial intelligence for multimodal image reconstruction in the MultiRecon ANR project (2021-2024)<sup>3</sup>, or on investigating parametric digital PET imaging in theranostic applications for <sup>177</sup>Lu-based cancer treatments (2021-2024)<sup>4</sup>.

Another perspective could also be the simulation of patient images to evaluate dose distributions such as in the study of Roncali et al. (2020) and validate their methods using CFD for radioembolisation treatment prediction. Therefore, to put it consisely, the proposed model has a wide range of potential applications and can support a number of future projects, in particular to optimise imaging performance, identify the influence of acquisition and reconstruction parameters on image quality and absorbed dose estimation, evaluate new reconstruction and correction methods.

The GATE toolkit has been used for the Monte Carlo simulation of different types of imaging and detection systems. It is however more than 15 years old, is community driven and the code is complex and evolves continuously. A recent review by Sarrut et al. (2021b) outlined the numerous simulations of emission tomographs in GATE, where the work during this thesis has been enhanced. Indeed, GATE (and other similar platforms) remain the gold standard for designing, optimising and assessing imaging systems and is still useful to industrials, researchers and students. One of the limitations of GATE is its Monte Carlo approach and simulations are slow and demand large computational power. Optical tracking simulations therefore cannot be performed on a complete PET detector ring and is limited to single pairs of detectors.

In my opinion, GATE will remain a useful tool for Monte Carlo simulations of complex imaging systems and can be easily adapted to future systems, however relying on volunteer contributions to maintain and implement new modules. Current considerations exist in the OpenGATE collaboration to propose a major GATE evolution exploiting Python tools<sup>5</sup> for faster analysis and PyTorch integrations which might open doors to developments within GATE exploiting Artificial Intelligence (AI). GATE is also of interest to students and is increasingly used to teach Monte Carlo methods for medical physics at universities. For an easier understanding, a more complete and clear documentation should be made available especially for students who are new to GATE. Efforts are being made on that side and GATE users are actually responsive to specific issues. Finally, a completely new GATE platform would be the future integration of the early stage AI tools for simulation and integration of complete optical analysis and data output, since the growing interest in

---

2. See [MoCaMed](#)

3. See [MultiRecon](#)

4. See [Parametric PET](#)

5. See [GateTools](#)

Cerenkov luminescence detection for faster TOF resolution (Lecoq et al., 2020). Input and output data files are also generally too bulky and AI could help in reducing their size.

### Reconstruction for dosimetry

The short term perspectives of the second contribution to this thesis on the evaluation of reconstruction parameters meet the ones that can be performed with the PET Monte Carlo model, as described earlier. The evaluation allowed us to understand the behaviour of the OSEM algorithm under low counts statistics and conditions intrinsic to the decay of  $^{90}\text{Y}$ . It can be useful to different institutions and research works to build their protocols following the same methodologies, starting with our own institution at the CLB. The evaluation also allowed **to reduce patient acquisition duration** following  $^{90}\text{Y}$ -radioembolisation by 30%, which makes the examination more comfortable for the patient. The methodology using DVH and RMSD can be applied to other isotopes, and other imaging modalities, such as for SPECT imaging following Lutathera therapy using the  $^{177}\text{Lu}$  isotope. Future studies might evaluate the PSF influence on quantification, by varying the parameters (fixed to 1 iteration with a 6 mm regularisation kernel in this thesis according to recommendations for  $^{18}\text{F}$ ) using the acquired phantom *listmode* phantom datasets, which might help to obtain a more accurate quantification. The study was based on simple phantom geometries with no heterogeneity and, therefore, new phantoms can now be easily designed by a 3D printer to take into account more realistic geometries. Modelling heterogeneous activity distributions in experimental setups is also something on which research should be focused. Indeed, the phantoms used had homogeneous activity distributions in the different compartments of the different phantoms.

### Predictive vs. monitoring dosimetry

Finally, the selected evaluated reconstruction parameters in the second contribution were used in the third and last contribution to this thesis, which provides preliminary results, evaluating retrospectively the predictive value of  $^{99m}\text{Tc}$ -MAA to  $^{90}\text{Y}$  microspheres for radioembolisation treatment. The primary aim in this work remained on the choice of the most suitable registration methods for comparisons between the predictive and actual activity distribution per-treatment and cannot be used to interpret on the  $^{99m}\text{Tc}$ -MAA predictive value yet, limited to 10 patients. This work will be continued prospectively in a short term, with a better selection and classification of patients for analysis. Indeed, several aspects were not taken into account for adequate patient selection. It would require a committee validating each patient based on specific inclusion criteria (such as liver-only disease, ECOG performance status, ...) and exclusion criteria (such as prior radioembolisation or external beam radiotherapy, ...). Tools and metrics such as proposed by Levillain et al. (2020) could be tested to validate their methodology using QVH and quality factors (QF) combined with DVH which could reinforce ours. As they stated, QVHs also provide a visual and quantitative assessment of the agreement between predictive and post-treatment dosimetry. Their Python code for QVH calculation is available on [Github/QVH](#). Furthermore, a synthesis using statistical analyses will be performed.

### Further perspectives

The patient datasets available at the CLB (around 45 patients) could be used in a future study to incorporate radiobiological parameters specific for radioembolisation using  $^{90}\text{Y}$  microspheres, even if TRT still lacks fundamental understanding of the underlying radiobiology and dose response. This would allow to further optimise a dosimetric and treatment approaches since dose effects have been established for  $^{90}\text{Y}$ -radioembolisation (Hoven et al., 2016). Other metrics besides the mean absorbed dose can be used for evaluation such as the equivalent uniform dose (EUD), biologically effective dose (BED) and equivalent uniform biologically effective dose (EUBED) such as used in Chiesa et al. (2015). There also seems to be interests in the determination of radiosensitivity parameters towards  $^{90}\text{Y}$ -radioembolisation and better understanding of the dose response of lesions in the liver, such as in a recent study from Lee et al. (2019). Future research on future patients receiving  $^{90}\text{Y}$ -radioembolisation treatment at the CLB should consider characterising the relationship between tumour absorbed dose and response after  $^{90}\text{Y}$ -radioembolisation, such as in the SARAH study (Hermann et al., 2020) and the DOSISPHERE-01 study (Garin et al., 2021).  $^{90}\text{Y}$  PET-derived radiomics could be combined to absorbed dose to improve model building to predict tumour response and progression in  $^{90}\text{Y}$ -radioembolisation treatment, using metrics suggested by Wei et al. (2020) in a recent publication. All these studies could allow to reinforce recommendations as published recently by Salem et al. (2019) and Levillain et al. (2021).

Even if major progress has been made in PET imaging during the recent years, with an improvement of the timing resolution by a factor of 2 using SiPMs instead of PMTs, PVE is still a major limitation to PET image quality and therefore absorbed dose assessments (Rousset, Ma, and Evans, 1998; Soret, Bacharach, and Buvat, 2007; Brodin, 2011; Erlandsson et al., 2012). Our research team at CREATIS/CLB are actually working on the feasibility to further correct PVEs following image reconstruction by a toolkit suggested by Thomas et al. (2016), and recover information using the image datasets acquired during this thesis. PET technology is still perfectible, and the search for better temporal resolution desired at less than 100 ps on clinical systems and increasingly wide axial coverage promises satisfactory results that would improve image quality and quantification. In lab, a 95 ps CTR using SiPMs has been achieved (Seifert et al., 2012). A quest for a 10 picoseconds timing resolution has also been launched, with the use of ultra-fast Cerenkov emission for TOF PET detectors which may allow PET technology to bypass the use of reconstruction algorithms, there can be real time image formation and only attenuation correction would be necessary (Lecoq, 2017; Lecoq et al., 2020). The use of reconstruction algorithms as a matter of fact adds further bias on quantitative data independent of PET performance, as shown in this thesis. Indeed, the TOF information alone may be sufficient to obtain a distribution of the activity concentration with an improved temporal and subsequently spatial resolution, and improved quantification towards post-treatment  $^{90}\text{Y}$ -radioembolisation monitoring. Furthermore, a major step forward has been taken with the installation of the first clinical and commercial eFOV whole-body PET in 2020, featuring a 1 metre compared to traditional 15-30 centimetres long axial FOVs, besides being SiPM-equipped. Benefiting from larger solid angles for detection with various long FOV PET systems being under development (Zhang et al., 2017; Badawi et al., 2019; Vandenberghe, Moskal, and Karp, 2020), PET therefore provides an even more fortifying technology and impact in clinical use.

## Résumé étendu

Le foie est l'une des causes croissantes de mortalité liée au cancer chez les deux sexes, alors que la mortalité due à la plupart des cancers est en baisse<sup>6</sup>. En fonction du diagnostic, du stade de la maladie, de l'état de santé relatif et de la condition physique de chaque patient atteint d'un cancer du foie, plusieurs alternatives thérapeutiques sont toutefois disponibles, y compris le traitement par radioembolisation, également appelé SIRT. La radioembolisation par l'utilisation de microsphères d'<sup>90</sup>Y encapsulées dans du verre ou en résine marquées à l'<sup>90</sup>Y est une méthode intra-artérielle utilisée en pratique clinique pour traiter les tumeurs malignes hépatiques non résécables et chimiorésistantes. Pendant la radioembolisation à l'<sup>90</sup>Y, des millions de microsphères sont administrées dans des branches sélectionnées de l'artère hépatique qui alimentent les tumeurs. La désintégration de l'<sup>90</sup>Y émet des particules  $\beta^-$  de haute énergie qui délivrent des doses absorbées élevées aux tissus environnants du foie où sont situées les tumeurs, tout en préservant de l'irradiation les régions saines non perfusées et les autres organes à risque (OARs). Suite à l'administration du traitement par radioembolisation à l'<sup>90</sup>Y, l'imagerie PET peut être réalisée pour surveiller la biodistribution des microsphères d'<sup>90</sup>Y et évaluer le succès technique de la procédure. Ce suivi est de première importance pour la sécurité du patient et pour progresser vers une dosimétrie personnalisée, permettant d'évaluer la distribution spatiale de la dose absorbée et de faire d'autres prédictions sur le résultat du traitement.

La PET est aujourd'hui la modalité d'imagerie fonctionnelle la plus sensible pour l'étude des interactions moléculaires dans le corps humain. En constante évolution, elle a récemment été équipée de photomultiplicateurs en silicium (SiPMs), remplaçant les tubes photomultiplicateurs (PMT) conventionnels, permettant ainsi une amélioration globale des performances et notamment de la résolution en temps-de-vol (TOF). La PET a également été jugée intéressante par ses performances pour l'imagerie de l'<sup>90</sup>Y. En effet, l'<sup>90</sup>Y est un émetteur pur de  $\beta^-$ , mais possède un rapport d'embranchement lié à une production de paires d' $e^-/e^+$  de  $32.6 \times 10^{-6}$  paires/désintégration. Même si les statistiques de production de positons sont faibles, l'imagerie PET est devenue, depuis une dizaine d'années, la référence pour la surveillance de la radioembolisation par des microsphères d'<sup>90</sup>Y.

Le contexte de cette thèse s'inscrit dans le cadre du suivi du traitement par radioembolisation au moyen de microsphères d'<sup>90</sup>Y en utilisant l'imagerie PET basée sur les SiPMs numérique et les calculs Monte Carlo. La radioembolisation à l'<sup>90</sup>Y est généralement pratiquée dans l'hôpital où s'est déroulée ma thèse, le CLB, cependant, le calcul de la dose absorbée n'est pas systématiquement effectué après le traitement bien qu'une imagerie PET soit toujours réalisée. Le succès technique du traitement est uniquement évalué par la distribution visuelle de la radioactivité des images PET.

L'objectif de cette thèse était double. Tout d'abord, l'accent a été mis sur la simulation du Vereos dans la plateforme GATE afin de la rendre disponible à la communauté scientifique à des fins de recherche. Ensuite, la thèse s'est concentrée sur

6. Voir [The Surveillance, Epidemiology and End Results \(SEER\) Program \(USA\)](#)

l'évaluation des paramètres de reconstruction d'image et des conditions d'imagerie utilisant  $^{90}\text{Y}$  en vue d'une amélioration de la quantification de la dose absorbée pour la radioembolisation à  $^{90}\text{Y}$ . Les analyses ont été réalisées à l'aide de données de fantômes mais également appliquées aux données de patients. Enfin, des comparaisons préliminaires ont été effectuées entre la dosimétrie prédictive au  $^{99\text{m}}\text{Tc-MAA}$  à celle obtenue suite au traitement par microsphères d' $^{90}\text{Y}$ .

Le manuscrit est divisé en deux parties, chacune d'elles comprenant trois chapitres. La *Partie I* (Chapitres 1 à 3) décrit en détail l'état de l'art du traitement par radioembolisation à l'aide de microsphères d' $^{90}\text{Y}$  et de l'imagerie PET. Les techniques de planification du traitement du patient et de dosimétrie pour le suivi du traitement par imagerie PET et les questions relatives à ces techniques y sont détaillées. La *Partie II* (Chapitres 4 à 6) présente les différentes contributions apportées au cours de cette thèse, notamment les simulations Monte Carlo de la PET Vereos de Philips dans GATE, les études expérimentales sur fantôme pour l'évaluation des paramètres de reconstruction pour l'imagerie PET à  $^{90}\text{Y}$  et appliquées aux données des patients pour le calcul de la dose absorbée.

Le *Chapitre 1* décrit d'abord la justification et le contexte clinique du traitement par radioembolisation. Il présente également l'état de l'art des méthodes actuelles de calcul de la dose absorbée à l'aide d'images voxélisées en PET et SPECT. Le *Chapitre 2* est un état de l'art générique sur la PET, de l'émission de positons à la détection de photons par annihilation et à la reconstruction d'images. De plus, il présente les concepts des SiPMs numériques de Philips (DPC), qui sont utilisés dans le système du Vereos, et résume les performances de plusieurs nouveaux systèmes PET cliniques actuels. Le *Chapitre 3* décrit enfin la physique de la désintégration de  $^{90}\text{Y}$  et les facteurs de confusion liés à l'imagerie PET pour la quantification.

Le *Chapitre 4* détaille les travaux réalisés pour la première contribution de cette thèse sur la simulation Monte Carlo de la PET numérique, décrivant les performances simulées du système, avec comparaison aux données expérimentales en accord avec les recommandations de la NEMA. Ce travail a été publié dans *EJNMMI Physics* (Labour et al., 2020). Le *Chapitre 5* présente les résultats de la deuxième contribution réalisée au cours de cette thèse sur l'étude quantitative utilisant le Vereos pour l'imagerie à  $^{90}\text{Y}$ . L'étude visait à évaluer les paramètres de reconstruction et en même temps à réduire la durée d'acquisition avec une dégradation acceptable de la précision des informations obtenues dans les images reconstruites. Cette contribution a été publiée dans *EJNMMI Physics* (Labour et al., 2021). Le *Chapitre 6* utilise les résultats des paramètres de reconstruction et d'acquisition sélectionnés dans la contribution du *Chapitre 5* sur un ensemble de données de patients ayant bénéficié d'une radioembolisation à  $^{90}\text{Y}$  dans notre établissement. Une évaluation préliminaire de la valeur prédictive du substitut  $^{99\text{m}}\text{Tc-MAA}$  aux microsphères d' $^{90}\text{Y}$  a été réalisée en suggérant des approches cohérentes pour l'enregistrement des images.

## I Contexte clinique

### I.1 Le cancer du foie

L'incidence et la mortalité des cancers du foie sont décrites par l'IARC<sup>7</sup>. En 2018, le nombre de nouveaux cas enregistrés pour le cancer du foie chez les deux sexes

7. Voir *Observatoire Mondial du Cancer (OGC) - CIRC/OMS (France,ONU)*

était de 841 100 pour 781 600 décès (Bray et al., 2018), ce qui en fait le sixième cancer le plus fréquemment diagnostiqué et la quatrième cause de mortalité par cancer (Bray et al., 2018 ; Dasgupta et al., 2020). La Figure 1.1 fournit quelques statistiques sur les taux d'incidence et de mortalité des pays de l'EU, où la France se classe respectivement au troisième et au quatrième rang des taux d'incidence et de mortalité. En plus, le cancer du foie est une maladie à prédominance masculine, associée à l'augmentation de l'âge et à de nombreux types de maladies chroniques du foie consécutives à des infections par le virus de l'hépatite B ou C, à une maladie du foie liée à l'alcool ou à une stéatose hépatique non alcoolique, qui est étroitement liée au syndrome métabolique et à l'obésité.

Les deux cancers primaires du foie les plus redoutés sont le HCC, qui représente 75%-85% de la totalité des tumeurs malignes primaires du foie, suivi du ICC qui représente 10%-15% des cas, ainsi que quelques autres types rares (Tischoff et Tannapfel, 2007 ; Bray et al., 2018). Le foie est également un site métastatique courant pour une grande variété de tumeurs primaires provenant d'autres sites de l'organisme (Namasivayam, Martin et Saini, 2007), comme les adénocarcinomes du système GI (par exemple, les cancers colorectaux).

## I.2 Le traitement du cancer du foie

En fonction du diagnostic, du stade, de l'état de santé relatif et de la condition physique de chaque patient atteint d'un cancer du foie, une équipe multidisciplinaire discutera du traitement approprié à administrer. Bien que le pronostic soit souvent mauvais, il existe de nombreuses alternatives pour le traitement du cancer du foie, allant de la guérison aux soins palliatifs ou au BSC. Les patients dont le cancer est détecté à un stade précoce disposent d'un plus large éventail de possibilités de traitement et ont plus de chances de vivre plus longtemps, par rapport à ceux qui se présentent à un stade plus tardif.

## I.3 Justification de la radioembolisation

La radioembolisation ou SIRT est une méthode intra-artérielle utilisée en pratique clinique pour traiter les tumeurs malignes hépatiques non résécables et chimiorésistantes (Lau et al., 1994 ; Salem et al., 2010 ; Sangro et al., 2011 ; Tafti et Padia, 2019). Au cours de la SIRT, des millions de microsphères sont administrées dans une artère, délivrant des doses absorbées élevées aux régions perfusées sélectionnées du foie où se trouvent les lésions hépatiques, tout en préservant les régions saines non perfusées du foie et les autres OARs de l'irradiation (Kennedy et al., 2012), voir la Figure 1.3. La SIRT peut être administrée aux patients atteints de tumeurs malignes du foie qui sont bien vascularisées puisque les microsphères sont transportées par le sang jusqu'à la tumeur, qu'il s'agisse de tumeurs primaires, HCC et ICC, ou de tumeurs secondaires, mCRC, mNETs et SHM de cancers du sein, etc.



## I.4 Propriétés des microsphères

Actuellement, la SIRT peut être réalisée avec deux isotopes, soit avec des microsphères d' $^{90}\text{Y}$  ou de  $^{166}\text{Ho}$ . Trois types de dispositifs médicaux existent, les SIR-Spheres® (Sirtex Medical Limited, North Sydney NSW, Australia, 2020) et TheraSphere™ (Boston Scientifics, Massachusetts, United States, 2020) pour les microsphères d' $^{90}\text{Y}$ , et QuiremSpheres® pour les microsphères d' $^{166}\text{Ho}$  (Quirem Medical BV, Deventer, the Netherlands, 2020). Les propriétés des trois types de microsphères sont résumées dans le Tableau 1.1.

## I.5 La radioembolisation à l' $^{90}\text{Y}$

Lors d'une radioembolisation à l' $^{90}\text{Y}$ , les particules d' $^{90}\text{Y}$  émettrices de  $\beta^-$  de haute énergie, encapsulées dans des microsphères de verre ou de résine marquée, voir le Tableau 1.1, sont administrées par des branches sélectionnées de l'artère hépatique qui alimentent les tumeurs. Cette méthode assure une biodistribution locale des microsphères d' $^{90}\text{Y}$  délivrant une dose absorbée très localisée dans les régions perfusées, épargnant les OARs et les tissus sains voisins avec l'avantage d'une irradiation négligeable des parties non embolisées et des tissus extra-hépatiques (compte tenu de la portée maximale des particules  $\beta^-$  autour du site de dépôt), consultez la Figure 1.3. La radioembolisation à l' $^{90}\text{Y}$  est largement utilisée en raison de son efficacité clinique et de sa sécurité relative (Lau et al., 1994 ; Sato et al., 2008 ; Kennedy et al., 2009 ; Salem et al., 2010 ; Sangro et al., 2011 ; Garin et al., 2021).

Avant le traitement par SIRT, les patients subissent une angiographie approfondie pour cartographier les vaisseaux artériels alimentant la tumeur et des particules de substitution qui imitent la distribution des microsphères sont administrées pour évaluer la présence de shunts pulmonaires et GI. Ces différentes étapes sont nécessaires pour une planification individualisée du traitement afin de maximiser et de garantir la sécurité et l'efficacité de la thérapie.

### I.5.1 Étape du pré-traitement

Afin d'éviter ou de limiter l'impact des effets secondaires et de la toxicité possibles, une procédure d'examen de simulation préalable au traitement est effectuée avant et pas plus de 2 semaines avant la radioembolisation à l' $^{90}\text{Y}$  (en raison de la progression possible de la maladie) en utilisant les particules de substitution, le  $^{99m}\text{Tc}$ -MAA, dont la taille correspond approximativement à celle des microsphères. Le  $^{99m}\text{Tc}$  est un émetteur gamma pur ( $\gamma$ ) avec un pic d'énergie photonique de 140 keV et sa demi-vie physique est relativement courte ( $\sim 6$  heures), ce qui permet un large éventail de procédures d'imagerie, tout en maintenant l'exposition totale du patient aux rayonnements à un niveau faible. Les propriétés du  $^{99m}\text{Tc}$ -MAA sont indiquées dans le Tableau 1.1.

**Scintigraphie planaire et SPECT/CT.** Après l'injection de  $^{99m}\text{Tc}$ -MAA, une scintigraphie planaire et/ou, si possible, une imagerie par gamma-caméra 3D-SPECT sont réalisées, comme le montrent les Figures 1.6 et 1.7. L'utilisation de ces deux dernières plateformes est multiple. Elles permettent de : (1) de détecter également tout dépôt extrahépatique de l'activité transportée par le système vasculaire hépatique vers le parenchyme hépatique non ciblé ou les OARs, (2) calculer la LSF qui est la proportion de matière radioactive qui a atteint les poumons vraisemblablement en raison

d'une migration via les shunts hépatopulmonaires, consultez la Section 1.4.1.1, (3) simuler le résultat de la distribution spatiale de  $^{90}\text{Y}$  pendant la phase de traitement, (4) adapter l'activité de  $^{90}\text{Y}$  à injecter pendant le traitement qui dépend du type de microsphère et (5) estimer si possible la distribution de la dose absorbée dans les régions tumorales perfusées d'intérêt et le tissu hépatique. L'imagerie doit être réalisée dans l'heure qui suit l'injection en raison de la dégradation des particules de  $^{99\text{m}}\text{Tc-MAA}$  (Grosser et al., 2016).

### I.5.2 Étape du traitement

Dans les deux semaines qui suivent la prescription de  $^{90}\text{Y}$  avec la procédure utilisant le  $^{99\text{m}}\text{Tc-MAA}$  de substitution, l'administration des microsphères d' $^{90}\text{Y}$  est réalisée en utilisant la même position de cathétérisation dans la vasculature hépatique sélectionnée qui est le site de traitement. Levillain et al. (2021) recommandent (recommandation R17) de réaliser SIRT dès que possible après la simulation et au maximum quatre semaines après la simulation pour les microsphères en résine.

**Suivi post-traitement.** Bien que si le shunt pulmonaire calculé par les images de la planification de traitement à l'aide de  $^{99\text{m}}\text{Tc-MAA}$  prédit le shunt pulmonaire pour les microsphères d' $^{90}\text{Y}$  (Jha et al., 2012), des différences peuvent apparaître entre la biodistribution du MAA et des microsphères, ce qui donne lieu à des prédictions imprécises (voir Section 1.7 et Chapitre 6 pour les limitations du  $^{99\text{m}}\text{Tc-MAA}$ ). Il convient donc de surveiller la biodistribution des microsphères après la procédure d'administration des SIRT afin d'évaluer le succès technique de la procédure et de détecter un éventuel dépôt non ciblé pour prendre les mesures nécessaires le plus tôt possible après le traitement en cas de dépôts extra-hépatiques (par exemple dans le tractus GI). Les normes d'excellence pour ce contrôle peuvent être réalisées en utilisant le BremSPECT/CT ou PET/CT, qui permettent en plus une évaluation de la distribution spatiale de la dose absorbée et d'autres prédictions sur le résultat du traitement (Lhommel et al., 2010; D'Arienzo et al., 2012). La Figure 1.9 montre une comparaison visuelle des images obtenues après l'injection de  $^{99\text{m}}\text{Tc-MAA}$  et après l'injection de microsphères d' $^{90}\text{Y}$ .

### I.6 Prescription de l'activité

Une description détaillée de la prescription de l'activité personnalisée par type de dispositif médical est présentée dans la Section 1.4. La SPECT/CT est préférablement utilisée, voir la Figure 1.7, pour surmonter les limites des images planaires telles que le manque d'informations 3D, la correction des densités et hétérogénéités tissulaires et la correction de l'atténuation. L'objectif de cette évaluation est l'adaptation de l'activité d' $^{90}\text{Y}$  à administrer pendant la SIRT pour une dosimétrie personnalisée pour chaque patient.

### I.7 Radionucléides alternatifs à $^{90}\text{Y}$ pour la radioembolisation

Les microsphères contenant du  $^{166}\text{Ho}$  (Quirem Medical BV, Deventer, the Netherlands, 2020) constituent une alternative aux microsphères d' $^{90}\text{Y}$ . Les spécifications du  $^{166}\text{Ho}$  par rapport aux microsphères d' $^{90}\text{Y}$  sont également fournies dans le Tableau 1.1. Les microsphères d' $^{166}\text{Ho}$  émettent des rayons  $\gamma$  de faible énergie, ce qui rend possible la visualisation des microsphères perfusées dans les patients à l'aide

de la SPECT/CT ; mais la spécificité supplémentaire étant que le  $^{166}\text{Ho}$  et son produit de désintégration  $^{166}\text{Er}$  sont tous deux des lanthanides<sup>8</sup> et présentent donc des propriétés paramagnétiques. La visualisation des microsphères est donc possible par MRI du métal. Cependant, même si la MRI a une résolution plus élevée et peut facilement être combinée avec des scanners anatomiques, il n'est pas adapté aux tissus contenant de l'air ou aux tissus contenant des métaux (tels que les coils placés pour le traitement) (Reinders et al., 2019). En raison de sa demi-vie plus courte que celle de  $^{90}\text{Y}$  et des différences dans les spectres d'énergie, une activité plus importante est nécessaire lors de l'utilisation du  $^{166}\text{Ho}$  pour atteindre des doses absorbées comparables. Par conséquent, 90% du rayonnement est libéré dans les 4 premiers jours d'irradiation, contre 11 jours pour  $^{90}\text{Y}$ .

## I.8 Calculs dosimétriques en radiothérapie interne

La Section 1.6 décrit les différents algorithmes possibles pour calculer la dose absorbée pour la TRT et pour la SIRT. Les méthodes de calcul utilisées pour la dosimétrie de la TRT partent de la macrodosimétrie de référence la plus courante, basée sur un modèle et utilisant des *S-values* pour des organes cibles entiers. Cette dernière méthode néglige toutefois les hétérogénéités dans les distributions des sources radioactives biologiques et les densités des tissus cibles et n'est pas représentative de toutes les variations de la morphologie réelle des patients.

D'autres méthodes basées sur des distributions d'activité non uniformes ont été proposées pour permettre une dosimétrie plus précise basée sur les voxels. Les méthodes actuelles font appel à des simulations numériques de Monte Carlo, à des méthodes de convolution analytiques utilisant des modélisations PK ou VK utilisant de *S-values* et le formalisme du MIRD (Bolch et al., 2009) et également à une dosimétrie voxel analytique plus simplifiée du MIRD utilisant le LDM. Ces dernières méthodes tiennent en compte les distributions de sources plus réalistes et, si possible, des hétérogénéités tissulaires, mais avec des niveaux de précision différents.

Les calculs en dosimétrie interne peuvent être effectués sur une large gamme de dimensions de la cible, en commençant par les organes entiers jusqu'aux niveaux cellulaires, en passant par les tissus à petite échelle. Cependant, ils dépendent des modalités d'imagerie disponibles et de la résolution des ensembles d'images de sortie, qui sont aujourd'hui de préférence présentés sous forme de cartes de voxels 3D. Les images fonctionnelles SPECT et PET sont généralement employées dans la dosimétrie clinique des patients pour évaluer l'absorption biologique des radiopharmaceutiques, tandis que la modalité anatomique CT peut fournir des informations sur la composition des tissus. Aujourd'hui, les systèmes bi-modaux tels que l'imagerie SPECT/CT et PET/CT ont été évalués pour le calcul de la dose absorbée dans les applications de médecine nucléaire.

## I.9 Conclusion

La radioembolisation nécessite l'utilisation de plusieurs techniques d'imagerie afin de planifier, délivrer et vérifier le succès technique du traitement. Plusieurs méthodes existent pour prescrire l'activité des microsphères et des recommandations ont récemment été publiées par Salem et al. (2019) et Levillain et al. (2021) afin d'adapter au mieux le traitement à chaque patient pour chaque type de microsphère. L'utilisation de la SPECT/CT pour le prétraitement ainsi que de la PET/CT pour le suivi du traitement est cruciale pour personnaliser le traitement (Garin et al., 2021).

8. Voir [Wikipedia/Lanthanides](#)

L'accent est mis sur l'imagerie PET/CT dans les sections suivantes, étudiée dans cette thèse pour la radioembolisation.

## II La tomographie par emission de positons

Des progrès majeurs ont été réalisés ces dernières années en imagerie PET. En plus de l'amélioration de la précision de la position de l'interaction et du gain SNR par l'incorporation des informations TOF dans la reconstruction tomographique, des développements significatifs avec l'émergence de la technologie SiPM et de l'électronique plus rapide permettent des capacités de détection de coïncidence plus efficaces. Les SiPM apportent des avantages supplémentaires, renforçant le rôle des PET dans le diagnostic et la stadification des maladies humaines. La PET semble donc rester la modalité d'imagerie fonctionnelle la plus sensible en médecine nucléaire, permettant de visualiser le métabolisme des cellules et des organes, par opposition au CT ou à la MRI morphologique qui permettent d'imager l'anatomie avec une bonne résolution spatiale. Aujourd'hui, tous les systèmes PET sont équipés d'un CT (ou MRI) qui fournit des informations supplémentaires pour aider à localiser plus précisément les anomalies fonctionnelles, avec des corrections d'atténuation des photons (CTAC) et PVE.

### II.1 Radionucléides utilisés en PET

L'imagerie PET bénéficie avant tout de la physique des isotopes émetteurs de positons ( $\beta^+$  ou  $e^+$ ). Les propriétés d'une liste de radionucléides utilisés en PET sont présentées dans le Tableau 2.1. Bon nombre des émetteurs les plus utilisés ont une demi-vie courte ( $T_{1/2}$ ), par exemple l' $^{15}\text{O}$  et le  $^{13}\text{N}$ , ce qui limite leur utilisation en recherche ou dans les hôpitaux à la disponibilité d'un cyclotron sur place ou à proximité<sup>9</sup>. Il est également possible de produire des isotopes en utilisant des générateurs, par exemple les générateurs  $^{68}\text{Ge}/^{68}\text{Ga}$  et  $^{82}\text{Sr}/^{82}\text{Rb}$  (Knapp et Mirzadeh, 1994; Dash et Chakravarty, 2019).

### II.2 Désintégration $\beta^+$

#### II.2.1 Émission de positons

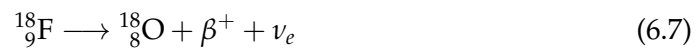
Le positon ( $e^+$ ) est l'antiparticule de l'électron ( $e^-$ ). Ils ont des masses similaires mais diffèrent en ce qu'un positon a une charge électrique positive, alors qu'un électron a une charge négative. Les positons sont émis par le processus de désintégration nucléaire  $\beta^+$  des noyaux instables qui ont un excès de protons ( $p$ ), l'émission de  $\beta^+$  est donc induite par l'interaction faible<sup>10</sup>. Fondamentalement, un proton dans le noyau de l'atome est transformé en un neutron ( $n$ ) et un positon comme le montrent les équations 6.5 et 6.6, la seconde étant générique pour tout isotope parent se désintégrant  $^A_Z\text{X}$  en son produit fils  $^A_{Z-1}\text{Y}$ , et l'atome retrouve sa stabilité nucléaire.



9. Voir [Wikipedia/Cyclotron](#)

10. Voir [Wikipedia/Weak interaction](#)

Le positon est éjecté du noyau accompagné d'un neutrino ( $\nu_e$ ). Un exemple pour le  $^{18}\text{F}$  qui émet un rayonnement  $\beta^+$  et se désintègre en  $^{18}\text{O}$  est présenté dans l'équation 6.7.



## II.2.2 Annihilation de positon

Le positon se thermalise rapidement après avoir été éjecté du noyau. Dès qu'il s'est thermalisé, il se combine directement avec un électron de spin opposé au repos, ce qui entraîne une annihilation de 2 photons gamma ( $2\text{-}\gamma$ ), ou bien il peut former des particules neutres de courte durée ( $10^{-7}\text{s}$ ) appelées positroniums (l'état lié d'un électron et d'un positon). Les positroniums existent sous la forme soit de para-positronium qui entraîne également une annihilation en  $2\text{-}\gamma$ , soit d'ortho-positronium qui se désintègre en  $3\text{-}\gamma$  (Harpen, 2003). Malgré cela, la plupart des annihilations dans les tissus donnent lieu à une émission utile de rayons  $2\text{-}\gamma$  (Harpen, 2003), qui est à la base de la détection de la PET.

## II.2.3 Interactions des $\gamma$ s de 0,511 MeV avec la matière

Pour rappel, les définitions des différentes interactions des photons dans la matière sont données ci-après. L'effet photoélectrique et la diffusion Compton sont les deux principales interactions photoniques qui nous intéressent en PET. Les photons ne provoquent pas directement des ionisations comme cela se produit avec le transport de particules chargées (qui ne sera pas détaillé ici), mais peuvent être classés comme rayonnement d'ionisation secondaire. Les interactions les plus probables des photons de 0,511 MeV sont représentées sur la Figure 2.4 (gauche).

**L'effet photoélectrique.** Le photon subit un effet photoélectrique lorsqu'il est absorbé complètement par un atome et que la totalité de son énergie est transférée à un électron orbital dans les couches internes. Si la valeur de  $E_\gamma$  est supérieure à l'énergie de liaison de l'électron, ce dernier gagne suffisamment d'énergie et s'échappe de son orbitale (le photoélectron), laissant une place vacante dans la couche électronique interne. Il y a alors libération d'énergie (due au déplacement d'un électron de la couche externe vers la coquille interne vacante) qui peut provoquer l'émission d'un photon de fluorescence X, ou être transmise à un électron atomique qui sera éjecté de l'atome, appelé électron Auger. Plus le numéro atomique ( $Z$ ) ou le  $Z$  effectif ( $Z_{eff}$ ) du milieu est élevé, plus l'interaction photoélectrique est probable. À 0,511 MeV, cette probabilité est approximativement proportionnelle à  $Z^3$  ou  $4$ ,  $E_\gamma^{-3}$  à  $-5$  et varie linéairement avec la densité ( $\rho$ , c'est-à-dire la masse par unité de volume) des matériaux.

**Diffusion incohérente ou Compton.** Le photon subit une interaction de préférence avec un électron en orbite dans la couche externe, transférant une partie de son énergie (supérieure à l'énergie de liaison) à l'électron. Cet électron est éjecté (l'électron de recul) et le photon est dévié par un angle de diffusion avec son énergie restante. Une relation claire existe entre l' $E_\gamma$  du photon diffusé et l'angle de diffusion  $\theta$  compte tenu des lois de conservation de l'énergie et de la quantité de mouvement (qui ne seront pas détaillées ici, voir Agarwal (1991), Cherry et Dahlbom (2006) et Cherry, Sorenson et Phelps (2012)). Comme l'interaction de diffusion Compton dépend principalement des électrons considérés comme 'libres' avec des liaisons

faibles avec le noyau, elle dépend donc moins de  $Z$  et de  $E_\gamma$  de l'électron incident, mais surtout de la densité électronique  $\rho_e$ . La diffusion Compton est le principal type d'interaction des photons dans les tissus mous.

À 0,511 MeV, le photon a trop ou trop peu d'énergie et il est moins probable qu'il subisse une diffusion cohérente ou une production de paires (respectivement) qu'un effet photoélectrique ou une diffusion Compton.

### II.3 Atténuation des photons dans la matière

Les photons ne provoquent pas directement d'ionisations, lorsqu'ils traversent la matière mais sont atténués par les diverses interactions, en fonction de leur propre énergie cinétique  $E_\gamma$  et des propriétés de  $Z$  ou  $Z_{eff}$ , de la densité  $\rho$  et de l'épaisseur  $D$  du milieu de transport. L'atténuation des photons peut être calculée à l'aide de l'équation 6.8.

$$I(x = D) = I_0 \cdot e^{-\int_0^D \mu_l(E_\gamma, x) dx} \quad (6.8)$$

où  $I_0$  et  $I(x = D)$  sont les intensités de photons : 1) sans matériaux atténuants (absorbeurs, par exemple le corps du patient avec différentes densités de tissu) et 2) transmis après avoir traversé les absorbeurs (par exemple le corps du patient avec une épaisseur variable  $0 \leq x \leq D$ ), respectivement. Le paramètre  $\mu_l(E_\gamma, x)$  est le coefficient d'atténuation linéaire. Il correspond à la probabilité d'interaction par unité de distance en fonction de  $E_\gamma$ , et  $x$ .  $\mu_l$  peut être donné par l'équation 6.9 en considérant l'atténuation linéaire pour l'effet photoélectrique ( $\mu_{PE}$ ) et la diffusion Compton ( $\mu_C$ ).

$$\mu_l \approx \mu_{PE} + \mu_C \quad (6.9)$$

Dans le cas de l'imagerie PET, trois types de milieux sont susceptibles d'atténuer les photons d'annihilation : 1) les tissus mous et les os, 2) les matériaux scintillateurs tels que LSO/LYSO et 3) les matériaux utilisés pour le blindage. Le Tableau 2.2 fournit les  $\mu_l$  à 0,511 MeV dans différents matériaux susceptibles d'agir comme milieux absorbants dans l'imagerie PET.

### II.4 Les principes de l'imagerie PET

Des photons d'annihilation  $2_\gamma$  de  $0,511 \pm \Delta E_\gamma$  MeV sont émis à  $180^\circ \pm \Delta\theta$  en coïncidence et sont détectés par des détecteurs placés dans des directions opposées, sur un ou plusieurs anneaux pour la détection 3D. Une logique simplifiée de détection de coïncidence est illustrée dans la Figure 2.5. Un ensemble de nouvelles méthodes de détection des 3D et une électronique de pointe améliorée sont utilisées pour discriminer les photons entrants, car différents types de rayonnements de photons primaires et secondaires peuvent être émis et confondre la détection des photons d'annihilation.

**Types d'événements pour la détection des coïncidences :** Une fois qu'un événement de coïncidence est enregistré par un LOR, la position de l'interaction des photons (dans le détecteur), l'énergie et le temps d'arrivée dans les fenêtres de coïncidence de chaque paire de photons sont enregistrés. La différence de TOF entre les deux photons est également enregistrée, consultez la Section 2.7. Cependant, en raison des performances et des limites des systèmes de détection et des interactions des

photons dans le volume d'émission (par exemple le corps humain), les informations de tous les LOR ne fournissent pas les informations correctes et la détection est confondue par des événements indésirables. Les coïncidences sont classées en quatre groupes différents : les *vraies* (les seules souhaitées), les *diffusées* et *fortuites* (les indésirables), et les *multiplés* (un choix ambigu doit être fait pour le bon LOR dans ce cas). Chacune d'entre elles est appelée une *coïncidence*, représentée sur la Figure 2.6.

## II.5 Sources d'erreur contribuant à la résolution spatiale de la PET

Différentes sources d'erreur influent sur la résolution spatiale des systèmes PET. Le biais intrinsèque (avant la reconstruction de l'image PET) dans la détection PET a été abordé dans le Chapitre 2, voir la Figure 2.1 pour les erreurs du parcours du positon et la de non-collinéarité des photons d'annihilation. Les contributions des autres sources d'erreur sont aussi discutées et décrites quantitativement.

Un résumé des différentes contributions à la résolution spatiale est schématisé dans la Figure 2.8. On suppose que leur addition se fait en quadrature (bien que toutes ne soient pas décrites par des fonctions Gaussiennes). Par conséquent, la résolution spatiale reconstruite  $\Gamma$  pour une source ponctuelle située à un rayon  $r$  du centre du FOV radial est décrite par l'équation 6.10.

$$\Gamma \text{ [mm à FWHM]} = 1.25 \sqrt{(d/2)^2 + s^2 + (0.0022D)^2 + b^2 + \frac{(12.5r)^2}{r^2 + (D/2)^2}} \quad (6.10)$$

où  $s$  est la distance parcourue par le positon,  $D$  le diamètre du tomographe et  $b$  est l'erreur du facteur de décodage du cristal ( $b = d/3$  pour les détecteurs qui utilisent un décodage optique ou 0 sinon).

## II.6 PET temps-de-vol

L'incorporation de l'information TOF a amélioré les capacités de l'imagerie PET (Surti, 2015), en améliorant le NEC et le SNR, donc la qualité de l'image. La localisation du point d'émission des photons d'annihilation dépend de l'information TOF, à savoir la détection de la différence de temps entre les deux photons d'annihilation, comme le montre la Figure 2.9. La rétroprojection de l'information sur les LOR est limitée à un nombre restreint de voxels utilisant l'information TOF par rapport aux PET sans TOF dans la matrice de l'image reconstruite. L'équation 6.11 donne la relation simple pour déterminer la position de l'interaction  $\Delta X$  à partir du centre du LOR (c'est-à-dire la distance entre deux détecteurs opposés).

$$\Delta X = \frac{|t_2 - t_1| \times c}{2} = \frac{\Delta T \times c}{2} \quad (6.11)$$

où  $c$  est la vitesse de la lumière et  $\Delta T$  la différence d'information temporelle, se référer à la Figure 2.9.

## II.7 Cristaux scintillateurs

Le système de détection de photons est basé sur deux détecteurs assemblés ensemble, le scintillateur (organique ou inorganique) et le photodétecteur (par exemple, les PMTs, les photodiodes, les SiPMs). Les scintillateurs convertissent l'énergie déposée par les  $\gamma$ s de 0,511 MeV par luminescence en photons visibles

et sont détectés par des photodétecteurs. Pour l'imagerie PET, on utilise des scintillateurs inorganiques sous forme de cristaux solides. Le Tableau 2.3 fournit les propriétés de différents cristaux scintillateurs intrinsèques et extrinsèques activés (par exemple, impureté dopé au césium) couramment utilisés en PET. Consultez la Section 2.8.

## II.8 Principes de fonctionnement des photodétecteurs

### II.8.1 Tubes photomultiplicateurs (PMTs)

Les PMTs convertissent la lumière de scintillation en une impulsion électrique détectable par multiplication des électrons. Les PMT ont été les premiers à être utilisés pour l'imagerie PET, mais ils sont aujourd'hui supplantés par les progrès récents de la technologie SiPM pour la détection optique des photons. La figure 2.10 présente une esquisse de la structure d'un PMT conventionnel, composé d'une photocathode et de plusieurs électrodes enfermées dans un tube à vide (en verre, céramique, métaux) dans un champ électrique. Pour plus de détail sur le fonctionnement des PMTs, Consultez la Section 2.9.1.

### II.8.2 Photomultiplicateurs en silicium (SiPMs)

Le principal développement en matière de détection de photons pour l'imagerie PET au cours de cette dernière décennie est la technologie SiPM. Elle utilise des réseaux de SPAD, qui sont des APD fonctionnant en mode de polarisation inverse quelques volts au-dessus de la tension de claquage, fonctionnant en mode Geiger, voir la Figure 2.11. Les SiPMs offrent beaucoup plus d'avantages que les APDs. Ils peuvent être de taille beaucoup plus petite ( $\mu\text{m}$  de côtés) et peuvent être compactés par milliers. Ils permettent la détection de photons uniques avec une excellente résolution temporelle (le SPTR) en raison de la faible gigue temporelle en mode Geiger (augmentation exponentielle du courant) et de l'étroite région d'amplification où le signal est produit. Les SPADs offrent un meilleur contrôle de la linéarité, des résolutions temporelles et spatiales améliorées et des applications TOF pour l'imagerie PET, par rapport aux APD, voir la Section 2.10. Ils ont un gain comparable à celui des PMT, de l'ordre de  $10^6$  et peuvent fonctionner numériquement en comptant les photons incidents au lieu de produire un courant amplifié comme avec les APD. Un aperçu des principes du composant de base de la cellule SiPM, c'est-à-dire le SPAD, et des types de SiPM existants : aSiPM et dSiPM, sont abordés dans la Section 2.9.3. Les principes de fonctionnement du DPC de Philips y sont aussi détaillées.

## II.9 Acquisition et reconstruction tomographique des données PET

L'objectif de la reconstruction d'image en PET est de transformer les informations des LORs individuels acquis en données quantitatives 3D, qui sont la concentration d'activité en  $\text{Bq.mL}^{-1}$  dans chaque voxel reconstruit présent dans le FOV. Les Sections 2.13 et 2.14 présentent les modes d'acquisition 2D et 3D pour l'imagerie PET, le format de stockage de données en sinogrammes ou mode liste, ainsi que les algorithmes de reconstruction tomographiques.



### III La physique de $^{90}\text{Y}$ pour l'imagerie PET

Comme exposé dans le Chapitre 1,  $^{90}\text{Y}$  est utilisé comme radioisotope pour le traitement des cancers du foie par radioembolisation. Alors qu'il s'agit d'un émetteur bêta pur, ce qui le rend adapté à la thérapie, il existe également un phénomène de production interne de paires ( $e^-e^+$ ) dans le schéma de désintégration de  $^{90}\text{Y}$ , provenant d'une transition monopolaire électrique rare (E0) entre les états  $0^+ / 0^+$  du  $^{90}\text{Zr}$ . Cette propriété peut donc être exploitée pour la détection de photons d'annihilation de 0,511 MeV à l'aide de systèmes d'imagerie PET, dont l'état de l'art est présenté dans le Chapitre 2.

#### III.1 Propriétés et schéma de désintégration de $^{90}\text{Y}$

$^{90}\text{Y}$  est un émetteur  $\beta^-$  pur, qui ne produit que des électrons au cours de sa désintégration en ses produits de filiation, principalement au niveau fondamental du  $^{90}\text{Zr}$ , et dans une bien moindre mesure à un état excité du  $^{90}\text{Zr}$ . Il fait partie d'une minorité de radionucléides qui n'émettent pas de rayons gamma à un taux significatif après leur désintégration. Son schéma de désintégration est présenté dans la Figure 3.1. Les propriétés de  $^{90}\text{Y}$  ont été fournies dans le Tableau 1.1 du Chapitre 1.  $^{90}\text{Y}$  a une demi-vie de 64,04 h. L'énergie moyenne du spectre du  $\beta^-$  est égale à 0,927 MeV (avec un maximum de 2,28 MeV). L'ensemble du spectre  $\beta^-$  est représenté sur la Figure 3.2. Nous verrons qu'il y a aussi une très petite production de positons pendant le processus de désintégration de  $^{90}\text{Y}$ , ce qui est intéressant pour cette thèse.

#### III.2 La production de paires internes et son rapport de branchement

##### III.2.1 Transition $0^+ \rightarrow 0^+$ du $^{90}\text{Zr}$

$^{90}\text{Y}$  a une partie rare de son rapport de branchement ( $\beta_{01}^-$ ) qui se désintègre au premier état excité  $0^+$  du  $^{90}\text{Zr}$  à un niveau d'énergie égal à 1,76 MeV. La déséxcitation qui suit du premier état excité  $0^+$  vers l'état stable fondamental du  $^{90}\text{Zr}$  peut entraîner la création d'une paire interne électron-positon ( $\beta^- / \beta^+$ ) si l'énergie excitée est supérieure à 1,022 MeV. La transition qui se produit est une transition monopolaire électrique  $0^+ \rightarrow 0^+$  du  $^{90}\text{Zr}$  et il n'y a aucune modification de la composition des noyaux parent (excité) et fille (stable) et les transitions gamma simples sont absolument interdites (contrairement aux états excités typiques). Pour une revue détaillée des modes de désintégration de  $^{90}\text{Y}$  et l'explication de la transition monopolaire  $0^+ \rightarrow 0^+$  des états du  $^{90}\text{Zr}$ , les lecteurs peuvent se référer à D'Arienzo (2013) et Deutsch (1957) (entre autres).

##### III.2.2 Rapport de branchement des positons et contexte historique

Ford (1955) prévoyait théoriquement que le premier état excité du  $^{90}\text{Zr}$  pourrait être un  $0^+$ . Cette prédiction a été mise en évidence la même année par Johnson, Johnson et Langer (1955) travaillant dans le même laboratoire. À l'époque, ils ont observé une raie de transition de 1,75 MeV (avec un FWHM de 0,5%) sur leur spectromètre dans leur montage expérimental utilisant une source d' $^{90}\text{Y}$  correspondant à des événements de conversion interne avec une intensité de 0,005% par rapport au spectre  $\beta^-$  de 2,26 MeV. Plusieurs études expérimentales ont suivi pour mesurer plus précisément la production de paires internes par désintégration de  $\beta^-$ ,  $w_p/w_\beta$ . Les valeurs trouvées dans la littérature sont fournies dans le Tableau 3.2.

### III.3 Facteurs de confusion de l'imagerie PET à $^{90}\text{Y}$

Pour rappel, le but premier de l'utilisation de  $^{90}\text{Y}$  en médecine nucléaire est la thérapie. Ses caractéristiques d'émission radioactive permettent un suivi post-traitement par imagerie tomographique d'émission. L'utilisation de la SPECT et ses inconvénients inhérents ont été mis discutés dans les chapitres précédents.  $^{90}\text{Y}$  est également un traceur PET défavorable par rapport à ceux couramment utilisés à des fins de diagnostic. Cette section mentionne les facteurs de confusion dans la quantification utilisant la PET pour l'imagerie de  $^{90}\text{Y}$ . Il s'agit des faibles statistiques dues au faible rapport d'embranchement du  $\beta^+$  décrit précédemment et de la difficulté de détecter des coups utiles parmi le fond naturel de radioactivité du  $^{176}\text{Lu}$  (présente dans les cristaux de LYSO/LSO) émettant des impulsions gamma qui tombent dans la fenêtre d'énergie pour la détection de coïncidence et le rayonnement X du spectre de désintégration du  $^{90}\text{Y}$  autour du pic de 511 keV.

Strydhorst et al. (2016) ont étudié l'impact des facteurs de confusion compromettant la quantification de  $^{90}\text{Y}$  à l'aide de la PET, en comparant leurs expériences sur fantôme (comparant les mesures de  $^{90}\text{Y}$  et de  $^{18}\text{F}$ ) aux simulations Monte Carlo utilisant GATE. Pour résumer leurs résultats, aucune influence significative n'a été détectée sur la quantification de  $^{90}\text{Y}$  qui pourrait être attribuée à la présence de comptages aléatoires en utilisant les simulations et rejoignent les résultats de Carlier et al. (2015), permettant aux données d'être corrigées de la désintégration pour obtenir une quantification adéquate.

### III.4 Autres facteurs limitant la quantification en PET

Plusieurs autres facteurs confondent la quantification en tomographie d'émission, moins spécifiques à un radiotraceur PET particulier. Les limites des processus physiques impliqués (parcours des positons, non-collinéarité des photons d'annihilation, atténuation, diffusion) et du système de détection du PET ont été présentées dans le Chapitre 2 et ajoutent un biais supplémentaire à la quantification de l'activité, voir la Section 2.6 et la Figure 2.8. Pour la PET, plusieurs méthodes de correction sont disponibles pour limiter ces facteurs de dégradation, notamment les effets d'arc, la normalisation, l'atténuation, les coïncidences aléatoires et diffusés, les corrections de temps mort et d'empilements et les effets de volume partiel. Les méthodes de correction ne seront pas détaillées dans cette thèse, mais un état de l'art complet peut être trouvé dans Salvadori (2020), *Partie I-Chapitre VI-Corrections et quantification*.

### III.5 Imagerie de $^{90}\text{Y}$ par tomographie par émission

L'imagerie SPECT de  $^{90}\text{Y}$  exploite les rayons X de freinage, avec différentes fenêtres d'énergie publiées, et a été utilisée pour l'évaluation post-SIRT. Cependant, malgré l'utilisation courante de la SPECT/CT, elle présente un certain nombre d'inconvénients.

Nickles et al. (2004) ont d'abord exploité le rapport de branchement des positons mineurs pour l'imagerie PET de  $^{90}\text{Y}$  pour montrer la distribution de la dose absorbée délivrée par les thérapies à  $^{90}\text{Y}$ . L'évaluation de la distribution de l'activité après la radioembolisation à  $^{90}\text{Y}$  s'est avérée possible en 2010 par Lhommel et al., 2009, 2010, grâce aux informations TOF ajoutées sur les systèmes PET/CT. D'autres études ont suivi et ont montré que les PET avec TOF comparés aux PET sans TOF fournissaient une meilleure récupération dans les données quantitatives reconstruites. Bien qu'il ait été démontré que les scanners PET de routine peuvent produire

des images  $^{90}\text{Y}$  de bonne qualité, d'autres études sont nécessaires pour déterminer quelles méthodes de reconstruction et quels paramètres d'acquisition doivent être utilisés (Van Elmbt et al., 2011 ; Pasciak et al., 2014).

### III.6 Conclusion

La PET/CT avec l'information TOF incorporée dans la reconstruction de l'image offre la possibilité de mesurer avec précision la concentration de l'activité  $^{90}\text{Y}$  malgré le faible rapport de branchement des positons de l' $^{90}\text{Y}$ , avec un degré de précision raisonnable. Il a été démontré que la contribution des rayons X de freinage et la radioactivité de fond ont une contribution négligeable sur la quantification de l' $^{90}\text{Y}$  en utilisant la PET et il y a peu de marge pour prendre en compte ces propriétés spécifiques. Les principales limites sont la production de positons rares, les performances de la PET elle-même (par exemple, la résolution spatiale) et la précision des algorithmes de reconstruction. Il est donc nécessaire de sélectionner avec précaution les paramètres de reconstruction qui peuvent améliorer la précision quantitative et le choix optimal dépendra du scanner et du logiciel de reconstruction.

## IV Simulation Monte Carlo de la PET numérique

Un modèle Monte Carlo GATE du Vereos DPC-PET utilisant des détecteurs SiPM est proposé. Ce chapitre est adapté de Labour et al. (2020) et cette publication est le résultat d'une collaboration fructueuse avec Julien Salvadori du laboratoire IADI de Nancy. Julien Salvadori et moi-même contribuons à parts égales à la publication en tant que premiers auteurs joints.

### IV.1 Introduction

L'imagerie PET joue un rôle essentiel dans la médecine moderne, tant pour le diagnostic que pour le suivi des traitements oncologiques (Cherry, Sorenson et Phelps, 2012), comme décrit dans la Partie I de cette thèse. Il a été démontré que la technologie PET a connu d'énormes améliorations en termes de performances au cours des dernières décennies et les nouvelles tendances font appel à des détecteurs SiPM, tels que le DPC Vereos PET/CT de Philips introduit en 2013, le GE Discovery<sup>TM</sup> MI PET/CT lancé en 2016 et le Siemens Biograph Vision<sup>TM</sup> et eFOV Vision Quadra<sup>TM</sup> PET/CT lancés respectivement en 2018 et 2020.

La détection et le traitement des signaux à l'aide des DPC dSiPMs évitent de devoir traiter les signaux analogues, par un comptage binaire direct des photons optiques, réduisant ainsi le bruit dans la sortie traitée, offrant de meilleures conditions pour l'imagerie que les PMTs à faibles comptages comme décrit dans les Chapitres 1 et 3. Le DPC du Vereos présente les caractéristiques d'un couplage 1 : 1 entre le groupement de cristaux et le groupement des dSiPMs, ce qui diminue l'incertitude de la position d'interaction et améliore finalement la résolution volumétrique sur les images reconstruites. Le Vereos a été préalablement évalué selon les recommandations expérimentales de la NEMA (Zhang, Maniawski et Knopp, 2018 ; Rausch et al., 2019). La résolution spatiale, définie comme le FWHM, était de 4,2 mm au centre du FOV, la sensibilité moyenne était estimée à 5200 coups par seconde (cps)/MBq, et le pic du NECR était de 153,4 kcps à une concentration d'activité du  $^{18}\text{F}$  de 54,9 kBq.mL<sup>-1</sup>, selon Rausch et al. (2019). Plusieurs études ont montré que le Vereos DPC peut améliorer la qualité des images PET par rapport aux systèmes analogues, tels que dans Wright et al. (2018), Salvadori et al. (2019a,b) et López-Mora et al. (2019). De

plus, la confiance et la précision du diagnostic pour les maladies oncologiques sont également améliorées (Nguyen et al., 2015; Wright et al., 2017a; Fuentes-Ocampo et al., 2019).

Les simulations utilisant des modèles Monte Carlo sont des outils importants et utiles pour l'imagerie PET. Elles permettent de concevoir, d'optimiser et d'évaluer les systèmes d'imagerie, de prédire les performances, d'optimiser les paramètres d'acquisition et les algorithmes de reconstruction et d'évaluer les effets des facteurs de confusion sur la qualité des images. Sarrut et al. (2021b) ont fait la synthèse des dernières avancées en matière de simulation de détecteurs actuels et ont présenté un rapport détaillé sur les systèmes d'imagerie qui ont été simulés et évalués dans GATE<sup>11</sup>/Geant4<sup>12</sup> (Jan et al., 2004; Jan et al., 2011; Sarrut et al., 2014). Cette revue a été alimentée par le travail fourni au cours de cette thèse (Labour et al., 2020), et a été un travail collaboratif de la collaboration OpenGATE.

Plusieurs travaux ont été proposés pour simuler les systèmes PET en utilisant GATE. Divers systèmes d'imagerie PET cliniques ont été modélisés et comparés à des mesures expérimentales, comme les systèmes PET ECAT HRRT (Bataille et al., 2004) et EXACT HR+ (Jan et al., 2005; Karakatsanis et al., 2006), Philips Allegro et GEMINI (Lamare et al., 2004; Lamare et al., 2006), GE Advance et Discovery LS (Schmidtlein et al., 2006) et Siemens Biograph 2 (Karakatsanis et al., 2006), Biograph 6 (Gonias et al., 2007), Biograph mcT (Poon et al., 2015) et Inveon (Lu et al., 2016). D'autres incluent des études de Buvat et Castiglioni (2002), Assie et al. (2004), Lamare et al. (2004), Michel et al. (2006), Lamare et al. (2006), Stute et al. (2011), Poon et al. (2012) et Lee, Gregor et Osborne (2013). Consultez le *Tableau 1* dans Sarrut et al. (2021b) pour une bibliographie complète incluant les systèmes de petits animaux commercialisés et prototypes cliniques et précliniques. Plusieurs plateformes sont également disponibles pour les simulations de Monte Carlo, comme SimSET (Badawi et al., 1999; MacDonald et al., 2008; Guérin et El Fakhri, 2008; Poon et al., 2015), PeneloPET (Abushab et al., 2016) (Penelope), SORTEO (Boisson et al., 2013), Eidolon (Zaidi et Morel, 1999) (MCNP), PETSIM (Thompson, Moreno-Cantu et Picard, 1992), Geant4 (Moehrs et al., 2006) ou GAMOS (Mikhaylova et al., 2011, 2013).

À notre connaissance, aucun modèle Monte Carlo d'un système commercial PET basé sur des SiPM n'a été publié en *OpenSource* et comparé aux données expérimentales. Dans ce travail, la DPC-PET de Philips a été modélisé à l'aide de la plateforme GATE et comparé aux mesures effectuées selon les protocoles NEMA NU 2-2018 (*NEMA NU 2-2018 - Performance measurements of positron emission tomographs 2018*). Toutes les comparaisons ont été effectuées en utilisant des données en mode liste afin de rester indépendant de l'algorithme de reconstruction d'image.

## IV.2 Matériels et méthodes

### IV.3 La géométrie de la PET Vereos

La DPC-PET a été modélisée avec la plateforme GATE 8.2, utilisant Geant4 10.5. La géométrie, les dimensions et la composition des matériaux du scanner ont été fournies par Philips. La PET cylindrique a été défini par un ensemble d'éléments hiérarchisés avec quatre niveaux de profondeur différents, comme décrit dans la Section 4.2.1. Le composant de premier niveau était le *module* (1<sup>er</sup> niveau). 18 modules étaient disposés en anneau et chaque module était composé d'un ensemble de 4×5 blocs, les *stacks* (2<sup>nd</sup> niveau). Les blocs étaient individuellement subdivisées en

11. Voir [OpenGATE collaboration](#)

12. Voir [Geant4 overview](#)

$4 \times 4$  mini-bloc, les *dice* (3<sup>ème</sup> niveau). Chaque mini-bloc était constitué d'une grille de  $2 \times 2$  LYSO, qui sont les éléments de cristaux scintillateur (4<sup>ème</sup> niveau). L'espace-ment et les matériaux d'emballage entre les différents blocs de détecteurs ont été pris en compte. La configuration finale conduit à un anneau de détection avec un total de 23040 cristaux scintillateurs LYSO nécessaires, avec des dimensions individuelles de  $4 \times 4 \times 19 \text{ mm}^3$ , résultant en un FOV axial de 164 mm et un cylindre de détection de 764 mm de diamètre intérieur, voir le Tableau 4.1.

#### IV.4 Chaîne de détection et circuit de coïncidences

Dans toutes les simulations, la liste nommée `emstandard_opt4` a été utilisée<sup>13</sup>. Les sources radioactives du  $^{18}\text{F}$  ont été simulées par des sources  $\beta^+$  avec des spectres d'énergie paramétrés selon les tables de Landolt-Börnstein (Jan et al., 2004). Le nombre de particules primaires a été adapté pour toutes les simulations selon le protocole NEMA.

Le nombre de photons de scintillation générés étant proportionnel à l'énergie déposée dans le cristal, un modèle analytique est utilisé par le biais d'un *digitizer* spécifique qui convertit les interactions des photons dans le cristal en comptages numériques et gère l'horodatage de tous les événements (Jan et al., 2004). Le *digitizer* est composé d'opérations successives de traitement du signal qui imitent le processus de photodétection<sup>14</sup>. La Figure 4.3 illustre la représentation schématique de la chaîne de traitement du signal proposée. Pour plus de détails sur la construction du *digitizer*, veuillez consulter la Section 4.2.

#### IV.5 Validation de la modélisation de la PET Vereos

Le modèle de simulation de la DPC-PET proposé a été évalué selon les recommandations de la NEMA. Les recommandations NEMA pour la PET fournissent une méthode uniforme et cohérente pour la mesure expérimentale et l'évaluation des paramètres de performance. Les tests d'évaluation choisis pour la validation étaient (1) les taux de comptage, le NECR et la fraction de diffusion, (2) la résolution TOF et la résolution énergétique, (3) la sensibilité et (4) la résolution spatiale avant reconstruction. Les trois premiers tests sont indépendants de la reconstruction d'image. Pour la résolution spatiale, une méthode basée sur LOR a été proposée afin d'estimer la résolution spatiale à partir des données *listmode*, avant la reconstruction de l'image.

Pour plus de détails sur les matériels et méthodes, veuillez consulter la Section 4.2.

#### IV.6 Résultats

##### IV.6.1 Taux de comptage

Comme le montre la Figure 4.8A, un bon accord a été obtenu entre les simulations et les expériences pour les taux d'événements dits *singles*, avec un maximum de 0,7% de différence relative jusqu'à une concentration d'activité de  $80 \text{ kBq.mL}^{-1}$ . Il convient de noter que les activités habituellement utilisées en clinique avec le traceur  $^{18}\text{F}$ -FDG ne dépassent pas environ  $6 \text{ kBq.mL}^{-1}$  (Sluis et al., 2019).

13. Voir [Geant4/PhysicsList](#)

14. Voir [OpenGATE/readthedocs](#)

Les différences relatives maximales entre les données simulées et expérimentales, jusqu'à  $80 \text{ kBq.mL}^{-1}$ , étaient de 3%, 3%, 5% et 18% pour les taux de comptage de coïncidence *totales*, *fortuites*, *vraies* et *diffusées*, respectivement (Figure 4.8B). La différence pour le taux de *diffusées* est inférieure à 5% jusqu'à une concentration de  $10 \text{ kBq.mL}^{-1}$ .

#### IV.6.2 Résolutions TOF et énergétiques

Comme le montre la Figure 4.9A, un bon accord a été obtenu avec moins de 4% de différence relative observée entre les données simulées et expérimentales pour les résolutions TOF et énergétiques sur toute la gamme des concentrations d'activité explorées dans cette étude. Des exemples d'histogrammes de TOF et d'énergie à partir desquels les valeurs FWHM ont été extraites, obtenus pour une concentration d'activité de  $5,2 \text{ kBq.mL}^{-1}$  sont présentés dans la Figure 4.9B.

#### IV.6.3 Sensibilité

Un accord de 7,9% a été trouvé entre la sensibilité sans atténuation pour les données simulées et expérimentales, montrant 5591 et 5184  $\text{cps.MBq}^{-1}$ , respectivement. Comme le montre la Figure 4.10, les profils de sensibilité axiale entre les données simulées et expérimentales étaient en bon accord. Les différences relatives les plus importantes étaient de l'ordre de 14% pour les tranches de faible sensibilité de part et d'autre du FOV.

#### IV.6.4 Résolution spatiale intrinsèque

Le Tableau 4.6 présente les FWHM de résolution spatiale intrinsèque des 10 positions recommandées par les normes NEMA. Un accord global de moins de 0,25 mm de différence absolue a été obtenu entre les données simulées et expérimentales, sauf pour l'axe  $z$  (axial) où des valeurs allant jusqu'à 0,92 mm ont été obtenues. La Figure 4.11 fournit un exemple des histogrammes à partir desquels les PSF ont été extraits pour la position transversale (0,20,0) cm. Le Tableau 4.7 présente les FWHM à la position centrale (0,1,0) cm obtenus 1) avant, 2) après reconstruction avec modélisation des PSF basée sur l'image et 3) après reconstruction avec la méthode standard de *Sieve*.

Pour plus de résultats, veuillez consulter la Section 4.3.

### IV.7 Discussions et conclusions

#### IV.7.1 Contexte

Dans cette étude, un modèle GATE du Vereos DPC-PET a été développé et validé en comparant les données simulées avec les données obtenues expérimentalement en utilisant les tests NEMA. Ce travail a été publié (Labour et al., 2020), et à notre connaissance, fournit pour la première fois le modèle Monte Carlo d'un système PET du corps entier à base de SiPM. Le Tableau 4.9 résume les modèles Monte Carlo publiés de systèmes PET cliniques utilisant GATE. Une liste plus exhaustive des systèmes PET précliniques et validés sur petits animaux publiés peut être trouvée dans Sarrut et al. (2021b), Tableau 1, où la présente étude a été valorisée.

### IV.7.2 Taux de comptage

En général, le modèle de simulation proposé a été comparé favorablement aux mesures. Un excellent accord a été trouvé entre les taux de comptage simulés et expérimentaux, avec des différences relatives inférieures à 1% sur toute la gamme de concentrations d'activité ( $< 80 \text{ kBq.mL}^{-1}$ ). Pour les taux de coïncidence *totales*, *fortuites* et *vraies*, des accords ont été trouvés avec des différences maximales égales ou inférieures à 5% dans l'ensemble. Cependant, pour les taux de comptage des *diffusés*, le pourcentage de différence augmentait avec la concentration d'activité, passant de 3% à 5% à 1 et 30  $\text{kBq.mL}^{-1}$  (respectivement) et atteignait un maximum de 18% de différence à 80  $\text{kBq.mL}^{-1}$ . La cause de cet écart à haute activité n'est pas encore expliquée; elle pourrait être due au fait que les éléments qui produisent un rayonnement diffusé sont inclus dans la simulation par des modèles géométriques simplifiés, comme les plaques de refroidissement, le couvercle en Lexan ou la table du patient. Cela pourrait également être dû à la composition simulée des matériaux du fantôme cylindrique qui pourrait ne pas être exactement la même que dans le fantôme réel. Cependant, pour une fraction de diffusion inférieure à 10  $\text{kBq.mL}^{-1}$ , les différences en pourcentage étaient inférieures à 6% entre les valeurs simulées et expérimentales et sont restées inférieures à 15% pour des concentrations d'activité plus élevées.

### IV.7.3 Modules d'addition et de lecture

En fixant la logique comme *winner-takes-all* et le module de lecture, le *reader* à profondeur *depth 3*, sur le *dice* (voir Figure 4.2), nous décrivons théoriquement un modèle qui répond à l'architecture d'intégration du DPC-PET. Cependant, cette configuration a conduit à une sous-estimation des taux de comptage et de la sensibilité de l'ordre de 40% par rapport aux mesures expérimentales. En revanche, en fixant le domaine de lecture à *depth 1* (le plus haut niveau correspondant au *module*), les résultats obtenus en termes de taux de comptage et de sensibilité étaient beaucoup plus cohérents avec les données expérimentales. Cela pourrait être dû à des événements diffus (dans les cristaux) qui sont rejetés à des profondeurs inférieures puisque toute leur énergie ne sera pas intégrée et déposée dans d'autres parties du *module*. Comme la modélisation en GATE récupérant les événements diffus n'est pas encore disponible, il a été décidé de définir le *readout* au plus haut niveau sur les modules à *depth 1*.

### IV.7.4 Le temps mort

L'une des principales caractéristiques du Vereos, par rapport aux PET analogues conventionnels, est ses bonnes performances en termes de taux de comptage, caractérisées par un faible temps mort et des effets de pile-up. Cette propriété est principalement due à l'utilisation de SiPM permettant un couplage 1:1 avec les cristaux de scintillation en raison de leurs petites dimensions et permettant plus de canaux de déclenchement. En conséquence, la différence relative entre le taux théorique et le taux expérimental de *singles* obtenu par la régression linéaire de faible activité en l'absence de temps mort, était inférieure à 5% jusqu'à une concentration d'activité de 15  $\text{kBq.mL}^{-1}$ . Cependant, même si la perte due au temps mort était relativement faible avec le Vereos DPC-PET, il était nécessaire de modéliser cet effet pour obtenir des taux de comptage précis, notamment pour les concentrations d'activité élevées.

#### IV.7.5 Le bruit de fond

Aux concentrations d'activité observées en routine clinique, le bruit de fond provenant de l'électronique et la radioactivité naturelle des cristaux sont souvent considérés comme négligeables et ne sont donc pas modélisés dans les simulations Monte Carlo pour la PET. Cependant, il était nécessaire de le considérer pour reproduire les courbes de comptage expérimentales à faible activité. Par exemple, à la plus faible concentration mesurée de  $0,3 \text{ kBq.mL}^{-1}$ , le bruit de fond représentait 60% du nombre total de *singles* détectés. Ce pourcentage a diminué avec la concentration d'activité, mais était encore de 6% à  $5 \text{ kBq.mL}^{-1}$ , ce qui est représentatif de l'activité clinique du  $^{18}\text{F}$ -FDG. Il est tombé en dessous de 1% à partir d'une concentration d'activité de  $35 \text{ kBq.mL}^{-1}$ .

#### IV.7.6 Résolutions TOF et énergie

La Figure 4.9A montre la stabilité des résolutions TOF et énergétiques jusqu'à  $80 \text{ kBq.mL}^{-1}$ . Un accord de moins de 4% entre les résolutions temporelles et énergétiques simulées et expérimentales a été trouvé sur toute la gamme d'activité. Les valeurs de simulation étaient légèrement inférieures aux valeurs expérimentales.

#### IV.7.7 La sensibilité

La valeur de sensibilité obtenue par simulation ( $5591 \text{ cps.MBq}^{-1}$ ) s'est avérée supérieure de 7,9% à la valeur expérimentale ( $5184 \text{ cps.MBq}^{-1}$ ). Un bon accord a été obtenu entre les profils de sensibilité axiale (Figure 4.10B), avec une différence maximale de 13% aux bords du FOV. Cependant, en comparaison avec les valeurs publiées par Zhang *et al.* ( $5721 \text{ cps.MBq}^{-1}$ ) (Zhang, Maniawski et Knopp, 2018) et celles de Philips ( $5390 \text{ cps.MBq}^{-1}$ ) (Miller, 2016), l'accord était plus proche avec des différences relatives de 2,3% et 3,7%, respectivement. Cette disparité entre les valeurs de sensibilité expérimentales pourrait s'expliquer par l'incertitude sur la calibration de l'activité ainsi que sur le positionnement du fantôme qui est critique pour ce test.

#### IV.7.8 La résolution spatiale intrinsèque

L'estimation de la résolution spatiale intrinsèque avant reconstruction était proche entre la simulation et les données expérimentales, avec moins de 0,25 mm de différence entre les FWHM pour les directions transversales ( $x, y$ ). Les résolutions spatiales intrinsèques étaient meilleures dans la direction transversale que dans la direction axiale ( $z$ ) qui a atteint 0,92 mm de différence entre les données simulées et expérimentales, voir la Figure 4.11 et le Tableau 4.6.

Cette asymétrie dans les trois directions est inhérente à la méthode proposée. En effet, en raison de la forme cylindrique du scanner, seuls quelques angles azimutaux sont disponibles dans la direction axiale. La distance projetée le long de  $z$  ne peut prendre que des valeurs comprises entre un scalaire  $b = \|\vec{S}\vec{A}\| \cos(\theta_{max})$  et  $\|\vec{S}\vec{A}\|$ , avec  $\theta_{max}$  étant l'angle azimutal maximal pour une distance donnée  $\|\vec{S}\vec{A}\|$ . De plus, la valeur de  $b$  dépend de la position axiale en raison de la troncature des données axiales dans le PET 3D. Par conséquent, les valeurs de distance projetée les plus faibles (entre 0 et  $b$ ) n'étaient pas présentes dans la distribution de la distance projetée axiale  $z$ , ce qui entraîne une FWHM dégradée par rapport à celles mesurées dans les directions transversales  $x$  et  $y$ . La troncature des projections entraîne également un échantillonnage axial non uniforme, ce qui rend la mesure de la



résolution imprécise avec la méthode présentée pour les positions trop éloignées du centre du FOV axial. Une solution pour améliorer cette méthode serait d'utiliser un algorithme de rebinning exact, tel que celui proposé par Defrise et al. (1997), suivi d'un rééchantillonnage pour obtenir un taux d'échantillonnage axial comparable à celui obtenu transversalement.

#### IV.7.9 Résolution spatiale reconstruite

Quel que soit le type de convolution choisi, un bon accord a été observé entre les résolutions simulées et expérimentales reconstruites, avec une différence absolue maximale de 0,35 mm, voir le Tableau 4.7. Il est intéressant de noter que ce n'est que lorsque la convolution a été appliquée dans le modèle de reconstruction et que l'algorithme OSEM a convergé suffisamment (5 itérations et 10 sous-ensembles), que les valeurs FWHM étaient proches de celles obtenues avec la méthode de résolution intrinsèque développée. Lorsque des filtres de convolution post-reconstruction ont été ajoutés, les valeurs de FWHM étaient proches de l'évaluation du fabricant (environ 4mm).

#### IV.7.10 Reconstructions d'images illustratives

Les images reconstruites étaient en bon accord entre les données simulées et reconstruites avec un écart relatif maximum de 13% pour le CRC et 14% pour le BRN. Le compromis entre le CRC et le BRN était systématiquement légèrement meilleur pour les données simulées que pour les données expérimentales. Cette différence peut s'expliquer par les coïncidences éparses qui n'ont pas été également corrigées : les données expérimentales ont été corrigées par la méthode standard de single-scatter simulation (SSS) (Ye, Song et Hu, 2014), qui corrige uniquement la diffusion de photons uniques, tandis que les données simulées ont été reconstruites en ignorant toutes les coïncidences de diffusion (cas idéal).

#### IV.7.11 Incertitude statistique

L'incertitude statistique relative Monte Carlo était inférieure à 1% sur les taux de comptage estimés. Les temps de calcul des simulations étaient relativement importants, avec une moyenne d'environ 3000 particules primaires simulées par seconde, ce qui a conduit, par exemple, à environ 80 heures de calcul pour l'une des 26 acquisitions avec le fantôme cylindrique de diffusion. Aucune attention particulière n'a été portée au gain de vitesse de simulation. En particulier, la liste la plus lente (emstandard\_opt4) a été utilisée et les énergies de coupures de production et de suivi de particules n'ont pas été optimisées. Le compromis optimal entre la vitesse de calcul et la précision reste à étudier, mais ce travail peut servir de référence pour des résultats de précision optimale. Des méthodes rapides, telles que le logiciel SMART (Pfaehler et al., 2018), peuvent être utilisées pour accélérer la simulation.

#### IV.7.12 Conclusion

En conclusion, le modèle GATE PET proposé a été validé par rapport aux données expérimentales conformes à la norme NEMA NU 2-2018. À notre connaissance, c'est la première fois qu'un modèle Monte Carlo complet d'un système commercial PET basé sur des SiPMs est proposé et publié. Il est accessible en ligne par la collaboration OpenGate. Ce modèle peut être utile pour de nombreuses études,

notamment pour optimiser les performances d'imagerie, évaluer les algorithmes de reconstruction et estimer les effets des facteurs de confusion sur la qualité de l'image.

## V Étude quantitative de $^{90}\text{Y}$ à l'aide de la PET numérique

Le Chapitre 5 est adapté de Labour et al. (2021), qui a été publié dans la revue EJNMMI (Physics). L'objectif principal était d'évaluer les paramètres de reconstruction pour différentes configurations de fantômes et différentes durées d'acquisition en mode liste afin d'améliorer la précision quantitative de la dosimétrie de  $^{90}\text{Y}$ , en utilisant la DPC-PET.

### V.1 Introduction

La radioembolisation ou SIRT a été détaillée dans le Chapitre 1, et est une méthode intra-artérielle utilisée en pratique clinique pour traiter les tumeurs malignes hépatiques non résecables (Salem et al., 2010; Sangro et al., 2011). Actuellement, la SIRT peut être réalisée avec des microsphères d' $^{90}\text{Y}$  ou de  $^{166}\text{Ho}$ . Au cours de la SIRT à  $^{90}\text{Y}$ , les particules d' $^{90}\text{Y}$  qui sont des émetteurs  $\beta^-$  de haute énergie, encapsulées dans du verre ou marquées dans des microsphères de résine, sont administrées par des branches sélectionnées de l'artère hépatique qui alimentent les tumeurs. Cette méthode assure une biodistribution régionale des microsphères d' $^{90}\text{Y}$  délivrant une dose absorbée très localisée dans les régions perfusées, épargnant les organes à risque voisins et les tissus sains, avec l'avantage d'une irradiation négligeable des parties non embolisées et des tissus extra-hépatiques. La méthode  $^{90}\text{Y}$ -SIRT est largement utilisée en raison de son efficacité clinique et de sa sécurité relative (Lau et al., 1994; Sato et al., 2008; Kennedy et al., 2009; Salem et al., 2010; Sangro et al., 2011).

À l'heure actuelle, la prédiction de la biodistribution des microsphères d' $^{90}\text{Y}$  est généralement effectuée à l'aide de MAA marquées au  $^{99m}\text{Tc}$  avant le traitement, consultez la Section 1.3.1. Cependant, la biodistribution du  $^{99m}\text{Tc}$ -MAA ne correspond pas toujours à la distribution post-thérapeutique des microsphères d' $^{90}\text{Y}$  (Cremonesi et al., 2014; Garin et al., 2016; Gnesin et al., 2016; Haste et al., 2017; Ricchetta et al., 2019). Une évaluation de la biodistribution des radionucléides doit être effectuée après le traitement, au moyen d'une SPECT, ou d'une PET. Cette évaluation vise principalement à détecter tout dépôt extrahépatique éventuel de microsphères et à déterminer la distribution intrahépatique des microsphères sur le tissu hépatique perfusé, tumoral et non tumoral.

L'imagerie SPECT de  $^{90}\text{Y}$  exploite les photons de freinage, avec différentes fenêtres d'énergie publiées, de taille du collimateur, avec ou sans correction (Dezarn et al., 2011; Wright et al., 2015) et a été utilisée pour l'évaluation du traitement post-SIRT (Walrand et al., 2011). Cependant, la SPECT souffre de la diffusion, d'une faible résolution spatiale et d'une analyse quantitative délicate. Par ailleurs, l'imagerie de  $^{90}\text{Y}$  en utilisant la PET exploite une désintégration positronique mineure (Johnson, Johnson et Langer, 1955; Ford, 1955), consultez le Chapitre 3. En 2004, Nickles et al. (2004) ont exploité pour la première fois cette propriété pour montrer la distribution de la dose absorbée localisée délivrée par les thérapies à  $^{90}\text{Y}$  à l'aide de la PET, bien que cela soit difficile et coûteux en temps en raison des statistiques de comptage des photons d'annihilation. L'évaluation de la distribution de l'activité après une thérapie à  $^{90}\text{Y}$ -SIRT s'est avérée réalisable en 2010 par Lhommel et al. (2009, 2010) grâce aux informations TOF ajoutées sur les systèmes PET/CT. D'autres études ont

suivi et ont montré que la PET avec TOF comparé à la PET sans TOF offrait une meilleure récupération dans les données quantitatives reconstruites (Lhommel et al., 2009, 2010; Elschot et al., 2011; Carlier et al., 2013; Gates et al., 2011; Kao et al., 2012; Kao et al., 2013a), surpassant en même temps l' $^{90}\text{Y}$  BremSPECT (Walrand et al., 2011; Elschot et al., 2011). En 2007, Selwyn et al. (2007) ont vérifié que le rapport d'embranchement lié à la production de paires  $e^+/e^-$  au cours de la désintégration de l' $^{90}\text{Y}$  était de  $(31,86 \pm 0,47) \times 10^{-6}$ , suite à la désexcitation de l'état excité  $0^+$  du  $^{90}\text{Zr}$ . La dernière valeur publiée est celle de Dryák et Šolc (2020) en 2020, qui ont mesuré le rapport d'embranchement à  $(32,6 \pm 0,4) \times 10^{-6}$ .

Les systèmes PET numériques récents sont équipés de la technologie SiPM qui remplace les PMT conventionnels, consultez le Chapitre 2. Ils permettent d'améliorer les capacités TOF et CTR grâce à une électronique plus rapide et plus compacte (Lecoq, 2017; Gundacker et al., 2020). Ils présentent de meilleures performances en termes de sensibilité, de résolution spatiale, de taux de comptage et de qualité globale de l'image (Zhang, Maniawski et Knopp, 2018; Rausch et al., 2019; Van Sluis et al., 2019; Labour et al., 2020; Gnesin et al., 2020; Chicheportiche, Marciano et Orevi, 2020).

**Contexte de la présente étude.** En faisant une revue bibliographique des études antérieures, les évaluations de l'imagerie de l' $^{90}\text{Y}$  ont été réalisées en grande partie en se basant sur des critères fondés dans les recommandations de la NEMA, et par l'évaluation de la détectabilité à des fins de diagnostic plutôt que de calculs dosimétriques. Willowson et al. (2012) et Carlier et al. (2013) ont montré qu'avec le bénéfice des informations TOF, une détectabilité plus élevée était atteinte avec un petit nombre d'itérations OSEM sur les systèmes Siemens Biograph mCT. Peu d'études ont évalué les paramètres de reconstruction de l'algorithme OSEM à l'aide d'outils se basant sur le calcul de la dose absorbée. En 2014, Pasciak, Bourgeois et Bradley (2014) basée sur les résultats précédents de Willowson et al. (2012) et Carlier et al. (2013) ont trouvé qu'une FWHM supplémentaire de 4,5 mm de la PSF améliore la précision des distributions de la dose absorbée en utilisant des DVHs. Siman et al. (2019) ont étudié un GE D690 PET/CT et ont trouvé que 3 itérations avec 12 sous-ensembles avec une modélisation PSF supplémentaire et une taille de filtre Gaussien post-reconstruction de 5,2 mm FWHM fournissaient le plus faible RMSD entre leur DVH expérimental et de référence.

Cette étude porte sur l'utilisation d'un DPC-PET pour la quantification de l' $^{90}\text{Y}$  à des fins de dosimétrie suite à un SIRT. Nous avons considéré le système Vereos PET/CT équipé d'un SiPM entièrement numérique décrit dans la Section 4.2.1, avec un couplage 1 :1 entre les cristaux scintillateurs LYSO et les SiPMs (Zhang, Maniawski et Knopp, 2018), démontrant une résolution temporelle et un SNR améliorés par rapport aux PMT-PET conventionnels (Salvadori et al., 2020b). Wright et al. (2016, 2017b) et Wright et al. (2018) ont montré que la détection des photons d'annihilation par la DPC-PET à la suite d'un traitement par SIRT à l' $^{90}\text{Y}$  est possible, en montrant une visualisation concordante avec un meilleur contraste entre la distribution des microsphères d' $^{90}\text{Y}$  et le fond avec la DPC-PET par rapport aux systèmes SPECT et PMT-PET.

Des études précédentes (Willowson et al., 2012; Carlier et al., 2013; Pasciak, Bourgeois et Bradley, 2014; Siman et al., 2019) ont évalué les paramètres de reconstruction OSEM pour les systèmes PMT-PET avec des résolutions TOF autour de 550 ps. Par conséquent, les paramètres suggérés dans la littérature pourraient ne pas être adaptés au DPC-PET avec une résolution TOF d'environ 320 ps (Rausch et al., 2019; Zhang, Maniawski et Knopp, 2018; Labour et al., 2020), en raison de la dépendance

de la convergence des algorithmes OSEM sur l'information TOF (Salvadori et al., 2020b). De plus, les implémentations des algorithmes basés sur l'algorithme OSEM diffèrent au sein des systèmes et l'algorithme OSEM mis en œuvre dans la DPC-PET est basé sur des données en mode liste, au lieu de sinogrammes, et utilise des éléments de volume à symétrie sphérique pour modéliser l'image, au lieu de voxels (Wang et al., 2006; Narayanan et Perkins, 2013).

Dans cette étude, nous avons étudié la précision de la DPC-PET pour  $^{90}\text{Y}$  en évaluant l'effet des paramètres de reconstruction OSEM et de la durée d'acquisition sur l'estimation de la distribution de la dose absorbée basée sur les DVHs (Drzymala et al., 1991), comme proposé par Siman et al. (2019).

## V.2 Matériels et méthodes

Afin d'évaluer la précision des estimations de la dose absorbée basées sur l'image à partir de  $^{90}\text{Y}$  DPC-PET/CT, 3 fantômes ont été sélectionnés et imagés en utilisant une série de paramètres. Les images PET acquises ont été utilisées comme cartes d'activité d'entrée pour calculer les distributions de dose absorbée et des DVHs. Les distributions obtenues à partir des images ont été comparées aux distributions de dose absorbée de référence calculées à l'aide de simulations de Monte Carlo et l'impact de plusieurs paramètres, notamment sur les différents VOIs, les niveaux de concentration d'activité, les paramètres de reconstruction et les durées d'acquisition, ont été évalués.

### V.2.1 Configuration expérimentale

Deux différents fantômes cylindrique, Ph1 et Ph2, ont été utilisés pour la validation des données quantitatives récupérées après l'étalonnage PET pour  $^{90}\text{Y}$ . Ph1 et Ph2 sont représentés sur les Figures 5.1A et 5.1B, respectivement.

Un fantôme NEMA IEC, Ph3, illustré dans la Figure 5.1C, a ensuite été utilisé pour les mesures quantitatives destinées aux évaluations dosimétriques. Il se compose d'un compartiment de fond d'environ 9700 ml, d'un insert pulmonaire et d'un insert avec six sphères remplies de 10, 13, 17, 22, 28 et 37 mm de diamètre. Les fantômes utilisés dans cette étude permettent de réaliser des évaluations quantitatives de la récupération de l'activité (ou de la concentration de l'activité) et de la dosimétrie dans des objets de différentes tailles. Une activité de 2355 MBq de  $^{90}\text{YCl}_3$  a été ajoutée au fond d'eau de 9700 mL. Les  $AC_{ref,init}$  dans les sphères et le compartiment du fond étaient respectivement de 2,25 MBq.mL<sup>-1</sup> et 0,24 MBq.mL<sup>-1</sup> au moment de l'injection. Un SBR de 9 :1 a été obtenu, similaire à celui de l'étude QUEST (Willowson, Tapner, Bailey et al., 2015).

### V.2.2 Acquisition et reconstruction d'images

Les acquisitions d'images pour tous les fantômes ont été effectuées sur six jours consécutifs (deux demi-vies de  $^{90}\text{Y}$ ) afin d'analyser la réponse de la PET avec des concentrations d'activité décroissantes. Les acquisitions de données ont été effectuées au format *listmode*.

Toutes les reconstructions d'images ont été réalisées avec des informations TOF et en utilisant l'algorithme LMOSEM relaxé (Wang et al., 2006) implémenté sur les systèmes PET de Philips, avec des voxels isotropes de  $2 \times 2 \times 2$  mm<sup>3</sup>. Elles ont été post-traitées avec une version régularisée de l'algorithme de Richardson-Lucy

pour la récupération de la résolution (Richardson, 1972; Lucy, 1974) avec les paramètres recommandés par défaut de la modélisation PSF (1 itération avec un noyau de régularisation FWHM de 6 mm) qui permettent une récupération raisonnable du contraste sans artefacts de Gibbs perceptibles (Narayanan et Perkins, 2013; Golla, Lammertsma et Boellaard, 2015). Plusieurs paramètres ont été comparés pour Ph3, listés dans le Tableau 5.1, avec au total, 45 combinaisons de reconstructions.

### V.2.3 Calcul de la dose absorbée et analyses

**Calcul de la dose absorbée.** Les distributions de dose absorbée ont été calculées à partir des images PET avec DOSIsoft® (Cachan, France) par l'algorithme de convolution du noyau de dose VSV selon le formalisme MIRD (Bolch et al., 2009; Dieudonné et al., 2010, 2011). Les calculs ont également été effectués en utilisant la méthode LDM à des fins de comparaison.

**Dose absorbée de référence.** Des simulations Monte Carlo ont été réalisées avec la plateforme GATE 9.0 (Jan et al., 2011; Sarrut et al., 2014) utilisant Geant4 10.5 (Collaboration, Agostinelli et al., 2003). La géométrie, les dimensions et la composition des matériaux de chaque fantôme ont été modélisées. Le nombre de particules primaires a été adapté pour chaque région du fantôme dans une seule simulation pour l'ensemble du fantôme en fonction du  $AC_{ref,init}$  expérimental relatif dans chaque région, de manière à atteindre une incertitude statistique de type A inférieure à 1% sur les valeurs estimées de la dose moyenne absorbée. Les valeurs finales de la dose absorbée ont été mises à l'échelle en fonction des activités cumulées connues dans toutes les régions injectées.

**Comparaisons.** Le calcul de la dose absorbée de référence par Monte Carlo, la convolution VSV basée sur l'image et la LDM basée sur l'image sont désignées respectivement par  $DVH_{ref}^{MC}$ ,  $DVH_{pet}^{VSV}$  et  $DVH_{pet}^{LDM}$ . Pour chaque ensemble de paramètres,  $r$ , utilisé pour la reconstruction de l'image et la taille de la sphère,  $\varnothing$ , dans Ph3, les différences entre les distributions de dose absorbée utilisant la convolution VSV ont été évaluées par le RMSD entre leurs  $DVH_{ref,\varnothing}^{MC}$  et  $DVH_{pet,\varnothing}^{VSV}$  respectifs, voir l'équation 6.12.

$$RMSD_{\varnothing,r} = \sqrt{\frac{\sum_{i=0}^{N-1} (DVH_{ref,\varnothing,i}^{MC} - DVH_{pet,\varnothing,r,i}^{VSV})^2}{N}} \quad (6.12)$$

où N est le nombre total de points dans lesquels les axes de dose absorbée des DVHs sont échantillonnés.

Pour plus de détails sur les matériels et méthodes, veuillez consulter la Section 5.2.

## V.3 Résultats du fantôme NEMA, Ph3

Au total, 270  $DVH_{pet}^{VSV}$  basés sur des images (45 ensembles de paramètres de reconstruction décrits dans la Section 5.2.3 pour les 6 sphères) ont été calculés, et 6  $DVH_{ref}^{MC}$  de référence, correspondant à chaque sphère, ont été simulés. Pour chaque sphère et chaque reconstruction, le  $DVH_{pet}^{VSV}$  a été comparé au  $DVH_{ref}^{MC}$ . La Figure 5.3 représente les  $DVH_{ref}^{MC}$  simulés (courbes noires) pour chaque sphère et les  $DVH_{pet}^{VSV}$

pour 8 reconstructions par sphère (seules les valeurs extrêmes sont représentées : 1 et 3 itérations, 10 et 30 sous-ensembles, tailles de filtre FWHM de 0 et 8 mm).

### V.3.1 Variation du filtre Gaussien post-reconstruction

Comme attendu pour toutes les sphères, l'augmentation de la taille du filtre a réduit le  $D_{max}$  du  $DVH_{pet}^{VSV}$ , par exemple entre i1s30-0mm et i1s30-8mm, comme le montre la Figure 5.3. On a pu observer qu'un filtre trop large ne pouvait pas convenir à la dosimétrie, en particulier avec des tailles de sphères décroissantes où l'aire sous la courbe peut être réduite de manière significative (en comparant les  $DVH_{pet}^{VSV}$  cyan et vert des Figures 5.3D, 5.3E and 5.3F).

### V.3.2 Variation des sous-ensembles

Comme attendu, l'augmentation du nombre de sous-ensembles a conduit à une augmentation du  $D_{max}$  du  $DVH_{pet}^{VSV}$  pour toutes les sphères, par exemple entre i3s10-0mm et i3s30-0mm, comme le montre la Figure 5.3. Pour les plus grosses sphères de 28 et 37 mm, 30 itérations par rapport à 10 itérations ont favorisé l'amplification du bruit au détriment des doses absorbées intermédiaires (comparaison des  $DVH_{pet}^{VSV}$  rouge et bleu).

### V.3.3 Variation du nombre d'itérations

La relation en variant le nombre d'itérations était moins claire et intuitive qu'avec la taille du filtre de post-reconstruction ou le nombre de sous-ensembles. Pour les sphères  $> 20$  mm (22, 28 et 37 mm), l'augmentation du nombre d'itérations n'a pas entraîné de changement significatif de la forme de la  $DVH_{pet}^{VSV}$  ou a entraîné une légère augmentation de la  $D_{max}$ , par exemple entre i1s10-0mm et i3s10-0mm, comme le montre la Figure 5.3. L'augmentation des itérations de 1 à 3 n'a pas semblé favoriser l'amplification du bruit pour les plus grosses sphères. En revanche, des variations plus importantes ont été observées pour les sphères  $< 20$  mm (10, 13, 17 mm) en utilisant la même comparaison, par exemple entre i1s10-0mm et i3s10-0mm.

### V.3.4 Nombre de mises à jour équivalents

Le nombre équivalent de mises à jour (produit du nombre d'itérations et de sous-ensembles) n'a pas donné la même précision dans  $DVH_{pet}^{VSV}$  que celle à laquelle on pourrait s'attendre, par exemple entre i1s30-0mm et i3s10-0mm ou entre i1s30-8mm et i3s10-8mm.

### V.3.5 Effet de la durée d'acquisition

La Figure 5.5 représente l'effet de la durée d'acquisition sur le  $DVH_{pet}^{VSV}$ , pour les 6 sphères de Ph3. Les RMSDs en comparant une acquisition de 15 à 10 min/pas de table  $DVH_{pet}^{VSV}$  étaient de 3,2, 8,0, 1,6, 1,8, 23,2 et 19,4 pour les sphères de 37 à 10 mm, respectivement. Ces RMSD correspondants ont augmenté à 10,1, 12,7, 5,6, 6,8, 43,6 et 24,2, en comparant un  $DVH_{pet}^{VSV}$  de 15 à 5 min/pas de table, respectivement.

Pour plus de résultats, veuillez consulter la Section 5.3.

## V.4 Discussions et conclusions

### V.4.1 Contexte

L'objectif principal de ce travail était d'évaluer l'influence des statistiques de comptage acquises (durée d'acquisition), de la configuration du fantôme et des paramètres de reconstruction à l'aide d'une DPC-PET pour améliorer la précision quantitative de la dosimétrie de  $^{90}\text{Y}$ . Une vérification initiale a été effectuée en utilisant deux fantômes cylindriques uniformes. Un troisième fantôme, le NEMA IEC a été utilisé pour évaluer les paramètres de l'algorithme LMOSEM mis en œuvre dans les plateformes de reconstruction Philips pour l'imagerie PET. Les paramètres OSEM ont été variés afin de trouver les combinaisons d'itérations, de sous-ensembles et de tailles de filtres Gaussiens post-reconstruction qui fourniraient la plus petite différence entre le  $DVH_{ref}^{MC}$  utilisant GATE et le  $DVH_{pet}^{VSV}$  utilisant DOSIsoft® (Cachan, France). Les modélisations TOF et PSF ont été prises en compte dans toutes les reconstructions. La durée d'acquisition a été variée par rééchantillonnage des jeux de données de fantômes et de patients en mode liste afin de déterminer la durée d'acquisition la plus courte permettant de maintenir une précision acceptable. En utilisant la méthode suggérée par Siman *et al.*, le RMSD entre  $DVH_{ref}^{MC}$  et  $DVH_{pet}^{VSV}$  a été utilisé pour comparer les doses absorbées obtenues avec différents ensembles de données et méthodologies de dosimétrie. Une analyse à l'aide de  $DVH_{pet}^{LDM}$  a également été effectuée, en utilisant des paramètres de reconstruction déterminés après évaluation. Aucune intention particulière n'a été prise pour améliorer la qualité de l'image en utilisant les normes NEMA sur les mesures de performance, NEMA (2018), puisque l'objectif était d'améliorer la précision de la dosimétrie.

### V.4.2 Ph3 et évaluation par DVH

Les différences de  $DVH_{ref}^{MC}$  et de  $DVH_{pet}^{VSV}$  sont représentées sur les Figures 5.3, 5.4 et 5.5. La limitation due à la faible statistique intrinsèque et la PVE compromettent la quantification précise des objets de petit volume, montrant des  $DVH_{pet}^{VSV}$  et des RMSDs qui ont de grandes variations selon les paramètres de reconstruction utilisés. Siman *et al.* ont également montré des RMSDs relativement importants entre leur référence et les DVHs basés sur les images, illustrant la perte de précision apportée par l'utilisation des images. Les Figures 5.5E et 5.5F illustrent la limite de la réduction de la durée d'acquisition pour les petites lésions. Les écarts entre les acquisitions de 10 à 15 minutes par position de table étaient significatifs pour les sphères de 10 et 13 mm par rapport aux 4 autres sphères plus grandes. D'un autre côté, la durée d'acquisition peut être réduite à 10 min/position de table en utilisant un DPC-PET si la taille de la lésion est d'au moins 17 mm de diamètre sur la base des distributions de dose absorbée obtenues dans cette étude. Les résultats ont montré que dans les données du fantôme et du patient, la différence de  $DVH_{pet}^{VSV}$  entre les acquisitions de 10 et 15 minutes était faible, comme le montre la Figure 5.7.

### V.4.3 Calculs de la dose absorbée

La convolution VSV pour le calcul de la dose absorbée est basée sur des noyaux précalculés par des méthodes de Monte Carlo. Elle a été validée et s'est avérée cliniquement adaptée à la dosimétrie post-SIRT à  $^{90}\text{Y}$  (Dieudonné *et al.*, 2011). Le LDM est une méthode rapide basée sur le voxel et facile à appliquer en clinique, qui ne nécessite pas de post-traitement et où un facteur multiplicatif similaire à l'équation 5.1 est appliqué par voxel, par opposition à un noyau de convolution

précalculé pour le VSV. Le LDM est une alternative offrant une bonne précision comme le suggèrent Pasciak, Bourgeois et Bradley (2014). Les simulations Monte Carlo ont été utilisées dans cette étude mais n'avaient pas pour but de remplacer la dosimétrie clinique utilisant la convolution VSV ou LDM. Elles ont été utilisées comme un outil pour obtenir une référence dans les distributions de dose absorbée et étaient plus accessibles à utiliser que les logiciels industriels pour le traitement par batch. Cela n'a pas été détaillé ici, mais les distributions de dose absorbée utilisant la convolution VSV ont été comparées aux simulations Monte Carlo basées sur l'image PET où d'excellents accords ont été obtenus entre eux, illustrant à nouveau la dégradation majeure de l'image provenant de la performance non idéale de PET ayant un impact sur les distributions de dose absorbée.

#### V.4.4 Variation des paramètres de l'algorithme OSEM

L'évaluation des paramètres de reconstruction pour la dosimétrie est nécessaire pour chaque système, d'abord en raison des différentes performances PET en termes de sensibilité, de résolution spatiale, de taux de comptage, résolution en énergie et de résolution temporelle (Labour et al., 2020; Rausch et al., 2019; Vandendriessche et al., 2019; Carlier et al., 2020). L'évaluation est nécessaire pour différents algorithmes de reconstruction, par exemple l'OSEM ou le BPL, et les implémentations des algorithmes basés sur le OSEM varient d'un fabricant à l'autre. De plus, les configurations très spécifiques des protocoles d'imagerie varient d'un hôpital à l'autre.

La combinaison des paramètres pour les reconstructions OSEM n'est pas un choix simple et est spécifique pour une configuration de SBR,  $AC_{ref}$ , la taille du voxel de l'image et la taille de la lésion. Dans cette étude, la variation du nombre d'itérations, limitée de 1 à 3, n'a pas eu d'impact significatif sur les distributions de dose absorbée calculées, voir la Figure 5.3. En revanche, la variation des sous-ensembles et du FWHM du filtre Gaussien de post-reconstruction a eu un impact. L'utilisation de 30 sous-ensembles pourrait contribuer à améliorer la précision de la dosimétrie pour les petites sphères, mais pourrait favoriser l'amplification du bruit dans l'image par rapport à 10 sous-ensembles. Le nombre de mises à jour, qui est le produit du nombre d'itérations et de sous-ensembles, n'a pas été utilisé comme critère objectif d'évaluation car différentes combinaisons pour le même nombre de mises à jour pourraient donner des résultats différents, par exemple 30 mises à jour pour i1s30-0mm et i3s10-0mm dans la Figure 5.3.

#### V.4.5 Les limites

Dans la présente étude, nous avons évalué plusieurs  $DVH_{pet}^{VSV}$  pour l'acquisition dans des conditions spécifiques (SBR de 9 :1, taille de voxel d'image isotrope de 2 mm,  $AC_{ref}$  de 2,18 MBq.mL<sup>-1</sup>). Pour des recherches plus approfondies, des évaluations de  $DVH_{pet}^{VSV}$  devraient être faites pour les différents  $AC_{ref}$  présentes dans les sphères à différents temps d'imagerie et également en faisant varier la résolution de l'image, par exemple pour des voxels de 4 mm au lieu de 2 mm. Les évaluations faisant varier le SBR nécessiteraient davantage de données expérimentales, avec un dispositif expérimental différent pour chaque SBR. Les évaluations en faisant varier et en réglant les paramètres choisis pour la version régularisée de l'algorithme de Richardson-Lucy pour la récupération de la résolution (fixée à 1 itération avec un noyau de régularisation de 6 mm dans cette étude selon les recommandations) et leur influence sur la précision des informations quantitatives récupérées dans les images reconstruites peuvent être le sujet de



futures études. Les paramètres de reconstruction sélectionnés étaient basés sur des évaluations utilisant la convolution VSV, mais des évaluations similaires peuvent être effectuées en utilisant le LDM. Les résultats présentés ici peuvent être utiles dans le choix des paramètres de reconstruction OSEM, par exemple dans les études telles que celles publiées par Wei et al. (2020), Levillain et al. (2020), Morán et al. (2020) et Hesse et al. (2020) pour une meilleure précision dans le calcul de la dose absorbée suite à une SIRT à  $^{90}\text{Y}$  utilisant la DPC-PET.

#### V.4.6 Conclusion

Cette étude visait à évaluer divers paramètres pour l'imagerie PET de  $^{90}\text{Y}$  avec un système DPC-PET de Philips pour la dosimétrie basée sur l'image post-SIRT. À notre connaissance, aucune étude concernant l'évaluation des paramètres d'acquisition et de reconstruction par DVHs n'a été publiée précédemment pour les systèmes PET basés sur des SiPMs. Dans l'ensemble, à des fins de dosimétrie, nous recommandons d'appliquer un filtre Gaussien post-reconstruction de 2 mm FWHM, qui pourrait réduire le bruit dans l'image reconstruite tout en conservant la même précision que lorsqu'aucun filtre n'est appliqué. Le jeu de paramètres de reconstruction sélectionné pourrait être  $3s10\text{-}2\text{mm}$  pour les grandes sphères, mais ce choix dépend de l'information sur la dose absorbée requise. Cette étude pourrait être utile pour le choix des paramètres de reconstruction avec la DPC-PET, en fonction des conditions d'imagerie pour  $^{90}\text{Y}$ . La durée d'acquisition peut également être réduite de 15 à 10 min/pas de table pour  $^{90}\text{Y}$ -SIRT avec une dégradation acceptable de la distribution de la dose absorbée, améliorant ainsi le confort du patient.

## VI Comparaison de la dosimétrie prédictive et la dosimétrie post-traitement pour le suivi de la radioembolisation

Les images pouvant présenter des différences spatiales, différentes techniques de recalage d'images sont proposées et comparées. Les données d'images de plusieurs patients ayant subi un traitement de radioembolisation au Centre Léon Bérard ont été évaluées rétrospectivement. Par conséquent, cette étude contribue à une évaluation préliminaire de la valeur prédictive des particules de MAA, substitut des microsphères, de la distribution spatiale de la dose absorbée dans différents volumes d'intérêt dans le foie, ainsi qu'une évaluation et une comparaison de la distribution de la dose absorbée après un traitement de radioembolisation. L'objectif principal ici est le choix de la méthode de recalage d'images la plus appropriée qui permettrait une meilleure correspondance des volumes hépatiques sans avoir besoin de procéder à des recalages manuels et d'effectuer des comparaisons.

### VI.1 Introduction

Contrairement à d'autres formes de radiothérapie ou de curiethérapie, il est difficile de réaliser une dosimétrie précise avant le traitement pour prédire la faisabilité technique et le résultat du traitement par radioembolisation. Des particules de substitution, du  $^{99m}\text{Tc}$ -MAA, ont été suggérées et c'est la pratique courante aujourd'hui pour la simulation préalable à l'administration du traitement par radioembolisation par l'utilisation de microsphères d' $^{90}\text{Y}$ , comme décrit dans le Chapitre 1, Section 1.3.1. Le  $^{99m}\text{Tc}$ -MAA est injecté à travers des parties sélectives du foie et

après l'injection, une scintigraphie planaire et/ou, si disponible, des images 3D-SPECT/CT sont acquises. La prédiction est principalement effectuée pour les raisons 1 à 5 données dans la Section 1.3.1.2.

À la suite de l'administration du traitement par microsphères d' $^{90}\text{Y}$ , on procède soit à une BremSPECT/CT soit, de préférence, à une TOF-PET/CT pour évaluer le succès technique du traitement, voir la Section 1.3.2.2. Plusieurs inconvénients et défis ont été abordés dans la littérature, par exemple la qualité d'image et la résolution spatiale limitées du BremSPECT pour l' $^{90}\text{Y}$ , et l'absence de statistiques sur les positons après la désintégration de l' $^{90}\text{Y}$  en utilisant la PET. Néanmoins, cela reste un atout de pouvoir vérifier systématiquement la délivrance du traitement et d'évaluer les distributions de dose absorbée intra et extra-hépatiques.

C'est également un atout de pouvoir utiliser les images pour prédire le résultat du traitement, ce qui permet une planification plus personnalisée, donne plus de confiance dans l'administration du traitement et supprime la nécessité d'une imagerie de suivi. Toutefois, les corrélations constatées entre les distributions de  $^{99m}\text{Tc}$ -MAA et des microsphères  $^{90}\text{Y}$  restent controversées. Une liste non exhaustive de publications passant en revue des études rétrospectives ayant évalué l'importance des prédictions à partir du  $^{99m}\text{Tc}$ -MAA est examinée ci-après.

Ahmadzadehfar et al. (2010) ont montré que le  $^{99m}\text{Tc}$ -MAA SPECT/CT est approprié pour minimiser les effets secondaires en minimisant les dépôts extra-hépatiques sur 76 patients atteints de plusieurs types de maladies, avec une comparaison entre le SPECT planaire, non corrigé en atténuation et le SPECT/CT, mais n'a pas évalué les distributions intra-hépatiques du  $^{99m}\text{Tc}$ -MAA. Knešaurek et al. (2010) ont également comparé les distributions de microsphères d'Yttrium-90 et de MAA pour 20 patients et ont souligné que la précision dépend fortement de la correspondance des images dans les 3 dimensions. Les transformées rigides automatiques qu'ils ont utilisées ne pouvaient pas fournir une correspondance suffisamment précise entre les images CT en raison du positionnement différent des patients entre les scans MAA et  $^{90}\text{Y}$ , et ont donc procédé à des recalages manuels dans ces cas. Ils ont obtenu une gamme de corrélations allant d'une corrélation élevée à une corrélation très faible entre les distributions d'activité prédictive et réelle. Leurs résultats suggèrent donc que la prédiction de la réponse du traitement peut ne pas être précise si elle est basée sur des distributions MAA. Wondergem et al. (2013) ont mené une autre étude sur 31 patients, et ont fait la même conclusion qu'il n'y a pas une prédiction précise de la distribution de l'activité avec les pratiques cliniques de cette époque, et que des recommandations spécifiques peuvent conduire à une dosimétrie plus personnalisée.

Garin et al. (2012) ont mené une étude sur 36 patients atteints de HCC traités avec des microsphères en verre pour évaluer si la réponse et la survie des patients peuvent être prédites en utilisant la dosimétrie des examens de  $^{99m}\text{Tc}$ -MAA SPECT/CT. Ils ont conclu que le MAA SPECT/CT fournit des prédictions précises, mais que des études doivent être menées pour les configurations SHM (Garin et al., 2016). Les études menées par Song et al. (2015) sur 23 patients atteints de tumeurs malignes du foie et Gnesin et al. (2016) sur 25 patients atteints d'HCC ont abouti à des conclusions similaires avec des relations étroites entre la planification de l'activité MAA et les distributions des microsphères d' $^{90}\text{Y}$ . Kao et al. (2013b) ont également obtenu de bonnes corrélations sur 23 patients et ont encouragé la poursuite des recherches sur la dosimétrie prédictive pour une dosimétrie plus personnalisée. Haste et al. (2017) ont réalisé des études similaires en utilisant la distribution de microsphères en verre d' $^{90}\text{Y}$  chez 62 patients atteints de HCC. Ils ont cependant constaté une grande variabilité dans les distributions de la dose absorbée pour les

régions tumorales définies, même si une bonne corrélation a été trouvée pour l'ensemble du tissu hépatique normal. Ils ont conclu que le  $^{99m}\text{Tc}$ -MAA était un indicateur peu fiable pour prédire quantitativement les distributions de microsphères d' $^{90}\text{Y}$  pour les HCC. Kafrouni et al. (2019) ont procédé aux mêmes comparaisons pour 23 patients atteints de HCC en utilisant des microsphères en verre, en étudiant les facteurs liés aux risques cliniques et aux problèmes d'équipement, tels que la préparation et l'administration de l'activité, la modalité d'imagerie utilisée et la radiologie interventionnelle. Ils ont constaté une bonne corrélation entre la prédiction à l'aide du  $^{99m}\text{Tc}$ -MAA et la distribution de la dose absorbée pour l' $^{90}\text{Y}$  dans le foie normal et les volumes tumoraux. Ils ont toutefois souligné l'importance de la reproductibilité de la position de l'extrémité du cathéter dans la concordance entre les distributions de dose prédictive et réelle lorsque des divergences ont été constatées. Une étude de Jadoul et al. (2019) a également conclu que les distributions de dose absorbée dans le foie normal peuvent être raisonnablement prédites en utilisant les MAA, mais pas pour la tumeur, pour les HCC et les métastases, quel que soit le type de microsphères.

Des études plus récentes gravitant autour de ce sujet controversé sont celles de Morán et al. (2020) qui ont étudié l'impact de quatre approches dosimétriques différentes pour le calcul des doses absorbées sur 14 patients et ont trouvé des disparités importantes entre les méthodes. Ils ont suggéré que les approches basées sur les voxels 3D (convolution du noyau de convolution et LDM) peuvent être utilisées de manière indistincte. Ils n'ont toutefois pas comparé les distributions prédictives des MAA et des microsphères  $^{90}\text{Y}$  pour ces patients. Levillain et al. (2020) ont combiné le concept de DVH et le concept de QVH (Vanderstraeten et al., 2006) pour améliorer la dosimétrie de la radioembolisation et ont obtenu des résultats prometteurs bien qu'ils n'aient pas conclu sur le résultat clinique sur la correspondance entre la dosimétrie prédictive et post-traitement sur les patients. Leur méthode devrait être validée dans des études prospectives.

La liste des publications susmentionnées n'est pas exhaustive et d'autres publications peuvent être trouvées dans la littérature. On peut observer que la corrélation entre les distributions de MAA et de microsphères reste encore peu claire et que des études prospectives doivent être réalisées. Il existe des incertitudes à plusieurs étapes du traitement, comme décrit ci-dessus, et la raison de l'inadéquation entre ces distributions d'activité peut être due à un certain nombre de facteurs, tels que les variations de la position du cathéter, les procédures d'injection, la différence de dimensions et de flux des particules entre les microsphères et les MAA, la progression de la maladie entre les étapes pré et post-traitement, et la différence d'énergie de rayonnement entre l' $^{90}\text{Y}$  et le  $^{99m}\text{Tc}$ . En outre, au cours des étapes du traitement de l'image, plusieurs types d'incertitudes s'ajoutent à la quantification de la distribution de l'activité dans les parties du foie : comme la performance intrinsèque non idéale des différentes modalités d'imagerie utilisées (SPECT pour la prédiction et PET pour la surveillance) et le choix des paramètres de reconstruction qui ajoute un biais sur la récupération de l'information dans les images reconstruites, comme évalué dans le Chapitre 5. Enfin, les différences dans les doses absorbées doivent être prises en compte en utilisant différentes méthodes de dosimétrie (Morán et al., 2020).

**Contexte de cette étude.** Le système numérique Vereos (basé sur des dSiPM) est installé au CLB depuis 2018, et le suivi du traitement par radioembolisation par microsphère d' $^{90}\text{Y}$  est depuis lors effectué à l'aide de ce système. La distribution des microsphères peuvent ainsi être comparées aux distributions prédictives aux

MAA telles que décrites dans les études référencées ci-dessus. À cette fin, le recalage des images est nécessaire pour mettre en relation les images pré et post-traitement. Plusieurs études ont fait état d'un manque de correspondance et ont procédé à des enregistrements manuels entre les images prédictives et les images de contrôle post-traitement.

L'objectif de ce travail était donc de proposer une approche cohérente pour les comparaisons d'images sans avoir à procéder à des ajustements manuels en cas de non correspondance avec des outils existants. Différents schémas pour recalcr les volumes d'intérêt (VOI), délimités avant traitement sur les images au  $^{99m}\text{Tc}$ -MAA SPECT/CT aux images PET/CT suite au traitement sont comparés. En effet, le choix de la méthode de recalage de l'image est un paramètre potentiel qui peut être responsable de divergences quantitatives dans les distributions de dose absorbée lors de cette comparaison, en raison de structures mal positionnées et délimitées (par exemple, de petites tumeurs), en raison des effets connus, mais difficiles à corriger, des déplacements des organes internes et des mouvements respiratoires. Cette étude rétrospective ne présente cependant que des résultats préliminaires et servira de perspective à la suite de cette thèse pour des études futures.

## VI.2 Matériels et méthodes

Dans cette étude, la prédiction au  $^{99m}\text{Tc}$ -MAA SPECT/CT a été utilisée pour calculer la distribution intrahépatique des doses absorbées chez 10 patients, en simulant la distribution des microsphères d' $^{90}\text{Y}$ . Dans la mesure du possible, les phases de préparation et de traitement ont été réalisées au cours de la même journée, sans qu'il y ait plus de trois semaines entre les deux procédures. Le suivi du traitement par radioembolisation à l' $^{90}\text{Y}$  a été réalisé à l'aide de la PET/CT et la distribution intrahépatique des doses absorbées a été calculée. Les distributions prédictives des MAA et des microsphères après le traitement ont été comparées en utilisant quatre méthodes de recalage d'image différents. Les doses absorbées ont été comparées grâce aux DVHs et aux valeurs de dose absorbée extraites. Les caractéristiques des patients étudiés sont présentées dans le Tableau 6.1. Les activités utilisées pour chaque patient sont indiquées dans le Tableau 6.2.

### VI.2.1 Protocoles d'imagerie et de reconstruction

**$^{99m}\text{Tc}$ -MAA, SPECT/CT.** Un collimateur LEHR a été utilisé avec une fenêtre d'énergie centrée à 140 keV et large de 10% (126,45-154,55 keV). 120 images (60 projections, 25 s par projection) ont été acquises en mode 3D. Les images ont été reconstruites avec des corrections d'atténuation basées sur CT et de diffusion par fenêtrage, et calibrées en  $\text{MBq}\cdot\text{mL}^{-1}$ . Un algorithme OSEM a été utilisé avec 8 itérations et 4 sous-ensembles, avec un filtre Gaussien post-reconstruction supplémentaire de 8,4 mm à FWHM. Les reconstructions ont été effectuées pour des tailles de voxels isotropes de 4,4 mm et une matrice d'image de  $128 \times 128$  voxels.

**Microsphères d' $^{90}\text{Y}$ , DPC PET/CT.** La durée d'acquisition pour chaque patient était de 10 min/pas de table, centrée sur la région du foie. Les images ont été reconstruites à l'aide des paramètres de reconstruction OSEM évalués et choisis, avec 3 itérations et 10 sous-ensembles, avec un filtre Gaussien post-reconstruction supplémentaire de 2 mm à FWHM, sur la base des résultats précédents (voir Chapitre 5). Les paramètres recommandés par défaut de la modélisation PSF (1 itération avec un noyau

de régularisation de 6 mm FWHM) pour la récupération de la résolution ont été utilisés. Les reconstructions ont été effectuées pour des tailles de voxels isotropes de 2 mm de côté et une matrice d'image de  $288 \times 288$  voxels.

### VI.2.2 Délimitation des volumes d'intérêt

Pour chaque patient, les contours des structures hépatiques ont été utilisés. Ils ont été définis par des cliniciens selon des protocoles cliniques locaux au CLB en utilisant la station de travail clinique PlanetOnco de DOSIsoft® (Cachan, France). Les VOI primaires définis étaient : 1) WLTV, 2)  $TV_{Total}$  et 3) PLV, représentées sur la Figure 6.1. D'autres VOI à des fins de comparaison ont pu être définis en utilisant les trois premières structures, qui étaient : 4)  $NLV_{Target}$ , 5) NPLV, et 6)  $NLV_{WholeLiver}$ . Tous les VOIs sont résumés dans le Tableau 6.4. Ils ont tous été propagés et enregistrés sur les images SPECT.

### VI.2.3 Calcul de la dose absorbée

Les cartes de dose absorbée pour chaque patient ont été calculées indépendamment des : 1)  $^{99m}\text{Tc}$ -MAA SPECT pour prédire la distribution des microsphères d' $^{90}\text{Y}$  et 2) des images de contrôle post-traitement PET pour la distribution réelle des microsphères d' $^{90}\text{Y}$  en utilisant la station de travail PlanetOnco. Les algorithmes de convolution de noyau de dose VSV et de LDM ont été utilisés.

### VI.2.4 Propagation des contours

L'alignement des séries de données d'images a été effectué à l'aide du logiciel *elastix*<sup>15</sup>, qui consiste en une collection d'algorithmes couramment utilisés pour résoudre les problèmes de recalage d'images médicales (Klein et al., 2009). Différents protocoles de recalage d'images ont été développés et comparés. Les contours  $RT\text{-}struct_{SPECT}$  ont été propagés aux images PET à l'aide de quatre méthodes de recalage, dénotées : 1)  $rigid_{global}$ , 2)  $deformable_{global}$ , 3)  $rigid_{local}$  et 4)  $rigide_{local, fonctionnal}$ . Le Tableau 6.5 fournit un résumé des méthodes utilisées.

Pour plus de détails sur les matériels et méthodes et les résultats, veuillez consulter les Section 6.2 et 6.3, respectivement.

## VI.3 Conclusions et discussions

### VI.3.1 Contexte

L'objectif principal de cette étude était d'examiner plusieurs protocoles de propagation des contours délimités à partir d'acquisitions SPECT/CT vers PET/CT pour la radioembolisation aux microsphères d' $^{90}\text{Y}$ . Ceux-ci permettent d'effectuer des comparaisons entre les dosimétries prédictives et post-traitement en sélectionnant les transformations d'images appropriées pour ajuster au mieux les structures de référence d'une image à l'autre. En effet, des études rétrospectives doivent encore être réalisées pour évaluer la valeur prédictive du  $^{99m}\text{Tc}$ -MAA SPECT/CT pour la radioembolisation à l' $^{90}\text{Y}$  pour différents scénarios, comme décrit dans l'*Introduction*, Section 6.1.

Les méthodes de propagation des contours et la segmentation de VOI constituent encore aujourd'hui des facteurs limitants pour une évaluation précise de la

15. Voir [elastix software webpage](#)

dosimétrie (Morán et al., 2020). L'étude actuelle s'est concentrée sur cette source d'incertitude afin d'obtenir les outils nécessaires et de renforcer les futures analyses dosimétriques sur des ensembles de données de patients au CLB. Elle démontre clairement que, selon le cas du patient, différentes techniques de recalage doivent être appliquées. Cette étude quantifie l'influence d'une bonne concordance ou d'une discordance entre la dosimétrie prédictive et la dosimétrie post-traitement sur les patients.

### VI.3.2 Comparaisons

Le Tableau 6.18 récapitule les différences obtenues, 1) entre les quatre méthodes, et 2) entre la prédiction et les doses moyennes absorbées après traitement. Une première difficulté réside dans le fait qu'il n'est pas évident de fixer des valeurs seuils pour évaluer si les résultats obtenus sont corrects, mais l'ampleur des différences peut être observée entre les différentes VOIs.

### VI.3.3 La dosimétrie prédictive

Si une prédiction précise des différents VOI peut être effectuée, la sélection des patients peut être optimisée et cela peut fournir une planification de traitement efficace et individualisée. Les doses moyennes absorbées prédites pour les grands volumes que sont les WL<sub>V</sub>, les NLV<sub>WholeLiver</sub> et les NPLV dans cette étude étaient à moins de 10 Gy des valeurs obtenues après traitement. Cependant, ce n'est pas le cas pour les PLV et TV<sub>Total</sub> où des différences beaucoup plus importantes ont été trouvées comme décrit dans le Chapitre 6.

La différence entre les prévisions et les doses moyennes absorbées après traitement par la méthode  $rigid_{local,functional}$  pour le NLV<sub>Target</sub> varie entre 0,6 et 13,6 Gy. Le PLV est la somme du TV<sub>Total</sub> et du NLV<sub>Target</sub>. Cela signifierait donc que la prédiction utilisant la dose moyenne absorbée à la TV<sub>Total</sub> n'est pas précise. En effet, les différences entre la prédiction et la méthode  $\bar{D}_{treatment}$  variaient entre 18,1 et 82,7 Gy avec la méthode  $rigid_{local,functional}$ . Les comparaisons à l'aide de D<sub>50%</sub> et D<sub>2%</sub> entre les prédictions et les doses absorbées obtenues telles que présentées dans la Section 6.3.2 ne sont que sommaires jusqu'à ce que d'autres analyses soient utilisées pour la comparaison.

### VI.3.4 Les limites

Les limites de cette étude sont présentés dans la Section 6.4.2. Il s'agit des volumes d'intérêt définis, des critères d'inclusion et d'exclusion, du mouvement respiratoire et d'autres facteurs de confusion y sont discutés.

### VI.3.5 Orientations futures

Cette étude préliminaire a évalué l'impact des méthodes de recalage pour la propagation des contours sur la quantification de la dose absorbée dans le foie après une radioembolisation à I<sup>90</sup>Y. Les distributions de la dose absorbée dans les régions traitées ainsi que dans les volumes parenchymateux normaux, non tumoraux, ont été réalisées. Les études prospectives peuvent mettre en œuvre les métriques suggérées par Morán et al. (2020), avec des QVH qui sont basés sur une comparaison de la dose absorbée voxel à voxel et traitent directement les différences de dose absorbée. Cependant, leur méthode devrait être validée dans des études

prospectives qui pourraient renforcer cette validation pour apporter des informations supplémentaires dans l'évaluation de la conformité entre les distributions de dose prédictive et absorbée après traitement.

Les résultats de cette étude peuvent également être utiles pour adapter les méthodes de recalage en fonction du cas du patient, en évitant les recalages manuels en cas d'inadéquation lors de la propagation des contours.

### VI.3.6 Conclusion

Ce travail a été réalisé pour valider un protocole de travail pour les techniques de recalage d'images avant de réaliser d'autres études rétrospectives en utilisant les mêmes ensembles de données d'images. Il a permis d'évaluer dans quelle mesure des différences peuvent être obtenues en fonction de la méthode de recalage et sensibilise aux grandes différences qui peuvent conduire à une mauvaise interprétation des données. Par conséquent, différentes méthodes doivent être adaptées à chaque cas de patient. Dans l'ensemble, le  $rigid_{global}$  a été suffisant pour les grands volumes comme le WL<sub>V</sub>, mais pas pour les plus petits comme le TV<sub>Total</sub>.

## VII Conclusions et perspectives

L'objectif de cette thèse était double : d'une part, proposer un modèle de simulation Monte Carlo d'un système PET numérique basé sur des SiPMs et d'autre part, étudier les sources d'erreur qui pourraient avoir un impact sur la quantification de  $^{90}\text{Y}$  en utilisant des simulations Monte Carlo pour le suivi du traitement de radioembolisation à  $^{90}\text{Y}$ . Au cours de cette thèse, nous avons 1) proposé un modèle Monte Carlo du DPC PET/CT, validé à l'aide de simulations GATE par rapport à des mesures expérimentales; 2) étudié l'influence des paramètres de reconstruction OSEM et des durées d'acquisition *listmode* sur la précision quantitative pour la dosimétrie de  $^{90}\text{Y}$  et 3) fourni une évaluation préliminaire de la valeur prédictive du substitut  $^{99m}\text{Tc}$ -MAA aux microsphères en suggérant des approches cohérentes pour le recalage des images.

### VII.1 Modèle Monte Carlo de la PET numérique

Le modèle Monte Carlo du Vereos présenté dans le *Chapitre 4* peut être utile pour de nombreuses études. Au lieu de réaliser des expériences, des évaluations complètes peuvent être effectuées en utilisant le modèle pour ajuster les paramètres, comme l'évaluation expérimentale des paramètres de reconstruction réalisée au cours de cette thèse en utilisant  $^{90}\text{Y}$ . Une perspective à court terme pour suivre le travail de cette thèse pourrait être de valider un protocole utilisant le logiciel CASToR pour la reconstruction des données de sortie GATE pour l'imagerie de  $^{90}\text{Y}$ . Cette validation peut être effectuée en comparant les données simulées aux données expérimentales acquises au cours de cette thèse. Un protocole de reconstruction utilisant l'algorithme OSEM a été validé par rapport aux données du  $^{18}\text{F}$  par Salvadori (2020), ce qui pourrait aider à élaborer le même protocole pour  $^{90}\text{Y}$  dans CASToR. Ceci fait, il est possible de réaliser des études évaluant par exemple l'étendue des effets de volume partiel (PVEs) (Soret, Bacharach et Buvat, 2007) sur des objets de différentes formes et tailles complexes, et contenant des concentrations d'activité variables. Les coefficients de recouvrement de la dose absorbée peuvent être dérivés en utilisant des données simulées et non expérimentales, et corrigés en utilisant des géométries connues et des métriques adaptées.

De plus, les évaluations des paramètres de reconstruction effectuées dans le *Chapitre 5* peuvent être poursuivies pour différents scénarios à l'aide du modèle Monte Carlo de la PET, en faisant varier les concentrations d'activité pour différents SBRs, ce qui est expérimentalement coûteux en temps et pose des problèmes de radioprotection. Cette démarche permettrait de constituer un ensemble complet de paramètres de reconstruction évalués pouvant être adaptés à des cas spécifiques de patients ou à des régions spécifiques de distributions d'activité, et ce pour différents isotopes utilisés en imagerie PET, qui pourraient faire partie de la dosimétrie individualisée pour les patients. En effet, les paramètres évalués au cours de cette thèse l'ont été pour un SBR de 9 :1 tout au long des expériences utilisant le fantôme NEMA, et pourraient varier dans les configurations des patients. Des géométries de fantômes plus complexes que les volumes sphériques peuvent être étudiées. De plus, les facteurs de confusion de la qualité de l'image et de la quantification peuvent être étudiés comme dans Strydhorst et al. (2016) pour plusieurs isotopes.

Dans une perspective à plus long terme, le modèle peut également être utile pour : 1) la génération d'ensembles de données à des fins d'apprentissage pour des techniques d'intelligence artificielle et 2) le test des données générées en utilisant la reconstruction d'images avec le protocole de travail tel que décrit ci-dessus. Par exemple, dans un futur projet de recherche, appelé projet ANR MoCaMed (2021-2025)<sup>16</sup> en collaboration avec différentes équipes de recherche (CREATIS, LATIM, LIRIS et CLB) à partir de septembre 2021, le modèle peut être d'une utilité potentielle pour simuler à partir des fichiers *espace de phase* générés, stockant les particules quittant le patient imagé, comme dans une étude récemment publiée dans notre équipe de recherche à Lyon appliquée à la radiothérapie externe par Sarrut, Krah et Létang (2019) en utilisant des GANs, et la preuve de concept à l'imagerie SPECT par Sarrut et al. (2021a). Ces fichiers *espace des phases* peuvent être utilisés comme entrée dans les simulations Monte Carlo des systèmes d'imagerie nucléaire et de notre modèle PET. Le modèle pourrait également être utile pour d'autres travaux de doctorat à venir dans notre équipe à CREATIS en collaboration avec d'autres institutions, sur l'utilisation de l'intelligence artificielle pour la reconstruction d'images multimodales dans le projet ANR MultiRecon (2021-2024)<sup>17</sup>, ou sur l'étude de l'imagerie PET numérique paramétrique dans les applications théranostiques pour les traitements du cancer à base du <sup>177</sup>Lu (2021-2024)<sup>18</sup>.

Une autre perspective pourrait également être la simulation d'images de patients pour évaluer les distributions de dose, comme dans l'étude de Roncali et al. (2020) et tester leurs méthodes en utilisant le CFD pour la prédiction du traitement par radioembolisation. Pour résumer, le modèle proposé a un large éventail d'applications potentielles et peut soutenir un certain nombre de projets futurs, en particulier pour optimiser les performances d'imagerie, identifier l'influence des paramètres d'acquisition et de reconstruction sur la qualité de l'image et l'estimation de la dose absorbée, évaluer de nouvelles méthodes de reconstruction et de correction.

La plateforme GATE a été utilisée pour la simulation Monte Carlo de différents types de systèmes d'imagerie et de détection. Elle a cependant plus de 15 ans, est gérée par la communauté et son code est complexe et évolue en permanence. Une revue récente de Sarrut et al. (2021b) a souligné les nombreuses simulations de tomographes à émission dans GATE, où le travail au cours de cette thèse a été mis en valeur. En effet, GATE (et d'autres plateformes similaires) reste le standard pour la conception, l'optimisation et l'évaluation des systèmes d'imagerie et est toujours

16. Voir [MoCaMed](#)

17. Voir [MultiRecon](#)

18. Voir [Parametric PET](#)



utile aux industriels, aux chercheurs et aux étudiants. L'une des limites de GATE est cependant son approche Monte Carlo et les simulations sont lentes et demandent une grande puissance de calcul. Les simulations de suivi de photons optique ne peuvent donc pas être réalisées sur un anneau de détecteurs PET complet et sont limitées à des paires de détecteurs.

À mon avis, GATE restera un outil utile pour les simulations Monte Carlo de systèmes d'imagerie complexes et peut être facilement adapté aux systèmes futurs, en s'appuyant toutefois sur des contributions volontaires pour maintenir et mettre en œuvre de nouveaux modules. Il est actuellement envisagé, dans le cadre de la collaboration OpenGATE, de proposer une évolution majeure du système GATE en exploitant les outils Python<sup>19</sup> pour une analyse plus rapide et des intégrations PyTorch qui pourraient ouvrir la voie à des développements au sein de GATE exploitant l'IA. GATE présente également un intérêt pour les étudiants et est de plus en plus utilisé pour enseigner les méthodes de Monte Carlo pour la physique médicale dans les universités. Pour une meilleure compréhension, une documentation plus complète et plus claire devrait être mise à disposition, en particulier pour les étudiants qui découvrent GATE. Des efforts sont faits de ce côté et les utilisateurs de GATE sont réellement réceptifs à des questions spécifiques. Enfin, une toute nouvelle plateforme serait l'intégration future des premiers outils de simulation et d'intégration de l'analyse de photons optique complète et de la sortie des données, étant donné l'intérêt croissant pour la détection de la luminescence de Cerenkov pour une résolution TOF plus rapide (Lecoq et al., 2020). Les fichiers de données d'entrée et de sortie sont aussi généralement trop volumineux et l'IA pourrait aider à réduire leur taille.

## VII.2 Reconstruction pour la dosimétrie

Les perspectives à court terme de la deuxième contribution à cette thèse sur l'évaluation des paramètres de reconstruction rejoignent celles qui peuvent être réalisées avec le modèle Monte Carlo de la PET, comme décrit précédemment. L'évaluation nous a permis de comprendre le comportement de l'algorithme OSEM sous des conditions de statistiques de comptage faibles et des conditions intrinsèques à la désintégration de  $^{90}\text{Y}$ . Il peut être utile pour différentes institutions et travaux de recherche de construire leurs protocoles en suivant les mêmes méthodologies, en commençant par notre propre institution au CLB. L'évaluation a également permis de réduire de 30% la durée d'acquisition du patient après une radioembolisation à  $^{90}\text{Y}$ , ce qui rend l'examen plus confortable pour le patient. La méthodologie utilisant le DVH et le RMSD peut être appliquée à d'autres isotopes, et à d'autres modalités d'imagerie, comme pour l'imagerie SPECT après une thérapie au Lutathera utilisant le  $^{177}\text{Lu}$ . Des études futures pourraient évaluer l'influence du PSF sur la quantification, en faisant varier les paramètres (fixés à 1 itération avec un noyau de régularisation de 6 mm dans cette thèse, conformément aux recommandations pour le  $^{18}\text{F}$ ) en utilisant les jeux de données *listmode* du fantôme acquis, ce qui pourrait permettre d'obtenir une quantification plus précise. L'étude était basée sur des géométries de fantômes simples, sans hétérogénéité. Par conséquent, de nouveaux fantômes peuvent désormais être facilement conçus par une imprimante 3D pour prendre en compte des géométries plus réalistes. La modélisation de distributions d'activité hétérogènes dans les montages expérimentaux est également un point sur lequel la recherche devrait se concentrer. En effet, les fantômes utilisés

19. Voir [GateTools](#)

présentaient des distributions d'activité homogènes dans les différents compartiments des différents fantômes.

### VII.3 Dosimétrie prédictive vs. dosimétrie de contrôle

Les paramètres de reconstruction sélectionnés et évalués dans la deuxième contribution ont été utilisés dans la troisième et dernière contribution à cette thèse, qui fournit des résultats préliminaires, évaluant rétrospectivement la valeur prédictive des microsphères d' $^{90}\text{Y}$  pour le traitement par radioembolisation. L'objectif principal de ce travail a été de choisir les méthodes de recalage les plus appropriées pour comparer la distribution de l'activité prédictive et celle obtenue suite au traitement et ne peut pas encore être utilisé pour interpréter la valeur prédictive du  $^{99m}\text{Tc}$ -MAA, limitée à 10 patients. Ce travail sera poursuivi de manière prospective à court terme, avec une meilleure sélection et classification des patients pour l'analyse. En effet, plusieurs aspects n'ont pas été pris en compte pour une sélection adéquate des patients. Il faudrait un comité validant chaque patient sur la base de critères d'inclusion spécifiques (tels que la maladie hépatique seule, le statut de performance ECOG, ...) et de critères d'exclusion (tels qu'une radioembolisation ou une radiothérapie externe préalable, ...). Des outils et des mesures tels que ceux proposés par Levillain et al. (2020) pourraient être testés pour valider leur méthodologie en utilisant des QVH et QF combinés avec DVH qui pourraient renforcer la nôtre. Comme ils l'ont précisé, les QVH fournissent également une évaluation visuelle et quantitative de la concordance entre la dosimétrie prédictive et la dosimétrie post-traitement. Leur code Python pour le calcul des QVH est disponible à l'adresse suivante [Github/QVH](#). En outre, une synthèse utilisant des analyses statistiques sera réalisée.

### VII.4 Autres perspectives

Les jeux de données de patients disponibles au sein du CLB (environ 45 patients) pourraient être utilisés dans une étude future pour intégrer des paramètres radiobiologiques spécifiques à la radioembolisation à l'aide de microsphères d' $^{90}\text{Y}$ , même si le TRT n'a pas encore une compréhension fondamentale de la radiobiologie sous-jacente et de la réponse à la dose. Cela permettrait d'optimiser davantage les approches dosimétriques et thérapeutiques puisque des effets de la dose commencent à être établis pour la radioembolisation à l' $^{90}\text{Y}$  (Hoven et al., 2016). D'autres paramètres que la dose moyenne absorbée peuvent être utilisés pour l'évaluation, comme le EUD, le BED et le EUBED, tels qu'ils sont utilisés dans la Chiesa et al. (2015). Il semble également intéressant de déterminer les paramètres de radiosensibilité à l' $^{90}\text{Y}$  et de mieux comprendre la dose-réponse des lésions hépatiques, comme dans une étude récente de Lee et al. (2019). Les recherches futures sur les futurs patients recevant un traitement par radioembolisation à l' $^{90}\text{Y}$  au CLB devraient envisager de caractériser la relation entre la dose absorbée par la tumeur et la réponse après la radioembolisation à l' $^{90}\text{Y}$ , telle que dans l'étude SARAH (Hermann et al., 2020) et l'étude DOSISPHERE-01 (Garin et al., 2021). La radiomique dérivée de la PET pour l' $^{90}\text{Y}$  pourrait être combinée à la dose absorbée afin d'améliorer la construction de modèles pour prédire la réponse et la progression tumorale dans le traitement par radioembolisation, en utilisant les métriques suggérées par Wei et al. (2020) dans une publication récente. Toutes ces études pourraient permettre de renforcer les recommandations telles que publiées récemment par Salem et al. (2019) et Levillain et al. (2021).

Même si des progrès majeurs ont été réalisés dans l'imagerie PET au cours des dernières années, avec une amélioration de la résolution temporelle d'un facteur 2 en utilisant des SiPMs au lieu de PMTs, le PVE reste un obstacle majeur à la qualité des images PET et donc à l'évaluation de la dose absorbée (Rousset, Ma et Evans, 1998; Soret, Bacharach et Buvat, 2007; Brodin, 2011; Erlandsson et al., 2012). Notre équipe de recherche au sein de CREATIS/CLB travaille actuellement sur la faisabilité de corriger davantage les PVEs suite à la reconstruction d'images par une boîte à outils proposée par Thomas et al. (2016), et de récupérer des informations en utilisant les jeux de données d'images acquises au cours de cette thèse. La technologie PET est encore perfectible, et la recherche d'une meilleure résolution temporelle souhaitée à moins de 100 ps sur les systèmes cliniques et d'une couverture axiale de plus en plus large promet des résultats satisfaisants qui amélioreraient la qualité et la quantification des images. En laboratoire, une CTR de 95 ps utilisant des SiPMs a été atteinte (Seifert et al., 2012). La quête d'une résolution temporelle de 10 picosecondes a également été lancée, avec l'utilisation d'une émission Cerenkov ultra-rapide pour les détecteurs TOF PET qui pourrait permettre à la technologie PET de contourner l'utilisation d'algorithmes de reconstruction, il peut y avoir une formation d'image en temps réel et seule la correction de l'atténuation serait nécessaire (Lecoq, 2017; Lecoq et al., 2020). En fait, l'utilisation d'algorithmes de reconstruction ajoute un biais supplémentaire aux données quantitatives, indépendamment des performances de la PET, comme le montre cette thèse. En effet, l'information TOF seule peut être suffisante pour obtenir une distribution de la concentration d'activité avec une meilleure résolution temporelle puis spatiale, et une meilleure quantification pour le suivi de la radioembolisation à l' $^{90}\text{Y}$  suite au traitement. Par ailleurs, une étape majeure a été franchie avec l'installation du premier eFOV corps entier clinique et commercial en 2020, doté d'un FOV axial d'un mètre de long contrairement aux FOV traditionnels de 15 à 30 centimètres, et équipé de SiPMs. Bénéficiant d'angles solides plus larges pour la détection avec divers systèmes de FOV longs en cours de développement (Zhang et al., 2017; Badawi et al., 2019; Vandenberghe, Moskal et Karp, 2020), la PET offre donc une technologie et un impact encore plus fortifiants dans l'utilisation clinique.

# Appendices



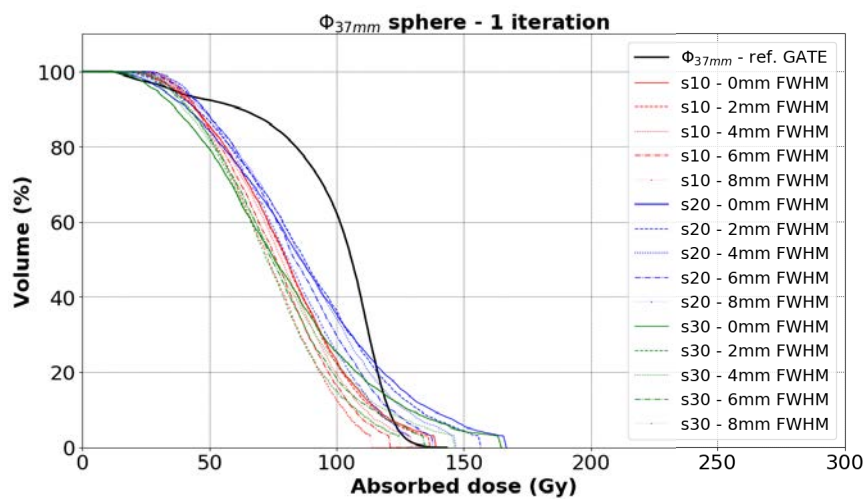
## Appendix A

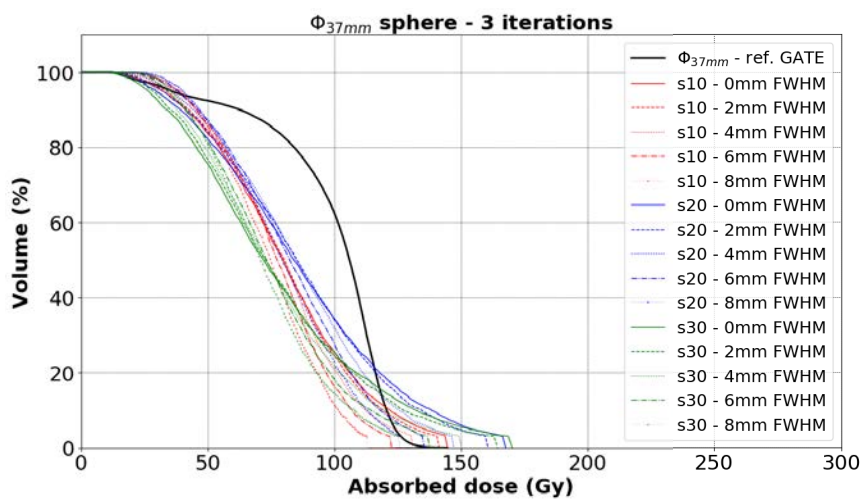
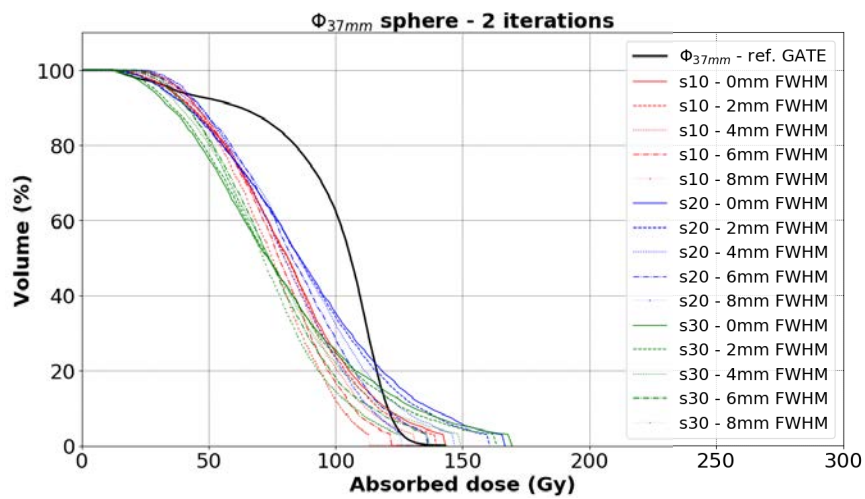
# Evaluation of reconstruction parameters using DVH

Appendices A1 to A6 hereafter provide the  $DVH_{pet}^{VSV}$  for all reconstruction parameter sets evaluated for the 37 to 10 mm spheres in decreasing diameter order, respectively.

### A1 37 mm sphere

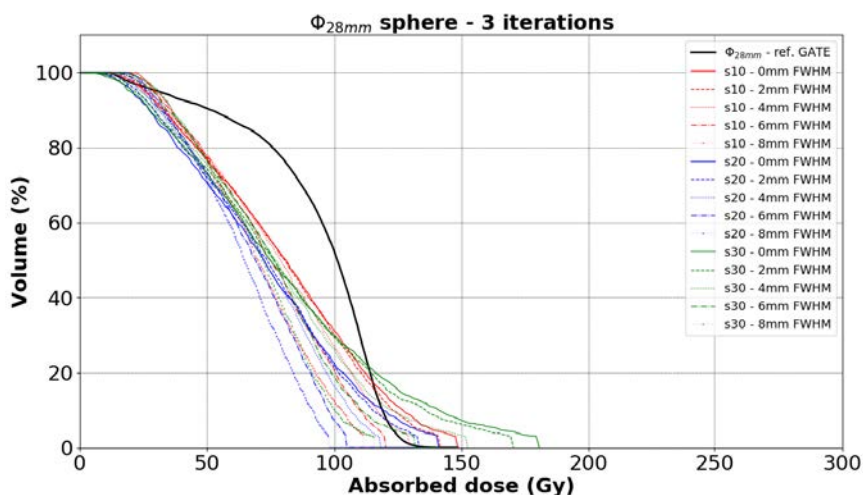
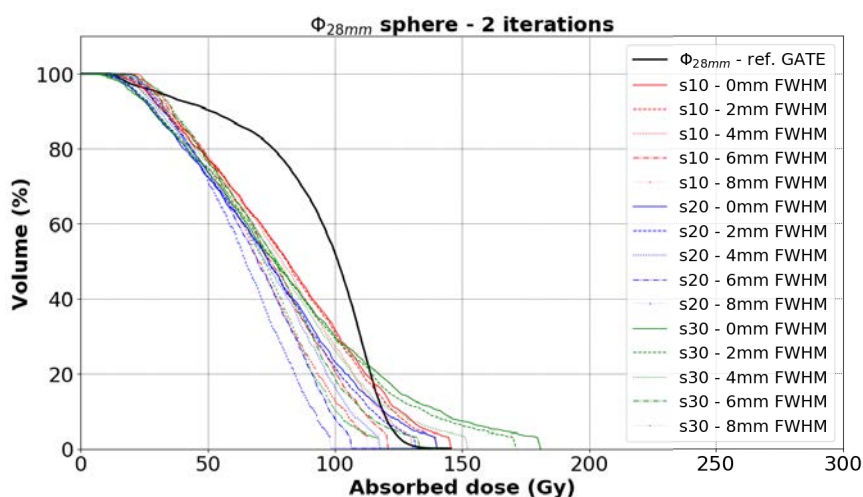
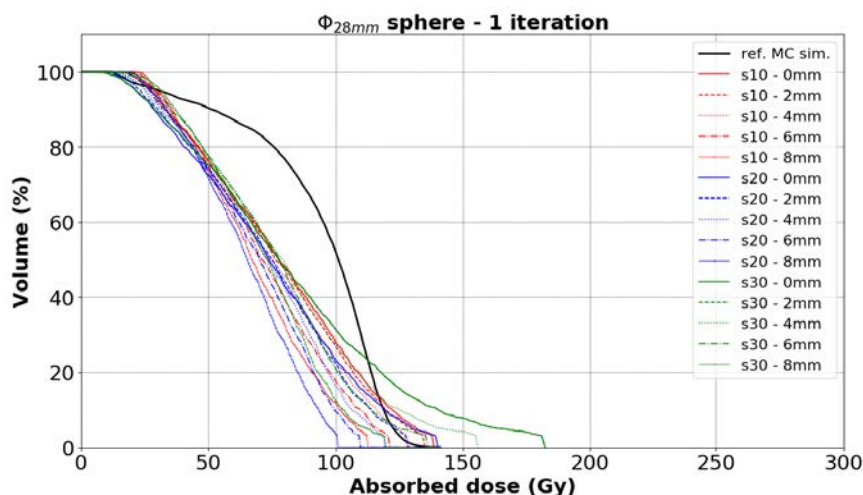
The  $DVH_{pet}^{VSV}$  for all 45 reconstructions (15 reconstructions per number of iterations) are compared to  $DVH_{ref}^{MC}$  (black curves) for the 37 mm sphere in the figures below. Each of the three figures are for a fixed number of iterations.





## A2 28 mm sphere

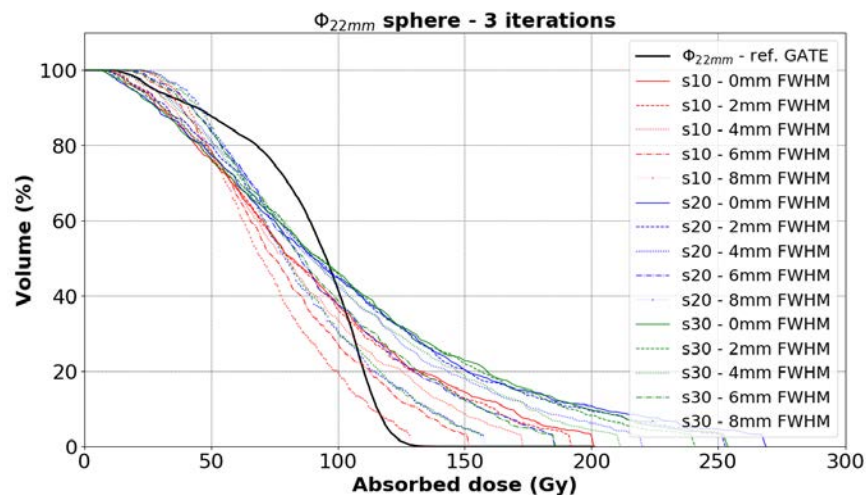
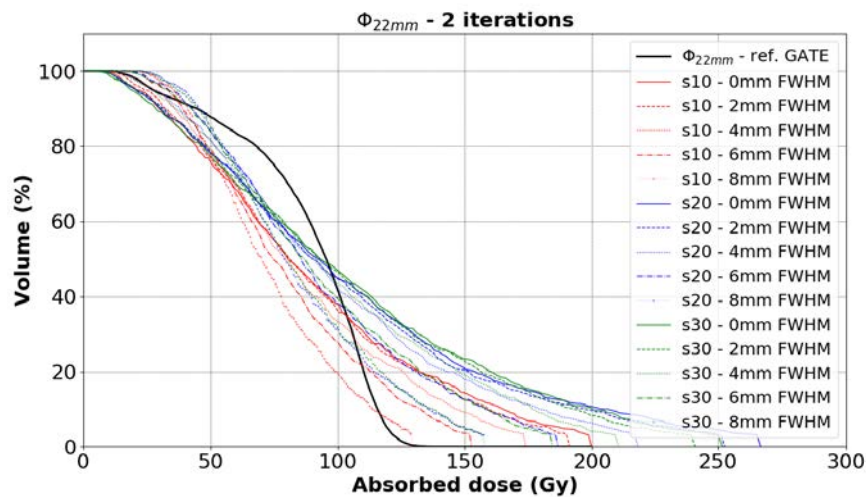
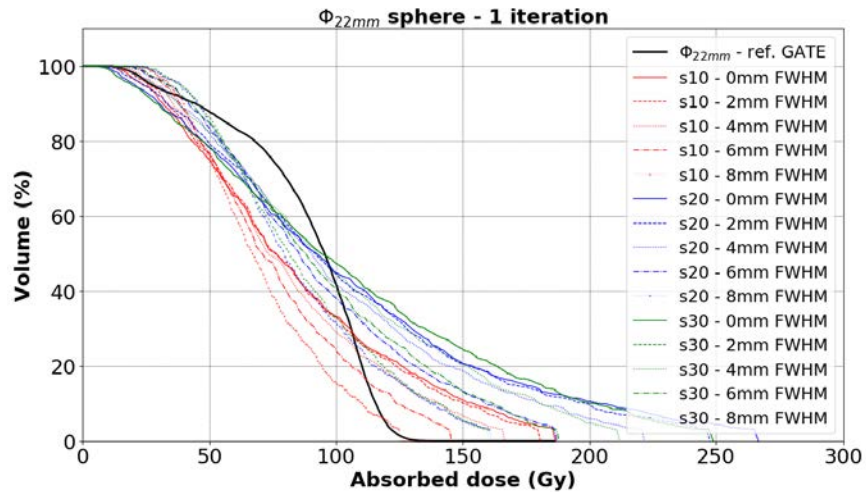
The  $DVH_{pet}^{VSV}$  for all 45 reconstructions (15 reconstructions per number of iterations) are compared to  $DVH_{ref}^{MC}$  (black curves) for the 28 mm sphere in the figures below. Each of the three figures are for a fixed number of iterations.





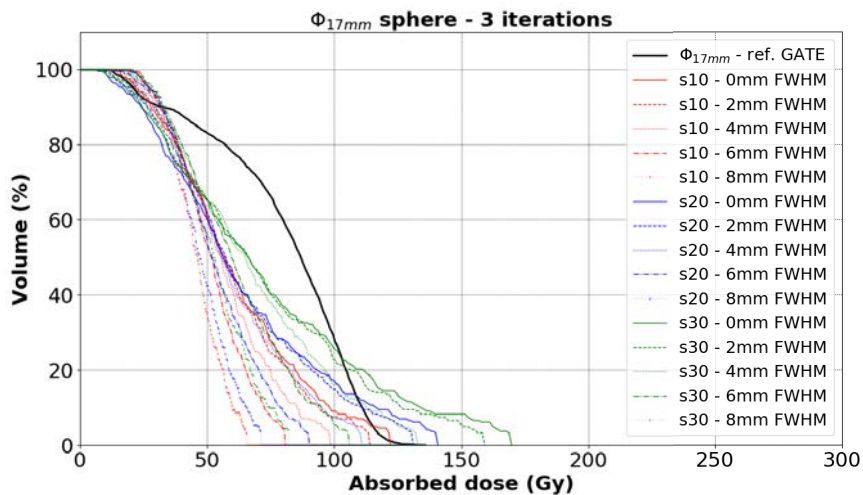
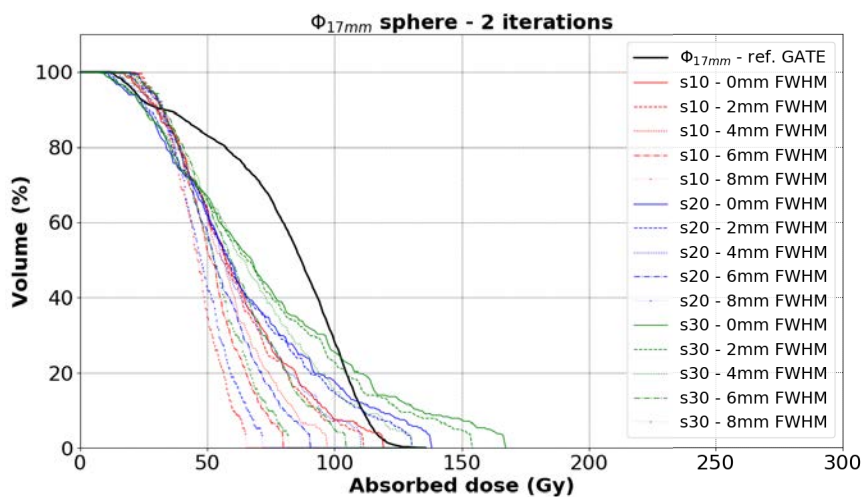
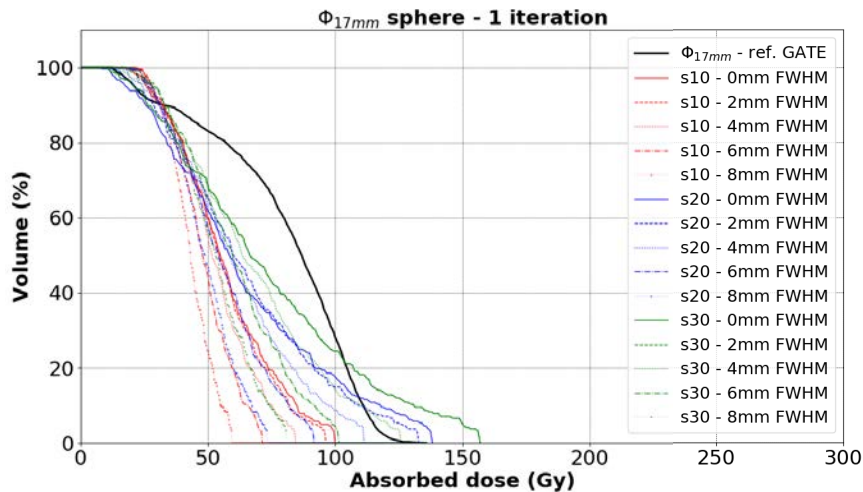
### A3 22 mm sphere

The  $DVH_{pet}^{VSV}$  for all 45 reconstructions (15 reconstructions per number of iterations) are compared to  $DVH_{ref}^{MC}$  (black curves) for the 22 mm sphere in the figures below. Each of the three figures are for a fixed number of iterations.



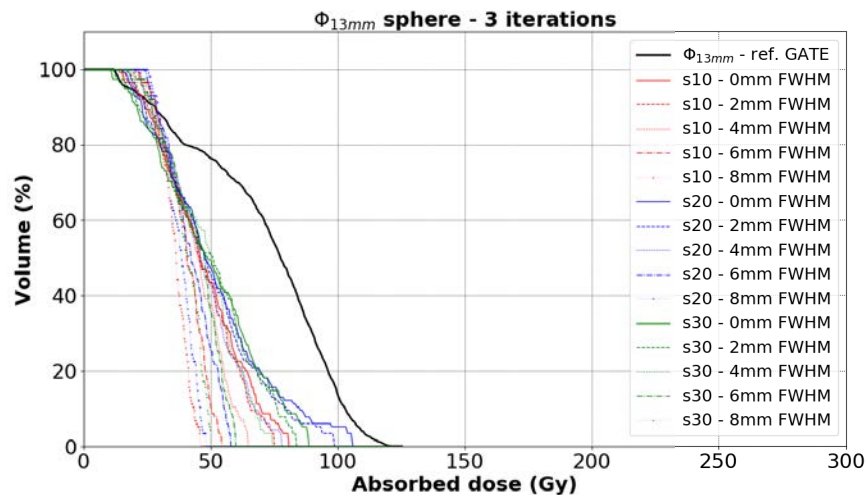
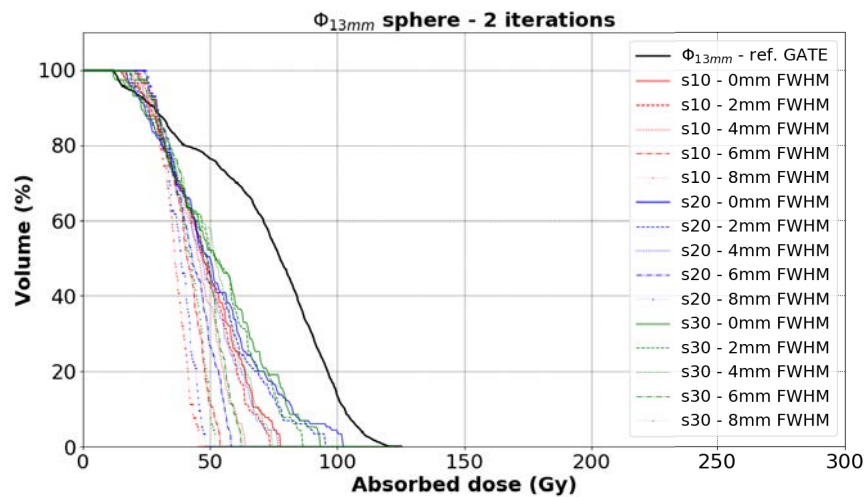
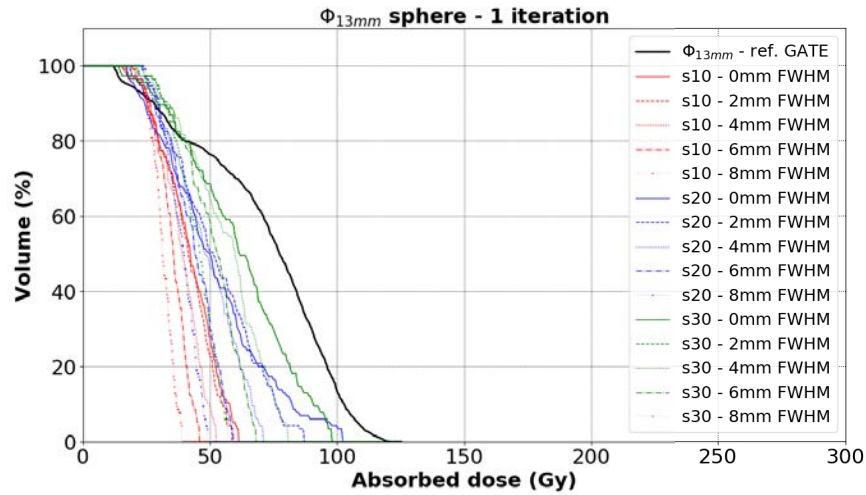
## A4 17 mm sphere

The  $DVH_{pet}^{VSV}$  for all 45 reconstructions (15 reconstructions per number of iterations) are compared to  $DVH_{ref}^{MC}$  (black curves) for the 17 mm sphere in the figures below. Each of the three figures are for a fixed number of iterations.



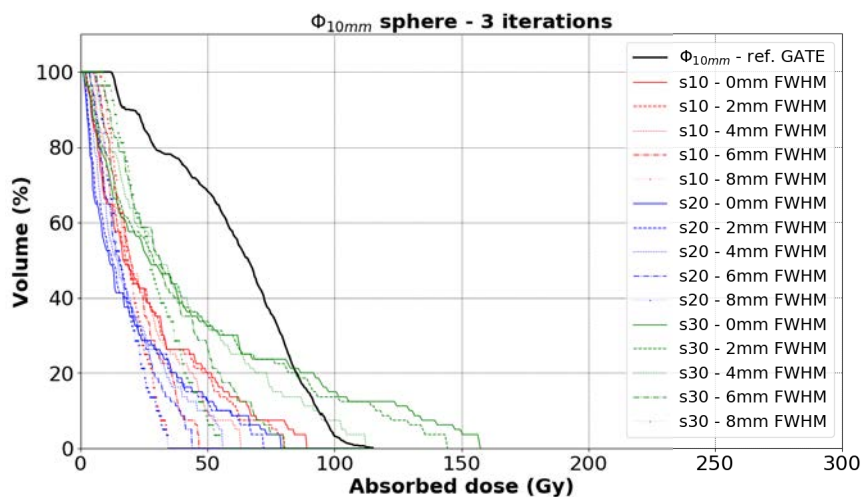
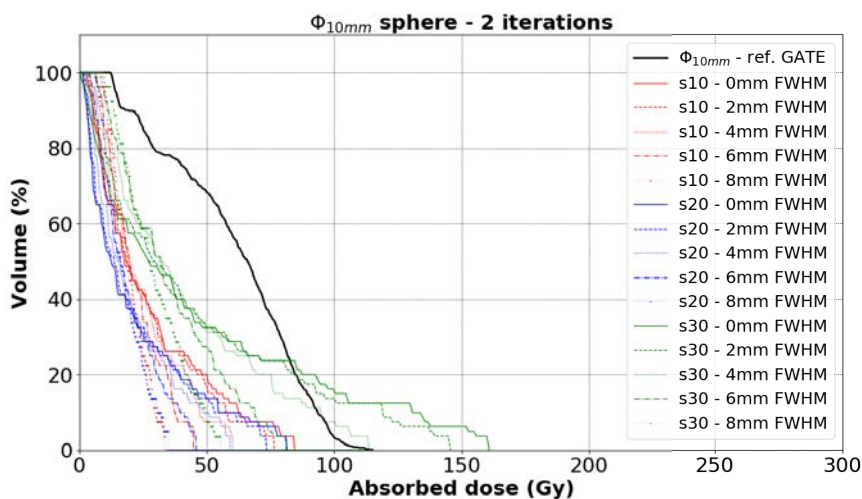
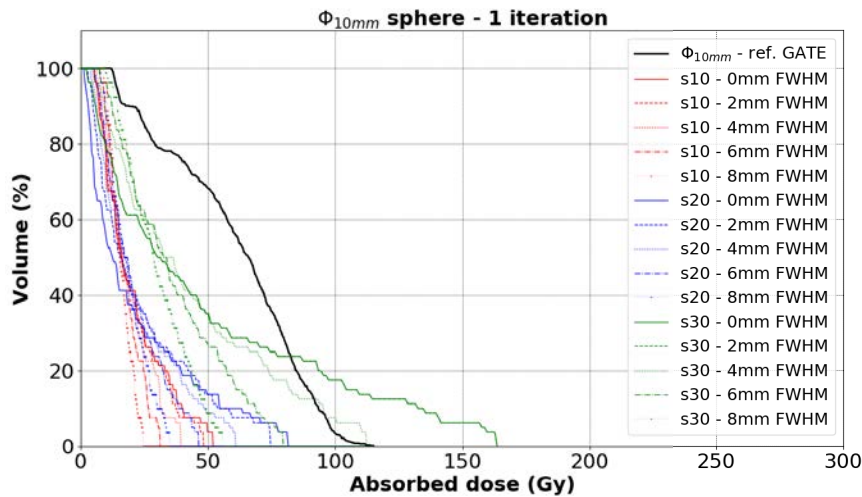
## A5 13 mm sphere

The  $DVH_{pet}^{VSV}$  for all 45 reconstructions (15 reconstructions per number of iterations) are compared to  $DVH_{ref}^{MC}$  (black curves) for the 13 mm sphere in the figures below. Each of the three figures are for a fixed number of iterations.



## A6 10 mm sphere

The  $DVH_{pet}^{VSV}$  for all 45 reconstructions (15 reconstructions per number of iterations) are compared to  $DVH_{ref}^{MC}$  (black curves) for the 10 mm sphere in the figures below. Each of the three figures are for a fixed number of iterations.

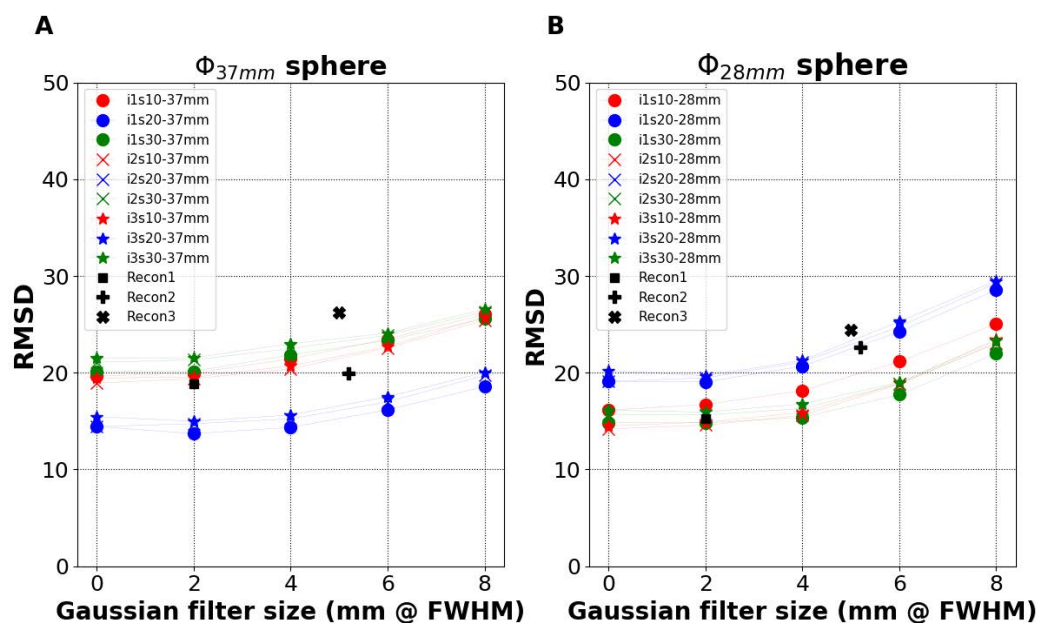


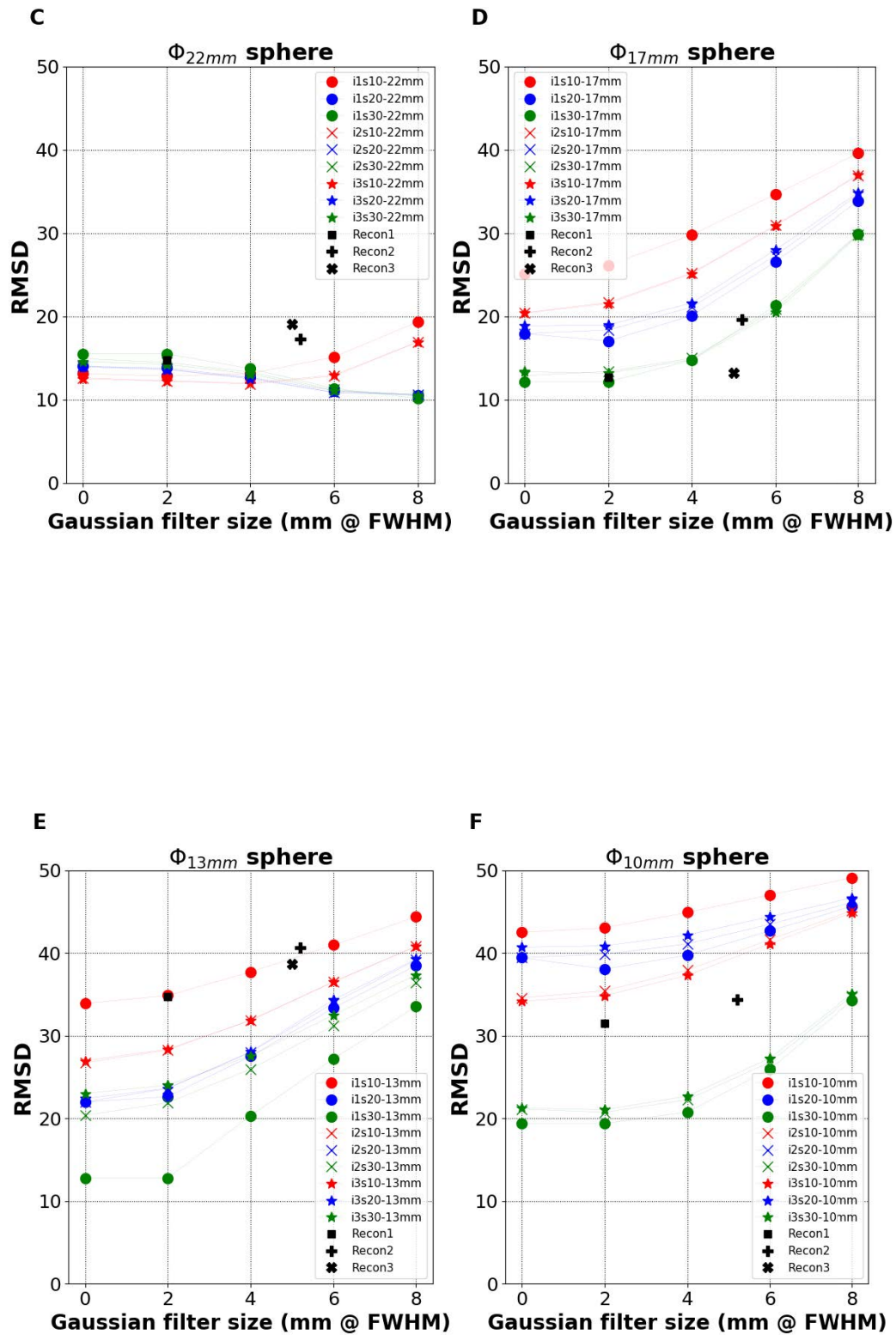


## Appendix B

# Evaluation of reconstruction parameters using RMSD

The figures hereafter depict RMSD values between  $DVH_{pet}^{VSV}$  and  $DVH_{ref}^{MC}$  against the post-reconstruction Gaussian filter size (FWHM) for all spheres (45 reconstructions per sphere).

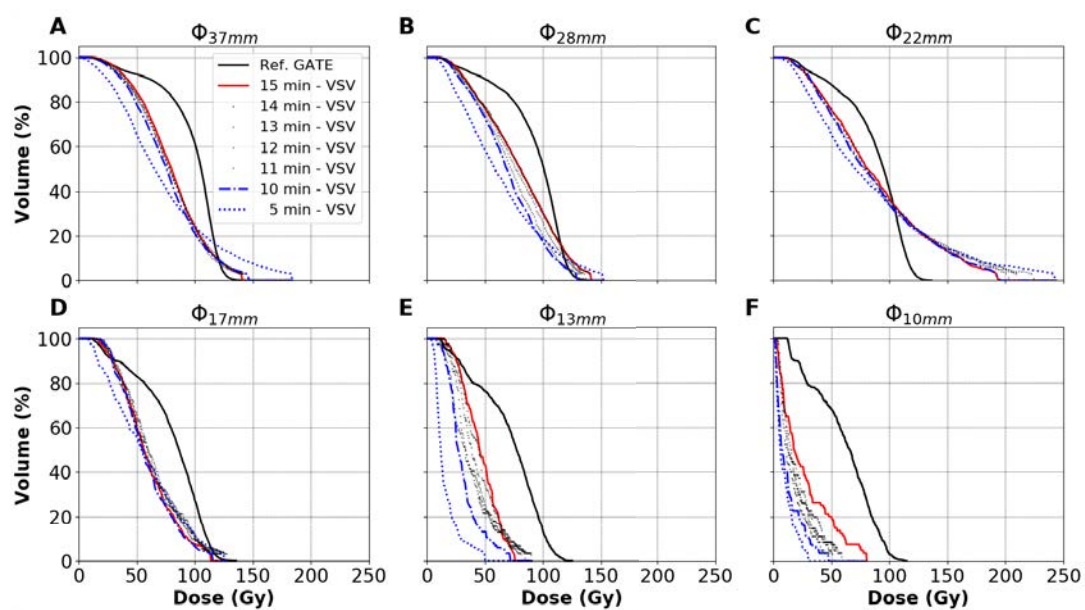




## Appendix C

# Influence of acquisition duration

The figures hereafter depict the  $DVH_{pet}^{VSV}$  variation (5, 10, 11, 12, 13, 14 and 15 mins) for all spheres.







## Appendix D

# Comparing pre- and per-treatment DVHs

### D1 Delineated volumes.

The three tables below provide the volumes of the delineated VOIs for the WLW, PLV and TV<sub>Total</sub> on the SPECT/CT and obtained volumes after propagation of structures on the PET/CT images.

Volumes for the WLW.

Patient number	Volumes in cm <sup>3</sup> - WLW				Predictive SPECT/CT
	Post-treatment PET/CT				
	<i>rigid<sub>global</sub></i>	<i>deformable<sub>global</sub></i>	<i>rigid<sub>local</sub></i>	<i>rigid<sub>local,functional</sub></i>	
#1	3103.0	3331.8	3103.0	3103.6	3102.6
#2	2092.0	2375.7	2091.3	2091.5	2091.3
#3	2821.9	2544.0	2821.9	2822.0	2822.1
#4	2998.7	3397.7	2998.8	2998.4	2998.2
#5	1532.9	1495.4	1532.8	1532.1	1532.9
#6	1319.9	1320.0	1319.7	1319.7	1319.7
#7	2145.8	2647.7	2145.8	2145.9	2146.1
#8	995.8	906.8	996.0	996.4	996.0
#9	1452.5	1479.6	1452.5	1452.2	1452.2
#10	1284.8	1331.6	1284.8	1284.2	1284.5

Volumes for the PLV.

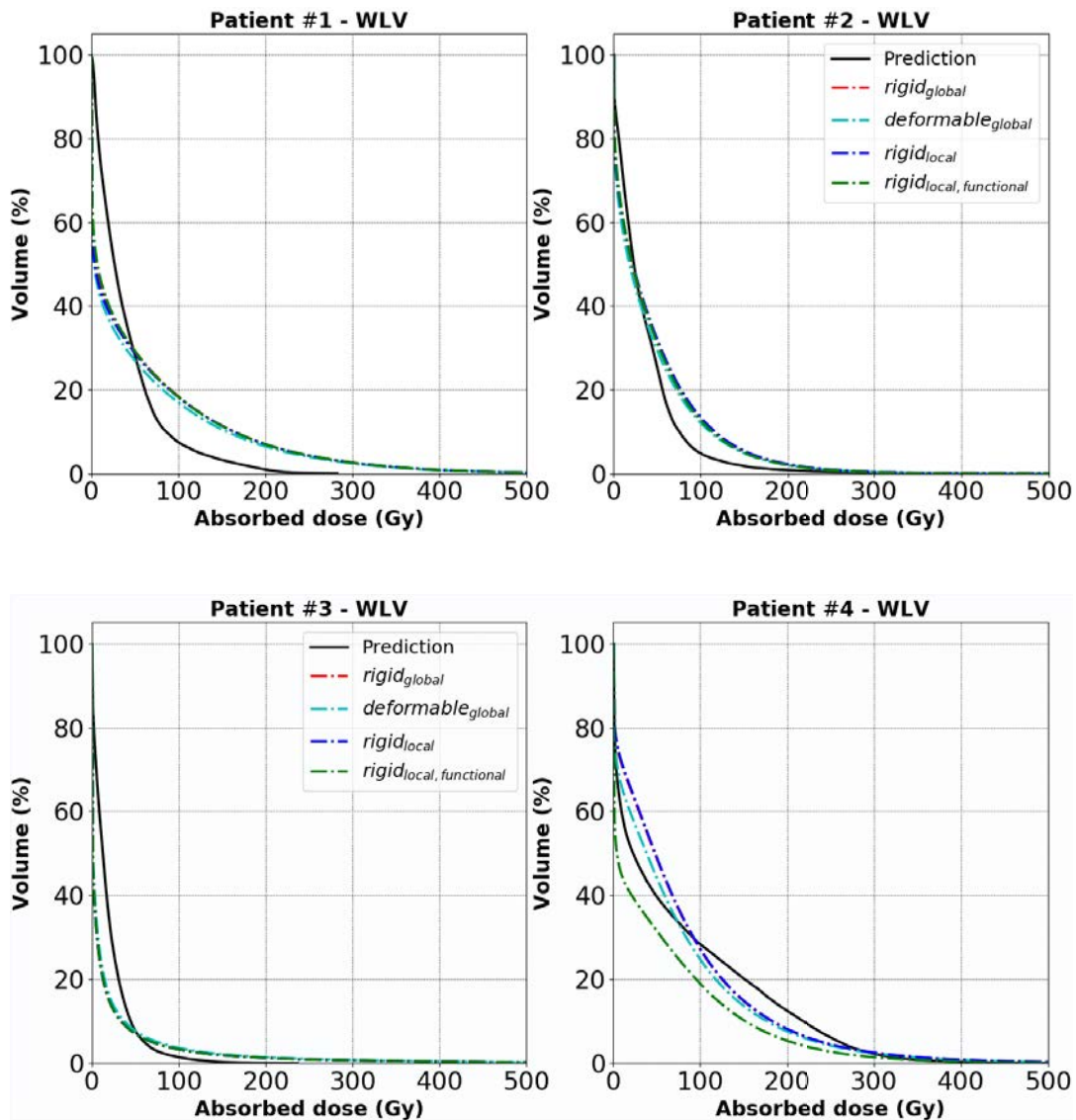
Patient number	Volumes in cm <sup>3</sup> - PLV				Predictive SPECT/CT
	Post-treatment PET/CT				
	<i>rigid<sub>global</sub></i>	<i>deformable<sub>global</sub></i>	<i>rigid<sub>local</sub></i>	<i>rigid<sub>local,functional</sub></i>	
#1	2119.0	2243.6	2119.0	2120.0	2118.3
#2	1138.2	1315.0	1138.2	1138.4	1138.2
#3	1461.4	1274.4	1461.4	1461.4	1461.4
#4	1482.4	1620.7	1482.3	1482.6	1482.2
#5	609.9	595.8	609.9	610.2	609.9
#6	139.8	138.4	139.4	139.5	139.4
#7	1214.5	1532.8	1214.3	1214.6	1214.5
#8	610.1	538.5	610.1	610.0	610.1
#9	324.4	302.3	324.4	324.5	324.8
#10	798.5	846.6	798.5	797.9	799.0

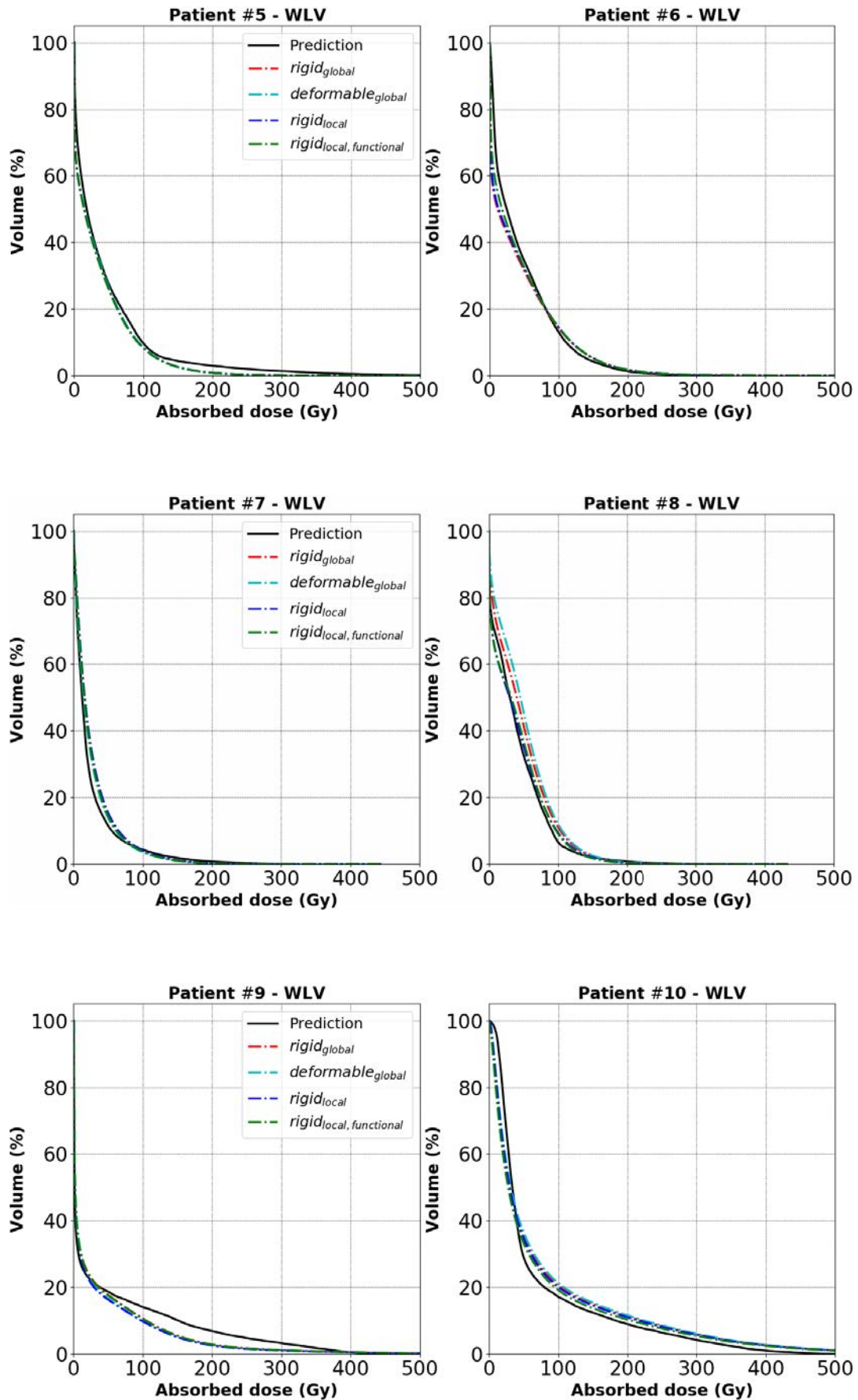
Volumes for the  $TV_{Total}$ .

Patient number	Volumes in $cm^3$ - $TV_{Total}$				Predictive SPECT/CT
	Post-treatment PET/CT				
	<i>rigid<sub>global</sub></i>	<i>deformable<sub>global</sub></i>	<i>rigid<sub>local</sub></i>	<i>rigid<sub>local,functional</sub></i>	
#1	335.2	386.4	335.3	335.3	335.5
#2	228.5	316.9	228.6	228.7	228.6
#3	106.3	85.7	106.3	106.7	106.7
#4	-	-	-	-	-
#5	175.6	166.9	175.6	175.5	175.9
#6	751.9	712.7	751.7	752.1	751.7
#7	152.3	190.9	152.3	153.3	152.3
#8	-	-	-	-	-
#9	-	-	-	-	-
#10	174.8	199.6	174.7	174.5	175.0

## D2 Whole liver

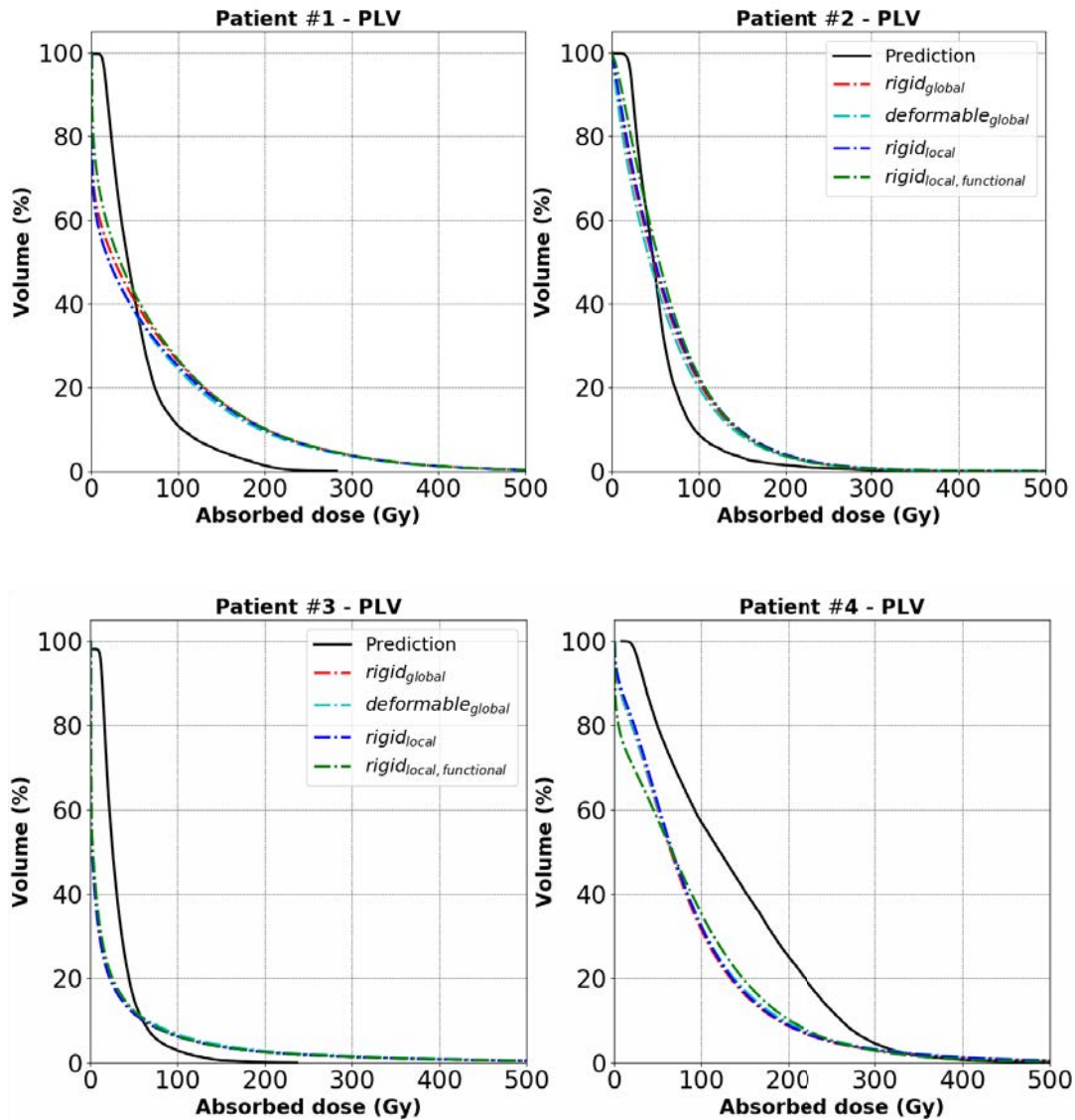
The figures below depict the obtained  $DVH_{j,treatment}$  considering the WLV (whole liver volume) using each of the four registration methods,  $j$ , for all patients. The  $DVH_{predicted}$  is also depicted on each figure. Refer to Section 6.3.1.1 for a summary of the results for the WLV.

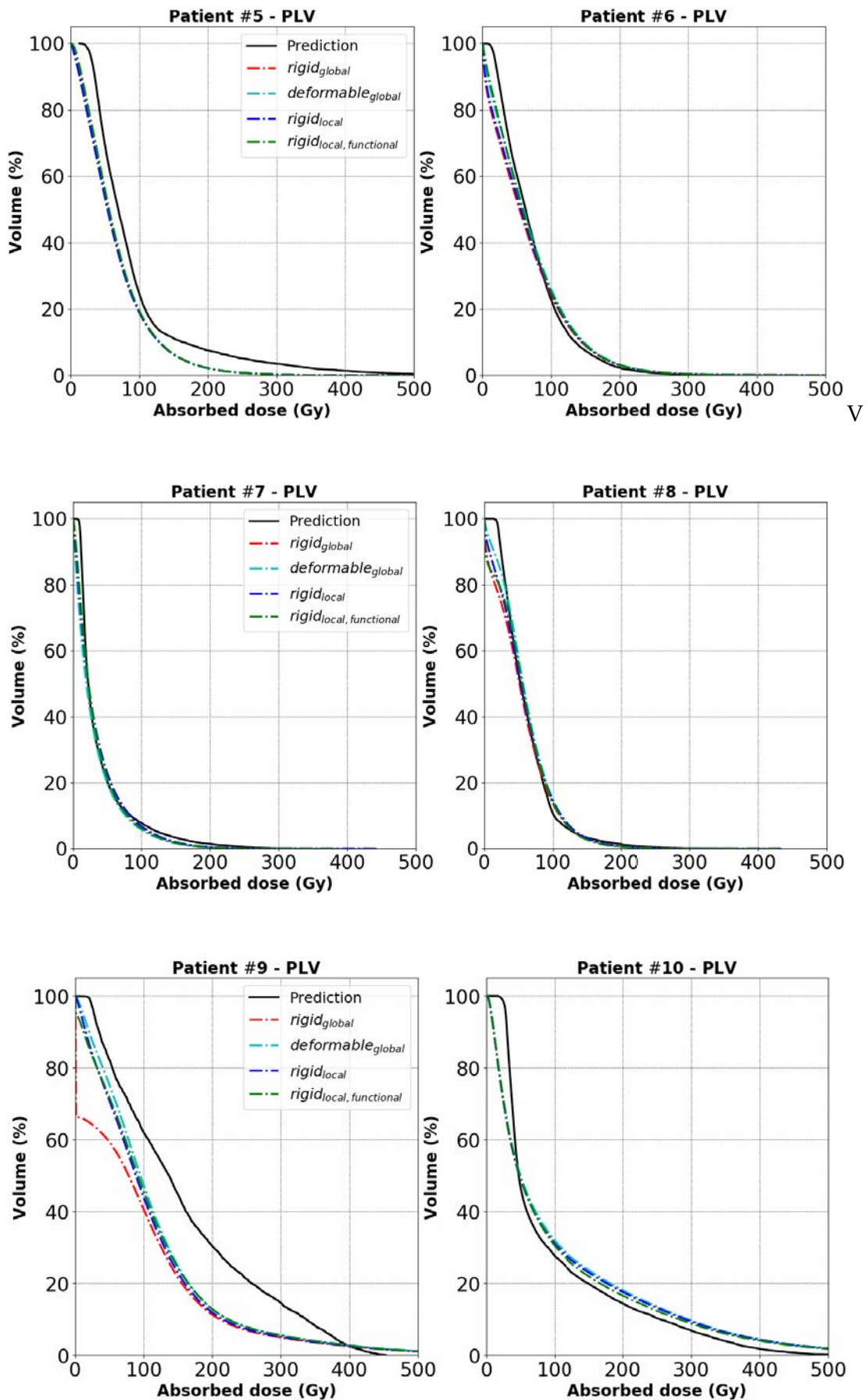




## D3 Perfused liver

The figures below depict the obtained  $DVH_{j,treatment}$  considering the PLV (perfused liver volume) using each of the four registration methods,  $j$ , for all patients. The  $DVH_{predicted}$  is also depicted on each figure. Refer to Section 6.3.1.2 for a summary of the results for the PLV.





## D4 Activity distribution

The  $ADV_{5\%}$  was used to define the PLV. Obtained results for the  $ADV_{5\%}$  in each patient are provided hereafter. The first table below is similar to those presented in Section 6.3.1. The second table following is similar to those presented in Section 6.3.2.

The figures afterwards depict the obtained  $DVH_{j,treatment}$  for the  $ADV_{5\%}$  (activity distribution volume) using each of the four registration methods,  $j$ , for all patients. The  $DVH_{predicted}$  is also depicted on each figure.

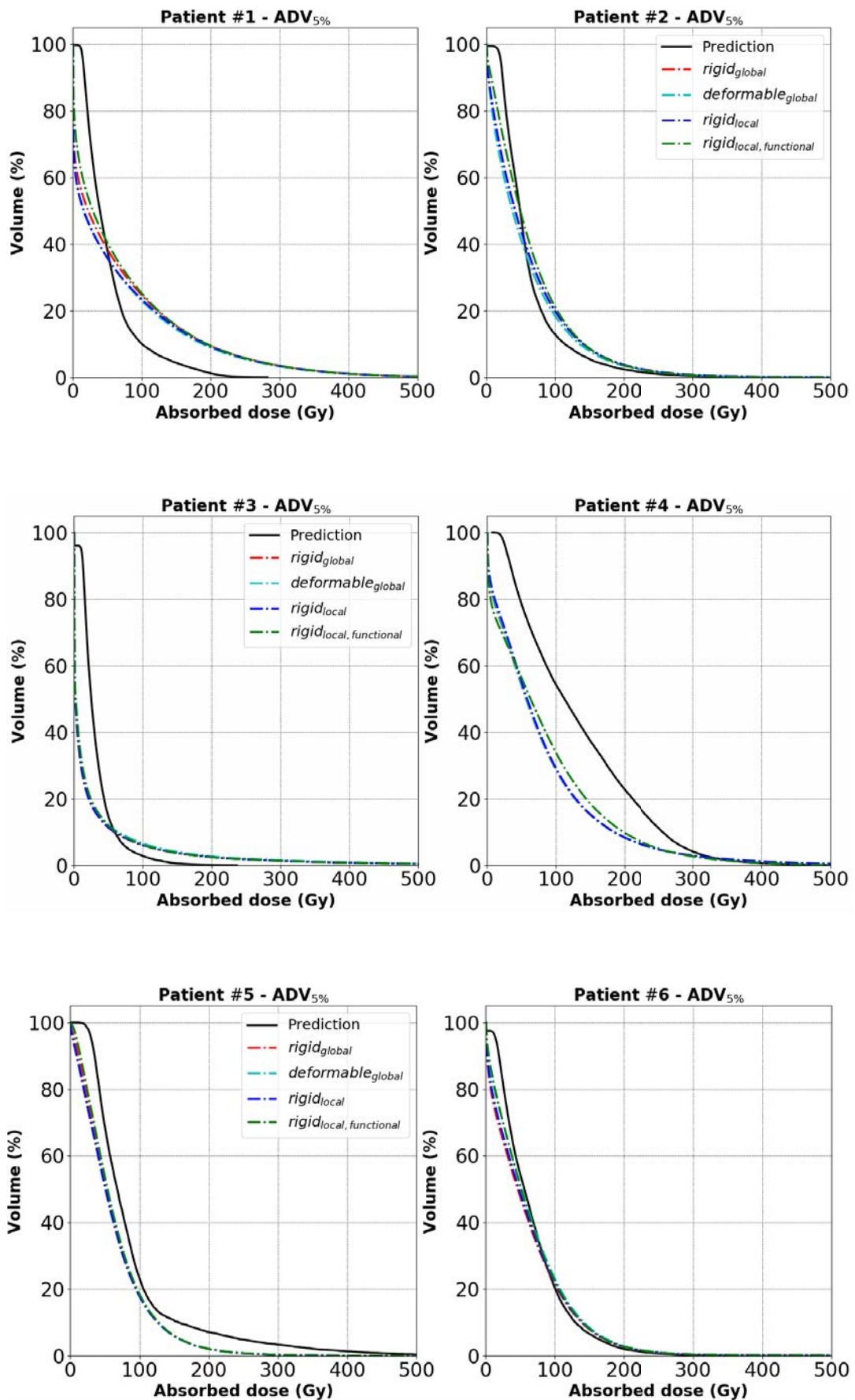
$\bar{D}_{treatment}$  for the  $ADV_{5\%}$  using different registration methods between SPECT/CT and PET/CT images. Values for  $\bar{D}_{predicted}$  are also provided.

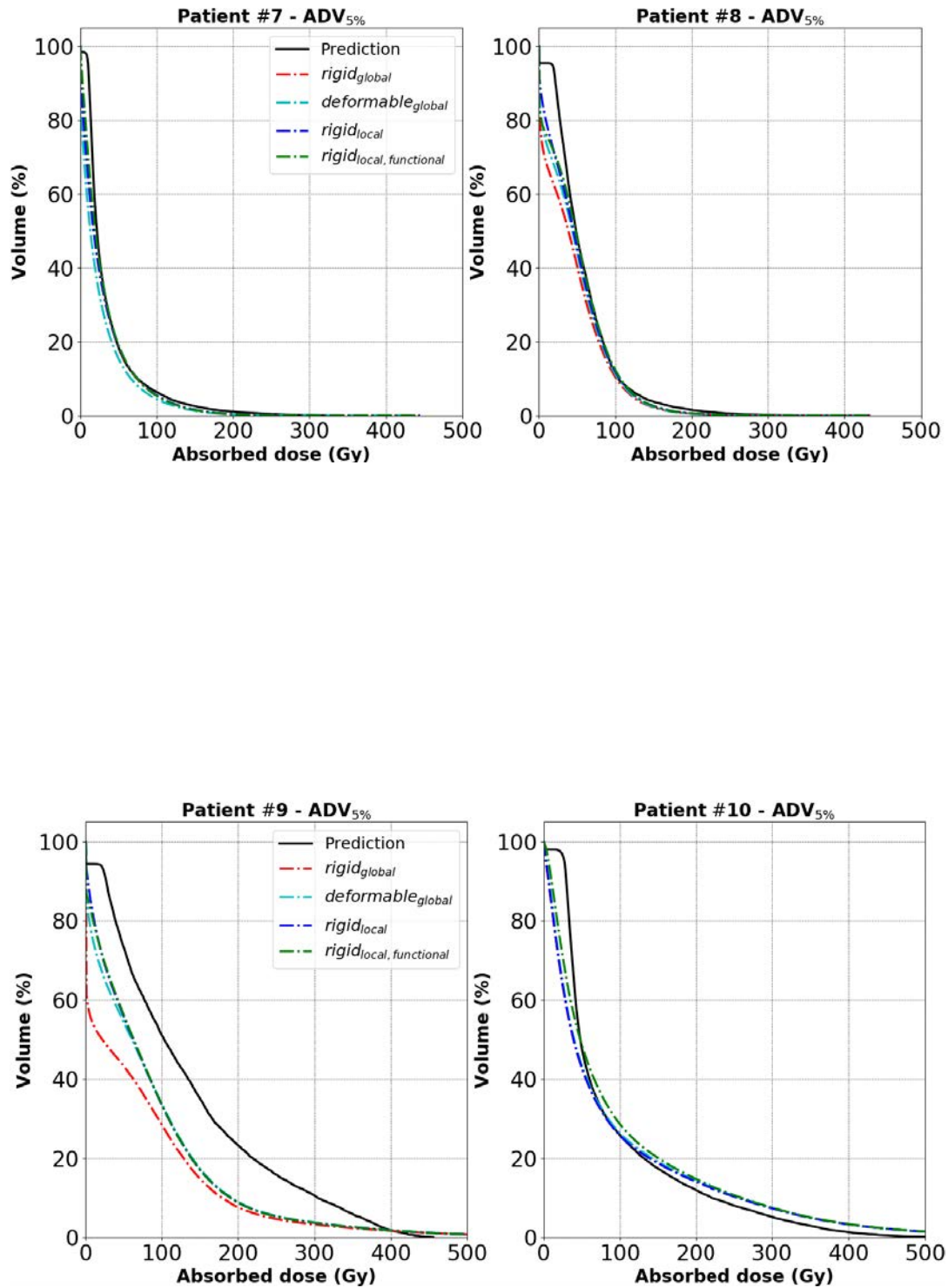
Patient number	Mean absorbed doses in Gy - $ADV_{5\%}$				Predictive SPECT/CT
	Post-treatment PET/CT				
	$rigid_{global}$	$deformable_{global}$	$rigid_{local}$	$rigid_{local,functional}$	
#1	69.3	61.3	62.0	68.3	51.5
#2	59.8	56.3	59.8	64.5	60.9
#3	23.0	24.4	22.7	23.8	32.1
#4	79.2	79.3	80.5	83.6	131.2
#5	62.8	61.5	61.3	64.5	88.0
#6	60.0	64.5	61.2	63.9	66.9
#7	29.6	25.2	29.6	31.0	35.4
#8	44.3	47.9	50.4	51.1	58.6
#9	67.8	84.1	85.9	85.7	132.7
#10	88.2	89.2	87.9	95.1	88.8

Predicted absorbed doses compared to obtained absorbed doses following treatment for the  $ADV_{5\%}$ , using the  $rigid_{local,functional}$ .

Patient number	Absorbed doses in Gy - $ADV_{5\%}$					
	Predicted SPECT/CT			Treatment monitoring PET/CT		
	$D_{mean}$	$D_{50\%}$	$D_{2\%}$	$D_{mean}$	$D_{50\%}$	$D_{2\%}$
#1	51.5	39.5	186.4	68.3	29.2	350.3
#2	60.9	49.2	211.6	64.5	49.4	234.2
#3	32.1	25.3	111.0	23.8	2.8	227.1
#4	131.2	112.4	335.1	83.6	63.3	320.0
#5	88.0	67.8	354.8	64.5	53.9	201.0
#6	66.9	55.9	201.1	63.9	51.3	215.0
#7	35.4	21.8	162.8	31.0	19.7	139.1
#8	58.6	48.7	186.5	51.1	48.1	158.4
#9	132.7	103.1	396.1	85.8	63.4	385.6
#10	89.0	48.2	373.1	95.1	47.9	461.3

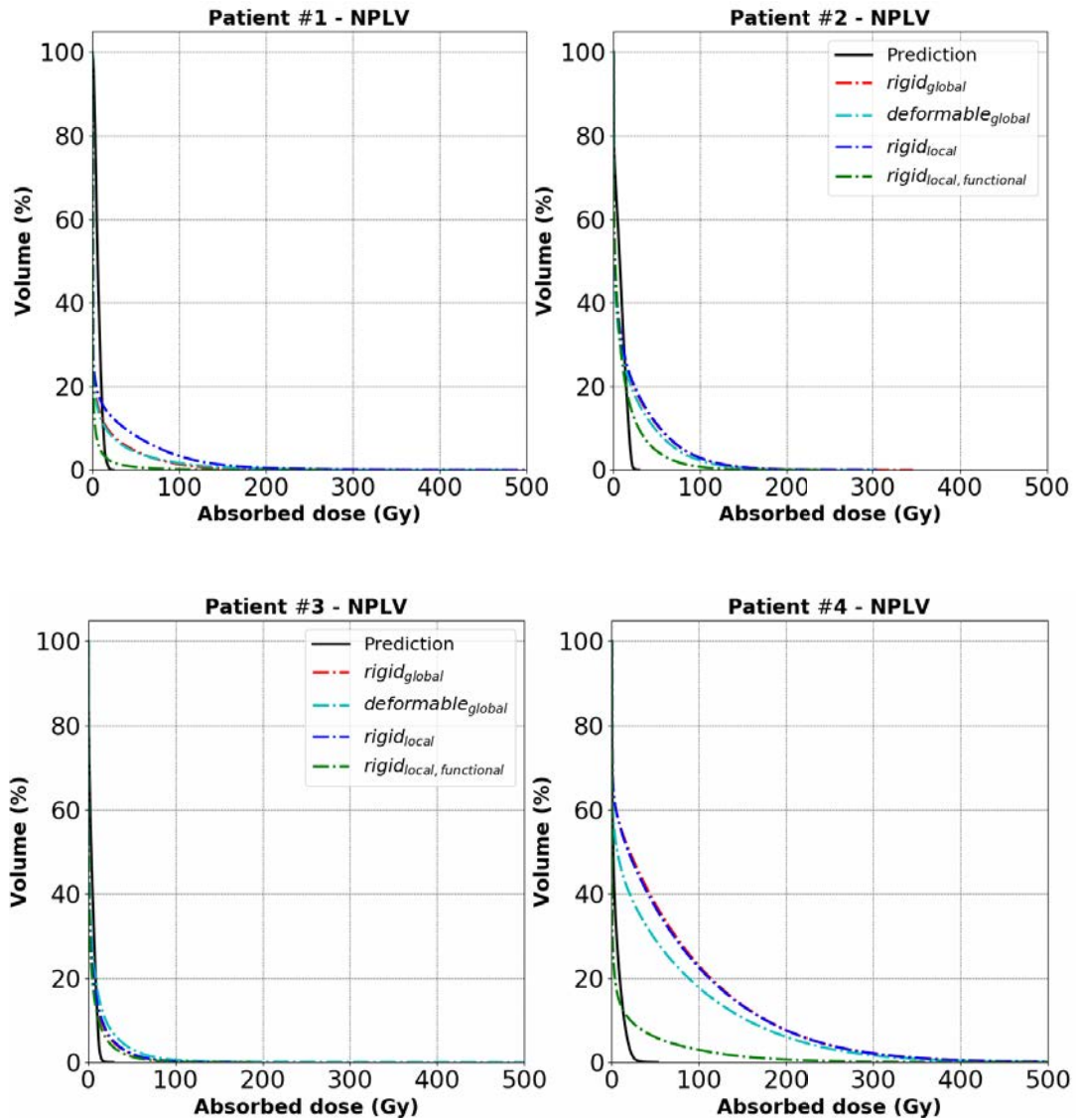


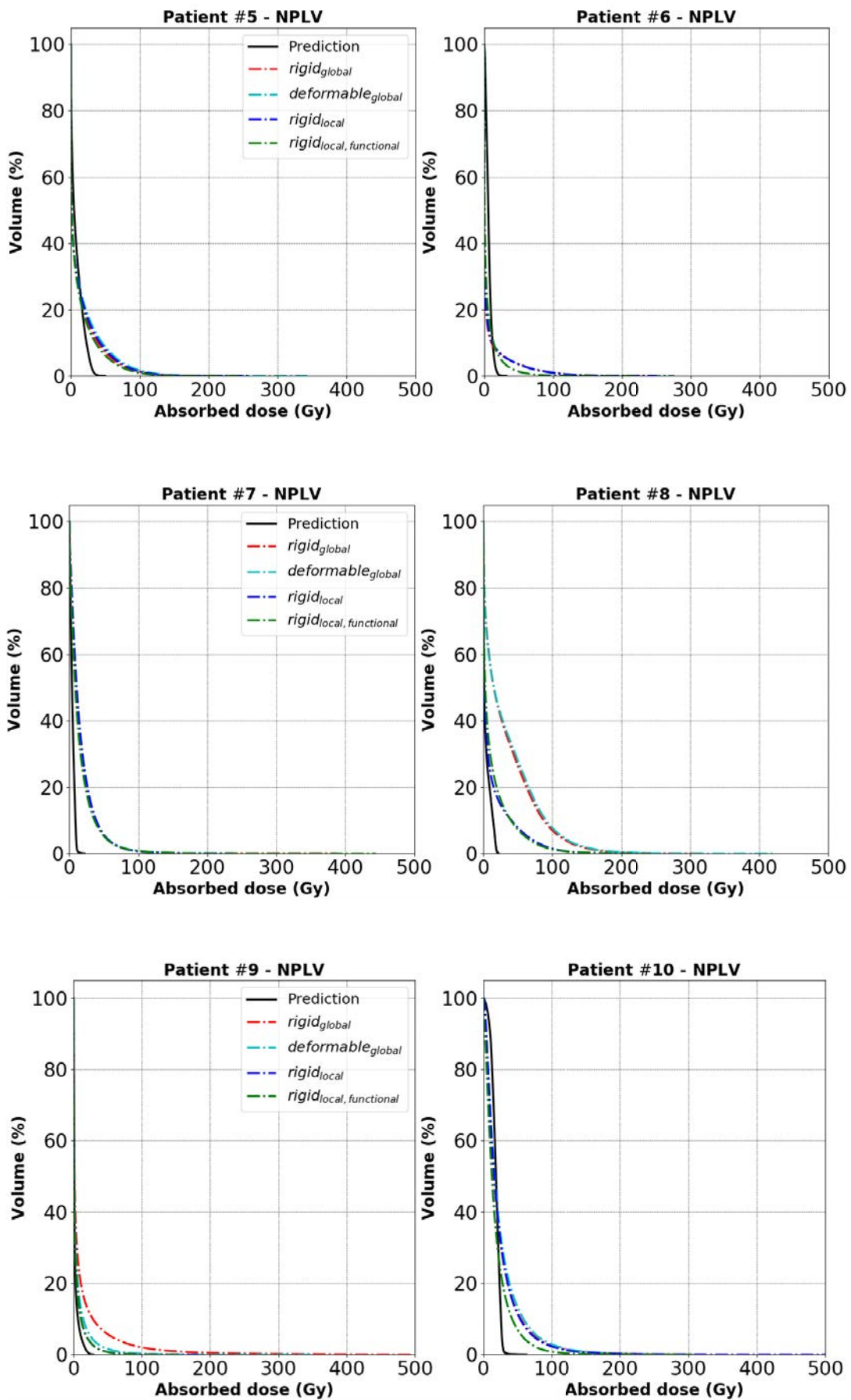




## D5 Non-perfused liver

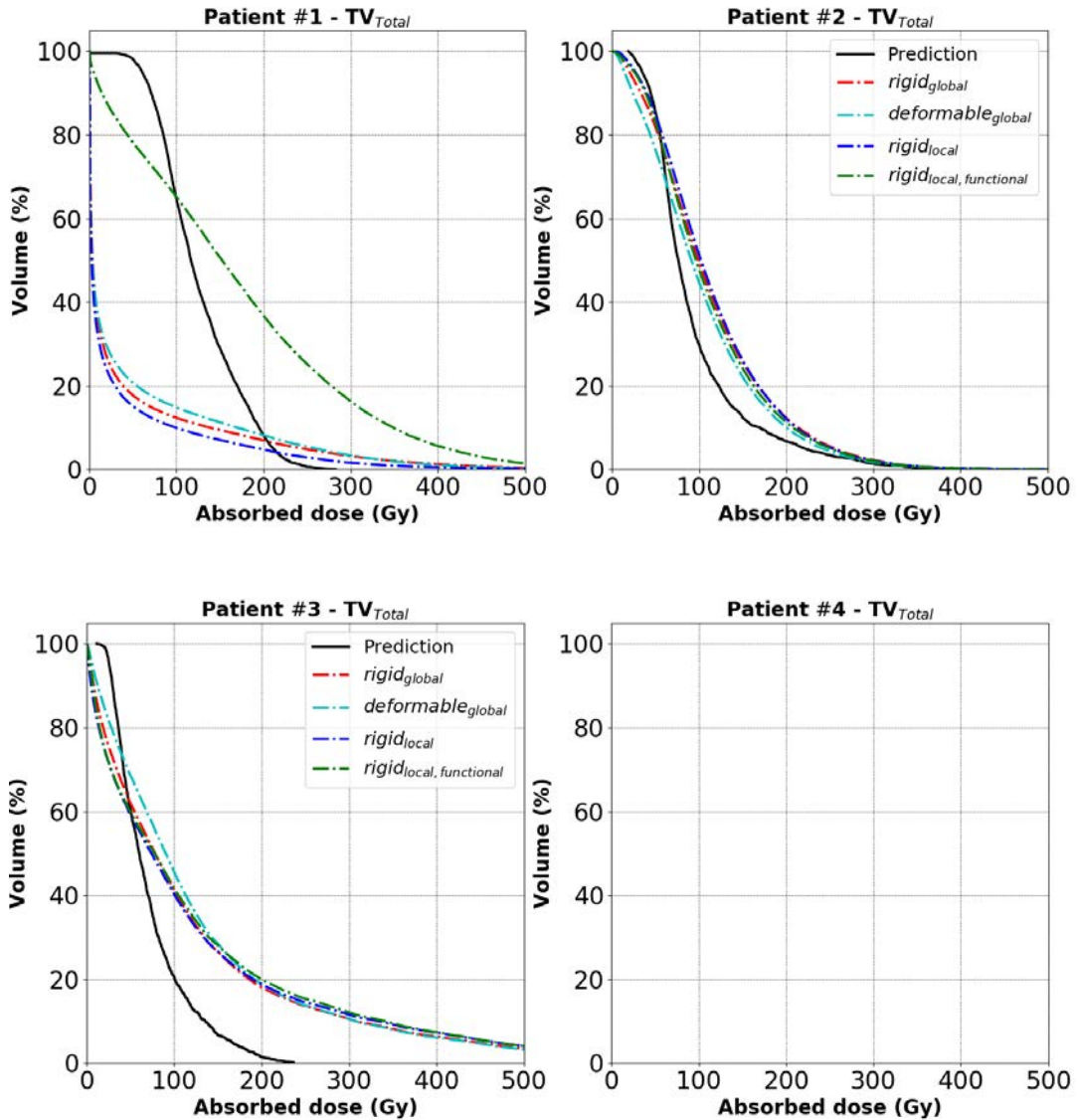
The figures below depict the obtained  $DVH_{j,treatment}$  considering the NPLV (non-perfused liver volume) using each of the four registration methods,  $j$ , for all patients. The  $DVH_{predicted}$  is also depicted on each figure. Refer to Section 6.3.1.3 for a summary of the results for the NPLV.

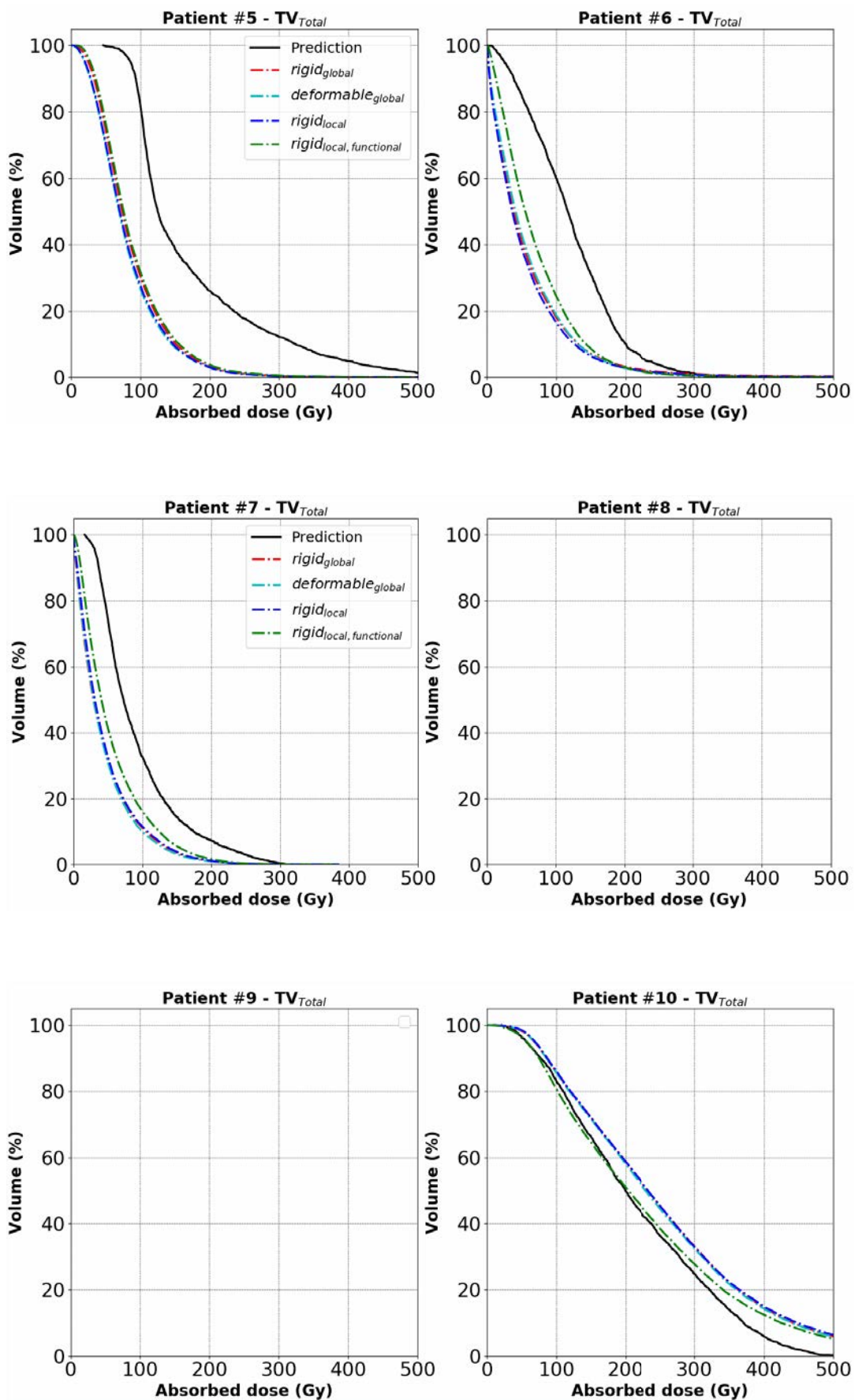




## D6 Total tumour

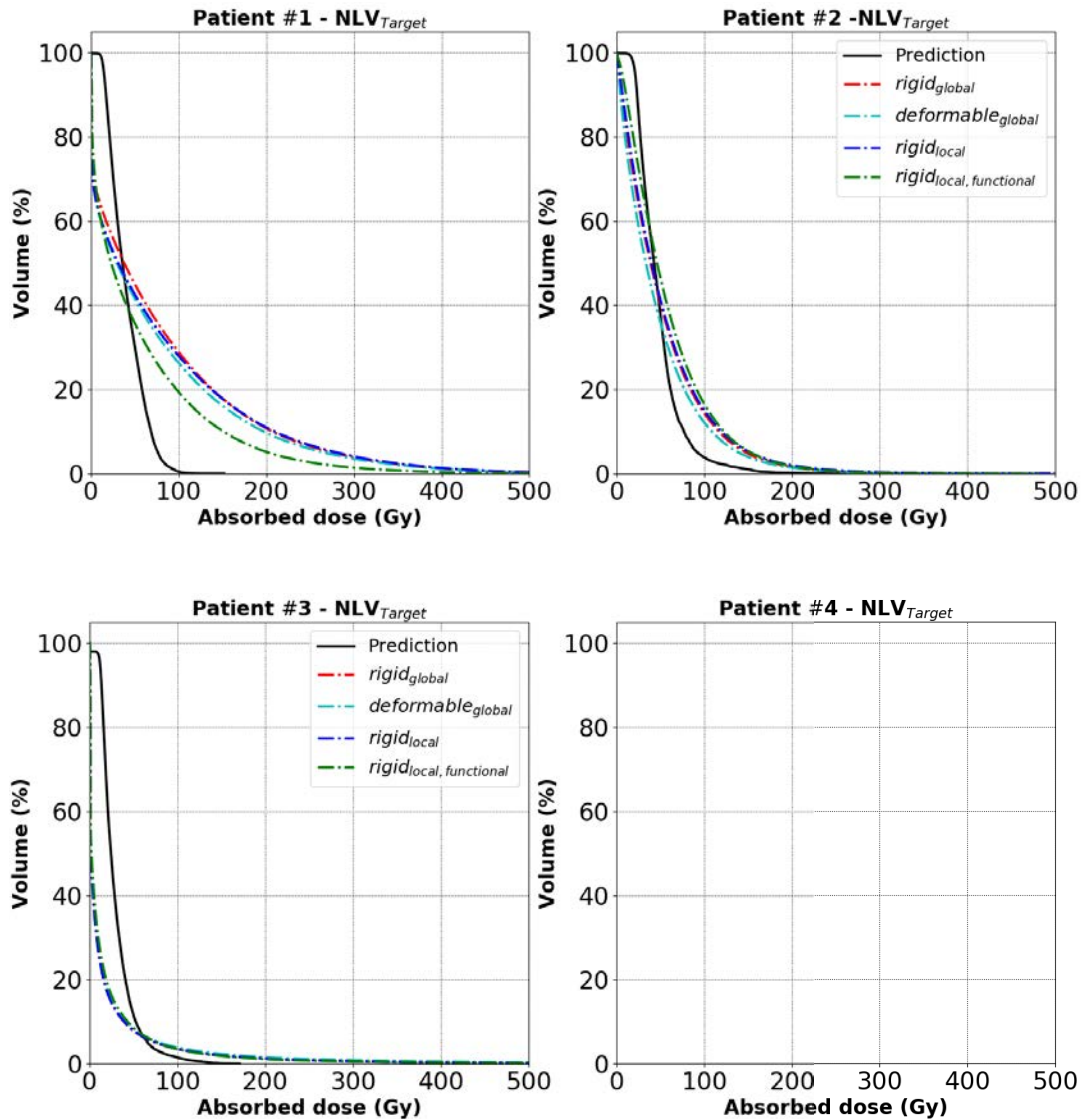
The figures below depict the obtained  $DVH_{j,treatment}$  considering the  $TV_{Total}$  (total tumour volume) using each of the four registration methods,  $j$ , for all patients. The  $DVH_{predicted}$  is also depicted on each figure. Refer to Section 6.3.1.4 for a summary of the results for the  $TV_{Total}$ .

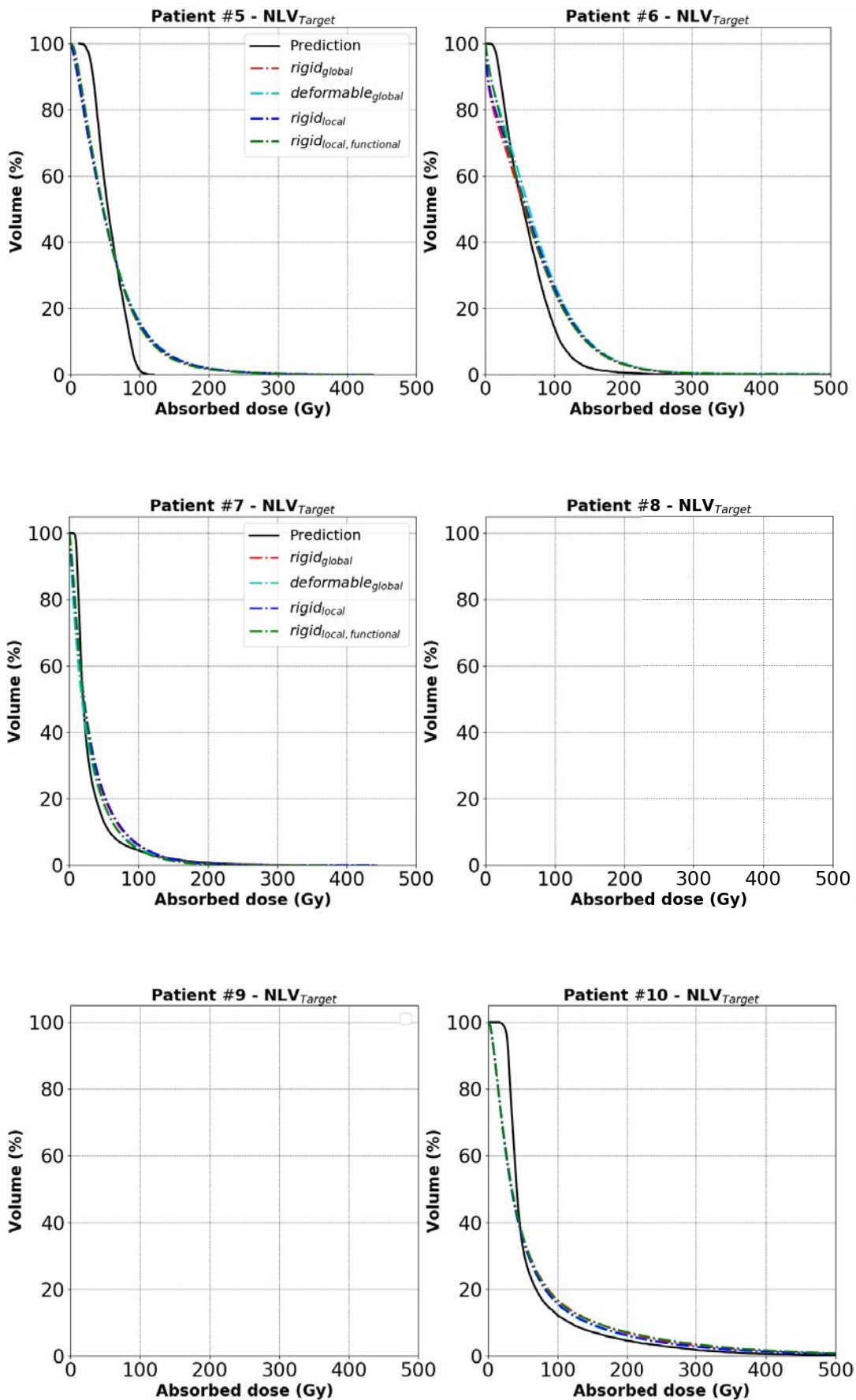




## D7 Target normal liver

The figures below depict the obtained  $DVH_{j,treatment}$  considering the  $NLV_{Target}$  (target normal liver volume) using each of the four registration methods,  $j$ , for all patients. The  $DVH_{predicted}$  is also depicted on each figure. Refer to Section 6.3.1.5 for a summary of the results for the  $NLV_{Target}$ .

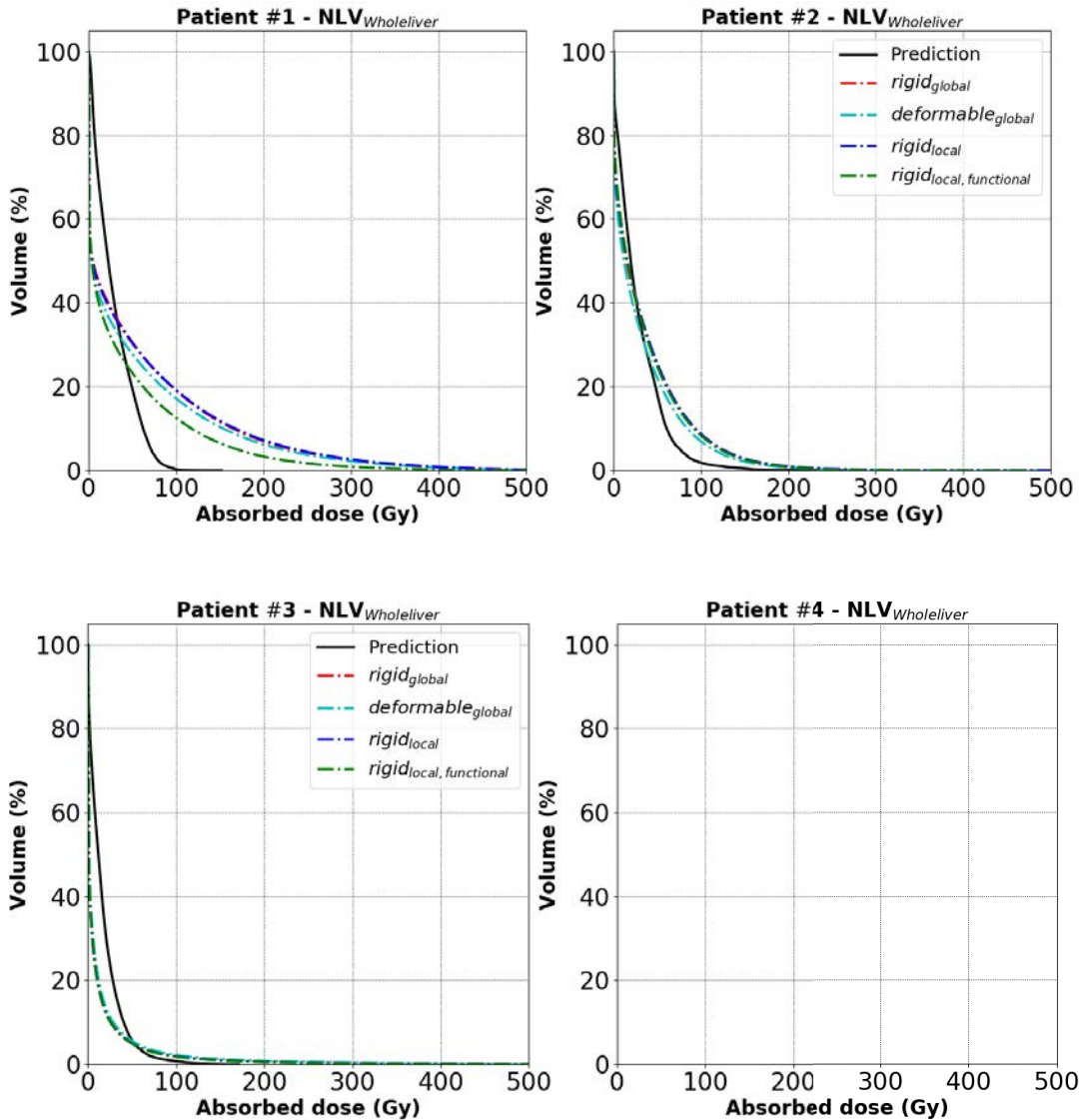


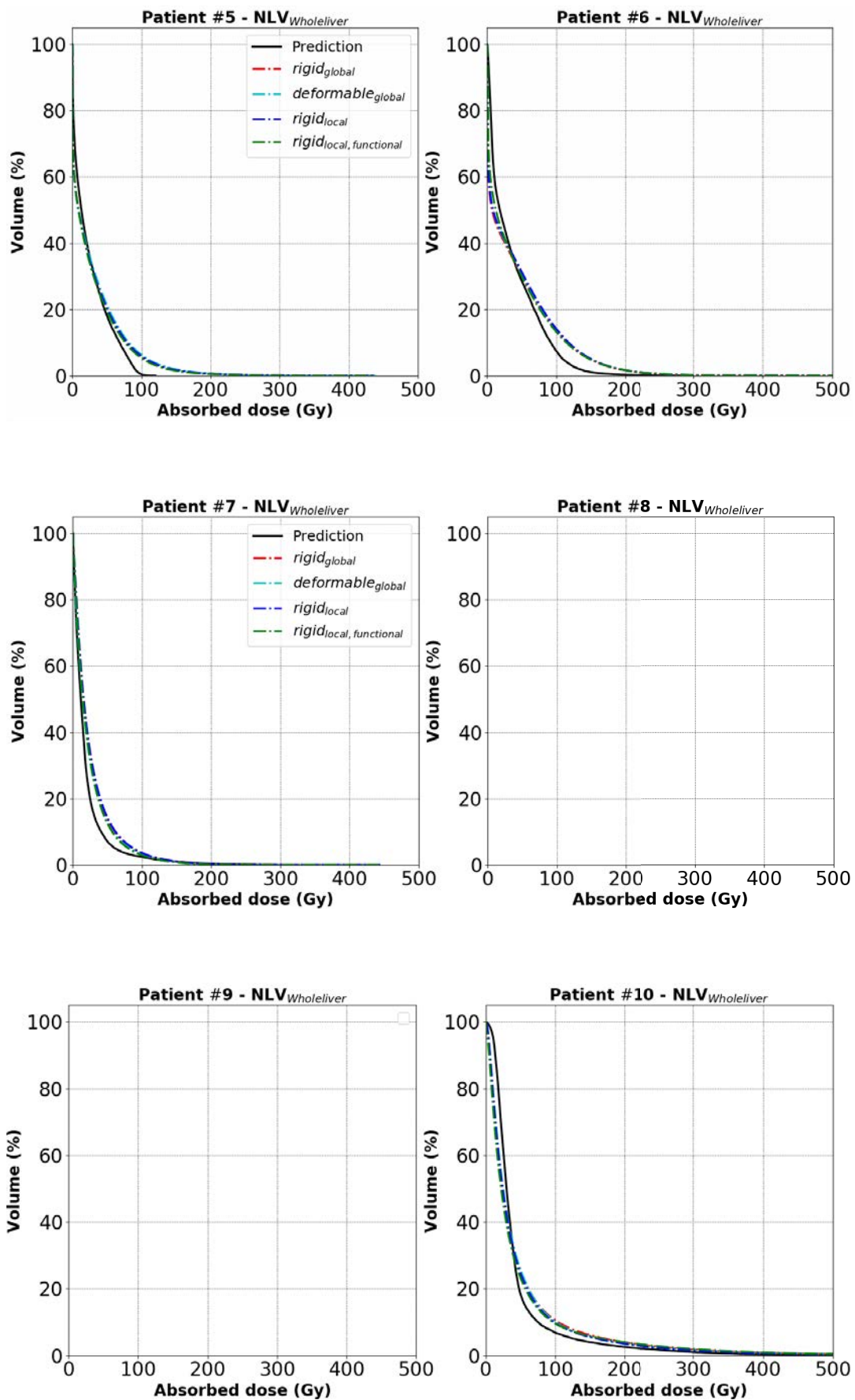




## D8 Whole normal liver

The figures below depict the obtained  $DVH_{j,treatment}$  for the  $NLV_{WholeLiver}$  (whole normal liver volume) using each of the four registration methods,  $j$ , for all patients. The  $DVH_{predicted}$  is also depicted on each figure. Refer to Section 6.3.1.5 for a summary of the results for the  $NLV_{WholeLiver}$ .







# Bibliography

- Abushab, K. et al. (2016). "Evaluation of PeneloPET simulations of Biograph PET/CT scanners". In: *IEEE Transactions on Nuclear Science* 63.3, pp. 1367–1374.
- Agarwal, B. K. (1991). *X-ray spectroscopy: an introduction*. Vol. 15. Springer.
- Ahmadzadehfar, H. et al. (2010). "The significance of  $^{99m}\text{Tc}$ -MAA SPECT/CT liver perfusion imaging in treatment planning for  $^{90}\text{Y}$ -microsphere selective internal radiation treatment". In: *Journal of Nuclear Medicine* 51.8, pp. 1206–1212.
- Aklan, B et al. (2015). "GATE Monte Carlo simulations for variations of an integrated PET/MR hybrid imaging system based on the Biograph mMR model". In: *Physics in Medicine & Biology* 60.12, p. 4731.
- Alberts, I. et al. (2021). "Clinical performance of long axial field of view PET/CT: a head-to-head intra-individual comparison of the Biograph Vision Quadra with the Biograph Vision PET/CT". In: *European Journal of Nuclear Medicine and Molecular Imaging*, pp. 1–10.
- Alessio, A., P. Kinahan, et al. (2006). "PET image reconstruction". In: *Nuclear medicine* 1.1, pp. 1–22.
- Alessio, A. and L. MacDonald (2008). "Spatially variant positron range modeling derived from CT for PET image reconstruction". In: *2008 IEEE Nuclear Science Symposium Conference Record*. IEEE, pp. 3637–3640.
- Ananthakrishnan, A., V. Gogineni, and K. Saeian (2006). "Epidemiology of primary and secondary liver cancers". In: *Seminars in interventional radiology*. Vol. 23. 1. Thieme Medical Publishers, p. 47.
- Arce, P et al. (2021). "Report on G4-Med, a Geant4 benchmarking system for medical physics applications developed by the Geant4 Medical Simulation Benchmarking Group". In: *Medical physics* 48.1, pp. 19–56.
- Ariño-Estrada, G. et al. (2018). "Towards time-of-flight PET with a semiconductor detector". In: *Physics in Medicine & Biology* 63.4, 04LT01.
- Assie, K. et al. (2004). "Monte Carlo simulation in PET and SPECT instrumentation using GATE". In: *Nuclear Instruments and Methods in Physics Research Section A: Accelerators, Spectrometers, Detectors and Associated Equipment* 527.1-2, pp. 180–189.
- Attarwala, A. A. et al. (2014). "Quantitative and qualitative assessment of Yttrium-90 PET/CT imaging". In: *PloS one* 9.11.
- Badawi, R. D. et al. (1999). "The effect of camera geometry on singles flux, scatter fraction and trues and randoms sensitivity for cylindrical 3D PET-a simulation study". In: *1999 IEEE Nuclear Science Symposium. Conference Record. 1999 Nuclear Science Symposium and Medical Imaging Conference (Cat. No. 99CH37019)*. Vol. 3. IEEE, pp. 1522–1526.
- Badawi, R. D. et al. (2019). "First human imaging studies with the EXPLORER total-body PET scanner". In: *Journal of Nuclear Medicine* 60.3, pp. 299–303.
- Bagni, O. et al. (2012). " $^{90}\text{Y}$ -PET for the assessment of microsphere biodistribution after selective internal radiotherapy". In: *Nuclear Medicine Communications* 33.2, pp. 198–204.

- Bardiès, M., C. Kwok, and G. Sgouros (2002). "Dose point-kernels for radionuclide dosimetry". In: *Therapeutic applications of Monte Carlo calculations in nuclear medicine*. CRC Press, pp. 158–174.
- Bastiaannet, R. et al. (2018). "The physics of radioembolization". In: *EJNMMI physics* 5.1, p. 22.
- Bataille, F et al. (2004). "Monte Carlo simulation for the ECAT HRRT using GATE". In: *IEEE Symposium Conference Record Nuclear Science 2004*. Vol. 4. IEEE, pp. 2570–2574.
- Bé, M. et al. (2006). "Table of radionuclides (Vol. 3-A= 3 to 244)". In: *Bureau International des Poids et Mesures, France: Sèvres*.
- Beaudoux, V. et al. (2019). "Geant4 physics list comparison for the simulation of phase-contrast mammography (XPulse project)". In: *Phys Med* 60, pp. 66–75.
- Berard, P. et al. (2008). "LabPET II, a novel 64-channel APD-based PET detector module with individual pixel readout achieving submillimetric spatial resolution". In: *2008 IEEE Nuclear Science Symposium Conference Record*. IEEE, pp. 5457–5462.
- Bergeron, M. et al. (2009). "Performance evaluation of the LabPET™ APD-based digital PET scanner". In: *IEEE Transactions on Nuclear Science* 56.1, pp. 10–16.
- Bierman, H. R. et al. (1951). "Studies on the blood supply of tumors in man. III. Vascular patterns of the liver by hepatic arteriography in vivo". In: *Journal of the National Cancer Institute* 12.1, pp. 107–131.
- Bilbao, J. I., M. F. Reiser, et al. (2008). *Liver radioembolization with 90Y microspheres*. Springer.
- Bochkarev, V. et al. (1972). "Distribution of absorbed energy from a point beta-source in a tissue-equivalent medium". In: *The International journal of applied radiation and isotopes* 23.11, pp. 493–504.
- Boisson, F et al. (2013). "NEMA NU 4-2008 validation and applications of the PET-SORTEO Monte Carlo simulations platform for the geometry of the Inveon PET preclinical scanner". In: *Physics in Medicine & Biology* 58.19, p. 6749.
- Bolch, W. E. et al. (1999). "MIRD pamphlet no. 17: the dosimetry of nonuniform activity distributions—radionuclide S values at the voxel level". In: *Journal of Nuclear Medicine* 40.1, 11S–36S.
- Bolch, W. E. et al. (2009). "MIRD pamphlet no. 21: a generalized schema for radiopharmaceutical dosimetry—standardization of nomenclature". In: *Journal of Nuclear Medicine* 50.3, pp. 477–484.
- Boston Scientifics, Massachusetts, United States (2020). *Package insert: TheraSphere™ Yttrium-90 Glass Microspheres*. URL: <https://www.bostonscientific.com/en-US/products/cancer-therapies/therasphere-y90-glass-microspheres/therasphere-y90-microspheres-brief-summary.html> (visited on 01/19/2021).
- Botta, F et al. (2011). "Calculation of electron and isotopes dose point kernels with FLUKA Monte Carlo code for dosimetry in nuclear medicine therapy". In: *Medical physics* 38.7, pp. 3944–3954.
- Brasse, D. et al. (June 2005). "Correction Methods for Random Coincidences in Fully 3D Whole-Body PET: Impact on Data and Image Quality". In: *Journal of Nuclear Medicine: official publication, Society of Nuclear Medicine* 46, pp. 859–67.
- Bray, F. et al. (2018). "Global cancer statistics 2018: GLOBOCAN estimates of incidence and mortality worldwide for 36 cancers in 185 countries". In: *CA: a cancer journal for clinicians* 68.6, pp. 394–424.
- Brolin, G. (2011). "Image-Based Partial-Volume Correction in SPECT: Application to 177Lu radionuclide therapy".

- Brunner, S. and D. Schaart (2017). "Enabling cost-effective TOF-PET by exploiting the Cherenkov emission in BGO". In: *Journal of Nuclear Medicine* 58.supplement 1, pp. 150–150.
- Budinger, T. F. (1983). "Time-of-flight positron emission tomography: status relative to conventional PET". In: *Journal of nuclear medicine* 24.1, pp. 73–78.
- Buvat, I and I Castiglioni (2002). "Monte Carlo simulations in SPET and PET". In: *QJ Nucl. Med* 46.1, pp. 48–61.
- Cal-González, J. et al. (2013). "Positron range estimations with PeneloPET". In: *Physics in Medicine & Biology* 58.15, p. 5127.
- Caribé, P. R. et al. (2019). "NEMA NU 2–2007 performance characteristics of GE Signa integrated PET/MR for different PET isotopes". In: *EJNMMI physics* 6.1, pp. 1–13.
- Carlier, T. et al. (2013). "Assessment of acquisition protocols for routine imaging of Y-90 using PET/CT". In: *EJNMMI Research* 3.1, pp. 1–12.
- Carlier, T. et al. (2015). "90Y-PET imaging: Exploring limitations and accuracy under conditions of low counts and high random fraction". In: *Medical physics* 42.7, pp. 4295–4309.
- Carlier, T. et al. (2020). "From a PMT-based to a SiPM-based PET system: a study to define matched acquisition/reconstruction parameters and NEMA performance of the Biograph Vision 450". In:
- Champion, C and C Le Loirec (2007). "Positron follow-up in liquid water: II. Spatial and energetic study for the most important radioisotopes used in PET". In: *Physics in Medicine & Biology* 52.22, p. 6605.
- Chang, T. et al. (2012). "Reliability of predicting image signal-to-noise ratio using noise equivalent count rate in PET imaging". In: *Medical physics* 39.10, pp. 5891–5900.
- Chauvin, M. et al. (2020). "OpenDose: Open-access resource for nuclear medicine dosimetry". In: *Journal of Nuclear Medicine* 61.10, pp. 1514–1519.
- Cherry, S. R. and M. Dahlbom (2006). "PET: physics, instrumentation, and scanners". In: *PET*. Springer, pp. 1–117.
- Cherry, S. R., J. A. Sorenson, and M. E. Phelps (2012). *Physics in Nuclear Medicine*. Elsevier Health Sciences.
- Chicheportiche, A., R. Marciano, and M. Orevi (2020). "Comparison of NEMA characterizations for Discovery MI and Discovery MI-DR TOF PET/CT systems at different sites and with other commercial PET/CT systems". In: *EJNMMI Physics* 7.1, p. 4.
- Chiesa, C et al. (2015). "Radioembolization of hepatocarcinoma with 90 Y glass microspheres: development of an individualized treatment planning strategy based on dosimetry and radiobiology". In: *European journal of nuclear medicine and molecular imaging* 42.11, pp. 1718–1738.
- Ciarrocchi, E. and N. Belcari (2017). "Cerenkov luminescence imaging: physics principles and potential applications in biomedical sciences". In: *EJNMMI physics* 4.1, pp. 1–31.
- Clarke, L. P. et al. (1992). "Bremsstrahlung imaging using the gamma camera: factors affecting attenuation". In: *Journal of Nuclear Medicine* 33.1, pp. 161–166.
- Collaboration, G., S Agostinelli, et al. (2003). "GEANT4—a simulation toolkit". In: *Nucl. Instrum. Meth. A* 506.25, p. 0.
- Colombino, P, B Fiscella, and L Trossi (1965). "Study of positronium in water and ice from 22 to-144 C by annihilation quanta measurements". In: *Il Nuovo Cimento (1955-1965)* 38.2, pp. 707–723.

- Conti, M. (2011). "Focus on time-of-flight PET: the benefits of improved time resolution". In: *European journal of nuclear medicine and molecular imaging* 38.6, pp. 1147–1157.
- Cremonesi, M. et al. (2014). "Radioembolization of hepatic lesions from a radiobiology and dosimetric perspective". In: *Frontiers in Oncology* 4, p. 210.
- D'Arienzo, M. (2013). "Emission of  $\beta^+$  particles via internal pair production in the  $0^+ \rightarrow 0^+$  transition of  $^{90}\text{Zr}$ : historical background and current applications in nuclear medicine imaging". In: *Atoms* 1.1, pp. 2–12.
- Dasgupta, P. et al. (2020). "Global trends in incidence rates of primary adult liver cancers: A systematic review and meta-analysis". In: *Frontiers in oncology* 10, p. 171.
- Dash, A. and R. Chakravarty (2019). "Radionuclide generators: The prospect of availing PET radiotracers to meet current clinical needs and future research demands". In: *American journal of nuclear medicine and molecular imaging* 9.1, p. 30.
- Daube-Witherspoon, M. E. and G. Muehllehner (1987). "Treatment of axial data in three-dimensional PET". In: *Journal of nuclear medicine* 28.11, pp. 1717–1724.
- De Gersem, R. et al. (2013). "Influence of time delay on the estimated lung shunt fraction on  $^{99\text{m}}\text{Tc}$ -labeled MAA scintigraphy for  $^{90\text{Y}}$  microsphere treatment planning". In: *Clinical nuclear medicine* 38.12, pp. 940–942.
- Defrise, M. and P. Kinahan (1998). "Data acquisition and image reconstruction for 3D PET". In: *The theory and practice of 3D PET*. Springer, pp. 11–53.
- Defrise, M. et al. (1997). "Exact and approximate rebinning algorithms for 3-D PET data". In: *IEEE transactions on medical imaging* 16.2, pp. 145–158.
- Degenhardt, C. et al. (2009). "The digital silicon photomultiplier—a novel sensor for the detection of scintillation light". In: *2009 IEEE Nuclear Science Symposium Conference Record (NSS/MIC)*. IEEE, pp. 2383–2386.
- Degenhardt, C. et al. (2010). "Arrays of digital silicon photomultipliers—intrinsic performance and application to scintillator readout". In: *IEEE Nuclear Science Symposium & Medical Imaging Conference*. IEEE, pp. 1954–1956.
- Delso, G. et al. (2011). "Performance measurements of the Siemens mMR integrated whole-body PET/MR scanner". In: *Journal of nuclear medicine* 52.12, pp. 1914–1922.
- Derenzo, S. E. (1979). "Precision measurement of annihilation point spread distributions for medically important positron emitters". In:
- Derenzo, S. E. et al. (1981). "Imaging properties of a positron tomograph with 280 BGO crystals". In: *IEEE Transactions on Nuclear Science* 28.1, pp. 81–89.
- Derenzo, S. E. et al. (1982). *Dynamic positron emission tomography in man using small bismuth germanate crystals*. Tech. rep. Lawrence Berkeley Lab.
- Deutsch, M. (1957). "Electric monopole transition rate in  $\text{Zr}^{90}$ ". In: *Nuclear Physics* 3.1, pp. 83–93.
- Dewaraja, Y. K. et al. (2017). "Improved quantitative  $^{90\text{Y}}$  bremsstrahlung SPECT/CT reconstruction with Monte Carlo scatter modeling". In: *Medical physics* 44.12, pp. 6364–6376.
- Dezard, W. et al. (2011). "Recommendations of the American Association of Physicists in Medicine on dosimetry, imaging, and quality assurance procedures for  $^{90\text{Y}}$  microsphere brachytherapy in the treatment of hepatic malignancies". In: *Med. Phys.* 38.8, p. 4824.
- Dezso, K. et al. (2009). "Development of arterial blood supply in experimental liver metastases". In: *The American journal of pathology* 175.2, pp. 835–843.
- Dieudonné, A. et al. (2010). "Fine-resolution voxel S values for constructing absorbed dose distributions at variable voxel size". In: *Journal of nuclear medicine* 51.10, pp. 1600–1607.

- Dieudonné, A. et al. (2011). "Clinical feasibility of fast 3-dimensional dosimetry of the liver for treatment planning of hepatocellular carcinoma with  $^{90}\text{Y}$ -microspheres". In: *Journal of Nuclear Medicine* 52.12, pp. 1930–1937.
- Dieudonné, A. et al. (2013). "Study of the impact of tissue density heterogeneities on 3-dimensional abdominal dosimetry: comparison between dose kernel convolution and direct Monte Carlo methods". In: *Journal of nuclear medicine* 54.2, pp. 236–243.
- Divoli, A. et al. (2009). "Effect of patient morphology on dosimetric calculations for internal irradiation as assessed by comparisons of Monte Carlo versus conventional methodologies". In: *Journal of Nuclear Medicine* 50.2, pp. 316–323.
- Dryák, P. and J. Šolc (2020). "Measurement of the branching ratio related to the internal pair production of  $\text{Y-90}$ ". In: *Applied Radiation and Isotopes* 156, p. 108942.
- Drzymala, R. et al. (1991). "Dose-volume histograms". In: *International Journal of Radiation Oncology Biology Physics* 21.1, pp. 71–78.
- D'Arienzo, M. et al. (2012). " $^{90}\text{Y}$  PET-based dosimetry after selective internal radiotherapy treatments". In: *Nuclear Medicine Communications* 33.6, pp. 633–640.
- D'Arienzo, M. et al. (2017). "Phantom validation of quantitative  $^{90}\text{Y}$  PET/CT-based dosimetry in liver radioembolization". In: *EJNMMI Research* 7.1, p. 94.
- Eckerman, K (2008). "Nuclear decay data for dosimetric calculations. ICRP Publication 107". In: *Ann ICRP* 38, pp. 7–96.
- Eckerman, K. F. and A. Endo (2007). *MIRD: radionuclide data and decay schemes*. Society of Nuclear Medicine.
- Elschot, M. et al. (2011). "Quantitative evaluation of scintillation camera imaging characteristics of isotopes used in liver radioembolization". In: *PLoS One* 6.11.
- Elschot, M. et al. (2013). "Quantitative comparison of PET and Bremsstrahlung SPECT for imaging the in vivo Yttrium-90 microsphere distribution after liver radioembolization". In: *PloS one* 8.2.
- Elschot, M. et al. (2014). " $^{99\text{m}}\text{Tc}$ -MAA overestimates the absorbed dose to the lungs in radioembolization: a quantitative evaluation in patients treated with  $^{166}\text{Ho}$ -microspheres". In: *European journal of nuclear medicine and molecular imaging* 41.10, pp. 1965–1975.
- Emami, A. et al. (2020). "Validation and evaluation of a GATE model for MAMMI PET scanner". In: *Iranian Journal of Nuclear Medicine* 28.1, pp. 33–38.
- Erlandsson, K. et al. (2012). "A review of partial volume correction techniques for emission tomography and their applications in neurology, cardiology and oncology". In: *Physics in Medicine & Biology* 57.21, R119.
- España, S. et al. (2009). "PeneloPET, a Monte Carlo PET simulation tool based on PENELOPE: features and validation". In: *Physics in Medicine & Biology* 54.6, p. 1723.
- Etxebeste Barrena, A. M. (2017). "Performance enhancement of a small animal positron emission tomograph based on continuous crystals and silicon photomultipliers". PhD thesis. Universitat de València.
- Fahey, F. H. (2002). "Data acquisition in PET imaging". In: *Journal of Nuclear Medicine Technology* 30.2, pp. 39–49.
- Farsaii, B. (Aug. 2005). "A solution to arc correction in cylindrical PET scanner". In: *Proceedings of SPIE - The International Society for Optical Engineering*.
- Fernández, M. et al. (2013). "A fast method for rescaling voxel S values for arbitrary voxel sizes in targeted radionuclide therapy from a single Monte Carlo calculation". In: *Medical physics* 40.8, p. 082502.
- Ferrari, M. E. et al. (2012). "3D dosimetry in patients with early breast cancer undergoing Intraoperative Avidination for Radionuclide Therapy (IART®) combined



- with external beam radiation therapy". In: *European Journal of Nuclear Medicine and Molecular Imaging* 39.11, pp. 1702–1711.
- Fessler, J. A. (2002). "Statistical methods for image reconstruction". In: *NSS-MIC Short Course on Statistical Image Reconstruction Methods, (annotated slides for attendees)* 87.
- Ford, K. W. (1955). "Predicted 0+ Level in  $Zr_{40}^{90}$ ". In: *Physical Review* 98.5, p. 1516.
- Frach, T. et al. (2009). "The digital silicon photomultiplier—Principle of operation and intrinsic detector performance". In: *2009 IEEE Nuclear Science Symposium Conference Record (NSS/MIC)*. IEEE, pp. 1959–1965.
- Frach, T. et al. (2010). "The digital silicon photomultiplier—System architecture and performance evaluation". In: *IEEE Nuclear Science Symposium & Medical Imaging Conference*. IEEE, pp. 1722–1727.
- Fuentes-Ocampo, F. et al. (2019). "Digital vs. analog PET/CT: intra-subject comparison of the SUVmax in target lesions and reference regions". In: *EJNMMI* 46.8, pp. 1745–1750.
- Gajos, A. et al. (2016). "Trilateration-based reconstruction of ortho-positronium decays into three photons with the J-PET detector". In: *Nuclear Instruments and Methods in Physics Research Section A: Accelerators, Spectrometers, Detectors and Associated Equipment* 819, pp. 54–59.
- Gardin, I. et al. (2003). "Voxeldose: a computer program for 3-D dose calculation in therapeutic nuclear medicine". In: *Cancer Biotherapy and Radiopharmaceuticals* 18.1, pp. 109–115.
- Garin, E. et al. (2012). "Dosimetry based on  $^{99m}Tc$ -macroaggregated albumin SPECT/CT accurately predicts tumor response and survival in hepatocellular carcinoma patients treated with  $^{90}Y$ -loaded glass microspheres: preliminary results". In: *Journal of Nuclear Medicine* 53.2, pp. 255–263.
- Garin, E. et al. (2016). "Clinical impact of ( $^{99m}Tc$ -MAA SPECT/CT)-based dosimetry in the radioembolization of liver malignancies with  $^{90}Y$ -loaded microspheres". In: *European Journal of Nuclear Medicine and Molecular Imaging* 43.3, pp. 559–575.
- Garin, E. et al. (2021). "Personalised versus standard dosimetry approach of selective internal radiation therapy in patients with locally advanced hepatocellular carcinoma (DOSISPHERE-01): a randomised, multicentre, open-label phase 2 trial". In: *The Lancet Gastroenterology & Hepatology* 6.1, pp. 17–29.
- Gates, V. L. et al. (2011). "Internal pair production of  $^{90}Y$  permits hepatic localization of microspheres using routine PET: proof of concept". In: *Journal of Nuclear Medicine* 52.1, pp. 72–76.
- Geramifar, P. et al. (2009). "Performance comparison of four commercial GE discovery PET/CT scanners: A monte carlo study using GATE". In: *Iranian Journal of Nuclear Medicine* 17.2, pp. 26–33.
- Giammarile, F. et al. (2011). "EANM procedure guideline for the treatment of liver cancer and liver metastases with intra-arterial radioactive compounds". In: *European journal of nuclear medicine and molecular imaging* 38.7, p. 1393.
- Gnesin, S. et al. (2016). "Partition model-based  $^{99m}Tc$ -MAA SPECT/CT predictive dosimetry compared with  $^{90}Y$  TOF PET/CT posttreatment dosimetry in radioembolization of hepatocellular carcinoma: a quantitative agreement comparison". In: *Journal of Nuclear Medicine* 57.11, pp. 1672–1678.
- Gnesin, S. et al. (2020). "Phantom-based image quality assessment of clinical  $^{18}F$ -FDG protocols in digital PET/CT and comparison to conventional PMT-based PET/CT". In: *EJNMMI physics* 7.1, pp. 1–16.
- Góbel, E., I. Mills, and A. Wallard (2006). "The International System of Units (SI)". In:

- Golla, S., A. Lammertsma, and R. Boellaard (2015). "Performance of the resolution recovery method on the Ingenuity PET/CT". In: *Journal of Nuclear Medicine* 56.supplement 3, pp. 1836–1836.
- Gonias, P et al. (2007). "Validation of a GATE model for the simulation of the Siemens biograph™ 6 PET scanner". In: *Nuclear Instruments and Methods in Physics Research Section A: Accelerators, Spectrometers, Detectors and Associated Equipment* 571.1-2, pp. 263–266.
- Götz, T. et al. (2019). "A comparison of methods for adapting dose-voxel-kernels to tissue inhomogeneities". In: *Physics in Medicine & Biology* 64.24, p. 245011.
- Götz, T. I. et al. (2021). "Dose voxel kernel prediction with neural networks for radiation dose estimation". In: *Zeitschrift für Medizinische Physik* 31.1, pp. 23–36.
- Grant, A. M. et al. (2016). "NEMA NU 2-2012 performance studies for the SiPM-based ToF-PET component of the GE SIGNA PET/MR system". In: *Medical Physics* 43.5, pp. 2334–2343.
- Gray, B et al. (2001). "Randomised trial of SIR-Spheres® plus chemotherapy vs. chemotherapy alone for treating patients with liver metastases from primary large bowel cancer". In: *Annals of Oncology* 12.12, pp. 1711–1720.
- Greenberg, J. S. and M. Deutsch (1956). "Positrons from the decay of  $P^{32}$  and  $Y^{90}$ ". In: *Physical Review* 102.2, p. 415.
- Grosser, O. S. et al. (2016). "Pharmacokinetics of  $^{99m}Tc$ -MAA- and  $^{99m}Tc$ -HSA-microspheres used in preradioembolization dosimetry: Influence on the liver-lung shunt". In: *Journal of Nuclear Medicine* 57.6, pp. 925–927.
- Gruppen, C. and I. Buvat (2011). *Handbook of particle detection and imaging*. Springer Science & Business Media.
- Guérin, B. and G. El Fakhri (2008). "Realistic PET Monte Carlo simulation with pixelated block detectors, light sharing, random coincidences and dead-time modeling". In: *IEEE Transactions on Nuclear Science* 55.3, pp. 942–952.
- Guez, D. et al. (2008). "Counting rates modeling for PET scanners with GATE". In: *IEEE Transactions on Nuclear Science* 55.1, pp. 516–523.
- Gulec, S. A., G. Mesoloras, and M. Stabin (2006). "Dosimetric techniques in  $^{90}Y$ -microsphere therapy of liver cancer: the MIRD equations for dose calculations". In: *Journal of Nuclear Medicine* 47.7, pp. 1209–1211.
- Gundacker, S. et al. (2020). "Experimental time resolution limits of modern SiPMs and TOF-PET detectors exploring different scintillators and Cherenkov emission". In: *Physics in Medicine & Biology* 65.2, p. 025001.
- Haemisch, Y. et al. (2012). "Fully digital arrays of silicon photomultipliers (dSiPM)—a scalable alternative to vacuum photomultiplier tubes (PMT)". In: *Physics Procedia* 37, pp. 1546–1560.
- Harpen, M. D. (2003). "Positronium: Review of symmetry, conserved quantities and decay for the radiological physicist". In: *Medical physics* 31.1, pp. 57–61.
- Haste, P. et al. (2017). "Correlation of Technetium-99m Macroaggregated Albumin and Yttrium-90 Glass Microsphere Biodistribution in Hepatocellular Carcinoma: A Retrospective Review of Pretreatment Single Photon Emission CT and Post-treatment Positron Emission Tomography/CT". In: *Journal of Vascular and Interventional Radiology* 28.5, pp. 722–730.
- Haute Autorité de Santé, France (2018). *SIR-Sphere, Microsphères d'Yttrium-90. Avis de la CNEDiMITS du 06 novembre 2018*. URL: [https://www.has-sante.fr/upload/docs/evamed/CEPP-5693\\_SIR\\_SPHERE\\_5693\\_avis\\_6\\_novembre\\_2018\\_occultation\\_accord\\_MJ.pdf](https://www.has-sante.fr/upload/docs/evamed/CEPP-5693_SIR_SPHERE_5693_avis_6_novembre_2018_occultation_accord_MJ.pdf) (visited on 01/31/2021).
- Haute Autorité de Santé, France (2020). *Theraspheres, Microsphères d'Yttrium-90. Avis de la CNEDiMITS du 28 janvier 2020*. URL: <https://www.has-sante.fr/upload/>

- docs/evamed/CNEDIMTS-6082\_THERASPHERE\_28\_janvier\_2020\_(6082)\_avis.pdf (visited on 01/31/2021).
- Heller, M. et al. (2013). *Study of a Digital SiPM for TOF-PET (No. PH-EP-Tech-Note-2013-003)*. Tech. rep.
- Hermann, A.-L. et al. (2020). "Relationship of tumor radiation-absorbed dose to survival and response in hepatocellular carcinoma treated with transarterial radioembolization with  $^{90}\text{Y}$  in the SARAH study". In: *Radiology* 296.3, pp. 673–684.
- Hesse, M. et al. (2020). "Yttrium-90 TOF-PET based EUD predicts response post liver radioembolizations using standard manufacturer reconstruction parameters". In: *arXiv preprint arXiv:2010.00303*.
- Ho, S et al. (1996). "Partition model for estimating radiation doses from yttrium-90 microspheres in treating hepatic tumours". In: *European Journal of Nuclear Medicine* 23.8, pp. 947–952.
- Hoeschen, C., M. Rafecas, and T. Aspelmeier (2011). "Algorithms for Image Reconstruction". In: *Radiation Physics for Nuclear Medicine*. Springer, pp. 211–232.
- Hoffman, E. J. et al. (1982). "Quantitation in positron emission computed tomography: 6. effect of nonuniform resolution." In: *Journal of computer assisted tomography* 6.5, pp. 987–999.
- Hou, X. et al. (2020). "Impact of image reconstruction method on dose distributions derived from  $^{90}\text{Y}$  PET images: phantom and liver radioembolization patient studies". In: *Physics in Medicine & Biology*.
- Hoven, A. F. van den et al. (2016). "Insights into the dose-response relationship of radioembolization with resin  $^{90}\text{Y}$ -microspheres: a prospective cohort study in patients with colorectal cancer liver metastases". In: *Journal of Nuclear Medicine* 57.7, pp. 1014–1019.
- Howell, R. W. et al. (1999). "The MIRD perspective 1999". In: *Journal of Nuclear Medicine* 40.1, 3S–10S.
- Hudson, H. M. and R. S. Larkin (1994). "Accelerated image reconstruction using ordered subsets of projection data". In: *IEEE transactions on medical imaging* 13.4, pp. 601–609.
- Huizing, D. M. V., M. Verheij, M. P. M. Stokkel, et al. (2018). "Dosimetry methods and clinical applications in peptide receptor radionuclide therapy for neuroendocrine tumours: a literature review". In: *EJNMMI research* 8.1, pp. 1–11.
- Iwata, K., R. Greaves, and C. Surko (1997). " $\gamma$ -ray spectra from positron annihilation on atoms and molecules". In: *Physical Review A* 55.5, p. 3586.
- Jadoul, A. et al. (2019). "Comparative dosimetry between  $^{99\text{m}}\text{Tc}$ -MAA SPECT/CT and  $^{90}\text{Y}$  PET/CT in primary and metastatic liver tumors". In: *European journal of nuclear medicine and molecular imaging*, pp. 1–10.
- Jan, S. et al. (Feb. 2011). "GATE V6: A Major Enhancement of the GATE Simulation Platform Enabling Modelling of CT and Radiotherapy." eng. In: *Phys Med Biol* 56.4, pp. 881–901.
- Jan, S. et al. (2004). "GATE: a simulation toolkit for PET and SPECT". In: *Physics in Medicine & Biology* 49.19, p. 4543.
- Jan, S. et al. (2005). "Monte Carlo simulation for the ECAT EXACT HR+ system using GATE". In: *IEEE Transactions on Nuclear Science* 52.3, pp. 627–633.
- Jha, A. K. A. et al. (2012). "Comparative analysis of hepatopulmonary shunt obtained from pretherapy  $^{99\text{m}}\text{Tc}$  MAA scintigraphy and post-therapy  $^{90}\text{Y}$  Bremsstrahlung imaging in  $^{90}\text{Y}$  microsphere therapy". In: *Nuclear medicine communications* 33.5, pp. 486–490.

- Ji, Y. et al. (2020). "High-Intensity Focused Ultrasound Ablation for Unresectable Primary and Metastatic Liver Cancer: Real-World Research in a Chinese Tertiary Center With 275 Cases". In: *Frontiers in Oncology* 10, p. 2307.
- Jiang, H.-Y. et al. (2018). "Noninvasive imaging of hepatocellular carcinoma: From diagnosis to prognosis". In: *World journal of gastroenterology* 24.22, p. 2348.
- Jiang, W., Y. Chalich, and M. J. Deen (2019). "Sensors for positron emission tomography applications". In: *Sensors* 19.22, p. 5019.
- Johnson, O., R. Johnson, and L. Langer (1955). "Evidence for a 0+ first excited state in  $Zr^{90}$ ". In: *Physical Review* 98.5, p. 1517.
- Joseph, P. M. (1982). "An Improved Algorithm for Reprojecting Rays through Pixel Images". In: *IEEE Transactions on Medical Imaging* 1.3, pp. 192–196. ISSN: 1558-254X.
- Kafrouni, M. et al. (2019). "Analysis of differences between 99m Tc-MAA SPECT-and 90 Y-microsphere PET-based dosimetry for hepatocellular carcinoma selective internal radiation therapy". In: *EJNMMI research* 9.1, pp. 1–9.
- Kallini, J. R. et al. (2017). "Comparison of the adverse event profile of TheraSphere® with SIR-Spheres® for the treatment of unresectable hepatocellular carcinoma: a systematic review". In: *Cardiovascular and interventional radiology* 40.7, pp. 1033–1043.
- Kao, Y. et al. (2012). "Yttrium-90 internal pair production imaging using first generation PET/CT provides high-resolution images for qualitative diagnostic purposes". In: *The British Journal of Radiology* 85.1015, pp. 1018–1019.
- Kao, Y.-H. et al. (2013a). "Post-radioembolization Yttrium-90 PET/CT-part 1: diagnostic reporting". In: *EJNMMI Research* 3.1, p. 56.
- Kao, Y.-H. et al. (2013b). "Post-radioembolization yttrium-90 PET/CT-part 2: dose-response and tumor predictive dosimetry for resin microspheres". In: *EJNMMI research* 3.1, pp. 1–12.
- Kaplon, Ł. et al. (2014). "Plastic scintillators for positron emission tomography obtained by the bulk polymerization method". In: *Bio-Algorithms and Med-Systems* 10.1, pp. 27–31.
- Kappadath, S. (2010). "SU-GG-I-163: A Scatter Correction Algorithm for Quantitative Yttrium-90 SPECT Imaging". In: *Medical Physics* 37.6Part5, pp. 3139–3139.
- Karakatsanis, N et al. (2006). "Comparative evaluation of two commercial PET scanners, ECAT EXACT HR+ and Biograph 2, using GATE". In: *Nuclear Instruments and Methods in Physics Research Section A: Accelerators, Spectrometers, Detectors and Associated Equipment* 569.2, pp. 368–372.
- Kennedy, A. et al. (2012). "Radioembolization for the treatment of liver tumors: general principles". In: *American journal of clinical oncology* 35.1, pp. 91–99.
- Kennedy, A. S. et al. (2009). "Treatment parameters and outcome in 680 treatments of internal radiation with resin 90Y-microspheres for unresectable hepatic tumors". In: *International Journal of Radiation Oncology Biology Physics* 74.5, pp. 1494–1500.
- Khazaei Moghadam, M. et al. (2016). "Evaluating the application of tissue-specific dose kernels instead of water dose kernels in internal dosimetry: a Monte Carlo study". In: *Cancer Biotherapy and Radiopharmaceuticals* 31.10, pp. 367–379.
- Kinahan, P. E. and J. Rogers (1988). *Analytic 3D image reconstruction using all detected events*. Tech. rep. Triumf.
- Klein, S. et al. (2009). "Elastix: a toolbox for intensity-based medical image registration". In: *IEEE transactions on medical imaging* 29.1, pp. 196–205.
- Knapp, F. R. and S Mirzadeh (1994). "The continuing important role of radionuclide generator systems for nuclear medicine". In: *European Journal of Nuclear Medicine* 21.10, pp. 1151–1165.

- Knešaurek, K. et al. (2010). "Quantitative comparison of yttrium-90 (90 Y)-microspheres and technetium-99m (99m Tc)-macroaggregated albumin SPECT images for planning 90 Y therapy of liver cancer". In: *Technology in cancer research & treatment* 9.3, pp. 253–261.
- Knoll, G. F. (2010). *Radiation detection and measurement*. John Wiley & Sons.
- Knudsen, E. S., P. Gopal, and A. G. Singal (2014). "The changing landscape of hepatocellular carcinoma: etiology, genetics, and therapy". In: *The American journal of pathology* 184.3, pp. 574–583.
- Kowalski, P. et al. (2018). "Estimating the NEMA characteristics of the J-PET tomograph using the GATE package". In: *Physics in Medicine & Biology* 63.16, p. 165008.
- Labour, J. et al. (2020). "Monte Carlo simulation of digital photon counting PET". In: *EJNMMI Physics* 7.1, pp. 1–19.
- Labour, J. et al. (2021). "Yttrium-90 Quantitative Phantom Study Using Digital Photon Counting PET". In: *EJNMMI Physics* 8(1).56.
- Lam, M. G. et al. (2014). "Limitations of body surface area-based activity calculation for radioembolization of hepatic metastases in colorectal cancer". In: *Journal of Vascular and Interventional Radiology* 25.7, pp. 1085–1093.
- Lamare, F. et al. (2006). "Validation of a Monte Carlo simulation of the Philips Allegro/GEMINI PET systems using GATE". In: *Physics in Medicine & Biology* 51.4, p. 943.
- Lamare, F. et al. (2004). "Simulation of the Allegro PET system using GATE". In: *Medical Imaging 2004: Physics of Medical Imaging*. Vol. 5368. International Society for Optics and Photonics, pp. 890–897.
- LANCONELLI, N. et al. (2012). "A free database of radionuclide voxel S values for the dosimetry of nonuniform activity distributions". In: *Physics in Medicine & Biology* 57.2, p. 517.
- Langhoff, H and H.-H. Hennies (1961). "Zum experimentellen Nachweis von Zwei-quantenzerfall beim 0+-0+-Übergang des Zr 90". In: *Zeitschrift für Physik* 164.2, pp. 166–173.
- Lau, W.-Y. et al. (2012). "Patient selection and activity planning guide for selective internal radiotherapy with yttrium-90 resin microspheres". In: *International Journal of Radiation Oncology\* Biology\* Physics* 82.1, pp. 401–407.
- Lau, W. et al. (1994). "Treatment of inoperable hepatocellular carcinoma with intrahepatic arterial yttrium-90 microspheres: a phase I and II study". In: *British Journal of Cancer* 70.5, pp. 994–999.
- Lawrence, T. S. et al. (1995). "Hepatic toxicity resulting from cancer treatment". In: *International Journal of Radiation Oncology\* Biology\* Physics* 31.5, pp. 1237–1248.
- Lecomte, R. (2009). "Novel detector technology for clinical PET". In: *European journal of nuclear medicine and molecular imaging* 36.1, pp. 69–85.
- Lecoq, P. (2017). "Pushing the limits in time-of-flight PET imaging". In: *IEEE Transactions on Radiation and Plasma Medical Sciences* 1.6, pp. 473–485.
- Lecoq, P. et al. (2020). "Roadmap toward the 10 ps time-of-flight PET challenge". In: *Physics in Medicine & Biology* 65.21, 21RM01.
- Lee, B. Q. et al. (2019). "Radiosensitivity of colorectal cancer to 90Y and the radiobiological implications for radioembolisation therapy". In: *Physics in Medicine & Biology* 64.13, p. 135018.
- Lee, S., J. Gregor, and D. Osborne (2013). "Development and validation of a complete GATE model of the Siemens Inveon trimodal imaging platform". In: *Molecular Imaging* 12.7, pp. 7290–2013.

- Lenz, M. (2021). "Design and characterisation of an MRI compatible human brain PET insert by means of simulation and experimental studies". PhD thesis. Universität Wuppertal, Fakultät für Mathematik und Naturwissenschaften.
- Levillain, H. et al. (2020). "Combined quality and dose-volume histograms for assessing the predictive value of  $^{99m}\text{Tc}$ -MAA SPECT/CT simulation for personalizing radioembolization treatment in liver metastatic colorectal cancer". In: *EJNMMI Physics* 7.1, pp. 1–19.
- Levillain, H. et al. (2021). "International recommendations for personalised selective internal radiation therapy of primary and metastatic liver diseases with yttrium-90 resin microspheres". In: *European Journal of Nuclear Medicine and Molecular Imaging*, pp. 1–15.
- Levin, C. S. and E. J. Hoffman (1999). "Calculation of positron range and its effect on the fundamental limit of positron emission tomography system spatial resolution". In: *Physics in Medicine & Biology* 44.3, p. 781.
- Lewellen, T. K. (1998). "Time-of-flight PET". In: *Seminars in Nuclear Medicine*. Vol. 28. 3. Elsevier, pp. 268–275.
- Lewitt, R. M., G. Muehllehner, and J. S. Karp (1994). "Three-dimensional image reconstruction for PET by multi-slice rebinning and axial image filtering". In: *Physics in Medicine & Biology* 39.3, p. 321.
- Lhommel, R. et al. (2009). "Yttrium-90 TOF PET scan demonstrates high-resolution biodistribution after liver SIRT". In: *European Journal of Nuclear Medicine and Molecular Imaging* 36.10, pp. 1696–1696.
- Lhommel, R. et al. (2010). "Feasibility of  $^{90}\text{Y}$  TOF PET-based dosimetry in liver metastasis therapy using SIR-Spheres". In: *European Journal of Nuclear Medicine and Molecular Imaging* 37.9, pp. 1654–1662.
- Li, S. et al. (2017). "Monte Carlo simulation of Ray-Scan 64 PET system and performance evaluation using GATE toolkit". In: *Journal of Instrumentation* 12.02, T02001.
- Liu, Z et al. (2016). "Performance study of Philips digital silicon photomultiplier coupled to scintillating crystals". In: *Journal of Instrumentation* 11.01, P01017.
- Llovet, J. M., J. Fuster, and J. Bruix (2004). "The Barcelona approach: diagnosis, staging, and treatment of hepatocellular carcinoma". In: *Liver transplantation* 10.S2, S115–S120.
- Loevinger, R. and M. Berman (1968a). "A formalism for calculation of absorbed dose from radionuclides". In: *Physics in Medicine & Biology* 13.2, pp. 205–217.
- (1968b). *A schema for absorbed-dose calculations for biologically-distributed radionuclides*. MIRD Pamphlet No. 1. New York, NY: Society of Nuclear Medicine.
- Loevinger, R., T. F. Budinger, and E. E. Watson (1988). *MIRD primer for absorbed dose calculations*. Society of Nuclear Medicine.
- (1991). "MIRD Primer for dose calculations—Revised Editions". In: *Society of Nuclear Medicine, New York*.
- López-Mora, D. A. et al. (2019). "Comparison of image quality and lesion detection between digital and analog PET/CT". In: *EJNMMI* 46.6, pp. 1383–1390.
- Louie, J. D. et al. (2009). "Incorporating cone-beam CT into the treatment planning for yttrium-90 radioembolization". In: *Journal of Vascular and Interventional Radiology* 20.5, pp. 606–613.
- Lu, L. et al. (2016). "Validation of a Monte Carlo simulation of the Inveon PET scanner using GATE". In: *Nuclear Instruments and Methods in Physics Research Section A: Accelerators, Spectrometers, Detectors and Associated Equipment* 828, pp. 170–175.
- Lucy, L. B. (1974). "An iterative technique for the rectification of observed distributions". In: *The Astronomical Journal* 79, p. 745.

- Luo, J. and X. Kong (2006). "Half-life of  $^{176}\text{Lu}$ ". In: *Applied Radiation and Isotopes* 64.5, pp. 588–590. ISSN: 0969-8043.
- MacDonald, L. et al. (2008). "Measured count-rate performance of the Discovery STE PET/CT scanner in 2D, 3D and partial collimation acquisition modes". In: *Physics in Medicine & Biology* 53.14, p. 3723.
- Marcatili, S. (2015). "Multi-scale dosimetry for targeted radionuclide therapy optimisation". PhD thesis. Université Paul Sabatier-Toulouse III.
- Martí-Climent, J. M. et al. (2014). "PET optimization for improved assessment and accurate quantification of  $^{90}\text{Y}$ -microsphere biodistribution after radioembolization". In: *Medical Physics* 41.9, p. 092503.
- Maughan, N. M. et al. (2018). "Multi institutional quantitative phantom study of Yttrium-90 PET in PET/MRI: the MR-QUEST study". In: *EJNMMI Physics* 5.1, p. 7.
- Mehadji, B. (2021). "Modélisation Monte Carlo d'une caméra Compton basée sur l'utilisation de détecteurs à scintillation sensibles à la position couplés à des SiPM". PhD thesis. Aix-Marseille Université.
- Merlin, T. et al. (2018). "CASToR: a generic data organization and processing code framework for multi-modal and multi-dimensional tomographic reconstruction". In: *Physics in Medicine & Biology* 63.18, p. 185005.
- Michel, C et al. (2006). "Influence of crystal material on the performance of the HiRez 3D PET scanner: A Monte-Carlo study". In: *2006 IEEE Nuclear Science Symposium Conference Record*. Vol. 4. IEEE, pp. 2528–2531.
- Miften, M. et al. (2018). "Radiation dose-volume effects for liver SBRT". In: *International Journal of Radiation Oncology\* Biology\* Physics*.
- Mikhaylova, E. et al. (2011). "Simulation of pseudo-clinical conditions and image quality evaluation of PET scanner based on pixelated CdTe detector". In: *2011 IEEE Nuclear Science Symposium Conference Record*. IEEE, pp. 2716–2722.
- Mikhaylova, E. et al. (2013). "Simulation of the expected performance of a seamless scanner for brain PET based on highly pixelated CdTe detectors". In: *IEEE Transactions on Medical Imaging* 33.2, pp. 332–339.
- Miller, M (2016). "Focusing on high performance". In: Philips Advanved Molecular Imaging.
- Moehrs, S. et al. (2006). "A detector head design for small-animal PET with silicon photomultipliers (SiPM)". In: *Physics in Medicine & Biology* 51.5, p. 1113.
- Monnier, F. et al. (2015). "Validation of a simultaneous PET/MR system model for PET simulation using GATE". In: *EJNMMI physics*. Vol. 2. 1. Springer, pp. 1–1.
- Moraes, E. R. et al. (2015). "Towards component-based validation of GATE: Aspects of the coincidence processor". In: *Physica Medica* 31.1, pp. 43–48.
- Morán, V. et al. (2020). "Impact of the dosimetry approach on the resulting  $^{90}\text{Y}$  radioembolization planned absorbed doses based on  $^{99m}\text{Tc}$ -MAA SPECT-CT: is there agreement between dosimetry methods?" In: *EJNMMI Physics* 7.1, pp. 1–22.
- Moreau, M. (2019). *Introduction à l'imagerie par Tomographie d'Émission de Positons: définitions, approches de reconstruction et initiation aux isotopes complexes*. URL: <https://hal.archives-ouvertes.fr/hal-01660503v2/document>.
- Moses, W. W. (2011). "Fundamental limits of spatial resolution in PET". In: *Nuclear Instruments and Methods in Physics Research Section A: Accelerators, Spectrometers, Detectors and Associated Equipment* 648, S236–S240.
- Moskal, P. et al. (2019). "Feasibility study of the positronium imaging with the J-PET tomograph". In: *Physics in Medicine & Biology* 64.5, p. 055017.

- Namasivayam, S., D. R. Martin, and S. Saini (2007). "Imaging of liver metastases: MRI". In: *Cancer Imaging* 7.1, p. 2.
- Narayanan, M and A Perkins (2013). "Resolution recovery in the Ingenuity TF PET/CT". In: *White Paper, Philips NM Clinical Science*.
- NEMA NU 2-2012 - *Performance measurements of positron emission tomographs* (2012). National Electrical Manufacturers Association. Rosslyn, USA.
- NEMA NU 2-2018 - *Performance measurements of positron emission tomographs* (2018). National Electrical Manufacturers Association. Rosslyn, USA.
- Nguyen, N. C. et al. (2015). "Image quality and diagnostic performance of a digital PET prototype in patients with oncologic diseases: initial experience and comparison with analog PET". In: *Journal of Nuclear Medicine* 56.9, pp. 1378–1385.
- Nickles, R. J. et al. (2004). "Assaying and PET imaging of Yttrium-90:  $1 \gg 34$  ppm  $> 0$ ". In: *IEEE Symposium Conference Record Nuclear Science 2004*. Vol. 6. IEEE, pp. 3412–3414.
- Niedźwiecki, S. et al. (2017). "J-PET: a new technology for the whole-body PET imaging". In: *arXiv preprint arXiv:1710.11369*.
- NIST. *NIST: Description of the ESTAR database*. URL: <https://physics.nist.gov/PhysRefData/Star/Text/method.html> (visited on 01/25/2021).
- *NIST stopping-power and range tables: Electrons, protons, and helium ions*. URL: <https://www.nist.gov/pml/stopping-power-range-tables-electrons-protons-and-helium-ions> (visited on 01/25/2021).
- Orth, R. C. et al. (2008). "C-arm cone-beam CT: general principles and technical considerations for use in interventional radiology". In: *Journal of Vascular and Interventional Radiology* 19.6, pp. 814–820.
- Otte, N et al. (2006). "The SiPM—A new photon detector for PET". In: *Nuclear Physics B-Proceedings Supplements* 150, pp. 417–420.
- Pacilio, M et al. (2009). "Differences among Monte Carlo codes in the calculations of voxel values for radionuclide targeted therapy and analysis of their impact on absorbed dose evaluations". In: *Medical physics* 36.5, pp. 1543–1552.
- Pacilio, M. et al. (2015). "Differences in 3D dose distributions due to calculation method of voxel S-values and the influence of image blurring in SPECT". In: *Physics in Medicine & Biology* 60.5, p. 1945.
- Pan, T. et al. (2019). "Performance evaluation of the 5-Ring GE Discovery MI PET/CT system using the national electrical manufacturers association NU 2-2012 Standard". In: *Medical physics* 46.7, pp. 3025–3033.
- Papadimitroulas, P. et al. (2012). "A dose point kernel database using GATE Monte Carlo simulation toolkit for nuclear medicine applications: comparison with other Monte Carlo codes". In: *Medical physics* 39.8, pp. 5238–5247.
- Parra, L. and H. H. Barrett (1998). "List-mode likelihood: EM algorithm and image quality estimation demonstrated on 2-D PET". In: *IEEE transactions on medical imaging* 17.2, pp. 228–235.
- Pasciak, A. S., A. C. Bourgeois, and Y. C. Bradley (2014). "A comparison of techniques for  $^{90}\text{Y}$  PET/CT image-based dosimetry following radioembolization with resin microspheres". In: *Frontiers in Oncology* 4, p. 121.
- Pasciak, A. S. et al. (2014). "Radioembolization and the dynamic role of  $^{90}\text{Y}$  PET/CT". In: *Frontiers in oncology* 4, p. 38.
- Peer-Firozjaei, M. et al. (2021). "Implementation of dose point kernel (DPK) for dose optimization of  $^{177}\text{Lu}/^{90}\text{Y}$  cocktail radionuclides in internal dosimetry". In: *Applied Radiation and Isotopes*, p. 109673.
- Pérez, P. et al. (2011). "Dosimetry for betaemitter radionuclides by means of Monte Carlo simulations". In: *Gholamrezanezhad A, editor* 12, pp. 265–286.



- Petoussi-Henss, N. et al. (2007). "Patient-specific scaling of reference S-values for cross-organ radionuclide S-values: what is appropriate?" In: *Radiation protection dosimetry* 127.1-4, pp. 192–196.
- Pfaehler, E. et al. (2018). "SMART (SiMulAtion and ReconsTruction) PET: an efficient PET simulation-reconstruction tool". In: *EJNMMI Phys* 5.1, p. 16.
- Pizzichemi, M. et al. (2016). "A new method for depth of interaction determination in PET detectors". In: *Physics in Medicine & Biology* 61.12, p. 4679.
- Poon, J. K. et al. (2012). "Optimal whole-body PET scanner configurations for different volumes of LSO scintillator: a simulation study". In: *Physics in Medicine & Biology* 57.13, p. 4077.
- Poon, J. K. et al. (2015). "Validation of the SimSET simulation package for modeling the Siemens Biograph mCT PET scanner". In: *Physics in Medicine & Biology* 60.3, N35.
- Prenosil, G. et al. (2021). "NEMA NU 2-2018 performance measurements of Biograph Vision Quadra PET/CT system". In: *Nuklearmedizin* 60.02, p. V47.
- Quirem Medical BV, Deventer, the Netherlands (2020). *Product documentation: QuiremSpheres® - Instructions for use*. URL: <https://www.quirem.com/ifu/> (visited on 01/28/2021).
- Radon, J. (1986). "On the determination of functions from their integral values along certain manifolds". In: *IEEE transactions on medical imaging* 5.4, pp. 170–176.
- Rausch, I. et al. (2019). "Performance evaluation of the Vereos PET/CT system according to the NEMA NU2-2012 standard". In: *Journal of Nuclear Medicine* 60.4, pp. 561–567.
- Reader, A. J. et al. (1998). "Fast accurate iterative reconstruction for low-statistics positron volume imaging". In: *Physics in Medicine & Biology* 43.4, p. 835.
- Reddin, J. S. et al. (2018). "Performance evaluation of the SiPM-based Siemens Biograph Vision PET/CT system". In: *2018 IEEE Nuclear Science Symposium and Medical Imaging Conference Proceedings (NSS/MIC)*. IEEE, pp. 1–5.
- Reinders, M. T. et al. (2019). "Holmium-166 microsphere radioembolization of hepatic malignancies". In: *Seminars in nuclear medicine*. Vol. 49. 3. Elsevier, pp. 237–243.
- Reiner, D., M. Blaickner, and F. Rattay (2009). "Discrete beta dose kernel matrices for nuclides applied in targeted radionuclide therapy (TRT) calculated with MCNP5". In: *Medical physics* 36.11, pp. 4890–4896.
- Richardson, W. H. (1972). "Bayesian-based iterative method of image restoration". In: *JoSA* 62.1, pp. 55–59.
- Richetta, E. et al. (2019). "PET-CT post therapy dosimetry in radioembolization with resin  $^{90}\text{Y}$  microspheres: Comparison with pre-treatment SPECT-CT  $^{99\text{m}}\text{Tc}$ -MAA results". In: *Physica Medica* 64, pp. 16–23.
- Ridder, J. de et al. (2016). "Incidence and origin of histologically confirmed liver metastases: an explorative case-study of 23,154 patients". In: *Oncotarget* 7.34, p. 55368.
- Robert, A. et al. (2019). "4D respiration-correlated whole-body SPECT reconstruction". In: *2019 IEEE NSS-MIC*.
- Roncali, E. et al. (2020). "Personalized Dosimetry for Liver Cancer  $^{90}\text{Y}$  Radioembolization Using Computational Fluid Dynamics and Monte Carlo Simulation". In: *Annals of biomedical engineering* 48.5, pp. 1499–1510.
- Rousset, O. G., Y. Ma, and A. C. Evans (1998). "Correction for partial volume effects in PET: principle and validation". In: *Journal of Nuclear Medicine* 39.5, pp. 904–911.
- Rowley, L. M. et al. (2017). "Optimization of image reconstruction for  $^{90}\text{Y}$  selective internal radiotherapy on a lutetium yttrium orthosilicate PET/CT system using

- a Bayesian Penalized Likelihood reconstruction algorithm". In: *Journal of Nuclear Medicine* 58.4, pp. 658–664.
- Salem, R. et al. (2010). "Radioembolization for hepatocellular carcinoma using Yttrium-90 microspheres: a comprehensive report of long-term outcomes". In: *Gastroenterology* 138.1, pp. 52–64.
- Salem, R. et al. (2019). "Clinical and dosimetric considerations for Y90: recommendations from an international multidisciplinary working group". In: *European journal of nuclear medicine and molecular imaging* 46.8, pp. 1695–1704.
- Salvadori, J. (2020). "Caractérisation, optimisation et simulation des performances d'un TEP-TDM numérique". PhD thesis. Université de Lorraine.
- Salvadori, J. et al. (2019a). "Head-to-head comparison of image quality between brain 18F-FDG images recorded with a fully digital versus a last-generation analog PET camera". In: *EJNMMI Research* 9.1, p. 61.
- Salvadori, J. et al. (2019b). "High-Resolution Brain 18F-FDG Images Provided by Fully Digital PET." In: *Clinical Nuclear Medicine* 44.4, pp. 301–302.
- Salvadori, J. et al. (2020a). "Head-to-head comparison between digital and analog PET of human and phantom images when optimized for maximizing the signal-to-noise ratio from small lesions". In: *EJNMMI Physics* 7.11, pp. 1–14.
- (2020b). "Head-to-head comparison between digital and analog PET of human and phantom images when optimized for maximizing the signal-to-noise ratio from small lesions". In: *EJNMMI Physics* 7.1, pp. 1–14.
- Sanaat, A. and H. Zaidi (2020). "Depth of interaction estimation in a preclinical PET scanner equipped with monolithic crystals coupled to SiPMs using a deep neural network". In: *Applied Sciences* 10.14, p. 4753.
- Sangro, B., M. Iñarrairaegui, and J. I. Bilbao (2012). "Radioembolization for hepatocellular carcinoma". In: *Journal of hepatology* 56.2, pp. 464–473.
- Sangro, B. et al. (2011). "Survival after yttrium-90 resin microsphere radioembolization of hepatocellular carcinoma across Barcelona clinic liver cancer stages: a European evaluation". In: *Hepatology* 54.3, pp. 868–878.
- Sarfaraz, M. et al. (2004). "Radiation absorbed dose distribution in a patient treated with yttrium-90 microspheres for hepatocellular carcinoma". In: *Medical Physics* 31.9, pp. 2449–2453.
- Sarrut, D et al. (2021a). "Modeling complex particles phase space with GAN for Monte Carlo SPECT simulations: a proof of concept". In: *Physics in Medicine & Biology* 66.5, p. 055014.
- Sarrut, D., N. Krah, and J.-M. Létang (2019). "Generative adversarial networks (GAN) for compact beam source modelling in Monte Carlo simulations". In: *Physics in Medicine & Biology* 64.21, p. 215004.
- Sarrut, D. et al. (2014). "A review of the use and potential of the GATE Monte Carlo simulation code for radiation therapy and dosimetry applications". In: *Medical physics* 41.6Part1, p. 064301.
- Sarrut, D. et al. (2021b). "Advanced Monte Carlo simulations of emission tomography imaging systems with GATE". In: *Physics in Medicine & Biology*.
- Sato, K. T. et al. (2008). "Unresectable chemorefractory liver metastases: radioembolization with <sup>90</sup>Y microspheres—safety, efficacy, and survival". In: *Radiology* 247.2, pp. 507–515.
- Scarinci, I., M. Valente, and P. Pérez (2013). "Dose Point Kernel calculation and modelling with nuclear medicine dosimetry purposes". In: *PoS (X LASNPA)* 84, p. 45.

- Schaart, D. R. et al. (2016). "Advances in digital SiPMs and their application in biomedical imaging". In: *Nuclear Instruments and Methods in Physics Research Section A: Accelerators, Spectrometers, Detectors and Associated Equipment* 809, pp. 31–52.
- Schmid, R. K. et al. (2019). "The Dosimetric Impact of Interfractional Organ-at-Risk Movement During Liver Stereotactic Body Radiation Therapy". In: *Practical radiation oncology* 9.6, e549–e558.
- Schmidtlein, C. R. et al. (2006). "Validation of GATE Monte Carlo simulations of the GE Advance/Discovery LS PET scanners". In: *Medical Physics* 33.1, pp. 198–208.
- Scott, N. P. and D. R. McGowan (2019). "Optimising quantitative  $^{90}\text{Y}$  PET imaging: an investigation into the effects of scan length and Bayesian Penalised Likelihood reconstruction". In: *EJNMMI Research* 9.1, p. 40.
- Seifert, S. et al. (2012). "A comprehensive model to predict the timing resolution of SiPM-based scintillation detectors: theory and experimental validation". In: *IEEE Transactions on nuclear science* 59.1, pp. 190–204.
- Selwyn, R. et al. (2007). "A new internal pair production branching ratio of  $^{90}\text{Y}$ : The development of a non-destructive assay for  $^{90}\text{Y}$  and  $^{90}\text{Sr}$ ". In: *Applied Radiation and Isotopes* 65.3, pp. 318–327.
- Seo, Y. et al. (2020). "Quantitative and Qualitative Improvement of Low-Count [ $^{68}\text{Ga}$ ] Citrate and [ $^{90}\text{Y}$ ] Microspheres PET Image Reconstructions Using Block Sequential Regularized Expectation Maximization Algorithm". In: *Molecular Imaging and Biology* 22.1, pp. 208–216.
- Sheikhzadeh, P. et al. (2017). "Development and validation of an accurate GATE model for NeuroPET scanner". In: *Physica Medica* 40, pp. 59–65.
- Shepp, L. A. and Y. Vardi (1982). "Maximum Likelihood Reconstruction for Emission Tomography". In: *IEEE Transactions on Medical Imaging* 1.2, pp. 113–122. ISSN: 1558-254X.
- Shibuya, K. et al. (2007). "Limit of spatial resolution in FDG-PET due to annihilation photon non-collinearity". In: *World Congress on Medical Physics and Biomedical Engineering 2006*. Springer, pp. 1667–1671.
- Siman, W. et al. (2019). "Dose volume histogram-based optimization of image reconstruction parameters for quantitative  $^{90}\text{Y}$ -PET imaging". In: *Medical Physics* 46.1, pp. 229–237.
- Sirtex Medical Limited, North Sydney NSW, Australia (2020). *Package insert: SIR-Spheres® Yttrium-90 Resin Microspheres*. URL: <https://www.sirtex.com/eu/clinicians/instructions-for-use/> (visited on 01/18/2021).
- Sluis, J. van et al. (2019). "Performance Characteristics of the Digital Biograph Vision PET/CT System". In: *Journal of Nuclear Medicine* 60.7, pp. 1031–1036.
- Smits, M. L. et al. (2015). "Radioembolization dosimetry: the road ahead". In: *Cardiovascular and interventional radiology* 38.2, pp. 261–269.
- Snyder, D. L. and M. I. Miller (1985). "The use of sieves to stabilize images produced with the EM algorithm for emission tomography". In: *IEEE Transactions on Nuclear Science* 32.5, pp. 3864–3872.
- Snyder, W. S. et al. (1975a). "MIRD pamphlet no. 11: S, absorbed dose per unit cumulated activity for selected radionuclides and organs". In: *New York: Society of Nuclear Medicine*.
- (1975b). *Tabulation of dose equivalent per microcurie-day for source and target organs of an adult for various radionuclides*. Tech. rep. Oak Ridge National Lab., Tenn.(USA).
- Song, Y. S. et al. (2015). "PET/CT-based dosimetry in  $^{90}\text{Y}$ -microsphere selective internal radiation therapy: single cohort comparison with pretreatment planning

- on  $^{99m}\text{Tc}$ -MAA imaging and correlation with treatment efficacy". In: *Medicine* 94.23.
- Soret, M., S. L. Bacharach, and I. Buvat (2007). "Partial-volume effect in PET tumor imaging". In: *Journal of nuclear medicine* 48.6, pp. 932–945.
- Spinelli, A. E. and F. Boschi (2015). "Novel biomedical applications of Cerenkov radiation and radioluminescence imaging". In: *Physica Medica* 31.2, pp. 120–129.
- Stabin, M. G. et al. (1994). "Bremsstrahlung radiation dose in yttrium-90 therapy applications". In: *Journal of Nuclear Medicine* 35.8, pp. 1377–1380.
- Stockhoff, M. et al. (2017). "Advanced optical simulation of scintillation detectors in GATE V8.0: first implementation of a reflectance model based on measured data". In: *Physics in Medicine & Biology* 62.12, p. L1.
- Strother, S., M. Casey, and E. Hoffman (1990). "Measuring PET scanner sensitivity: relating countrates to image signal-to-noise ratios using noise equivalents counts". In: *IEEE Transactions on Nuclear Science* 37.2, pp. 783–788.
- Strydhorst, J. and I. Buvat (2016). "Redesign of the GATE PET coincidence sorter". In: *Physics in Medicine & Biology* 61.18, N522.
- Strydhorst, J. et al. (2016). "A GATE evaluation of the sources of error in quantitative  $^{90}\text{Y}$  PET". In: *Medical Physics* 43.10, pp. 5320–5329.
- Stute, S et al. (2011). "Monte Carlo simulations of clinical PET and SPECT scans: Impact of the input data on the simulated images". In: *Physics in Medicine & Biology* 56.19, p. 6441.
- Surti, S. (2015). "Update on time-of-flight PET imaging". In: *Journal of Nuclear Medicine* 56.1, pp. 98–105.
- Taebi, A., C. T. Vu, and E. Roncali (2021). "Multiscale Computational Fluid Dynamics Modeling for Personalized Liver Cancer Radioembolization Dosimetry". In: *Journal of Biomechanical Engineering* 143.1, p. 011002.
- Taebi, A. et al. (2020). "Computational Modeling of the Liver Arterial Blood Flow for Microsphere Therapy: Effect of Boundary Conditions". In: *Bioengineering* 7.3, p. 64.
- Tafti, B. A. and S. A. Padia (2019). "Dosimetry of Y-90 microspheres utilizing Tc-99m SPECT and Y-90 PET". In: *Seminars in nuclear medicine*. Vol. 49. 3. Elsevier, pp. 211–217.
- Takahashi, M and K Ogawa (1997). "Selection of projection set and the order of calculation in ordered subsets expectation maximization method". In: *1997 IEEE Nuclear Science Symposium Conference Record*. Vol. 2. IEEE, pp. 1408–1412.
- Tang, L. et al. (2020). "Gamma-ray spectra in the positron-annihilation process of molecules at room temperature". In: *Physics Letters A* 384.24, p. 126593.
- Thomas, B. A. et al. (2016). "PETPVC: a toolbox for performing partial volume correction techniques in positron emission tomography". In: *Physics in Medicine & Biology* 61.22, p. 7975.
- Thomas, D. J. (2012). *ICRU report 85: fundamental quantities and units for ionizing radiation*.
- Thompson, C., J Moreno-Cantu, and Y Picard (1992). "PETSIM: Monte Carlo simulation of all sensitivity and resolution parameters of cylindrical positron imaging systems". In: *Physics in Medicine & Biology* 37.3, p. 731.
- Tischoff, I and A Tannapfel (2007). "Hepatocellular carcinoma and cholangiocarcinoma—different prognosis, pathogenesis and therapy". In: *Zentralblatt fur Chirurgie* 132.4, pp. 300–305.
- Townsend, D. W. and M. Defrise (1993). *Image-reconstruction methods in positron tomography*. CERN-93-02. CERN.

- Trindade, A. et al. (2012). "Validation of GATE Monte Carlo simulations of the Philips GEMINI TF and TruFlight Select PET/CT scanners based on NEMA NU2 standards". In: *2012 IEEE Nuclear Science Symposium and Medical Imaging Conference Record (NSS/MIC)*. IEEE, pp. 2546–2549.
- Usman, S. and A. Patil (June 2018). "Radiation detector deadtime and pile up: A review of the status of science". In: *Nuclear Engineering and Technology* 50.
- Uusijärvi, H. et al. (2009). "Comparison of electron dose-point kernels in water generated by the Monte Carlo codes, PENELOPE, GEANT4, MCNPX, and ETRAN". In: *Cancer biotherapy and radiopharmaceuticals* 24.4, pp. 461–467.
- Van Elmbt, L. et al. (2011). "Comparison of Yttrium-90 quantitative imaging by TOF and non-TOF PET in a phantom of liver selective internal radiotherapy". In: *Physics in Medicine & Biology* 56.21, p. 6759.
- Van Sluis, J. et al. (2019). "Performance characteristics of the digital Biograph Vision PET/CT system". In: *Journal of Nuclear Medicine* 60.7, pp. 1031–1036.
- Vandenberghe, S., P. Moskal, and J. S. Karp (2020). "State of the art in total body PET". In: *EJNMMI physics* 7, pp. 1–33.
- Vandendriessche, D. et al. (2019). "Performance characteristics of silicon photomultiplier based 15-cm AFOV TOF PET/CT". In: *EJNMMI Physics* 6.1, p. 8.
- Vanderstraeten, B. et al. (2006). "[18F] fluoro-deoxy-glucose positron emission tomography ([18F] FDG-PET) voxel intensity-based intensity-modulated radiation therapy (IMRT) for head and neck cancer". In: *Radiotherapy and oncology* 79.3, pp. 249–258.
- Vauthey, J.-N. et al. (2002). "Body surface area and body weight predict total liver volume in Western adults". In: *Liver transplantation* 8.3, pp. 233–240.
- Walrand, S. et al. (2011). "Yttrium-90-labeled microsphere tracking during liver selective internal radiotherapy by bremsstrahlung pinhole SPECT: feasibility study and evaluation in an abdominal phantom". In: *EJNMMI Research* 1.1, p. 32.
- Walrand, S. et al. (2014). "The low hepatic toxicity per Gray of  $^{90}\text{Y}$  glass microspheres is linked to their transport in the arterial tree favoring a nonuniform trapping as observed in posttherapy PET imaging". In: *Journal of Nuclear Medicine* 55.1, pp. 135–140.
- Wang, G.-C. et al. (2016). "PET timing performance measurement method using NEMA NEC phantom". In: *IEEE Transactions on Nuclear Science* 63.3, pp. 1335–1342.
- Wang, W et al. (2006). "Systematic and distributed time-of-flight list mode PET reconstruction". In: *2006 IEEE Nuclear Science Symposium Conference Record*. Vol. 3. IEEE, pp. 1715–1722.
- Wang, W., Z. Hu, and D. Gagnon (2007). "A new component approach to efficiency normalization for 3D PET". In: *IEEE Transactions on Nuclear Science* 54.1, pp. 92–99.
- Wei, L. et al. (2020). "Tumor Response Prediction in  $^{90}\text{Y}$  Radioembolization with PET-based Radiomics Features and Absorbed Dose Metrics". In: *EJNMMI Physics* 7.1.
- Werner, M. K. et al. (2010). "PET/CT for the assessment and quantification of  $^{90}\text{Y}$  biodistribution after selective internal radiotherapy (SIRT) of liver metastases". In: *European Journal of Nuclear Medicine and Molecular Imaging* 37.2, pp. 407–408.
- Wernick, M. N. and J. N. Aarsvold (2004). *Emission tomography: the fundamentals of PET and SPECT*. Elsevier.
- Wieczorek, A. (2017). "Development of novel plastic scintillators based on polyvinyltoluene for the hybrid J-PET/MR tomograph". In: *arXiv preprint arXiv:1710.08136*.

- Willowson, K. et al. (2012). "Quantitative  $^{90}\text{Y}$  image reconstruction in PET". In: *Medical Physics* 39.11, pp. 7153–7159.
- Willowson, K. P., M. Tapner, D. L. Bailey, et al. (2015). "A multicentre comparison of quantitative  $^{90}\text{Y}$  PET/CT for dosimetric purposes after radioembolization with resin microspheres". In: *European Journal of Nuclear Medicine and Molecular Imaging* 42.8, pp. 1202–1222.
- Wondergem, M. et al. (2013). " $^{99\text{m}}\text{Tc}$ -macroaggregated albumin poorly predicts the intrahepatic distribution of  $^{90}\text{Y}$  resin microspheres in hepatic radioembolization". In: *Journal of Nuclear Medicine* 54.8, pp. 1294–1301.
- Wright, C. et al. (2018). "Yttrium-90 imaging with Digital Photon Counting PET/CT: An intra-individual comparison with conventional photomultiplier tube-based PET/CT following radioembolization". In: *Journal of Nuclear Medicine* 59.supplement 1, pp. 600–600.
- Wright, C. L. et al. (2015). "Theranostic imaging of Yttrium-90". In: *BioMed research international* 2015.
- Wright, C. L. et al. (2016). " $^{90}\text{Y}$  Digital PET/CT Imaging Following Radioembolization". In: *Clinical Nuclear Medicine* 41.12, pp. 975–976.
- Wright, C. L. et al. (May 2017a). "Advanced functional tumor imaging and precision nuclear medicine enabled by digital PET technologies". In: *Contrast Media & Molecular Imaging* 2017, pp. 1–7.
- Wright, C. L. et al. (2017b). "Clinical feasibility of  $^{90}\text{Y}$  digital PET/CT for imaging microsphere biodistribution following radioembolization". In: *European Journal of Nuclear Medicine and Molecular Imaging* 44.7, pp. 1194–1197.
- Xiang, H. et al. (2020). "A deep neural network for fast and accurate scatter estimation in quantitative SPECT/CT under challenging scatter conditions". In: *European journal of nuclear medicine and molecular imaging* 47.13, p. 2956.
- Ye, J., X. Song, and Z. Hu (2014). "Scatter correction with combined single-scatter simulation and Monte Carlo simulation for 3D PET". In: *2014 IEEE Nuclear Science Symposium and Medical Imaging Conference (NSS/MIC)*, pp. 1–3.
- Zaidi, H. and C. Morel (1999). "Eidolon: A Monte Carlo Simulator for Multi-ring 3D PET Scanners". In: *PARAPET, Geneva University Hospital Division of Nuclear Medicine, Switzerland*.
- Zatcepin, A. et al. (2020). "Improving depth-of-interaction resolution in pixellated PET detectors using neural networks". In: *Physics in Medicine & Biology* 65.17, p. 175017.
- Zhang, J., P. Maniawski, and M. V. Knopp (2018). "Performance evaluation of the next generation solid-state digital photon counting PET/CT system". In: *EJN-MMI Research* 8.1, p. 97.
- Zhang, X. et al. (2017). "Quantitative image reconstruction for total-body PET imaging using the 2-meter long EXPLORER scanner". In: *Physics in Medicine & Biology* 62.6, p. 2465.



## FOLIO ADMINISTRATIF

### THESE DE L'UNIVERSITE DE LYON OPEREE AU SEIN DE L'INSA LYON

NOM : LABOUR

DATE de SOUTENANCE : 21 septembre 2021

Prénoms : Joey

TITRE : Yttrium-90 quantification using Digital Photon Counting PET and Monte Carlo simulations for radioembolisation monitoring

NATURE : Doctorat

Numéro d'ordre : 2021LYSEI054

Ecole doctorale : Électronique, Électrotechnique, Automatique

Spécialité : Traitement du Signal et de l'Image

RESUME : La tomographie par émission de positrons (TEP) est aujourd'hui la modalité d'imagerie fonctionnelle la plus sensible pour étudier les interactions moléculaires dans le corps humain. L'avènement de la technologie des photomultiplicateurs au silicium (SiPM) a apporté des avantages supplémentaires à la résolution du temps-de-vol (TOF), améliorant le rapport signal sur bruit (SNR) et donc la qualité de l'image, remplaçant au cours des dernières années les tubes photomultiplicateurs conventionnels (PMT) pour l'imagerie TEP. La TEP combinée à la tomodensitométrie (TDM) est une méthode établie et recommandée pour le suivi post-traitement de la radiothérapie interne sélective (SIRT) utilisant  $^{90}\text{Y}$ . La SIRT  $^{90}\text{Y}$  est régulièrement pratiquée au Centre Léon Bérard mais aucune évaluation de la dose absorbée n'est effectuée, même si l'imagerie TEP/TDM est systématiquement réalisée après le traitement. Le succès technique du traitement est uniquement évalué par la distribution visuelle de la radioactivité à l'aide des images TEP. Cette thèse s'inscrit dans le cadre (1) du suivi d'un traitement SIRT avec des microsphères d' $^{90}\text{Y}$  à l'aide du système TEP Vereos, qui est équipé de SiPMs à comptage numérique de photons (DPC) et (2) de la simulation Monte Carlo de ce même système TEP afin de fournir un modèle validé pour les simulations. En effet, les performances des systèmes TEP actuels permettent l'imagerie de  $^{90}\text{Y}$ , même si l'isotope est un émetteur bêta pur (c'est-à-dire émettant 100 % d'électrons), mais  $^{90}\text{Y}$  présente un faible rapport de branchement positronique mesuré à  $32 \times 10^{-6}$  (par opposition à  $97 \times 10^{-2}$  pour le  $^{18}\text{F}$ ). Le travail au cours de cette thèse a mis l'accent sur la simulation du Vereos dans GATE afin de le rendre disponible à la communauté scientifique à des fins de recherche concernant  $^{90}\text{Y}$  ou tout autre aspect. Ensuite, il s'est concentré sur l'évaluation des conditions d'imagerie, concernant les paramètres de reconstruction et la durée d'acquisition en utilisant  $^{90}\text{Y}$  pour plus de précision dans les calculs de dose absorbée et en utilisant les simulations Monte Carlo comme référence. Les résultats ont été vérifiés sur des fantômes mais également appliqués aux images de patients. Une comparaison dosimétrique entre l'imagerie prédite au  $^{99\text{mTc}}\text{-MAA}$  et l'imagerie post-traitement à  $^{90}\text{Y}$  a été effectuée. Les chapitres 1 à 3 du manuscrit présentent un état de l'art du SIRT et de la TEP. Les chapitres 4 à 6 décrivent les contributions apportées au cours de cette thèse.

MOTS-CLÉS : Tomographie par émission de positrons, radioembolisation, simulations monte carlo, médecine nucléaire, yttrium-90, dosimétrie

Laboratoire (s) de recherche : CREATIS

Directeur de thèse : David Sarrut

Président de jury : Christian Morel

Composition du jury : Christian Morel (Président), Etienne Garin (Rapporteur), Yuni Dewaraja (Rapporteuse), Emilie Roncali (Examinatrice), Arnaud Dieudonné (Examinateur), David Sarrut (Directeur de thèse), Jean-Noël Badel (co-Directeur de thèse)